Antenna Handbook

THEORY, APPLICATIONS, AND DESIGN

Edited by
Y. T. Lo
Electromagnetics Laboratory
Department of Electrical and Computer Engineering
University of Illinois–Urbana

S. W. Lee
Electromagnetics Laboratory
Department of Electrical and Computer Engineering
University of Illinois–Urbana

Contents

Chapter 11

Array Theory

Y. T. Lo
University of Illinois

CONTENTS

Yuen T. Lo is a professor and the director of the Electromagnetics Laboratory (formerly the Antenna Laboratory) in the Electrical and Computer Engineering Department, University of Illinois at Urbana-Champaign. He is a member of the National Academy of Engineering, a Fellow of IEEE, and a member of the International Union of Radio Science. He received the 1964 IEEE AP-S Bolljahn Memorial Award, and the 1964 IEEE AP-S Best Paper Award, the 1979 IEEE AP-S Best Paper Award, the IEEE Centennial Medal, and the Halliburton Education Leadership award. He served as an AP-S AdCom member, the Chairman of the AP-S Education and Tutorial Papers Committee, and twice (1979–1982 and 1984–1987) as the IEEE AP-S National Distinguished Lecturer. Dr. Lo is an honorary professor of the Northwest Telecommunication Engineering Institute and also the Northwestern Polytechnical University, both at Xian, China. He has published over 100 technical articles in refereed journals covering a wide spectrum, from theoretical to experimental works. His works include large-antenna arrays, radiotelescopes, multiple-beam antennas, multiple scattering, antenna synthesis, antijamming antennas, antenna in plasmas, corrugated guides and horns, artificial dielectrics, and microstrip antennas. He designed the University of Illinois Radiotelescope, considered to be the world's largest antenna, in the early 1960s.

11-2

1. Introduction

fascis controllable

Single-element antennas are discussed in other chapters in the book but their performance is somewhat limited. To obtain high directivity, narrow beams, low side lobes, <u>steerable beams</u>, particular pattern characteristics, etc., commonly a group of antenna elements, called an *antenna array*, or simply *array*, is used. The design of an array involves mainly first the selection of elements and array geometry, and then the determination of the element excitations required for achieving a particular performance, sometimes under a given constraint. The realization of the desired excitation requires a detailed knowledge of element input impedance characteristics as well as the mutual impedance between any two elements in the given array environment. In general, this is a difficult problem which may be solved approximately for large arrays with an infinite array model and for small arrays in a two-element environment model. While discussions on these models for some simple elements can be found elsewhere in the book, in this chapter we confine our discussion to the problems stated above.

There is no reason why all elements in an array must be of the same type other than simplicity in fabrication and analysis. In fact, radioastronomers have made use of two or more existing radiotelescopes of different types for interferometry measurement. Furthermore, even with the same type of elements, the shape of current or aperture field distribution of the element near the edge of the array can be different from that of the element in the central portion of the array, depending on the array geometry, element spacing and orientation, and, of course, the element type. Generally such a difference may not cause a serious deterioration in the array performance in some applications.

There is also no particular reason why the array structure must be periodic other than the two reasons just stated above. In fact, a periodic structure can result in grating lobes, frequency sensitivity, blind angles, etc. Even a periodic structure of scatterers, such as those used in artificial dielectrics, possesses some interesting but undesirable properties, such as birefringence, anisotropy, and dispersion. For analytic simplicity, however, uniformly spaced arrays, particularly the linear ones, have been studied in a great detail [1–120]. At least for these arrays the performance can be predicted accurately. Therefore we shall consider uniformly spaced linear arrays first. With some understanding of linear arrays, for convenience in later discussions, we then consider a general transformation theory and its application to planar, circular, and elliptical arrays. Finally, a few array synthesis problems are discussed.

2. General Formulation

For radiation characteristics, only the far field is of interest. In all the following discussions the use of the far-field approximation will be understood. Let $A(r)$ be

the magnetic vector potential due to a typical element. Then

$$\mathbf{A}(\mathbf{r}) \cong \frac{\mu}{\pi} \frac{e^{-jkr}}{r} \int_V \mathbf{J}(\mathbf{r}') e^{jkr' \cos \xi} dV'$$

(1)

where

$\mathbf{J}(\mathbf{r}') = $ the electrical current distribution in the element

$\mathbf{r} = $ the position vector of an observation point

$\mathbf{r}' = $ the position vector of a typical source point

$V = $ the volume of the source element

$dV' = $ a differential volume element of the source

$\cos \xi = \hat{\mathbf{r}} \cdot \hat{\mathbf{r}}'$

$k = \omega \sqrt{\mu \epsilon} = 2\pi/\lambda = $ free-space wave number

The important consequence of the far-field approximation is that the dependence of $\mathbf{A}(\mathbf{r})$ on $\mathbf{r}$ is separated into two parts: one depending on r only and the other on (θ, ϕ) through $\hat{\mathbf{r}}$ (or $\cos \xi$ in the integral). Thus, for a sphere with fixed r, we can write the factor $(jkr' \cos \xi)$ as $(j\mathbf{k} \cdot \mathbf{r}')$ and $\mathbf{A}(\mathbf{r})$ as $\mathbf{A}(\mathbf{k})$ with $\mathbf{k} = k\hat{\mathbf{r}}$, the direction in which $\mathbf{A}$ is to be evaluated. In practice, only the directional characteristic is of main interest; therefore, we shall focus our attention on the integral and rewrite (1) in the following form:

$$\mathbf{K} = \mathbf{K} \hat{\mathbf{r}}$$

$$\mathbf{A}(\mathbf{r}) = \hat{\mathbf{r}}A_r + \hat{\boldsymbol{\theta}}A_\theta + \hat{\boldsymbol{\phi}}A_\phi \cong \frac{\mu e^{-jkr}}{4\pi r} [\hat{\mathbf{r}}f_r(\hat{\mathbf{k}}) + \hat{\boldsymbol{\theta}}f_\theta(\hat{\mathbf{k}}) + \hat{\boldsymbol{\phi}}f_\phi(\hat{\mathbf{k}})]$$

(2a)

where

$$\left.\begin{array}{c} f_\theta(\theta, \phi) \\ f_\phi(\theta, \phi) \end{array}\right\} = \left\{\begin{array}{c} f_\theta(\hat{\mathbf{k}}) \\ f_\phi(\hat{\mathbf{k}}) \end{array}\right\} = \left\{\begin{array}{c} \hat{\boldsymbol{\theta}} \\ \hat{\boldsymbol{\phi}} \end{array}\right\} \cdot \int \mathbf{J}(\mathbf{r}') e^{j\mathbf{k} \cdot \mathbf{r}'} dV'$$

(2b)

Then the far fields are

$$\mathbf{E}(\mathbf{r}) = -j\omega \mathbf{A} + \frac{1}{j\omega\epsilon}\nabla\nabla\cdot\mathbf{A} \cong -j\omega[\hat{\boldsymbol{\theta}}\hat{\boldsymbol{\theta}} + \hat{\boldsymbol{\phi}}\hat{\boldsymbol{\phi}}]\cdot\mathbf{A}$$

$$\mathbf{H}(\mathbf{r}) \cong \frac{1}{\eta}\hat{\mathbf{r}} \times \mathbf{E}$$

(3)

where $\eta = \sqrt{\mu/\epsilon}$.

The angular-dependent parts $f_\theta(\theta, \phi)$ and $f_\phi(\theta, \phi)$ give the directional characteristics of E_θ and E_ϕ. It should be noted that f_θ and f_ϕ are complex functions. Their absolute values, or magnitudes, $|f_\theta(\theta, \phi)|$ and $|f_\phi(\theta, \phi)|$, are

generally referred to as the *pattern functions*; in fact, often one of them is termed the major component (or copolarization) pattern function and the other the cross-polarization pattern function. Their phases, namely $\angle f_\theta(\theta,\phi)$ and $\angle f_\phi(\theta,\phi)$, are referred to as the *phase pattern functions*. Obviously the significance of a phase pattern function should be weighted by its associated pattern function $|f(\theta,\phi)|$. The phase pattern is of interest in some applications, such as the determination of the phase center. Sometimes one is also interested in evaluating the patterns in terms of circularly, instead of linearly, polarized components. In that case

$$\mathbf{E}(\hat{r}) \propto \hat{\mathbf{L}} f_L(\theta,\phi) + \hat{\mathbf{R}} f_R(\theta,\phi) \tag{4}$$

where

$$\hat{L} = \frac{\hat{\theta} + j\hat{\phi}}{\sqrt{2}}$$

$$f_L(\theta,\phi) = f_\theta(\theta,\phi) - jf_\phi(\theta,\phi) = \text{LCP pattern}$$
$$f_R(\theta,\phi) = f_\theta(\theta,\phi) + jf_\phi(\theta,\phi) = \text{RCP pattern} \qquad \hat{R} = \frac{\hat{\theta} - j\hat{\phi}}{\sqrt{2}} \tag{5}$$

Finally, it may also be noted that, in practice, for simplicity, $f(\theta,\phi)$ is often called the pattern function, rather than the precise term *complex* pattern function.

For an array of N arbitrary elements, as shown in Fig. 1, the far field is

$$\mathbf{E}(\mathbf{r}) \cong \frac{-j\omega\mu e^{-jkr}}{4\pi r}\mathbf{f}(\theta,\phi) \quad = -j\,\frac{K^2}{4\pi}\,\frac{e^{-jkr}}{r}\,f(\theta,\phi) \tag{6}$$

where

$$\mathbf{f}(\theta,\phi) = \sum_{n=1}^{N} \mathbf{f}_n(\theta,\phi)$$

$$\mathbf{f}_n(\theta,\phi) = (\hat{\theta}\hat{\theta} + \hat{\phi}\hat{\phi})\int_{\substack{n\text{th}\\ \text{element}}} \mathbf{J}_n(\mathbf{r}'_n)\, e^{jk\hat{r}\cdot(\mathbf{r}'-\mathbf{r}_n)}\, dV'_n \tag{7}$$
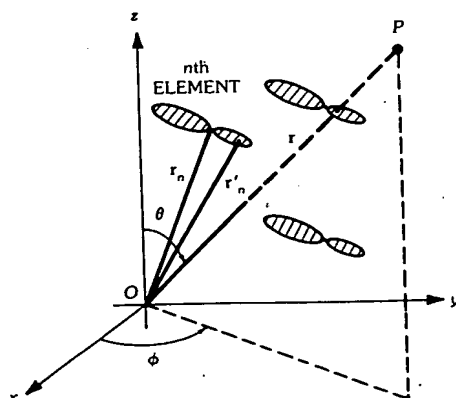
Fig. 1. Geometry of an array with identical elements.

$\mathbf{r}_n$ = a convenient reference point, such as the phase center, of the nth element

$\mathbf{r}'_n$ = a typical point on the nth element

$\mathbf{f}_n(\theta, \phi)$ = the nth-element pattern function

If all elements are identical and also identically oriented, with the assumption that the current distribution of all elements in the array have identical shape except for a constant multiplier, one can write

$$\mathbf{f}_n(\theta, \phi) = I_n \mathbf{f}_0(\theta, \phi) \tag{8}$$

where

$\mathbf{f}_0(\theta, \phi)$ = complex pattern function of a single element

I_n = relative complex excitation to the nth element

It should be noted again that element patterns in different array environments could be significantly different from each other (see Chapters 13 and 14). For large arrays or arrays with simple elements the neglect of this difference may still lead to a useful approximation. Then, using (8), one can rewrite (6) as follows:

$$\mathbf{E}(\mathbf{r}) \cong -\frac{j\omega\mu e^{-jkr}}{4\pi r} \mathbf{f}_0(\theta, \phi) F(\theta, \phi) \tag{9}$$

where

$$F(\theta, \phi) = \sum_n I_n e^{jk\hat{\mathbf{r}}\cdot\mathbf{r}_n} \tag{10}$$

is usually called the (complex) array factor, or the array pattern function for N isotropic point sources at $\{\mathbf{r}_n\}$. Equation 9 also states the *pattern multiplication principle*, namely, that the array pattern for N identical elements, similarly oriented, is equal to the product of the element pattern and the array factor (or the array pattern for isotropic sources). The study of an array usually implies the study of the array factor, which is often called simply the *array pattern function*. In the following we shall devote most of our discussions to this function.

3. Linear Arrays

Linear arrays occupy a unique position in array theory and have received great attention. This is probably because for uniformly spaced elements the pattern function can simply be expressed in terms of a polynomial for which the analytic tool is well-known. Let the elements be placed along the z axis with interelement spacing d; then for the nth element $\mathbf{r}_n = \hat{z}nd$ and for an array of $(N + 1)$ elements

$$F(\theta) = \sum_{n=0}^{N} I_n e^{jknd\cos\theta} = \sum_{n=0}^{N} I_n Z^n \qquad (11)$$

where

$$Z = e^{j\psi} \quad \text{and} \quad \psi = kd\cos\theta \qquad (12)$$
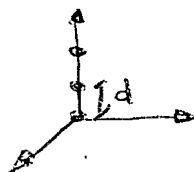
For the physically observable region $0 \leq \theta \leq \pi$, the function $F(\theta)$ is given by the value of the polynomial in (11) with Z only on a unit circle and its phase angle ψ bounded between $-kd$ and $+kd$, which is called the *visible region*. Polynomials have been thoroughly studied and it is therefore not surprising to find a large number of contributions in the literature on linear arrays. A few important results are summarized below.

Arrays with Prescribed Nulls

These are useful for antijamming and interference elimination. Let $\{\theta_n\}$, $n = 1, 2, \ldots, N$, be the set of null angles. Then the desired array pattern function is

$$F(\theta) = c\prod_{n=1}^{N} (Z - Z_n) = c[I_0 + I_1 Z + \cdots + I_N Z^N] \qquad (13)$$

where c = a constant, commonly a normalization factor such that

$$\max|F(\theta)| = 1,$$
$$Z_n = e^{j\psi_n},$$
$$\psi_n = kd\cos\theta_n,$$
$$I_n = \text{the required complex excitation for the } n\text{th element}$$

Comments:

(a) The magnitude pattern is

$$|c|\prod_{n=1}^{N} |Z - Z_n| = 20\left(\log|c| + \sum_{n=1}^{N} \log|Z - Z_n|\right)$$

in decibels, where $|Z - Z_n|$ is the length between a typical point $Z(\theta)$ on the unit circle and Z_n, which is also on the circle as shown in Fig. 2.

(b) Excitations are given by the coefficients of the polynomial expansion as in (13).

(c) Because of the axial symmetry the 3D pattern is the generation of the above pattern function rotated about the array axis.

(d) To obtain a deep null at, say, θ_n, multiplicity of the root Z_n can be imposed. In fact, $(Z - Z_n)^p$, with p an integer, implies that all derivatives up to the $(p - 1)$th order vanish at $Z = Z_n$.

(e) These excitations are determined only by the desired null directions without
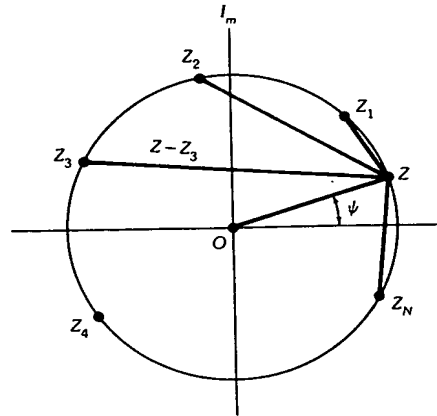
Fig. 2. Zeros of an array polynomial on a unit circle.

considering the desired signal. For a more meaningful solution see Section 6, where signal-to-interference ratio is to be maximized.

(*f*) Since each element can be a subarray, the element could be designed against the jamming signals while the entire array is designed for receiving the desired signal, or vice versa, provided the desired signal is in a direction different from that of any of the jamming signals.

(*g*) Null steering can be achieved by varying Z_n on a unit circle, but in general this change will alter excitations of many elements.

(*h*) Of course, some roots $\{Z_n\}$ need not be on the unit circle nor in the visible region. In that case the array will not have deep nulls at $\{\theta_n\}$.

Binomial Arrays

If all roots $\{Z_n\}$ coincide and are equal to Z_1, then

$$F(\theta) = c(Z - Z_1)^N$$

$$= c[Z^N + N(-Z_1)Z^{N-1} + \frac{N(N-1)}{2}(-Z_1)^2 Z^{N-2}$$

$$+ \cdots + C_k^N(-Z_1)^k Z^{N-k} + \cdots + (-Z_1)^N] \tag{14}$$

where

$Z_1 = e^{jkd\cos\theta_1}$

$\theta_1 =$ null angle

$C_k^N =$ binomial coefficient, which can be found more easily by using the Pascal triangle

Thus $I_1 = 1$, $I_2 = NZ_1$, $\ldots$, $I_k = C_k^N(-Z_1)^k$, $\ldots$, $I_N = (-Z_1)^N$.

Comments:

(a) The magnitude pattern indecibels is

$$|c|\,|Z - Z_1|^N = 20(\log|c| + N\log|Z - Z_1|)$$

(b) This array has no "side lobes" if $d \leqq \lambda/2$. For example, if $d = \lambda/2$ and $\theta_1 = 0$, then $Z_1 = -1$ and all element excitations are in phase with weight $\{C_k^N\}$. The pattern has only a broadside beam, irrespective of the array length. If $\theta_1 = \pi/2$, $Z_1 = 1$, all element excitations will be alternatively opposite in phase. The pattern will consist of two separate beams along $\theta = 0$ and $\theta = \pi$, respectively, and a null at $\theta = \pi/2$. Again there are no other lobes, no matter how long the array is. If d is near or larger than λ, grating lobes appear partially or totally.

Uniform Arrays

When all excitations are equal, say 1,

$$F(\theta) = \sum_{n=0}^{N-1} Z^n = \frac{Z^N - 1}{Z - 1} \tag{15}$$

If the array center is chosen as the origin,

$$F(\theta) = \frac{\sin(N\psi/2)}{\sin(\psi/2)} \tag{16}$$

where

$$\psi = kd\cos\theta \tag{17}$$

The normalized pattern function of (16) as a function of ψ for a few values of N is shown in Fig. 3. The graphical method for determining $F(\theta)$ through (17) is demonstrated in Fig. 4 for two cases: broadside and scan angle θ_0.

Comments:

(a) As will be seen in Section 6 the uniform array for d nearly equal to or greater than $\lambda/2$ has a directivity close to maximum. For $d < \lambda/2$, a substantial increase in directivity over that of the uniform excitation is only possible in theory but not in practice. Thus the directivity of a uniformly excited array is about the maximum achievable in practice and therefore is often used as a reference for comparing directivities of various designs.

(b) The beam maximum of (16) appears at $\theta = \pi/2$ and, therefore, the array is called a *broadside array*. The beam can be steered to any direction θ_0 if the excitation I_n contains a progress phase factor $nkd\cos\theta_0$, for all ns, as will be seen in a general discussion in Section 4, under "Application to Planar Periodic Arrays." This phase shift results in a translation of ψ by $kd\cos\theta_0$. Thus, instead of (17),

$$\psi = kd(\cos\theta - \cos\theta_0) \tag{18}$$
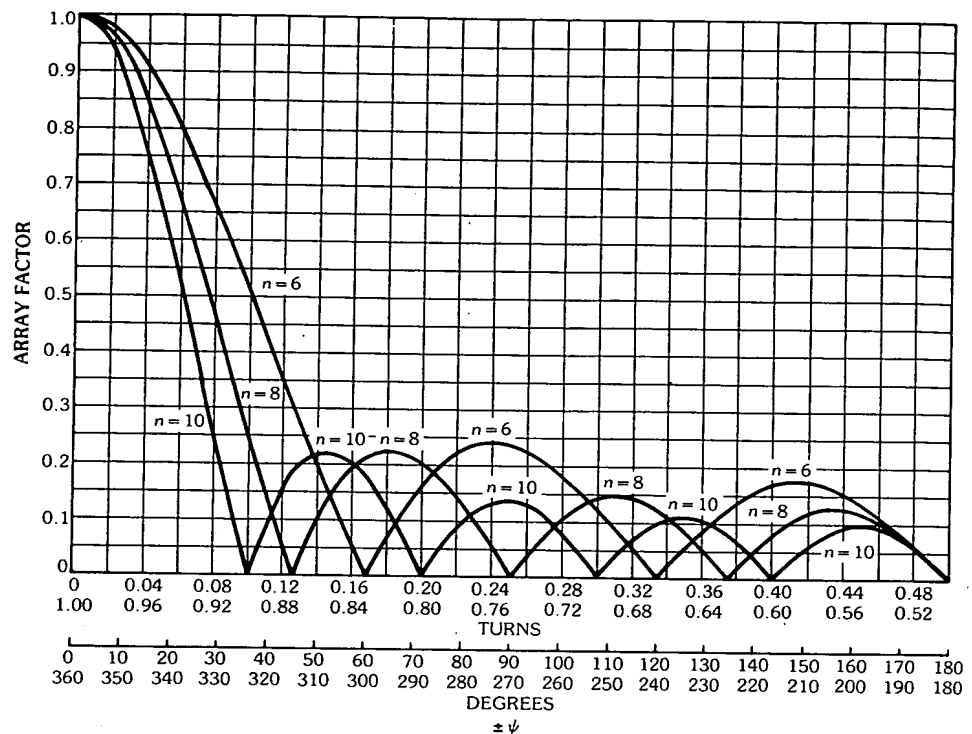
Fig. 3. Plots of $\sin(N\psi/2)/\sin(\psi/2)$ vs ψ for $N = 6$ through 11. (*After Kraus [60]*, © *1950; reprinted with permission of McGraw-Hill Book Co.*)

In other words, what happened at $\theta = \pi/2$ before introducing the phase shift will happen afterwards at $\theta = \theta_0$. The pattern function does not change with respect to ψ except for a simple translation. But this is not true when plotted against θ due to the nonlinear functional dependence of ψ on θ. Therefore it is often more convenient to study the pattern as a function of ψ, or the so-called u space in Section 4. When $\theta_0 = 0°$, the main beam will be along the array axis and the array will be called end-fire.

(c) A few important formulas, such as directivity D, half-power beamwidth, beamwidth between first nulls, null angular position, and side lobe maximum position, for broadside and end-fire uniform arrays are listed in Table 1.

(d) Also listed in Table 1 are the formulas for Hansen-Woodyard end-fire arrays. Hansen and Woodyard [50] found that for a long uniform end-fire array when element spacing is small the directivity in the $\theta = 0°$ direction can be increased from that of the ordinary end-fire if the phase shift per element is [4]

$$\beta = -\left(kd + \frac{2.94}{N}\right) \cong -\left(kd + \frac{\pi}{N}\right) \tag{19}$$

and if
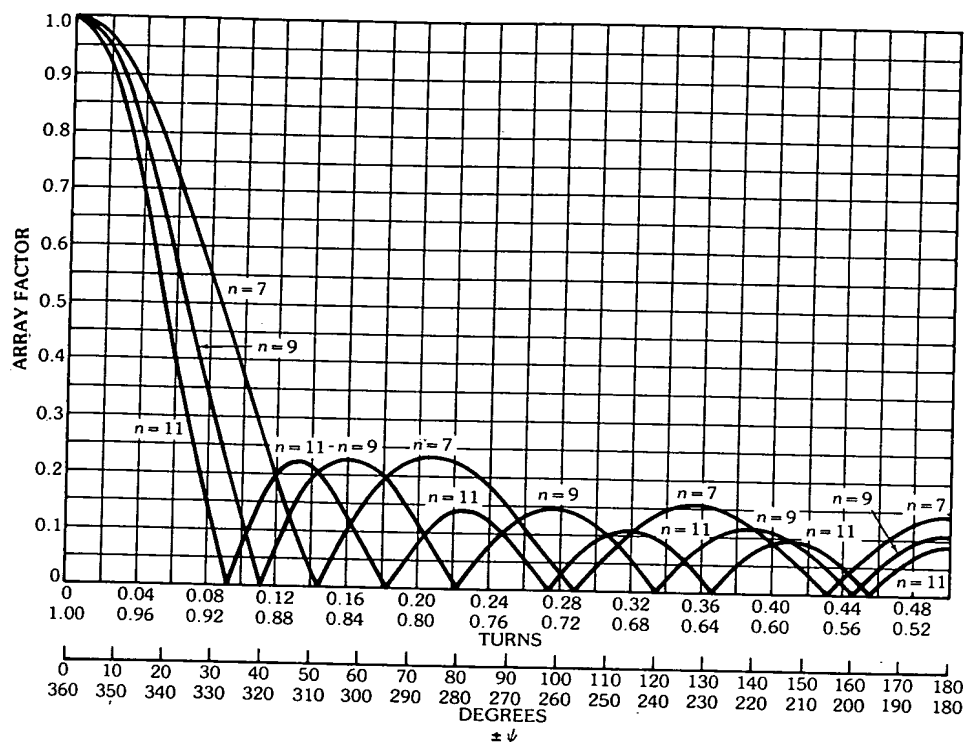
Fig. 3, *continued.*

$$|\psi| = |kd\cos\theta + \beta|_{\theta=0°} \cong \pi/N$$

$$|\psi| = |kd\cos\theta + \beta|_{\theta=180°} \cong \pi \tag{20}$$

It will be seen in Section 6 that this excitation does not give the maximum directivity and, in fact, for $d \cong \lambda/2$ or larger, its directivity is even smaller than that of the ordinary end-fire.

Dolph-Chebyshev Arrays

It is well known that the antenna aperture distribution and pattern function (in the wave vector **k** space, or the *u* space) are a Fourier transform pair. Since for any practical antenna the aperture function must vanish outside a finite region, its Fourier transform, namely the pattern function, is analytic. An analytic function which is zero (or constant) over a finite region must vanish (or be constant) everywhere. This result, if translated into antenna language, implies that any physically realizable antenna pattern must either have a broad beam covering the entire visible region, or have side lobes. From the Parseval's theorem the L_2 norm of the pattern function must be finite. Thus if one side lobe is pushed down, somewhere else the pattern function must go up. Therefore a meaningful optimum
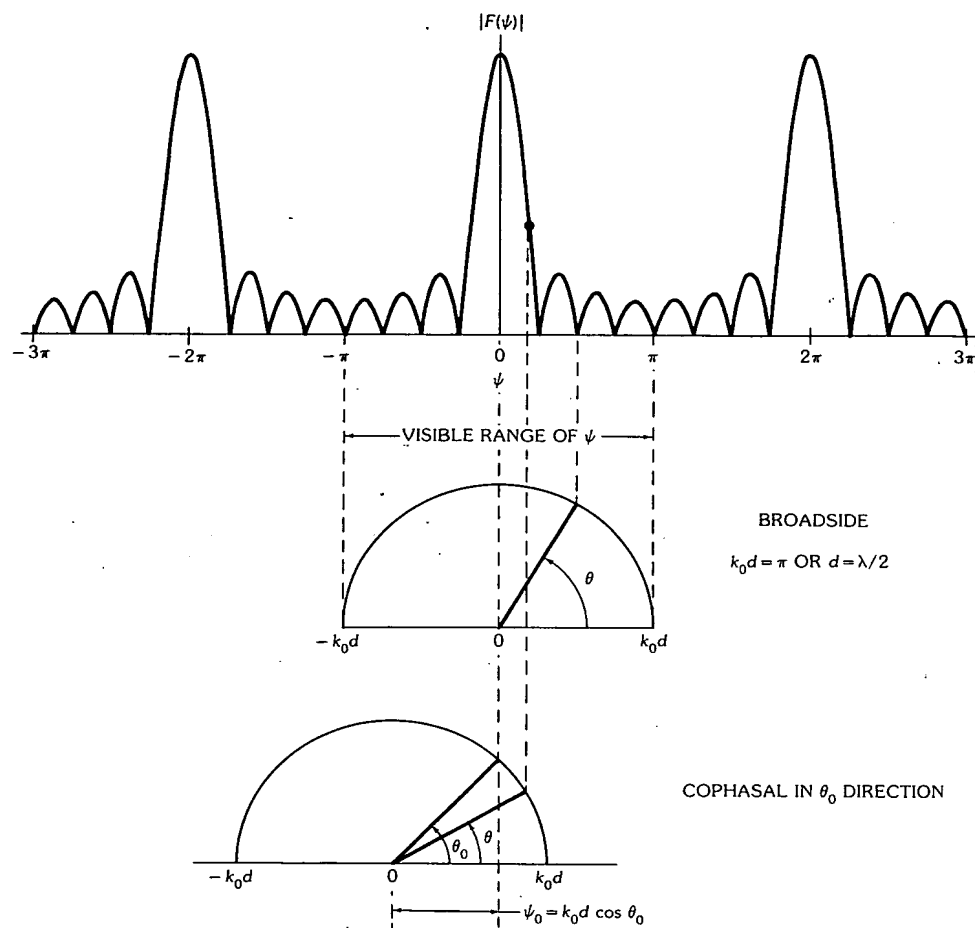
Fig. 4. Graphical method of constructing the radiation pattern from a universal pattern for a uniformly excited broadside array and a uniformly excited cophasal array with the beam in the θ_0 direction.

design would be one in which no one side lobe has a level higher than any others, i.e., equal side lobe levels. For an aperture antenna this is impossible because of the finite L_2 norm of the pattern function for $|u| < \infty$, and the pattern function must approach zero as $|u|$ approaches infinity. Thus the best design one can hope for will be one in which only a *finite* number of side lobes are of equal level. Taylor [100] has provided a solution to this problem which is discussed in Chapter 4.

Since a discrete array can be considered as an aperture antenna sampled at a discrete set of points, all previously stated results are generally applicable. However, when all elements are uniformly spaced, the pattern function becomes periodic (see Chapters 13 and 14). In this case the L_2 norm can be defined over a period, and the Parseval's theorem becomes the well-known power relation. It is thus possible to realize a design of a pattern function with a finite L_2 norm and all

Table 1. Approximate Formulas for a Few Linear Arrays

	Uniform Broadside	Uniform End-fire	Hansen-Woodyard End-fire
Directivity $\cong$ ($Nd \gg \lambda$)	$2N(d/\lambda)$	$4N(d/\lambda)$	$1.79 \times [4N(d/\lambda)]$
Half-power beamwidth $\cong$ ($\pi d/\lambda \ll 1$)	$2\left[\dfrac{\pi}{2} - \cos^{-1}\left(\dfrac{1.391\lambda}{\pi Nd}\right)\right]$	$2\cos^{-1}\left(1 - \dfrac{1.391\lambda}{\pi Nd}\right)$	$2\cos^{-1}\left(1 - 0.1398\dfrac{\lambda}{Nd}\right)$
Beamwidth between nulls	$2\left[\dfrac{\pi}{2} - \cos^{-1}\left(\dfrac{\lambda}{Nd}\right)\right]$	$2\cos^{-1}\left(1 - \dfrac{\lambda}{Nd}\right)$	$2\cos^{-1}\left(1 - \dfrac{\lambda}{2Nd}\right)$
Null angular position $n = 1, 2, \ldots$ $n \neq N, 2N, \ldots$	$\cos^{-1}\left(\pm\dfrac{n}{N}\dfrac{\lambda}{d}\right)$	$\cos^{-1}\left(1 - \dfrac{n\lambda}{Nd}\right)$	$\cos^{-1}\left[1 + (1 - 2n)\dfrac{\lambda}{2Nd}\right]$
Side lobe maximum position $\cong$ ($\pi d/\lambda \ll 1$) ($s = 1, 2, \ldots$)	$\cos^{-1}\left[\pm\dfrac{(2s + 1)\lambda}{2Nd}\right]$	$\cos^{-1}\left[1 - \dfrac{(2s + 1)\lambda}{2Nd}\right]$	$\cos^{-1}\left(1 - \dfrac{s\lambda}{Nd}\right)$

(After Balanis [4], © 1982 Harper & Row, Publishers, Inc.; reprinted by permission of the publisher)

side lobes in one period of equal level. This is achieved by Dolph [22] by making use of the Chebyshev polynomials.

(*a*) For the Dolph-Chebyshev array first consider the Chebyshev polynomials. They can be expressed in either of two equivalent forms, the use of which depends on a particular consideration. For the *m*th degree, they are

$$T_m(x) = \begin{cases} \cos(m\alpha) = \cos(m\cos^{-1}x), & |x| \leqq 1 \\ \cosh(m\alpha) = \cosh(m\cosh^{-1}x), & |x| \geqq 1 \end{cases} \tag{21}$$

or

$$\begin{aligned} T_m(x) &= \text{Re}\{e^{jm\alpha}\} = \text{Re}\{(\cos\alpha + j\sin\alpha)^m\} \\ &= \cos^m\alpha - \binom{m}{2}(\cos^{m-2}\alpha)(\sin^2\alpha) + \cdots \\ &\quad + (-1)^n\binom{m}{2n}(\cos^{m-2n}\alpha)(\sin^{2n}\alpha) + \cdots + \text{Re}\{(j)^m\sin^m\alpha\} \\ &= x^m - \binom{m}{2}x^{m-2}(1 - x^2) + \cdots + \text{Re}\{(j)^m(1 - x^2)^{m/2}\} \\ &= A_m \prod_{p=1}^{m}(x - x_p) \end{aligned} \tag{22}$$

where

$$x = \cos \alpha \tag{23}$$

$$x_p = \cos \alpha_p = \cos\left(\frac{2p - 1}{2m} \pi\right) = p\text{th root, with } p = 1, 2, \ldots, m \tag{24}$$

$$\binom{m}{2n} = \frac{m!}{(2n)!(m - 2n)!} = \text{binomial coefficient} \tag{25}$$

$$A_0 = A_1 = 1$$
$$A_m = 2A_{m-1}, \qquad m \geqq 2 \tag{26}$$

A few of these polynomials are sketched in Fig. 5. Note that $T_m(x)$ is a
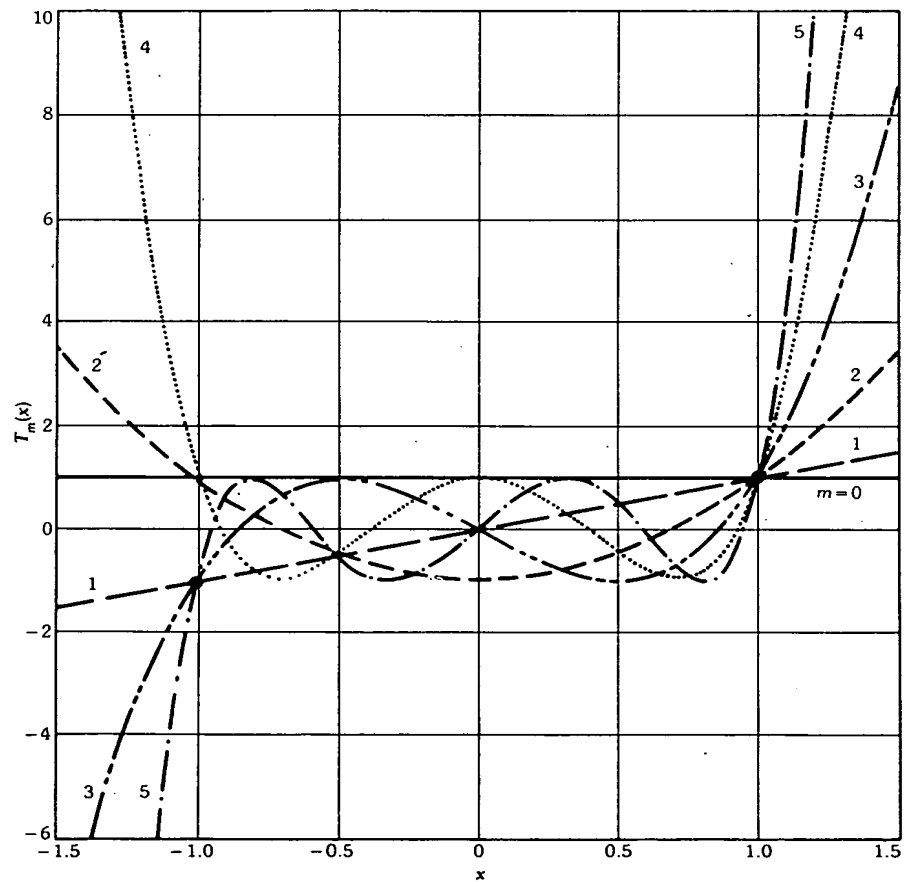
Fig. 5. Chebyshev polynomial $T_m(x)$ for $m = 0, 1, \ldots, 5$. (*After Balanis [4]*, © *1982, Harper & Row, Publishers, Inc.; reprinted by permission of the publisher*)

polynomial of mth degree, having only even-power terms of x if m is even and only odd-power terms of x if m is odd. The recursion formula, useful for generation, is

$$T_{m+1}(x) + T_{m-1}(x) = 2xT_m(x) \tag{27}$$

with $T_0(x) = 1$ and $T_1(x) = x$. Thus $T_m(x)$ is $1/x$ times the arithmetic mean of its two adjacent neighbors, $T_{m-1}(x)$ and $T_{m+1}(x)$.

(b) Pattern function of an array with N equally spaced and symmetrically excited elements:

If N is odd,

$$
\begin{aligned}
F(\theta) &= I_0 + (I_1 e^{j\psi} + I_{-1} e^{-j\psi}) + (I_2 e^{j2\psi} + I_{-2} e^{-j2\psi}) \\
&\quad + \cdots + [I_{N-1/2} e^{j(N-1)\psi/2} + I_{-N-1/2} e^{-j(N-1)\psi/2}] \\
&= I_0 + \sum_{n=1}^{(N-1)/2} I_n(Z^n + Z^{-n})
\end{aligned} \tag{28}
$$

If N is even,

$$
\begin{aligned}
F(\theta) &= I_1 e^{j\psi/2} + (I_{-1} e^{-j\psi/2}) + (I_2 e^{j3\psi/2} + I_{-2} e^{-j3\psi/2}) \\
&\quad + \cdots + [I_{N/2} e^{j(N-1)\psi/2} + I_{-N/2} e^{-j(N-1)\psi/2}] \\
&= \sum_{n=1}^{N/2} I_n[Z^{(2n-1)/2} + Z^{-(2n-1)/2}]
\end{aligned} \tag{29}
$$

where $\psi = kd \cos \theta$, $Z = e^{j\psi}$, and d is the interelement spacing.

(c) To relate (a) and (b), let

$$x = a \cos \psi/2 = a(Z^{1/2} + Z^{-1/2})/2 \tag{30}$$

Then

$$
\begin{aligned}
T_{N-1}(x) &= A_{N-1} \prod_{p=1}^{N-1} (x - x_p) \\
&= A_{N-1} \prod_{p=1}^{N-1} a(Z^{1/2} + Z^{-1/2} - Z_p^{1/2} - Z_p^{-1/2})/2
\end{aligned} \tag{31}
$$

$$x_p = a \cos(\psi_p/2) = \cos\left[\frac{2p-1}{2(N-1)}\pi\right] \tag{32}$$

$$
\begin{aligned}
Z_p &= e^{j\psi} p \\
\psi_p &= kd \cos \theta_p
\end{aligned} \tag{33}
$$

$$\theta_p = \text{angular position of the } p\text{th pattern null} \tag{34}$$

Note that the pattern function as given by (28) or (29) is a polynomial in $Z^{1/2}$ of power from $-(N-1)$ to $(N-1)$, and so is $T_{N-1}(x)$ as given by (31). They can be equated to determine the excitation $\{I_n\}$ once the spacing d/λ and the parameter a are chosen. To find a, one needs to specify the desired side lobe level. Let the main beam to side lobe level ratio be b. Then

$$b = T_{N-1}(a) = \cosh[(N-1)\cosh^{-1}a]$$

or

$$a = \cosh\left(\frac{1}{N-1}\cosh^{-1}b\right) \tag{35}$$

as θ varies from $0 \to \pi/2 \to \pi$

      ψ varies from $2\pi d/\lambda \to \ 0 \ \to -2\pi d/\lambda$

      x varies from $a\cos(\pi d/\lambda) \to \ a \ \to a\cos(\pi d/\lambda)$ (36)

From Fig. 6 it is seen that to avoid grating lobes

$$a\cos(\pi d/\lambda) \leqq -1 \tag{37}$$

Although tables for $\{I_n\}$ are available [93], today, with the availability of computers, it is simple to compute them according to the formula given by Elliott [28]:

$$I_n = I_{-n} = \sum_{p=n}^{(N-1)/2} (-1)^{(N-1)/2-p}\frac{N-1}{N-1+2p}\begin{bmatrix}(N-1)/2+p\\2p\end{bmatrix}\begin{bmatrix}2p\\p-n\end{bmatrix}a^{2p},$$
$$\text{if } N \text{ is odd} \tag{38}$$

$$I_n = I_{-n} = \sum_{p=n}^{N/2} (-1)^{(N/2)-p}\frac{N-1}{N+2(p-1)}\begin{bmatrix}N/2+p-1\\2p-1\end{bmatrix}\begin{bmatrix}2p-1\\p-n\end{bmatrix}a^{2p-1},$$
$$\text{if } N \text{ is even} \tag{39}$$

(d) Design procedure: Choose number of elements N and main beam-to-side-lobe ratio b; then successively determine the following quantities, using the equations shown in the boxes, and finally the required excitation $\{I_n\}$

$$\downarrow \quad \boxed{(35)}$$
$$a$$

$$\downarrow \quad \boxed{(37)}$$

the largest permissible value of d

$$\downarrow \boxed{(32)}$$

roots $\{x_k\}$ of $T_{N-1}(x)$

$$\downarrow \boxed{(33) \text{ and } (34)}$$

ψ_k and Z_k

$$\downarrow \boxed{(31)}$$

expand $T_{N-1}(x)$ in terms of $Z^{\pm 1/2}$ (ignoring the factor A_{N-1} and a)

$$\downarrow$$

compare with (28) or (29) to obtain $\{I_n\}$, or use (38) and (39).

(e) To find the pattern, use (30) and (31) [or (28) and (29)]. Or, graphically, as shown in Fig. 6, first construct $T_{N-1}(x)$ and a circle with radius a and center at $x = 0$, and then use (36) to find a point on the circle corresponding to a given value θ and project on the x axis to find $T_{N-1}(x)$, which is $F_{N-1}(\theta)$ except for a constant multiplier.

(f) Cophasal Dolph-Chebyshev array. Let θ_0 be the main beam angle and replace ψ in the above discussion by $\psi - \psi_0 = (2\pi d/\lambda)(\cos\theta - \cos\theta_0)$; then what happened at $\theta = \pi/2$ (i.e., the main beam) will occur at $\theta = \theta_0$. However, for the visible region,

$$\theta = \qquad 0 \qquad\qquad \to \theta_0 \to \pi$$

$$\psi - \psi_0 = \frac{2\pi d}{\lambda}(1 - \cos\theta_0) \qquad \to 0 \to -\frac{2\pi d}{\lambda}(1 + \cos\theta_0)$$

$$x = a\cos[(\psi - \psi_0)/2] = a\cos\left[\frac{\pi d}{\lambda}(1 - \cos\theta_0)\right] \to a \to a\cos\left(\frac{\pi d}{\lambda}\right)(1 + \cos\theta_0)$$

$$(40)$$

To avoid the presence of grating lobes, neither of the end points of x in the above range should be less than -1. This will determine the largest allowable element spacing d.

Comments:

(1) For large arrays and for side lobe levels in the range of -20 to -60 dB, the excitation transformation method of Elliott [28] gives an approximation solution for the half-power beamwidth in terms of the beam-broadening factor f, which is defined as the ratio of the half-power beamwidth of the array with the Dolph-Chebyshev excitation and that with a uniform excitation. Fig. 7a shows the plot of f versus side lobe level in decibels.

(2) A Dolph-Chebyshev array is optimum only in the sense of narrowest beamwidth for a given side lobe level, or lowest side lobe level for a given beamwidth, but not for maximum directivity. Elliott [28] gives an approximate expression for the directivity of a large Dolph-Chebyshev array:
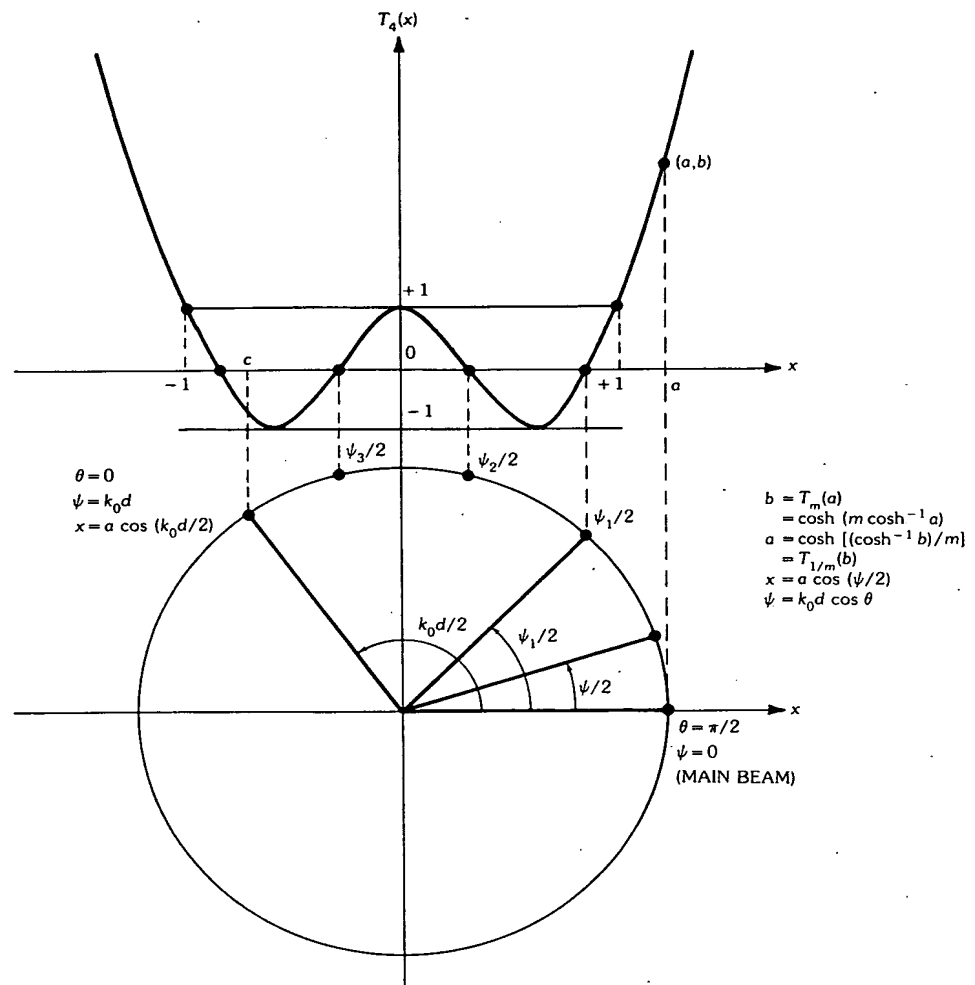
Fig. 6. Graphical method for constructing the radiation pattern of a five-element Dolph-Chebyshev array with side lobe level $20 \log b$ and element spacing d.

$$D \cong \frac{2b^2}{1 + (b^2 - 1)f\lambda/(L + d)}$$

where

L = the total array length

f = the beam-broadening factor given in Fig. 7a

b = determined by the desired side lobe level [see (35)]

Fig. 7b shows the plots of D versus $(L + d)/\lambda$ for several side lobe levels. The directivity is generally lower than that of a uniform array, particularly for large L and high side lobe levels.
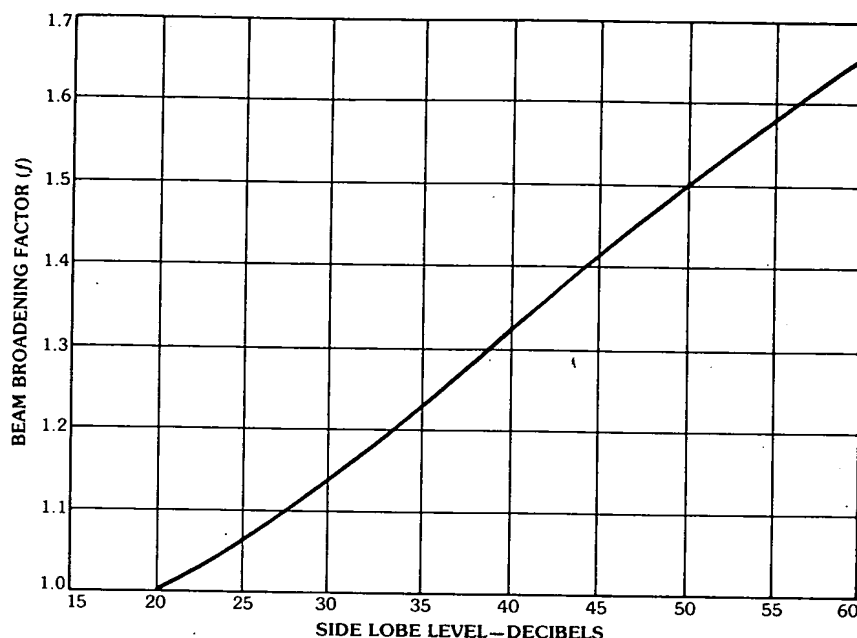
Fig. 7. Beam broadening factor and directivity of a Chebyshev array as functions of side lobe level. (a) Beam broadening factor f versus side lobe level. (b) Directivity versus $(L + d)/\lambda$ for various side lobe levels from 15 to 40 dB. (*After Elliott [121], reprinted with permission of* Microwave Journal, *from the December 1963 issue, © 1963 Horizon House–Microwave, Inc.*)

(g) An alternative Dolph-Chebyshev array design. So far the Chebyshev polynomial in (a) and the pattern function in (b) are related by (30) as shown graphically in Fig. 6, where the center of the circle is at $x = 0$. The visible region as given by (36) may not necessarily reach the point $x = -1$, depending on the value of $a \cos \pi d/\lambda$. To make full use of the interval $(-1, a)$ for x, one may let

$$x = c \cos \psi + h = 2c(Z + Z^{-1}) + h \qquad (41)$$

where

$$\psi = kd \cos \theta$$

$$a = \cosh\left(\frac{2 \cosh^{-1} b}{N - 1}\right)$$

$$c = \frac{a + 1}{1 - \cos kd} \qquad (42)$$

$$h = -\frac{a \cos kd + 1}{1 - \cos kd}$$

In this case,
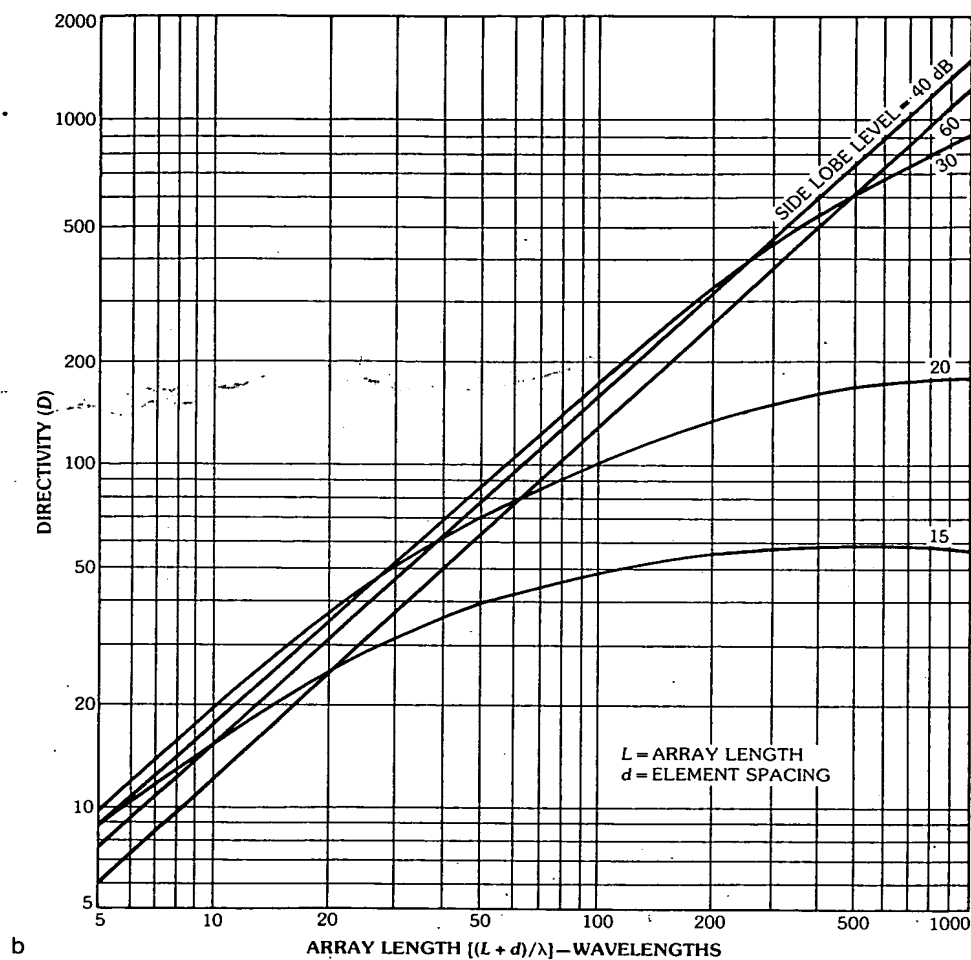
Fig. 7, *continued.*

$$\theta = 0 \rightarrow \pi/2 \rightarrow \pi$$

$$\psi = kd \rightarrow 0 \rightarrow -kd$$

$$x = -1 \rightarrow a \rightarrow -1$$

To find $\{I_n\}$, the term x defined by (41), instead of (30), must be substituted in (31) and the polynomial is compared with (28) for odd N, since now the polynomials in (28) and (31) are both in powers of Z, not $Z^{1/2}$, and also there is a zero-degree term due to h in (41). Furthermore, the power of Z in (28) ranges from $(N-1)/2$ to $-(N-1)/2$ [or similarly from $(N-1)$ to 0 by multiplying all terms by $Z^{-(N-1)/2}$], whereas that in (31) with x substituted by (41) ranges from $(N-1)$ to $-(N-1)$.

Since the number of terms in the polynomial must equal the number of elements, N, only the Chebyshev polynomial of $(N-1)/2$ degree, i.e., $T_{(N-1)/2}(x)$, is needed for (31). Drane [23] has given the following formula for the excitation of an array with N (odd) number of elements:

$$I_n = \frac{\varepsilon_n}{4M} \sum_{m=0}^{M_1} \varepsilon_m \varepsilon_{M_2-m} T_n(Y_m) S_M^n(c, h, y_m) \tag{43}$$

where

$$\varepsilon_0 = 1 \text{ and } \varepsilon_n = 2 \quad \text{for } n \neq 0,$$

$$y_m = \cos(m\pi/M)$$

$$M = (N-1)/2$$

$M_1, M_2 = $ the integer parts of $M/2$ and $(M+1)/2$, respectively,

$$S_M^n(c, h, y_m) = T_M(cy_m + h) + (-1)^n T_M(h - cy_m) \tag{44}$$

If M is even,

$$S_M^n(c, h, y_{M/2}) = T_M(cy_{M/2} + h) \tag{45}$$

4. Linear Transformations in Antenna Arrays

A linear transformation can be applied to array pattern functions in two different ways: (1) When applied to element positions it relates the pattern function of an array of one geometry to that of another [64]. In other words, the pattern of one member of a family of arrays determines the patterns of the entire family, if their geometries are linearly transformable. (2) When applied to excitations it can express the pattern function of an array with one type of excitation in terms of the patterns of the same array with different types of excitations, in particular, the patterns for some simple canonical excitations, such as uniform cophasal excitations. Of course, the application of some of these transformations is valid only if the mutual coupling effect among elements can be ignored, since this effect, in general, is not linearly dependent on element spacings. But the transformation can also be used if the feeding network is redesigned to compensate for the coupling effect after transformation. We shall discuss some fundamental results in this section.

Linear Transformations in Array Geometry

Let us consider a Cartesian coordinate system with bases $\{\hat{e}_1, \hat{e}_2, \hat{e}_3\}$ in which all lengths are expressed in terms of free-space wavelength λ. First we define the following vectors in matrix notations:

$$\mathbf{E} = (\hat{e}_1, \hat{e}_2, \hat{e}_3) \tag{46}$$

$$\mathbf{X} = (x_1, x_2, x_3)^t \tag{47}$$

$$\mathbf{U} = (u_1, u_2, u_3)^t \tag{48}$$

where the superscript t, as usual, designates the transpose, and the us are Cartesian components of a unit vector $\hat{\mathbf{u}}$ in spherical coordinates, namely

$$u_1 = \sin\theta\cos\phi, \qquad u_2 = \sin\theta\sin\phi, \qquad u_3 = \cos\theta \tag{49}$$

In the following discussion we shall use either vector notations or matrix notations, depending on which one is more convenient in a particular discussion. Thus

$$\mathbf{x} = x_1\hat{\mathbf{e}}_1 + x_2\hat{\mathbf{e}}_2 + x_3\hat{\mathbf{e}}_3 = \mathbf{EX} \tag{50}$$

$$\hat{\mathbf{u}} = u_1\hat{\mathbf{e}}_1 + u_2\hat{\mathbf{e}}_2 + u_3\hat{\mathbf{e}}_3 = \mathbf{EU} \tag{51}$$

Then from (2a) for each component, the pattern, due to a source called x, with distribution $J(\mathbf{x})$, as a function of (θ, ϕ), or $\hat{\mathbf{u}}$, is

$$F_x(\hat{\mathbf{u}}) = \int_{\text{source } x} J(\mathbf{x}) \, e^{j2\pi\hat{\mathbf{u}}\cdot\mathbf{x}} \, d\mathbf{x} \tag{52}$$

where $d\mathbf{x} = dx_1\,dx_2\,dx_3$, the subscript x of $F_x(\cdot)$ denotes the pattern function for source x, and $J(\mathbf{x})$ can be any source distribution function, with continuous, sectionally continuous, or discrete point sources. For the latter case,

$$J(\mathbf{x}) = \sum_n I(\mathbf{x}_n)\,\delta(\mathbf{x} - \mathbf{x}_n) \tag{53}$$

and

$$F_x(\hat{\mathbf{u}}) = \sum_n I(x_n)\,e^{j2\pi\hat{\mathbf{u}}\cdot\mathbf{x}_n} \tag{54}$$

which is simply the array factor for point elements at $\{\mathbf{x}_n\}$ with excitations $\{I_n\}$. Thus the so-called array factor can be regarded as a special case of (52).

Equation 52 indicates that $F_x(\hat{\mathbf{u}})$ and $J(\mathbf{x})$ are a Fourier transform pair. However, in physical space (θ, ϕ) are real, and, because of (49), the observable pattern function is described by only a part of the Fourier transform of $J(x)$ which lies on a unit sphere in the transform space u.

Now let $\mathbf{X}$ and $\mathbf{U}$ undergo linear transformations described by matrices $\mathbf{A}$ and $\mathbf{B}$, respectively, which takes $\mathbf{X}$ to $\mathbf{Y} = \mathbf{AX}$ and $\mathbf{U}$ to $\mathbf{V} = \mathbf{BU}$. If

$$\mathbf{B}^{-1} = \mathbf{A}^t \tag{55}$$

then the scalar product

$$\mathbf{v}\cdot\mathbf{y} = \mathbf{V'Y} = (\mathbf{BU})'(\mathbf{AX}) = \mathbf{U'X} = \mathbf{u}\cdot\mathbf{x} \tag{56}$$

remains invariant. Hence (52) can be written as

$$F_x(\hat{\mathbf{u}}) = \int_{\text{source } x} J(\mathbf{x})\, e^{j2\pi\hat{\mathbf{u}}\cdot\mathbf{x}}\, d\mathbf{x}$$

$$= \int_{\text{source } y} J(\mathbf{A}^{-1}\mathbf{Y})\, e^{j2\pi\mathbf{v}\cdot\mathbf{y}}\, |\mathbf{A}|^{-1} d\mathbf{Y} = F_y(\mathbf{v}) \tag{57}$$

where $|\mathbf{A}|$ is the determinant of $\mathbf{A}$. This relation states in effect that the field $J(\mathbf{x})$ observed in the direction $\hat{\mathbf{u}}$ due to the source x is the same as that in the direction $\mathbf{v}$ due to the source y, that is, $J(\mathbf{y}) = |\mathbf{A}|^{-1}J(\mathbf{A}^{-1}\mathbf{Y})$. Thus the pattern function of a member of a family of arrays which are related to each other by a linear transformation in geometry determines the patterns of all members of the family. However, since in general $\mathbf{u} \neq \mathbf{v}$, part of the invisible region in the u space may become visible in the v space after the transformation, or vice versa. To see this transformation in detail, let us consider first the scalar product invariant transformation, from (55):

$$\mathbf{B'A} = \mathbf{A'B} = \mathbf{E}$$

Let $\mathbf{a}_1, \mathbf{a}_2, \mathbf{a}_3$ be the column vector of $\mathbf{A}$ and $\mathbf{b}_1, \mathbf{b}_2, \mathbf{b}_3$ be those of $\mathbf{B}$. Then $\mathbf{Y} = \mathbf{AX}$ implies that

$$\mathbf{y} = y_1\hat{\mathbf{e}}_1 + y_2\hat{\mathbf{e}}_2 + y_3\hat{\mathbf{e}}_3 = x_1\mathbf{a}_1 + x_2\mathbf{a}_2 + x_3\mathbf{a}_3 \tag{58}$$

This transformation can be regarded as a *mapping* (rotation and linear stretching) of $\mathbf{x}$ into $\mathbf{y}$, or, by comparing the right-hand side of (58) with (50), simply a *relabeling* of the base vectors of $\mathbf{x}$ from $\mathbf{e}_n$ into $\mathbf{a}_n$. Similar interpretations can be given to $\mathbf{V} = \mathbf{BU}$,

$$\mathbf{v} = v_1\hat{\mathbf{e}}_1 + v_2\hat{\mathbf{e}}_2 + v_3\hat{\mathbf{e}}_3 = u_1\mathbf{b}_1 + u_2\mathbf{b}_2 + u_3\mathbf{b}_3 \tag{59}$$

For invariant scalar product, (55) states that

$$\mathbf{b}_i\cdot\mathbf{a}_j = \delta_{ij}, \qquad i,j = 1,2,3 \tag{60}$$

where the Kronecker delta $\delta_{ij} = 0$ if $i \neq j$ and 1 if $i = j$. Thus $\mathbf{b}_i$ has a projection on $\mathbf{a}_i$ equal to $1/a_i$ and a direction perpendicular to all other $\mathbf{a}_j$s. Specifically,

$$\mathbf{b}_1 = |\mathbf{A}|^{-1}(\mathbf{a}_2 \times \mathbf{a}_3), \qquad \mathbf{b}_2 = |\mathbf{A}|^{-1}(\mathbf{a}_3 \times \mathbf{a}_1), \qquad \mathbf{b}_3 = |\mathbf{A}|^{-1}(\mathbf{a}_1 \times \mathbf{a}_2) \tag{61}$$

Here $\{\mathbf{a}_i\}$ and $\{\mathbf{b}_i\}$ are called *reciprocal bases* to each other. These are very useful in the study of periodic structures and Floquet space harmonics.

Application to Planar Periodic Arrays

Fig. 8a shows a broadside planar array with elements at the square grid intersection points in the $x_1 x_2$ plane and spacing d (in wavelengths). Its pattern function in the $u_1 u_2$ space is also periodic as shown in Fig. 8b, where the small circles indicate the locations of the grating lobes (including the main beam). If the array is of infinite extent, each circle corresponds to a space harmonic. The spacing between two circles along the u_1 or u_2 axis is $1/d$. The visible region is bounded by a unit circle and a typical point in this $u_1 u_2$ plane has the polar coordinates $(\sin\theta, \phi)$. Thus a given point (u_1, u_2) determines uniquely (θ, ϕ) in the physical region $0 \leq \theta \leq \pi$, $0 \leq \phi < 2\pi$, and vice versa.

For a cophasal array with main beam at (θ_0, ϕ_0)

$$J(\mathbf{x}) = |J(\mathbf{x})| \exp(-j2\pi \hat{\mathbf{u}}_0 \cdot \mathbf{x}) \qquad (62)$$

where

$$u_{01} = \sin\theta_0 \cos\phi_0, \qquad u_{02} = \sin\theta_0 \sin\phi_0 \qquad (63)$$

This additional phase results simply in a translation of the origin of the $u_1 u_2$ space by $(-u_{01}, -u_{02})$ as shown in Fig. 9 with all grating beam circles fixed, or with the origin remains fixed and all grating beam circles translated by (u_{01}, u_{02}). The visible region in this case is given by a unit disc with (u_{01}, u_{02}) as center as shown in Fig. 9a. For a phased array with full scan range, $0 \leq \theta_0 \leq \pi$ and $0 \leq \phi_0 < 2\pi$, the *overall* visible region is bounded by a disc with radius 2 and center at the original origin as shown in Fig. 9b. For a particular scan range, say $0 \leq \theta_0 \leq \theta_0''$ and $\phi_0' \leq \phi_0 \leq \phi_0''$, the total visible region is bounded by that part of the $u_1 u_2$ plane which is covered by all unit discs with their centers (u_{01}, u_{02}) satisfying the inequalities

a   b   CIRCLE OF
                                                                VISIBLE REGION
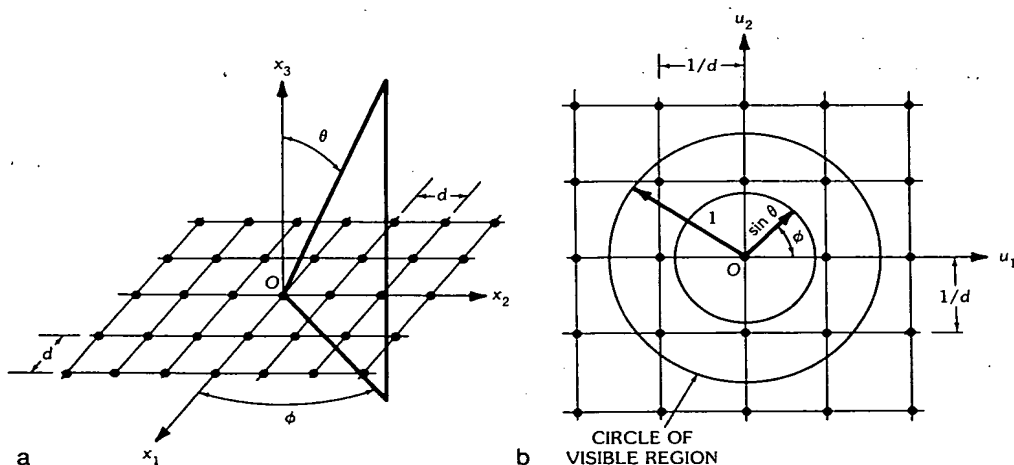
Fig. 8. Broadside planar array and pattern function. (*a*) A periodic planar array with square cells in the $x_1 x_2$ plane. (*b*) Periodic structure of the pattern function of the array (*a*) in the $u_1 u_2$ plane. (*After Lo and Lee [64], © 1965 IEEE*)

a

b

c
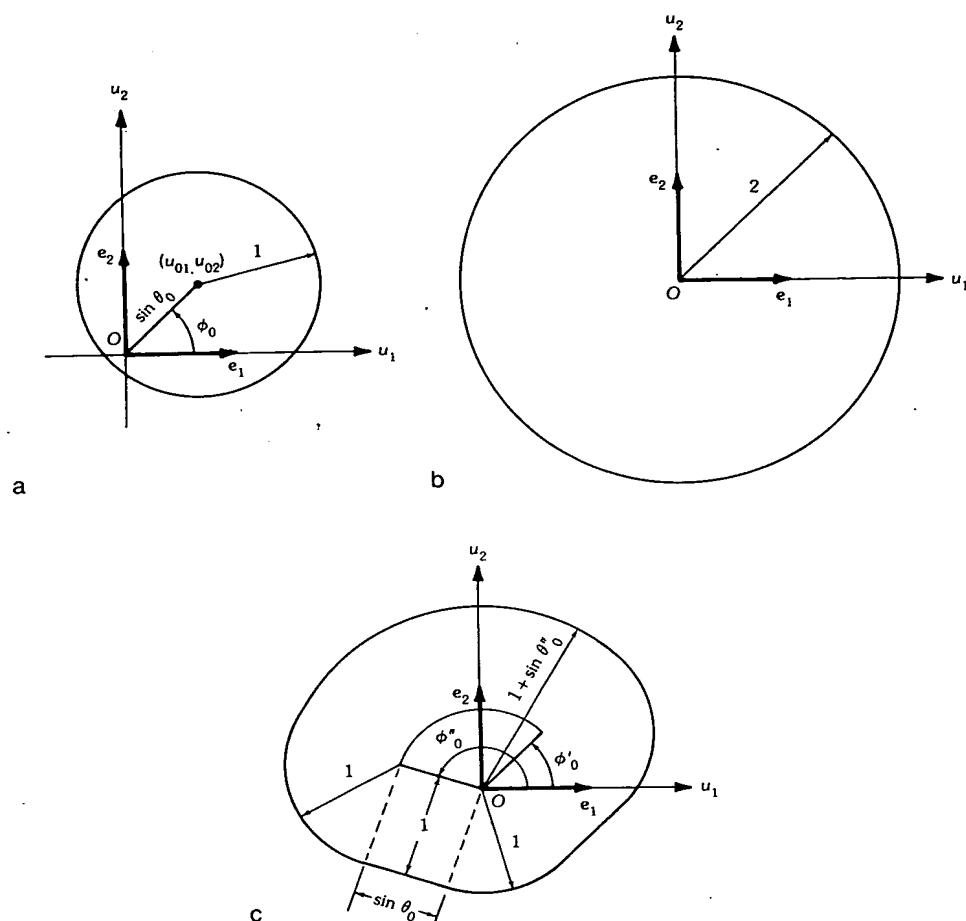
Fig. 9. Visible region in the $u_1 u_2$ plane. (a) As the beam is scanned to (θ_0, ϕ_0). (b) For a full scan: $0 \leqq \theta_0 \leqq \pi$ and $0 \leqq \phi_0 \leqq 2\pi$. ($c$) For a limited scan: $\phi'_0 \leqq \phi_0 \leqq \phi''_0$ and $0 \leqq \theta_0 \leqq \theta''_0$. (*After Lo and Lee [64], © 1965 IEEE*)

$$0 \leqq (u_{01}^2 + u_{02}^2)^{1/2} \leqq \sin \theta_0'' \quad \text{and} \quad \phi'_0 \leqq \tan^{-1}\left(\frac{u_{02}}{u_{01}}\right) \leqq \phi''_0 \qquad (64)$$

as illustrated in Fig. 9c.

An Example—Consider a uniform array (called the x array) with square grid size $d = 1$ as shown in Fig. 8a. Then the mnth element position is

$$\mathbf{x}_{mn} = m\hat{\mathbf{e}}_1 + n\hat{\mathbf{e}}_2, \qquad 1 \leqq m \leqq M, \qquad 1 \leqq n \leqq N \qquad (65)$$

Its pattern is

$$F_x(\mathbf{u}) = \frac{\sin M\pi u_1}{\sin \pi u_1} \frac{\sin N\pi u_2}{\sin \pi u_2} \tag{66}$$

Next we consider a more general uniform planar array, called the y array, as shown in Fig. 10a, whose mnth element is at

$$\mathbf{y}_{mn} = m\mathbf{a}_1 + n\mathbf{a}_2, \qquad 1 \leqq m \leqq M, \qquad 1 \leqq n \leqq N \tag{67}$$

where $\mathbf{a}_1$ and $\mathbf{a}_2$ need not be orthogonal, nor of equal length. From (58) we see that the y array can be obtained from the x array with the transformation

$$\mathbf{A} = (\mathbf{a}_1, \mathbf{a}_2, \hat{\mathbf{e}}_3) \tag{68}$$

since for planar arrays there is no need for the transformation for the axis normal to the array, i.e., $\mathbf{a}_3 = \hat{\mathbf{e}}_3$. Now, from (55),

$$\mathbf{U} = \mathbf{B}^{-1}\mathbf{V} = \mathbf{A}'\mathbf{V}$$

or

$$\mathbf{u}_1 = \mathbf{a}_1\cdot\mathbf{v}, \qquad \mathbf{u}_2 = \mathbf{a}_2\cdot\mathbf{v}, \qquad \mathbf{u}_3 = \hat{\mathbf{e}}_3\cdot\mathbf{v} \tag{69}$$

where
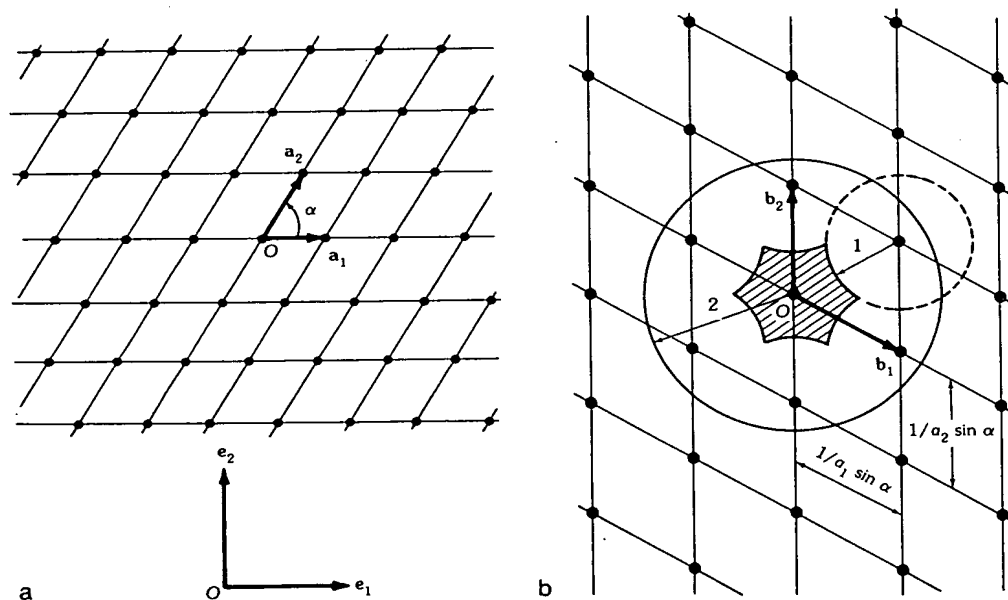
Fig. 10. Periodic planar array and pattern function. (*a*) Periodic planar array with parallelogram cells defined by vectors $\mathbf{a}_1$ and $\mathbf{a}_2$ in y space. (*b*) Periodic pattern function structure in the $v_1 v_2$ plane. (*After Lo and Lee [64]*, © *1965 IEEE*)

$$v = \sin\theta\cos\phi\hat{e}_1 + \sin\theta\sin\phi\hat{e}_2 + \cos\theta\hat{e}_3 \qquad (70)$$

Therefore from (66) and (69) the pattern of the y array is simply

$$F_y(v) = \frac{\sin(M\pi a_1 \cdot v)}{\sin(\pi a_1 \cdot v)} \frac{\sin(N\pi a_2 \cdot v)}{\sin(\pi a_2 \cdot v)} \qquad (71)$$

Since $F_x(u)$ has grating lobes at u_1 and u_2 equal to $0, \pm 1, \pm 2, \ldots$, or

$$u = m\hat{e}_1 + n\hat{e}_2, \qquad m, n = 0, \pm 1, \pm 2, \ldots, \qquad (72)$$

$F_y(v)$ will have grating lobes at $(a_1 \cdot v)$ and $(a_2 \cdot v)$ equal to $0, \pm 1, \pm 2, \ldots$, or

$$v = m b_1 + n b_2 \qquad (73)$$

where b_1 and b_2 are determined from a_1 and a_2 from (61) as shown in Fig. 10b. Note that b_1 and b_2 are perpendicular to a_1 and a_2, respectively, and that the lengths of b_1 and b_2 are equal to the reciprocals of $a_1 \sin\alpha$ and $a_2 \sin\alpha$, respectively. If $a_1 = a_2$ and the angle between a_1 and a_2, namely α, is 60°, the y array becomes an equilateral-triangular grid. It is very simple to determine the range of scan for which no grating lobe will appear. This region is bounded by the arcs of unit circles with centers at all adjacent grating lobe locations shown as the shaded parts in Fig. 10b. To translate the boundary of this region into one in the $\theta\phi$ plane, one needs to recall that any point in the $v_1 v_2$ plane has the polar coordinates $(\sin\theta, \phi)$. Thus by placing a transparent overlay with ordinary polar coordinates (except that the concentric circles are marked with θ according to the value of $\sin\theta$ as their radii) on the top of Fig. 10b, one can determine immediately the scanning region in θ and ϕ (see Fig. 14). This method is not only simpler but also more illuminating than others [88].

Nonuniform Excitation and Relation between Aperture Antenna and Discrete Array

Often an array with discrete elements can be considered as a sampled set of an aperture antenna with a distribution function $f_0(y)$. A question of interest will be how close the pattern of the sampling array is to that of the aperture antenna. To see this, let $f_0(y)$ be the given excitation for y inside the aperture and zero outside the aperture. Then for the array $\{y\}$ one may have

$$f(y) = f_0(y) \sum_{m,n} \delta(y - y_{mn}) \qquad (74)$$

where $\delta(y - y_{mn})$ is the two-dimensional delta function and the summation is taken over all the integers for both m and n. Now applying the transformation A, one obtains a corresponding array $\{x\}$ with excitation

$$f(AX) = f_0(AX) \sum_{m,n} \delta(AX - AX_{mn}) \qquad (75)$$

By substituting (75) into (52) and making use of the convolution integral theorem, one has

$$F_x(\mathbf{u}) = F_{0x}(\mathbf{u}) * \sum_{m,n} \delta(\mathbf{U} - \mathbf{X}_{mn})|\mathbf{A}|^{-1} \tag{76}$$

where the asterisk denotes the convolution integration and $F_{0x}(\mathbf{u})$ is the Fourier tranform or the pattern function of an aperture antenna with excitation $f_0(\mathbf{AX})$. As in (67), if $\mathbf{y}_{mn} = m\mathbf{a}_1 + n\mathbf{a}_2$, then $\mathbf{x}_{mn} = m\hat{\mathbf{e}}_1 + n\hat{\mathbf{e}}_2$ and $F_x(\mathbf{u})$ is periodic in u_1 and u_2 of unity period. Equation 76 states that $F_x(\mathbf{u})$ is the sum of infinitely many $F_{0x}(\mathbf{u})$s, each displaced from the other by a unit along the u_1 and u_2 axes. Since $f_0(\mathbf{AX})$ is an aperture limited function, $F_{0x}(\mathbf{u})$ becomes negligible for large u. Therefore, for (u_1, u_2) in the neighborhood of (m, n), $F_x(\mathbf{u})$ is essentially equal to $F_{0x}(\mathbf{u})$. From (76) the pattern function of array $\{y\}$ is given immediately by*

$$F_y(\mathbf{v}) = F_x(\mathbf{B}^{-1}\mathbf{V}) = |\mathbf{B}| F_{0x}(\mathbf{B}^{-1}\mathbf{V}) * \sum_{m,n} \delta(\mathbf{V} - \mathbf{BX}_{mn})$$

$$= |\mathbf{B}| F_{0x}(\mathbf{B}^{-1}\mathbf{V}) * \sum_{m,n} \delta(\mathbf{v} - m\mathbf{b}_1 - n\mathbf{b}_2) \tag{77}$$

As in Fig. 10b the pattern function of array $\{y\}$ is also a periodic function with periods inversely proportional to $a_1 \sin\alpha$ and $a_2 \sin\alpha$ along $\mathbf{b}_1$ and $\mathbf{b}_2$, respectively, and it is thus a linearly distorted pattern of $F_x(\mathbf{u})$. Obviously (76) and (77) also show the exact difference between the pattern function for continuous (or sectionally continuous) excitation and that for discrete excitation with periodically spaced elements.

Hexagonal Arrays

Periodic arrays with unit cells other than parallelograms may also be analyzed in a similar manner. As an example, consider a hexagonal array of uniform excitation, as shown in Fig. 11a, where the element positions are marked by crosses. The array may be regarded simply as a superposition of two parallelogram arrays with equal excitations but opposite in sign. The sides of the two parallelograms are defined by

$$\mathbf{a}_1 = \hat{\mathbf{e}}_1, \qquad \mathbf{a}_2 = \cos(60°)\hat{\mathbf{e}}_1 + \sin(60°)\hat{\mathbf{e}}_2$$

$$\mathbf{a}_1' = 3\hat{\mathbf{e}}_1, \qquad \mathbf{a}_2' = \sqrt{3}\cos(30°)\hat{\mathbf{e}}_1 + \sqrt{3}\sin(30°)\hat{\mathbf{e}}_2 \tag{78}$$

From the relation $\mathbf{B} = (\mathbf{A}')^{-1}$, one immediately obtains

---

*It is understood that the convolution integral in (77) refers to the variable **v** whereas in (76) it refers to the variable **u**.
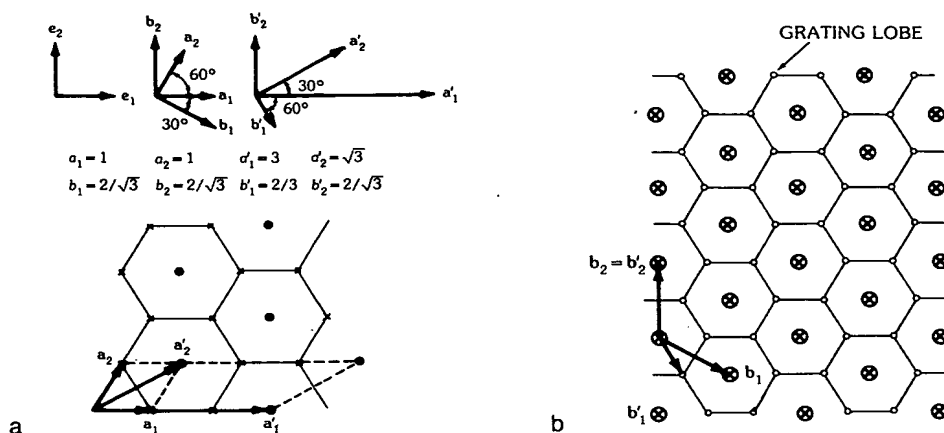
Fig. 11. Periodic array with hexagonal cells and hexagonal pattern function structure. (a) Array with cells in y space. (b) Pattern function structure in v space. (*After Lo and Lee [64],* © *1965 IEEE*)

$$\mathbf{b}_1 = \frac{2}{\sqrt{3}}\cos(-30°)\,\hat{\mathbf{e}}_1 + \frac{2}{\sqrt{3}}\sin(-30°)\,\hat{\mathbf{e}}_2, \qquad \mathbf{b}_2 = \frac{2}{\sqrt{3}}\hat{\mathbf{e}}_2$$

$$\mathbf{b}_1' = \frac{2}{3}\cos(-60°)\,\hat{\mathbf{e}}_1 + \frac{2}{3}\sin(-60°)\,\hat{\mathbf{e}}_2, \qquad \mathbf{b}_2' = \frac{2}{\sqrt{3}}\hat{\mathbf{e}}_2$$

$$(79)$$

as shown in Fig. 11b. It is seen that the grating lobes, denoted by the small circles without crosses, also form a hexagonal periodic structure.

Periodic Arrays with Minimum Number of Elements

In practice it is often desirable to have only a single main beam in the visible region. This condition sets an upper limit on the element spacing of a period array. For the array with elements at the vertices of square cells, as shown in Fig. 8a, it is well known that for the case of full scan the element spacing must be smaller than half wavelength, as seen from Fig. 8b. As a result this sets a lower limit on the required number of elements. In the following we shall show that, for some other periodical arrays, this lower limit can be reduced.

First, it should be understood that the previous statement about a single main beam in the visible region, in fact, has different meanings, depending on the types of arrays under discussion. For example, for a linear array, due to symmetry, a single main beam may actually be a disklike beam when it is broadside, a cone-shaped beam when it is fired at an angle, and a unidirectional beam when it is end-fired. On the other hand, for a planar array, whenever there is beam firing above the plane of the array, there is always one below the plane, due to symmetry, except for the limiting case of end-fire. Customarily, one may regard all of these as being degenerated cases of a three-dimensional array which, in general, can possess a truly single beam in the visible range.

Now consider a periodic array with parallelograms as unit cells, as shown in Fig. 10a. Then, as previously shown, the grating lobes will appear at

$$\mathbf{u} = m\mathbf{b}_1 + n\mathbf{b}_2, \qquad m, n = \text{integers} \tag{80}$$

Let

$$\begin{aligned}\mathbf{b}_1 &= b_{11}\hat{\mathbf{e}}_1 + b_{12}\hat{\mathbf{e}}_2 \\ \mathbf{b}_2 &= b_{21}\hat{\mathbf{e}}_1 + b_{22}\hat{\mathbf{e}}_2\end{aligned} \tag{81}$$

Then, in matrix notation, (80) becomes

$$\begin{bmatrix} u_1 \\ u_2 \end{bmatrix} = \begin{bmatrix} b_{11} & b_{21} \\ b_{12} & b_{22} \end{bmatrix} \begin{bmatrix} m \\ n \end{bmatrix}$$

The objective is to determine all bs under the condition that no grating lobes appear in the visible region* and then determine all as which fix the array arrangement. In order to make the number of elements minimum for a given aperture one must add a condition that the area of each unit cell, namely $|\mathbf{A}|$, should be made as large as possible, or $|\mathbf{B}|$ as small as possible.

To give an example, first consider the case of *full* scan. Then it is required that:

(1) for all grating lobes outside the *full* scan circle in u space: $(b_{11}m + b_{21}n)^2 + (b_{12}m + b_{22}n)^2 \geqq 4$, for m, n, equal to all integers except $m = n = 0$;
(2) for minimum number of elements:
     $|\mathbf{B}| = b_{11}b_{22} - b_{12}b_{21}$ to be minimum

The solution is

$$\mathbf{a}_1 = \frac{1}{\sqrt{3}}\hat{\mathbf{e}}_1 \quad \text{and} \quad \mathbf{a}_2 = \frac{1}{\sqrt{3}}[\cos(60°)\,\hat{\mathbf{e}}_1 + \sin(60°)\,\hat{\mathbf{e}}_2] \tag{82}$$

This is the well-known equilateral-triangular grid structure.

If the scan range is limited to

$$0 \leqq \theta_0 \leqq \theta_0'' \quad \text{and} \quad 0 \leqq \phi_0 \leqq 2\pi$$

the solution can be determined similarly as

$$\begin{aligned}\mathbf{a}_1 &= \frac{2}{\sqrt{3}(1 + \sin\theta_0'')}\hat{\mathbf{e}}_1 \\ \mathbf{a}_2 &= \frac{2}{\sqrt{3}(1 + \sin\theta_0'')}(\hat{\mathbf{e}}_1 \cos 60° + \hat{\mathbf{e}}_2 \sin 60°)\end{aligned} \tag{83}$$

---

*This condition is regarded as one where the grating lobe begins to show up in the visible region at the extreme scanning angle. This determines the upper limit of the element spacings. Actually, to avoid the grating lobe *completely*, the spacings should be somewhat *smaller*, depending on the beam shape, width, or the aperture and the excitation function.

Now comparing this array with a conventional one with square cells, as shown in Fig. 8a, the number of elements is reduced approximately by

$$\frac{|\mathbf{B}_{sq}| - |\mathbf{B}|}{|\mathbf{B}_{sq}|} = \frac{4 - 2\sqrt{3}}{4} = 13.4 \text{ percent}$$

where $|\mathbf{B}_{sq}|^{-1}$, $|\mathbf{B}|^{-1}$ are, respectively, the areas of a square cell and a parallelogram given by (83). It can be easily shown that this percentage is dependent on ϕ_0'' only, and the previous value applies when ϕ_0 covers the whole range $(0, 2\pi)$. If ϕ_0 covers only part of this range, condition 1 should be revised. For the special case, $0 \leqq \theta_0 < 45°$, $0 \leqq \phi_0 < 2\pi$, $a_1 = a_2 = 0.676$.

It is easy to extend the previous results to a three-dimensional periodic array with elements over vertices of parallelopiped cells. In this case, for *full* scan, $\mathbf{b}_1$, $\mathbf{b}_2$, and $\mathbf{b}_3$ are found to form an oblique coordinate system with 60° between any two vectors, and each with length 2. With respect to the orthonormal basis $\{\hat{\mathbf{e}}_1, \hat{\mathbf{e}}_2, \hat{\mathbf{e}}_3\}$, they are

$$\mathbf{b}_1 = 2\hat{\mathbf{e}}_1, \qquad \mathbf{b}_2 = \hat{\mathbf{e}}_1 + \sqrt{3}\,\hat{\mathbf{e}}_2, \qquad \mathbf{b}_3 = \hat{\mathbf{e}}_1 + \frac{1}{\sqrt{3}}\hat{\mathbf{e}}_2 + \frac{2\sqrt{2}}{\sqrt{3}}\hat{\mathbf{e}}_2 \tag{84}$$

From the relation between as and bs, one obtains

$$\mathbf{a}_1 = \frac{1}{2}\hat{\mathbf{e}}_1 - \frac{1}{2\sqrt{3}}\hat{\mathbf{e}}_2 - \frac{1}{2\sqrt{6}}\hat{\mathbf{e}}_3, \qquad \mathbf{a}_2 = \frac{1}{\sqrt{3}}\hat{\mathbf{e}}_2 - \frac{1}{2\sqrt{6}}\hat{\mathbf{e}}_3, \qquad \mathbf{a}_3 = \frac{\sqrt{3}}{2\sqrt{2}}\hat{\mathbf{e}}_3 \tag{85}$$

It is readily verified that all as have a length equal to $\sqrt{3}/2\sqrt{2}$ and make an angle of $\cos^{-1}(-1/3) = 109.5°$ between any two of them. In comparison with a conventional array with cubic cells, the number of elements is reduced approximately by 29.3 percent.

Transformation between Circular and Elliptical Arrays

The pattern of a circular array or aperture antenna can be expressed in terms of Bessel functions (see later in this section, under "Circular Arrays"). In a similar manner the pattern of an elliptical array or aperture antenna can be expressed in terms of Mathieu functions. But the numerical computation of the latter is much more difficult than that of the former. By using linear transformation, this difficulty can be alleviated.

Let the Cartesian coordinates of the nth element with excitation I_n of an elliptical array, called the x array, be $\mathbf{x}_n = (x_{n_1}, x_{n_2})$ in the $\hat{\mathbf{e}}_1\hat{\mathbf{e}}_2$ plane; then

$$(x_{n_1}/a)^2 + (x_{n_2}/b)^2 = 1 \tag{86}$$

where $2a$ and $2b$ are the major and minor axes, respectively. The pattern function of the x array is

$$F_x(\mathbf{u}) = \sum_n I_n e^{j2\pi \mathbf{u} \cdot \mathbf{x}_n} \tag{87}$$

Now, applying the transformation

$$\mathbf{A} = \begin{bmatrix} 1 & 0 \\ 0 & \tau \end{bmatrix} \quad \text{and} \quad \mathbf{B} = (\mathbf{A}^{-1})^t = \begin{bmatrix} 1 & 0 \\ 0 & t \end{bmatrix} \tag{88}$$

where $\tau = 1/t = a/b = $ axial ratio, one obtains

$$F_x(\mathbf{u}) = \sum_n I_n e^{j2\pi \mathbf{u} \cdot \mathbf{x}_n} = \sum_n I_n e^{j2\pi \mathbf{v} \cdot \mathbf{y}_n} = F_y(\mathbf{v}) \tag{89}$$

where

$$\mathbf{y}_n = \begin{bmatrix} y_{n_1} \\ y_{n_2} \end{bmatrix} = \mathbf{AX} = \begin{bmatrix} 1 & 0 \\ 0 & \tau \end{bmatrix} \begin{bmatrix} x_{n_1} \\ x_{n_2} \end{bmatrix} = \begin{bmatrix} x_{n_1} \\ \tau x_{n_2} \end{bmatrix} \tag{90}$$

and

$$\mathbf{V} = \begin{bmatrix} v_1 \\ v_2 \end{bmatrix} = \mathbf{BU} = \begin{bmatrix} 1 & 0 \\ 0 & t \end{bmatrix} \begin{bmatrix} u_1 \\ u_2 \end{bmatrix} = \begin{bmatrix} u_1 \\ t u_2 \end{bmatrix} \tag{91}$$

From (86) and (90)

$$y_{n_1}^2 + y_{n_2}^2 = a^2 \tag{92}$$

Thus the y array is a circular array whose nth element excitation is still I_n. Similarly, since

$$u_1^2 + u_2^2 = \sin^2\theta^{(u)}\cos^2\phi^{(u)} + \sin^2\theta^{(u)}\sin^2\phi^{(u)} = \sin^2\theta^{(u)} \tag{93}$$

one obtains from (91)

$$v_1^2 + (\tau v_2)^2 = \sin^2\theta^{(v)}\cos^2\phi^{(v)} + \tau^2\sin^2\phi^{(v)}\sin^2\phi^{(v)} = \sin^2\theta^{(u)} \tag{94}$$

where the superscript u is used to denote the values of θ and ϕ associated with a certain point in the u space and the superscript v is used to denote the values of θ and ϕ for its transformed point in the v space. All the above results can be summarized as in the following:

"The pattern of an elliptical array, with excitation $\{I_n\}$, major axis $2a$, and axial ratio τ when computed over a circle of radius $\sin\theta^{(u)}$ and $0 \leq \phi^{(u)} < 2\pi$ in the u plane is the same as that of a circular array, with excitations $\{I_n\}$ and radius a when computed over an ellipse with major axis $2\sin\theta^{(u)}$ and axial ratio τ in the v plane, as shown in Fig. 12."

Sometimes it is more convenient to specify element position and observation point by azimuthal angles as shown in Fig. 12. One finds that the element located at angle
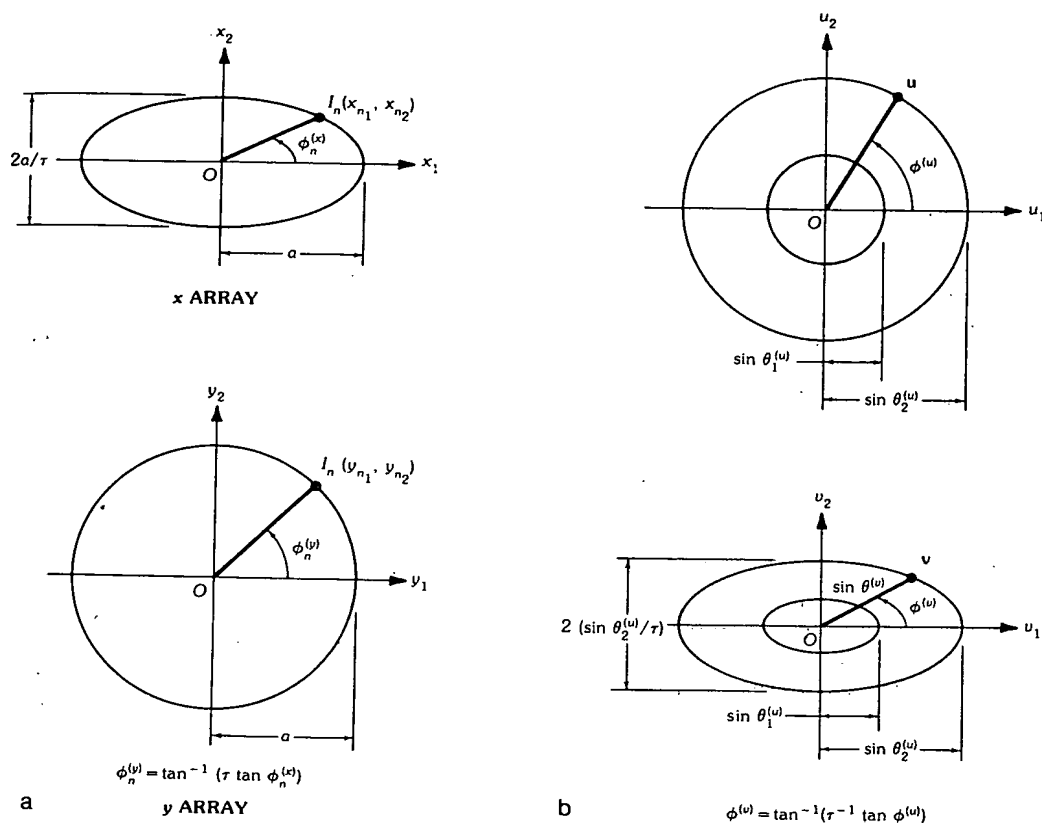
Fig. 12. Far field at u with polar coordinates $(\sin\theta^{(u)}, \phi^{(u)})$ in the $u_1 u_2$ plane due to an elliptical array x is the same as that at v with polar coordinates $(\sin\theta^{(v)}, \phi^{(v)})$ in the $v_1 v_2$ plane due to a circular array y. (a) Array plane. (b) Field plane. (*After Lo and Hsuan [66], © 1965 IEEE*)

$\phi_n^{(x)}$ of the x array will be located for the y array at

$$\phi_n^{(y)} = \tan^{-1}(\tau\tan\phi_n^{(x)}) \tag{95}$$

Similarly, an observation at $\phi^{(u)}$ on the circle of radius $\sin\theta^{(u)}$ in the u plane will be on the ellipse with major axis $2\sin\theta^{(u)}$ and axial ratio τ in the v plane at angle

$$\phi^{(v)} = \tan^{-1}(\tau^{-1}\tan\phi^{(u)}) \tag{96}$$

All of these are shown in Fig. 12, and also Fig. 13 for $\tau = 3, 7$, and 10. A few examples will be given in later in this section, under "Circular Arrays." This technique can also be applied to aperture antennas. In particular the Taylor distribution for a circular aperture [99, 43, 45] can be extended to that for an elliptical aperture [66].
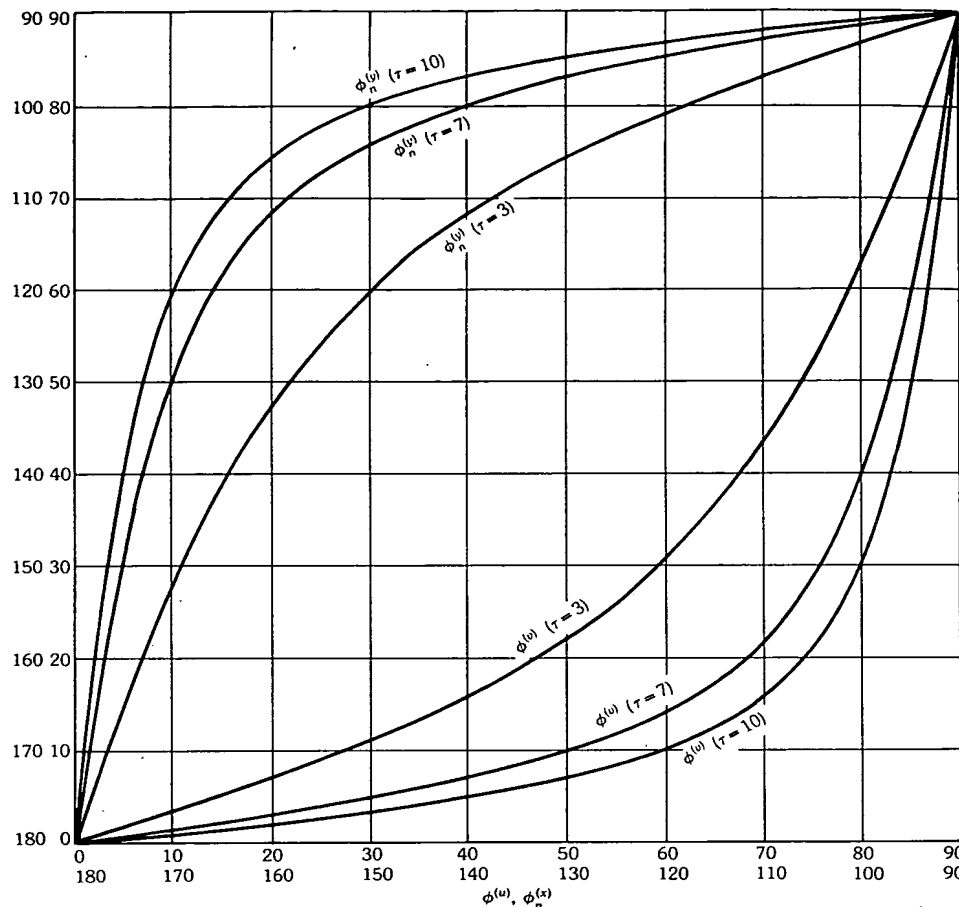
Fig. 13. Transformation of the angular position $\phi_n^{(x)}$ of the nth element of the x array to that of the y array, $\phi_n^{(y)}$, for various axial ratios τ; also, transformations of the observation angle $\phi^{(u)}$ in the u plane to that in the v plane, $\phi^{(v)}$, for various values of τ. (*After Lo and Hsuan [66], © 1965 IEEE*)

Beam and Pattern Distortion Due to Scanning

It is well known that the beam broadens and the pattern distorts in the $\theta\phi$ space as the beam scans away from the broadside direction [28]. However, if the pattern is presented in the u space, the beam scanning due to progressive phase shift as in (62) results only in a translation of the origin of the u space, leaving the beam and the pattern unchanged. The so-called distortion is really a result of the nonlinear-functional relationship between (θ, ϕ) and $\mathbf{u} - \mathbf{u}_0$. An understanding of this relationship is therefore important for determining the distortion, no matter which array is considered.

Consider a hemisphere of unit radius as shown in Fig. 14. A point on the sphere
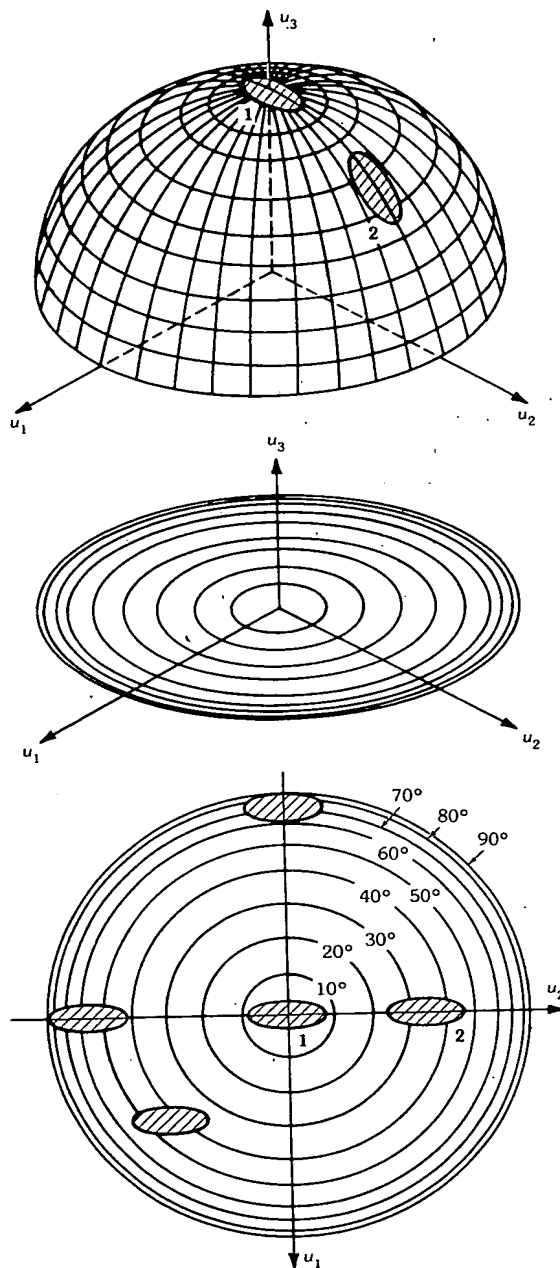
Fig. 14. Beam and pattern distortion as the beam scans away from the polar axis, a result from the nonlinear projection of the u_1u_2 plane on the sphere (the beam shape in the u_1u_2 plane remains unchanged as the beam scans).

with coordinates $(1, \theta, \phi)$ when projected on the $u_1 u_2$ plane will have the Cartesian coordinates $(u_1, u_2) = (\sin \theta \cos \phi, \sin \theta \sin \phi)$. To find how a beam (or pattern) appears on the sphere, it need only project the beam contour lines in the $u_1 u_2$ plane onto the spherical surface. One can even construct a three-dimensional pattern model by making the radial length in the $u_1 u_2$ plane proportional to the level of the contour in that direction.

Suppose in the broadside direction the beam cross section at a certain level looks like the cross-hatched region 1 at the bottom of Fig. 14. If this beam is scanned to $\theta = 33°$ and $\phi = 90°$ by a progressive phase shift, the origin of the $u_1 u_2$ plane will be moved by $\sin 33°$ in the $-u_2$ direction, or the beam is moved by $\sin 33°$ along the $+u_2$ direction as shown by region 2 in the figure (with *no* distortion). However, when beam 2 is projected on the sphere, the width along the ϕ direction remains unchanged but that along the θ direction is widened. Since the azimuthal angle of the sphere is the same as that of the $u_1 u_2$ coordinate system, there is no distortion in the ϕ direction. The distortion is therefore due to $\sin \theta$ only.

It is somewhat awkward to make projections from a plane onto a sphere. Instead, one can project latitude circles of the sphere on the $u_1 u_2$ plane, or simply draw a series of concentric circles with radius equal to $\sin \theta$ as shown at the bottom of Fig. 14. If the circles are marked with their corresponding values of θ, one obtains a set of nonlinear scales which can measure any beam distortion due to scan simply by moving the same beam contour structure to the desired scan angle (θ_0, ϕ_0) in this set of scales.

One can also compute the beam broadening from the following formula:

$$\sin \Delta\theta_p = \sin(\theta_0 + \Delta\theta_p') - \sin \theta_0 = 2\cos(\theta_0 + \Delta\theta_p'/2)\sin(\Delta\theta_p'/2) \qquad (97)$$

where

$\Delta\theta_p =$ the polar-angular position of a point at the p-dB level of the beam when the beam is in the broadside direction

$\Delta\theta_p' + \theta_0 =$ the polar-angular position of the p-dB level point of the beam when it is scanned to θ_0

Once $\Delta\theta_p'$ is found for $\Delta\theta_p$ and θ_0 the amount of beam broadening is determined. For *narrow* beams the above formula can be approximated as

$$\Delta\theta_p'/\Delta\theta_p \cong \sec\theta_0$$

in particular, for half-power

$$\Delta\theta_{HP}' = \Delta\theta_{HP}/\cos\theta_0 \qquad (98)$$

which is the well-known result; namely, the half-power beamwidth broadens according to the cosine of the scan angle from the broadside direction.

Linear Transformations on Excitations

For simplicity, consider a linear array of N elements at $z = z_1, z_2, \ldots, z_N$ (in wavelengths) and with excitations $I_1, I_2, \ldots, I_N$, respectively. Consider further a nonsingular matrix $\mathbf{A}$ and let

$$\mathbf{I}' = \mathbf{A}^{-1}\mathbf{I} \quad \text{or} \quad \mathbf{I} = \mathbf{A}\mathbf{I}' \tag{99}$$

where $\mathbf{I}$ is the column vector with elements $I_1, I_2, \ldots, I_N$ and $\mathbf{I}'$ is another column vector, with elements $I_1', I_2', \ldots, I_N'$. Then the pattern of the array can be written as

$$
\begin{aligned}
f(\theta) &= \sum_n^N I_n e^{j\psi_n} = \mathbf{V}'\mathbf{I} = \mathbf{V}'\mathbf{A}\mathbf{I}' \\
&= \mathbf{V}'(\mathbf{A}_1, \mathbf{A}_2, \ldots, \mathbf{A}_N)\mathbf{I}' \\
&= \mathbf{V}'\mathbf{A}_1 I_1' + \mathbf{V}'\mathbf{A}_2 I_2' + \cdots + \mathbf{V}'\mathbf{A}_N I_N' \\
&= F_1(\theta)I_1' + F_2(\theta)I_2' + \cdots + F_N(\theta)I_N'
\end{aligned}
\tag{100}
$$

where the superscript t denotes the transpose, and

$$\mathbf{V}' = (e^{j\psi_1}, e^{j\psi_2}, \ldots, e^{j\psi_N}) \tag{101}$$

$$\psi_n = 2\pi z_n \cos\theta \tag{102}$$

$\mathbf{A}_1, \mathbf{A}_2, \ldots, \mathbf{A}_N$ are the first, second, $\ldots$, and Nth *columns* of matrix $\mathbf{A}$

$$F_n(\theta) = \mathbf{V}'\mathbf{A}_n = \sum_m^N A_{mn} e^{j\psi_m} \tag{103}$$

Equation 103 states that $F_n(\theta)$ is the pattern of an array with excitations $A_{1n}, A_{2n}, \ldots, A_{Nn}$, and (100) states that the pattern of the array with excitations $I_1, I_2, \ldots, I_N$ is the sum of $F_1(\theta), F_2(\theta), \ldots, F_N(\theta)$ weighed by $I_1', I_2', \ldots, I_N'$, respectively. In other words, the pattern of an array with excitations $\{I_n\}$ can be expressed in terms of the patterns associated with some other, say canonical, excitations. An interesting application is given below.

Consider a linear uniformly spaced array of N elements with interelement spacing d (in wavelengths) and excitations $I_1, I_2, \ldots, I_N$. Let

$$\mathbf{A} = \begin{bmatrix}
1 & 1 & 1 & 1 & \cdots & 1 \\
1 & e^{-j2\pi/N} & e^{-j4\pi/N} & e^{-j6\pi/N} & \cdots & e^{-j2\pi(N-1)/N} \\
1 & e^{-j4\pi/N} & e^{-j8\pi/N} & e^{-j12\pi/N} & \cdots & e^{-j4\pi(N-1)/N} \\
\vdots & \vdots & \vdots & \vdots & & \vdots \\
1 & e^{-j2\pi(N-1)/N} & e^{-j4\pi(N-1)/N} & e^{-j6\pi(N-1)/N} & \cdots & e^{-j2\pi(N-1)^2/N}
\end{bmatrix} \tag{104}$$

Then

$$F(\theta) = \frac{1}{N} \sum_{n}^{N} I_n e^{j\psi_n} = I_1' F_1(\theta) + I_2' F_2(\theta) + \cdots + I_N' F_N(\theta) \tag{105}$$

where the factor $1/N$ has been added for convenience, and

$$F_1(\theta) = \mathbf{V}' \mathbf{A}_1 = \frac{1}{N} \sum_{n=0}^{N-1} e^{j2\pi nd \cos \theta} = \frac{1}{N} \frac{\sin(N\psi/2)}{\sin(\psi/2)} \tag{106}$$

$$F_2(\theta) = \mathbf{V}' \mathbf{A}_2 = \frac{1}{N} \sum_{n=0}^{N-1} e^{j2\pi nd(\cos \theta - 1/Nd)} = \frac{1}{N} \frac{\sin[N(\psi - \psi^{(1)})/2]}{\sin[(\psi - \psi^{(1)})/2]} \tag{107}$$

$$F_3(\theta) = \mathbf{V}' \mathbf{A}_3 = \frac{1}{N} \sum_{n=0}^{N-1} e^{j2\pi nd(\cos \theta - 2/Nd)} = \frac{1}{N} \frac{\sin[N(\psi - \psi^{(2)})/2]}{\sin[(\psi - \psi^{(2)})/2]} \tag{108}$$

$$F_N(\theta) = \mathbf{V}' \mathbf{A}_N = \frac{1}{N} \sum_{n=0}^{N-1} e^{j2\pi nd[\cos \theta - (N-1)/Nd]} = \frac{1}{N} \frac{\sin[N(\psi - \psi^{(N-1)})/2]}{\sin[(\psi - \psi^{(N-1)})/2]} \tag{109}$$

$$\psi = 2\pi d \cos \theta$$
$$\psi^{(m)} = 2\pi m/N$$

Equations 106–109 are simply uniform array patterns with a progressive phase shift such that the main beam appears at

$$\psi = \psi^{(m)} \quad \text{or} \quad \theta = \cos^{-1}(m/Nd) \tag{110}$$

The set of functions $\{F_n(\theta)\}$ has the following interesting properties:

(a)   All their nulls coincide.

(b)   Let the beam maximum of $F_n(\theta)$ be at $\theta_{\max}^{(n)}$. Then at this angle all other members of $\{F_n(\theta)\}$ vanish, i.e., $F_p(\theta_{\max}^{(n)}) = 1$ as $p = n$, and 0 as $p \neq n$. This result has been used for pattern synthesis [117, 118]. From (105)

$$F(\theta_{\max}^{(n)}) = I_n', \qquad n = 1, 2, \ldots, N \tag{111}$$

Thus let the desired pattern be sampled at equispaced points in $\psi_{\max}^{(n)} = 2\pi d \cos \theta_{\max}^{(n)}$, for $n = 1, 2, \ldots, N$; then (111) states that these samples are simply $\{I_n'\}$ and from (99) one determines the required excitations:

$$\mathbf{I} = \mathbf{A} \mathbf{I}' = \mathbf{A} F(\theta_{\max}^{(n)}) \tag{112}$$

Of course, the synthesizing pattern agrees with the desired pattern exactly *only* at this set of points. Since in general there is some arbitrariness in selecting this set (such as the starting point, sampling rate, and sampling numbers—see "An Example," below), the solution is not unique. One should in general try a few possibilities, bearing in mind that the sampling rate depends on d, sampling number is the number of elements N, and array size is Nd (in wavelengths). For close agreement with the desired pattern, a high sampling rate and a large sampling

number are required, resulting in closely spaced elements. In that case impractical unstable solutions, as for the so-called superdirectivity problem, may occur (see Section 7 for more discussion).

To recapitulate, the philosophy of this method can be viewed as a linear transformation from the N degrees of freedom of $\{I_n\}$ to another N degrees of freedom of $\{I'_n\}$ as shown in (99). Therefore its application can be very general. For example, $F(\theta)$ can also be expressed in terms of a *set* of patterns, each associated with a *uniform aperture* excitation function $f_n(z)$ along z:

$$I'_n f_n(z) = I'_n e^{j2\pi z \cos\theta_n}, \qquad n = 1, 2, \ldots, N \tag{113}$$

The array so synthesized will be an aperture antenna. Mathematically speaking, the difference between this and the discrete array is rather trivial, mainly in the choice of "basis" functions only.

An Example—Fig. 15 shows an example considered by Balanis [4] in which the desired pattern is

$$F_d(\theta) = \begin{cases} 1 & \text{if } \pi/4 \leqq \theta \leqq 3\pi/4 \\ 0 & \text{elsewhere} \end{cases}$$

It is synthesized first by a linear array with 11 elements and $d = 1/2$, then by a continuous aperture distribution of length 5λ, both sampled at 11 points as shown in Table 2. Fig. 15b shows seven nonzero composing functions $\{F_n(\theta)\}$ and their sum.

Another Example—Fig. 16 shows two among many possible solutions for synthesizing a $\csc\theta$ pattern with a linear array of 21 elements and spacing $d = 1/2$. The first solution is obtained by sampling $\csc\theta$ such that the synthesizing array pattern is zero at $\theta = 0°$. The second solution is obtained by choosing the sampling points such that the synthesizing pattern is 0.45 at $\theta = 0°$. It is seen that the latter gives a closer solution to the desired pattern $\csc\theta$ over the useful region.

Circular Arrays

First consider a circular array of N elements uniformly excited and uniformly distributed over a circle of radius a (in wavelengths). Then the nth element will be located at

$$\mathbf{r}_n = \hat{x}a\cos\phi_n + \hat{y}a\sin\phi_n \tag{114}$$

where

$$\phi_n = 2\pi n/N, \qquad n = 1, 2, \ldots, N \tag{115}$$

Then the pattern function is
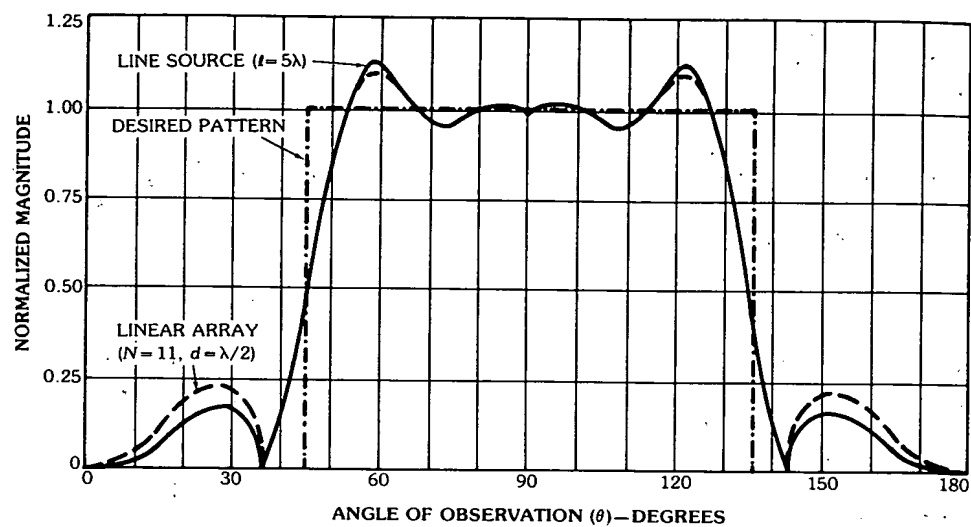
a
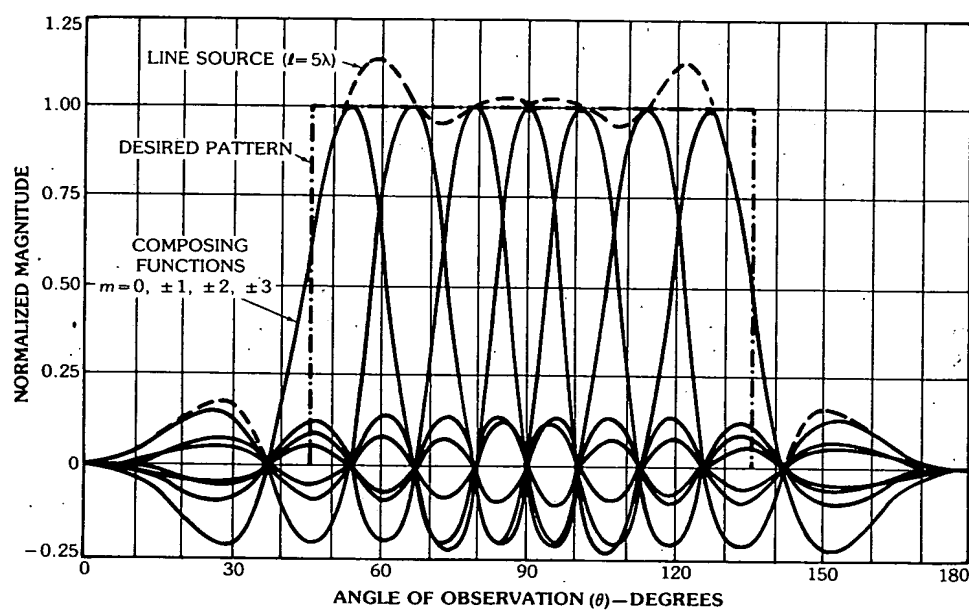
b

Fig. 15. Desired and synthesized patterns and composing functions, using Woodward's method [117, 4] for a linear array with 11 elements at $\lambda/2$ spacing and a line aperture 5 wavelengths long. (*a*) Normalized amplitude patterns. (*b*) Composing functions for line source ($l = 5\lambda$). (*After Balanis [4], © 1982, Harper & Row, Publishers, Inc.; reprinted by permission of the publisher*)

Table 2. Pattern Synthesized at $\{\theta_m\}$

m	θ_m	$F(\theta_m)$	m	θ_m	$F(\theta_m)$
0	90°	1			
1	78.46°	1	−1	101.54°	1
2	66.42°	1	−2	113.58°	1
3	53.13°	1	−3	126.87°	1
4	36.87°	0	−4	143.13°	0
5	0°	0	−5	180°	0

(After Balanis [4], © 1982 Harper & Row, Publishers, Inc., reprinted by permission of the publisher)

Fig. 16. Two possible synthesized patterns for the $\csc\theta$ in dashed line. (*a*) With a value of 0 at $\theta = 0°$. (*b*) With a value of 0.45 at $\theta = 0°$. (*After Woodward and Lawson [119]*, © *British Crown Copyright 1948*)

$$F(\theta,\phi) = \frac{1}{N}\sum_{n=1}^{N} e^{j2\pi r_n \cdot \mathbf{u}} = \frac{1}{N}\sum_{n=1}^{N} e^{j2\pi a \sin\theta \cos(\phi-\phi_n)}$$

$$= \sum_{m=-\infty}^{\infty} J_{mN}(2\pi a \sin\theta)\, e^{jmN(\pi/2-\phi)} \qquad (116)$$

$$\cong J_0(2\pi a \sin\theta) \qquad \text{if } 2\pi a/N \ll 1 \qquad (117)$$

where use has been made of the expansion

$$e^{jz\cos\phi} = \sum_{m=-\infty}^{\infty} (j)^m J_m(z) e^{jm\phi} \tag{118}$$

and

$$\frac{1}{N} \sum_{n=1}^{N} e^{j2\pi mn/N} = \begin{cases} 1 & \text{if } m = Np, \, p = 0, \pm 1, \pm 2, \ldots \\ 0 & \text{otherwise} \end{cases} \tag{119}$$

The last approximation in (117) applies if $N \gg 2\pi a$, i.e., if the circumferential distance between any two adjacent elements, $2\pi a/N$, is sufficiently less than λ. In that case the pattern varies with $\sin\theta$ according to the $J_0(\cdot)$ function and independent of ϕ, as shown in Fig. 17a, where $|J_0(\cdot)|$ is plotted. When the above

a

b
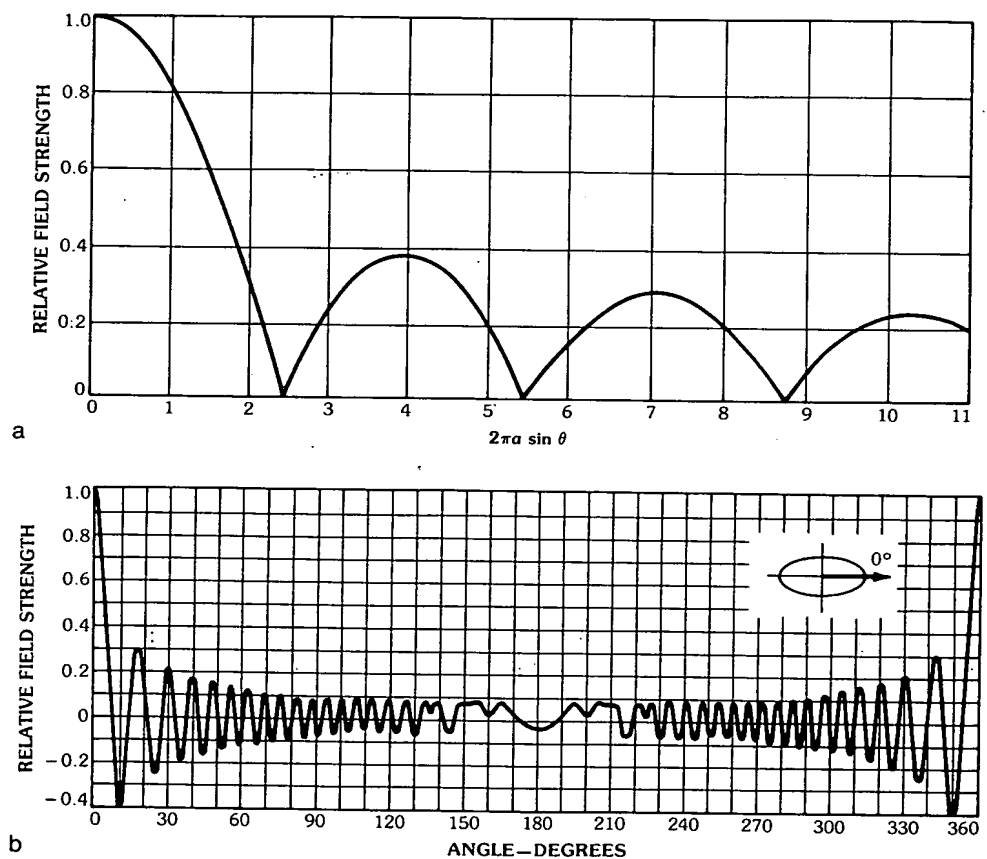
Fig. 17. Patterns of uniformly excited circular and elliptical arrays. (a) Pattern of a circular array with radius a and small element spacing. (b) Pattern of a cophasal elliptical array with major axis $2a = 20\lambda$, axial ratio $\tau = 3$, and main beam at $\phi_0 = 0°$. (c) Same as (b) but with $\phi_0 = 30°$. (d) Same as (b) but with $\phi_0 = 60°$. (e) Same as (b) but with $\phi_0 = 90°$. (After Lo and Hsuan [66], © 1965 IEEE)
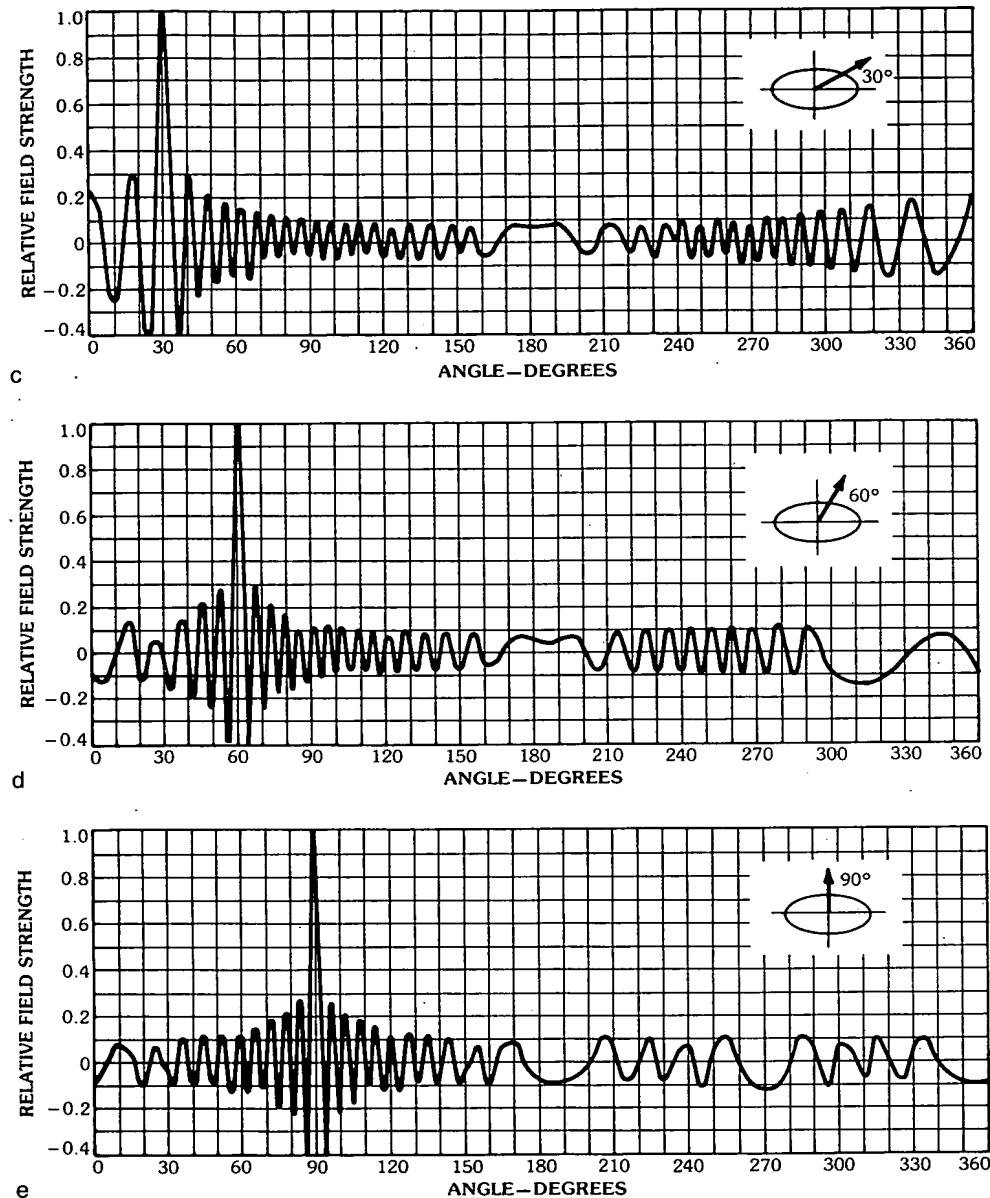
Fig. 17, *continued.*

condition is not satisfied, higher-order terms become significant and the pattern varies with ϕ. Using the transform discussed earlier in this section, under "Transformation between Circular and Elliptical Arrays," one can readily find the patterns of a uniformly excited cophasal elliptical array with major axis $2a = 20\lambda$,

axial ratio $= \tau = 3$, and main beam in $\phi_0 = 0°$, $30°$, $60°$, and $90°$ directions as shown in Figs. 17b to 17e.

Cophasal Uniform Circular Arrays

For an array cophasal in the (θ_0, ϕ_0) direction the nth-element excitation is

$$I_n = e^{j2\pi r_n \cdot \mathbf{u}_0} \tag{120}$$

where $\mathbf{u}_0 = \hat{\mathbf{x}} \sin \theta_0 \cos \phi_0 + \hat{\mathbf{y}} \sin \theta_0 \sin \phi_0$. Then

$$F(\theta, \phi) = \frac{1}{N} \sum_{n=1}^{N} e^{j2\pi r_n \cdot (\hat{\mathbf{u}} - \mathbf{u}_0)} \tag{121}$$

Using (114) and the geometry in Fig. 18, one finds that

$$\mathbf{r}_n \cdot (\hat{\mathbf{u}} - \mathbf{u}_0) = a|\mathbf{u}_{xy} - \hat{\mathbf{u}}_0| \cos(\xi - \phi_n) \tag{122}$$

where

$\mathbf{u}_{xy} = \hat{\mathbf{u}} \cdot (\hat{\mathbf{x}}\hat{\mathbf{x}} + \hat{\mathbf{y}}\hat{\mathbf{y}}) = $ projection of $\tilde{\hat{\mathbf{u}}}$ on the xy plane

$\xi = $ the azimuthal angle of $(\mathbf{u}_{xy} - \mathbf{u}_0) = \cos^{-1} \dfrac{\hat{\mathbf{x}} \cdot (\hat{\mathbf{u}} - \mathbf{u}_0)}{|\mathbf{u}_{xy} - \mathbf{u}_0|}$

$$= \cos^{-1} \left\{ \frac{\sin \theta \cos \phi - \sin \theta_0 \cos \phi_0}{[(\sin \theta \cos \phi - \sin \theta_0 \cos \phi_0)^2 + (\sin \theta \sin \phi - \sin \theta_0 \sin \phi_0)^2]^{1/2}} \right\} \tag{123}$$

Inserting (122) in (121) and comparing it with (116), nothing is really changed except that $|\mathbf{u}_{xy} - \mathbf{u}_0|$ replaces $\sin \theta$, and ξ replaces ϕ. Therefore
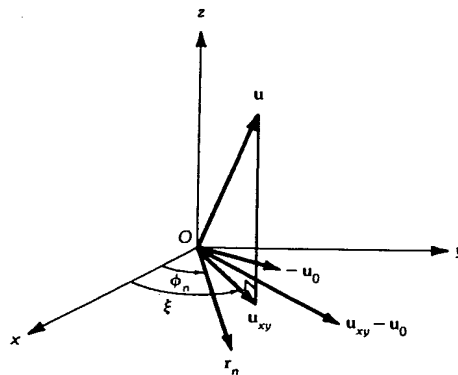
Fig. 18. Geometrical relation for cophasal circular array formulas (123)–(125).

$$F(\theta, \phi) = \sum_{m=-\infty}^{\infty} J_{mN}(2\pi a |\mathbf{u}_{xy} - \mathbf{u}_0|) e^{jmN(\pi/2 - \xi)}$$

$$\cong J_0(2\pi a |\mathbf{u}_{xy} - \mathbf{u}_0|), \qquad \text{if } 2\pi a/N \ll 1 \tag{124}$$

where ξ is given by (123) and

$$|\mathbf{u}_{xy} - \mathbf{u}_0| = [(\sin\theta\cos\phi - \sin\theta_0\cos\phi_0)^2$$
$$+ (\sin\theta\sin\phi - \sin\theta_0\sin\phi_0)^2]^{1/2} \tag{125}$$

Nonuniformly Excited Circular Arrays

A nonuniformly excited circular array can be analyzed in terms of uniformly excited circular arrays by applying a linear transformation on excitation. For example let $\{I_n\}$ be any given excitation. Now applying the transformation

$$\mathbf{I}' = \mathbf{A}^{-1}\mathbf{I} \quad \text{or} \quad \mathbf{I} = \mathbf{A}\mathbf{I}' \tag{126}$$

where

$$\mathbf{A} = \begin{bmatrix} 1 & e^{j2\pi/N} & e^{j4\pi/N} & \cdots & e^{j2\pi(N-1)/N} \\ 1 & e^{j4\pi/N} & e^{j8\pi/N} & \cdots & e^{j4\pi(N-1)/N} \\ \cdot & \cdot & & \cdots & \cdot \\ 1 & e^{j2\pi N/N} & e^{j4\pi N/N} & \cdots & e^{j2\pi(N-1)N/N} \end{bmatrix}$$

Then, similar to (105) through (109),

$$F(\theta, \phi) = \frac{1}{N} \sum_{n=1}^{N} I_n e^{j2\pi \mathbf{r}_n \cdot \mathbf{\hat{u}}}$$

$$= I_1' F_1(\theta, \phi) + I_2' F_2(\theta, \phi) + \cdots + I_N' F_N(\theta, \phi) \tag{127}$$

where

$$F_1(\theta, \phi) = \mathbf{V}^t \mathbf{A}_1 = \frac{1}{N} \sum_{n=1}^{N} e^{j2\pi a \sin\theta \cos(\phi - \phi_n)}$$

$$= \sum_{m=-\infty}^{\infty} J_{mN}(2\pi a \sin\theta) e^{jmN(\pi/2 - \phi)} \cong J_0(2\pi a \sin\theta) \tag{128}$$

$$F_2(\theta, \phi) = \mathbf{V}^t \mathbf{A}_2 = \frac{1}{N} \sum_{n=1}^{N} e^{j2\pi[a \sin\theta \cos(\phi - \phi_n) + (n/N)]}$$

$$= \sum_{m=-\infty}^{\infty} J_{mN+1}(2\pi a \sin\theta) e^{j(mN+1)(\pi/2 + \phi)}$$

$$\cong J_1(2\pi a \sin\theta) e^{j(\pi/2 + \phi)} \tag{129}$$

$$F_3(\theta, \phi) = \mathbf{V}^t \mathbf{A}_3 = \frac{1}{N} \sum_{n=1}^{N} e^{j2\pi[a\sin\theta\cos(\phi - \phi_m) + (2n/N)]}$$

$$= \sum_{m=-\infty}^{\infty} J_{mN+2}(2\pi a\sin\theta)\, e^{j(mN+2)(\pi/2+\phi)}\, e^{j4\pi/N}$$

$$\cong J_2(2\pi a\sin\theta)\, e^{j2(\pi/2+\phi)}$$

$$F_N(\theta, \phi) = \mathbf{V}^t \mathbf{A}_N = \sum_{m=-\infty}^{\infty} J_{mN+N-1}(2\pi a\sin\theta)\, e^{j(mN+N-1)(\pi/2+\phi)}$$

$$\cong J_{N-1}(2\pi a\sin\theta)\, e^{j(N-1)(\pi/2+\phi)} \tag{130}$$

As before, all the approximate solutions are valid only if $2\pi a/N \ll 1$. Similar to the linear array in (105), the nonuniform excitation is now expressed in terms of the uniform excitation given by (126). This transformation is known as the method of symmetrical components in power engineering for analyzing an unbalanced polyphase system in terms of the balanced ones and also multiple-arm spiral antennas [122].

Elliptical Arrays With Nonuniform Excitations

By applying the linear transformations (95) and (96) to each of the $\{F_n(\theta, \phi)\}$ of (127) one can then analyze an elliptical array with nonuniform excitation in terms of that with *uniformly* excited *circular* arrays. This case serves as an interesting example for applying simultaneously both transformations, one for the geometry and the other for the excitations. If the minor axis of the ellipse approaches zero, the transformation will give a closed-form solution for an *unequally* spaced *nonuniformly* excited linear array.

5. Planar Arrays

When a planar array has a separable excitation, say in x and y, an analysis can be made simply by regarding each row (or column) subarray as a single element and then considering all rows (or columns) to form a "linear" column (or row) array. In so doing, the theory for linear arrays applies. For example, the pattern function of a uniform rectangular array cophasal in the (θ_0, ϕ_0) direction is given by

$$F(\theta, \phi) = \frac{1}{M} \frac{\sin(M\psi_x/2)}{\sin(\psi_x/2)} \frac{1}{N} \frac{\sin(N\psi_y/2)}{\sin(\psi_y/2)} \tag{131}$$

where M and N are the number of elements along the x and y axes, respectively, and

$$\psi_x = 2\pi d_x(\sin\theta\cos\phi - \sin\theta_0\cos\phi_0)$$

$$\psi_y = 2\pi d_y(\sin\theta\sin\phi - \sin\theta_0\sin\phi_0)$$

and d_x and d_y are interelement spacings (in wavelengths) along the x and y axes, respectively.

A three-dimensional pattern for a 5×5 element array with $d_x = d_y = \frac{1}{2}$ and $\theta_0 = 0°$ is shown in Fig. 19. The first side lobe level in the $\phi = 0°$ and $90°$ planes is approximately -12 dB (as compared with -13.2 dB for a uniformly excited linear aperture) while that in the $\phi = 45°$ and $135°$ planes is -24 dB. Fig. 20 shows the pattern for the same array but with $d_x = d_y = 1$. In this case four grating lobes appear at $\phi = 0°$, $90°$, $180°$, and $270°$ in the $\theta = 90°$ plane.

For nonseparable excitations the pattern function in general cannot be expressed in terms of a polynomial, and the pattern may have to be evaluated numerically.

Two-Dimensional Dolph-Chebyshev Arrays

One of the interesting problems is how to design a planar array which will have side lobes of equal level in the three-dimensional pattern. Evidently this cannot be achieved with two separable Dolph-Chebyshev excitations along the x and y directions as in the method discussed above, because in any plane other than $\phi = 0°$ and $90°$, the side lobes will not have the same level. Baklanov [123] and Tseng and Cheng [107] have given a simple but interesting solution to this problem. In essence, they introduced a transformation which generates from a linear Dolph-Chebyshev array a planar array with a pattern having equal side lobe levels
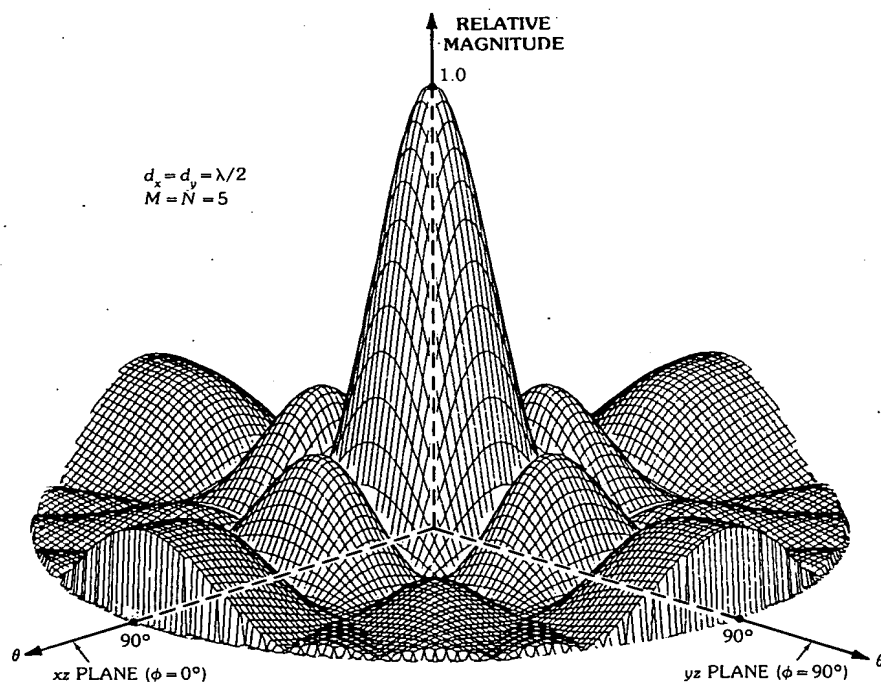
Fig. 19. Three-dimensional antenna pattern of a uniform planar array of isotropic elements with spacing $d_x = d_y = \lambda/2$. (After Balanis [4], © 1982, Harper & Row, Publishers, Inc.; reprinted by permission of the publisher)
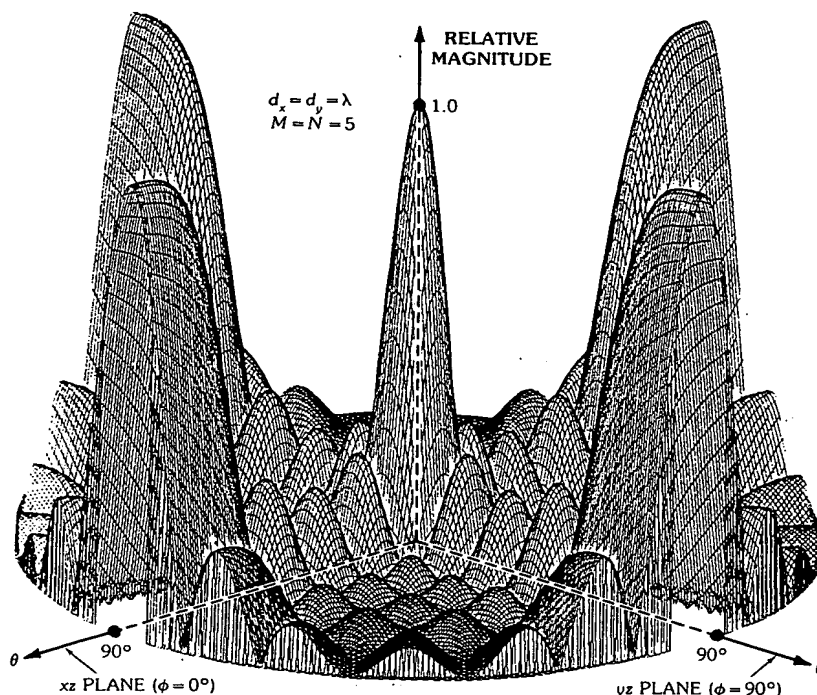
Fig. 20. Three-dimensional antenna pattern of a uniform planar array of isotropic elements with spacing $d_x = d_y = \lambda$. (*After Balanis [4], © 1982, Harper & Row, Publishers, Inc.; reprinted by permission of the publisher*)

in *every* cut of the ϕ = constant plane. Because of the nature of the transformation, however, the side lobe peaks do not occur at the same polar angle θ in all cuts, thus forming the so-called ringlike side lobes (i.e., not in concentric circles) in the three-dimensional patterns [28]. This, as will be seen later, is simply a result of the distortion introduced by the transformation in the u plane.

First, for simplicity, consider a square array in the xy plane with $2N \times 2N$ elements and interelement spacing d (in wavelengths) along both x and y directions. (If the unit cell is not a square, i.e., $d_x \neq d_y$, the pattern can be deduced from that of the square one simply by changing the scale of one of the u axes, not the magnitude of the pattern function as discussed in Section 4.) Let the center of the array be the origin and assume the excitation to be symmetrical with respect to both the x and y axes. Further let the excitation of the element at $x = md$ and $y = nd$ be I_{mn}, for $m, n = -N, \ldots, N$. Then

$$I_{mn} = I_{-m,n} = I_{m,-n} = I_{-m,-n} \tag{132}$$

and the pattern function

$$F(\theta,\phi) = \sum_{m,n=1}^{N} I_{mn} \cos[(2m-1)\cos^{-1}\alpha] \cos[(2n-1)\cos^{-1}\beta]$$

$$= \sum_{m,n=1}^{N} I_{mn} T_{2m-1}(\alpha) T_{2n-1}(\beta) \tag{133}$$

where

$$\cos^{-1}\alpha = u_1 = \pi d \sin\theta \cos\phi \tag{134}$$

$$\cos^{-1}\beta = u_2 = \pi d \sin\theta \sin\phi \tag{135}$$

$T_m(\cdot)$ = the Chebyshev polynomial of degree m

Equation 133 states that $F(\theta,\phi)$ is a polynomial in α and β; thus one can write

$$F(\theta,\phi) = \sum_{m,n=1}^{N} A_{mn} \alpha^{2m-1} \beta^{2n-1} \tag{136}$$

If I_{mn} can be chosen such that

$$A_{mn} = \delta_{mn} A_{mm} \tag{137}$$

i.e., all $A_{mn} = 0$ if $m \neq n$, then

$$F(\theta,\phi) = \sum_{m=1}^{N} A_{mm}(\alpha\beta)^{2m-1} \tag{138}$$

which is a polynomial of degree $2N-1$ in $\alpha\beta$. Let us equate this polynomial to the Chebyshev polynomial

$$F(\theta,\phi) = \sum_{m=1}^{N} A_{mm}(\alpha\beta)^{2m-1} = T_{2N-1}(w_0\alpha\beta) \tag{139}$$

with

$$T_{2N-1}(w_0) = R \tag{140}$$

Then, for every plane cut ϕ = constant, $\alpha\beta$ is a function of θ only; thus $F(\theta,\phi)$ follows a Chebyshev pattern in θ. As $\theta = 0$, $\alpha\beta = 1$, and, therefore,

$$F(0,\phi) = T_{2N-1}(w_0) = R \tag{141}$$

which is the main-beam magnitude with the side lobe level being 1. To recapitulate, the key point in this method is to reduce (136) to (139) by imposing (137). The former is a general planar array pattern while the latter is that of a linear array. One may thus consider this process as one which generates a two-dimensional

Dolph-Chebyshev pattern from a one-dimensional one, $T_{2n-1}(z)$, by using the transformation

$$z = w_0 \alpha \beta = w_0 \cos u_1 \cos u_2 \tag{142}$$

Beam Scanning—From the discussion for the one-dimensional case, if the main beam is scanned to (θ_0, ϕ_0), it is sufficient only to replace the definitions of u_1 and u_2 of (134) and (135) in the above analysis by

$$\cos^{-1}\alpha = u_1 - u_{01} = \pi d (\sin\theta \cos\phi - \sin\theta_0 \cos\phi_0)$$
$$\cos^{-1}\beta = u_2 - u_{01} = \pi d (\sin\theta \sin\phi - \sin\theta_0 \cos\phi_0)$$

Odd Number of Elements—From the basic principle given above, it is also evident that the method can also be applied to an array with $(2N + 1) \times (2N + 1)$ elements.

Symmetry—As a result of (137) one will find an additional symmetry of the excitation to those shown in (132):

$$I_{mn} = I_{nm} \tag{143}$$

Thus for such an array one needs to determine only $N(N + 1)/2$ excitation currents for an array with $2N \times 2N$ elements and $(N + 1)(N + 2)/2$ excitation currents for an array with $(2N + 1) \times (2N + 1)$ elements.

A Few Major Results*

(a) For an array with $L \times L$ elements, the excitation for the mnth element as determined from (133), (138), and (139) can be reduced to the following form:

$$I_{mn} = \left(\frac{4}{L}\right)^2 \sum_{p=1}^{N} \sum_{q=1}^{N} T_{L-1}\left(w_0 \cos p - \frac{1}{2}\frac{\pi}{L}\cos q - \frac{1}{2}\frac{\pi}{L}\right)$$
$$\times \cos\left(\frac{2\pi}{L}m - \frac{1}{2}p - \frac{1}{2}\right)\cos\left(\frac{2\pi}{L}n - \frac{1}{2}q - \frac{1}{2}\right), \qquad \text{for } L = 2N \tag{144}$$

and

$$I_{mn} = \left(\frac{2}{L}\right)^2 \sum_{p=1}^{N+1} \sum_{q=1}^{N+1} \varepsilon_p \varepsilon_q T_{L-1}\{w_0 \cos[(p-1)\pi/L]\cos[(q-1)\pi/L]\}$$
$$\times \cos\left[\frac{2\pi}{L}(m-1)(p-1)\right]\cos\left[\frac{2\pi}{L}(n-1)(q-1)\right], \qquad \text{for } L = 2N + 1 \tag{145}$$

---

*These are taken from Tseng and Cheng [107].

where $w_0 = \cosh\left(\dfrac{1}{L-1}\cosh^{-1}R\right)$.

(b) Beamwidth $\Delta\theta_c$ at level c/R, or $20\log_{10}(R/c)$ dB below the main-beam maximum at (θ_0,ϕ_0). Let θ_c be the solution to the equation

$$\cosh\left(\frac{1}{L-1}\cosh^{-1}c\right) = w_c = w_0\cos u_{1c}\cos u_{2c}$$

where

$$u_{1c} = \pi d(\sin\theta_c - \sin\theta_0)\cos\phi_0$$
$$u_{2c} = \pi d(\sin\theta_c - \sin\theta_0)\sin\phi_0$$

Because of the nonlinearity in transformation (i.e., nonlinear distortion from the u plane to the $\theta\phi$ plane) the beamwidth at level c/R, as determined by θ_c in the above equations, varies with ϕ_0. In particular, if $\phi_0 = 0$,

$$\Delta\theta_c = \sin^{-1}\left[\sin\theta_0 + \frac{1}{\pi d}\cos^{-1}\left(\frac{w_c}{w_0}\right)\right]$$
$$- \sin^{-1}\left[\sin\theta_0 - \frac{1}{\pi d\cos\theta_0}\cos^{-1}\left(\frac{w_c}{w_0}\right)\right]$$
$$\cong 2\sin^{-1}\left[\frac{1}{\pi d\cos\theta_0}\cos^{-1}\left(\frac{w_c}{w_0}\right)\right], \qquad \text{when } L \text{ is large} \qquad (146)$$

If $\phi_0 = \pi/4$,

$$\Delta\theta_c = \sin^{-1}\left[\sin\theta_0 + \frac{\sqrt{2}}{\pi d}\cos^{-1}\left(\frac{w_c}{w_0}\right)\right] - \sin^{-1}\left[\sin\theta_0 - \frac{\sqrt{2}}{\pi d}\cos^{-1}\left(\frac{w_c}{w_0}\right)\right]$$
$$\cong 2\sin^{-1}\left(\frac{\sqrt{2}}{\pi d\cos\theta_0}\right)\cos^{-1}\left(\frac{w_c}{w_0}\right), \qquad \text{when } L \text{ is large} \qquad (147)$$

(c) Minimum number of elements. This is determined by the maximum permissible spacing d for a given array area so that no grating lobe will appear in a given scanning range. As discussed in Section 4, under "Beam and Pattern Distortion Due to Scanning," since there is no distortion in azimuthal angles in the transformation from the (θ,ϕ) plane to the u plane, one may expect that the maximum value of d depends only on the maximum scan angle of θ_0, designated by θ_M. Then

$$d \leqq \frac{1 - (1/\pi)\cos^{-1}(1/w_0)}{1 + \sin\theta_M} \qquad (148)$$

(d) Some numerical results for (c). Figs. 21 and 22 show the largest beamwidth $(\Delta\theta_c)_M$ at the 30-dB level below the main beam for maximum scanning angles $\theta_M =$
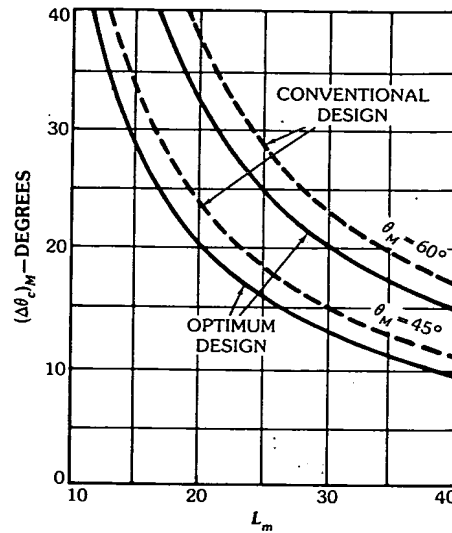
Fig. 21. Beamwidth versus minimum element number L_m on each side of a square array ($c/R = 0.03$, 30-dB side lobe level). (*After Tseng and Cheng [107], © 1968 IEEE*)
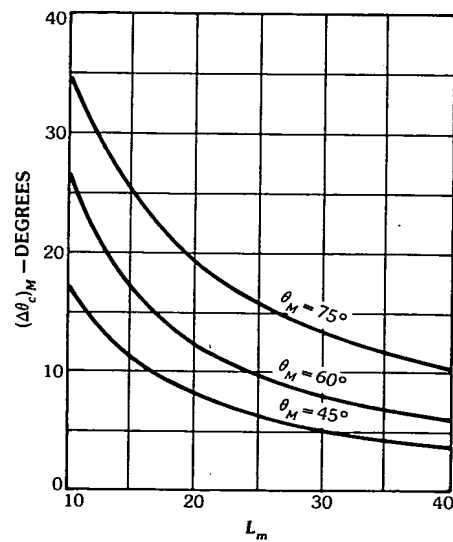
Fig. 22. Beamwidth versus minimum element number L_m on each side of a square array (optimum design: $c/R = 0.707$, 30-dB side lobe level). (*After Tseng and Cheng [107], © 1968 IEEE*)

60° and 45° and an array with minimum number of elements $L_m \times L_m$, or largest permissible spacing as given by (148). The design is for an equal side lobe level of -30 dB in all planes cutting through the main-beam maximum. Also shown for comparison is the beamwidth (in dashed curves) under the same condition but based on the conventional separable product of two Dolph-Chebyshev linear array designs. The beamwidth of the Baklanov-Tseng-Cheng design is always narrower than that of the conventional design, but the side lobes of the latter in planes other than the principal ones are lower. Fig. 22 shows the half-power beamwidth versus L_m for the same array condition as in Fig. 21. Fig. 23 shows the largest element spacing d_M permissible versus L for various scanning ranges $\theta_M = 45°$, $60°$, and $75°$ and for a -30-dB side lobe level. Directivity of this design may be higher or lower than that of the conventional design.

A Numerical Example—An array with 10×10 elements, spacing $d_x = 1/2$, $d_y = 3/4$, -20-dB side lobe level, and $\theta_0 = 0°$ has been considered by Elliott [28]. Table 3 shows the relative currents in all elements, and Figs. 24a through 24d show the patterns in four different planes $\phi = 0°$, $30°$, $60°$, and $90°$. It is seen that all side lobes have equal levels of -20 dB but are displaced along the θ axis. Since for this example $d_x \neq d_y$, the displacements are different in these planes. In fact the beamwidth is narrower in the $\phi = 90°$ plane than that in the $\phi = 0°$ plane because $d_y > d_x$. If $d_x = d_y$, the patterns in these two planes would be identical and the beamwidth would become the widest in the $\phi = 45°$ plane.
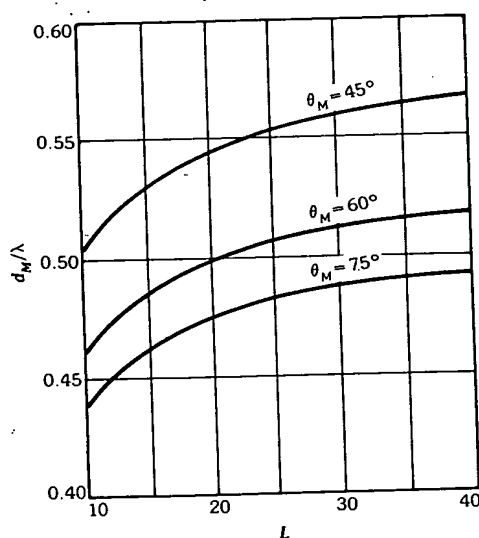
Fig. 23. Largest element spacing d_M (in wavelengths) versus L, the element number on each side of a square array, for nonappearance of grating lobes for a 30-dB side lobe level. (*After Tseng and Cheng [107], © 1968 IEEE*)

Table 3. Current Distributions for 10 × 10 Array to Give 20-dB Tseng-Cheng Pattern [28]

I_{mn}	20-dB Tseng-Cheng
I_{11}	0.773
$I_{21} = I_{12}$	0.569
$I_{31} = I_{13}$	0.796
$I_{41} = I_{14}$	0.029
$I_{51} = I_{15}$	1.000
I_{22}	0.946
$I_{32} = I_{23}$	0.119
$I_{42} = I_{24}$	0.618
$I_{52} = I_{25}$	0.667
I_{33}	0.486
$I_{43} = I_{34}$	0.777
$I_{53} = I_{35}$	0.286
I_{44}	0.387
$I_{54} = I_{45}$	0.071
I_{55}	0.008
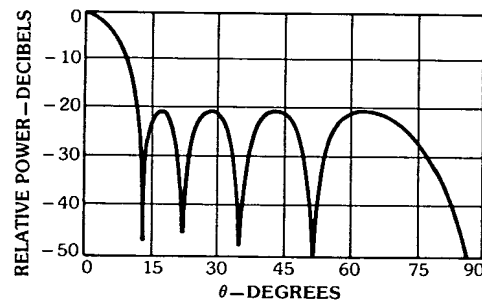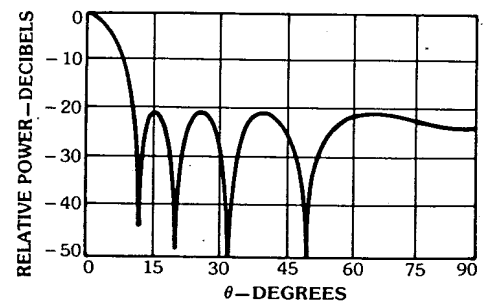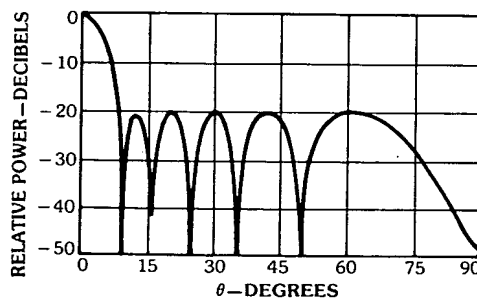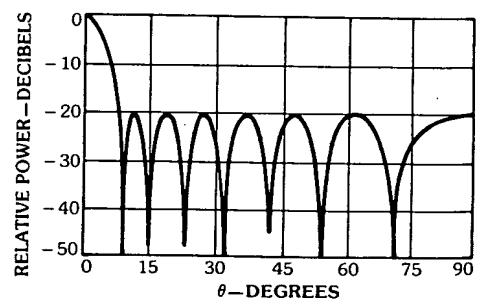
Fig. 24. Patterns in four ϕ cuts for a 10 × 10 rectangular Baklanov-Tseng-Cheng array with $d_x = 0.5\lambda$, $d_y = 0.75\lambda$, and side lobe level of 20 dB. (a) For $\phi = 0°$. (b) For $\phi = 30°$. (c) For $\phi = 60°$. (d) For $\phi = 90°$. (*After Tseng and Cheng*, Radio Science, *vol. 12, pp. 653–57*, © *American Geophysical Union*)

General Discussion of the Transformation

To see the distortion introduced by the transformation (142), a set of universal contour lines defined by

$$\cos u_1 \cos u_2 = c \quad \text{(constant)}$$

for various values of c from 0.01 to 1.00 are plotted in Fig. 25, with u_1 and u_2 defined by (134) and (135). Along the u_1 axis (i.e., $\phi = 0$) the pattern, as given by (139), is exactly that of a linear Dolph-Chebyshev array $T_{2N-1}(w_0\alpha)$ with $\alpha = \cos(\pi d_x \sin\theta)$. Along the u_2 axis the pattern is $T_{2N-1}(w_0\beta)$ with $\beta = \cos(\pi d_y \sin\theta)$. They are identical if $d_x = d_y$. (If $d_x \neq d_y$, only a linear change of the scale in u is needed.) For any $\phi = $ constant plane, the pattern is given by $T_{2N-1}(w_0 \cos u_1 \cos u_2)$, which is again the same as that of a linear Dolph-Chebyshev array except that the scale in $\sin\theta$ is changed, depending on
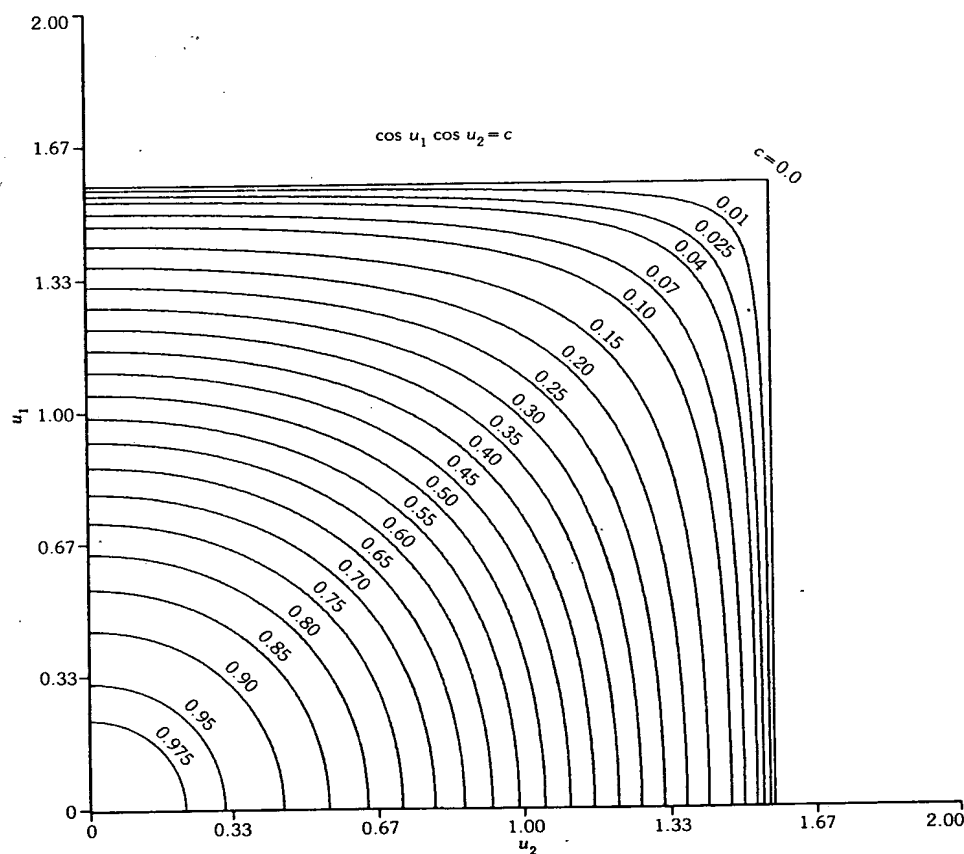
Fig. 25. Plots of $\cos u_1 \cos u_2 = c$ in the $u_1 u_2$ plane for various values of c. (*Prepared by Michael L. Oberhart*)

the value of ϕ. Fig. 25 shows exactly the dependence of this scale change on ϕ. (Note that the polar angle of any point (u_1, u_2) in the plane is simply ϕ.) As shown, the scale stretches to the largest extent at $\phi = 45°$. To find how this change is reflected in the $\theta\phi$ scale, one needs only to place an overlay on this figure as shown in Fig. 14.

As discussed earlier, a polynomial $P(z)$ can always be factorized in terms of its roots z_k:

$$P(z) = A \prod_k (z - z_k)$$

The pattern magnitude is thus proportional to the product of all the phasor magnitudes $|z - z_k|$. When z passes through a certain z_k to z_{k+1} one obtains either a main beam or a side lobe. In the latter case the locations of z_k and z_{k+1} will generally have a major influence on the height of that side lobe level, since all other roots are presumably farther away from them. Using this fact Elliott [28] is able to perturb certain roots of a Chebyshev polynomial for achieving a certain side lobe topology. For an array with an even number of elements, if the excitations of any two symmetrically located elements are equal in magnitude and opposite in phase, one obtains a sharp null, instead of a main beam, in the broadside direction. Optimum designs for nearly equal side lobes, except for the first two next to the broadside null of the so-called difference pattern, have been considered in great detail by Elliott [28] and Bayliss [6].

6. Optimization of Directivity (*D*) and Signal-to-Noise Ratio (*SNR*)

When an array is used for transmitting, the maximization of D is of interest, and when an array is used for reception, the maximization of SNR is of interest. These two problems can be solved in the same manner. In fact, the problem of jamming or interference can be treated similarly.

Formulation and Solution

Consider an arbitrary array with N elements. Let its nth element be located at $\mathbf{r}_n = (x_n, y_n, z_n)$ all measured in wavelengths and be excited with current

$$I_n = J_n e^{-j\mathbf{r}_n \cdot \mathbf{u}_0} \tag{149}$$

where

$$\mathbf{r}_n \cdot \mathbf{u}_0 = 2\pi(x_n \sin\theta_0 \cos\phi_0 + y_n \sin\theta_0 \sin\phi_0 + z_n \cos\theta_0) \tag{150}$$

(θ_0, ϕ_0) = angular direction in which D is to be maximized, or from which the signal is to be received

In (149), $\{J_n\}$ can be complex and will be determined. If $\{J_n\}$ is real, $\{I_n\}$ will be cophasal excitation.

For convenience, we shall use *bra-ket* notation as defined below:

$$\langle J = \text{a } row \text{ vector} = (J_1, J_2, \ldots, J_N) \tag{151}$$

$$\langle V = \text{a } row \text{ vector} = (\exp[j(\psi_1^0 - \psi_1)], \exp[j(\psi_2^0 - \psi_2)], \ldots, \\ \exp[j(\psi_N^0 - \psi_N)]) \tag{152}$$

$J\rangle$ and $V\rangle$ are transposes of $\langle J$ and $\langle V$, respectively, and are therefore column vectors

where

$$\psi_n = 2\pi(x_n \sin\theta\cos\phi + y_n\sin\theta\sin\phi + z_n\cos\theta) \tag{153}$$

$$\psi_n^0 = \psi_n\big|_{\theta=\theta_0,\,\phi=\phi_0.} \tag{154}$$

Then the pattern function is given by

$$F(\theta,\phi) = \sum_n^N J_n \exp[j(\psi_n - \psi_n^0)] = \langle JV^* \rangle \tag{155}$$

The power density, or the received signal in the direction (θ_0, ϕ_0), is proportional to

$$|F(\theta,\phi)|^2 = \langle JV_1^* \rangle \langle V_1 J^* \rangle = \langle JCJ^* \rangle \tag{156}$$

where

$V_1\rangle = V\rangle\big|_{\theta=\theta_0,\,\phi=\phi_0}$

$\mathbf{C} = $ a dyad, or a special $N \times N$ matrix:

$$\mathbf{C} = V_1^* \rangle \langle V_1 = V^* \rangle \langle V \big|_{\phi=\theta_0,\phi=\phi_0} = \begin{bmatrix} 1 & 1 & \cdots & 1 \\ 1 & 1 & \cdots & 1 \\ \cdot & \cdot & \cdots & \cdot \\ 1 & 1 & \cdots & 1 \end{bmatrix} \tag{157}$$

If the array is in a noisy environment with temperature distribution $T(\theta,\phi)$, the total received noise power is proportional to

$$P_n = \langle JAJ^* \rangle \tag{158}$$

where $\mathbf{A}$ is an $N \times N$ matrix given by

$$\mathbf{A} = \frac{1}{4\pi} \int_{4\pi} V^* \rangle \langle V\, T(\theta,\phi)\, d\Omega \tag{159}$$

Therefore the signal-to-noise ratio is proportional to

$$SNR = \frac{\langle JCJ^* \rangle}{\langle JAJ^* \rangle} \tag{160}$$

Similarly, the average of total radiated power is proportional to

$$P_{av} = \frac{1}{4\pi} \int_{4\pi} \langle JV^* \rangle \langle VJ^* \rangle \, d\Omega = \langle JBJ^* \rangle \tag{161}$$

where $\mathbf{B}$ is an $N \times N$ matrix given by

$$\mathbf{B} = \frac{1}{4\pi} \int_{4\pi} V^* \rangle \langle V d\Omega = \mathbf{A} \big|_{T=1} \tag{162}$$

Therefore the directivity is given by

$$D = \frac{\langle JCJ^* \rangle}{\langle JBJ^* \rangle} \tag{163}$$

The objective is to maximize D for directivity, or to maximize the SNR for reception in the given noise environment $T(\theta, \phi)$, with the N degrees of freedom $J_1, J_2, \ldots, J_N$. Before proceeding, it may be noted that

$$SNR = \frac{\langle JCJ^* \rangle}{\langle JBJ^* \rangle} \bigg/ \frac{\langle JAJ^* \rangle}{\langle JBJ^* \rangle} = D/T_{av} \tag{164}$$

where

$$T_{av} = \langle J(1/4\pi) \int_{4\pi} V^* \rangle \langle VT(\theta, \phi) \, d\Omega J^* \rangle \Big/ \langle J(1/4\pi) \int_{4\pi} V^* \rangle \langle V \, d\Omega J^* \rangle$$

= temperature of the received noise power if it were distributed uniformly in space

= equivalent uniform temperature distribution for the same noise power received by the array $\tag{165}$

It may also be noted that for interference, or jamming signal, with power density distribution, $I(\theta, \phi)$, uncorrelated in space, the signal-to-interference (S/I) ratio is also given by (160) with $T(\theta, \phi)$ replaced by $I(\theta, \phi)$.

Therefore (a) the problem of maximizing D/T_{av} is exactly the same as that of maximizing the SNR, (b) the problem of maximizing D is the same as that of maximizing the SNR with $T = 1$, i.e., uniform temperature distribution in space, and (c) the problem of maximizing S/I is the same as that of maximizing the SNR. Hence, for all these problems, one needs only to consider the maximization of the SNR; but the optimum solution for $\{I_n\}$ depends on the matrix $\mathbf{A}$, or $\mathbf{B}$, or both.

Solutions to all these problems may lead to unrealistic results which are generally referred to as the "supergain," "superdirectivity," "ill-conditioned," or "improperly posed" problems [9, 65, 120]. To make the solutions more physically meaningful, a constraint may be imposed on the so-called array Q factor

$$Q = \frac{\langle JJ^* \rangle}{\langle JVJ^* \rangle} \qquad (166)$$

which follows from Taylor's definition of *supergain ratio* for an aperture antenna [100]. Except for a constant and the quality factor of a single element, the above definition of the array Q factor has the usual meaning of 2π times the total stored energy divided by the energy radiated per cycle if the mutual impedance effect can be neglected.

The most general optimization problem can thus be stated as follows:

Given: Array geometry, direction of desired signal (θ_0, ϕ_0), $T(\theta, \phi)$, and constraint on the Q factor.

To find: $\langle J$ (or $\langle I$) such that the *SNR* is maximized.

Solution: Using the fact that matrices **A**, **B**, and **C** are Hermitian, the solutions can be found for various cases as summarized in Table 4 [65]. The optimum $\langle J$ as listed in the last row in Table 4 is for maximum *SNR* with a prescribed Q factor. When there is a constraint on the Q factor, one needs first to solve for p in the following eigenvalue equation:

$$\det(V_1\rangle, W_2\rangle, \ldots, W_N\rangle) = 0 \qquad (167)$$

where

$$\mathbf{I} = \text{identity matrix}$$
$$V_1\rangle = (1, 1, \ldots, 1)^t$$
$$W_n\rangle = p^2(Q\mathbf{B} - \mathbf{I})V_n^*\rangle + 2p\mathbf{A}V_n^*\rangle + \mathbf{A}(Q\mathbf{B} - \mathbf{I})^{-1}\mathbf{A}V_n^*\rangle,$$
$$\qquad \text{for } n = 2, 3, \ldots, N$$
$$V_2\rangle = (-1, 1, 0, 0, \ldots, 0)^t$$
$$\cdots \qquad \cdots$$
$$V_N\rangle = (-1, 0, 0, \ldots, 1)^t$$

In words, $V_n\rangle$, for $n = 2, \ldots, N$, is a column vector with -1 as its first element, $+1$ as its nth element, and 0 for all other elements. Once p is found, one can compute the matrix

$$\mathbf{K} = \mathbf{A} + p(Q\mathbf{B} - \mathbf{I}) \qquad (168)$$

and the optimum $J\rangle$ as shown in the last row in Table 4:

$$J\rangle = \mathbf{K}^{-1*}V_1\rangle \qquad (169)$$

Table 4. Formulas for Optimum Gain and SNR of an Arbitrary Array

	Current	D	SNR	Q Factor
Definition	$J\rangle$	$\dfrac{\|\langle JV_1^*\rangle\|^2}{\langle JBJ^*\rangle}$	$\dfrac{\|\langle JV_1^*\rangle\|^2}{\langle JAJ^*\rangle}$	$\dfrac{\langle JJ^*\rangle}{\langle JBJ^*\rangle}$
Uniform current excitation	$V_1^*\rangle$	$\dfrac{N^2}{\langle V_1BV_1^*\rangle}$	$\dfrac{N^2}{\langle V_1AV_1^*\rangle}$	$\dfrac{N}{\langle V_1BV_1^*\rangle}$
Optimum D without constraint on Q	$B^{*-1}V_1^*\rangle$	$\langle V_1B^{-1}V_1^*\rangle$	$\dfrac{\|\langle V_1B^{-1}V_1^*\rangle\|^2}{\langle V_1B^{-1}AB^{-1}V_1^*\rangle}$	$\dfrac{\langle V_1B^{-2}V_1^*\rangle}{\langle V_1B^{-1}V_1^*\rangle}$
Optimum D with a prescribed Q	$F^{*-1}V_1^*\rangle$	$\dfrac{\|\langle V_1F^{-1}V_1^*\rangle\|^2}{\langle V_1F^{-1}BF^{-1}V_1^*\rangle}$	$\dfrac{\|\langle V_1F^{-1}V_1^*\rangle\|^2}{\langle V_1F^{-1}AF^{-1}V_1^*\rangle}$	A given constant
Optimum SNR without constraint on Q	$A^{*-1}V_1^*\rangle$	$\dfrac{\|\langle V_1A^{-1}V_1^*\rangle\|^2}{\langle V_1A^{-1}BA^{-1}V_1^*\rangle}$	$\langle V_1A^{-1}V_1^*\rangle$	$\dfrac{\langle V_1A^{-2}V_1^*\rangle}{\langle V_1A^{-1}BA^{-1}V_1^*\rangle}$
Optimum SNR with a prescribed Q	$K^{*-1}V_1^*\rangle$	$\dfrac{\|\langle V_1K^{-1}V_1^*\rangle\|^2}{\langle V_1K^{-1}BK^{-1}V_1^*\rangle}$	$\dfrac{\|\langle V_1K^{-1}V_1^*\rangle\|^2}{\langle V_1K^{-1}AK^{-1}V_1^*\rangle}$	A given constant

Symbolism

Actual current in the nth element $= J_n e^{-j\psi_n^0}$

$\langle J = (J_1, J_2, \cdots, J_N), \qquad \langle V_1 = (1, 1, \cdots, 1)$

$\psi_n = 2\pi(x_n \sin\theta\cos\phi + y_n \sin\theta\sin\phi + z_n \cos\theta)$

$\psi_n^0 = \psi_n|_{\theta=\theta_0,\ \phi=\phi_0}$

$K = A + p(QB - I), \qquad\qquad F = K|_{A=B}$

$A = (1/4\pi)\int_{4\pi} V^*\rangle\langle VT(\theta,\phi)\,d\Omega, \qquad B = A|_{T=1}$

(After Lo, Lee, and Lee [65], © 1966 IEEE)

From (168) one can compute its associated directivity

$$D = \frac{\|\langle V_1K^{-1}V_1^*\rangle\|^2}{\langle V_1K^{-1}BK^{-1}V_1^*\rangle} \qquad (170)$$

and its associated SNR

$$SNR = \frac{\|\langle V_1K^{-1}V_1^*\rangle\|^2}{\langle V_1K^{-1}AK^{-1}V_1^*\rangle} \qquad (171)$$

One of the eigenvalues p of (167) which gives the largest value of SNR is the optimum solution. Since the solution $J\rangle$ is determined for maximum SNR, D as computed from (170) using that $J\rangle$ is not necessarily maximum.

● For maximum *SNR* without constraint on Q the solution is given in row 5 of Table 4. For this case, $p = 0$ and no eigenvalue needs to be computed. Therefore from (168) $\mathbf{K} = \mathbf{A}$ and

$$J\rangle = \mathbf{A}^{-1*}V_1\rangle \tag{172}$$

● For maximum D with and without constraint on the Q factor, the solutions are listed in rows 4 and 3 of Table 4, respectively. The solutions are exactly the same as those for maximum *SNR* except that $T(\theta,\phi) = 1$ and $\mathbf{A} = \mathbf{B}$. The corresponding $\mathbf{K}$ matrix is denoted by

$$\mathbf{F} = \mathbf{B} + p(Q\mathbf{B} - \mathbf{I}), \qquad \text{for a constraint on the } Q \text{ factor} \tag{173}$$

$$\dot{\mathbf{F}} = \mathbf{B}, \qquad \text{for no constraint} \tag{174}$$

● Since $V_1\rangle = (1, 1, \ldots, 1)'$, the optimum solution for J_n is simply the *sum* of all the elements in the nth row of $\mathbf{B}^{*-1}$, $\mathbf{F}^{-1*}$, $\mathbf{A}^{-1*}$, and $\mathbf{K}^{-1*}$, respectively, for each case. The actual current for the nth element, by definition, is given by (149).

Planar Array with Isotropic Elements or Vertical Dipoles in the (x, y) *Plane*

Referring to Fig. 26, the elements of matrix $\mathbf{B}$ for this array can be integrated in closed form:

$$b_{nm} = b^*_{mn} = e^{-j\psi^0_{nm}}\left[\frac{\sin 2\pi\varrho_{nm}}{2\pi\varrho_{mn}} + q\frac{\cos 2\pi\varrho_{nm}}{(2\pi\varrho_{nm})^2} - q\frac{\sin 2\pi\varrho_{nm}}{(2\pi\varrho_{nm})^2}\right],$$
$$\text{for } n < m \tag{175}$$

$$b_{nn} = 1 - q/3 \tag{176}$$

where
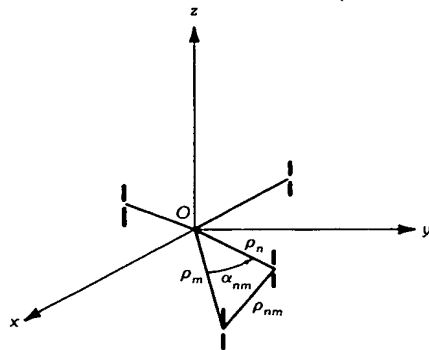
Fig. 26. A planar array with elements (vertical dipoles or isotropic) in the *xy* plane.

$$\psi_{mn}^0 = 2\pi\varrho_{nm} \sin\theta_0 \cos(\phi_0 - a_{nm})$$

$$\varrho_{nm} = [(x_n - x_m)^2 + (y_n - y_m)^2]^{1/2}$$
$$= \text{distance between the } n\text{th and } m\text{th elements}$$

$$(x_n, y_n) = \text{coordinates of the } n\text{th element}$$

$$a_{nm} = \tan^{-1}[(y_n - y_m)|(x_n - x_m)], \text{ where } 0 \leqq a_{nm} < \pi$$

$$q = \begin{cases} 0 & \text{for isotropic elements} \\ 1 & \text{for vertical dipoles} \end{cases}$$

From the above a few interesting results can be obtained:

(*a*) In particular for a linear array, say along the *x* axis, with *N* isotropic elements,

$$b_{nm} = b_{mn}^* = e^{-j\psi_{nm}^0} \frac{\sin 2\pi\varrho_{nm}}{2\pi\varrho_{mn}}, \qquad n < m \tag{177}$$

$$b_{nn} = 1 \tag{178}$$

where

$$\varrho_{nm} = x_n - x_m$$
$$\psi_{nm}^0 = 2\pi\varrho_{mn} \sin\theta_0 \cos\phi_0$$

For uniform interelement spacing equal to $\lambda/2$ or its multiples,

$$b_{nm} = \begin{cases} 0 & \text{for } n \neq m \\ 1 & \text{for } n = m \end{cases}$$

Thus

$$\mathbf{B} = \mathbf{I} = \text{identity matrix}$$
$$Q = 1, \text{ independent of } J\rangle$$
$$\max D = N \tag{179}$$

and

$$\text{optimum } \langle J = (1, 1, \ldots, 1) \tag{180}$$

In other words, if $d = m/2$ (a multiple of $\lambda/2$), the *cophasal uniform array is optimum*. This conclusion is approximately true for dipole arrays since, for $d = m/2$, the diagonal elements of **B** dominate over all others, and **B** is approximately **I**.

(*b*) For broadside planar array $\psi_{nm}^0 = 0$. Thus the **B** matrix is real and the optimum excitation is real. In other words, for broadside arrays *optimum*

excitations are either in phase or antiphase. A few examples are shown in Figs. 27 through 31. In Figs. 30 and 31 the term "cophasal" implies that only the excitation amplitudes are optimized while the phases are kept cophasal in the end-fire direction.

(c) For planar arrays with large interelement spacings, say much greater than a wavelength, $\mathbf{B} \cong \mathbf{I}$. *The uniform cophasal excitation is nearly optimum, max* $\mathbf{D} \cong \mathbf{N}$ *and* $\mathbf{Q} \cong 1$. Some workers have sought optimum spacings and excitations for a thinned array; this result shows that the uniform cophasal excitation is the solution no matter what element spacings are as long as they are sufficiently large as in a thinned array.

(d) From the definition of the array Q factor, the value of $1/Q$ is bounded between the smallest and the largest eigenvalue of the $\mathbf{B}$ matrix. For equally spaced linear arrays with isotropic elements, $Q = 1$ as $d = m/2, m = 1, 2, \ldots$, and $Q \cong 1$ as $d > 1$, no matter what $\langle J$ is.

(e) From the example to be discussed next, it will be seen that the optimum excitation for a linear end-fire array with uniform spacings is nearly *antiphase for* $d \leq 1/2$ *and nearly cophasal for* $d \geq 1/2$.

(f) Gilbert and Morgan [124] showed that the *average* of *maximum* directivity over all directions is equal to N, the number of isotropic elements, i.e.,

$$\frac{1}{4\pi} \int_{4\pi} \max D(\theta_0, \phi_0)\, d\Omega = N \tag{181}$$

Thus if max D is greater than N in some direction, it must be smaller than N in some other direction.

(g) In general, ohmic losses in most antennas with low Q are of little importance in antenna efficiency. However, for antennas with strong local fields and large circulating currents, such as in superdirective arrays, the efficiency for radiation in (θ_0, ϕ_0) may be defined as

$$\eta = \frac{\text{radiated power density in } (\theta_0, \phi_0)}{\text{radiated power density in } (\theta_0, \phi_0) + \text{ohmic power loss}} = \frac{1}{1 + rS} \tag{182}$$

where

r = ohmic resistance of each element,

$$S = \frac{Q}{D} = \frac{\langle JJ^* \rangle}{\langle JCJ^* \rangle} \tag{183}$$

The S parameter, called the *sensitivity factor* [109], is a measure of the mean-square variation of the maximum field with respect to the mean-square deviation of the excitation. Thus large Q results in not only low efficiency but also high sensitivity, as will be seen in the following example, Section 7, and [8, 9, 53, 120].

A Typical Example for Maximum Directivity

Consider an equally spaced linear end-fire array with 10 isotropic elements along the x axis. Using the results in row 3 of Table 4 the maximum directivity can be
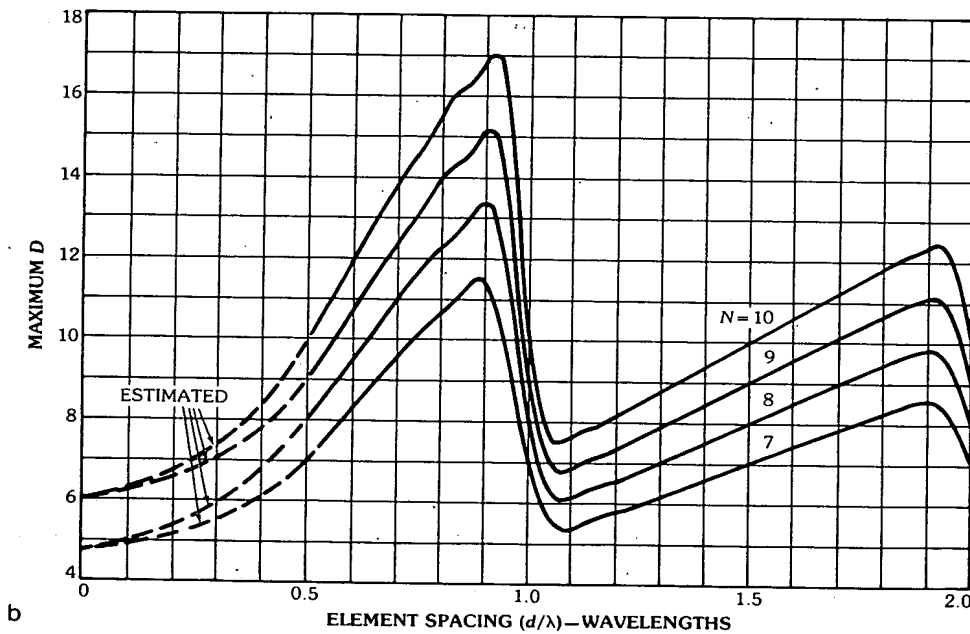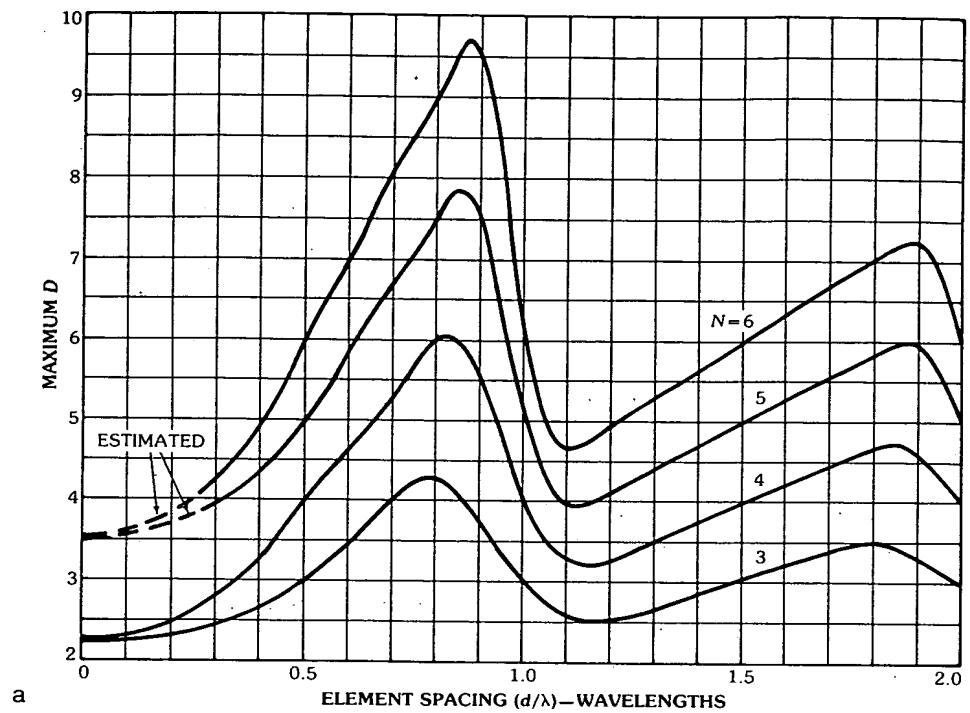
Fig. 27. Maximum directivity D of a linear broadside array of N isotropic elements versus element spacing d in wavelengths. (a) For $N = 3$ through 6. (b) For $N = 7$ through 11. (*Courtesy C. T. Tai*)

11-66

Fig. 28. Maximum directivity of a linear broadside array of N parallel dipoles versus element spacing d (in wavelengths) for $N = 4, 6, 8,$ and 10. (*Courtesy C. T. Tai*)

computed for various values of spacing d as shown by the curve $D(O)$ in Fig. 32. As expected, max $D = N = 10$ at $d = m/2, m = 1, 2, \ldots$. As d decreases below ½, D increases rapidly and approaches $N^2 = 100$ as d approaches zero. For comparison a few other cases are also shown in the figure:

$D(OC)$ = maximum directivity with only the excitation *magnitudes* subject to optimization and with the phases confined to the cophasal condition in the end-fire direction

$D(U)$ = directivity for a uniform cophasal excitation

$D(HW)$ = directivity for the Hansen-Woodyard (HW) excitation (see Section 3, under "Uniform Arrays With N Elements")

Fig. 33 shows the Q factor versus d for all the cases just stated. From these two figures the following remarks can be made:

(a) $D(O)$ is considerably higher than $D(U)$ only when $d \leqq 0.4$. A moderate

Fig. 29. Maximum directivity of a linear broadside array of N collinear dipoles versus element spacing d (in wavelengths) for $N = 4, 6, 8,$ and 10. (*Courtesy C. T. Tai*)

improvement of $D(O)$ over $D(U)$ can be obtained only at the price of astronomically large Q, which implies extremely high local field, dissipation loss, sensitivity, and extremely low efficiency and narrow bandwidth. Therefore a superdirective array is more a fantasy than reality.

(b) Hansen-Woodyard excitation is not truly optimum; in fact its directivity is much lower than $D(U)$ for $d > 1/2$.

(c) $D(U) \to 1$ as $d \to 0$, and $D(U) = N$ as $d = m/2$, $m = 1, 2, \ldots$.

(d) $D(O) \cong D(U)$ as $d \geqq 1/2$. In view of the simplicity of uniform excitation the uniform array is indeed an excellent practical antenna so far as the directivity is concerned.

(e) A superdirective antenna, according to the IEEE Standard, is one whose directivity is "significantly" higher than that of a uniform excitation. A top-loaded monopole, for example, is not a superdirective antenna since the top loading is in effect to make the excitation more uniform. The radiation leak from an open-circuit, balanced, two-wire transmission line with small spacing can be considered as a superdirective antenna, but obviously it is a very inefficient poor
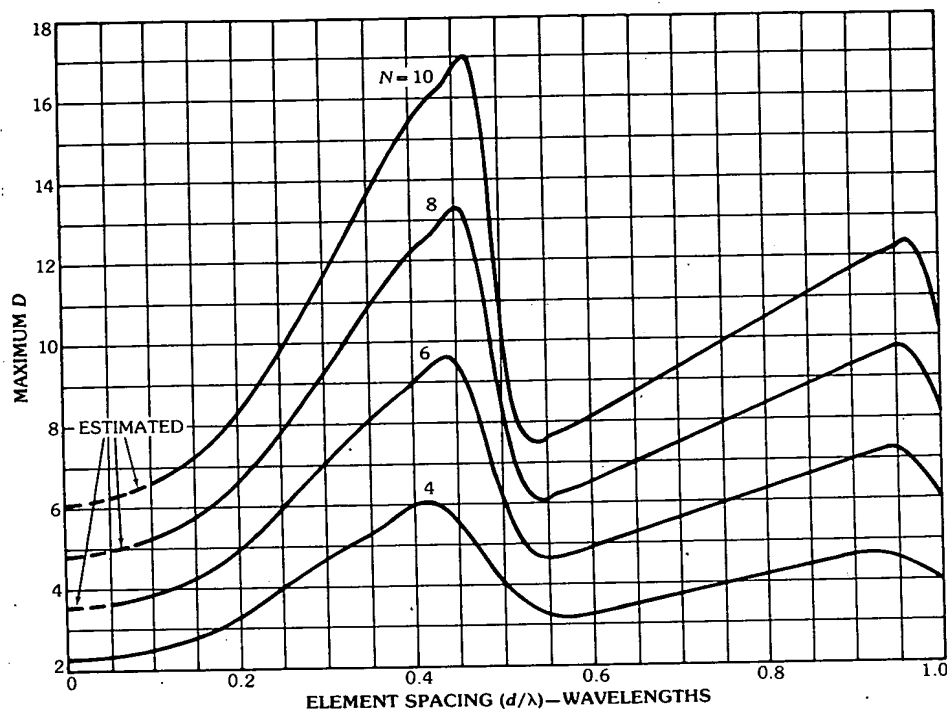
Fig. 30. Maximum directivity of a linear cophasal end-fire array of N isotropic elements versus element spacing d (in wavelengths) for $N = 4, 6, 8$, and 10. (*Courtesy C. T. Tai*)

antenna. So are some other small antennas whose largest dimensions are smaller than a few thousandths of a wavelength.

For academic interest the optimum excitation magnitude and phase for the above example are shown in Figs. 34 and 35. In both figures the curves for $d = 0.2\lambda$ should not be taken seriously, and in Fig. 35 the phases of the excitations of elements 9 and 10 are omitted for brevity, but they can be obtained by extrapolation from the curves shown. From these two figures the following remarks can be made:

(*a*) The optimum excitation for small spacing is highly tapered toward the ends of the array and approximately uniform for spacing equal to or larger than $\lambda/2$. This is consistent with the directivity characteristics stated above, namely, for $d \geqq 1/2$ the maximum directivity is nearly that of a uniform array.

(*b*) The optimum phase is nearly cophasal for $d \geqq 1/2$, again in agreement with the directivity characteristics stated above. However, for $d < 1/2$ the optimum phase distribution is nearly antiphase, about 170°, which results in large local field, low efficiency, etc.

(*c*) For $d = 0.4$ wavelength, where the strong superdirectivity begins to show $[D(O) - D(U) \cong 3.5 \text{ dB}]$, the optimum pattern is shown in Fig. 36a. For com-
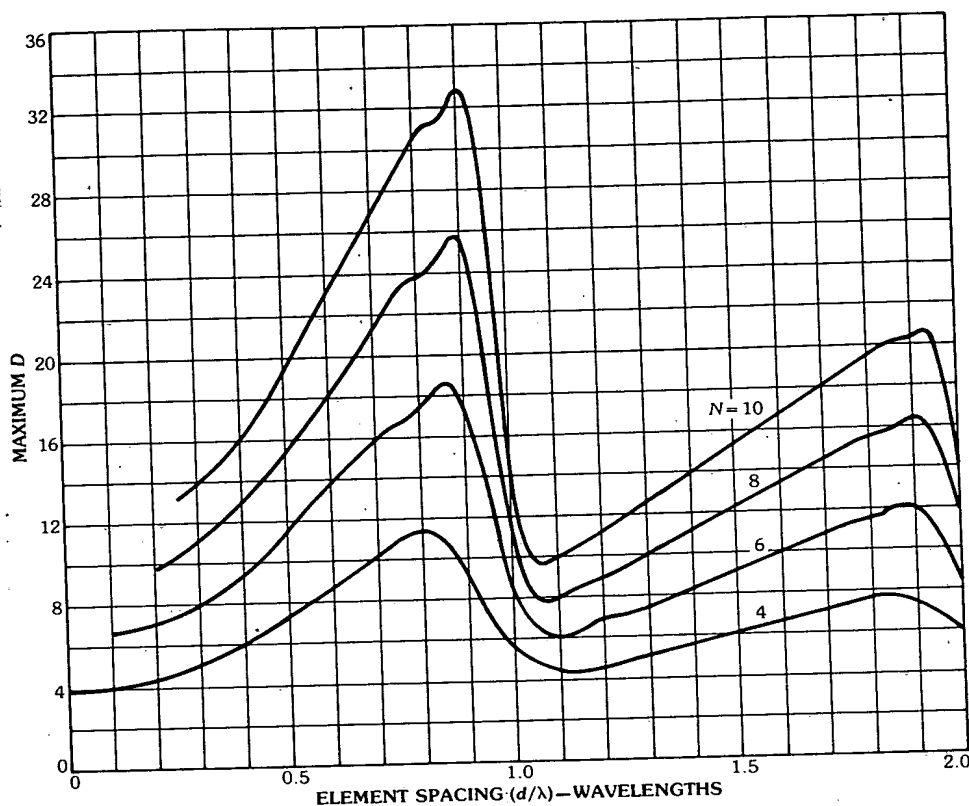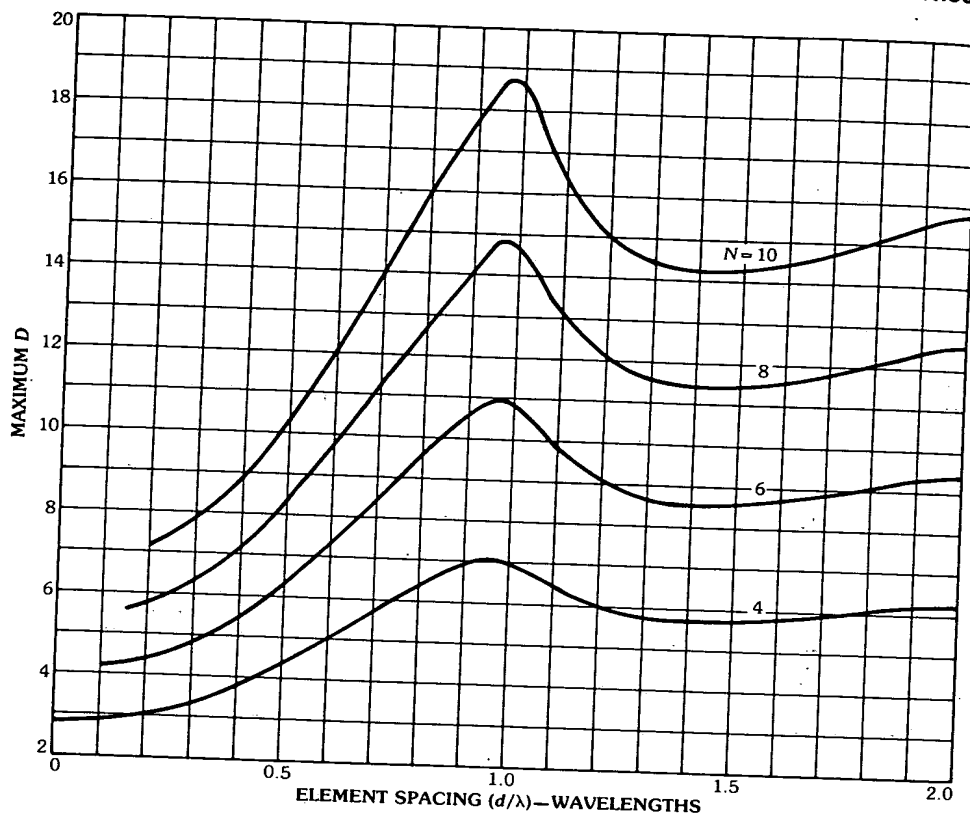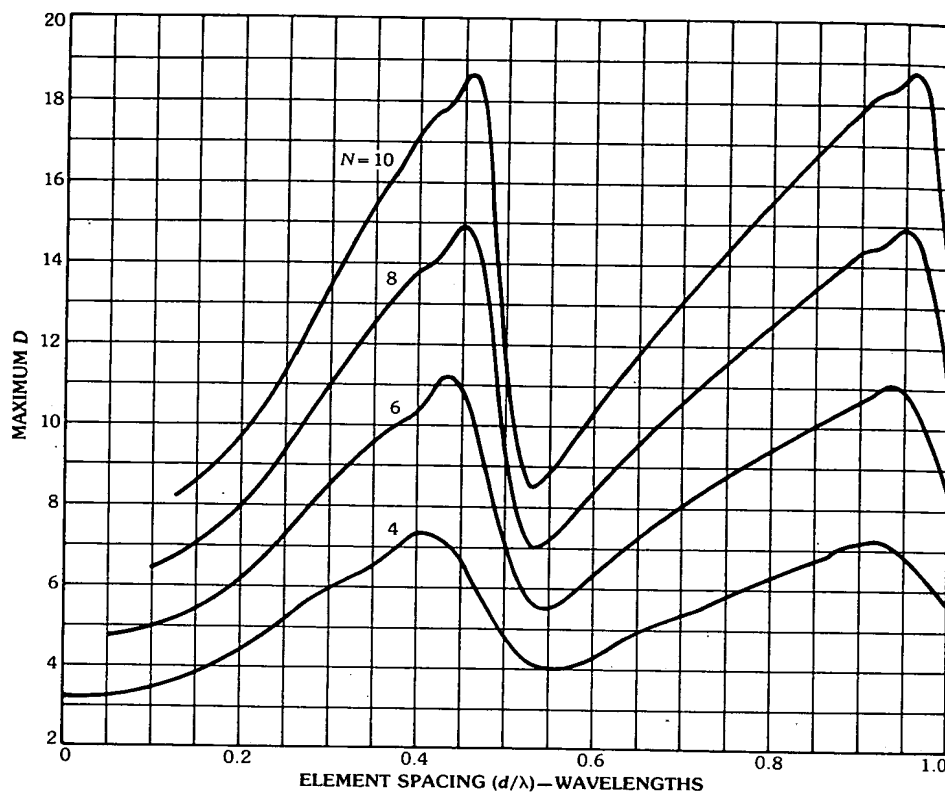
Fig. 31. Maximum directivity of a linear cophasal end-fire array of N parallel dipoles versus element spacing d (in wavelengths) for $N = 4, 6, 8,$ and 10. (*Courtesy C. T. Tai*)

parison, the pattern for the same array but with Hansen-Woodyard excitation is shown in Fig. 36b. It is seen that the latter has a much broader beam.

(d) Fig. 37 shows how the maximum D varies with the angle for which D is maximized for two different cases: $D(O)$ with both excitation magnitudes and phases subject to optimization and $D(OC)$ with only the magnitudes subject to optimization and cophasal phase distribution. It is seen that for both cases D is larger than N, namely 10 here, for small angles (i.e., near end-fire) and smaller than N, namely 10, in some other directions, as expected from (181).

An Example for Maximum SNR

Superdirective arrays are impractical as stated above. However, for reception, it is the SNR, not D, that is of concern. In particular, one is interested in finding out whether a significant improvement of SNR over that of a uniform array is possible without paying a high price on the Q factor. To show that this is possible a simple semicircular array, consisting of nine uniformly distributed isotropic elements in the xz plane is considered. Let the signal come from the z axis and $T(\theta, \phi) =$ constant for $z < 0$ and 0 for $z > 0$ as shown in Fig. 38. Using the formulas in Table 4

D(O)   = Both amplitudes and phases are optimized
D(OC) = Only amplitudes are optimized, phases are kept cophasal
         in the end-fire direction
D(U)   = The amplitudes are uniform and the phases are cophasal in
         the end-fire direction, i.e., ordinary uniform end-fire excitation
D(HW) = Hanson-Woodward excitation for increased directivity

$N = 10$
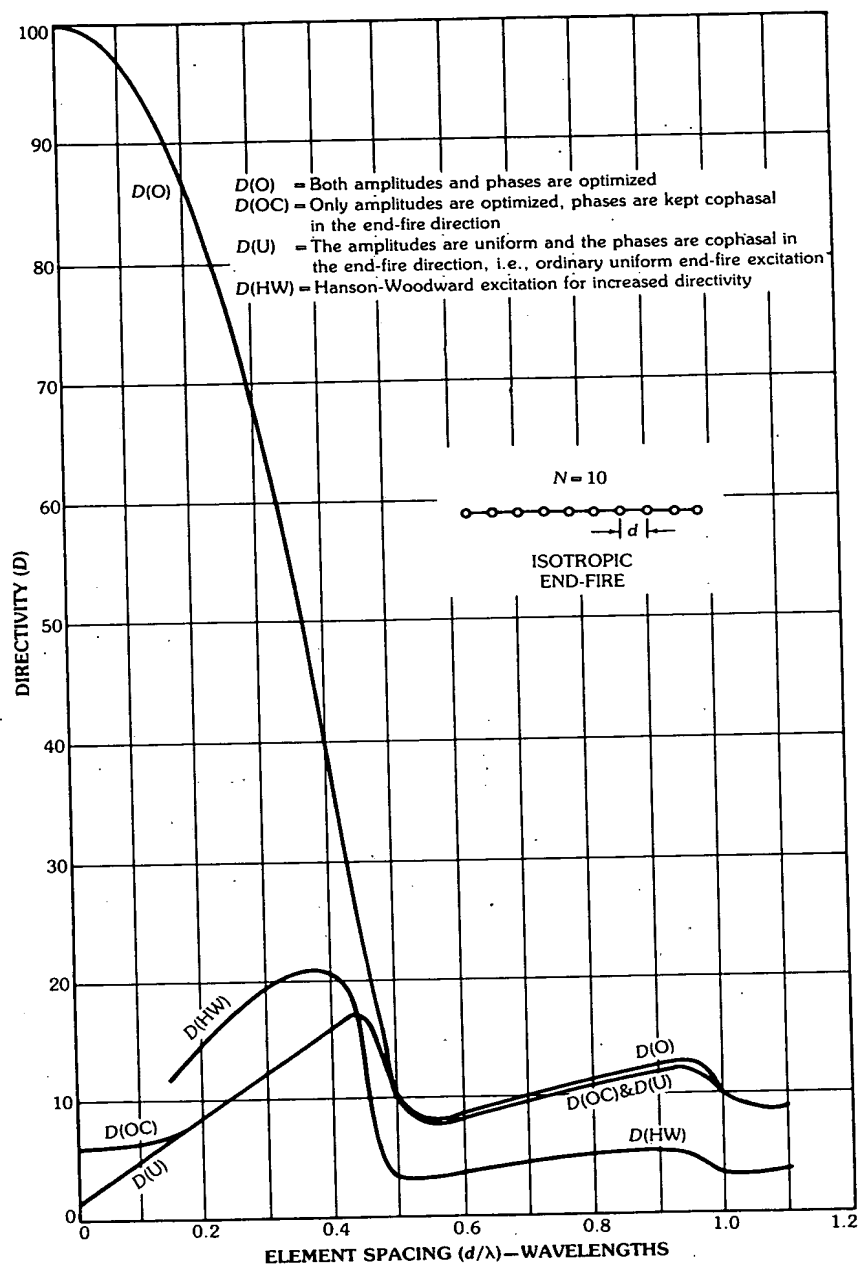
ISOTROPIC
END-FIRE

Fig. 32. Directivities of a linear end-fire array of 10 isotropic elements with various excitations. (*After Lo, Lee, and Lee [65], © 1966 IEEE*)
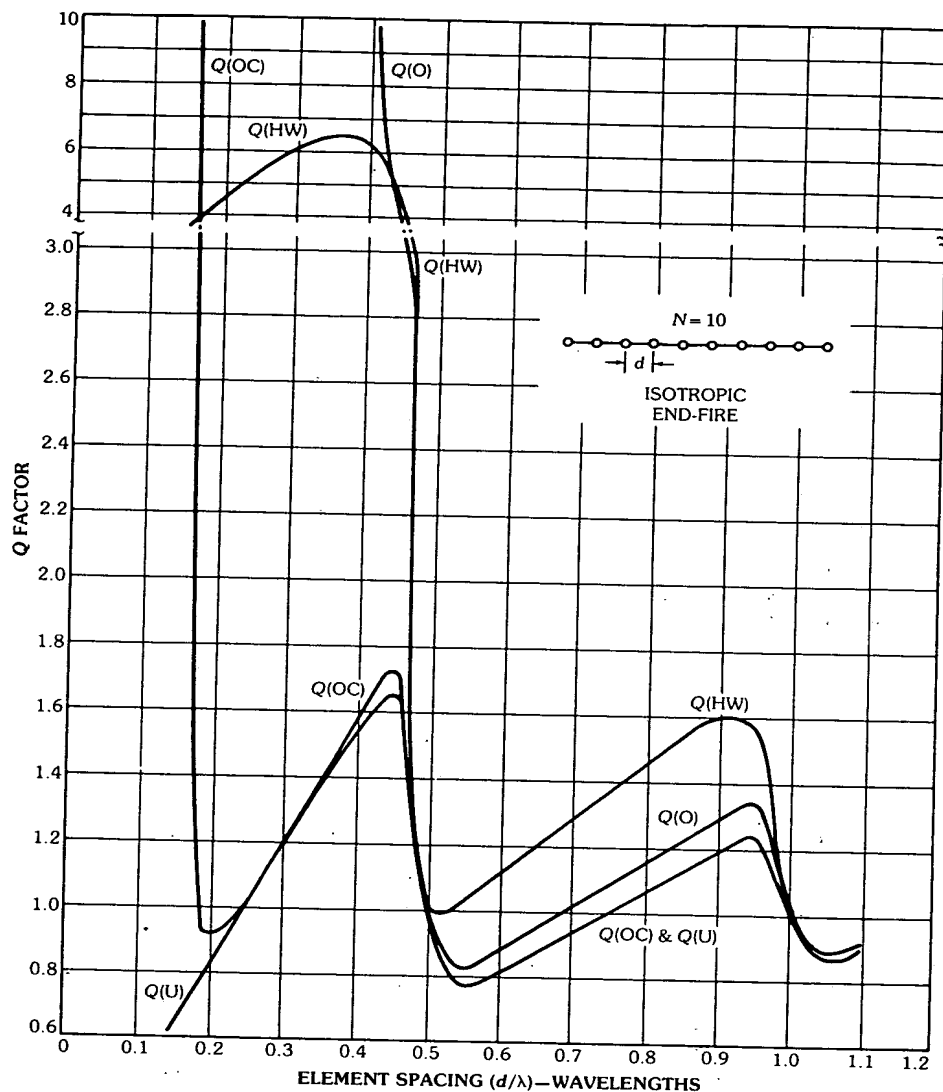
Fig. 33. Array Q factor for the array with the various excitations shown in Fig. 32. (*After Lo, Lee, and Lee [65], © 1966 IEEE*)

various results are computed as shown in Table 5 for the circle radius equal to λ and Table 6 for the circle radius equal to $\lambda/4$. From these the following remarks can be made:

(a) From Table 5 the highest *SNR* of 81.6 with $Q = 1.14$ is obtained, as compared with 35.5 with $Q = 0.916$ for a uniform excitation. Thus an improvement of 3.6 dB is obtained without paying a high price on the Q factor.

(b) From Table 6 where the elements are closely spaced, the highest *SNR* of
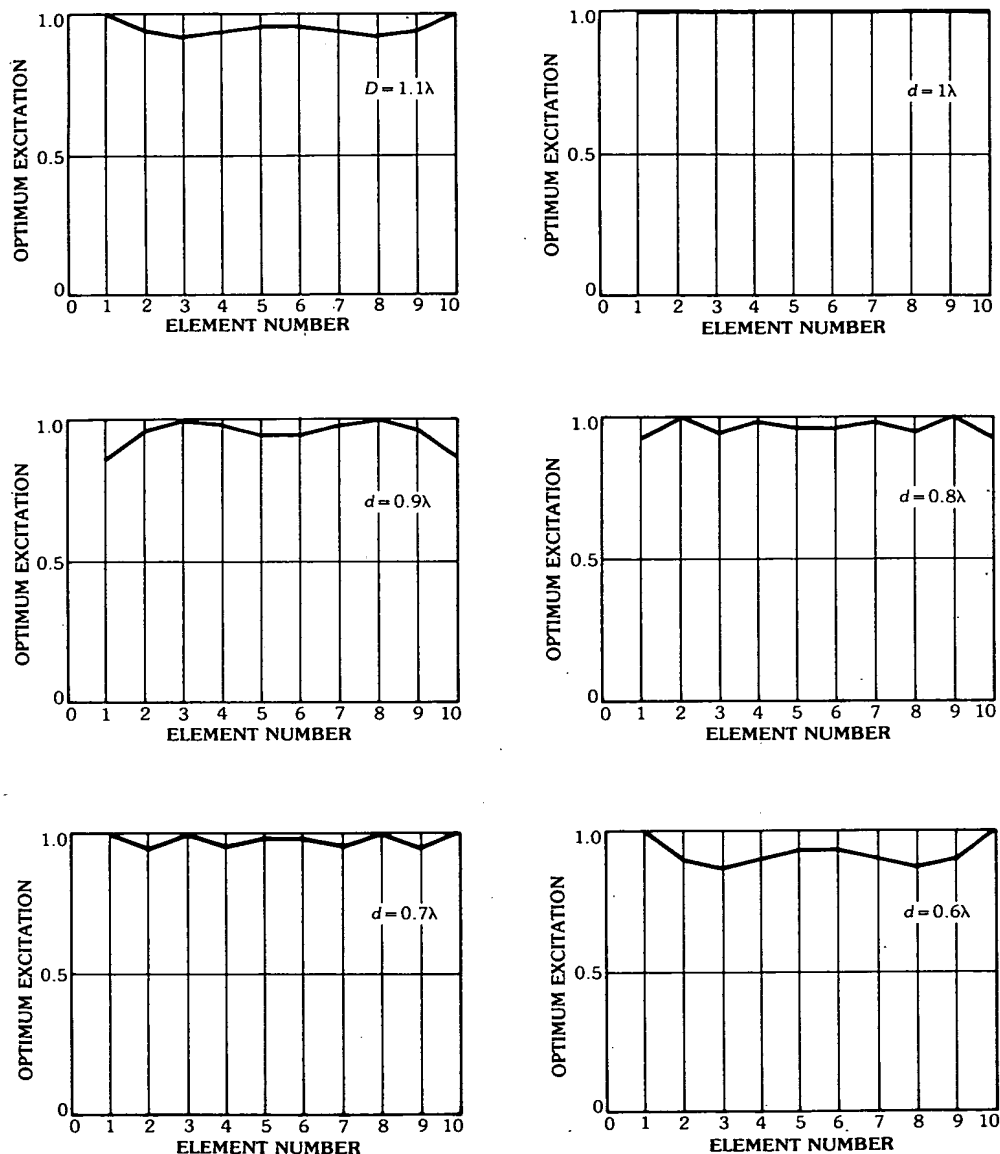
Fig. 34. Relative amplitudes of the optimum excitations for $D(O)$ in Fig. 32 for various element spacings d. (*After Lo, Lee, and Lee [65], © 1966 IEEE*)

47.1 is obtained at the price of $Q = 3.26 \times 10^3$. But with a prescribed value of 20 for the Q factor, $SNR = 21.8$, which is about 5.2 dB higher than that of a uniform excitation.

(c) If D, rather than the SNR, is optimized for the array to receive a signal from
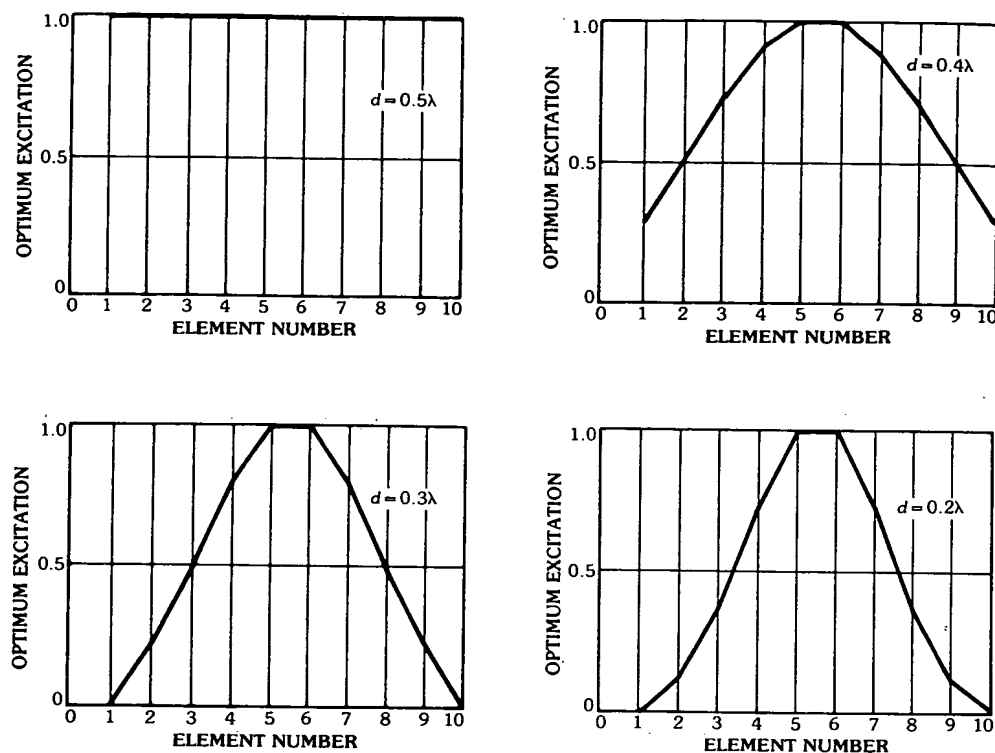
Fig. 34, *continued.*

the z axis in a noise environment as stated above, one would obtain a significantly lower *SNR*. Therefore, the criterion of maximum *SNR* may not be substituted with that of maximum D.

(*d*) In general, large Q is always associated with antiphase distribution.

Extensions

The theory and technique developed above can also be applied to the problem of maximizing the *beam efficiency* where the power radiated in a solid angle Ω_0 about the direction (θ_0, ϕ_0) for a given total radiated power, rather than D, is maximized. For this case, only the **C** matrix need be redefined as

$$\mathbf{C} = \int_{\Omega_0} V^* \rangle \langle V d\Omega \tag{184}$$

This solution is given by solving the eigenvalue problem $(\mathbf{C} - \lambda \mathbf{B})(J) = 0$. The optimization of an aperture antenna can also be solved in a similar manner except that a set of basis functions, or modal functions, over the aperture, instead of elements, should be considered [65].

The technique can also be applied for pattern synthesis. In that case the
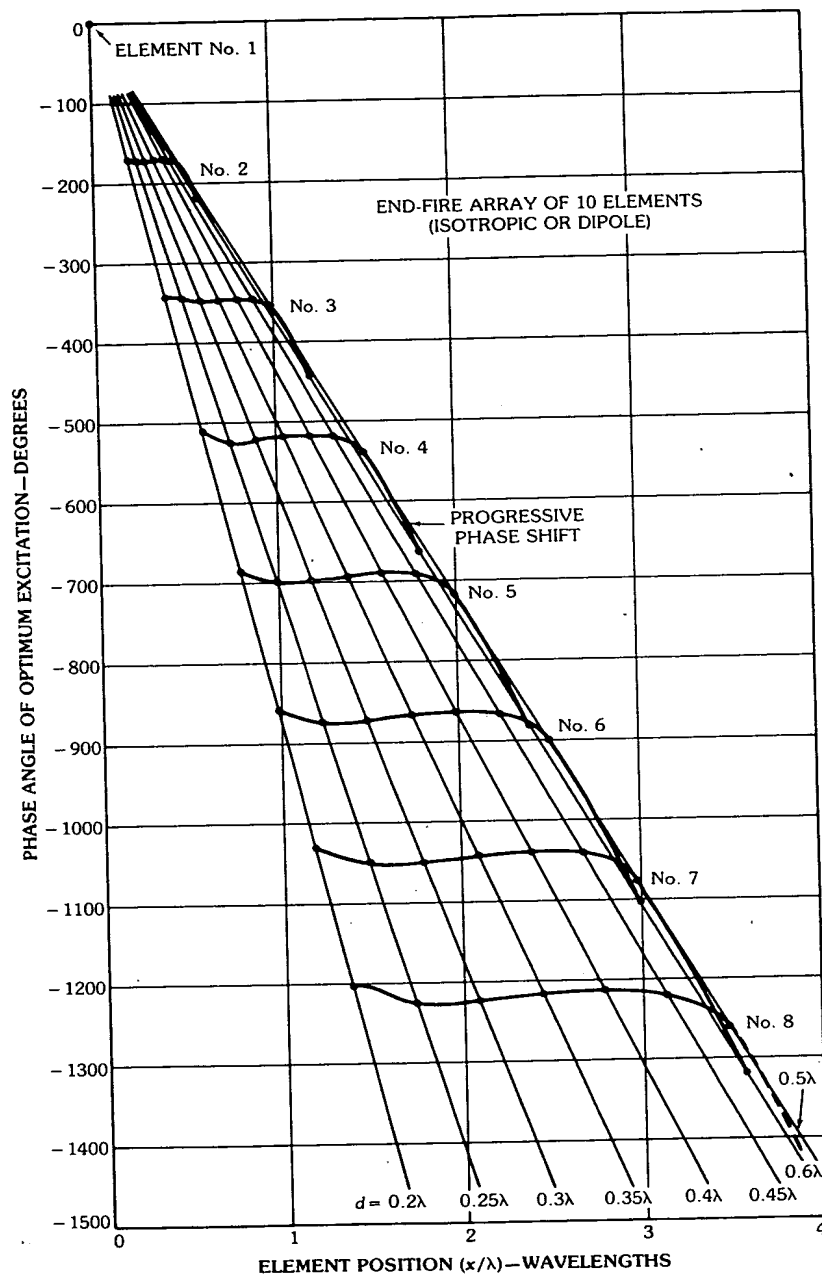
Fig. 35. Relative phases of the optimum excitations for $D(O)$ in Fig. 32 for various element spacings d, where only the phases for the first eight elements are shown.
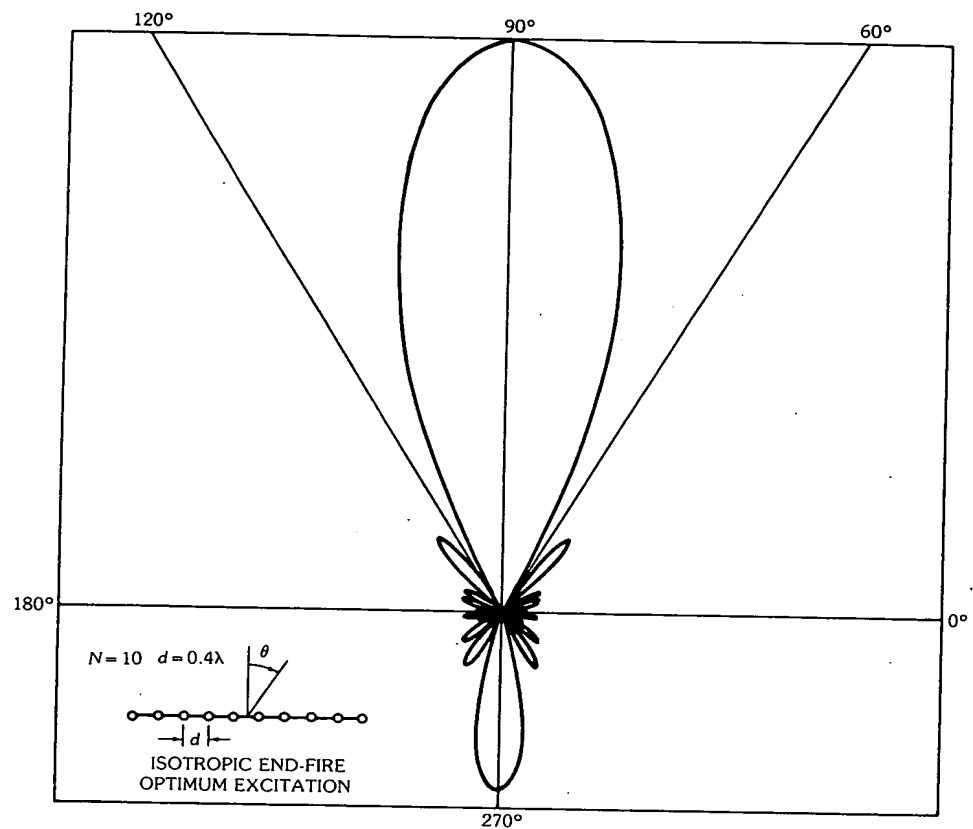
a

Fig. 36. Radiation patterns for end-fire isotropic array. (*a*) For the array in Fig. 32 with optimum excitations shown in Figs. 34 and 35 for $d = 0.4\lambda$. (*b*) For the array in (*a*) but with Hansen-Woodyard's increased directivity excitation. (*After Lo, Lee, and Lee [65],* © *1966 IEEE*)

mean-square difference between the array pattern and the desired pattern is minimized, as discussed in the next section.

7. Pattern Synthesis in the Probabilistic Sense

In the last section an array Q factor was defined to indicate the degree of superdirectivity. It was then shown that a moderate improvement in directivity over the uniform excitation can be obtained only at the price of an astronomically large Q factor. To make the design practical a constraint on the Q factor should be imposed. However, the question of how large a value of the Q factor can be considered practical is left unanswered. One possible approach to this problem is to take the parametric uncertainty into consideration. To illustrate this, a pattern synthesis problem is discussed. Let
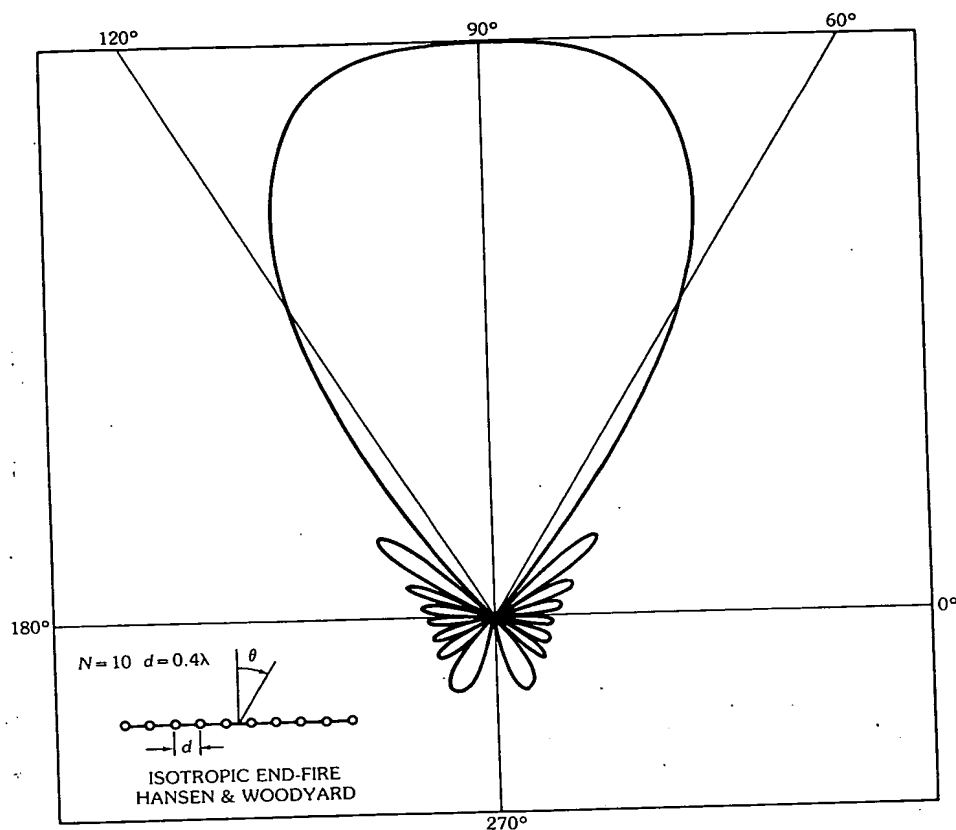
Fig. 36, continued.

$$f_d(\theta, \phi) = \text{desired pattern function} \tag{185}$$
$$f(\theta, \phi) = \text{actually realizable pattern of the array} = \langle JV^* \rangle$$

where

$\langle J = \text{a row vector} = (J_1, J_2, \ldots, J_N)$

$J_n = \text{excitation current for the } n\text{th element}$

$V \rangle = \text{a column vector} = (V_1, V_2, \ldots, V_N)^t$

$V_n^* = \text{pattern function of the } n\text{th element}$

Then, for least-square optimization, the following norm in the L_2 space is to be minimized:
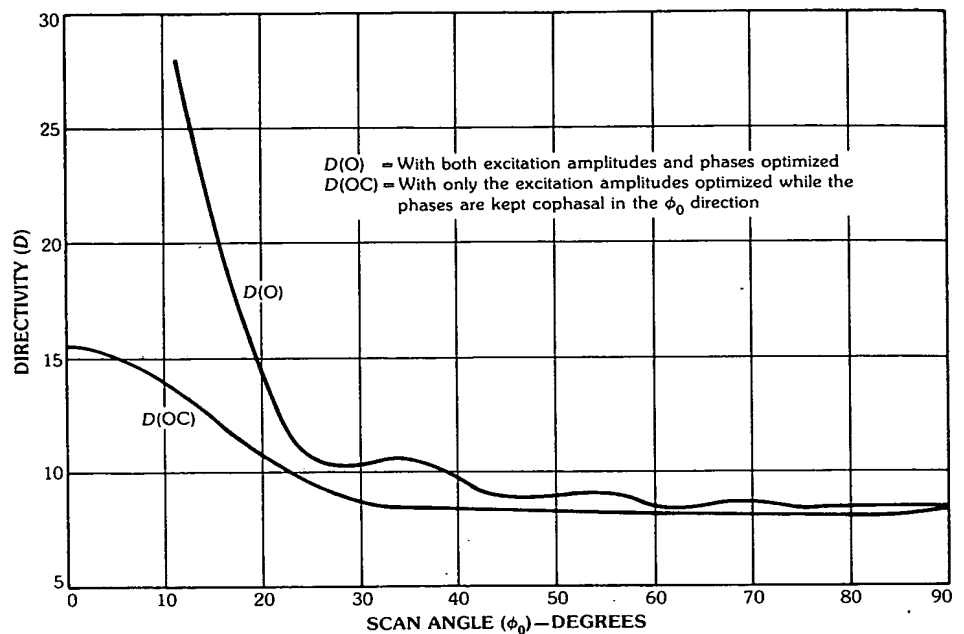
Fig. 37. The directivities $D(O)$ and $D(OC)$ versus scan angle ϕ_0 in which the directivity is maximized for a linear array with $N = 10$ isotropic elements along the x axis and element spacing $d = 0.4\lambda$. $D(O)$: with both excitation magnitudes and phases optimized. $D(OC)$: with only the excitation magnitudes optimized while the phases are kept cophasal in the ϕ_0 direction. (*After Lo, Lee, and Lee [65], © 1966 IEEE*)
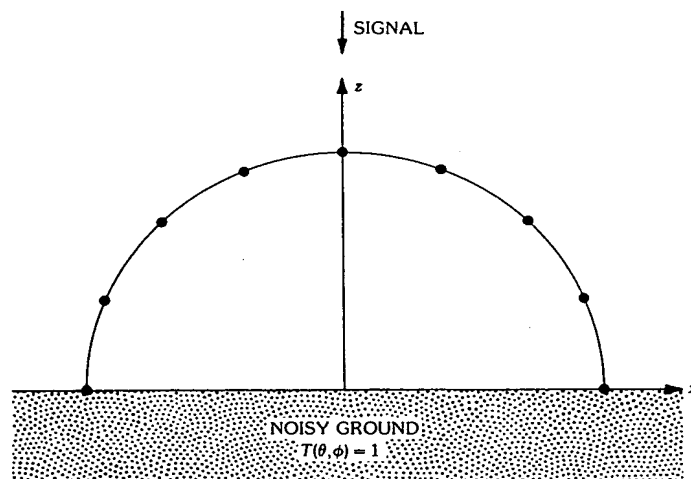
Fig. 38. Geometry of a semicircular array above a noisy ground to receive a signal from the z axis. (*After Lo, Lee, and Lee [65], © 1966 IEEE*)

Table 5. Optimum Semicircular Array ($r = \lambda$) of Nine Cophasally Excited Isotropic Elements

	Current	D	SNR	Q Factor
Uniform excitation	$J_1 = J_2 = J_3 = J_4 = J_5 =$ $J_6 = J_7 = J_8 = J_9 = 1$	8.24	35.5	0.916
Optimum D without constraint on Q factor	$J_1 = J_9 = 1.123$ $J_2 = J_8 = 1.29$ $J_3 = J_7 = 0.881$ $J_4 = J_6 = 0.757$ $J_5 = 0.600$	8.71	55.0	1.03
Optimum D with a prescribed Q factor	$J_1 = J_9 = 1.082$ $J_2 = J_8 = 1.218$ $J_8 = J_7 = 0.898$ $J_4 = J_6 = 0.816$ $J_5 = 0.659$	8.67	50.5	1.0 (prescribed)
Optimum SNR without constraint on Q factor	$J_1 = J_9 = 11.436$ $J_2 = J_8 = 15.396$ $J_3 = J_7 = 10.446$ $J_4 = J_6 = 3.746$ $J_5 = -0.421$	7.76	81.6	1.14
Optimum SNR with a prescribed Q factor	$J_1 = J_9 = 5.835$ $J_2 = J_8 = 7.719$ $J_3 = J_7 = 7.451$ $J_4 = J_6 = 5.223$ $J_5 = 2.664$	8.44	55.1	1.0 (prescribed)

Element positions (in wavelengths):
$x_1 = -x_9 = 1.000 \quad z_1 = z_9 = 0.0$
$x_2 = -x_8 = 0.924 \quad z_2 = z_8 = 0.383$
$x_3 = -x_7 = 0.707 \quad z_3 = z_7 = 0.707$
$x_4 = -x_6 = 0.383 \quad z_4 = z_6 = 0.924$
$x_5 = 0.0 \quad z_5 = 1.0$

Main beam: $\theta_0 = 0$

Thermal noise distribution: $T(\theta, \phi) = \begin{cases} 1 & \text{for } \pi/2 < \theta \leqq \pi \\ 0 & \text{otherwise} \end{cases}$

(After Lo, Lee, and Lee [65], © 1966 IEEE)

$$\varepsilon = \| f_d - f \|^2 = \int_{4\pi} (f_d - f)(f_d - f)^* \, w \, d\Omega$$

$$= \| f_d \|^2 + \int_{4\pi} |f|^2 \, w \, d\Omega - 2 \, \mathrm{Re} \left\{ \int f f_d^* \, w \, d\Omega \right\}$$

$$= \| f_d \|^2 + \left\langle J \int_{4\pi} V^* \right\rangle \left\langle V_d \, w \, d\Omega \, J^* \right\rangle - 2 \, \mathrm{Re} \left\{ \left\langle J \int_{4\pi} V^* \right\rangle f_d^* \, w \, d\Omega \right\}$$

$$= \| f_d \|^2 + \langle JGJ^* \rangle - 2 \, \mathrm{Re} \{ \langle JC \rangle \} \tag{186}$$

where

Table 6. Optimum Semicircular Array ($r = 0.25\lambda$) of Nine Cophasally Excited Isotropic Elements

	Current	D	SNR	Q Factor
Uniform excitation	$J_1 = J_2 = J_3 = J_4 = J_5 = J_6 = J_7 = J_8 = J_9 = 1$	2.19	6.63	0.244
Optimum D without constraint on Q factor	$J_1 = J_9 = 5.23$ $J_2 = J_8 = -15.74$ $J_3 = J_7 = 34.81$ $J_4 = J_6 = -55.83$ $J_5 = 66.69$	3.63	37.8	3.76×10^3
Optimum D with a prescribed Q factor	$J_1 = J_9 = 2.24$ $J_2 = J_8 = -2.92$ $J_3 = J_7 = 3.35$ $J_4 = J_6 = -2.23$ $J_5 = 2.37$	3.25	20.2	20.0 (prescribed)
Optimum SNR without constraint on Q factor	$J_1 = J_9 = 58.86$ $J_2 = J_8 = -179.6$ $J_3 = J_7 = 412.72$ $J_4 = J_6 = -686.83$ $J_5 = 836.80$	3.52	47.1	3.26×10^3
Optimum SNR with a prescribed Q factor	$J_1 = J_9 = 12.80$ $J_2 = J_8 = -15.58$ $J_3 = J_7 = 19.70$ $J_4 = J_6 = -18.96$ $J_5 = 25.87$	3.19	21.8	20.0 (prescribed)

Element positions (in wavelengths):
$x_1 = -x_9 = r$ $z_1 = z_9 = 0$
$x_2 = -x_8 = 0.9239r$ $z_2 = z_8 = 0.3827r$
$x_3 = -x_7 = 0.7071r$ $z_3 = z_7 = 0.7071r$
$x_4 = -x_6 = 0.3827r$ $z_4 = z_6 = 0.9239r$
$x_5 = 0$ $z_5 = r$

Main beam: $\theta_0 = 0$

Thermal noise distribution: $T(\theta, \phi) = \begin{cases} 1 & \text{for } \pi/2 < \theta \leqq \pi \\ 0 & \text{otherwise} \end{cases}$

(After Lo, Lee, and Lee [65], © 1966 IEEE)

w = a possible weighting function that stresses a closer approximation of f to f_d for some angular regions

$$\mathbf{G} = \int_{4\pi} V^*\rangle\langle V\, w\, d\Omega \text{ (a positive-definite Hermitian matrix)} \qquad (187)$$

$$\mathbf{C} = \int_{4\pi} V^*\rangle f_d^*\, w\, d\Omega \qquad (188)$$

Using the variational method, the solution of $J\rangle$ which minimizes ε is found to be

$$J_0\rangle = (\mathbf{G}^{-1}\mathbf{C}\rangle)^* = U\,\mathrm{diag}[(\lambda_1)^{-1}, (\lambda_2)^{-1}, \ldots, (\lambda_N)^{-1}]\,U^\dagger\mathbf{C}^*\rangle \qquad (189)$$

where

$$\lambda_1, \lambda_2, \ldots, \lambda_N = \text{the eigenvalues, in descent order, of } \mathbf{G}^*$$
$$U \doteq \text{a unitary matrix which diagonalizes } \mathbf{G}^*$$
$$U^\dagger = \text{the complex conjugate transpose of } U$$

Since $\mathbf{G}$ depends on the array geometry, its largest to smallest eigenvalue ratio, λ_1/λ_N, can increase very rapidly to an extremely large value as the array element spacing decreases. This finally leads to an ill-conditioned $\mathbf{G}$ and a very unstable solution $J_0\rangle$. Mathematically, this phenomenon is identical with the super-directivity. Such a solution is not only impractical, but is also difficult to compute accurately. Therefore, the so-called optimum solution (189) in such a case should not be taken seriously.

Because of the physical limitation, instrumental error, environmental variation, etc., the excitation $J\rangle$ can only be adjusted in practice within an uncertain random error, say $\delta\bar{J}\rangle$. Therefore for a more practically meaningful design, this error should be taken into consideration. Assume that the error $\delta\bar{J}\rangle$ is, as in most practical cases, only *relative* to $J\rangle$:

$$\delta\bar{J}\rangle = \bar{\mathbf{A}}J\rangle \qquad (190)$$

where $\bar{\mathbf{A}}$ is a matrix with stochastic elements, which may result from, for example, some uncertainties in the feeding network. Thus the pattern function due to the actual current $J\rangle + \delta\bar{J}\rangle$ will be a random function,

$$\bar{f}(\theta, \phi) = \langle (J + \delta\bar{J}), V^*(\theta, \phi)\rangle \qquad (191)$$

and so must be the difference between $\bar{f}(\theta, \phi)$ and $f_d(\theta, \phi)$. Following (186), let

$$\bar{\varepsilon} = \| f_d - \bar{f} \|^2 \qquad (192)$$

Then for a given $J\rangle$ and a given realization of the random error $\delta\bar{J}\rangle$, there is a realization of $\bar{f}$ and also $\bar{\varepsilon}$. Hence, for the totality of all these realizations there is a probability distribution $F(\varepsilon; J\rangle)$ which defines the probability for $\bar{\varepsilon} < \varepsilon$ for the given $J\rangle$. With this distribution function one can define the probability mean of a quantity in the following formula:

$$E\{\cdot\} = \int_{\substack{\text{entire prob.}\\ \text{space}}} (\cdot)\,dF(\varepsilon; J\rangle) \qquad (193)$$

With this preparation one can define the optimization problem in many different ways. Among them we may state three theoretically possible situations as shown in Fig. 39, each giving an optimum solution different from the others,
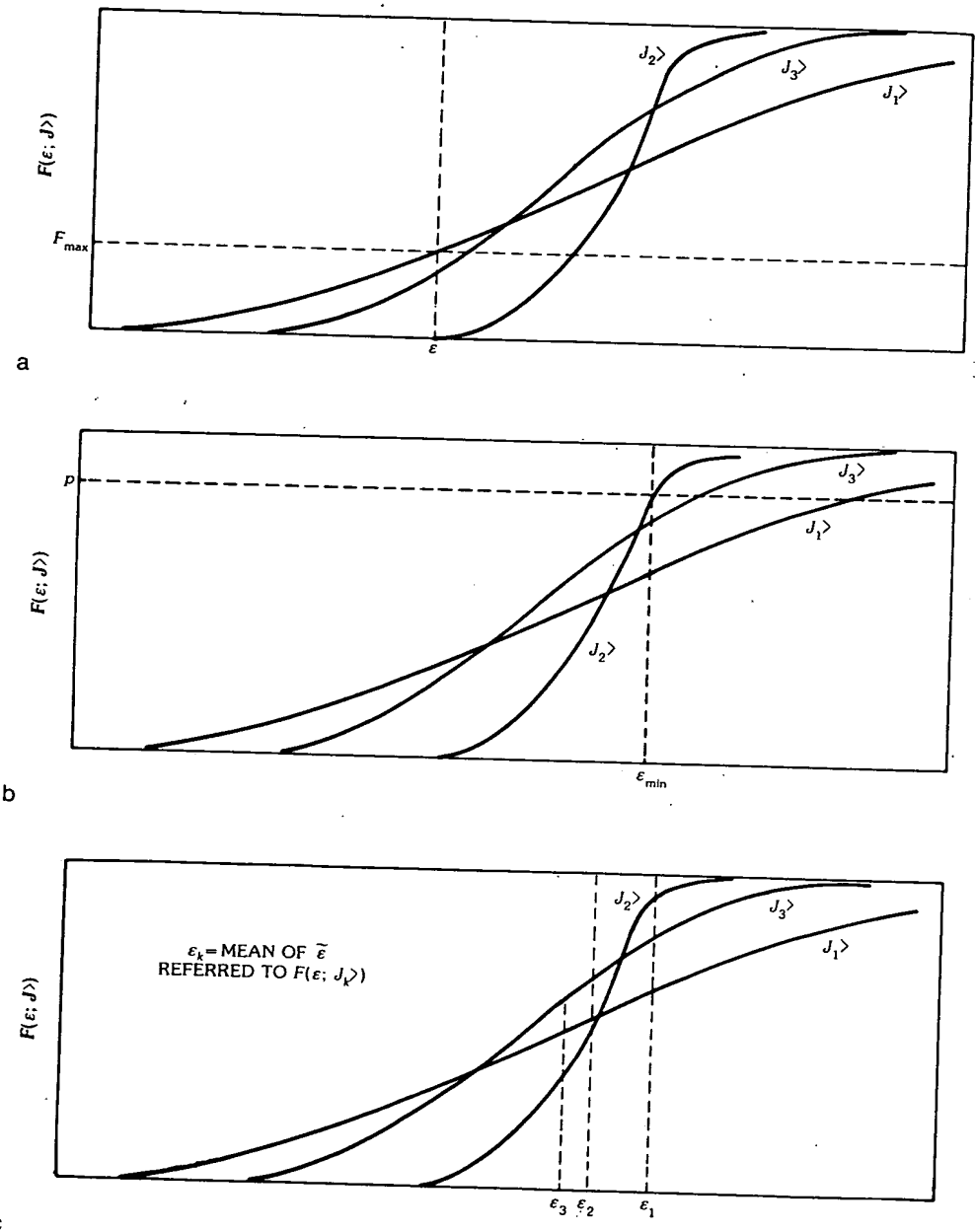
Fig. 39. Three possible philosophies of optimization. (*a*) Vertical optimization: $J_1\rangle$ is the optimum. (*b*) Horizontal optimization: $J_2\rangle$ is the optimum. (*c*) Optimization of $E\{\tilde{\varepsilon}\}$: $J_3\rangle$ is the optimum. (*After Richards and Lo [80], © 1975 IEEE*)

depending on the sense of optimization. The first scenario shown in Fig. 39a, which may be called the *vertical optimization*, illustrates that for a *given* tolerable error ε, $J\rangle$ is to be determined under the condition $F(\varepsilon; J\rangle)$ is the maximum, i.e., the largest probability for having error less than the given tolerance ε. Comparing the three possible distribution curves, $J_1\rangle$ is apparently the best solution since it gives the largest value of $F(\varepsilon; J\rangle)$ for the given ε.

The second possible optimization, which may be called the *horizontal optimization*, is defined by seeking $J\rangle$ such that for a given probability, say p, the error ε is the minimum as shown in Fig. 39b. It is seen that for this scenario $J_2\rangle$ is the best solution. The third possible optimization is to seek $J\rangle$ which minimizes the mean value of ε, namely $\bar{\varepsilon} = E\{\bar{\varepsilon}\}$. As can be seen from Fig. 39c, $J_3\rangle$ is the best solution. As stated, these three distribution curves are hypothetical and whether they would occur in a certain problem is not clear. For simplicity, in what follows the last sense of optimization is considered and it is found later that the solution so obtained also leads to approximately the optimum solutions in the other two senses.

Without loss of generality one may assume that

$$E\{\delta \bar{J}\rangle\} = 0 \tag{194}$$

Since now the excitation is $J\rangle + \delta \bar{J}\rangle$, similar to (186), the random error between the realized pattern f and desired pattern f_d is simply

$$\bar{\varepsilon} = \| f_d \|^2 + \langle (J + \delta \bar{J}) \, \mathbf{G} (J + \delta \bar{J})^* \rangle - 2 \operatorname{Re}\{ \langle (J + \delta \bar{J}) \, C \rangle \} \tag{195}$$

Since $\delta \bar{J}\rangle = \bar{A} J\rangle$,

$$\bar{\varepsilon} = E\{\bar{\varepsilon}\} = \| f_d \|^2 + \langle J \mathbf{G} J^* \rangle - 2 \operatorname{Re}\{ \langle J C \rangle \} + E\{ \langle \delta \bar{J} \, \mathbf{G} \, \delta \bar{J}^* \rangle \} \tag{196}$$

where

$$E\{ \langle \delta \bar{J} \, \mathbf{G} \, \delta \bar{J}^* \rangle \} = \langle J \mathbf{K}_2 J^* \rangle \quad \text{and} \quad \mathbf{K}_2 = E\{ \bar{A}^t \mathbf{G} \bar{A}^* \} \tag{197}$$

The *mn*th element of matrix $\mathbf{K}_2$ is given by

$$(\mathbf{K}_2)_{mn} = \sum_{i,j} G_{ij} E\{ \bar{A}_{jm} \bar{A}_{in}^* \} \tag{198}$$

where G_{ij} is the *ij*th element of $\mathbf{G}$, and $E\{ \bar{A}_{jm} \bar{A}_{in}^* \}$ is the covariance (or joint moment) of elements (jm) and (in) of $\bar{A}$. Using (196)–(198) the optimum solution of $J\rangle$ which minimizes $\bar{\varepsilon}$ for a given probabilistic property of $\delta \bar{J}$ (or $\bar{A}$) is given by

$$J\rangle = [(\mathbf{G} + \mathbf{K}_2)^{-1} C\rangle]^* \tag{199}$$

For a typical simple case where all array elements are identical, $\delta \bar{J}\rangle$ has uncorrelated elements and identical variance σ^2, the matrix $\mathbf{K}_2$ becomes diagonal:

$$\mathbf{K}_2 = \sigma^2 G_{11}\mathbf{I} = \alpha\mathbf{I} \tag{200}$$

where $\mathbf{I}$ is an identity matrix and α is a scalar equal to $\sigma^2 G_{11}$. Therefore, following (189), the optimum solution for this case is simply

$$J\rangle = \mathbf{U}\,\mathrm{Diag}[(\lambda_1 + \alpha)^{-1}, (\lambda_2 + \alpha)^{-1}, \ldots, (\lambda_N + \alpha)^{-1}]\,\mathbf{U}^\dagger C^*\rangle \tag{201}$$

where $\lambda_1, \ldots, \lambda_N$ are, as before, the eigenvalues of $\mathbf{G}$. It is interesting to compare (201) with (189) and note that the two solutions are identical except for the constant α. Now even if $\lambda_1, \ldots, \lambda_N$ march off to zero as the element spacing decreases, the solution $J\rangle$ is no longer unstable and dominated by those small λ_ns. Tihonov [125] introduced the so-called regularization method for ill-conditioned problems such as the one in (189). Cabayan's group [126], in making use of that method for the pattern synthesis problem, proposed to minimize $\| f_d - f \|^2 + \alpha\langle JJ^*\rangle$, instead of $\| f_d - f \|^2$. It is clear, however, that α must assume a proper value because if too large the minimization will be applied mainly for $\langle JJ^*\rangle$ and, if too small, the solution may be again unstable. For a given probability distribution of $\delta J\rangle$, Cabayan used the Monte Carlo method to determine the proper value of α numerically. The above analysis shows that the proper value is simply $\sigma^2 G_{11}$.

An Example—Richards and Lo [80] considered a planar array with 10 concentric rings as shown in Fig. 40. The radius of the kth ring is

$$\varrho_k = 2\pi\left[\frac{1}{4}\left(k - \frac{2}{\pi}\right) - \frac{1}{2\pi}\left(\frac{1}{2}\right)^{10-k}\right], \qquad k = 1, 2, \ldots, 10$$

A total of 200 vertical dipoles are placed over the intersecting points between the rings and 20 rays from the origin uniformly spaced in angles over 360° as illustrated in the figure. The objective is to determine the optimum excitation which will produce a pattern "closest" to a secant pattern:

$$f_d(\theta) = \begin{cases} \sec\theta & \text{for} \quad 0 < \theta \leq 70° \\ \sec 70° & \text{for } 70° \leq \theta \leq 90° \end{cases}$$

The solid curve in Fig. 41a is the nominal elevation pattern for $\sigma = 0$ using the solution given by (189) for no tolerance. The solid curve in Fig. 41b is the nominal pattern for $\sigma = 5$ percent using the solution given by (201). It is seen that the former is closer than the latter to the desired pattern f_d which is also shown in both figures. However, if the actual error $\delta J\rangle$ is added to $J\rangle$, the results are completely different. Using the Monte Carlo method, five sets of sample errors of $\delta \bar{J}\rangle$ with zero mean and 5 percent standard deviation are generated. From these five sets five sample patterns are computed for both cases, shown as the dotted curves in Fig. 41a and dots only in Fig. 41b. It is clearly seen that in the former case, where the unavoidable error is ignored in the optimization, none of the five realizations even remotely resembles the desired, or the nominal, pattern. As for the latter case, although the nominal pattern is less close to f_d than that of the first case, with all five sets of real errors included, the five realizations of the pattern are so close to
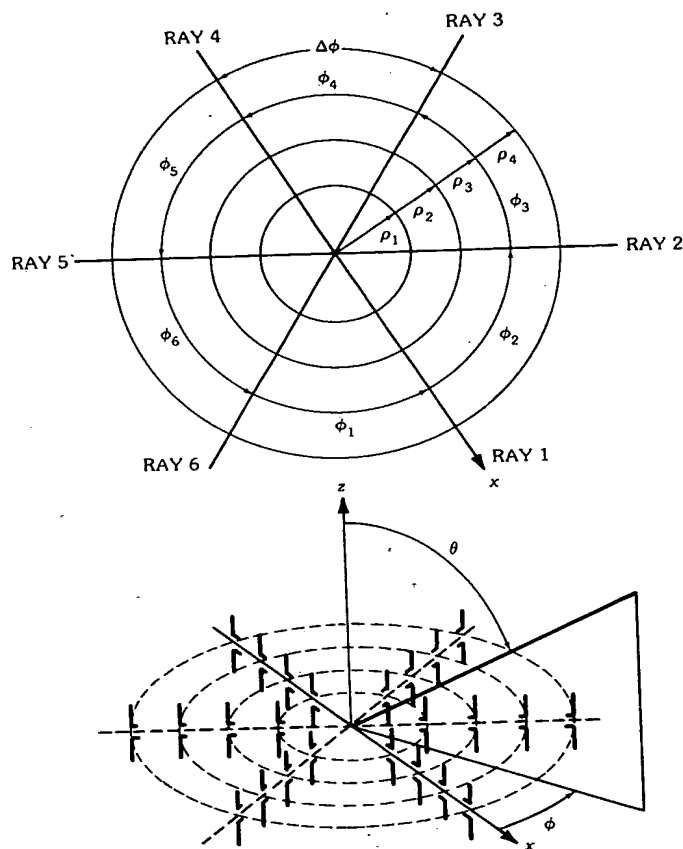
Fig. 40. Geometry of a planar array of vertical dipoles (or monopoles above the ground). (*After Richards and Lo [80], © 1975 IEEE*)

the nominal pattern that, to avoid confusion, no attempt was made to connect the dots for each realization. This result vividly confirms that in some design problems, where the stability is questionable, to demand less may *actually* obtain a better optimum solution.

For the example discussed above, Richards and Lo [80] has derived an Edgeworth series representation for the distribution function $F(\varepsilon; J\rangle)$ and also showed the validity of this solution with 2500 samples using the Monte Carlo simulation with a computer. They also verified the theoretical solution for one value of σ while using Monte Carlo simulations for a wide range of σ values. For the example studied, the sample distribution curves for $\sigma = 3$, 5, and 10 percent are very close to each other, indicating that a precise information of the statistics of δJ may not be very important for determining the optimum solution $J\rangle$. Another interesting result shows that $\| J \|$ for $\sigma = 0$ is several orders of magnitude larger than that for $\sigma = 5$ percent, implying very high Q, low efficiency, and unstable solution for the former, in agreement with previous discussion for maximum D.

a

b
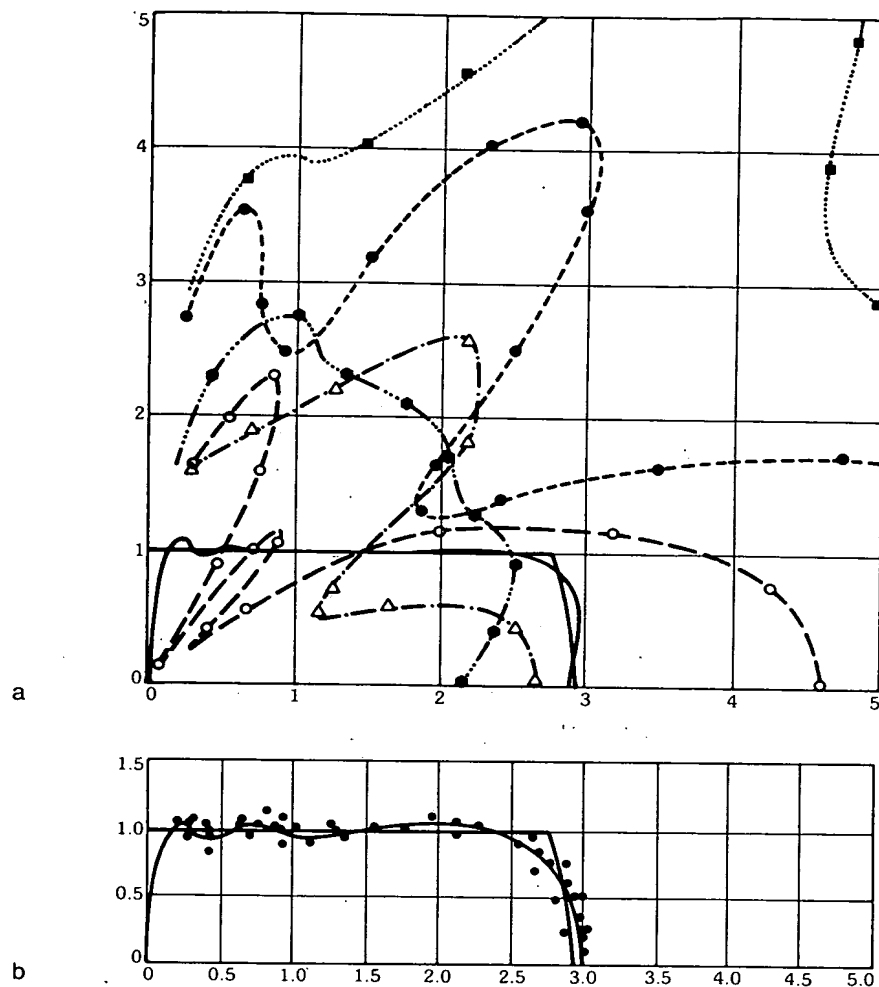
Fig. 41. Synthesis for a desired pattern function: $f_d = \sec\theta$ for $0° < \theta \leq 70°$ and $\sec 70°$ for $70° \leq \theta \leq 90°$. (a) Nominal pattern (solid curve), in polar plot, corresponding to the deterministic optimum solution with zero tolerance and five actual sample patterns (dotted) for 5% standard deviation of the tolerance, generated by the Monte Carlo method. (b) Nominal pattern (solid curve), in polar plot, corresponding to the probabilistic optimum with the 5% tolerance taken into consideration and five actual sample patterns (dots only), generated as in (a) by the Monte Carlo method. (*After Richards and Lo [80]*, © *1975 IEEE*)

8. References

[1] J. L. Allen et al., "Phased array radar studies," *Tech. Rep. 238*, MIT Lincoln Labs, August 1960.

[2] N. Amitay et al., *Theory and Analysis of Phased Array Antennas*, New York: John Wiley & Sons, 1972.

[3] H. Bach and J. E. Hansen, "Uniformly spaced arrays," chapter 5 in *Antenna Theory*,

Part 1, ed. by R. E. Collin and F. J. Zucker, New York: McGraw-Hill Book Co., 1969.

[4] C. A. Balanis, *Antenna Theory: Analysis and Design*, New York: Harper & Row, 1982.

[5] D. Barbiere, "A method for calculating the current distribution of Tschebyscheff arrays," *Proc. IRE*, vol. 40, pp. 78–82, 1952.

[6] E. T. Bayliss, "Design of monopulse antenna difference patterns with low side lobes," *Bell Syst. Tech. J.*, vol. 47, pp. 623–640, 1968.

[7] A. Bloch, R. G. Medhurst, and S. D. Pool, "A new approach to the design of super-directive aerial arrays," *IEE Proc.*, vol. 100, pt. III, pp. 303–314, 1953.

[8] A. Bloch, R. G. Medhurst, and S. D. Pool, "Superdirectivity," *Proc. IRE*, vol. 48, p. 1164, 1960.

[9] C. J. Bouwkamp and N. G. De Bruijn, "The problem of optimum antenna current distribution," *Philips Res. Rep.*, vol. 1, p. 135, 1946.

[10] P. A. Bricout, "Pattern synthesis using weighted functions," *IRE Trans. Antennas Propag.*, vol. AP-8, pp. 441–444, 1960.

[11] J. L. Brown, "A simplified derivation of the Fourier coefficients for Chebyshev patterns," *Proc. IEE*, vol. 105C, pp. 167–168, 1957.

[12] J. L. Brown, "On the determination of excitation coefficients for a Tchebycheff pattern," *IRE Trans. Antennas Propag.*, vol. AP-10, pp. 215–216, 1962.

[13] L. B. Brown and G. A. Scharp, "Tschebyscheff antenna distribution, beam-width, and gain tables," *NOLC Rep. 383*, February 1958.

[14] D. K. Cheng, "Optimization techniques for antenna arrays," *Proc. IEEE*, vol. 59, pp. 1664–1674, 1971.

[15] D. K. Cheng and M. T. Ma, "A new mathematical approach for linear array analysis," *IRE Trans. Antennas Propag.*, vol. AP-8, pp. 255–259, 1960.

[16] L. J. Chu, "Physical limitations of omnidirectional antennas," *J. Appl. Phys.*, vol. 19, pp. 1163–1175, 1948.

[17] H. P. Coleman, "An iterative technique for reducing side lobes of circular arrays," *IEEE Trans. Antennas Propag.*, vol. AP-18, pp. 566–567, July 1970.

[18] R. E. Collin and S. Rothschild, "Evaluation of antenna Q," *IEEE Trans. Antennas Propag.*, vol. AP-12, pp. 23–27, January 1964.

[19] A. G. Dermerud and J. J. Gustincic, "The interpolation of general active array impedance from multielement simulators," *IEEE Trans. Antennas Propag.*, vol. AP-27, pp. 68–71, 1979.

[20] B. L. Diamond, "A generalized approach to the analysis of infinite planar array antennas," *Proc. IEEE*, vol. 56, pp. 1837–1851, 1968.

[21] B. L. Diamond and G. H. Knittel, "A new procedure for the design of a waveguide element for a phased-array antenna," *Phased Array Antennas*, ed. by A. A. Oliner and G. H. Knittel, Dedham, Mass.: Artech House, 1972, pp. 149–156.

[22] C. L. Dolph, "A current distribution for broadside arrays which optimizes the relationship between beam width and side lobe level," *Proc. IRE*, vol. 34, pp. 335–348, 1946.

[23] C. J. Drane, "Derivation of excitation coefficients for Chebyshev arrays," *Proc. IEE*, vol. 110, pp. 1755–1758, 1963.

[24] C. J. Drane, "Dolph-Chebyshev excitation coefficient approximation," *IEEE Trans. Antennas Propag.*, vol. AP-12, pp. 781–782, 1964.

[25] C. J. Drane, "Useful approximations for the directivity and beamwidth of large scanning Dolph-Chebyshev arrays," *Proc. IEEE*, vol. 56, pp. 1779–1787, 1968.

[26] R. H. DuHamel, "Optimum patterns for end-fire arrays," *Proc. IRE*, vol. 41, pp. 652–659, 1953.

[27] R. H. DuHamel, "Pattern synthesis for antenna arrays on circular, elliptical, and spherical surfaces," *Tech. Rep. no. 16*, E. E. Research Lab, Univ. of Illinois, Urbana, 1952.

[28] R. S. Elliott, *Antenna Theory and Design*, Englewood Cliffs: Prentice-Hall, 1981.

[29] R. S. Elliott, "Mechanical and electrical tolerances for two-dimensional scanning

antenna arrays," *IRE Trans. Antennas Propag.*, vol. AP-6, pp. 114–120, 1958.

[30] R. S. Elliott, "The theory of antenna arrays," in chapter 1 of *Microwave Scanning Antennas, Volume II*, ed. by R. C. Hansen, New York: Academic Press, 1966.

[31] R. S. Elliott, "Design of line-source antennas for sum patterns with side lobes of individually arbitrary heights," *IEEE Trans. Antennas Propag.*, vol. AP-24, pp. 76–83, 1976.

[32] R. S. Elliott, "On discretizing continuous aperture distributions," *IEEE Trans. Antennas Propag.*, vol. AP-25, pp. 617–621, 1977.

[33] R. S. Elliott and R. M. Johnson, "Experimental results on a linear array designed for asymmetric side lobes," *IEEE Trans. Antennas Propag.*, vol. AP-26, pp. 351–352, 1978.

[34] J. E. Evans, "Synthesis of equiripple sector antenna patterns," *IEEE Trans. Antennas Propag.*, vol. AP-24, pp. 347–353, 1976.

[35] R. J. Evans and T. E. Fortmann, "Design of optimal line-source antennas," *IEEE Trans. Antennas Propag.*, vol. AP-23, pp. 342–347, 1975.

[36] R. L. Fante, "Optimum distribution over a circular aperture for best mean-square approximation to a given radiation pattern," *IEEE Trans. Antennas Propag.*, vol. AP-18, pp. 177–181, 1970.

[37] G. R. Forbes, "An end-fire array continuously proximity-coupled to a two-wire line," *IEEE Trans. Antennas Propag.*, vol. AP-8, pp. 518–519, 1960.

[38] A. C. Gately, Jr., et al., "A network description for antenna problems," *Proc. IEEE*, vol. 56, pp. 1181–1193, 1968.

[39] W. S. Gregorwich et al., "A waveguide simulator for the determination of a phased-array resonance," *IEEE G-AP Intl. Symp. Dig.*, pp. 134–141, 1968.

[40] J. J. Gustincic, "The determination of active array impedance with multielement waveguide simulators," *IEEE Trans. Antennas Propag.*, vol. AP-20, pp. 589–595, 1972.

[41] P. W. Hannan and M. A. Balfour, "Simulation of a phased-array antenna in waveguide," *IEEE Trans. Antennas Propag.*, vol. AP-13, pp. 342–353, 1965.

[42] P. W. Hannan, "Discovery of an array surface wave in a simulator," *IEEE Trans. Antennas Propag.*, vol. AP-15, pp. 574–576, 1967.

[43] R. C. Hansen, "Tables of Taylor distributions for circular aperture antennas," *IRE Trans. Antennas Propag.*, vol. AP-8, pp. 23–26, 1960.

[44] R. C. Hansen, "Comparison of square array directivity formulas," *IEEE Trans. Antennas Propag.*, vol. AP-20, pp. 100–102, 1972.

[45] R. C. Hansen, "A one-parameter circular aperture distribution with narrow beamwidth and low sidelobes," *IEEE Trans. Antennas Propag.*, vol. AP-24, pp. 477–480, 1976.

[46] R. C. Hansen, "Gain limitations of large antennas," *IRE Trans. Antennas Propag.*, vol. AP-8, pp. 490–495, 1970; see also correction in vol. AP-13, p. 997, 1965.

[47] R. C. Hansen, *Microwave Scanning Antennas, Volume 1*, chapter 1, New York: Academic Press, 1964.

[48] R. C. Hansen (ed.), Special issue on "Electronic scanning," *Proc. IEEE*, vol. 56, pp. 1761–2038, 1968.

[49] R. C. Hansen, *Significant Phased Array Papers*, Dedham: Artech House, 1973.

[50] W. W. Hansen and J. R. Woodyard, "A new principle in directional antenna design," *Proc. IRE*, vol. 26, pp. 333–345, 1938.

[51] R. F. Harrington, "Effect of antenna size on gain, bandwidth, and efficiency," *J. Res. Natl. Bur. Stand.* (US), vol. 64D, pp. 1–12, 1960.

[52] W. G. Jaeckle, "Antenna synthesis by weighted Fourier coefficients," *IEEE Trans. Antennas Propag.*, vol. AP-12, pp. 369–370, 1964.

[53] E. C. Jordan and K. G. Balmain, "Electromagnetic waves and radiating systems," section 14.08, Englewood Cliffs: Prentice-Hall, 1968.

[54] W. K. Kahn, "Ideal efficiency of a radiating element in an infinite array," *IEEE Trans. Antennas Propag.*, vol. AP-15, pp. 534–538, 1967.

[55] W. K. Kahn, "Impedance-match and element-pattern constraints for finite arrays," *IEEE Trans. Antennas Propag.*, vol. AP-25, pp. 747–755, 1977.

[56] H. E. King, "Directivity of a broadside array of isotropic radiator," *IRE Trans. Antennas Propag.*, vol. AP-7, pp. 197–198, 1959.

[57] M. J. King and R. K. Thomas, "Gain of large scanned arrays," *IRE Trans. Antennas Propag.*, vol. AP-8, pp. 635–636, 1960.

[58] R. W. P. King, *The Theory of Linear Antennas*, Cambridge: Harvard Univ. Press, 1956.

[59] H. L. Knudsen, "Radiation from ring quasi-arrays," *IRE Trans. Antennas Propag.*, vol. AP-4, pp. 452–472, 1956.

[60] J. D. Kraus, *Antennas*, New York: McGraw-Hill Book Co., 1950.

[61] H. N. Kritikos, "Optimal signal-to-noise ratio for linear arrays by the Schwartz inequality," *J. Franklin Inst.*, vol. 276, pp. 195–304, 1963.

[62] A. Ksienski, "Maximally flat and quasi-smooth sector beams," *IRE Trans. Antennas Propag.*, vol. AP-8, pp. 476–484, 1960.

[63] L. Lapaz and G. A. Miller, "Optimum current distributions on vertical antennas," *Proc. IRE*, vol. 31, pp. 214–232, 1943.

[64] Y. T. Lo and S. W. Lee, "Affine transformation and its application to antenna arrays," *IEEE Trans. Antennas Propag.*, vol. AP-13, pp. 890–896, 1965.

[65] Y. T. Lo, S. W. Lee, and Q. H. Lee, "Optimization of directivity and signal-to-noise ratio of an arbitrary antenna array," *Proc. IEEE*, vol. 54, pp. 1033–1045, 1966.

[66] Y. T. Lo and H. C. Hsuan, "An equivalence theory between elliptical and circular arrays," *IEEE Trans. Antennas Propag.*, vol. AP-13, pp. 247–256, 1965.

[67] M. T. Ma, *Theory and Application of Antenna Arrays*, New York: John Wiley & Sons, 1974.

[68] M. T. Ma, "A new mathematical approach for linear array analysis and synthesis," PhD dissertation, Syracuse University, 1961.

[69] M. T. Ma and L. C. Walters, "Synthesis of concentric ring antenna arrays yielding approximately equal sidelobes," *Radio Sci.*, vol. 3, pp. 465–470, May 1968.

[70] R. B. Mack, "A study of circular arrays," technical report, Cruft Lab, Harvard University, May 1963.

[71] B. A. Munk et al., "Scan independent phased arrays," *Radio Sci.*, vol. 14, pp. 979–990, 1979.

[72] E. A. Nelson, "Quantization sidelobes of a phased array with a triangular element arrangement," *IEEE Trans. Antennas Propag.*, vol. AP-17, pp. 363–365, 1969.

[73] E. H. Newman et al., "Superdirective receiving arrays," *IEEE Trans. Antennas Propag.*, vol. AP-26, pp. 629–635, 1978.

[74] R. L. Pritchard, "Optimum directivity patterns for linear point arrays," *J. Acoust. Soc. Am.*, vol. 25, pp. 879–891, 1953.

[75] D. R. Rhodes, "The optimum line source of the best mean-square approximation to a given radiation pattern," *IEEE Trans. Antennas Propag.*, vol. AP-11, pp. 440–446, 1963.

[76] D. R. Rhodes, "On an optimum line source for maximum directivity," *IEEE Trans. Antennas Propag.*, vol. AP-17, pp. 485–492, 1969.

[77] D. R. Rhodes, "On a fundamental principle in the theory of planar antennas," *Proc. IEEE*, vol. 52, pp. 1013–1021, 1965.

[78] D. R. Rhodes, *Synthesis of Planar Antenna Sources*, London: Clarendon Press, 1974.

[79] H. J. Riblet, "Discussion on 'A current distribution for broadside arrays which optimizes the relationship between beam width and side-lobe level,'" *Proc. IRE*, vol. 35, pp. 489–492, 1947.

[80] W. F. Richards and Y. T. Lo, "Antenna pattern synthesis based on optimization in a probabilistic sense," *IEEE Trans. Antennas Propag.*, vol. AP-23, pp. 165–172, 1975.

[81] G. M. Royer, "Directive gain and impedance of a ring array of antennas," *IEEE Trans. Antennas Propag.*, vol. AP-14, pp. 566–573, 1966.

[82] L. A. Rondinelli, "Effects of random errors on the performance of antenna arrays of many elements," *IRE Natl. Conv. Rec.*, pt. 1, pp. 174–189, 1959.

[83] J. Ruze, "Antenna tolerance theory—a review," *Proc. IEEE*, vol. 54, pp. 633–640, 1966.

[84] H. E. Salzer, "Calculating Fourier coefficients for Chebyshev patterns," *Proc.*

IEEE, vol. 63, pp. 195–197, 1975.

[85]   S. A. Schelkunoff, "A mathematical theory of linear arrays," *Bell Syst. Tech. J.*, vol. 22, pp. 80–107, 1943.

[86]   S. A. Schelkunoff and H. T. Friis, *Antenna Theory and Practice*, New York: John Wiley & Sons, 1942, pp. 368 and 401.

[87]   A. C. Schell and A. Ishimaru, "Antenna pattern synthesis," chapter 7. in *Antenna Theory*, ed. by R. E. Collin and F. J. Zucker, New York: McGraw-Hill Book Co., 1969.

[88]   E. D. Sharp, "A triangular arrangement of planar-array elements that reduces the number needed," *IRE Trans. Antennas Propag.*, vol. AP-9, pp. 126–129, 1961.

[89]   J. C. Simon, "Application of periodic functions approximation to antenna pattern synthesis and circuit theory," *IRE Trans. Antennas Propag.*, vol. AP-4, pp. 429–440, 1956.

[90]   G. C. Southworth, "Arrays of linear elements," in *Antenna Engineering Handbook*, ed. by H. Jasik, New York: McGraw-Hill Book Co., 1961.

[91]   R. J. Spellmire, "Tables of Taylor aperture distributions," *Rep. TM 581*, Hughes Aircraft Co., Culver City, CA, 1958.

[92]   L. Stark, "Radiation impedance of a dipole in an infinite planar phased array," *Radio Sci.*, vol. 1, pp. 361–377, 1966.

[93]   R. J. Stegen, "Excitation coefficients and beamwidths of Tschebyscheff arrays," *Proc. IRE*, vol. 41, pp. 1671–1674, 1953.

[94]   R. J. Stegen, "Gain of Tchebyscheff arrays," *IRE Trans. Antennas Propag.*, vol. AP-8, pp. 629–631, 1960.

[95]   W. L. Stutzman, "Synthesis of shaped-beam radiation patterns using the iterative sampling method," *IEEE Trans. Antennas Propag.*, vol. AP-19, pp. 36–41, 1971.

[96]   W. L. Stutzman, "Side lobe control of antenna patterns," *IEEE Trans. Antennas Propag.*, vol. AP-20, pp. 102–104, 1972.

[97]   W. L. Stutzman and G. A. Thiele, *Antenna Theory and Design*, New York: John Wiley & Sons, 1981.

[98]   C. T. Tai, "The optimum directivity of uniformly spaced broadside arrays of dipoles," *IEEE Trans. Antennas Propag.*, vol. AP-12, pp. 447–454, 1964.

[99]   T. T. Taylor, "Design of circular apertures of narrow beamwidth and low side lobes," *IRE Trans. Antennas Propag.*, vol. AP-8, pp. 17–22, 1960.

[100] T. T. Taylor, "Design of line-source antennas for narrow beamwidth and low side lobes," *IRE Trans. Antennas Propag.*, vol. AP-3, pp. 16–28, 1955.

[101] T. T. Taylor, "A synthesis method for circular and cylindrical antennas composed of discrete elements," *IRE Trans. Antennas Propag.*, vol. AP-1, pp. 251–261, 1952.

[102] J. D. Tillman, Jr., "The theory and design of circular antenna arrays," Univ. of Tennessee, Eng. Exp. Station, Knoxville, 1966.

[103] G. Toraldo Di Francia, "Directivity, super-gain, and information," *IRE Trans.*, 1956, pp. 473–478; also "Theory of antenna arrays," special issue, *Radio Sci.*, vols. 3–5, 1968.

[104] G. N. Tsandoulas, "Tolerance control in an array antenna," *Microwave J.*, vol. 20, pp. 24–30, 1977.

[105] F. I. Tseng, "Design of array and line-source antennas for Taylor patterns with a null," *IEEE Trans. Antennas Propag.*, vol. AP-27, pp. 474–479, 1979.

[106] F. I. Tseng and D. K. Cheng, "Antenna pattern response to arbitrary time signals," *Can. J. Phys.*, vol. 42, pp. 1358–1368, 1964.

[107] F. I. Tseng and D. K. Cheng, "Optimum scannable planar arrays with an invariant side lobe level," *Proc. IEEE*, vol. 56, pp. 1771–1778, 1968.

[108] A. I. Uzkov, "An approach to the problem of optimum directive antenna design," *C. R. Acad. Sci. URSS*, vol. 53, p. 35, 1946.

[109] M. Uzsoky and L. Solymar, "Theory of super-directive linear arrays," *Acta Phys. Hung.*, vol. 6, pp. 185–205, 1956.

[110] G. J. van der Maas, "A simplified calculation for Dolph-Tchebycheff arrays," *J. Appl. Phys.*, vol. 25, pp. 121–124, 1954.

[111] R. C. Voges and J. K. Butler, "Phase optimization of antenna array gain with constrained amplitude excitation," *IEEE Trans. Antennas Propag.*, vol. AP-20, pp. 432–436, 1972.

[112] W. H. von Aulock, "Properties of phased arrays," *Proc. IRE*, vol. 48, pp. 1715–1727, 1960.

[113] W. Wasylkiwskyj and W. J. Kahn, "Element pattern bounds in uniform phased arrays," *IEEE Trans. Antennas Propag.*, vol. AP-25, pp. 597–604, 1977.

[114] W. Wasylkiwskyj and W. K. Kahn, "Element patterns and active reflection coefficient in uniform phased arrays," *IEEE Trans. Antennas Propag.*, vol. AP-22, pp. 207–212, 1974.

[115] H. A. Wheeler, "A survey of the simulator technique for designing a radiating element," in *Phased Array Antennas*, ed. by A. A. Oliner and G. H. Knittel, pp. 132–148, Dedham: Artech House, 1972.

[116] L. P. Winkler and M. Schwartz, "A fast numerical method for determining the optimum snr of an array subject to a Q factor constraint," *IEEE Trans. Antennas Propag.*, vol. AP-20, pp. 503–505, 1972.

[117] P. M. Woodward, "A method for calculating the field over a plane aperture required to produce a given polar diagram," *Proc. IEE*, vol. 93, pt. IIIA, pp. 1554–1558, 1946.

[118] P. M. Woodward, "A method of calculating the field over a plane aperture required to produce a given polar diagram," *Proc. IEE*, vol. 93, pt. III, pp. 1554–1558, 1947.

[119] P. M. Woodward and J. D. Lawson, "The theoretical precision with which an arbitrary radiation pattern may be obtained from a source of finite size," *Proc. IEE*, vol. 95, pt. III, pp. 363–370, 1948.

[120] N. Yaru, "A note on supergain antenna arrays," *Proc. IRE*, vol. 39, pp. 1081–1085, 1951.

[121] R. S. Elliott, "Beamwidth and directivity of large scanning arrays," first of two parts, *Microwave J.*, December 1963.

[122] C. S. Liang and Y. T. Lo, "A multipole-field study for the multiarm log-spiral antennas," *IEEE Trans. Antennas Propag.*, vol. AP-16, pp. 656–664, 1968.

[123] Ye. V. Baklanov, "Chebyshev distribution of currents for a plane array of radiators," *Radio Eng. Electron. Phys.*, vol. 11, pp. 640–642, April 1966 (English translation from Russian).

[124] E. N. Gilbert and S. P. Morgan, "Optimum design of directive antenna arrays subject to random variations," *Bell Syst. Tech. J.*, vol. 34, pp. 637–661, 1955.

[125] A. H. Tihonov, "Solution of incorrectly formulated problems and the regularization method," *Sov. Math.*, vol. 4, pp. 1035–1038, 1964.

[126] H. S. Cabayan, P. E. Mayes, and G. A. Deschamps, "Techniques for computation and realization of stable solutions for synthesis of antenna patterns," *Antenna Lab Rep. 70-13*, Univ. of Illinois at Urbana, October 1970.

Chapter 13

Periodic Arrays

R. J. Mailloux
Rome Air Development Center, Electromagnetic Sciences Division

CONTENTS

Robert J. Mailloux was born in Lynn, Massachusetts. He received the BS degree in electrical engineering from Northeastern University, Boston, Massachusetts, in 1961, and the SM and PhD degrees from Harvard University, Cambridge, Massachusetts, in 1962 and 1965, respectively.

He was with the NASA Electronics Research Center, in Cambridge, from 1965 to 1970, and with the Air Force Cambridge Research Laboratories from 1970 to 1976. He is presently acting chief of the Antennas and Components Division, Rome Air Development Center, Electromagnetics Directorate. His research interests are in the area of periodic structures and antenna arrays. He has published numerous papers on antennas and arrays, and book chapters on antenna research topics, on hybrid systems of arrays and reflectors or lenses, and on conformal arrays. He was elected to the grade of Fellow of the IEEE in 1978.

Dr. Mailloux is a member of Tau Beta Pi, Eta Kappa Nu, Sigma Xi, and Commission B of URSI. He was Technical Activities Chairman for Commission B of URSI from 1979 to 1982, and President of the Hanscom Chapter, Sigma Xi, in 1980. He was President of the Antenna and Propagation Society in 1983 and has previously been AP-S Distinguished Lecturer, AdCom Member, and Meetings Chairman.

1. Introduction

Most scanning array antennas are composed of rows and columns of periodically spaced antenna elements. Periodic arrays can be designed to provide extremely low side lobes and high gain when element spacing is kept relatively small, and they are chosen in preference to arrays with aperiodic lattices for many radar and communications applications. In addition, when hundreds or thousands of closely spaced elements are required, it is also simpler and cheaper to construct periodic than aperiodic arrays. Aperiodic arrays, treated in the next chapter, have advantages in high-resolution thinned configurations, and when used to achieve equivalent amplitude taper without the use of a complex feed network.

Chapter 11 deals with a number of theoretical aspects of phased arrays and establishes a basis in mathematics by which one can compute or synthesize detailed radiation patterns. This chapter will provide some background in theory to increase comprehension, but is intended mainly to present fundamental engineering data to aid in antenna design and evaluation.

Although phase-scanned arrays are the main topic of the chapter, some consideration is given to time-delay scanned arrays. There are discussions of pattern distortions resulting from grating lobes and array errors and a brief treatment of mutual coupling effects. Pattern synthesis is covered in more detail in Chapter 11, so the treatment in this chapter is restricted to giving engineering data and some examples of the effects of discreting line source data. The results of organizing an array into subarrays are presented and several approaches described that achieve wide instantaneous bandwidth.

The discussion of specific devices for arrays is restricted to passive components (phase shifters, power dividers, array elements, etc.) and does not include amplifiers or any of a wide variety of array control systems, mixer steering, or signal processing means of pattern control.

Pattern and Excitation

The most general form of radiation pattern used in this section is given below. Each element at position (x_i, y_i, z_i) of Fig. 1 is excited by a complex weighting a_i and radiates with a vector element pattern $\mathbf{f}_i(\theta, \phi)$ so that the total far-field radiated field is given by

$$\mathbf{E}(\mathbf{r}) = \frac{e^{-jkR_0}}{R_0} \sum_i a_i \mathbf{f}_i(\theta, \phi) \, e^{+jk\mathbf{r}_i \cdot \hat{\varrho}} \tag{1}$$

where $k = 2\pi/\lambda$, the vectors $\mathbf{r}_i$ define the locations of array elements relative to the element with index zero, and the unit vector $\hat{\varrho}$ is the position vector locating the observation point P a distance R_0 from the origin at the zeroth element:

13-5
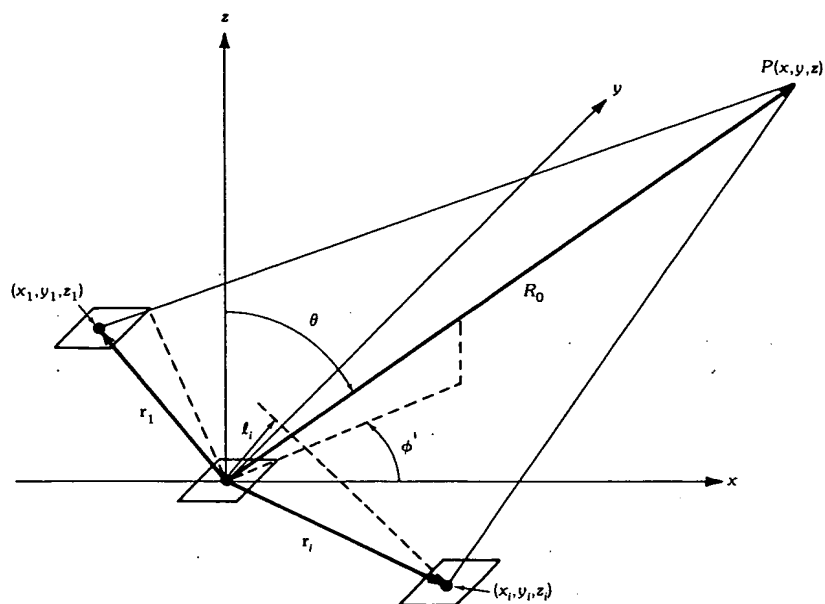
Fig. 1. Generalized array geometry.

$$\hat{\varrho} = \hat{x}u + \hat{y}v + \hat{z}\cos\theta$$
$$\mathbf{r}_i = \hat{x}x_i + \hat{y}y_i + \hat{z}z_i \qquad\qquad (2)$$
$$\mathbf{R}_0 = |r - r_0| = \sqrt{x^2 + y^2 + z^2}$$

The direction cosines u and v are

$$u = \sin\theta\cos\phi$$
$$v = \sin\theta\sin\phi$$

with $u^2 + v^2 \leqq 1$.

In this generalized form the weighting a_i is the *applied* excitation, an incident mode amplitude for a transmission-line or waveguide-fed array, or an *applied* voltage for an array of wire elements. The feeding sources are assumed matched to their characteristic impedance. The variables $\mathbf{f}_i(\theta, \phi)$ are the radiation patterns of each ith element, in the presence of all other elements, and so are called *element patterns* (sometimes termed "active element patterns"). The vector element patterns $\mathbf{f}_i$ are in general different, even in an array of like elements. The difference results from the interaction between individual elements and proximity to the array edge. In the formal treatment of antenna radiation the element patterns are unknowns, obtained by solving an electromagnetic boundary value problem.

Before leaving the topic of interpreting (1), it should be noted that an alternative but fully as general formalism considers the a_i to be the actual (unknown) currents for wire elements, or electric fields for slots or apertures. From this

perspective, when mutual coupling is considered, the $a_i f_i(\theta, \phi)$ are replaced by the radiation pattern of the unknown distribution of current or field on the ith element: a distribution that is found from the solution of a boundary value problem, and will not, in general, be directly proportional to the applied excitations. In the absence of mutual coupling, however, the two formalisms are identical.

Throughout this section the a_i will be the applied excitation, as in the element pattern formalism described earlier. Furthermore, throughout Sections 2, 3, and 5, the element patterns will be assumed equal and isotropic over the hemisphere $z \geqq 0$, but element pattern distortion will be described in Section 4, in connection with array mutual coupling. In addition, it is assumed that all expressions relate to the axis of principal polarization, and so the patterns are written as scalar functions.

The usual purpose of an array is to form a beam at some specific angle in space (θ_0, ϕ_0). In the absence of mutual coupling this can be done at all frequencies by choosing the excitation

$$a_i = |a_i| e^{-jk \mathbf{r}_i \cdot \hat{\mathbf{e}}_0} = |a_i| e^{-jk\ell_i} \qquad (3)$$

with ϱ_0 given by (2) using θ_0 and ϕ_0 in the direction cosine expressions. At such a point the fully collimated beam field strength is a simple vector summation of the element patterns weighted by the amplitudes $|a_i|$

$$\mathbf{E}_0(\mathbf{R}_0) = \frac{e^{-jkR_0}}{R_0} \sum_i \mathbf{f}_i(\theta_0, \phi_0)|a_i| \qquad (4)$$

and if the element patterns $\mathbf{f}_i$ are equal and isotropic, $(|\mathbf{f}_i| = 1)$; this is the largest possible value of the field $\mathbf{E}(\mathbf{r})$ for any given R_0 in the far field. Selection of the excitations of (3) is understood intuitively by considering that the projected distance to the observer at (R_0, θ_0, ϕ_0) is different for each array element by the length ℓ_i in Fig. 1. Removal of this path length difference will cause the contributions from each element to add in phase in the far field. The envelope of coefficients $|a_i|$ is the array illumination and is the primary determinant of the radiation side lobe levels, just as it is for aperture antennas.

Time Delay and Phase Steering

Applying signals of the form of (3) is called *time-delay steering* because the phase of the excitation signals exactly compensates for the time delay of a signal traveling in the projected distances ℓ_i. Time-delay steering results in a fully collimated beam at all frequencies, but is extremely expensive, bulky, and lossy since it depends on switching relatively long delay lines. For this reason true time delay is not often used at the array element level but more commonly incorporated into the feed circuits of arrays divided into subarrays. Examples of subarray excitation are described in Section 3.

Alternatively, at some fixed frequency f_0, with wavelength λ_0 and wave number $k_0 = 2\pi/\lambda_0$, phase weighting can be substituted for the time-delay steering. In such a case the weighting factors a_i are

$$a_i = |a_i| e^{-jk_0 \mathbf{r}_i \cdot \hat{\mathbf{e}}_0} \qquad (5)$$

and

$$E_0(\mathbf{r}) = \frac{e^{-jkR_0}}{R_0} \sum_i \mathbf{f}_i(\theta, \phi) |a_i| e^{+j\mathbf{r}_i \cdot (k\hat{\varrho} - k_0\hat{\varrho}_0)}$$

which represents exact collimation only at fixed frequencies $\lambda = \lambda_0$ and is called *phase steering*. Most arrays are phase steered, but when wide operating bandwidths are required it may be necessary to investigate options for time delay. Section 3 describes several broadbanding approaches.

Examples of Array Collimation

Several examples of array collimation are given below for the arrays of Fig. 2. Note m and n are half-integers, $\pm\frac{1}{2}, \ldots$, to $\pm(N_y - 1)/2$ or $\pm(N_x - 1)/2$ for arrays with even numbers of elements, or integers, $0, \pm 1, \ldots, (N_y - 1)/2$, etc.

Periodic Column Array in One Plane

$$\mathbf{r}_m = \hat{x}x_m = \hat{x}md_x, \qquad u_0 = \cos\theta_0 \tag{6}$$

Steering excitation:

$$a_m = |a_m| e^{-jk_0 md_x u_0}$$

Radiation pattern:

$$\mathbf{E}(\mathbf{r}) = \frac{e^{-jkR_0}}{R_0} \sum_m \mathbf{f}_m(\theta, \phi) |a_m| e^{jmd_x(ku - k_0u_0)}$$

Periodic Two-Dimensional Array (Rectangular Lattice)

$$\mathbf{r}_{mn} = \hat{x}md_x + \hat{y}nd_y, \qquad u_0 = \sin\theta_0 \cos\phi_0, \qquad v_0 = \sin\theta_0 \sin\phi_0$$

Steering excitation:

$$a_{mn} = |a_{mn}| e^{-jk_0(md_x u_0 + nd_y v_0)} \tag{7}$$

Radiation pattern:

$$\mathbf{E}(\mathbf{r}) = \frac{e^{-jkR_0}}{R_0} \sum_{m,n} \mathbf{f}_{mn}(\theta, \phi) |a_{mn}| e^{j[md_x(ku - k_0u_0) + nd_y(kv - k_0v_0)]}$$

Circular Array Section

The circular array section of Fig. 2c is another characteristic array shape that requires a simple regular excitation vector to form a beam in the principal plane $(\theta, 0)$:

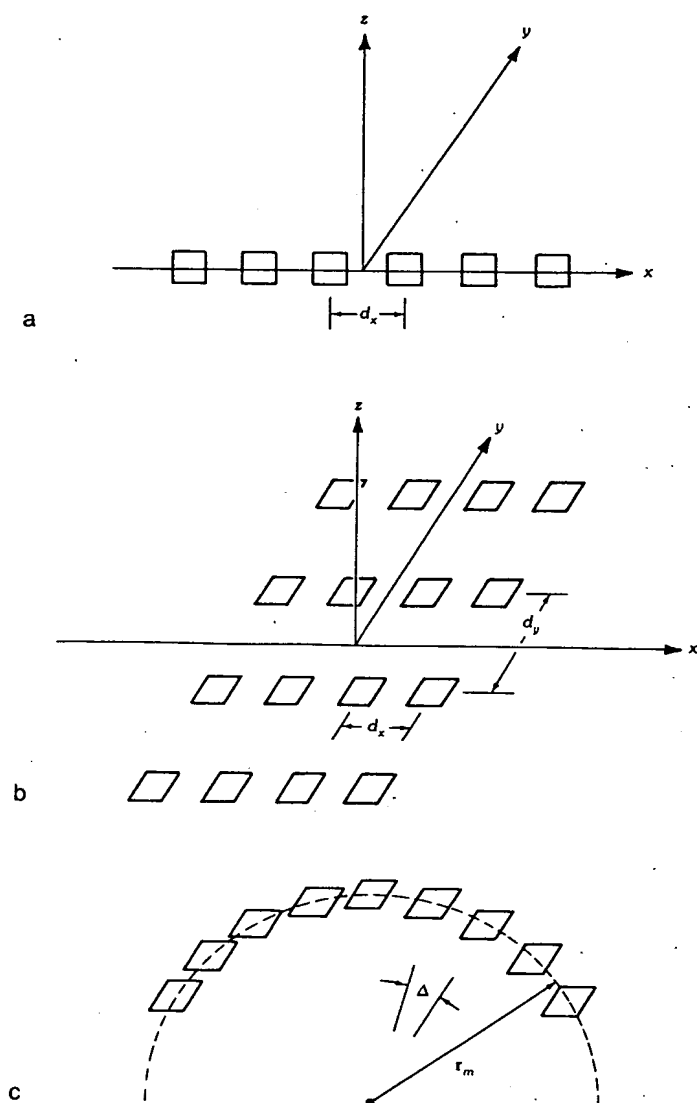**Fig. 2.** Common array orientations. (a) One-dimensional array. (b) Two-dimensional rectangular grid array. (c) Sector of circular array.

$$\mathbf{r}_m = \hat{\mathbf{x}}a\cos\theta_m + \hat{\mathbf{y}}a\sin\theta_m, \qquad \hat{\mathbf{\varrho}} = \hat{\mathbf{x}}\cos\theta + \hat{\mathbf{y}}\sin\theta \qquad (8)$$

Steering excitation:

$$a_m = |a_m|e^{-jk_0 a\cos(\theta_0 - \theta_m)}, \qquad \theta_m = m\Delta$$

Radiation pattern:

$$\mathbf{E}(\mathbf{r}) = \frac{e^{-jkR_0}}{R_0} \sum_m \mathbf{f}_m(\theta) |a_m| e^{ja[k\cos(\theta - \theta_m) - k_0\cos(\theta_0 - \theta_m)]}$$

In each of the above cases the phase steering beam collimation is changed to time-delayed collimation by substituting $k = 2\pi/\lambda$ for the phase steered term $k_0 = 2\pi/\lambda_0$.

Quality of the Array Beam

The quality of the beam formed by an array is measured by a number of factors. Chief among these are the directivity, beamwidth, and side lobe level of the array pattern, and the bandwidth over which satisfactory radiation characteristics can be obtained.

The *directivity* is the ratio of power density at the peak of the main beam ($\mathbf{r} = \mathbf{r}_0$) to the average power density, or in terms of (1):

$$D = E(\mathbf{r}_0) E^*(\mathbf{r}_0) \Big/ (4\pi)^{-2} \int_0^{2\pi} \int_0^{\pi} E(\mathbf{r}) E^*(\mathbf{r}) \sin\theta \, d\theta \, d\phi \tag{9}$$

The integral over θ is often carried only to $\pi/2$ for most planar arrays with a ground screen, as it is assumed that radiation is negligible for $\theta > \pi/2$, which is consistent with the assumption of hemispherical element patterns.

Equation 9 can be reduced to much simpler forms for linear and planar arrays.

Elliott [1] gives convenient formulas for the directivity of linear dipole arrays and derives an especially simple form for arrays of isotropic elements with half-wave spacing and currents a_m as in (6).

$$D = \left(\sum a_m \right)^2 \Big/ \sum a_m^2 \tag{10}$$

The directivity is increased by the factor 2 for hemispherical element patterns. This expression shows the directivity of a linear array to be independent of scan angle. As pointed out by Elliott, this behavior is peculiar to the linear array and results from the broad pattern perpendicular to the array axis. As the array is scanned toward end-fire the area of this conical shape is reduced and the effect offsets the beam broadening in the plane of scan that tends to reduce gain.

Fig. 3 shows the broadside directivity (dashed curve) of a linear array of eight isotropic elements with uniform excitation for various array element spacings [2]. It indicates that directivity is a severe function of element spacing. The solid curve shown in the figure is the maximum directivity for the array, as derived by Tai, and serves to indicate that the directivity of a broadside array is very nearly optimum except in the supergain region ($d/\lambda < 0.5$). The reduced directivity occurring near $d/\lambda = 1$ results directly from the radiation of an additional set of primary lobes, called *grating lobes*, which will be discussed in detail later. Since the presence of grating lobes is unacceptable for most applications, the directivity of a uniformly
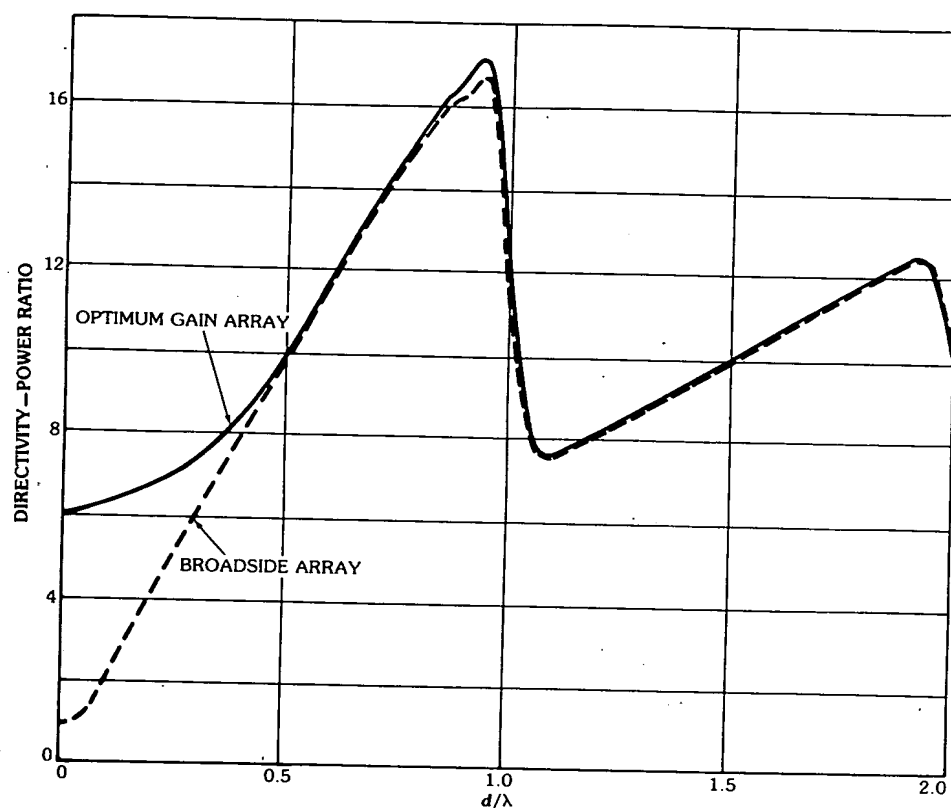
Fig. 3. Array gain for eight isotropic elements versus element spacing. (*After Tai [2]*, © *1964 IEEE*)

illuminated roadside array is well approximated by the following expression throughout the linear (useful) portion of the curve shown in Fig. 3:

$$D \cong 2Nd/\lambda \tag{11}$$

The directivity of an ideal planar array (one that is perfectly matched and has $\cos \theta$ hemispherical element patterns) is given approximately by

$$D = 32\,400/B \tag{12}$$

where B is the 3-dB beamwidth product for scan angle θ

$$B = \theta_{x_3}\theta_{y_3}\sec \theta \tag{13}$$

with beamwidths given in degrees.

2. Patterns of Periodic Arrays

Array antennas, with their numerous closely spaced elements, provide a degree of pattern control not achievable with reflector or lens apertures. Most early developments in this area emphasized electronic scanning, but more recently there has been substantial effort devoted to producing low side lobe and adaptively controlled patterns.

Characteristics of an Array Scanned in One Plane

The array illumination determines the pattern beamwidth, side lobes, and directivity. In general, the beamwidth is proportional to the inverse of the normalized array length, or

$$\Delta\theta = K\lambda/L \tag{14}$$

with $\Delta\theta$ in radians, K a constant, and L defined to be Nd, for N elements in the θ plane. This equation gives the half-power beamwidth of this radiation pattern for a linear array or in the principal planes of a rectangular array at broadside. Uniform illumination ($|a_i| = 1$), with $K = 0.886$, produces the highest directivity and narrowest beam of any illumination (except for certain special "superdirective" illuminations associated with rapid phase fluctuations and closely spaced elements), but this illumination produces relatively high side lobe patterns (about -13 dB). Selection of various tapered illuminations can result in much lower side lobes, accompanied by wider beamwidths and lower directivity. As the array is scanned from broadside the beamwidth widens, again like $\sec\theta_0$ except near end-fire. A more general formula and a plot of beamwidth versus scan angle are given later, but it is important to note that the array beamwidth does increase with scan when observed in the (θ, ϕ) space. The solid-line curves of Fig. 4 show the radiation pattern of an eight-element, one-dimensional array at broadside and scanned to 45° ($u = 0.7071$). The element spacing is 0.5λ. The comparison shows that the array pattern is invariant in the parameter $(d/\lambda)(u - u_0)$, so that no beam broadening or other pattern change is evident when plotted in direction cosine space. The observed $\sec\theta$ beam broadening factor for large arrays is thus the result of mapping the uniform beamwidth in u space onto the θ plane. The advantage of plotting antenna patterns in u ($\sin\theta$) space is that as far as the pattern function is concerned, there is no need to recompute patterns for any other scan angle. Later we shall see that mutual coupling introduces angle-dependent effects that can drastically alter the radiation characteristics.

Similarly, the form of the pattern is not dependent on the spacing d/λ, except that its scale in $u - u_0$ space expands or contracts with the choice of spacing d/λ. This subject is addressed in the next sections.

Array Lattice Spacings and Comparison With Continuous Line Source—The 0.5λ spacing used in the array of Fig. 4 was chosen to minimize the effects of periodicity and makes that array pattern very little different from that of a continuous aperture. Normalized broadside radiation patterns for an N-element array [of actual length $(N - 1)d_x$] and a line source of length L are given as follows:
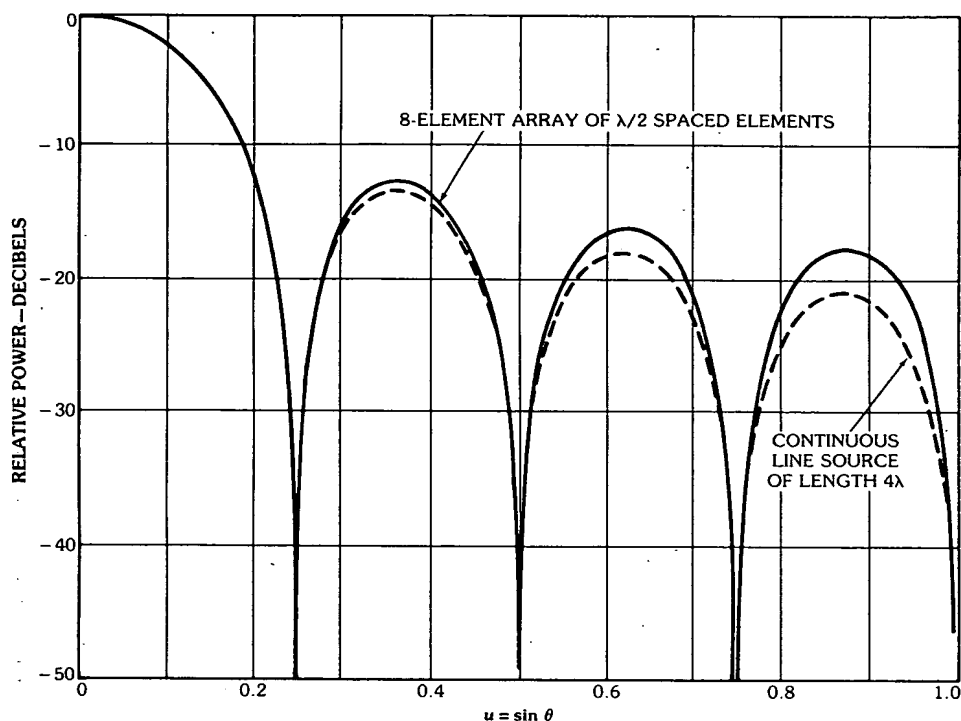
Fig. 4. Patterns of uniformly illuminated array and line source.

Linear array:

$$f(\theta) = \frac{\sin(N\pi d_x u/\lambda)}{N\sin \pi d_x u/\lambda} \tag{15}$$

Line source:

$$f(\theta) = \frac{\sin(L\pi u/\lambda)}{L\pi u/\lambda} \tag{16}$$

The radiation patterns for a continuous line source of length 4λ and an eight-element array of $\lambda/2$ spaced elements with uniform excitation are shown in Fig. 4. The line source pattern differs very little from the array pattern up to the second side lobe, and the null positions are unchanged, since these are determined from the numerators of the two expressions in (15) and (16). The similarity of these expressions makes it convenient to define the length parameter $L = Nd$ for arrays.

Fig. 5 shows the pattern (solid) of an eight-element array with 4λ spacings, as compared with the (dashed) pattern of a continuous line source with $L = 32\lambda$. Here the dramatic difference is the occurrence of lobes in the periodic array pattern at the zeroes of the denominator of (15). These lobes, which are called *grating*
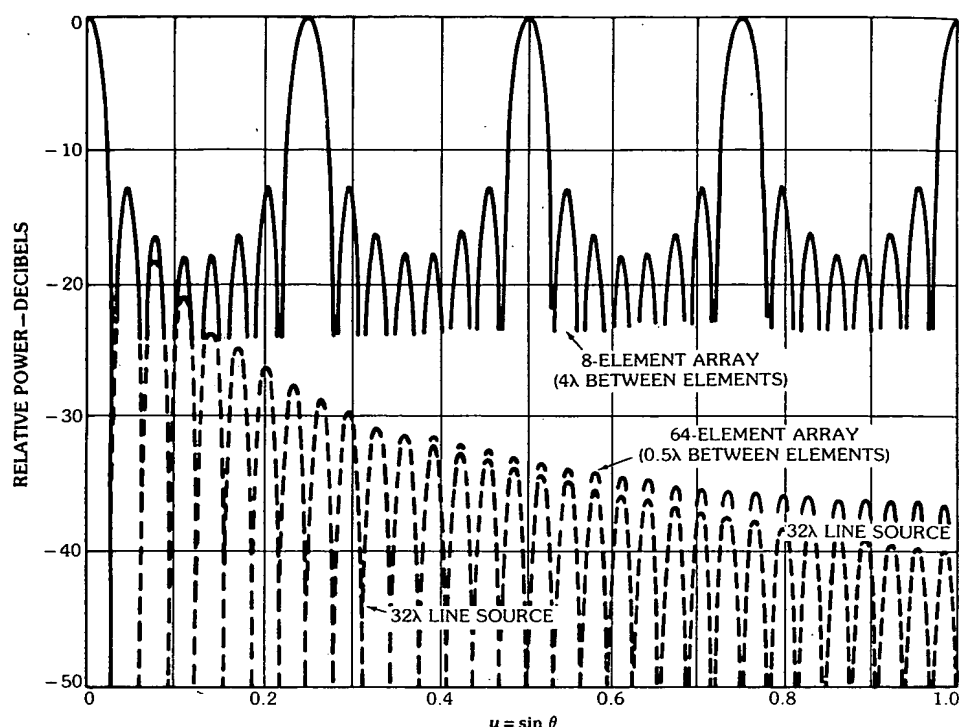
Fig. 5. Patterns of uniformly illuminated 64-element array with 0.5λ spacing, 32λ line source, and 8-element array with 0.5λ spacing.

lobes, have the same peak value as the main beam and are located at distances $p\lambda/d_x$ from the main beam in u space, for all integers p that define angles in real space ($|u| \leq 1$). Grating lobes are a direct consequence of the periodicity and occur independently of any chosen amplitude distribution across the array. When the array is scanned to u_0 they occur at angles

$$u_p = u_0 + p\frac{\lambda}{d_x}, \qquad \text{for } p = \pm 1, \pm 2, \cdots \tag{17}$$

subject to $-1 \leq u_p \leq +1$.

The array factor is thus completely periodic in u space (for $|u| \leq 1$), with period equal to grating lobe separation (λ/d_x). The region $|u| \leq 1$ is called *real space* because $\sin\theta$ has a geometric interpretation in this regime. Before leaving the comparison of continuous apertures and discrete arrays it should be noted that the similarity is maintained almost halfway between the main beam and the nearest grating lobe, because it is on this scale that the pattern of the periodic array is repeated. Fig. 5 also shows (solid) the side lobe peaks of the 64-element array with 0.5λ spacing.

Fig. 6 further emphasizes the pattern invariance in the scale parameters
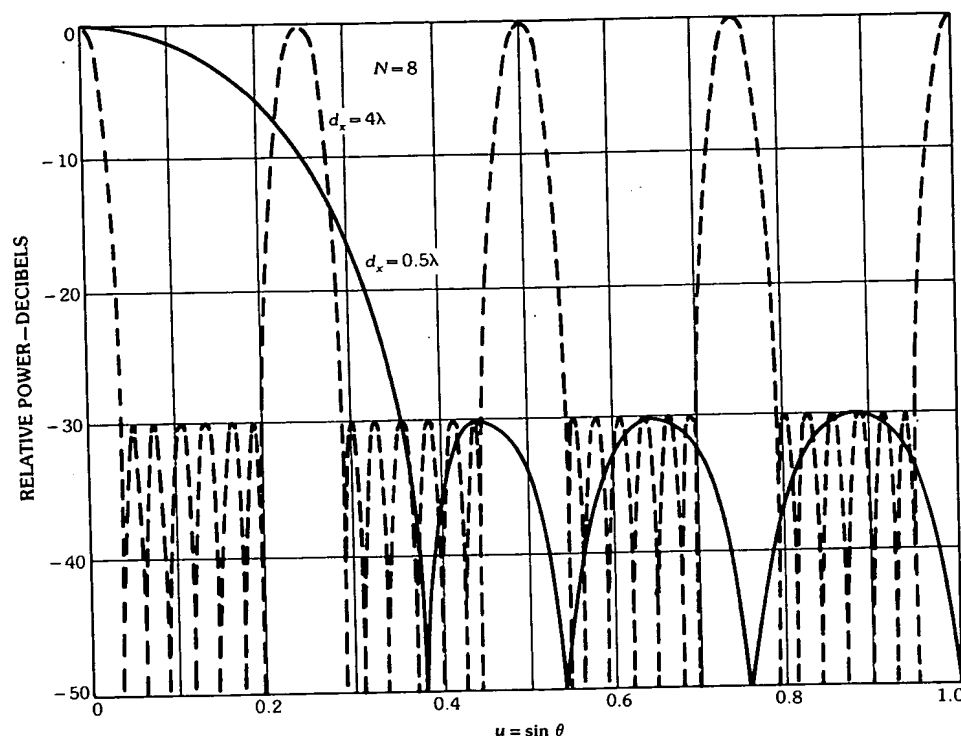
Fig. 6. Patterns of eight-element arrays with −30-dB Chebyshev illuminations: 0.5λ spacing, and 4λ spacing.

$d_x(u - u_0)/\lambda$ by showing the patterns of two eight-element arrays with one of the low side lobe excitations that will be described in a later section, a −30-dB Chebyshev taper. The two patterns are for arrays with $d_x = 0.5\lambda$ and 4λ. Increasing d_x shrinks the scale of the pattern and so brings additional grating lobes into real space but produces no other change in the pattern.

Scanning in Two Planes

Equation 7 gives the pattern of a rectangular planar array like that of Fig. 7a scanned in two planes. The occurrence of grating lobes in rectangular-grid two-dimensional arrays is directly apparent from (7), where the substitutions

$$u_p = u_0 + p\frac{\lambda}{d_x}, \qquad v_q = v_0 + q\frac{\lambda}{d_y} \qquad (18)$$

leave these expressions unchanged. Not all values of q and p correspond to allowed angles of radiation, however, for the direction θ of radiation measured from the array normal is given by

$$\cos\theta_{pq} = \sqrt{1 - u_p^2 - v_q^2} \qquad (19)$$

Rectangular Grid Array

a
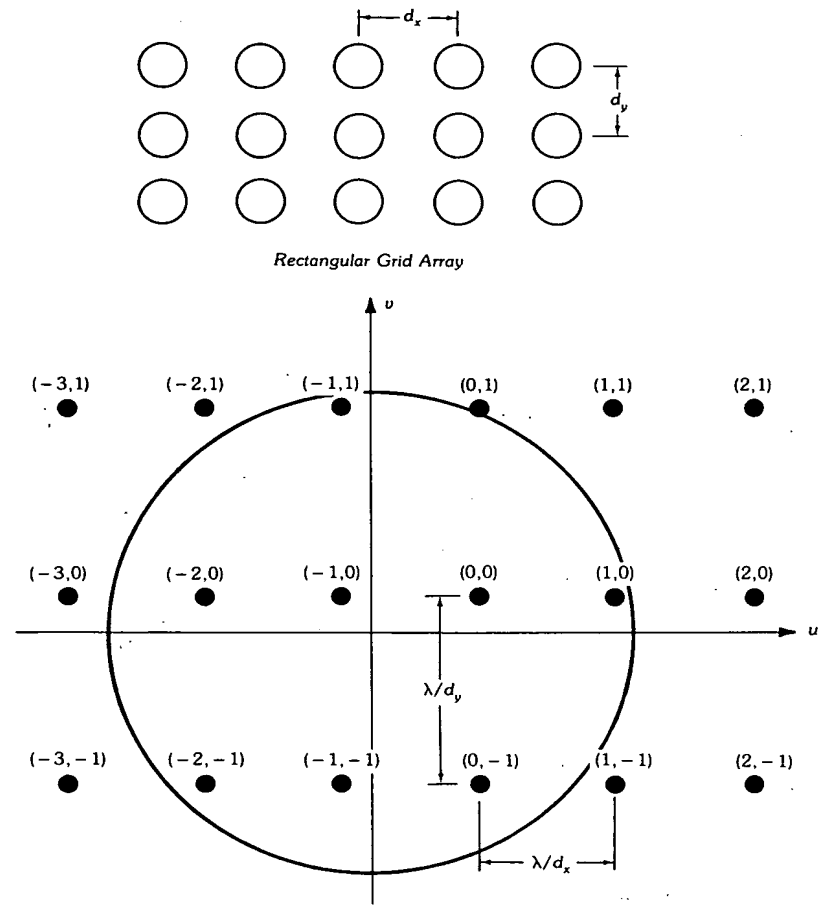
Fig. 7. Rectangular and triangular grid planar arrays and their grating lobe lattices. (*a*) Grating lobe lattice for rectangular grid. (*b*) Grating lobe lattice for triangular grid.

and so real angles of radiation θ_{pq} require that the allowed values of u_p and v_q are constrained by the condition

$$u_p^2 + v_q^2 < .1 \tag{20}$$

These points are shown in (u, v) space as a regularly spaced grating lobe lattice about the main beam location (u_0, v_0) in Fig. 7a. The circle with unity radius represents the bounds of the above inequality; all grating lobes within the circle represent those radiating into real space, and those outside do not radiate.

Fig. 7b shows a triangular array lattice and pertinent grating lobe locations for that lattice. In this case, (5) is still valid and there are still grating lobes, but the nearest lobes in the azimuth scan plane are removed. The grating lobe locations shown in Fig. 7b are given by

Triangular Grid Array
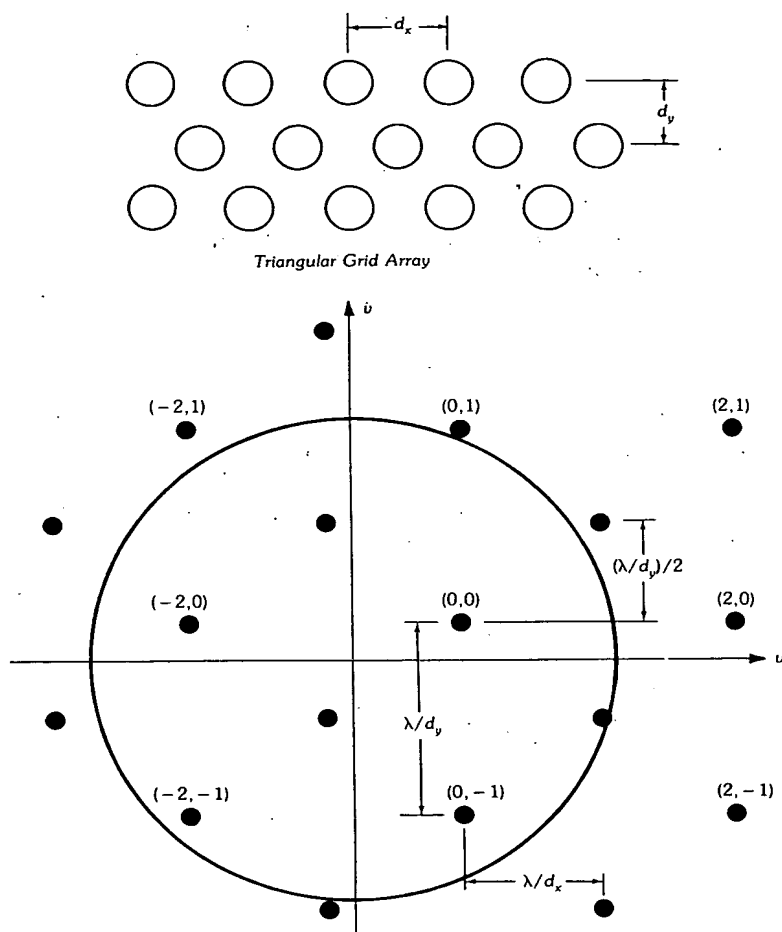
Fig. 7, *continued.*

$$u_p = u_0 + p\frac{\lambda}{d_x}$$

$$v_q = \begin{cases} v_0 + q\dfrac{\lambda}{d_y} & \text{for } p = 0, \pm 2, \cdots \\ v_0 + \left(q - \dfrac{1}{2}\right)\dfrac{\lambda}{d_y} & \text{for } p = \pm 1, \pm 3, \cdots \end{cases} \qquad (21)$$

Pattern Shape and Beam Broadening

In the previous section it was pointed out that for a periodic array the pattern shape does not change with scan angle if it is plotted in u space, and changes in array spacing alter only the scale (width) of the pattern. The actual shape of the

pattern, its relative width, side lobes, and slope values depend only on the applied amplitude and phase illumination. Fig. 8 indicates that one of the major results of reducing the side lobes for a given size array is to broaden the beamwidth. The figure shows three different Chebyshev patterns, with −20-, −30-, and −40-dB side lobe levels, and indicates beam broadening factors $B = K/0.886$ of 1.12, 1.29, and 1.43 relative to the pattern of the array with uniform illumination. In general, then, side lobes can be lowered by employing tapered array illuminations, but this is achieved at the expense of broadening the beamwidth and reducing the array gain. Fig. 9 gives the beamwidth in degrees for a scanned array with arbitrary taper as a function of the array length and beam broadening factor. By using the relationship

$$\Delta\theta = \sin^{-1}(u_0 + 0.443 B\lambda_0/L) - \sin^{-1}(u_0 - 0.443 B\lambda_0/L) \qquad (22)$$

which is valid to within a beamwidth of end-fire. The curves are not plotted beyond that point, because the array factor is symmetric about $\theta = 90°$. Here $F(\theta) = F(180° - \theta)$ and the pattern for $\theta < 90°$ coalesces with the pattern for $\theta > 90°$ to form a broader beamwidth. Elliott [1] gives the expression below for the beamwidth at end-fire. Further narrowing of the beam can be obtained using slow-wave excitation [3]:
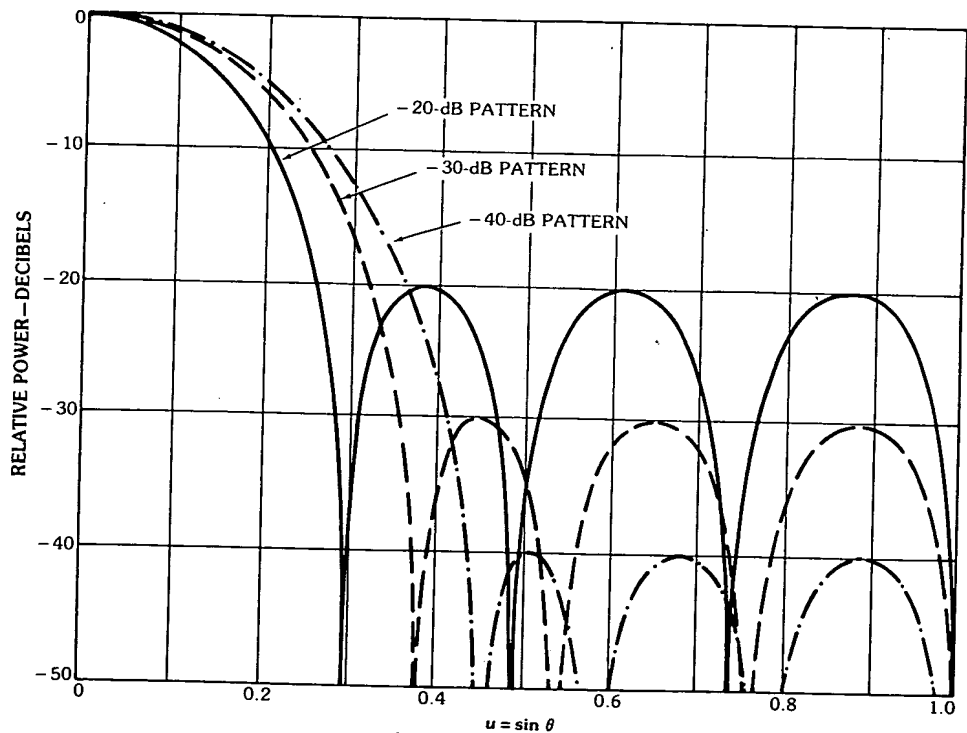
Fig. 8. Chebyshev patterns for an 8-element array ($\lambda/2$ spacing) with illuminations for −20 dB, −30 dB, and −40 dB.
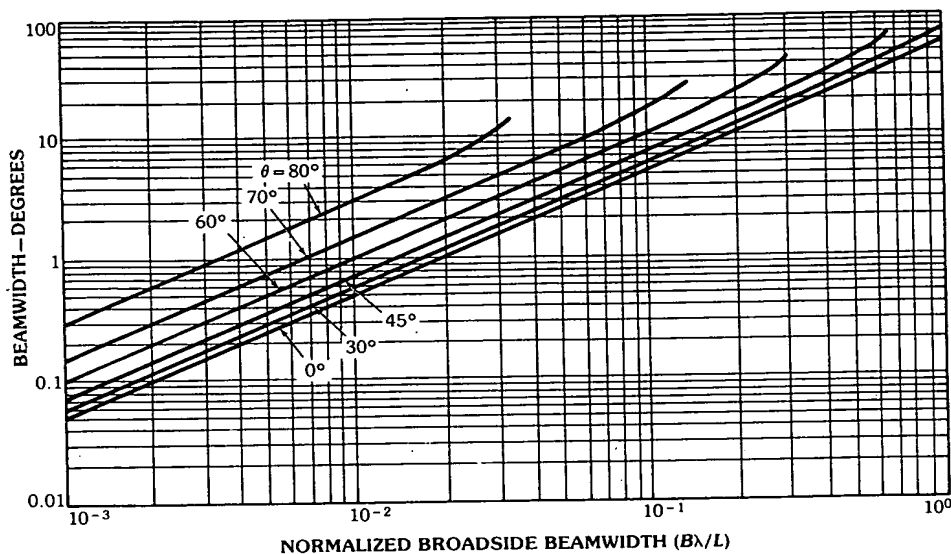
Fig. 9. Beamwidth versus normalized broadside beamwidth for a scanned array.

$$\Delta\theta = 2\cos^{-1}(1 - 0.443 B\lambda_0/L) \tag{23}$$

Phased Array Bandwidth

As indicated in Section 1, most arrays are designed using phase shifters, not time-delay units. A phase-steered array establishes a progressive phase front to match a wave at a single frequency. At a different frequency the progressive phase front corresponds to a wave at a different angle. This effect is shown schematically in Fig. 10.

Equations 3 and 5 give array excitation coefficients for time-delay and phase-
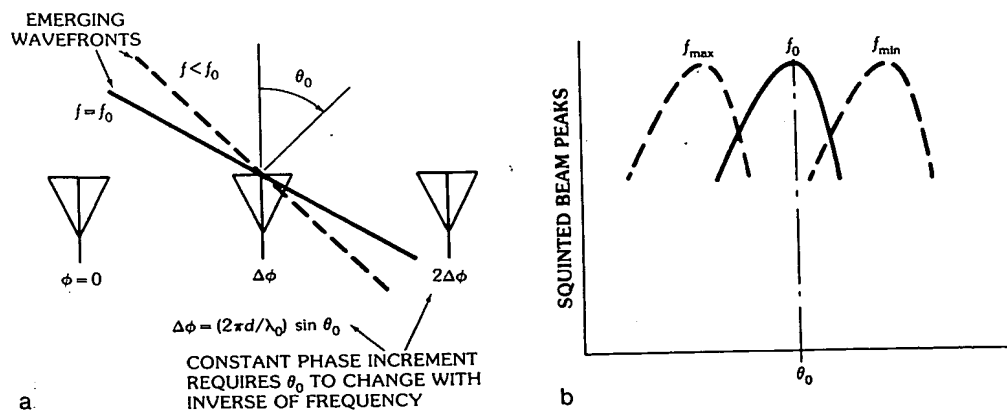
Fig. 10. Beam squint for a phase-scanned array. (*a*) Wavefronts. (*b*) Beam-pointing errors.

steered arrays. Scanning with phase shifters causes the peak gain angle of a phase-steered beam to not occur at the established (θ_0, ϕ_0) position except at $\lambda = \lambda_0$. For example, at center frequency f_0 the interelement phase shift ϕ_0 is given by

$$\phi_0 = \frac{2\pi}{\lambda_0} d_x \sin \theta_0 \qquad (24)$$

but the interelement phase required for this scan angle at some other frequency is

$$\phi = \frac{2\pi}{\lambda} d_x \sin \theta_0 \qquad (25)$$

The net effect, a beam-pointing error referred to as *beam squint*, is that the beam scans away from the desired θ_0 to an angle with $\sin \theta = (\lambda/\lambda_0) \sin \theta_0$; this is the most significant bandwidth limiting effect in array antennas.

Assuming an approximate half-power beamwidth $K\lambda/L$ (note $K = 0.886$ for uniform illumination) one can solve for the array bandwidth under the assumption that the gain at each frequency limit is reduced to half-power (that the squint is equal to a half-beamwidth at each limit). The resulting fractional bandwidth is given by

$$\frac{\Delta f}{f_0} = 0.886B \left(\frac{\lambda_0}{L}\right) \frac{1}{\sin \theta} \qquad (26)$$

and for small scan angles

$$\frac{\Delta f}{f_0} \cong \frac{1}{n_B} \qquad (27)$$

where n_B is the number of beamwidths scanned.

Fig. 11 shows how the 3-dB beamwidth varies with array length and scan angle for arrays with arbitrary side lobe levels.

For very large arrays it is necessary to divide the array into subarrays in order that some time-delay correction can be applied for each subarray. This is discussed in more detail in Section 3.

Antenna Pattern Synthesis

One of the primary advantages of the use of a phased array is the flexibility to form desired antenna patterns and so to match the radiation pattern to the technical requirement. The theory of antenna pattern synthesis is addressed in more detail in Chapter 2, hence the treatment that follows is restricted to remarks about several generalized procedures and a listing of relevant formulas and engineering data for the special case of low side lobe methods.
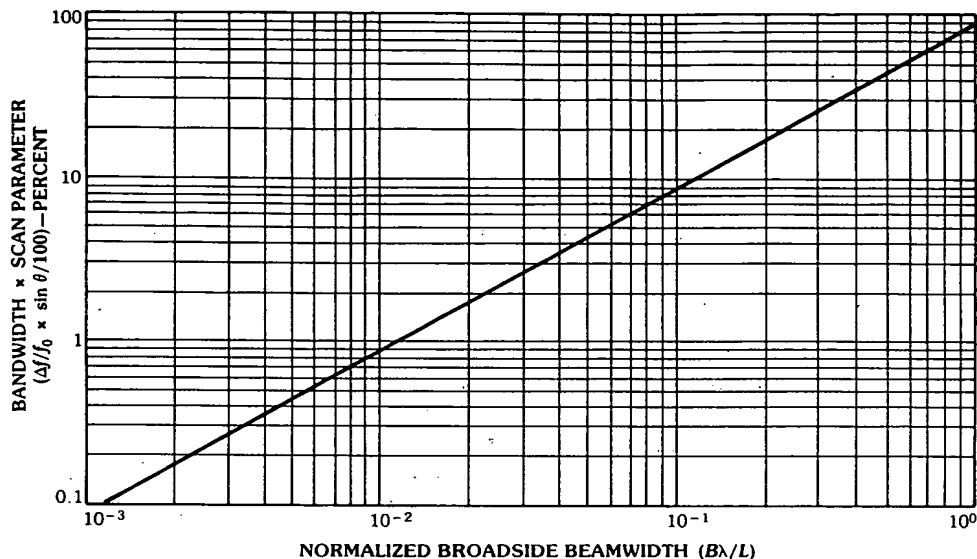
Fig. 11. Bandwidth scan product versus normalized broadside beamwidth for a scanned array.

General Procedures

Schelkunoff's method [4], introduced in Chapter 3, is based on the manipulation of zeros of the pattern function in the complex plane. The procedure is very useful of itself, and in addition is the foundation of computer-based methods with great power and flexibility. Elliott [5,6] has described a generalized method based on a null perturbation approach to modify the side lobe structure of Taylor and Bayliss line source patterns. The procedure develops simultaneous linear equations solved by matrix inversion for a perturbed pattern and is repeated iteratively to converge to the desired result.

Fourier series methods can be readily applied to array synthesis problems by recognizing that the pattern function

$$E(u) = \sum_{m=-(M-1)/2}^{(M-1)/2} a_m e^{jkmud_x} \qquad m = \begin{cases} \pm\frac{1}{2}, \pm\frac{3}{2}, \ldots, & \text{for } M \text{ even} \\ 0, \pm 1, \ldots, & \text{for } M \text{ odd} \end{cases} \qquad (28)$$

is a finite Fourier series and is periodic in u space with the interval of the grating lobe distance λ/d_x. Thus, given a desired field distribution $E(u)$, one can obtain an expression for the currents from orthogonality, with

$$a_m = \frac{d_x}{\lambda} \int_{-\lambda/2d_x}^{\lambda/2d_x} e^{-j(2\pi/\lambda)ud_x m} E(u)\, du \qquad (29)$$

Stutzman and Thiele [7] show the application of this procedure to synthesis of a sector pattern. The method provides the least mean squared error approximation

to the desired pattern as long as the element spacing $d_x \geq 0.5\lambda$. For closer spacing the domain of integration exceeds the visible region, and definition of a pattern function is ambiguous. The method provides a convenient test of required array size for synthesizing a given pattern, because one can vary the number of terms in the Fourier series and observe pattern convergence.

Synthesis with Orthogonal Beams

One of the most insightful methods, this approach is particularly useful for the synthesis of generalized sector coverage patterns, patterns without nulls, and certain low side lobe patterns. The method is due to Woodward [8] and Woodward and Lawson [9] and is referenced in several texts, so it will not be described in detail here. Although usually carried out for line source excitations, the method is very appropriate for array synthesis. It consists of using the multiple orthogonal beams of the periodic array as a basis for expanding the desired radiation field.

If the aperture length of an N-element array is defined to be $Nd_x = L$, N beams will fill a sector of width $(N - 1)\lambda/L$ in u space, as shown in Fig. 12. The desired shaped pattern can then be matched at N points by selecting the amplitude of each beam. The specific patterns shown in Fig. 12 are for $N = 8$.

To excite the ith beam the elements are excited by progressive phase distribution

$$a_n = e^{-j(2\pi/\lambda)d_x u_i n} \tag{30}$$

where

$$u_i = (\lambda/L)i = (1/N)(\lambda/d_x)i \quad \text{and} \quad i,n = \pm\tfrac{1}{2}, \cdots, \pm(N - 1)/2$$

The ith beam is given by

$$
\begin{aligned}
g_i(u) &= \sum_{n=-(N-1)/2}^{(N-1)/2} e^{j(2\pi/\lambda)x_n(u-u_i)} \\
&= N\left\{ \frac{\sin[(N\pi d_x/\lambda)(u - u_i)]}{N\sin[(\pi d_x/\lambda)(u - u_i)]} \right\}
\end{aligned} \tag{31}
$$

The set of beams $g_i(u)$ is also orthogonal and occupies the beam positions shown in Fig. 12 (the example was done for $N = 8$). Fig. 12b shows two of the normalized orthogonal beams ($i = -7/2$ and $i = +1/2$) and clearly indicates that the domain of pattern synthesis must be restricted to $|Nd_x \sin\theta| \leq 0.5(N - 1)$, for beyond that the grating lobes of the outermost beams present an ambiguity that leads to significant pattern distortion. One of the most significant results of synthesis with orthogonal beams is that the resultant feed networks can be lossless, since the progressive phase sequences can be formed by lossless Butler matrices or orthogonal beam lenses.

Section 3 shows an example of the use of orthogonal beams in a subarraying feed configuration to synthesize a pulse-type subarray pattern.
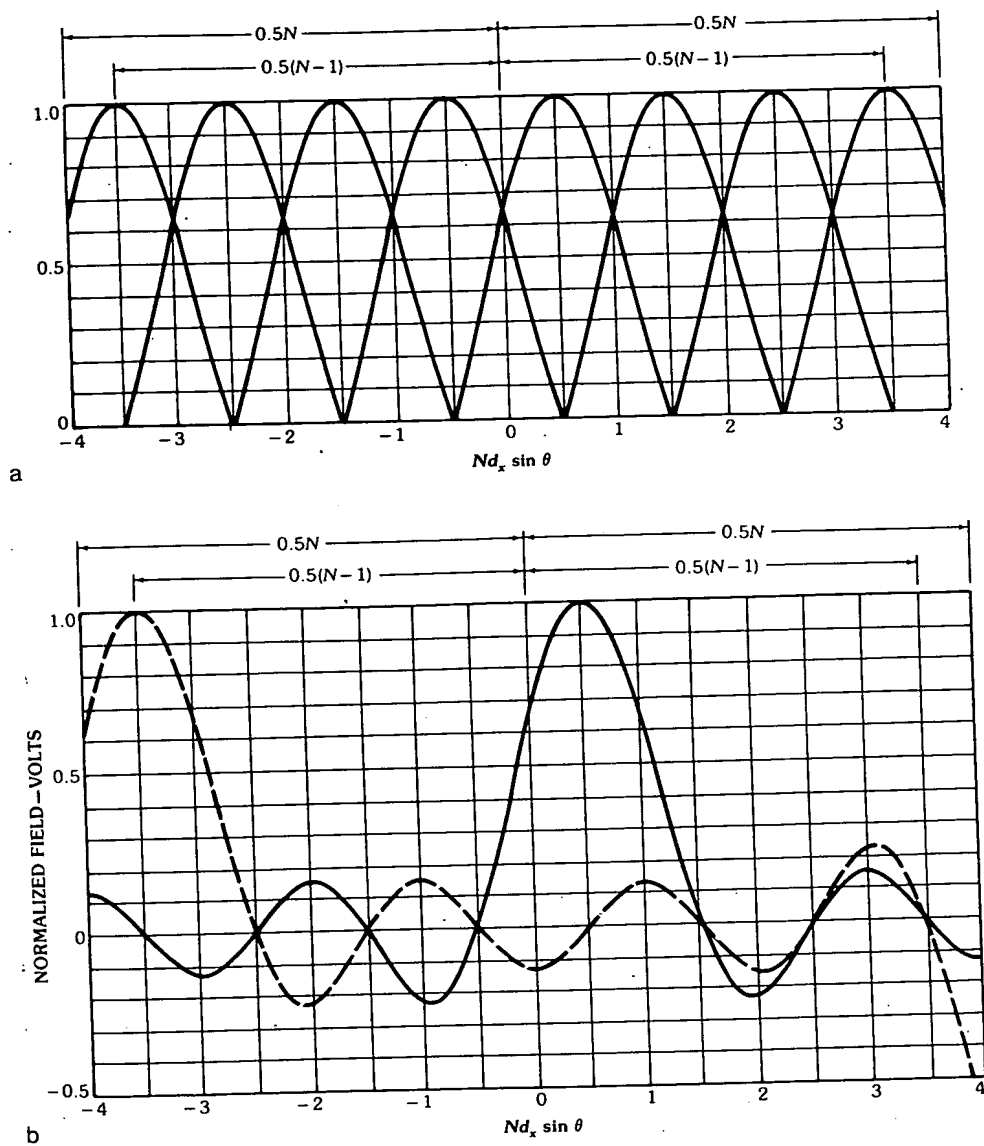
Fig. 12. Orthogonal beams for an N-element array. (a) Complete set of beams (plotted to first zeros). (b) Two orthogonal beams (plotted over domain of orthogonality) with $i = 1/2$ (solid) and $i = -7/2$ (dashed).

Low Side Lobe Solutions: Basic Formulas and Engineering Data

Among the most important and useful synthesis procedures are those that result in minimum beamwidth consistent with very low side lobes. From this class of methods three of the most important are Chebyshev and Taylor line source

methods for symmetric patterns and Bayliss line source synthesis for antisymmetric difference patterns. The basic formulas for these three methods follow.

Dolph-Chebyshev Synthesis

Based on equating the array polynomial expression to a given Chebyshev polynomial, the method [10] synthesizes patterns for an N-element array (N any integer) with the narrowest beamwidth subject to a given side lobe level. A characteristic of the patterns is that all side lobes are of equal amplitude.

The synthesized pattern is given by the expression below for an array of $M + 1$ elements, spaced d apart:

$$F(z) = T_M(z) \tag{32}$$

where $T_M(z)$ is the Chebyshev polynomial of order M and is defined by

$$\begin{aligned}
T_M(z) &= \cos(M \cos^{-1} z) && \text{for } |z| \leqq 1 \\
&= \cosh(M \cosh^{-1} z) && \text{for } |z| \geqq 1
\end{aligned} \tag{33}$$

The parameter z is given by

$$z = z_0 \cos[(\pi d/\lambda) \sin \theta] \tag{34}$$

where

$$z_0 = \cosh(M^{-1} \cosh^{-1} R)$$

for voltage side lobe level R ($\text{SL}_{\text{dB}} = 20 \log_{10} R$).

The original formulation of this problem is attributable to Dolph, who derived results for $\lambda/2$-spaced elements. Later Riblett [11] extended the analysis to elements greater than $\lambda/2$. Barbiere [12] derived the expression for z_0 above, and derived convenient relations for the currents. Stegen [13] derived the most widely used exact expressions for the required current distribution, and extensive tabulations of his results are given by Brown and Scharp [14], who also include gain and beamwidth values for arrays of up to 40 elements.

Stegen also gives a formula for Chebyshev array beamwidth, valid for large arrays. The following equation, derived by Drane [15], gives the beamwidth (here converted to degrees) for an array of length L with side lobe level $|\text{SL}|$(dB)

$$\text{BW} = \left(\frac{\lambda}{L}\right)(10.314)(|\text{SL}| + 4.52)^{1/2} \tag{35}$$

Fig. 13 shows the normalized beamwidth parameter $(L/\lambda)\text{BW}$ (in degrees) as a function of side lobe level R as computed from the above equation. Drane also gives an equation for directivity for array spacings greater or less than a half-wavelength. For spacings greater than $\lambda/2$ the directivity D is [15]
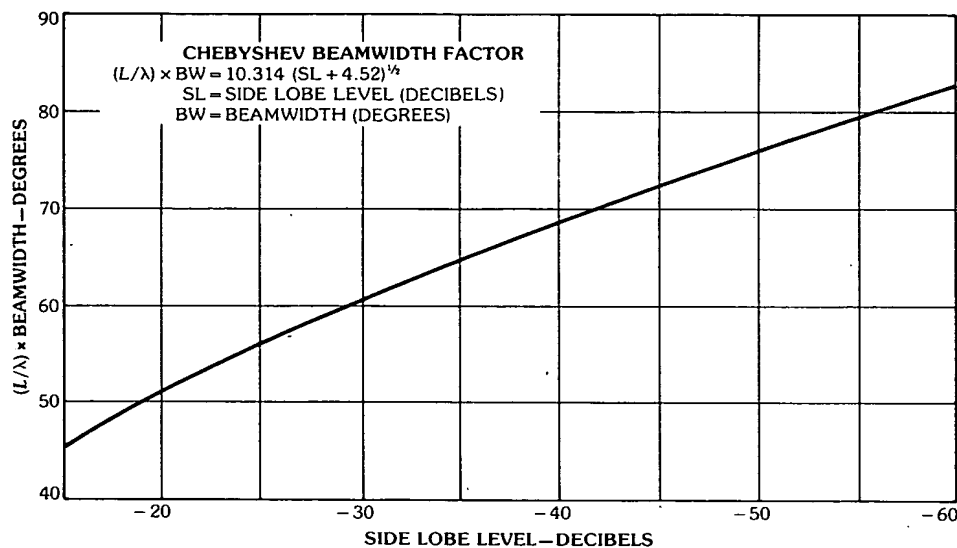
Fig. 13. Normalized beamwidth versus side lobe level for Chebyshev arrays. (*After Drane [15], © 1968 IEEE*).

$$D \cong \frac{2R^2}{1 + (\lambda/L)R^2\sqrt{(\ln 2R)/\pi}} \tag{36}$$

This result is in close agreement with the equation of Elliott [1]. For large arrays this directivity reaches the maximum value $2R^2$, or 3 dB greater than the specific side lobe level.

Chebyshev patterns have been used for purposes of illustration throughout this chapter, and so no additional patterns will be shown here.

Taylor Line Source Synthesis

The classic paper by Taylor [16] investigated the synthesis of equal side lobe patterns with continuous line source excitations and satisfying the same criteria as do the Chebyshev linear array patterns. He showed that the idealized pattern is the solution to this problem is not physically realizable but could be approximated arbitrarily closely by a function of two parameters, A and $\bar{n}$. The family of patterns derived by Taylor has the first $\bar{n}$ side lobes at the desired level, and all side lobes beyond the $\bar{n}$th fall off as $(\sin \pi z)/\pi z$ (for $z = Lu/\lambda$) for a line source of length L. The synthesized pattern, normalized to unity, is given by

$$F(z, A, \bar{n}) = \frac{\sin \pi z}{\pi z} \prod_{n=1}^{\bar{n}-1} \frac{1 - z^2/z_n^2}{1 - z^2/n^2} \tag{37}$$

for $z = (L/\lambda)u$.

The zeros of the function are at

$$z_n = \begin{cases} \pm\sigma\sqrt{A^2 + (n - \tfrac{1}{2})^2} & \text{for } 1 \leqq n \leqq \bar{n} \\ \pm n & \text{for } \bar{n} \leqq n < \infty \end{cases} \qquad (38)$$

where

$$\beta = \frac{\bar{n}}{\sqrt{A^2 + (\bar{n} - \tfrac{1}{2})^2}}$$

The parameter A is defined so that $\cosh(\pi A)$ is the voltage side lobe ratio, or

$$A = \frac{1}{\pi}\cosh^{-1}R \qquad (39)$$

An approximation for the beamwidth is given by

$$\Delta\theta \cong \sigma\beta_0(\lambda/L) = \frac{\beta_0\bar{n}(\lambda/L)}{\sqrt{A^2 + (\bar{n} - \tfrac{1}{2})^2}} \qquad (40)$$

where

$$\beta_0 = (2/\pi)\sqrt{(\cosh^{-1}R)^2 - (\cosh^{-1}R/\sqrt{2})^2}$$

The current or aperture field distribution necessary to produce this pattern family is

$$g(x) = F(0,A,\bar{n}) + 2\sum_{m=1}^{\bar{n}-1} F(m,A,\bar{n})\cos(2m\pi x/L) \qquad \text{for } -L/2 \leqq x \leqq L/2 \quad (41)$$

where the coefficients $F(z,A,\bar{n})$ are the pattern values of (37) at the integers $(z = m \leqq \bar{n})$. In abbreviated form these are

$$F(m,A,\bar{n}) = \frac{[(\bar{n} - 1)!]^2}{(\bar{n} - 1 + m)!(\bar{n} - 1 - m)!}\prod_{n=1}^{\bar{n}-1}(1 - m^2/z_n^2) \qquad (42)$$

These coefficients $F(m,A,\bar{n})$ are tabulated in Hansen [17] for various n for side lobe levels between -30 and -40 dB in 5-dB increments.

Fig. 14 shows two Taylor patterns. The solid one is the line source pattern computed from (37), while the dashed curve is the radiation pattern of the $g(x)$ distribution sampled at the points: $(L/N)i$ for $\pm i = \tfrac{1}{2}, \tfrac{3}{2}, \ldots, (N-1)/2$ for an array of N elements using the tabulated values of F. The patterns are for a -30-dB Taylor distribution with $\bar{n} = 4$ and $N = 16$. The figure indicates that the sampled line source distribution is a very good approximation of the line source pattern, even for an array with only 16 elements.

The practical selection of the $\bar{n}$ parameter is discussed by Taylor. This parameter must be large enough or the beam will be broader than necessary; $\bar{n}$
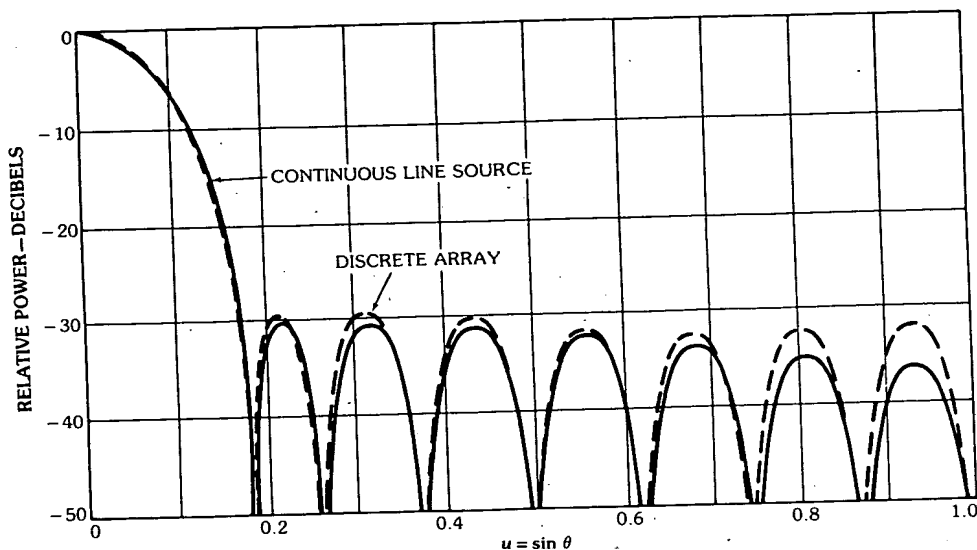
Fig. 14. Taylor $\bar{n} = 4$ line source patterns: continuous line source and discrete array pattern ($N = 16$) using sampled Taylor illumination.

should be at least 3 for -25-dB side lobes, and at least 6 for -40 dB. Increasing $\bar{n}$ further narrows the main beam, but supergaining results if it is made too large.

Bayliss Line Source Synthesis

E. T. Bayliss [18] has developed a method of synthesizing line source difference patterns that parallel the essential features of Taylor line source patterns. The difference pattern is fully described by two parameters, A and $\bar{n}$, which completely control the side lobe level and decay behavior. Bayliss' method results in a pattern of the following form:

$$F(z) = \pi z \cos \pi z \prod_{n=1}^{\bar{n}-1} [1 - (z/\sigma z_n)^2] \bigg/ \prod_{n=0}^{\bar{n}-1} \{1 - [z/(n + \tfrac{1}{2})]\} \qquad (43)$$

where

$$z = (L/\lambda)u$$
$$\sigma = \frac{\bar{n} + \tfrac{1}{2}}{z_{\bar{n}}}$$
$$z_{\bar{n}} = (A^2 + \bar{n}^2)^{1/2}$$

Here, as in the Taylor method, the first few side lobes are at the design level, and beyond about $z = \bar{n}$ the side lobes decay as $z^{-3/2}$. Unlike the Taylor line source method, the $z_{\bar{n}}$ terms are not available in closed form but are given in terms of the

coefficients of fourth-order polynomials relating the null positions and side lobe levels. The null positions are given by:

$$\sigma z_n = \begin{cases} 0 & \text{for } n = 0 \\ \pm\sigma\xi_n & \text{for } n = 1,2,3,4 \\ \pm\sigma(A^2 + n^2)^{1/2} & \text{for } n = 5,6,\ldots \end{cases} \qquad (44)$$

Bayliss computed ξ_n and A by iterative methods but presented coefficients of fourth-order polynomials to evaluate these constants and the location of the difference peak P_0 using Table 1 and the expression

$$\text{polynomial name} = \sum_{n=0}^{4} c_n(\text{SL})^n \qquad (45)$$

where SL is the side lobe level in decibels.

Elliott [19] gives a convenient table of A and ξ_n for patterns with SL = -15 through -40 dB in increments of 5 dB. The table is given here as Table 2.

The line source excitation required to produce this pattern is given by

$$g(x) = \sum_{n=0}^{\bar{n}-1} B_n \sin[(2\pi x/L)(n + \tfrac{1}{2})], \qquad -L/2 \leqq x \leqq L/2 \qquad (46)$$

with Fourier coefficients

Table 1. Polynomial Coefficients

Polynomial Name	c_0	c_1	c_2	c_3	c_4
A	0.303 875 30	−0.050 429 22	−0.000 279 89	−0.000 003 43	−0.000 000 02
ξ_1	0.985 830 20	−0.033 388 50	0.000 140 64	0.000 001 90	0.000 000 01
ξ_2	2.003 374 87	−0.011 415 48	0.000 415 90	0.000 003 73	0.000 000 01
ξ_3	3.006 363 21	−0.006 833 94	0.000 292 81	0.000 001 61	0.000 000 00
ξ_4	4.005 184 23	−0.005 017 95	0.000 217 35	0.000 000 88	0.000 000 00
p_0	0.479 721 20	−0.014 566 92	−0.000 187 39	−0.000 002 18	−0.000 000 01

Table 2. Values of A and ξ_n

Polynomial Name	Side Lobe Level (dB)					
	15	20	25	30	35	40
A	1.0079	1.2247	1.4355	1.6413	1.8431	2.0415
ξ_1	1.5124	1.6962	1.8826	2.0708	2.2602	2.4504
ξ_2	2.2561	2.3698	2.4943	2.6275	2.7675	2.9123
ξ_3	3.1693	3.2473	3.3351	3.4314	3.5352	3.6452
ξ_4	4.1264	4.1854	4.2527	4.3276	4.4093	4.4973

$$B_m = \frac{1}{2j}(-1)^m(m + \tfrac{1}{2})^2 \prod_{n=1}^{\bar{n}-1} \{1 - [(m + \tfrac{1}{2})/\sigma z_n]^2\} \Big/$$

$$\prod_{\substack{n=0 \\ n \neq m}}^{\bar{n}-1} \{1 - [(m + \tfrac{1}{2})/(n + \tfrac{1}{2})]^2\} \tag{47}$$

for $m = 0, 1, \cdots, \bar{n} - 1$. Also

$$B_m = 0, \qquad \text{for } m \geqq \bar{n}$$

Fig. 15 shows two Bayliss patterns. The solid one is computed directly from (43) and is the line source pattern, while the dashed one is the radiation pattern of the $g(x)$ distribution sampled at the points (L/Ni) for $\pm i = \tfrac{1}{2}, \tfrac{3}{2}, \ldots, (N-1)/2$. The patterns are for a -30-dB illumination with $\bar{n} = 4$ and $N = 16$.

Although the discretized pattern is a good approximation to the line source pattern, even for as few as 16 elements, in some cases it may be important to improve the discretized patterns. Elliott has applied perturbation methods for this purpose and derived a set of linear equations from the perturbations of peak side lobe values. The procedure is iterated until convergence is adequate.

The above methods have been extended to treat circular apertures by Taylor [20] and Bayliss [18], and in addition Tseng and Cheng [21] have synthesized a class of circularly rectangular arrays with rectangular lattices and circularly symmetric patterns.
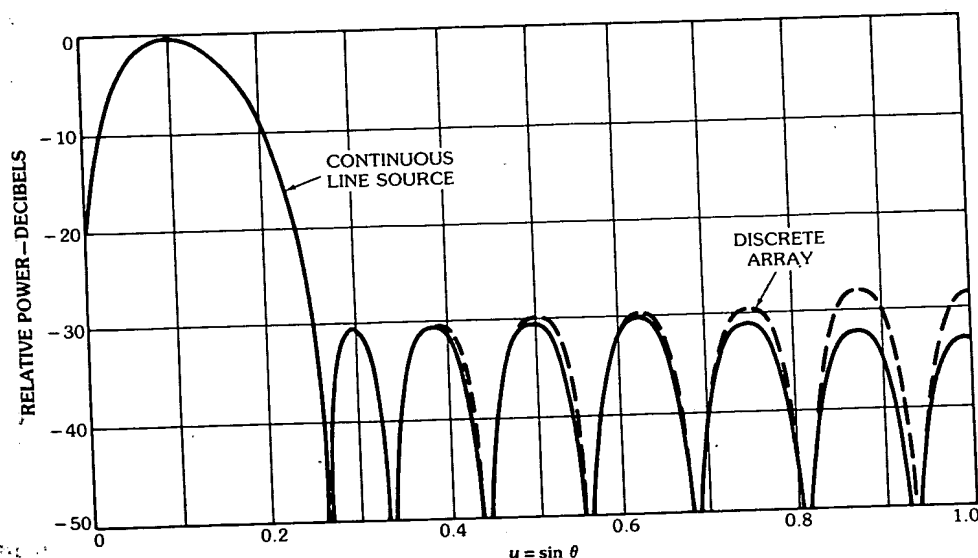

Fig. 15. Bayliss $\bar{n} = 10$ line source patterns: continuous line source and discrete array pattern ($N = 16$) using sampled Bayliss illumination.

3. Array Organization: Subarrays and Broadband Feeds

Often it is convenient to treat a large array as an array of smaller arrays. This is done to simplify power distribution networks, to incorporate low-power, light-weight, or compact circuitry that may have high losses, to integrate amplifier stages into the feed network, or to introduce time-delay networks to improve the broadband properties of the array.

Grouping the array into subarrays may be quite advantageous, but for several reasons it tends to increase the array side lobe level. In Section 4 it is shown that random errors in subarray excitation result in larger side lobes than errors at the array elements because there are so few subarrays. Furthermore, the periodic phase errors that occur in arrays of equal-size time-delayed subarrays produce grating lobes in the array factor. Techniques for producing wide-band behavior with an array of phase-steered elements are described in this section.

Aperture Illumination Control at Subarray Input Ports

One example of an application of subarrays is shown in Fig. 16. An array of $m \times M$ elements is divided into m arrays of M elements each. For simplicity the identical M-way power dividers provide in-phase, equal-amplitude output signals. The m-way beamformer provides feed coefficients a_i applied at the subarray ports. Since the subarrays are formed by equal-amplitude power dividers the array illumination has a staircase appearance shown in the figure, with steps at the a_i level. The normalized radiation pattern at center frequency, unscanned, is

a
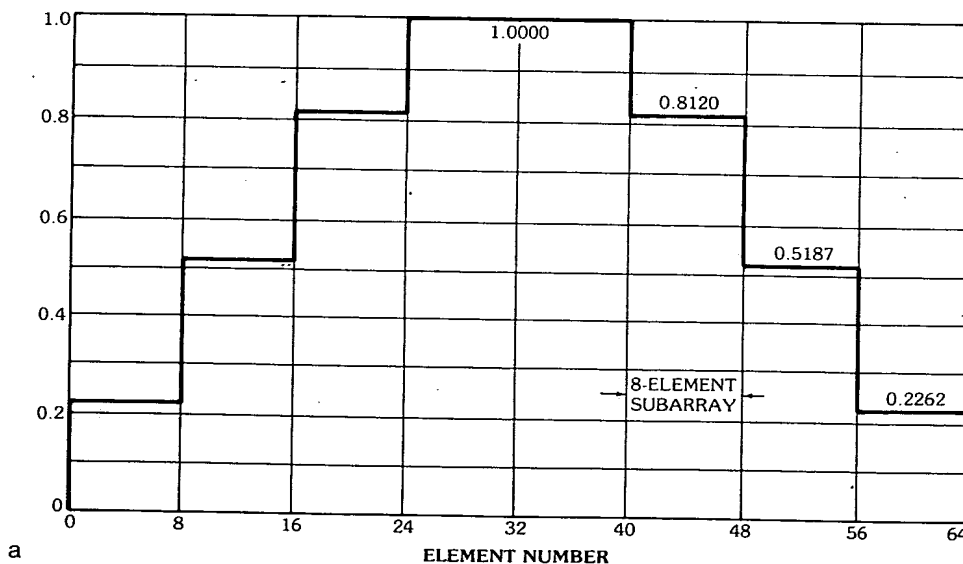
Fig. 16. An array of contiguous uniformly illuminated subarrays with −30-dB and −40-dB Chebyshev array illuminations. '(a) Array illumination (−30-dB case) for eight subarrays with eight elements each. (b) Subarray pattern and array factor (for −30-dB case). (c) Total array pattern for −30-dB case (−40-dB case shown partially).

ARRAY FACTOR
8-ELEMENT
CHEBYSHEV (−30 dB)
FOR SUBARRAYS
4λ APART

SUBARRAY PATTERN
(8 ELEMENTS, λ/2 SEPARATION)

RELATIVE POWER—DECIBELS

$u = \sin \theta$

b

−30-dB CHEBYSHEV ILLUMINATION

SPLIT GRATING LOBES FOR
−40-dB CHEBYSHEV ILLUMINATION·

RELATIVE POWER—DECIBELS

$u = \sin \theta$

c.

Fig. 16, *continued*.

13-31

$$E(r) = \frac{e(u,v)}{m} \frac{\sin[Mu\pi(d_x/\lambda)]}{M\sin[\pi u(d_x/\lambda)]} \sum_{i=-(m-1)/2}^{(m-1)/2} a_i e^{ji(2\pi/\lambda)u D_x} \tag{48}$$

Fig. 16 shows the pattern for a 64-element array with $M = m = 8$ and with the coefficients a_i shown in Fig. 16a selected to produce a -30-dB Chebyshev array factor. The final pattern, shown in Fig. 16c, is the product of the array factor 16b (solid) with low side lobes but large grating lobes and the subarray pattern 16b (dashed), and exhibits characteristic split grating lobe peaks that occur because of the broadened beamwidth of the low side lobe array factor. If the a_i coefficients were chosen for still lower near side lobes, the main beam and grating lobes in the array factor would broaden further and the subarray pattern nulls would be much narrower than the width of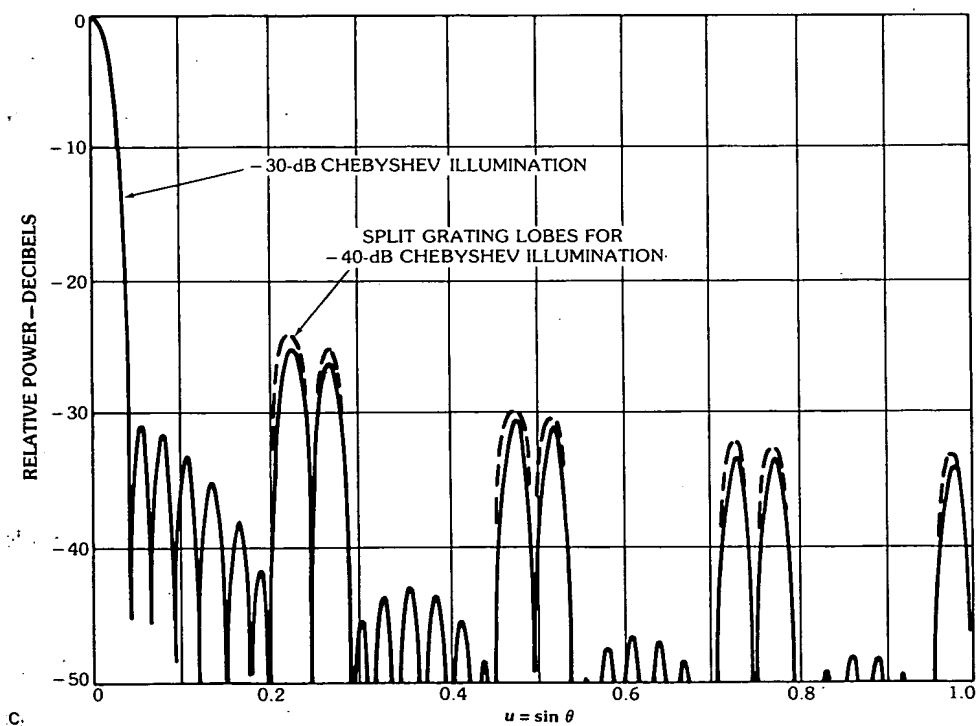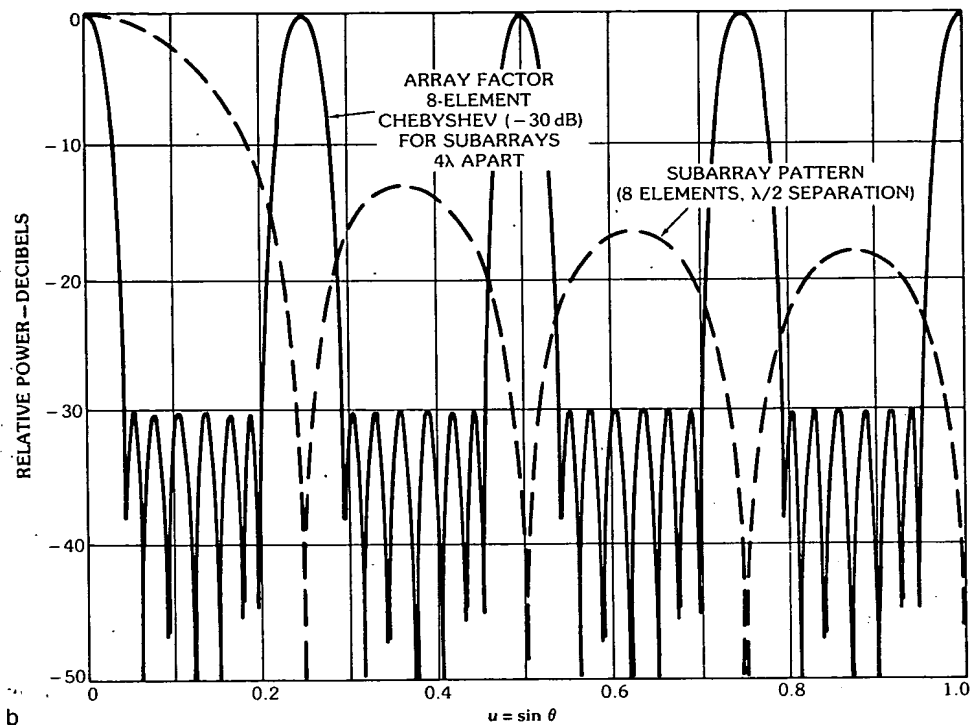 each grating lobe, thus leading to increased values of the split-peak grating lobes. Sample values corresponding to the -40-dB Chebyshev results are indicated dashed on the figure.

The above grating lobes could be lowered by using more and therefore smaller subarrays. The end result would be to broaden the subarray pattern nulls and so reduce the product of subarray pattern times array factor in the vicinity of the grating lobes.

In all of the cases treated in this section the grating lobe peaks can be suppressed by using unequally spaced subarrays. This modification leaves higher average side lobes than the array would have without subarraying, but is often the method selected for introducing time delay in a large array.
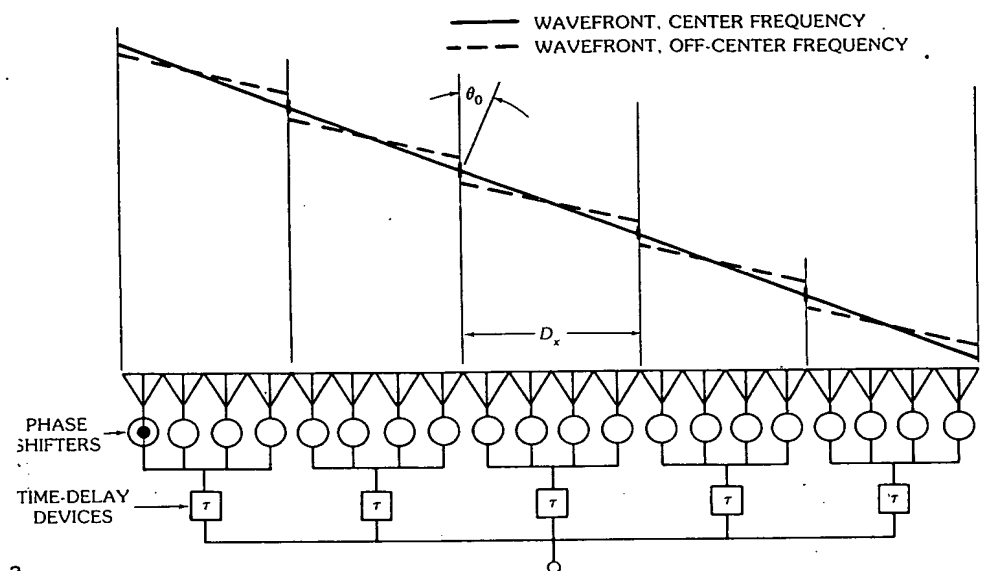
Wideband Characteristics of Time-Delayed Subarrays

The bandwidth limitations implied by (26) are often reasonable for small arrays but are usually too restrictive for large arrays. For this reason it is common practice to combine phase and time-delay steering by organizing the array into a relatively small number of subarrays and to use time-delay devices at the subarray input ports and phase steering at all the array elements. The resulting array bandwidth is a compromise between the cost of providing time-delay devices for a large number of subarrays and the pattern deterioration and bandwidth limitations of dividing the array into too few subarrays.

Contiguous Subarrays of Discrete Time-Delay Devices

The array of contiguous subarrays (Fig. 17) is conceptually simpler than other subarray approaches, and uses separate distribution networks to feed adjacent sections of the array. Phase shifters control the subarray pattern to produce a beam tilt, and the time-delay devices produce true time delay between the subarray centers. Fully equivalent is an array with time-delay devices behind each element, but with only a fixed number of discrete time-delay bits. The situations are mathematically equivalent if the number of available time-delay steps is made equal to the number of subarrays. In this case, for equal-size subarrays, the following results give peak grating lobe levels.

To consider an example, assume a one-dimensional array of elements spaced d_x apart, with element pattern $e(u,v)$. The elements are grouped into subarrays of M elements. The entire array has m equally spaced subarrays. Each of the subarrays has a subarray pattern that is the same as the middle term in (48), and
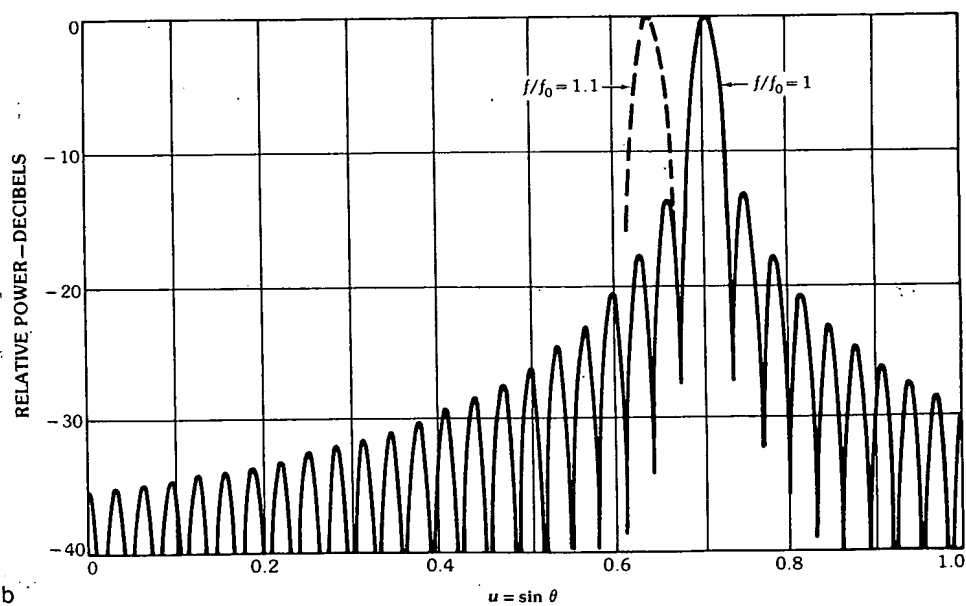
Fig. 17. Broadband characteristics of an array with time delay at subarray level, and contiguous phase-steered subarrays. (a) Array geometry, showing wavefront at center and off-center frequencies. (b) Patterns of 64-element array with phase shift steering. (c) Patterns of array organized with eight time-delayed subarrays.
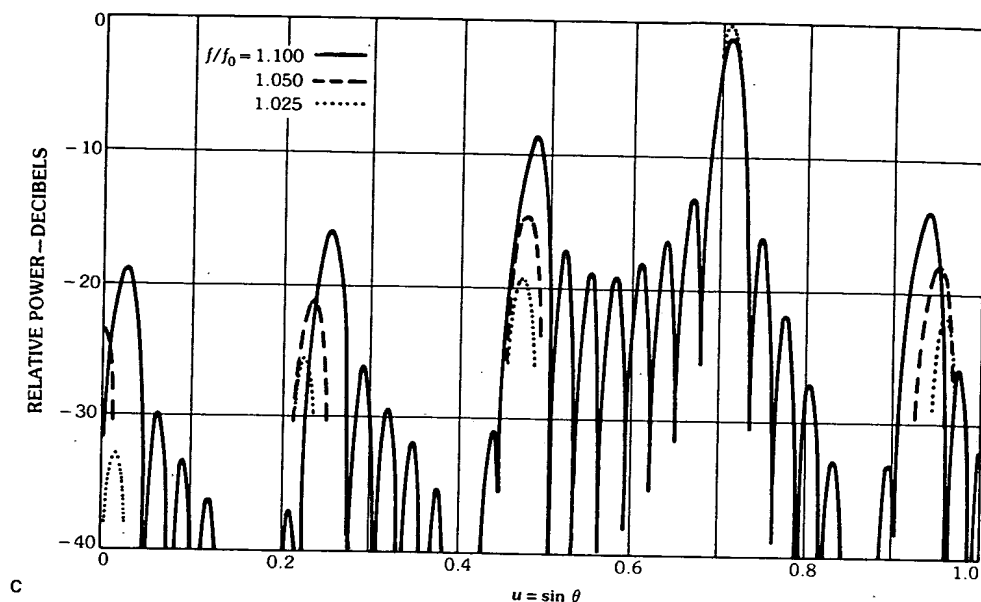
Fig. 17, *continued.*

when these subarrays are arrayed with time delay appropriate for beam collimation the complete field pattern is given by the expression

$$E(r) = e(u, v)\left\{\frac{\sin[M\pi d_x(u/\lambda - u_0/\lambda_0)]}{M\sin[\pi d_x(u/\lambda - u_0/\lambda_0)]}\right\}\left\{\frac{\sin[(m\pi D_x/\lambda)(u - u_0)]}{m\sin[(\pi D_x/\lambda)(u - u_0)]}\right\} \quad (49)$$

where $D_x = Md_x$ is the subarray size.

This expression shows the total field as the product of element pattern, phase-steered subarray pattern, and time-delayed array factor. If the array were purely phase controlled, with $M \times M$ elements each spaced d_x apart, its bandwidth given by (26) would be

$$\frac{\Delta f}{f_0} = \frac{K\lambda_0}{Mmd_x\sin\theta_0} \quad (50)$$

In its present subarrayed form, however, the time-delayed array factor exactly collimates the subarray contributions at all frequencies, and the system bandwidth is essentially the same as the subarray bandwidth:

$$\frac{\Delta f}{f_0} = \frac{K\lambda_0}{Md_x\sin\theta_0} \quad (51)$$

For example, an array of ten subarrays of ten elements each has approximately ten times the bandwidth of the phase-steered array of one hundred elements.

The above description emphasizes bandwidth based on gain, but in fact subarraying can introduce severe pattern degradation in the form of grating lobes that arise as frequency is changed. Grating lobes exist in this case, even though the subarray phase centers are appropriately delayed to form a beam at θ_0. This is because each subarray has a phase squint that causes the peak of the subarray pattern to move off the position θ_0 and the subarray pattern nulls to move so that they do not suppress the array pattern grating lobes. Fig. 17 shows the pattern of a uniformly illuminated array of 64 elements, arranged in subarrays of 8 elements, with each element 0.5λ apart. The array is scanned to 45°. In Fig. 17b, the array is steered by phase controls alone, and its main beam squints from the desired 45° to 40° for $f/f_0 = 1.10$. Fig. 17c shows that the same array with time delay at the sub-array input ports exhibits no beam squint, but that large grating lobes (about 8 dB below the main beam) seriously distort the pattern and cause a loss of gain at $f/f_0 = 1.1$. Grating lobes at $f/f_0 = 1.05$ and 1.025 are shown dashed and dotted, respectively. Clearly, the use of contiguous time-delayed subarrays leads to intolerable pattern deterioration for all but extremely small fractional bandwidths.

Overlapped Subarrays

A technique for implementing time-delay steering at the subarray level without the occurrence of large grating lobes involves the synthesis of subarray illuminations that are not merely contiguous but actually overlap. By using an aperture illumination wider than the intersubarray period it is possible to produce subarray patterns that have flat tops and are narrow enough to suppress the array pattern grating lobes [22]. This synthesis is achieved using two back-to-back transform networks in order to form a number of flat-topped subarray patterns, using the orthogonal beams as in a Woodward-type synthesis. The transform networks could be Butler matrices, as described here, or confocal lenses (Fig. 18), or reflectors, or some combination of these.

Fig. 18a shows the basic configuration of two Butler matrixes back to back used to excite an array that has phase shifters at each array element. The phase shifters are controlled in accordance with (24). A signal applied to the ith input port of the matrix at right (the $M \times M$ matrix) produces a progressive set of phases at the N array elements and radiates with the pattern

$$g_i(u) = Nf^e(u)\frac{\sin[(N\pi d_x/\lambda_0)(fu/f_0 - u_i)]}{N\sin[(\pi d_x/\lambda_0)(fu/f_0 - u_i)]} \tag{52}$$

where $f^e(u)$ is the array element pattern (assumed equal for all elements) and

$$u_i = i\frac{\lambda_0}{Nd_x} + u_0 \tag{53}$$

Each of the orthogonal beams is displaced from the angle of its peak radiation with all phase shifters set to zero by the amount u_0. When the matrix at left is used to provide the signals at the input to the $M \times N$ matrix at right, each input J_m excites a whole set of signals I_{im}, given by

a

b
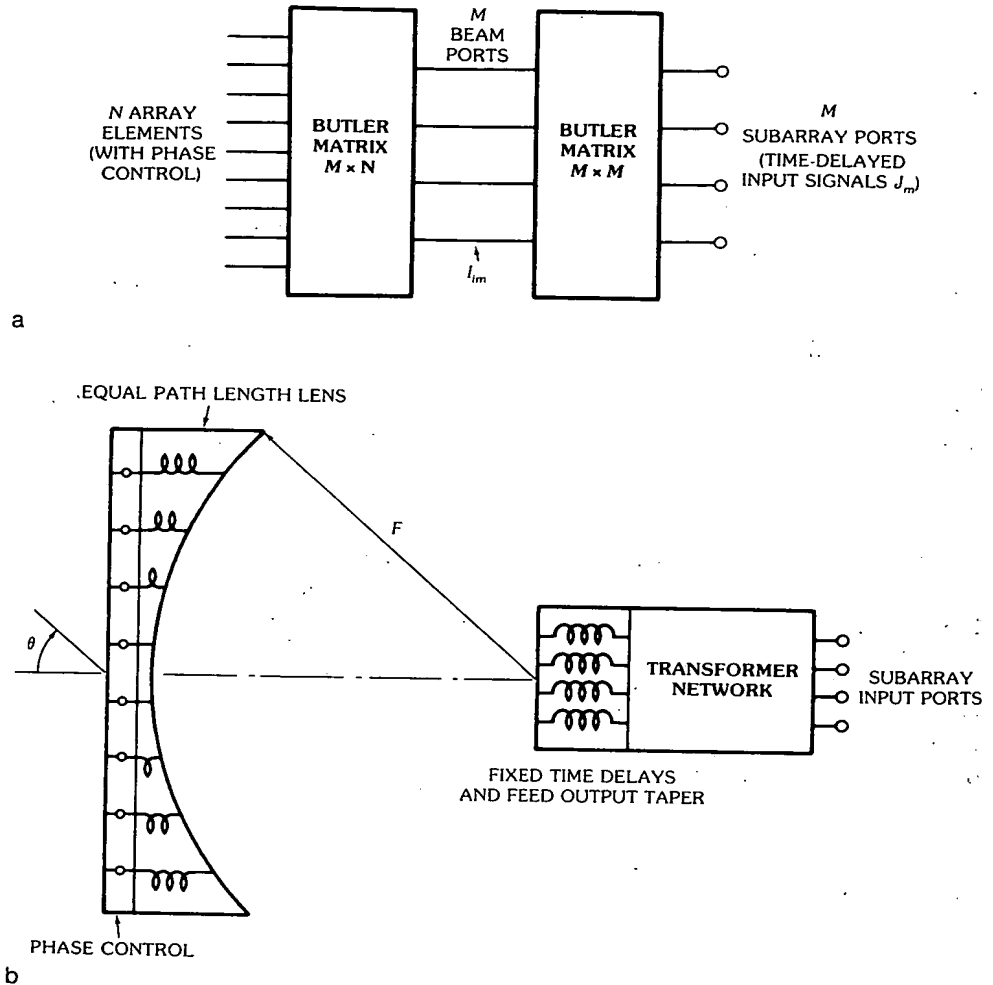
Fig. 18. Constrained and space-fed systems for overlapped subarray formation. (*a*) Constrained network. (*b*) Space-fed network.

$$I_{im} = \frac{J_m}{\sqrt{M}} e^{j2\pi(m/M)i}, \qquad -\left(\frac{M-1}{2}\right) \leqq i \leqq \frac{M-1}{2} \tag{54}$$

The aperture illumination (phase scanned to u_0) corresponding to the mth subarray is, for each nth element of the N-element array,

$$i_m^{(n)} = e^{-j(2\pi/\lambda_0)u_0} \frac{1}{\sqrt{N}} \sum_{i=-(M-1)/2}^{(M-1)/2} I_{im} e^{-j2\pi(n/N)i}$$

$$= \frac{N J_m e^{-j(2\pi/\lambda_0)u_0}}{\sqrt{NM}} \frac{\sin M\pi[(mN - nM)/MN]}{M \sin \pi[(mN - nM)/MN]} \tag{55}$$

This illumination has a maximum at the element with index $n = m(N/M)$, and overlaps all the elements of the array. An example of one such subarray illumination is the dashed curve of Fig. 19a for the subarray ($m = 4$) of an array of 64 elements ($N = 64$) with $\lambda/2$ separation. The array has eight subarrays ($M = 8$).

The radiated subarray patterns are given by

$$f_m(u) = \sum_i I_{im} g_i(u)$$

$$= \frac{NJ_m f^e(u)}{\sqrt{MN}} \sum_{i=-(M-1)/2}^{(M-1)/2} e^{j2\pi(m/M)i} \left(\frac{\sin[(N\pi d_x/\lambda_0)(fu/f_0 - u_i)]}{N \sin[(\pi d_x/\lambda_0)(fu/f_0 - u_i)]} \right) \qquad (56)$$

This expression is a sum of M orthogonal pencil beams arranged to fill the sector, and taken together to form a flat-topped pattern for the mth subarray, which is shifted in angle so that its center is at u_0 at center frequency.

Fig. 19b shows two subarray patterns at center frequency for the same 64-element array. The selected subarrays are an edge ($m = -7/2$) and one of the two central subarrays ($m = 1/2$). The edge subarray has higher side lobes and a highly rippled pass region because its illumination is truncated at the array edge.

The array excitation with all subarrays excited is

$$\mathscr{I}_n = \sum_{m=-(M-1)/2}^{(M-1)/2} J_m i_n^{(m)} \qquad (57)$$

where the $i_n^{(m)}$ are given in (55). An example of such a composite excitation is shown in the solid curve of Fig. 19a, for all subarrays weighted with a -30-dB Chebyshev illumination. This excitation is much smoother than the illumination
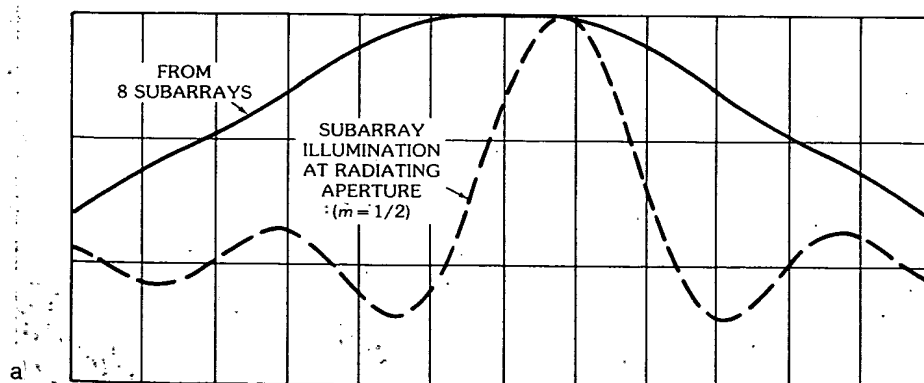
Fig. 19. Broadband characteristics of an array with time delay at the subarray level and completely overlapped phase-steered subarrays. (a) Typical subarray illumination at radiating aperture and total illumination from eight subarrays with -30-dB Chebyshev weighting. (b) Radiated subarray patterns near array edge and array center. (c) Array radiation pattern at broadside and $45°$ scan ($f = f_0$) and $45°$ scan ($f = 1.1f_0$).
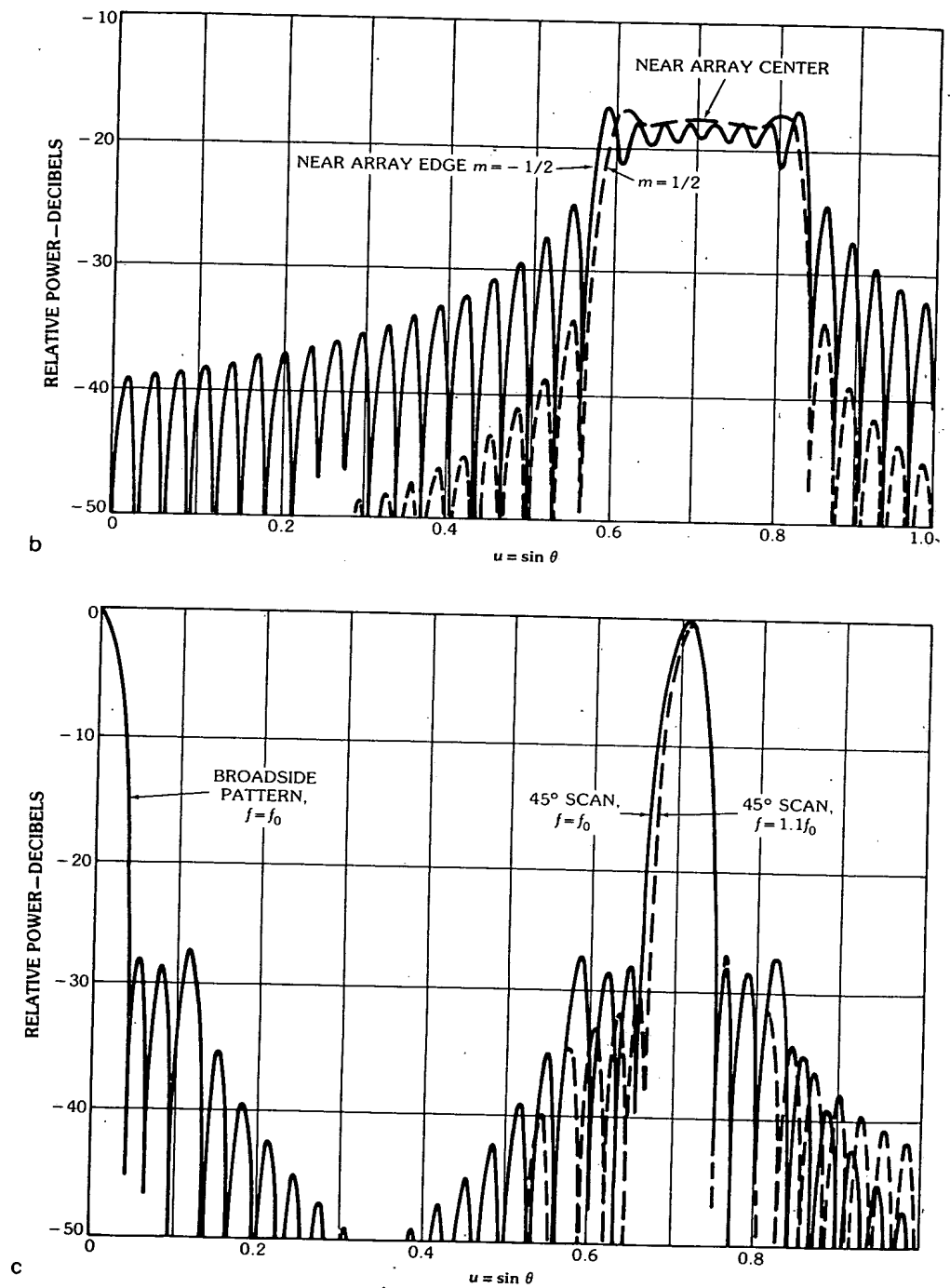
Fig. 19, *continued*.

shown in Fig. 16a, which shows the same weightings applied to an array of contiguous subarrays. So it can be expected that the side lobes would be lower for the overlapped subarray case.

The radiated array pattern is given by

$$F(u) = \sum_{M=-(M-1)/2}^{(M-1)/2} J_m f_m(u) \tag{58}$$

To scan the array beam to u_0 with time delay, one applies the signals

$$J_m = |J_m| e^{-j(2\pi/\lambda_0)D_x(f/f_0 - 1)u_0} \tag{59}$$

where $D_x = (N/M)d_x$ is the distance between subarray centers at the array face.

The absolute values of the input signals $|J_m|$ are weighted directly to provide the appropriate near side lobe distribution.

Figs. 19c and 19d show several array patterns for the array with the -30-dB illumination. As shown in the figures the side lobe levels exceed -30 dB because of the rippled subarray patterns. At center frequency ($f/f_0 = 1$) the pattern scanned to $u = 0.707$ (45°) has the same form as the broadside pattern, and even at 10 percent above center frequency ($f/f_0 = 1.1$) the main beam is not altered in location or gain, though the side lobe structure is.

The bandwidth of such a subarraying is on the order of

$$\frac{\Delta f}{f_0} \cong \frac{(M-1)}{N} \frac{\lambda}{d_x} \frac{1}{\sin \theta_0} \tag{60}$$

Overlapped subarray systems have been implemented using multiple-beam lens systems [22, 23, 24] and Butler matrix [25] networks. With the emergence of digital beam-forming technology it is likely that it will be convenient to form subarrayed patterns digitally for future system applications.

The networks described above produce completely overlapped subarrays; each subarray extends over the whole array. However, convenient networks have also been developed to overlap small groups of elements. Such techniques form approximations of the ideal flat-topped pattern and are useful for limited scan applications [26, 27].

Broadband Array Feeds with Time-Delayed Offset Beams

Equation 26 gives the fractional bandwidth of a phase-steered array as a function of its beamwidth and the maximum scan angle θ_0. The bandwidth can be relatively large if the array scan remains small, so that the product $(L/\lambda_0) \sin \theta_0$ does not become a large number. Similarly, if an array is fed by a system that produces a time-delayed beam at some angle θ_T, and the beam is phase steered to an angle θ_0 by phase shifters, then the bandwidth is given by

$$\frac{\Delta f}{f_0} = \frac{0.866B\lambda_0}{L|\sin \theta_T - \sin \theta_0|} \tag{61}$$

This equation shows that by using a feed system that provides a number of fixed-offset time-delayed beams it is possible to scan those beams over the limited angular regions between the beams, and so operate over substantially increased instantaneous bandwidth. One such implementation, suggested by Rotman and Franchi [28], is indicated in Fig. 20a, which shows an active lens with four feed horns equally spaced along the focal arc of a two-dimensional microwave-cons-
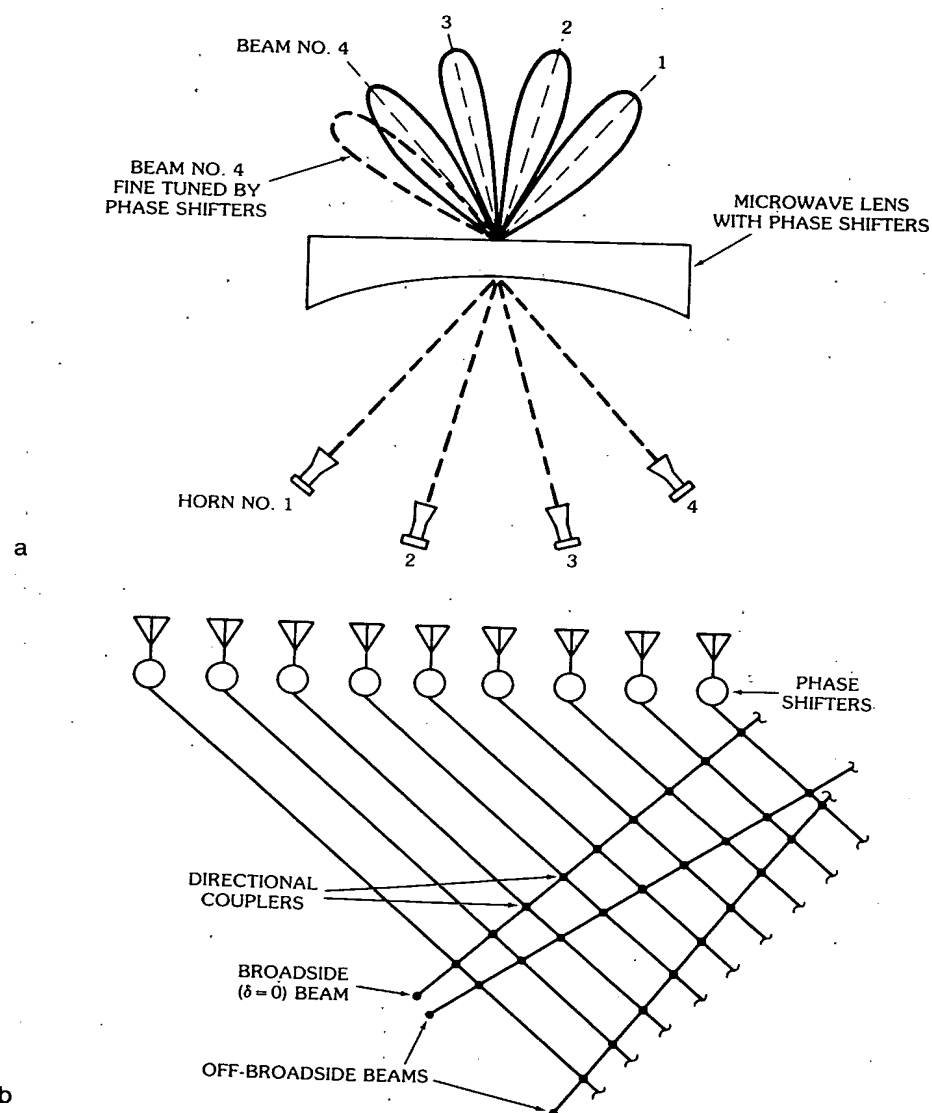

Fig. 20. Wideband scanning using phase shifter and fixed time-delayed beams. (a) Microwave lens configuration. (b) True time-delay matrix.

trained lens. Energy from a transmitter can be directed to any one of the horns by means of the switching tree. Each horn, in turn, will form a beam in a different azimuth direction for the zero phase shifter setting. A typical beam for the Mth horn is sketched as the solid curve (Mth beam). As the phase of the lens illumination is changed by the phase shifters the beam scans to either side of its no-phase-shift position. This effect is illustrated by the dotted curve (phase-scanned Mth beam). The bandwidth limitation imposed by this phase scanning is given by the following equation, with θ_0 the maximum scan angle and N the number of beam positions (4 for the example in the figure). The system bandwidth, given below and readily derived from (26), is wide because of the limited scan angle:

$$\frac{\Delta f}{f_0} \cong \frac{0.886BN}{(L/\lambda_0)\sin\theta_0} \tag{62}$$

Other means for achieving fixed offset beams include the use of constrained multiple-beam systems, such as the true time-delay matrix of Fig. 20b, or precut switched time delays at each array element. In addition to providing wideband gain, systems that use offset beams have no phase discontinuities and therefore no grating lobes. In principle they can have very low side lobes.

4. Practical Arrays

The previous sections on periodic arrays treat the array in an idealized case, with perfectly regular lattices, prescribed exact phase controls, half-space isotropic element patterns, and, most importantly, with all element patterns equal.

This section deals with a number of problems that confront array designers. Array mutual coupling leads to unequal element patterns and to a need to solve coupled integral equations before applying any of the synthesis methods mentioned earlier. Conformal nonplanar arrays have lattices that are, at most, periodic in one plane, and so present special problems in synthesis and pattern control. Finally, the section addresses array component errors of several types, and it reviews components used to distribute power and scan the beam of a phased array.

Mutual Coupling and Element Patterns

One of the most important and complex aspects of modern array design is that element excitation coefficients are not proportional to applied sources (voltages or currents) and that the element patterns are nonisotropic and not equal to the pattern of an isolated element. These phenomena occur because each of the elements couples through radiation to all of the others, and hence the relationship between applied sources and element excitation must be expressed in terms of a complex matrix. This phenomenon is called *mutual coupling*.

A detailed treatment of mutual coupling is beyond the scope or intent of this chapter. The solution of wire antenna problems, such as the dipole array of Fig. 21a, is carried out by satisfying a boundary condition (usually that the tangential electric field is zero) at the surface of the wire and equal but opposite to the applied field at the source point. For the dipole array of Fig. 21a, with dipole axes along the $\hat{y}$ direction and their centers located at $(x_m, y_m, c/2)$ with and without a ground
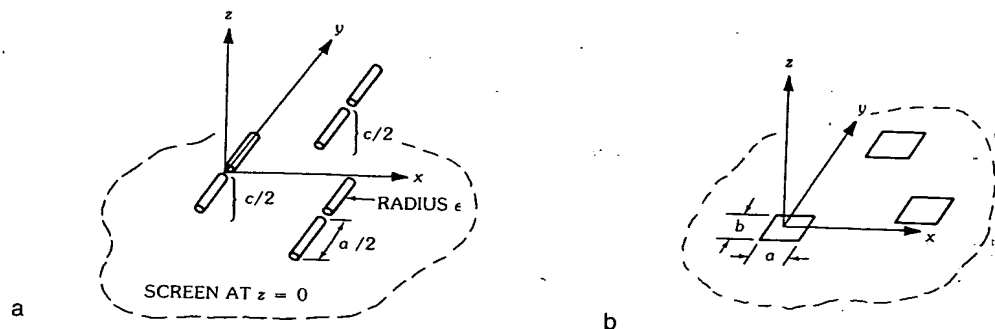
Fig. 21. Elements for scanning arrays. (*a*) Dipoles over ground screen. (*b*) Waveguide apertures in ground screen.

plane, it is convenient to introduce a single component of the vector potential defined at $\mathbf{r} = \hat{x}x + \hat{y}y + \hat{z}z$ as

$$A_y(x, y, z) = \frac{\mu_0}{4\pi} \sum_m \int_{v_m} I_m(y') G(r, r') dy' \tag{63}$$

where

$$G(r, r') = \frac{e^{-jk_0|\mathbf{r} - \mathbf{r}_m|}}{|\mathbf{r} - \mathbf{r}_m|}$$

$$|\mathbf{r} - \mathbf{r}_m| = \sqrt{(x - x_m)^2 + (y - y')^2 + (z - c/2)^2}$$

for the array without a ground plane, and

$$G(r, r') = \frac{e^{-jk_0|\mathbf{r} - \mathbf{r}_m|}}{|\mathbf{r} - \mathbf{r}_m|} - \frac{e^{-jk_0|\mathbf{r} - \mathbf{r}_m^{(i)}|}}{|\mathbf{r} - \mathbf{r}_m^{(i)}|}$$

$$|\mathbf{r} - \mathbf{r}_m^{(i)}| = \sqrt{(x - x_m)^2 + (y - y')^2 + (z - c/2)^2}$$

for the array with ground plane at $z = 0$.

The second expression accounts for the image dipole at $z = -c/2$.

The set of integral equations equating the tangential **E** field to zero at each dipole radius is written at the nth dipole

$$E_y(x_n, y, c/2) = -V^{(n)}\delta(y - y_n) = -j\frac{\omega}{k_0^2}\left[\frac{\partial^2 A_y}{\partial y^2} + k^2 A_y\right],$$

$$\text{for } -a/2 \leqq y - y_n \leqq a/2 \tag{64}$$

where $V^{(n)}$ is the potential across the source at the nth antenna. The source is assumed to be a delta function of the electric field located at the center of each dipole, and the equation sets the induced field equal to the negative of the source field at this point.

In this form the integral equation is often called *Pocklington's equation* and is frequently chosen for digital computer solution of dipole and wire antenna problems. In this procedure each dipole is considered as made up of a number of connected segments, with each segment radiating and coupling to all other segments in all of the radiators. For detailed descriptions of this procedure the reader is referred to [29] and [30].

Another traditional form of equation for dipole arrays is obtained by constructing a solution to the above differential form to obtain a generalized form of Hallen's equation [31]:

$$
\left.
\begin{aligned}
A_y(x_n, y, z_n) &= c_1^{(n)}\cos ky + c_2^{(n)}\sin ky - j\frac{k}{2}\frac{V^{(n)}}{\omega}\sin ky, & 0 \leqq y - y_n \leqq a/2 \\
&= c_3^{(n)}\cos ky + c_4^{(n)}\sin ky + j\frac{k}{2}\frac{V^{(n)}}{\omega}\sin ky, & -a/2 \leqq y - y_n \leqq 0
\end{aligned}
\right\}
\tag{65}
$$

The potential A_y on the left side of the equation is evaluated at the center line of each dipole (using $|\mathbf{r} - \mathbf{r}_m| = [\varepsilon^2 + (y - y')^2]^{1/2}$ for $n = m$). The evaluation of the potential function in this manner is valid for thin dipoles (with ε much less all other dimensions, including wavelength) and assumes the potential outside of and even at the surface of the dipole is the same as if there were a filament of current at the dipole axis.

The constant c_4 is equal to c_2.

The above is a set of M integral equations, written along each dipole, and consisting of M unknown current functions and $3M$ constants ($c_1^{(n)}, c_2^{(n)}, c_3^{(n)}$) that arose from the integration of the integrodifferential equations. The solution of the above equations is necessarily approximate and there have been numerous forms of published solutions, each with different degrees of validity and complexity. The simplest approximation is one that assumes that the form of the current distribution is the same on all dipoles,

$$
I_m(y) = I(m)f(y)
\tag{66}
$$

This approach is most appropriate for resonant dipoles with their source points all in the same plane ($y_n = 0$). Examples of this sort of solution exist in the literature and have been carried out by assuming a form $f(y)$ and solving the resulting simultaneous equations.

The end result after elimination of constants is an impedance matrix

$$
\mathbf{V} = \mathbf{ZI}
\tag{67}
$$

with column vectors $\mathbf{I}$ and $\mathbf{V}$ and square impedance matrix $\mathbf{Z}$ that one can use for computation of currents, given applied voltages, or, in the case of synthesizing required antenna patterns, can be used to compute the required voltages to provide desired current terms. Commonly used single-mode impedance formulas are given by Brown and King [32], Carter [33], and Tai [34].

King and his colleagues have employed several higher-order solutions that are

more realistic for computing near-field effects or coupling between column arrays of dipoles with parallel axes. The most comprehensive of these is the five-term theory [35,36] that includes asymmetric current terms for evaluation of the radiation properties of arrays scanned in two dimensions.

Of these two basic methods, the expansion of the current by a finite number of functions that span the entire dipole or by a piecewise approximation in sections across the dipole, solutions based on higher-order current expansions have to date seen far wider application to large arrays than the multisegment solutions, because the former involve the inversion of much smaller matrices.

Finite waveguide arrays can be treated in a similar manner. In this case there are no electric current sources in the half-space $z \geq 0$, and the only sources are the magnetic current sources as represented by the tangential aperture fields. In this case there is no single vector component that serves to completely represent the fields except for special two-dimensional cases. In general, however, for a finite waveguide aperture the solution is vector and is formulated by expanding the aperture field in a set of functions and matching fields in the waveguides and free space. For open-ended waveguides it is convenient to choose as basis functions the waveguide normal-mode fields, and for unloaded rectangular waveguides one can choose the orthogonally polarized transverse electric fields. The transverse electric field for the waveguide at the origin of the coordinate system of Fig. 21 is

$$\mathbf{E}^T = \mathbf{e}_0(x,y)e^{-jk_z(0)z} + \sum_n V_n \mathbf{e}_n(x,y)e^{+jk_z(n)z} \tag{68}$$

where the $\mathbf{e}_n(x,y)$ are the transverse-mode functions for the two possible polarizations, the $k_z(n)$ are the modal propagation constants, and V_n are undetermined modal amplitude coefficients. This expression represents a single incident mode in the waveguide and an infinite series of reflected modes. Typically all but the $k_z(0)$ propagation constants are imaginary, indicating that those are beyond waveguide cutoff, but they enter into the solution to match boundary conditions. The solution proceeds by expanding the transverse magnetic waveguide fields in terms of these and writing the half-space fields ($z > 0$) as the aperture field. Construction of the free-space Green's function ensures that the tangential E field is continuous, and imposed continuity of the magnetic field components results in a vector integrodifferential equation

$$\hat{\mathbf{z}} \times \mathbf{B}(z = 0^-) = \hat{\mathbf{z}} \times \mathbf{B}(z = 0^+)$$

$$= j2\omega\varepsilon\hat{\mathbf{z}} \times \sum_s \bar{\bar{\Gamma}}^0(r,r') \cdot (\hat{\mathbf{z}} \times \mathbf{E})ds' \tag{69}$$

where the free-space dyadic Green's function is given by

$$\bar{\bar{\Gamma}}^0(\mathbf{r},\mathbf{r}') = \left(\bar{\bar{\mathbf{U}}} + \frac{1}{k^2}\nabla\nabla\right)G(\mathbf{r},\mathbf{r}')$$

where

$$G(\mathbf{r}, \mathbf{r}') = \frac{e^{-jk|\mathbf{r}-\mathbf{r}'|}}{4\pi|\mathbf{r} - \mathbf{r}'|}$$

$$\mathbf{r} - \mathbf{r}' = \sqrt{(x - x')^2 + (y - y')^2 + z^2}$$

is the scalar Green's function. The unit dyad $\bar{\bar{\mathbf{U}}}$ is defined in rectangular coordinates as

$$\bar{\bar{\mathbf{U}}} = \hat{\mathbf{x}}\hat{\mathbf{x}} + \hat{\mathbf{y}}\hat{\mathbf{y}} + \hat{\mathbf{z}}\hat{\mathbf{z}}$$

The magnetic field $\mathbf{B}$ for $z = 0$ can be obtained from the expansion (68) using waveguide modal admittances. By following Galerkin's procedure the above can then be reduced to a matrix equation and solved for aperture fields. The details of this procedure will not be carried further, but are described in a number of available references [37, 38].

Waveguide array solutions using single-mode approximations in each aperture have much more limited applicability than the simple theories for dipole arrays. Single-mode waveguide coupling solutions fail to predict blindness effects (see next section) but can be used successfully for small arrays and for relatively closely spaced elements at scan angles far from the grating lobe onset. Single-mode solutions have also been used by Golden [39], Steyskal [40], and others for elements conformal to curved surfaces.

Fig. 22 [41] shows several of the most significant effects due to mutual coupling. Fig. 22a shows the element pattern of the central element in an array of N parallel plane elements with the incident waveguide fields in the plane of scan. The presence of multiple ripples in the element pattern is due to reflections from the array edge, as indicated by the higher angular frequency for increased N. The infinite array results, also shown in the figure, demonstrate element pattern narrowing due to mutual coupling that forces the pattern to be zero at the horizon. Fig. 22b shows the associated reflection coefficient for the central element and again evidences the rippling effect for finite arrays and the unity reflection coefficient for the infinite array model at end-fire (about $\psi = 140°$) and throughout the slow-wave region $\psi > 140°$.

Array Blindness

In certain circumstances it is possible to have mutual coupling effects that actually create a null in the array element patterns so that the array cannot transmit energy in given directions.

Fig. 23 shows the basic phenomena as described by Farrell and Kuhn [42, 43] in the first published analytical work on the subject. The figure shows a measured deep null in an element pattern of a waveguide array and compares the data with results computed using a single-mode grating lobe series for an infinite array and a full modal array solution. The null is due to the cumulative effects of mutual coupling and can be related to surface wave type behavior at the array face. In many cases the existence of the null is understood as a cancellation process involving waveguide higher-order modes, and this is why the single-mode grating lobe solution bears little correlation to the data in Fig. 23. In the years since this initial discovery these blindnesses have been found in most waveguide array
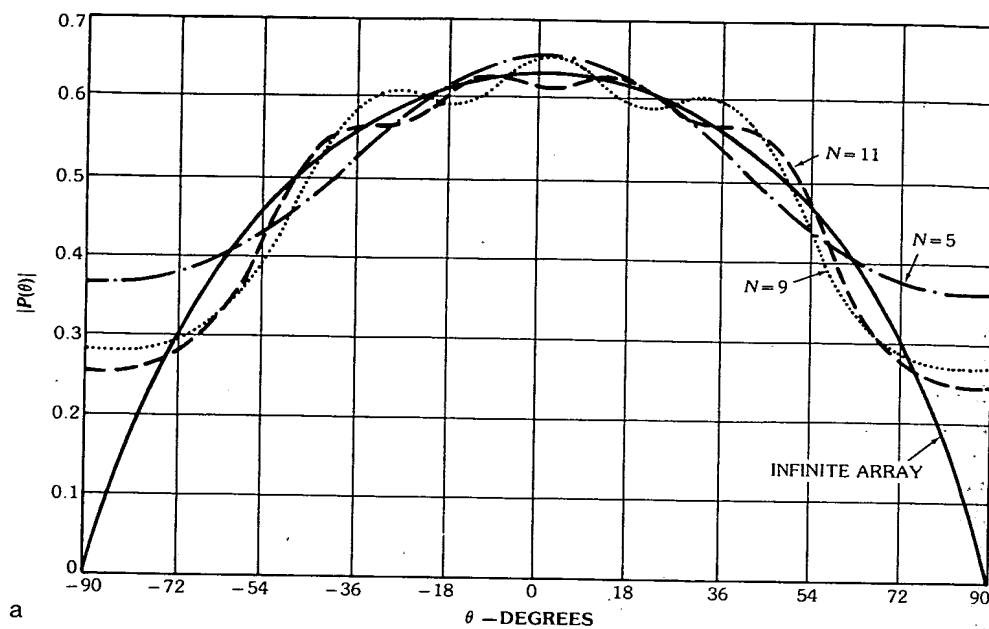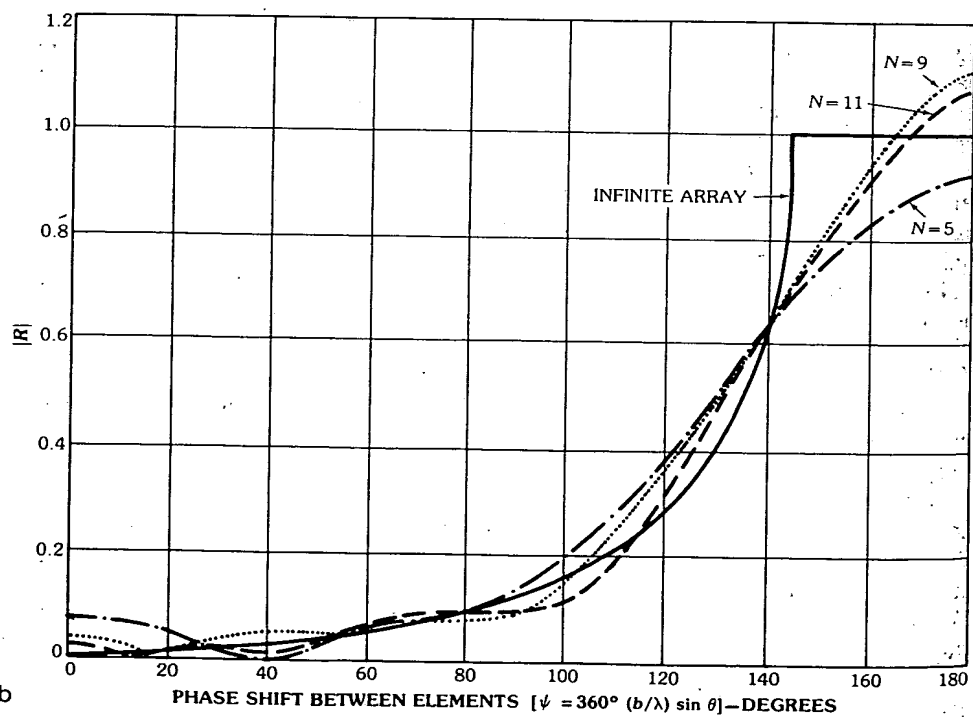
Fig. 22. Element patterns $P(\theta)$ and reflection coefficients R of center elements in unloaded waveguide array ($b/\lambda = a/\lambda = 0.4$). ($a$) Radiation patterns. ($b$) Reflection coefficients. (*After Wu [41], © 1970 IEEE*)

Fig. 23. Array element power pattern showing array blindness. (*After Farrell and Kuhn [42, 43], © 1968 IEEE*)
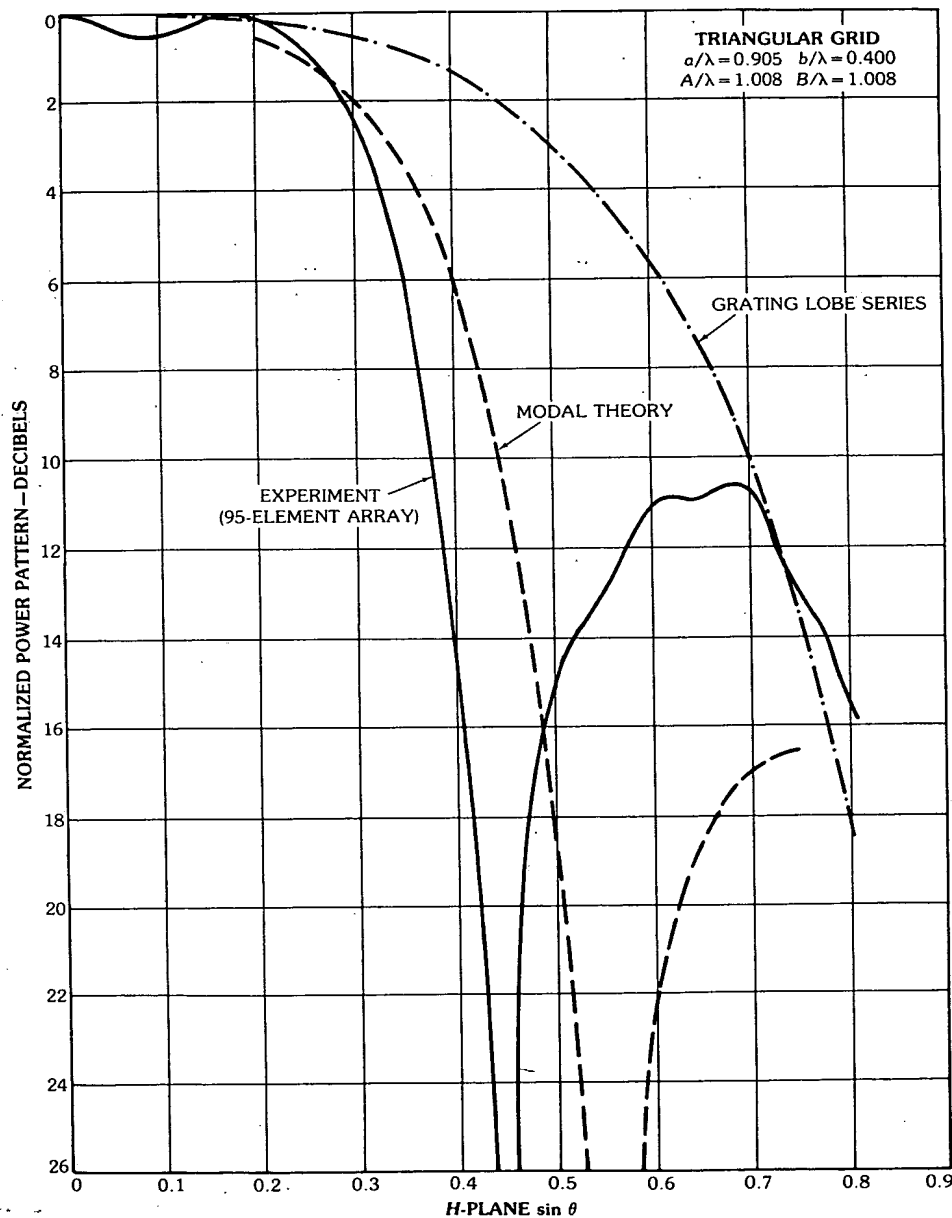
configurations and in some dipole and stripline arrays [44]. The problem can usually be reduced or eliminated by keeping the element lattice dimensions d_x and d_y small enough so that grating lobes are well beyond the maximum scan angle throughout the operating frequency range [45].

Reported blindnesses in dipole arrays seem to be related to the presence of dipole supports. Analytical studies of infinite dipole arrays [46] without supports do not exhibit array blindness. Mayer and Hessel [47] analyze a stripline dipole structure and show that for practical spacings the balanced stripline dipole feed structure supports a propagating TM mode in addition to two TEM modes. The TEM mode propagation constant is scan dependent, and for certain parameter selections it occurs before the onset of the grating lobe. It is conjectured that this mode might be the cause of blindness in dipole arrays.

Experience with array blindness has led to the practice of performing infinite-array studies, measuring the array element in simulator, or fabricating a small array for element pattern tests before embarking on the construction of a large array. Multimodal infinite array solutions are far simpler to obtain than multimode solutions for large arrays and such solutions have been obtained for many array types. Fig. 24 shows a few of the basic array configurations for which infinite array
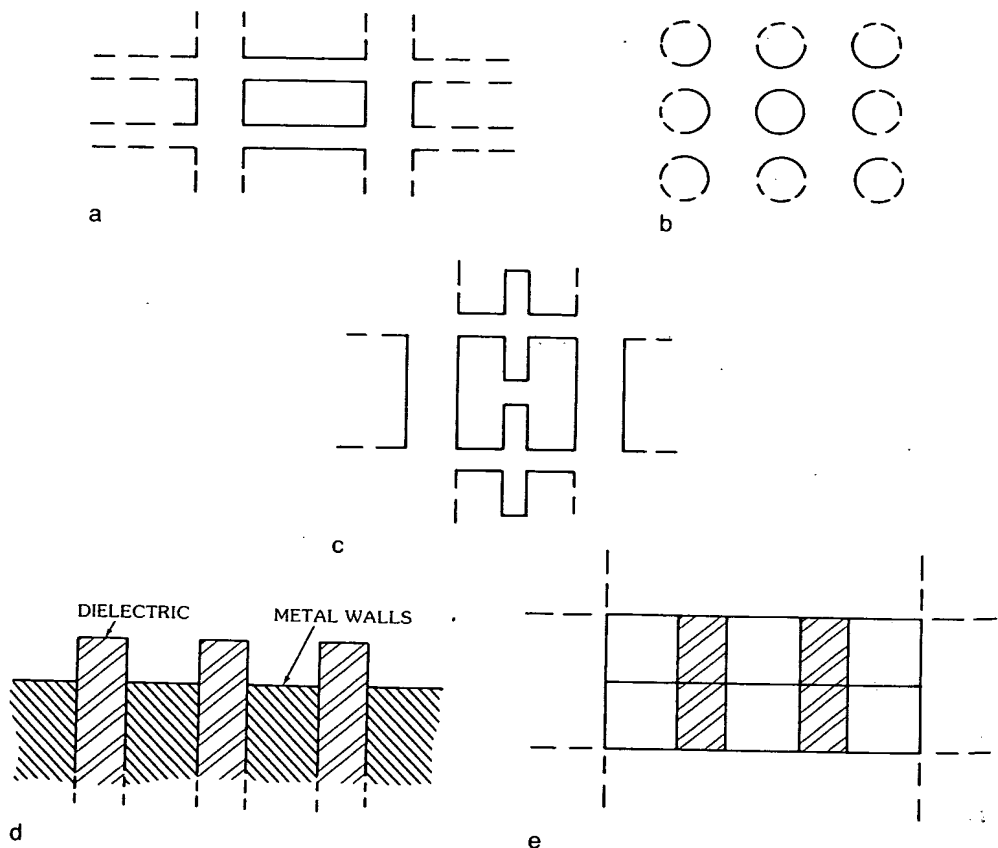

Fig. 24. Several configurations with existing infinite array solutions. (a) Rectangular waveguide array. (b) Circular waveguide array. (c) Ridge loaded waveguide array. (d) Protruding dielectric waveguide array. (e) Dual-frequency array.

solutions are published. Included in the figure are flush mounted arrays of rectangular [48] and circular [49] elements, ridge loaded elements [50, 51, 52], protruding dielectric (TEM solution) [53], and a dual-frequency dielectric loaded configuration [54]. Among other published solutions are numerous interlaced multiple-frequency configurations [55], examples of dielectric loading [56], iris loading [57] and fence [58], and corrugated plate [59] loadings for impedance match, as well as several very wide band configurations for waveguide [60] and stripline [61]. In addition there have been a number of infinite dipole array solutions published [62].

Conformal Arrays

The need for conformal or low profile arrays for aircraft and missile applications, and for ground-based arrays with 360° azimuth coverage or hemispherical coverage, has grown continually with requirements that emphasize maximum utilization of available space and minimum cost. The earliest and continuing stimulus for cylindrical and circular array development is the need for inexpensive systems with mechanical or electronic scanning with constant gain throughout the 360° coverage sector. There are also a number of spacecraft and aircraft applications requiring low profile or conformal arrays. Fig. 25 shows a possible configuration of an airborne array for satellite communication.

Array elements on curved bodies point in different directions, and so it is usually necessary to turn off those elements that radiate primarily away from the desired direction of radiation. For this reason also, one cannot factor an element pattern out of the total radiation pattern and therefore conformal array synthesis is very difficult. In addition, mutual coupling problems can be severe and difficult
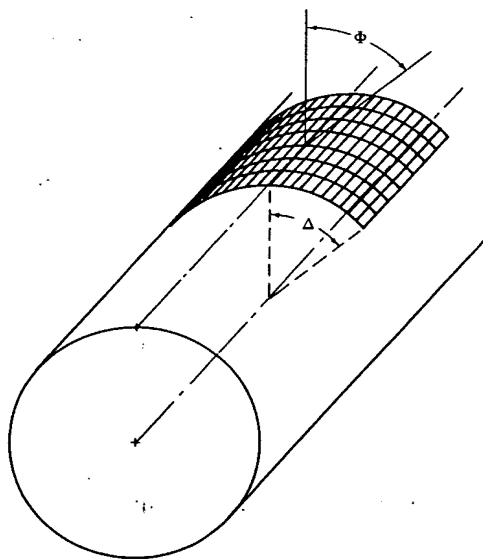
Fig. 25. Conformal array geometry for 2Δ arc array on cylinder.
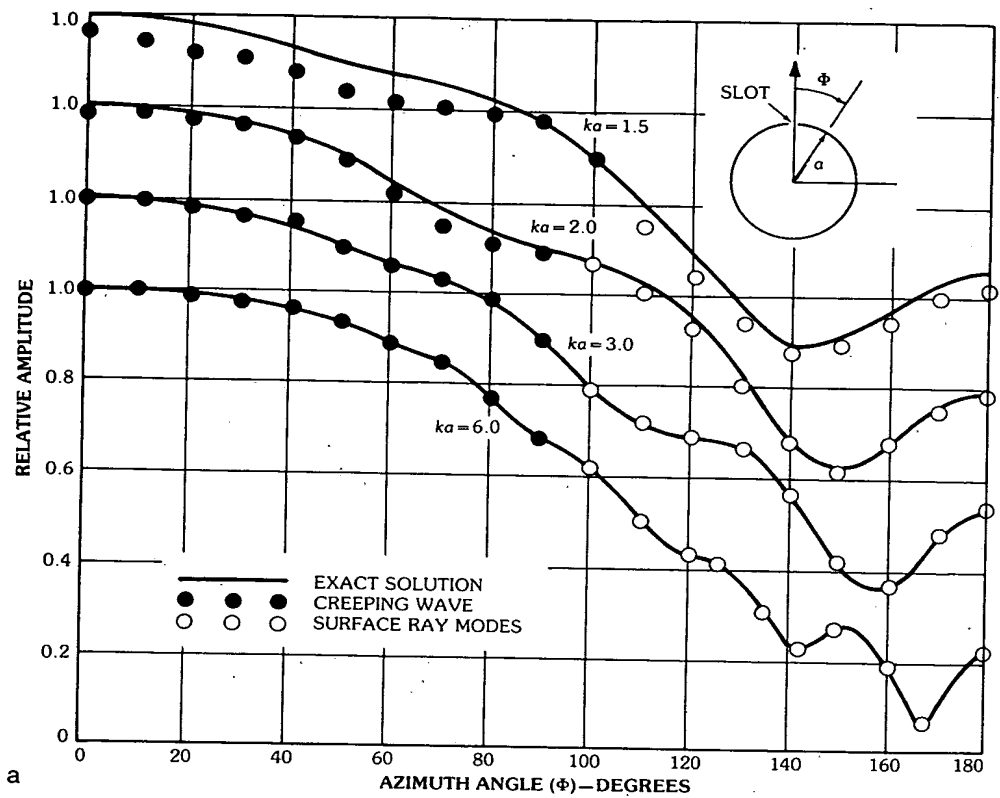
Fig. 26. Patterns of slots and arrays on cylinders. (*a*) Patterns of a thin axial slot in a perfectly conducting cylinder. (*After Pathak and Kouyoumjian [63],* © *1974 IEEE*) (*b*) Element patterns for dipole arrays on a cylinder. (*After Herper et al. [68],* © *1980 IEEE*)

to analyze because of the extreme asymmetry of structures like cones and because of multiple coupling paths between elements (for example, the clockwise and counterclockwise paths between two elements on a cylinder). Cross-polarization effects arise because of the different pointing directions for elements on curved surfaces causing the polarization vector projections to be nonaligned. There is also a need to use different collimating phase shifts in the azimuth plane of a cylindrical array scanned in elevation due to the fact that steering in azimuth and elevation planes is not separate. Another phenomenon related to mutual coupling is the evidence of ripples on the element patterns of cylindrical arrays. This phenomenon can be explained in terms of creeping-wave contributions.

The behavior of slot and dipole elements is altered by the presence of the curved surface. Pathak and Kouyoumjian [63] give a very convenient extension of the geometrical theory of diffraction (GTD) for apertures in curved surfaces. Fig. 26a shows the patterns of an axial slot element in perfectly conducting circular cylinders of various radii, as computed by Pathak and Kouyoumjian. The pattern compares the exact solution with that obtained using the appropriate GTD
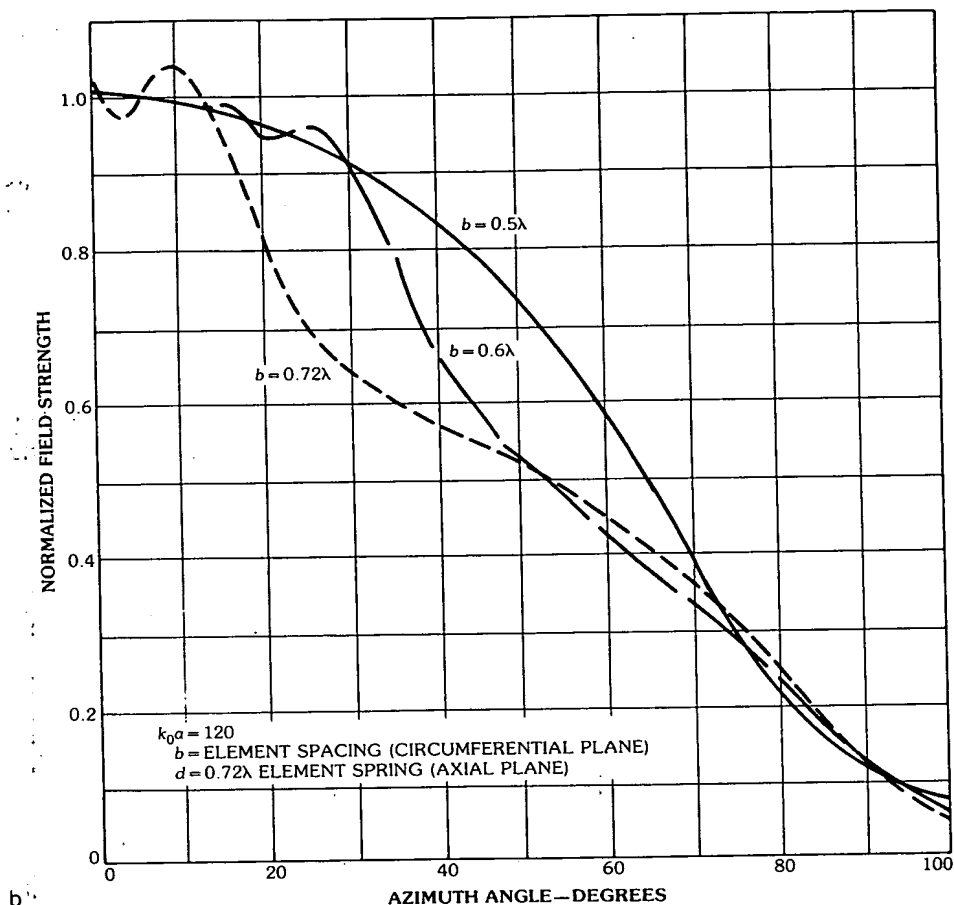
Fig. 26, *continued.*

expressions in several regions of space, and shows the GTD formalism to be highly accurate, even for relatively small cylinders. The figure also emphasizes the way in which the finite cylinder alters slot element patterns, for a similar slot in a flat ground plane would have a constant radiation pattern from $\phi = 0°$ to $180°$. A number of other references give the radiation patterns of slots and dipole elements on a variety of generalized surfaces [64, 65, 66].

Arrays of slots or dipoles on curved surfaces also behave differently from those on plane surfaces, and often have highly rippled element patterns [67] that make low side lobe synthesis impossible. Fig. 26b, however, shows that the rippled element pattern characteristic shown for a dipole array over a cylinder does not occur if the element spacing is restricted to about a half-wavelength [67]. The unwelcome rippled effect shown for larger spacings has been attributed [67] to interference between the grating lobe of the fast creeping wave and the direct ray.

At $\lambda/2$ element spacing this grating lobe does not radiate, and the resulting element patterns are free from ripples.

. Cylindrical arrays can have low side lobe patterns, but it is important to maintain close element spacing and not to wrap the array too far around the cylinder. Fig. 27 shows the results attributable to Sureau and Hessel [67] that illustrate both of these effects. This figure shows that for the array with elements wrapped entirely around the cylinder, doubling the size of the excited sector of the array only increases the gain by 1 dB due to inefficient radiation of the edge elements. The narrowed array element patterns, also shown in the figure, emphasize the fact that edge elements are required to provide coverage at the outer limits of their active element patterns.

Array Errors and Phase Quantization

The ability of an array to create a desired antenna pattern in space is limited by diffraction effects resulting from finite antenna size, by element pattern ripple, and by random and correlated errors in the array illumination.
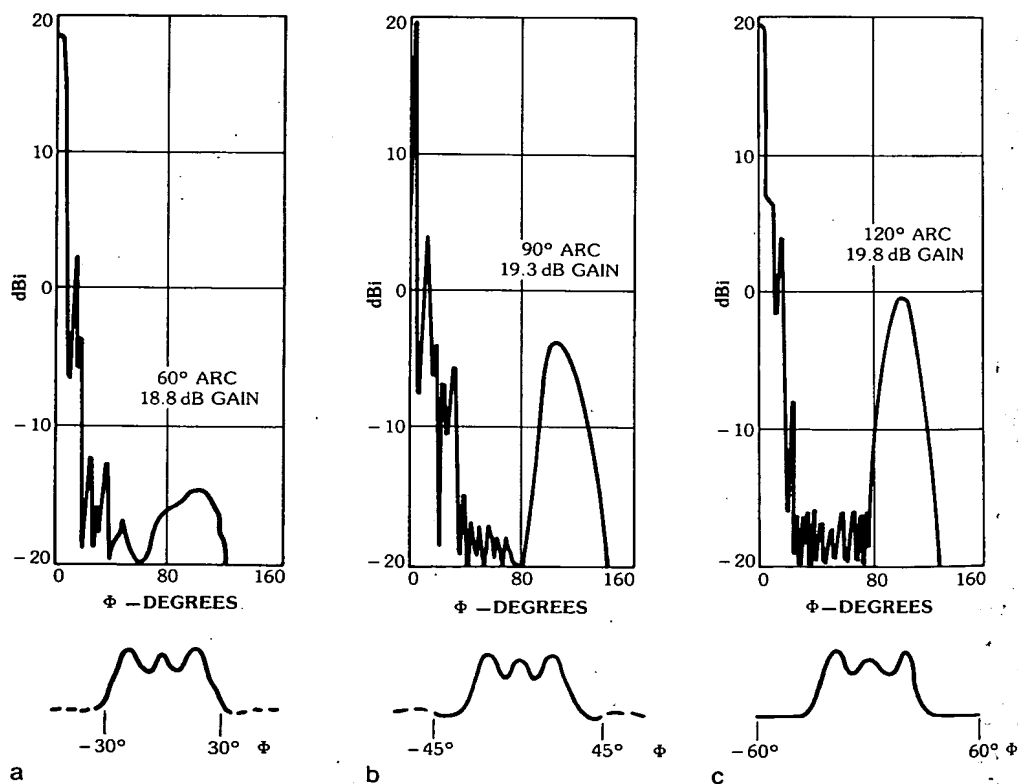
Fig. 27. Array gain (in dBi = dB relative to isotropic) and radiation patterns for 60°, 90°, and 120° arc arrays on a cylinder, where the lower curves show angular extent of element patterns used for given arc. (After.Sureau and Hessel [67], © 1972 Artech House)

In the case of an array with random phase and amplitude errors, and including randomly failed elements, the average side lobe level far from the beam peak is given by [69, 70]

$$\bar{\sigma}^2 = \frac{\bar{\varepsilon}^2}{P_e N \eta} = \frac{[(1 - P_e) + \bar{\Delta}^2 + P_e \bar{\delta}^2]}{P_e N \eta} \tag{70}$$

where

$\bar{\Delta}^2$ = the amplitude error variance normalized to unity

$\bar{\delta}^2$ = the phase error variance

$\bar{\varepsilon}^2$ = the error variance

P_e = the probability of survival for any element in the array

η = array efficiency

N = total number of elements

This equation gives the normalized side lobe level relative to the average array gain. The failed elements in the array are assumed to be randomly located, and the average value of the phase and amplitude errors is assumed to be zero. The side lobe level above should be considered the average of a number of antenna patterns, not the average level of any one antenna.

If the broadside, no-error gain of an array with elements $\lambda/2$ apart is $\pi P_e N \eta$, the side lobe level is given from (70) as

$$\bar{\sigma}^2 = \pi \bar{\varepsilon}^2 / G \tag{71}$$

in terms of the gain G and the error variance.

Peak side lobe levels are also given in the literature. A convenient result is obtained when the errors are sufficiently large compared to side lobes or null depths that structured minor-lobe radiation is negligible and the statistics of the field intensity pattern are described by a Rayleigh density function. In this case the probability $P(v > v_0)$ that a particular side lobe level $v_0{}^2$ is exceeded at any point is [70]

$$P(v > v_0) = e^{-v_0{}^2/\bar{\sigma}^2} \tag{72}$$

where $\bar{\sigma}^2$ is the average side lobe level of (70).

Starting with the expression above, valid at a particular point, Allen [69] derives the following rule of thumb for the error $\bar{\varepsilon}^2$ allowable for an array with gain G, in terms of the far side lobe level $1/R$, assuming 99-percent probability that all side lobes are below the given level

$$\bar{\varepsilon}^2 \leqq \frac{1}{10\pi} \frac{G}{R} \tag{73}$$

which results in an allowable phase error of about 10° when the side lobe level is numerically equal to the gain. This important relationship explains why it is not difficult to design arrays with side lobes at the isotropic level $(G = R)$, but to maintain side lobes of 20 dB below the isotropic level would require 1° phase error, an extremely difficult goal and one barely within the present state of the art.

In this expression, and in all equations given in this section, when the parameter N is the number of elements in the array, the side lobe levels are those distributed throughout all real space; but when the errors are correlated in one plane, as they would be for power divider or phase shifter errors in the plane of scan for an array of columns, then N is the number of columns, and the side lobe level given by these equations is in the principal scan plane.

For the case of an array of columns of $\lambda/4$-spaced elements the gain of a column is equal to $\sqrt{\pi}\eta N P_e$, and (70) becomes

$$\bar{\sigma}^2 = \frac{\sqrt{\pi}\,\bar{\varepsilon}^2}{G_1} \tag{74}$$

where G_1 is the column gain, $\bar{\varepsilon}^2$ is the error variance between columns, and $\bar{\sigma}^2$ the average side lobe level in the plane perpendicular to the columns. For a square array this reduces to

$$\bar{\sigma}^2 = \frac{\sqrt{\pi}\,\bar{\varepsilon}^2}{\sqrt{G}} \tag{75}$$

where now G is the total array gain.

Fig. 28 shows the average side lobe level, (71), for a square array with random phase shift errors, and a square array of columns (75) with errors completely
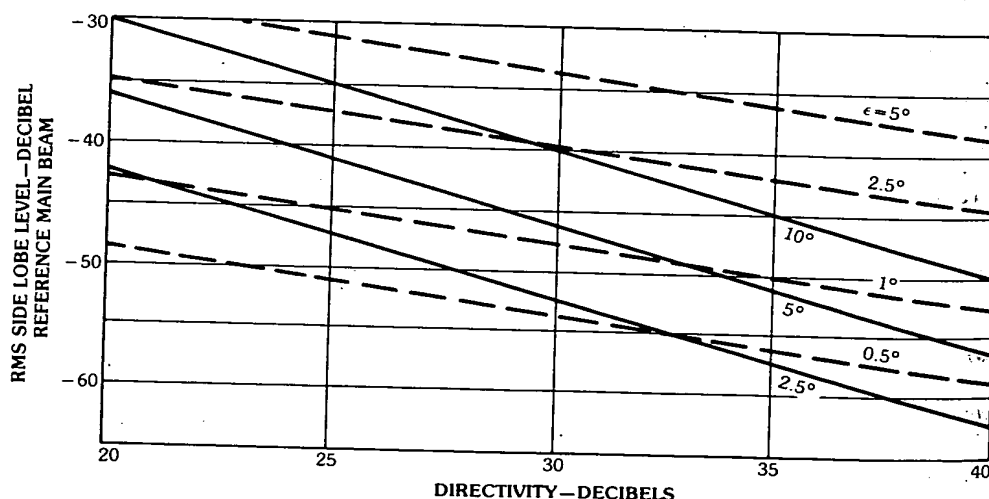

Fig. 28. Root-mean-square side lobe level versus directivity for square array with phase errors at elements (solid lines) or at columns (dashed lines, in plane of arrayed columns).

correlated in the plane of the columns, and the phase error between columns randomly distributed in the scan plane. This figure illustrates that extreme precision is required for arrays organized into columns when low principal-plane side lobes are required.

The reduction in directivity due to these errors is given by

$$\frac{D}{D_0} = \frac{P_e}{1 + \bar{\Delta}^2 + \bar{\delta}^2} \tag{76}$$

In the case of digitally controlled phase shifts, a p bit phase shifter has 2^p phase states separated by phase steps of $2\pi/(2^p)$. Miller [71] has analyzed the resulting peak and rms side lobe levels for this staircase approximation to the desired linear phase progression and has shown that the loss in array gain due to the triangular error distribution is

$$\Delta G = \frac{1}{3} \frac{\pi^2}{2^{2p}} \tag{77}$$

which is on the order of 0.23 for a 3-bit phase shifter and 0.06 for a 4-bit phase shifter. More significant are the average side lobe levels which, based on an average array loss of 2 dB to account for illumination taper and scan degradation, are

$$\text{rms side lobes} = \frac{5}{N \times 2^{2p}} \tag{78}$$

where N is the number of elements in the array. For a one-dimensionally scanned array, N is the number of phase controls, and the rms side lobe level above is measured in the plane of scan. The net result, as before, is to require extreme precision for unidimensional scanned arrays. Fig. 29 shows the side lobe level for various phase shifter bits p and N up to 10 000 elements. For -50-dB rms side lobes an array of 1000 elements requires 5-bit phase shifters, but an array of 10 000 elements can maintain 50-dB side lobes with only 3 phase bits.

Of greater significance to antenna design is that the phase errors have a periodic variation across the array and tend to collimate as individual side lobes, called *phase-quantization side lobes*, that are much larger than the rms levels. A detailed discussion of this phenomenon is given by Miller along with simple formulas for evaluating the resulting lobes. In the case of a perfectly triangular quantization error the quantization lobe level is $1/2^p$, which gives -30 dB for 5-bit phase shifters. Cheston and Frank [72] show that for discrete phase shifters the error is not triangular and that the maximum quantization lobe can be substantially larger.

One solution to the peak quantization lobe problem is to decorrelate the phase shifter errors. Decorrelation occurs naturally in space-fed arrays, where the phase shifters collimate the beam as well as steer it. In such arrays the phase error is distorted from the triangular shape and the quantization lobe is substantially reduced. Alternatively, in an array with in-phase power division one can introduce
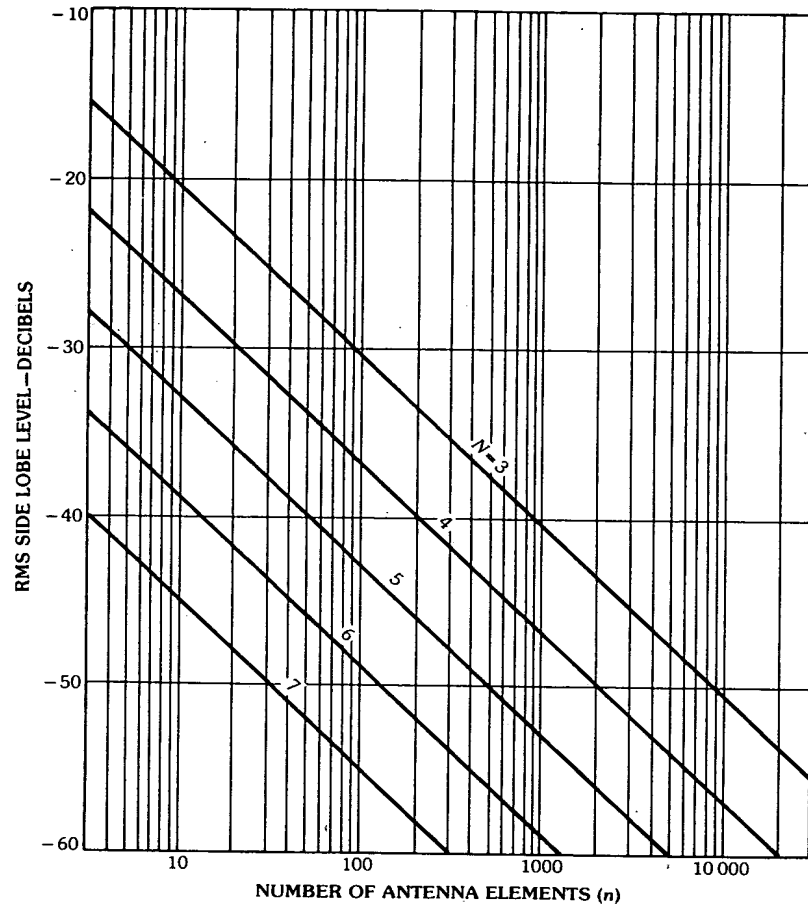
Fig. 29. Root-mean-square side lobes due to quantization, where N is the number of phase shifter bits. (*After Miller [71]*)

a phase error into each path and then program the phase shifter to remove the error in addition to steering the beam. Optimizing this error can reduce the peak side lobes very close to the rms side lobe level, but this is a consideration that must be carefully accounted for in the array design.

An entirely different solution to the quantization lobe problem is often achieved at the system level by recycling all the phase shifters between consecutive radar pulses or between transmit and receive. This process, called *beam dithering* [73], consists of adding a fixed phase shift to the phase command and recomputing phase shifts. The net result is to change all the phase states so that the quantization is made differently for each pulse (or between transmit and receive). If this procedure is compatible with other radar processing, one can use simple row-column steering but introduce randomness into the quantization steps to reduce the peak quantization lobes.

Array Elements

Array elements are usually some form of dipole or slot excited by a waveguide or other transmission line. Waveguide arrays, though heavy, tend to have low loss, good bandwidth, and relatively graceful scan degradation. They also have been the subject of numerous design studies, and so their behavior is well documented and predictable. Early examples of specific waveguide element designs are the studies of Wheeler [74, 75] in which matching networks were derived using waveguide transmission circuits like that shown in Fig. 30 consisting of dielectric slabs mounted in and above the waveguide. McGill and Wheeler [76] introduced the use of a dielectric sheet, often called a WAIM (wide-angle impedance-matching) sheet, to produce a susceptance variation with scan angle that partially cancels the scan mismatch of the array face. A significant development in impedance matching of waveguide arrays is the synthesis of double-tuned response characteristics achieved using dielectric loading and a cutoff waveguide section [77]. Fig. 31 shows a loaded rectangular waveguide (phase shifter), a transformer to circular guide, two dielectric disks, and an unloaded section of guide that is below cutoff at the operating frequencies.
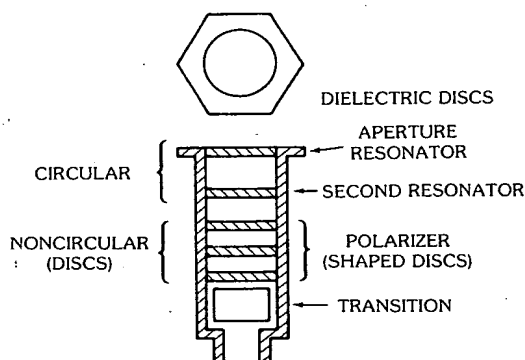

Fig. 30. Circular element for triangular grid array. (*After Wheeler [74, 75],* © *1968 IEEE*)
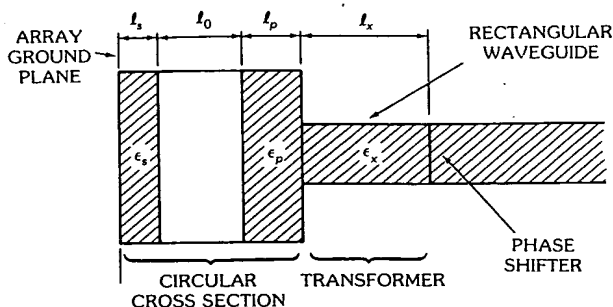
Fig. 31. Doubly tuned waveguide array element. (*After Lewis, Kaplan, and Hanfling [77],* © *1974 IEEE*)

Dipole arrays have also received substantial attention and have generally graceful scan properties when properly designed. Fig. 32 shows several common varieties of stripline printed dipoles. One design, attributable to Wilkinson [78], uses metallization on two sides of a microstrip line to produce a complete dipole fed by a two-wire line in the plane of the dipoles. This dipole and printed circuit distribution network is fabricated by two photographic exposures using a two-sided printed-circuit board, and so is an example of low-cost technology. The array was mounted a quarter wavelength above a ground plane and uniformally illuminated by a reactive power divider to form a pencil beam. Another convenient circuit for dipole design, shown in Fig. 32, is described in a report by Hanley and Perini [79] and is a printed-stripline folded dipole with a Schiffman balun. One major advantage of this element is that it is printed in a single process, all on one side of a circuit board and so is relatively inexpensive to produce.

Fig. 33 shows one means of exciting flush-mounted stripline slot antennas. Most often these elements are isolated from the rest of the stripline medium by the

a

b
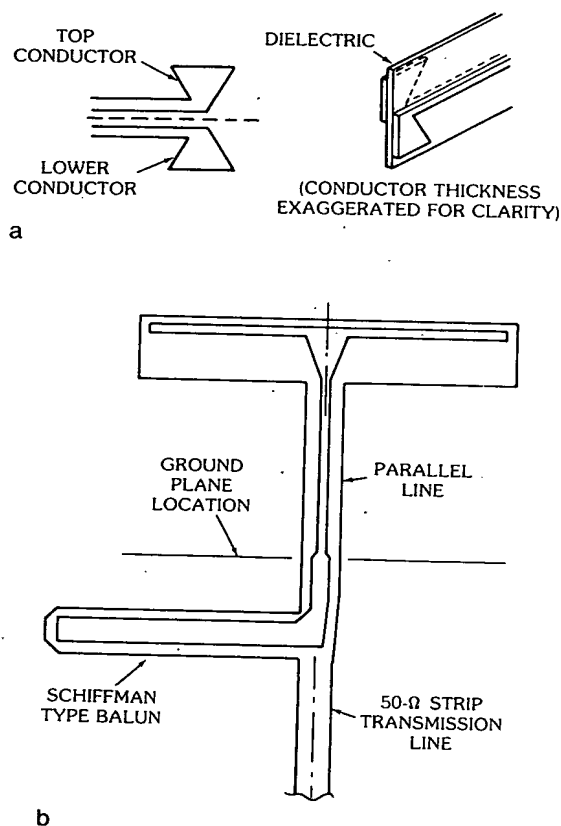
Fig. 32. Printed-circuit dipole configurations. (*a*) Conductors and dielectric. (*b*) Printed-stripline folded dipole and balun.
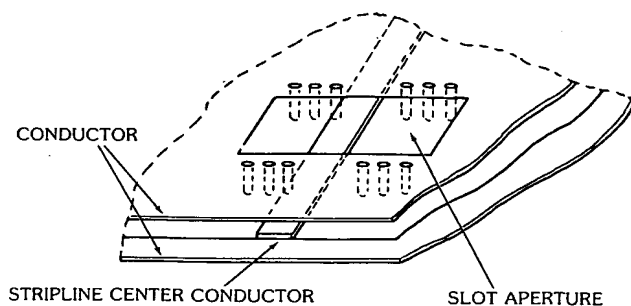
Fig. 33. Stripline slot radiator.

use of plated through holes or rivets that form a cavity as shown in the figure, which also serves to suppress higher-order modes.

Several very broadband elements have been described in the literature. Among these the broadest-band element is the flared-notch antenna (Fig. 34) studied by Lewis and others [61], which exhibits up to an octave band when used in an array, but needs careful design for any given array configuration because of the possibility of array blindness effects for critical frequencies and scan angles.

The microstrip patch element and its variations are inexpensive and light-weight, and have found increasing use in a variety of array applications. The basic path element (Fig. 35) is narrow-band, with percentage bandwidth given approximately by
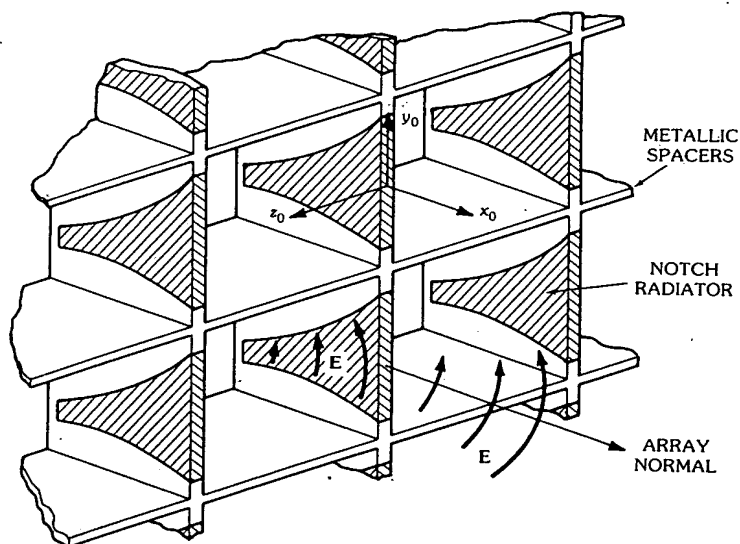
Fig. 34. Flared-notch array elements. (*After Lewis, Kaplan, and Hanfling [77], © 1974 IEEE*)
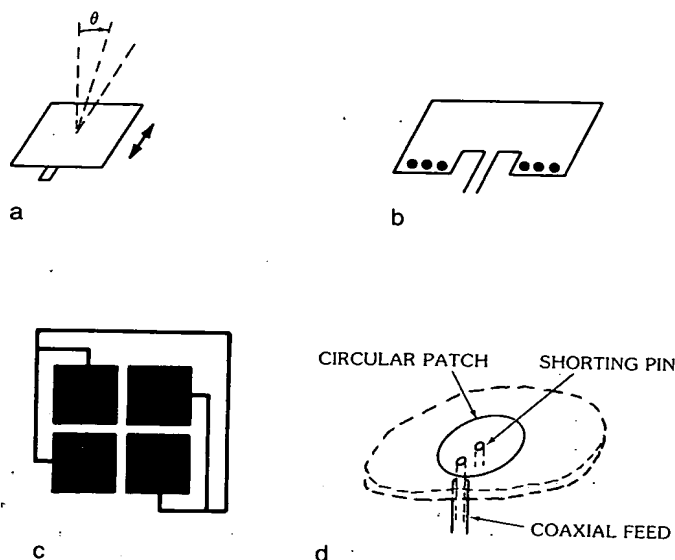
Fig. 35. Useful microstrip radiator types. (*a*) Patch antenna elements. (*b*) Shorted patch. (*c*) Crossed slot of four shorted patches. (*d*) Circular disk.

$$100\frac{\Delta f}{f_0} = 5tf_0 \qquad (79)$$

for a thickness *t* in centimeters for the air-loaded patch. A number of very creative microstrip elements have been developed. Fig. 35 shows a square patch design for radiating circular polarization, a shorted rectangular patch for producing a much wider element pattern in the scan plane, and a combination of shorted patches that radiates circular polarization and is the microstrip equivalent of crossed slot radiations [80]. Many other microstrip radiators have found practical application. Of these, the most significant is the circular disk radiator of Howell [81] (Fig. 35d), which can be excited by a microstrip line but which also is very suitably excited from below the ground plane, as shown in the figure. Still other transmission line media offer advantages for array use in a variety of applications.

Passive Components for Arrays: Polarizers and Power Dividers

The trends toward greater flexibility, more accurate pattern control, and lightweight, compact array structures are also having an impact on the type of components used in arrays. This section lists some of the passive components used to control radiated polarization and to provide power distribution networks for precise pattern synthesis.

Waveguide polarizers using a probe or obstacle to excite both polarizations and some variation of a quarter-wave plate to produce the requisite ±90° delay for circular polarization have long been used as phased array components.

Waveguide polarizers in current use include the tapered septum polarizer [82]

for converting linear to circular polarization, which operates over about a 2- to 5-percent bandwidth, and the stepped-septum polarizer of Chen and Tsandoulas, a three-port device that allows polarization agility over at least 20-percent bandwidth, with isolation greater than 26 dB [83].

Often it is less expensive to insert a polarizer in front of the whole array. The earliest polarizer of that type is the use of a grid of quarter-wave plates, but a much more popular recent solution that is compatible with wide-angle electronic scanning is the use of meander line polarizers following the work of Young's group [84].

Power divider networks for array feeds need to be extremely precise to synthesize low side lobe radiation patterns. Other requirements often impose extreme high-power specifications and still others demand very lightweight or compact construction practices. Waveguide and coaxial-line corporate feed networks are most often used for high-power arrays but the increasing ease and quality of stripline construction has made that the medium of choice for many new array developments. Often it is convenient to produce hybrid combinations of waveguide, coaxial line, and stripline to take advantage of inexpensive stripline network techniques for lower-power sections of the array while using waveguide or coaxial line at the high-power regions of the feed network.

Precise feed synthesis requires both equal and unequal power dividers. Among the various developments in stripline components the most commonly used are reactive tee power dividers, branch line couplers, and parallel coupled line and in-line power dividers. Although they are most simple and inexpensive to construct, reactive tee power divider networks have no isolated port and hence offer serious mismatch and isolation problems when used to feed mismatched elements. Reactive corporate-feed networks are therefore useful mainly for fixed beam arrays or for power division in the unscanned plane of arrays with one plane of scan. Single-section [85] branch line couplers occupy an area approximately $\lambda/4$ square and are most useful for coupling ranges from 3 to 9 dB. These couplers are easily fabricated using a conventional stripline by machining or etching the center conductor. Parallel coupled stripline power dividers for loose coupling (greater than 10 dB) can also be designed from conventional stripline using side coupled parallel lines, but tighter coupling requires the use of three-layer stripline for broadside coupled lines (3 to 6 dB coupling) or variable overlap couplers for intermediate values. Single-section parallel coupled power dividers are $\lambda/4$ long but occupy less area than branch line hybrids. Another likely choice for array feed networks is the Wilkinson [86] in-line power divider or its impedance-compensated derivative split-tee power dividers [87].

Single-section Wilkinson power dividers are $\lambda/4$ long for equal power division and $\lambda/2$ long for unequal power division. Split-tee power dividers have an extra stage of impedance matching and so are longer by approximately $\lambda/4$, although they have the advantage of wider bandwidth.

In either case the in-line power dividers have excellent broadband characteristics in comparison with branch and coupled line hybrids because the coupling ratio is determined by relative impedance ratios, not line length. Similarly, in-line hybrids are in-phase power dividers and so there is little phase error introduced with frequency change. The output ports of branch and coupled line hybrids have substantially different phases ($\pi/2$ for equal power division) and, although this can

be compensated at center frequency, networks of these hybrids tend to be very narrow band relative to in-line hybrids. Typical bandwidths for individual in-line hybrids can reach an octave. The selection of power division networks is critical to array design and the choice can vary substantially with the application.

Array Phase Control

A discussion of time-delay devices for arrays is omitted because the primary components used to date are switched transmission lines and are governed by the same critical components as phase shifters.

Phasing networks are most often implemented at the rf operating frequency because this is usually the most efficient process. Notable exceptions use phase shifters at intermediate frequencies and up-convert to rf with amplifiers to improve efficiency. In addition, many ingenious intermediate-frequency phase scanning systems have used harmonically derived phased shifts or frequency displaced signals across an array to produce time-varying beam positions. Systems of this type are described in the literature and their operation is beyond the scope of this chapter. In general, diode phase shifters dominate the frequency range below 2 GHz, and ferrites are usually selected above 5 GHz for high-power applications. Diode phase shifters are compact and very lightweight compared with ferrite devices and so are gaining popularity in lightweight array configurations through 40 GHz, often in combination with low-cost monolithic microstrip antenna circuits. The rapid development of solid-state amplifier modules for arrays also favors the use of diode phase shifters at all frequencies.

At present the most popular types of diode phase shifter designs for arrays are the hybrid coupled, switched-line, and loaded-line phase shifters using pin diodes. These three fundamental networks are shown in Fig. 36. Hybrid and loaded-line (transmission) phase shifters require two diodes per bit, and switched-line phase shifters require four per bit. Switched-line hybrids also have greater insertion loss and an undesirable phase dependence with frequency that usually makes them unsuitable for low side lobe array control. They do possess distinct advantages in weight and compactness, however, and have been used successfully in monolithic microstrip antennas for many years. Hybrid and transmission phase shifters have lower loss and better bandwidth performance. An S-band stripline hybrid phase shifter is reported by White [88] to have an average phase loss of only 3° over 20 percent bandwidth. This device had about 0.8 dB average loss from 3.0 to 3.5 GHz and was tested to high-power burnout at 4 kW peak with 0.1-ms pulses and 0.05 duty cycle. Insertion loss for X-band and K_u-band phase shifters was about 2 and 3 dB.

Broadband low–side-lobe array designs are possible using Schiffman phase shifters because this phase shifter produces a nearly constant phase shift over extremely wide frequency ranges. White gives data for a 90° bit over a frequency ratio of 2.27:1.

A precise low–side-lobe array developed by Tsandoulas [89] used six-bit diode phase shifters with phase tolerance limits of less than 0.0° rms for the 90° and 180° bits, 0.4° for 45°, 22.5°, and 11.25° bits, and 0.2° for the 5.625°. These remarkable results were achieved in a practical testbed array described in the reference.

Ferrite phase shifters have been built to operate up to 60 GHz and possess

a.

b $\Delta\phi = (2\pi/\lambda)(l_1-l_2)$

c $\Delta\phi \cong (B_1/Y_0) - (B_2/Y_0)$
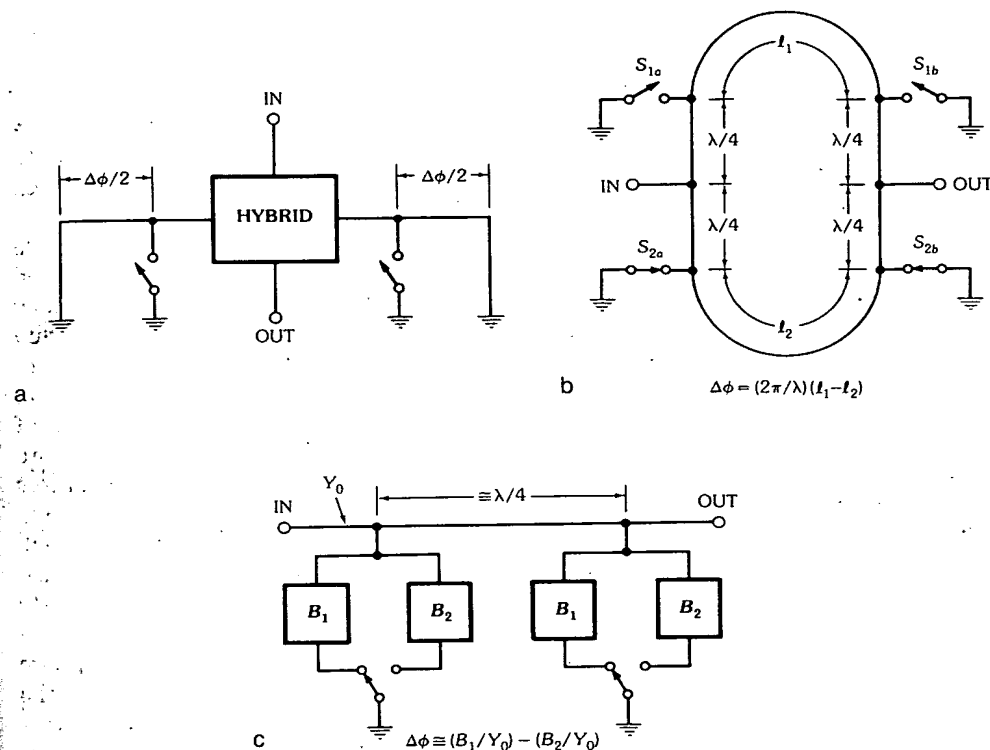
Fig. 36. Diode phase shifter circuits. (a) Hybrid coupled reflection phase shifter. (b) Switched-line phase shifter. (c) Loaded-line phase shifter.

excellent characteristics for many phased array applications. Several recent survey articles and an annotated bibliography [90, 91, 92] summarize progress in this field and list numerous references to devices and to the fundamental theory of ferrite phasor operation. Nonreciprocal ferrite phase shifters include early twin-slab designs (Fig. 37) that require a transverse-switched external magnetic field and the well-known toroid designs that use a longitudinal wire to drive the ferrite magnetization to saturation as in a latching phase shifter, or to various points on the magnetization curve with flux drive circuitry. Typical digital latching phase shifters
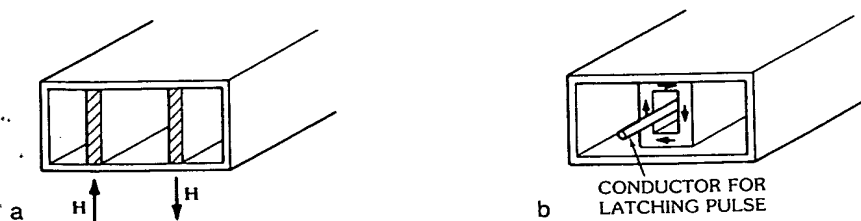
Fig. 37. Dual-slab and toroid ferrite phase shifters. (a) Dual-slab. (b) Toroid.

can have bandwidths in excess of 10 percent and insertion losses between 0.5 and 1 dB. Power levels supported by these devices can vary from 1 kW to as much as 150 kW peak with average power levels to 400 W. Latching phase shifters can be switched in about 1 μs and have become standard throughout the industry. Flux drive circuits with toroidal phase shifters are analog devices and not restricted to specific phase bits. Their major disadvantage is the need to reset them between transmit and receive functions for radar applications.

Among several varieties of reciprocal ferrite phase shifters the dual-mode phase shifters have replaced Reggia-Spencer phase shifters, which have been found to have low values of phase shift per wavelength. Dual-mode phasors are Faraday rotation devices in which a linearly polarized incident waveguide mode is converted to circularly polarized energy by a nonreciprocal ferrite quarter-wave plate, phase-shifted by Faraday rotation, and then converted back to linear polarization. A signal from the opposite direction is converted to circular polarization of the opposite sense, but since the directions of propagation and polarization are both opposite it incurs the same, reciprocal phase shift. Dual-mode phase shifters are very competitive with toroid phase shifters and have average power levels up to 1.5 kW at S-band and peak powers to 150 kW. Insertion loss can be 0.6 dB through X-band. Switching speed can be on the order of tens of microseconds for a latched design, depending on the application. The reference by Ince and Temme [90] compares specific phasor examples for S-band through K_a-band.

One other important reciprocal phase shifter is the analog rotary-field phase shifter of Boyd [93]. This phase shifter is based on the principle of the commercial rotary-vane phase shifters after Fox [94] and uses a ferrite rod of circular cross section fitted with a slotted stator in which are wound two sets of coils each generating a four-pole field. In comparison with the well-known rotating half-wave plate of the Fox phase shifter, the stator windings produce a rotating four-pole field distribution with the orientation of the principal axes proportional to the coil driving current values. The dc distribution in the ferrite serves to rotate a virtual half-wave plate that is converted to a phase shift just as is the mechanical half-wave plate rotation of the Fox phase shifter. This circuit has the disadvantages of requiring substantial drive power and having relatively long switching times (200 to 500 μs). Its advantages for many applications far outweigh these disadvantages because it has nearly dispersionless phase shift that can be maintained within a degree or two over substantial bandwidths, has insertion loss well under 1 dB, and can handle very high peak and average power levels. An S-band model operates at 90 kW peak, 3 kW average power, 0.5 dB insertion loss, and phase tracking within ±1.5° over about 9 percent bandwidth.

5. References

[1]   R. S. Elliott, "The theory of antenna arrays," in Chapter 1, in *Microwave Scanning Antennas*, vol. II, ed. by R. C. Hansen, New York: Academic Press, 1966, pp. 29–31.

[2]   C. T. Tai, "The optimum directivity of uniformly spaced broadside arrays of dipoles," *IEEE Trans. Antennas Propag.*, vol. AP-12, pp. 447–454, July 1964.

[3]   C. H. Walter, *Traveling-Wave Antennas*, New York: McGraw-Hill Book Co., 1965, pp. 121–122 and 322–325.

[4]   S. A. Schelkunoff, "A mathematical theory of linear arrays," *Bell Syst. Tech. J.*,

vol. 22, pp. 80–107, 1943.

[5] R. S. Elliott, "Design of line source antennas for sum patterns with side lobes of individually arbitrary heights," *IEEE Trans. Antennas Propag.*, vol. AP-24, pp. 76–83, June 1976.

[6] R. S. Elliott, "Design of line source antennas for difference patterns with side lobes of individually arbitrary heights," *IEEE Trans. Antennas Propag.*, vol. AP-24, pp. 310–316, June 1976.

[7] W. L. Stutzman and G. A. Thiele, *Antenna Theory and Design*, New York: John Wiley and Sons, 1966.

[8] P. M. Woodward, "A method of calculating the field over a plane aperture required to produce a given polar diagram," *J. IEE* (London), pt. IIIA, vol. 93, pp. 1554–1558, 1947.

[9] P. M. Woodward and J. P. Lawson, "The theoretical precision with which an arbitrary radiation pattern may be obtained from a source of finite size," *J. AIEE*, vol. 95, P1, pp. 362–370, September 1948.

[10] C. L. Dolph, "A current distribution for broadside arrays which optimizes the relationship between beamwidth and side lobe level," *Proc. IRE*, vol. 34, pp. 335–345, June 1946.

[11] H. J. Riblett, "Discussion of Dolph's paper," *Proc. IRE*, vol. 35, pp. 489–492, May 1947.

[12] D. Barbiere, "A method for calculating the current distribution of Tschebyscheff arrays," *Proc. IRE*, vol. 40, pp. 78–82, January 1952.

[13] R. J. Stegen, "Excitation coefficients and beamwidths of Tschebyscheff arrays," *Proc. IRE*, vol. 41, pp. 1671–1674, November 1953.

[14] L. B. Brown and G. A. Scharp, "Tschebyscheff antenna distribution, beamwidth, and gain tables," *NAVORD Rep. 4629 (NOLC Rep. 383)*, Naval Ordnance Lab., Corona, California, February 1958.

[15] C. J. Drane, Jr., "Useful approximations for the directivity and beamwidth of large scanning Dolph-Chebyshev arrays," *Proc. IEEE*, vol. 56, pp. 1779–1787, November 1968.

[16] T. T. Taylor, "Design of line source antennas for narrow beamwidth and low side lobes," *IEEE Trans. Antennas Propag.*, vol. AP-3, pp. 16–28, January 1955.

[17] R. C. Hansen, ed., *Microwave Scanning Antennas, Volume 1*, app. 1, New York: Academic Press, 1966.

[18] E. T. Bayliss, "Design of monopulse antenna difference patterns with low side lobes," *Bell Syst. Tech. J.*, vol. 47, pp. 623–640, 1968.

[19] R. S. Elliott, "Design of line source antennas for difference patterns with side lobes of individually arbitrary heights," *IEEE Trans. Antennas Propag.*, vol. AP-24, no. 3, pp. 310–316, May 1976.

[20] T. T. Taylor, "Design of circular apertures for narrow beamwidth and low side lobes," *IRE Trans. Antennas Propag.*, vol. AP-8, pp. 17–22, January 1960.

[21] F. I. Tseng and D. K. Cheng, "Optimum scannable planar arrays with an invariant side lobe level," *Proc. IEEE*, vol. 46, pp. 1771–1778, 1968.

[22] R. Tang, "Survey of time-delay beam-steering techniques," *Phased Array Antennas: Proceedings of the 1970 Phased Array Antenna Symposium*, Dedham: Artech House, pp. 254–260, 1972.

[23] V. Borgiotti, "An antenna for limited scan in one plane: design criteria and numerical simulation," *IEEE Trans. Antennas Propag.*, vol. AP-25, pp. 232–243, March 1977.

[24] R. L. Fante, "Systems study of overlapped subarrayed scanning antennas," *IEEE Trans. Antennas Propag.*, vol. AP-28, pp. 668–679, September 1980.

[25] P. D. Hrycak, "The theoretical and experimental investigation of a constrained-feed totally overlapped subarray antenna system," *IEEE 1982 AP-S Symp. Dig.*, pp. 695–698, May 24–28, 1982.

[26] R. J. Mailloux, "An overlapped subarray for limited scan application," *IEEE Trans. Antennas Propag.*, vol. AP-22, pp. 487–489, May 1974.

[27] E. C. Dufort, "Constrained feeds for limited scan arrays," *IEEE Trans. Antennas*

Propag., vol. AP-26, pp. 407–413, May 1978.

[28] W. Rotman and P. Franchi, "Cylindrical microwave lens antenna for wideband scanning application," *IEEE Intl. Symp. Dig.*, vol. AP-S, pp. 564–567, June 1980.

[29] J. H. Richmond, "Digital computer solutions of the rigorous equations for scattering problems," *Proc. IEEE*, vol. 53, pp. 796–804, August 1965.

[30] R. F. Harrington, *Field Computation by Moment Methods*, New York: Macmillan Co., 1968.

[31] R. W. P. King, *The Theory of Linear Antennas*, Cambridge: Harvard University Press, 1956, p. 79.

[32] G. H. Brown and R. King, "High-frequency models in antenna investigations," *Proc. IRE*, vol. 22, pp. 457–480, April 1934.

[33] P. S. Carter, "Circuit relations in radiating systems and applications to antenna problems," *Proc. IRE*, vol. 20, pp. 1004, 1041, June 1932.

[34] C. T. Tai, "Coupled antennas," *Proc. IRE*, vol. 36, pp. 487–500, April 1948.

[35] R. W. P. King, R. B. Mack, and S. S. Sandler, *Arrays of Cylindrical Dipoles*, London: Cambridge University Press, 1968, pp. 282–283.

[36] V. W. H. Chang and R. W. P. King, "Theoretical study of dipole arrays of N parallel elements," *Radio Sci.*, vol. 3 (New Series), no. 5, September–October 1968.

[37] N. Amitay, V. Galindo, and C. P. Wu, *Theory and Analysis of Phased Array Antennas*, New York: Wiley Interscience, 1972.

[38] R. J. Mailloux, "First-order solutions for mutual coupling between waveguides which propagate two orthogonal modes," *IEEE Trans. Antennas Propag.*, vol. AP-17, no. 6, pp. 740–746, November 1969.

[39] K. E. Golden et al., "Approximation techniques for the mutual admittance of slot antennas in metallic cones," *IEEE Trans. Antennas Propag.*, vol. AP-22, pp. 44, 48, 1979.

[40] H. Steyskal, "Analysis of circular waveguide arrays on cylinders," *IEEE Trans. Antennas Propag.*, vol. AP-25, pp. 610–616, 1977.

[41] C. P. Wu, "Analysis of finite parallel-plate waveguide arrays," *IEEE Trans. Antennas Propag.*, vol. AP-18, no. 3, pp. 328–334, May 1970.

[42] G. F. Farrell, Jr., and D. H. Kuhn, "Mutual coupling effects of triangular grid arrays by modal analysis," *IEEE Trans. Antennas Propag.*, vol. AP-14, pp. 652–654, September 1966.

[43] G. F. Farrell, Jr., and D. H. Kuhn, "Mutual coupling in infinite planar arrays of rectangular waveguide horns," *IEEE Trans. Antennas Propag.*, vol. AP-16, pp. 405–414, July 1968.

[44] J. C. Herper, C. J. Esposito, C. Rottenberg, and A. Hessel, "Surface resonances in a radome covered dipole array," *1977 IEEE AP-S Intl. Symp. Dig.*, pp. 198–201.

[45] G. H. Knittel, A. Hessel, and A. A. Oliner, "Element pattern nulls in phased arrays and their relation to guided waves," *Proc. IEEE*, vol. 56, no. 11, pp. 1822–1836, November 1968.

[46] V. W. H. Chang, "Infinite phased dipole array," *Proc. IEEE*, vol. 56, no. 11, pp. 1892–1900, November 1968.

[47] E. Mayer and A. Hessel, "Feed region modes in dipole phased arrays," *IEEE Trans. Antennas Propag.*, to be published.

[48] G. N. Tsandoulas and G. H. Knittel, "The analysis and design of dual-polarization square waveguide phased arrays," *IEEE Trans. Antennas Propag.*, vol. AP-21, pp. 796–808, November 1973.

[49] N. Amitay and V. Galindo, "The analysis of circular waveguide phased arrays," *Bell Syst. Tech. J.*, vol. 47, pp. 1903–1931, November 1968.

[50] M. H. Chen and G. N. Tsandoulas, "Bandwidth properties of quadruple ridge circular and square waveguide radiators," *IEEE AP-S Intl. Symp. Rec.*, pp. 391–394, June 1973.

[51] J. P. Montgomery, "Ridged waveguide phased array elements," *IEEE Trans. Antennas Propag.*, vol. AP-24, no. 1, pp. 46–53, January 1976.

[52] S. S. Wang and A. Hessell, "Aperture performance of a double-ridge rectangular

waveguide in a phased array," *IEEE Trans. Antennas Propag.*, vol. AP-26, pp. 204–214, March 1978.

[53] L. R. Lewis, A. Hessell, and G. H. Knittel, "Performance of a protruding-dielectric waveguide element in a phased array," *IEEE Trans. Antennas Propag.*, vol. AP-20, pp. 712–722, November 1972.

[54] R. J. Mailloux and H. Steyskal, "Analysis of a dual frequency array technique," *IEEE Trans. Antennas Propag.*, vol. AP-27, no. 2, pp. 130–134, March 1979.

[55] J. K. Hsiao, "Computer aided impedance matching of an interleaved waveguide phased array," *IEEE Trans. Antennas Propag.*, vol. AP-20, pp. 505–506, July 1972.

[56] V. Galindo and C. P. Wu, "Dielectric loaded and covered rectangular waveguide phased arrays," *Bell Syst. Tech. J.*, vol. 47, pp. 93–116, January 1978.

[57] S. W. Lee and W. R. Jones, "On the suppression of radiation nulls and broadband impedance matching of rectangular waveguide phased arrays," *IEEE Trans. Antennas Propag.*, vol. AP-19, pp. 41–51, May 1971.

[58] R. J. Mailloux, "Surface waves and anomalous wave radiation null phased arrays of TEM waveguides with fences," *IEEE Trans. Antennas Propag.*, vol. AP-20, pp. 160–166, January 1972.

[59] E. C. Dufort, "Design of corrugated plates for phased array matching," *IEEE Trans. Antennas Propag.*, vol. AP-16, pp. 37–46, January 1968.

[60] C. C. Chen, "Octave band waveguide radiators for wave-angle scan phased arrays," *IEEE AP-S Intl. Symp. Rec.*, pp. 376–377, June 1972.

[61] L. R. Lewis, M. Fassett, and J. Hunt, "A broadband stripline array element," *IEEE AP-S Intl. Symp. Dig.*, pp. 335–337, June 1974.

[62] W. H. Chang, "Infinite phased dipole array," *Proc. IEEE*, vol. 56, pp. 1892–1900, 1968.

[63] B. H. Pathak and R. G. Kouyoumjian, "An analysis of the radiation from apertures in curved surfaces by the geometrical theory of diffraction," *Proc. IEEE*, vol. 62, no. 11, pp. 1433–1447, November 1974.

[64] W. D. Burnside, R. J. Marhefka, and C. L. Yu, "Roll-plane analysis of on-aircraft antennas," *IEEE Trans. Antennas Propag.*, vol. AP-21, no. 6, pp. 780–786, November 1973.

[65] W. D. Burnside, M. C. Gilreath, R. J. Marhefka, and C. L. Yu, "A study of KC-135 aircraft antenna patterns," *IEEE Trans. Antennas Propag.*, vol. AP-23, no. 3, pp. 309–316, May 1975.

[66] B. H. Pathak, N. Wang, W. D. Burnside, and R. G. Kouyoumjian, "A uniform GTD solution for the radiation from sources on a convex surface," *IEEE Trans. Antennas Propag.*, vol. AP-29, pp. 609–622, July 1981.

[67] J. C. Sureau and A. S. Hessel, "Realized gain function for a cylindrical array of open-ended waveguides," *1970 Proc. Phased Array Antennas*, ed. by A. A. Oliner and G. H. Knittel, Dedham: Artech House, 1972, p. 283.

[68] J. C. Herper, C. Mandarino, R. Hessel, and B. Tomasic, "Performance of a dipole element in a cylindrical array—a modal approach," *IEEE AP-S Intl. Symp.*, pp. 162, 165, 1980.

[69] J. L. Allen, "The theory of array antennas," *Tech Rep. 323*, MIT Lincoln Labs, July 1963.

[70] R. E. Collin and F. J. Zucker, eds., *Antenna Theory*, New York: McGraw-Hill Book Co., 1969.

[71] C. J. Miller, "Minimizing the effects of phase quantization errors in an electronically scanned array," *Proc. 1964 Symp. on Electron. Scanned Array Tech. Appl.*, RADC TR-64-225, vol. 1, pp. 17–38, RADC, GAFB, NY.

[72] T. C. Cheston and J. Frank, *Radar Handbook*, Chapter 11, ed. by M. I. Skolnik, New York: McGraw-Hill Book Co., 1970, pp. 11–42.

[73] E. Brookner, ed., *Radar Technology*, Dedham: Artech House, 1977.

[74] H. A. Wheeler, "A systematic approach to the design of a radiator element for a phased array antenna," *Proc. IEEE*, vol. 56, pp. 1940–1951, November 1968.

[75] H. A. Wheeler, "A survey of the simulator techniques for designing a radiating

element," *Array Antennas: Proceedings of the 1970 Phased Array Antenna Symposium*, ed. by A. A. Oliner and G. H. Knittel, Dedham: Artech House, 1972.

[76] E. G. McGill and H. A. Wheeler, "Wide-angle impedance matching of a planar array antenna by a dielectric sheet," *IEEE Trans. Antennas Propag.*, vol. AP-14, no. 1, pp. 49–53, January 1966.

[77] L. R. Lewis, L. J. Kaplan, and J. L. D. Hanfling, "Synthesis of a waveguide phased array element," *IEEE Trans. Antennas Propag.*, vol. AP-22, no. 4, pp. 536–540, July 1974.

[78] W. C. Wilkinson, "A class of printed circuit antennas," *IEEE AP-S Intl. Symp. Dig.*, pp. 270–273, 1974.

[79] G. R. Hanley and H. R. Perini, "Column network study for a planar array used with an unattended radar," *RADC TR-80*, final report, RADC, GAFB, NY, March 1980.

[80] G. Sanford and L. Klein, "Increasing the beamwidth of a microstrip radiating element," *Intl. Symp. Dig. of Antennas Propag. Soc.*, Univ. of Washington, pp. 126–129, June 1979.

[81] J. Q. Howell, "Microstrip antennas," *IEEE Trans. Antennas Propag.*, vol. AP-23, pp. 90–93, January 1975.

[82] D. Davis, O. J. Digiandomenico, and J. A. Kempic, "A new type of circularly polarized antenna element," *IEEE G-AP Symp. Dig.*, pp. 2–23, 1967.

[83] M. H. Chen and G. N. Tsandoulas, "A wideband square waveguide array polarizer," *IEEE Trans. Antennas Propag.*, vol. AP-21, pp. 389–391, May 1973.

[84] L. Young, L. A. Robinson, and C. A. Hacking, "Meander line polarizer," *IEEE Trans. Antennas Propag.*, vol. AP-21, pp. 376–378, May 1973.

[85] H. Howe, *Stripline Circuit Design*, Dedham: Artech House, 1974.

[86] E. Wilkinson, "An *n*-way hybrid power divider," *IEEE Trans. Microwave Theory Tech.*, vol. MTT-8, no. 1, pp. 116–118, January 1960.

[87] L. I. Parad and R. L. Moynihan, "Split-tee power divider," *IEEE Trans. Microwave Theory Tech.*, vol. MTT-13, pp. 91–95, January 1965.

[88] J. F. White, *Semiconductor Control*, Dedham: Artech House, 1977.

[89] G. N. Tsandoulas, "Unidimensionally scanned phased arrays," *IEEE Trans. Antennas Propag.*, vol. AP-28, no. 1, pp. 86–98, January 1980.

[90] W. J. Ince and D. H. Temme, "Phasors and time-delay elements," *Advances in Microwaves*, vol. 4, pp. 2–183, New York: Academic Press, 1969.

[91] L. R. Whicker and C. W. Young, "The evolution of ferrite control components," *Microwave J.*, vol. 21, pp. 33–37, November 1978.

[92] L. R. Whicker and D. M. Bolle, "Annotated literature survey of microwave ferrite control components and materials for 1968–1974," *IEEE Trans. Microwave Theory Tech.*, vol. MTT-23, no. 11, pp. 908–918, November 1975.

[93] C. R. Boyd, "Analog rotary-field ferrite phase shifters," *Microwave J.*, vol. 20, pp. 41–43, December 1977.

[94] A. G. Fox, "An adjustable waveguide phase changer," *Proc. IRE*, vol. 35, pp. 1489–1498, December 1947.

Chapter 14

Aperiodic Arrays

Y. T. Lo
University of Illinois

CONTENTS

Yuen T. Lo is a professor and the director of the Electromagnetics Laboratory (formerly the Antenna Laboratory) in the Electrical and Computer Engineering Department, University of Illinois at Urbana-Champaign. He is a member of the National Academy of Engineering and a Fellow of IEEE, and a member of the International Union of Radio Science. He received the 1964 IEEE AP-S Bolljahn Memorial Award, the 1964 IEEE AP-S Best Paper Award, the 1979 IEEE AP-S Best Paper Award, the IEEE Centennial Medal, and the Halliburton Education Leadership award. He served as an AP-S AdCom member, the Chairman of the AP-S Education and Tutorial Papers Committee, and twice (1979–1982 and 1984–1987) as IEEE AP-S National Distinguished Lecturer. Dr. Lo is an honorary professor of the Northwest Telecommunication Engineering Institute and also the Northwestern Polytechnical University, both at Xian, China. He has published over a hundred technical articles in refereed journals covering a wide spectrum, from theoretical to experimental works. His works include large antenna arrays, radio telescopes, multiple-beam antennas, multiple scattering, antenna synthesis, antijamming antennas, antenna in plasmas, corrugated guides and horns, artificial dielectrics, and microstrip antennas. He designed the University of Illinois Radio Telescope, considered to be the world's largest antenna in the early 1960s.

1. Introduction

Arrays with uniformly spaced elements (often called *uniformly spaced arrays*) have been widely studied, mainly for two reasons: mathematical tractability in many cases and simplicity in fabrication. As discussed in Chapter 11, the pattern function of a uniformly spaced array, no matter how it is excited, is always periodic in the wave-vector k-space, or sometimes expressed in the so-called u-space. Thus a beam in the pattern function will repeat itself an infinite number of times. However, the visible region corresponds only to a finite region of this space. To ensure that only a single beam appears in the visible region (i.e., no grating lobes), adjacent element spacing must be kept sufficiently small, and as a result a large number of elements must be used to fill a given aperture, which is determined by the desired beamwidth and, sometimes, directivity also.

In contrast, arrays with incommensurable element spacings have aperiodic pattern functions, and are thus called *aperiodic arrays*. In general, they have no grating lobes, and, as a result, the required number of elements is not directly related to the grating lobe condition. Some nonuniformly spaced arrays, even with commensurable element spacings, may have very large periods in the pattern functions as compared with that of a uniformly spaced array and thus exhibit characteristics similar to those of aperiodic arrays. They may be regarded as pseudo-aperiodic arrays or, for all practical purposes, simply aperiodic arrays. This situation occurs actually in *all* practical arrays since all element spacings must be rounded up numerically to a finite number of the digits and are therefore divisible by a common unit.

Aperiodic arrays may be used in many different ways, but the most interesting applications are in array thinning, beamwidth narrowing, and element-interaction reduction. In regard to directivity it is shown in Chapter 11 that for element spacing greater than a half-wavelength the directivity for a uniform excitation is nearly maximum, approximately equal to the number of elements. This conclusion can also be deduced from the fact that, in general, the *mutual* radiation resistance becomes less significant in comparison with the self-radiation impedance. As an example, for half-wavelength dipoles, as the element spacing increases beyond a half-wavelength the total power radiated depends mainly on the self-radiation resistance and thus reaches approximately a constant value. From this point of view one can expect that the same conclusion can be drawn even for nonuniformly spaced arrays, as most element spacings, if not all, are greater than $\lambda/2$. On the other hand, if element spacings are allowed to assume any value, the result in Chapter 11 shows that maximum directivity can be reached when element spacings become vanishingly small. However, this is the so-called superdirectivity and cannot be realized in practice. From this argument one can therefore conclude that the optimization of element spacings for maximum directivity is a problem of little

14-3

practical significance. Thus in this chapter we shall direct our attention to other aspects of the array.

One of the interesting array synthesis problems is to find an optimum set of element spacings and excitations that would minimize the highest side lobe level in the entire visible region. Many attempts have been made, including some analytic methods (using the Poisson summation formula), numerical methods (using the quadrature approximation and the so-called dynamic programming), and statistical and probabilistic approaches [1–21]. It is shown [22] that none of these methods can yield a solution even close to the true optimum. The difficulty of this problem may be attributed to the fact that the side lobe level depends on the element spacings in a highly nonlinear manner, and that, in general, there is no known analytical method to determine the highest side lobe level, or the angular direction where the highest side lobe may occur, even with all element positions given. Except for small arrays a numerical search with a modern computer is considered impractical. The reason is that the highest side lobe position does not change *continuously* with the element positions; thus there is no simple way to keep track of the highest side lobe as the element position changes unless an entire three-dimensional pattern is computed. With this understanding it is not surprising to find that so far all the attempts are not successful. In the following we shall make a brief review of these works and finally focus our discussion on the probabilistic approach because, first, the theory is more complete, second, it has been supported by various experiments, and, last, it can provide a useful practical solution which, though not optimum in the ordinary sense, is optimum in some probabilistic sense (see below). It will be seen that the array so obtained can have a performance much superior to that of conventional arrays in many respects.

2. A Brief Review

Unz [1] used the Fourier-Bessel expansion to relate the pattern function to the element positions. As pointed out by various authors it is difficult to make use of this expansion to yield useful numerical results. King, Packard, and Thomas [2] computed the pattern functions of a few sample arrays with preassigned spacings. Their computed results reveal some interesting properties of nonuniformly spaced arrays. At about the same time, nonuniformly spaced arrays were studied at the University of Illinois in connection with the feed of a radio telescope [3]. In that paper a certain optimization procedure and the method of relating the element spacings to the excitation function were proposed and applied. Maffett [4] independently proposed the same method of relating the element position function to the excitation function. Andreason [5] suggested a procedure for using a computer to optimize the element positions such that the side lobe level in the visible region is minimized. This method has been independently applied by Lo [3], who also stated that, at best, the solution so obtained is only optimum locally. For large arrays this procedure becomes tedious and time consuming, if not completely impossible. In his article Andreason gave an interesting lower bound of the side lobe level of widely spaced arrays by using the fact that the directivity of these arrays is proportional to the number of elements.

Ishimaru [6], Yen and Chow [7], and Ishimaru and Chen [8], using the Poisson

summation formula, reduced the pattern function of a finite sum to an infinite sum. In general, this would make the computation more difficult; however, for small u, it is reasonable to assume that only the first term of the series is important. However, for large u or, equivalently, for very wide average element spacing, which, unfortunately, is the case of greater interest, other terms also become significant. Ishimaru and Chen in particular considered a spacing function of the type $x + (2A_1/\pi) \sin \pi x$ with $A_1 < \frac{1}{2}$, which is a perturbed uniform spacing, particularly when A_1 is small. As $A_1 = \frac{1}{2}$, this spacing function becomes identical with that considered earlier by Lo [3]. However, using this type of spacing function, Ishimaru expressed the pattern function in terms of the Anger function, and, for convenience, he and his associate compiled a table for this function [9]. In principle, for a general spacing function one may need to consider more terms of this type as indicated in their paper, but it is doubtful that the numerical convenience could be retained. Ishimaru and others claimed that the choice of a single term with $A_1 = \frac{1}{6}$ gave a pattern quite close to the optimum. As shown in [22], this is not so.

Skolnik, Nemhauser, and Sherman [11] realized that a straightforward search for an optimum set of element spacings, using a high-speed computer, is next to impossible, even for a moderately large array. As a result they proposed a systematical method using the so-called dynamic programming technique. Unfortunately, this method does not lead to a truly optimal solution since, as noted by the authors, the "principle of optimality" (which is essential in the successful use of the dynamic programming) does not apply to this problem [11]. In particular, the assumption that the optimal position of the first element depends *only* on the position of the second elements or in general that the $(n - 1)$st element depends on the nth element is not valid for large arrays.

In addition, it is perhaps proper to cite the works of Harrington [14] and Baklanov, Pokrovshi, and Surdotovich [15], whose investigations are not concerned with reducing the number of elements but rather with achieving certain pattern characteristics by spacing weighting. Baklanov, Pokrovshi, and Surdotovich, in particular, used some complicated numerical techniques in an attempt to derive a spacing-weighted array from the Dolph-Chebyshev counterpart. From a practical point of view this may appear to have some advantage since it is much easier to achieve spacing weighting than excitation weighting. In doing so, however, some element spacings have to be smaller than usual, and the strong coupling effects between elements may offset this apparent advantage appreciably. Furthermore, the method seems to be too cumbersome to be applicable to large arrays.

Finally, we may mention the probabilistic and statistical approaches to this problem. Rabinowitz and Kolar [16] analyzed the case that the placement of elements over a uniform grid system in an aperture is determined by the outcome of a random experiment. They obtained only the *mean* side lobe level which, for the example studied in their paper, is about 7 dB lower than what was computed actually. Later, Skolnik, Sherman, and Ogg [17] considered the same problem and made a very similar analysis. They too obtained only the mean side lobe level; likewise, their examples showed that the predicted level is about 7 to 8 dB lower than the actually computed result in what they called "principal" planes.

Maher and Cheng [18] studied the problem of random removal of elements in a uniformly spaced array. Their assumption that the removals of elements are statistically independent events may result in the removal of the same element many times.

Starting with the probability distribution function of the elements in the aperture, Lo [12] obtained the distribution function of the antenna response at each observation angle, the half-power beamwidth, and the directivity, etc. He also obtained an approximate distribution of the side lobe level in any range of u. Later, these results have been verified by using the Monte Carlo simulation [13] and actual holey plate experiment [23]. Later Agrawal and Lo [24] refined the analysis, extended the theory for small arrays, and included the effect of element interactions. Clearly this method does not lead to an optimum design in the true sense.

The confusion of various theories finally prompted Lo and Lee [22] to conduct a comparison study with a few small arrays. They found that none of the theories yields the optimum solution; in fact, most are far from it. Similar to the so-called space-tapered arrays, some of these designs can control near-in side lobes only to some extent, and the far-out side lobe level not at all.

3. Spaced-Tapered Arrays

A spaced-tapered array is one in which the interelement spacing varies in some fashion across the array, usually increasing from the center to the edge of an array. This method is motivated by an attempt to remove the following two disadvantages of a conventional uniformly spaced array [3]:

(1) *Inefficiency*, in the sense that, in most low side lobe level designs, a large number of elements in the outer portion of the array serves only the purpose to cancel partially the high side lobes produced by the central portion of the array but contributes very little to the radiated power.

(2) *Feeding difficulty*, in that the design may require the element excitation power to be level over a range of several orders of magnitude.

As discussed in Chapter 11 a discrete array could be regarded as a sampling of an aperture antenna with "continuous" illumination functions. When the sampling is uniform one obtains a uniformly spaced array with element excitation weighted according to the illumination function. If the sampling interval is small enough, one expects a close similarity between the pattern functions of the discrete and the continuous array, such as $\sin(N\psi/2)/\sin(\psi/2)$ for the former against $\sin(L\psi/2)/(\psi/2)$ for the latter in the case of a uniform excitation with aperture length $L = Nd/\lambda$. On the other hand, if the sampling is made such that each interval contains the same amount of excitation power, one obtains a space-tapered array with all elements excited equally in power as illustrated in Fig. 1.

Design Procedure for a Symmetrical Space-Tapered Array

(a) Choose a proper illumination function $f(x)$ (see comments below).

(b) Define and compute
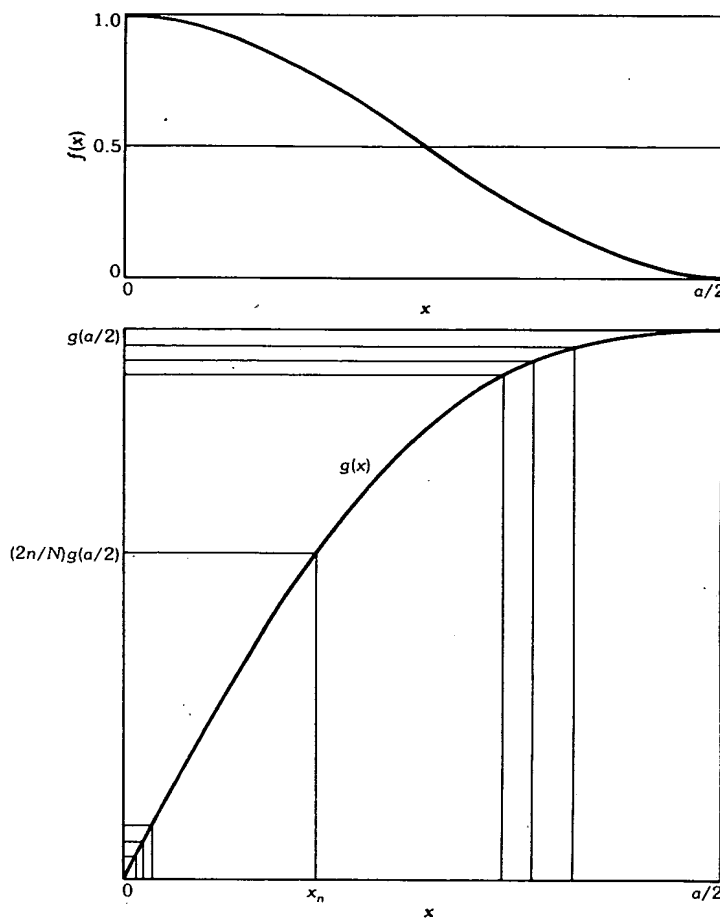
$$g(x) = \int_{-a/2}^{x} f(x)\, dx \tag{1}$$

Fig. 1. A graphical method for determining element location of a space-tapered array.

where a = aperture dimension in wavelengths.

(c) Let N be the number of elements, which is approximately equal to the array directivity.

(d) Solve for x_n, the nth element location, in

$$g(x_n) = \frac{2g(a/2)}{N} n, \qquad n = 1, 2, \ldots, N/2 \tag{2}$$

which could easily be solved graphically as illustrated in Fig. 1.

Advantages—Usually a smaller number of elements are needed and all elements excited *equally*.

Disadvantages—With the exception of the region near the main beam, the array pattern may differ greatly from that of the corresponding aperture antenna; usually the side lobe level increases with observation angle.

Comments—The design is useful if only a low near-in side lobe is desired, or directive elements are used.

The set of element positions obtained above can be used as a starting set for an iteration procedure in which the element positions are moved one at a time in a direction where the side level is decreasing. Of course, the final set so determined is at best an optimum locally [3].

The extension of this method to two- or even three-dimensional arrays is obvious, since it needs only to divide the illumination function in equal power per area or volume where an element will be placed.

4. Probabilistic Approach

Since the pattern function is an analytic function it is theoretically impossible to have contributions from all elements completely canceled for all observation angles except for a single direction in which the main beam maximum is intended. Therefore all patterns (except for the trivial case of a very wide beam) have side lobes. Consequently the best design one could hope for in many applications would be one having all side lobes equal in level. When a large number of elements is used the uniformly spaced Chebyshev-Dolph array has already provided the solution. But for economic reasons one may ask whether or not a similar performance could be achieved with substantially fewer elements. As discussed in the review section, so far all attempts have failed. In view of this fact it is natural to resort to a probabilistic approach so that contributions from all elements would be as incoherent as possible for all observation angles except in the main beam maximum direction where all contributions should be completely coherent. This can be achieved by using random element positions (or spacings, but with progressive phase excitation in case of scan). It will be seen later that, in so doing, the probability for the pattern to exceed a certain level at any observation angle outside the main beam region can be made the same as at any other angle. In the language of information theory this is a state of maximum entropy. It is only in this sense that the probabilistic design is optimum; in other words, all side lobes are equal in a probability sense. Therefore this design is, in a sense, a probabilistic approach to the Chebyshev-Dolph array.

For simplicity consider first a linear array, while the extension to the planar array is straightforward as will be shown later. In the following, all length dimensions are understood to be measured in wavelength λ. Let $g(X)$ = probability density function for placing an element at X, with $|X| \leq a/2$ and

$$\int_{-a/2}^{a/2} g(X)\, dX = 1 \tag{3}$$

If there are N equally excited elements each of which is to be placed within the array aperture $(-a/2, a/2)$ according to the same probability function $g(X)$ but independently of each other, then for each set of random samples $\{X\}$: $(X_1, X_2, \ldots, X_N)$ there is associated a sample pattern function

$$F(u) = \frac{1}{N}\sum_{n=1}^{N} \exp[j2\pi(\sin\theta - \sin\alpha)\,X_n] = \frac{1}{N}\sum_{n=1}^{N}\exp(jux_n) \qquad (4)$$

where the last expression is a normalized pattern function with

θ = any observation angle

α = main beam angle

$x_n = 2X_n/a$ = normalized element position

$u = a\pi(\sin\theta - \sin\alpha)$

As a result of the normalization in X, the aperture becomes $(-1, 1)$ and (3) can be rewritten as

$$g(x) \equiv 0 \quad \text{for } |x| > 1$$
$$\int_{-1}^{1} g(x)\,dx = 1 \qquad (5)$$

The ensemble of all sample sets $\{x\}$ constitutes a corresponding ensemble of $\{F(u)\}$. Our objective is to study the probabilistic properties of $F(u)$, in particular, those related to the array performance. For later discussion it is noted that the array dimension a appears *only* in the parameter u. Thus the pattern of an array with any value a can be obtained simply from that of a normalized array. In other words, if a is increased by a factor of, say, two, one needs only to extend the computation of $F(u)$ for twice the range of u while $F(u)$ in the first half range remains the same except that the scale of u changes by a factor of two. This scaling is not important if one is only interested in the highest side lobe level in the visible region.

Theoretical Results

Let $E\{\cdot\}$ be a probability average operator. A few important results are summarized below:

(a) The mean of $F(u)$ is

$$\phi(u) \equiv E\{F(u)\} = \int_{-\infty}^{\infty} g(x)\,e^{jux}\,dx \qquad (6)$$

which is simply the Fourier transform of $g(x)$, or in probability theory the characteristic function of the random variable x, or in antenna theory the pattern function of a "continuous" aperture antenna with illumination function $g(x)$. This implies that by choosing a proper $g(x)$, at least the mean pattern $\phi(u)$ can behave in some desired manner. It may also be noted that since $g(x)$ is an aperture-limited function, $\phi(u)$ is analytic.

(b) For *any given* u, the joined probability density function of the real and imaginary parts of $F(u)$, namely $F_1(u)$ and $F_2(u)$, is asymptotically normal:

$$f(F_1, F_2) = \frac{1}{2\pi\sigma_1\sigma_2}\exp\left\{-\left[\frac{1}{2}\frac{(F_1 - \phi)^2}{\sigma_1^2} + \frac{F_2^2}{\sigma_2^2}\right]\right\} \tag{7}$$

where the independent variable u has been suppressed, and $g(x)$, for simplicity, is assumed to be even, implying

$$\mathrm{Im}\{\phi(u)\} = 0$$
$$\sigma_1^2(u) = \text{variance of } F_1(u) = E\{[F_1(u) - \phi(u)]^2\}$$
$$= \frac{1}{2N}[1 + \phi(2u)] - \frac{1}{N}\phi^2(u) \tag{8}$$
$$\sigma_2^2(u) = \text{variance of } F_2(u) = E\{F_2^2(u)\}$$
$$= \frac{1}{2N}[1 - \phi(2u)] \tag{9}$$

(c) Let $\mathrm{Pr}\{\cdot\}$ be the probability measure for the event in the curly braces; then

$$\mathrm{Pr}\{|F(u)| < r\} = \iint_{(F_1^2 + F_2^2) < r^2} f(F_1, F_2)\, dF_1 dF_2 \tag{10}$$

which is a generalized noncentral chi-square distribution with two degrees of freedom. Tables of percentiles in r for various values of the parameters are available [25]. When r is large compared with σ_1 and σ_2, an asymptotic solution is given by

$$\mathrm{Pr}\{|F| < r\} = \frac{1}{2}\mathrm{erf}(sr)[\mathrm{erf}(r + m) + \mathrm{erf}(r - m)]$$
$$- \frac{1}{4\sqrt{\pi}s^2 r}\exp\left(-\delta^2\left\{1 + \frac{3\delta}{4s^2 r} + \left[\frac{3}{8s^2} + \frac{15(2\delta^2 - 1)}{48s^4}\right]\frac{1}{r^2}\right.\right.$$
$$\left.\left. + 0(s^{-4}r^{-3}) + 0[\sqrt{skr}\exp(-s^2 k^2 r^2)]\right\}\right) \tag{11}$$

where $m = \phi/\sigma_1$, $s = \sigma_1/\sigma_2$, $\delta = r - m$, and $0 < k < 1$.

For the special case when $\sigma_1 = \sigma_2$ (i.e., $s = 1$) which occurs for u outside the main beam region, the above expansion reduces to that given by Rice [26], who utilized the asymptotic expansion of the Bessel function in his derivation. For large $|u|$, $\phi(u) \cong 0$, and the distribution becomes simply Rayleigh. For the general case, however, it can approximately be computed by a method due to Patnaik [27] which approximates a noncentral chi-square distribution by a central one with different degrees of freedom. The latter can then be read from an incomplete gamma function table prepared by Pearson [28], which is shown as $I(v,p)$ in Fig. 2 with

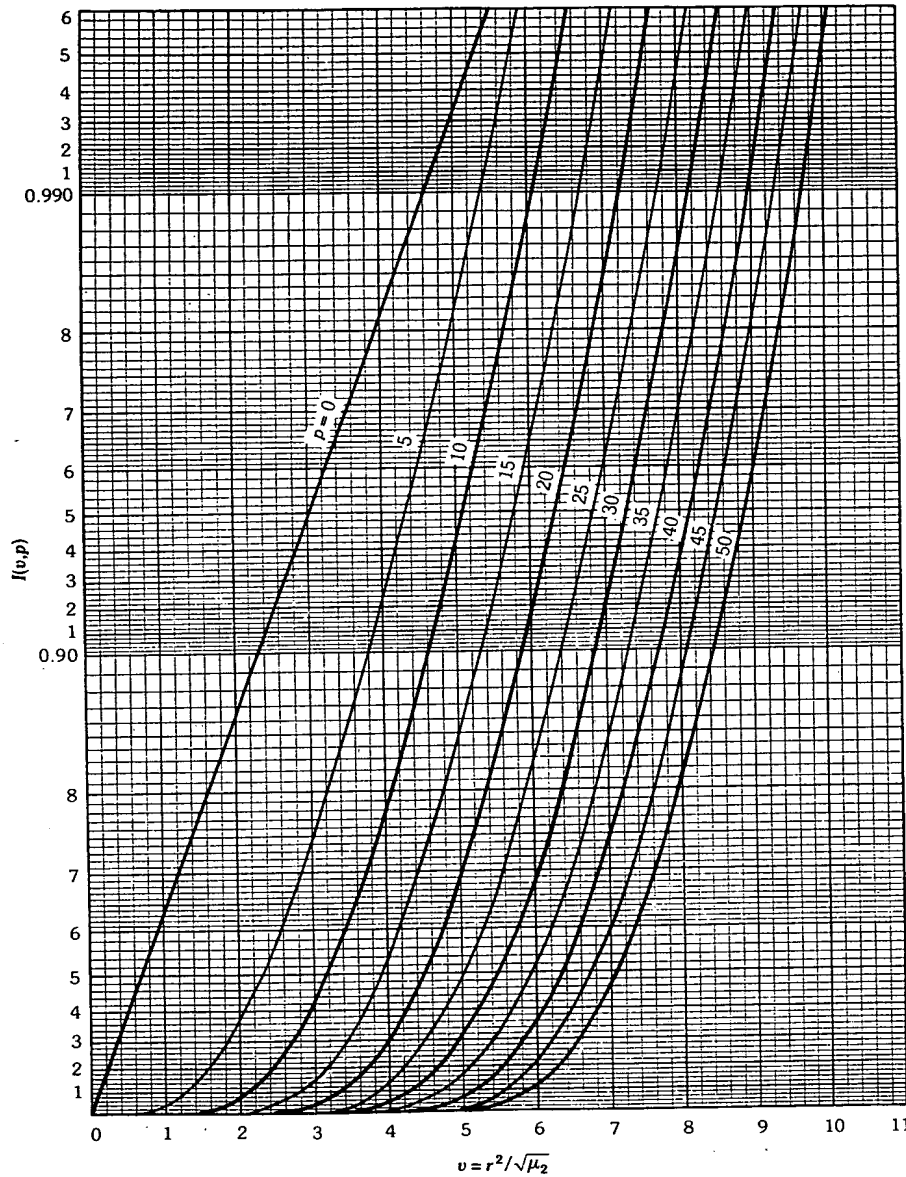$$\mathrm{Pr}\{|F| < r\} \cong I(v,p) \tag{12}$$

where

Fig. 2. Incomplete gamma function approximation for noncentral chi-square distribution. The curve for $p = 0$ is the Gausian distribution. (*After Lo [13],* © *1964 by the American Geophysical Union*)

$$v = r^2/\sqrt{\mu_2}$$

$$p = \mu_1^2/\mu_2 - 1$$

$$\mu_1 = \sigma_1^2 + \sigma_2^2 + \phi^2$$

$$\mu_2 = 2(\sigma_1^4 + \sigma_2^4 + 2\phi^2\sigma_1^2)$$

In general, except for u in the main beam region, $\sigma_1^2 \cong \sigma_2^2 \cong 1/2N$, $\phi \cong 0$ and $p \cong 0$, and therefore the distribution becomes simply Rayleigh $I(Nr^2, 0)$ in Fig. 2 and independent of u. This implies that, although the pattern behavior in the main beam region is determined by $g(x)$, outside the main beam region it is determined *only* by N, the number of elements. Unless the near-in side lobe level is of interest it is advantageous to use the uniform density function for $g(x)$ so that a narrow beam is obtained.

As an example, consider

$$g(x) = \begin{cases} \cos^2(\pi x/2) & \text{for } |x| \leq 1 \\ 0 & \text{for } |x| > 1 \end{cases}$$

Fig. 3 shows the mean pattern $\phi(u)$ and variances $\sigma_1^2(u)$ and $\sigma_2^2(u)$ for each value of u/π. It is seen that in the neighborhood of main beam maximum the variances are nearly zero, indicating that in this region the beam is almost deterministic. Outside the main beam the variances quickly reach a constant value $1/2N$. Figs. 4 through 6 show the level curve as well as the mean pattern $|\phi(u)|$ for comparison, for $N = 10^2$, 10^4, and 10^5, respectively. A *p-percent* level curve is a plot of r_p
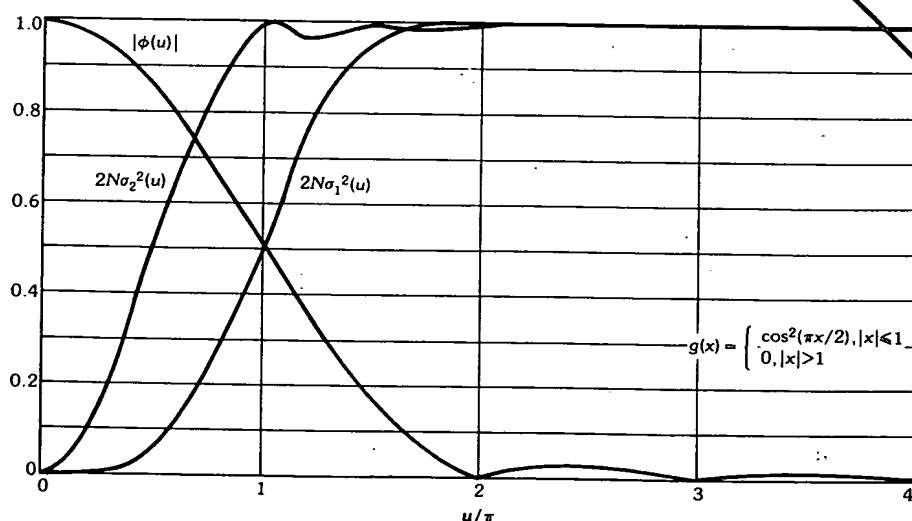

Fig. 3. The mean $\phi(u)$ and variances σ_1^2 and σ_2^2 of the real and imaginary parts of the random pattern function $|F(u)|$ as functions of u, for a cosine-square probability density function and uniform excitation. (*After Lo [12]*, © *1964 IEEE*)

Fig. 4. Level curves of $|F(u)|$ for cumulative probability equal to 99 percent, 80 percent, and 50 percent with a cosine-square probability density function and uniform excitation, for $N = 10^2$. (*After Lo [12], © 1964 IEEE*)
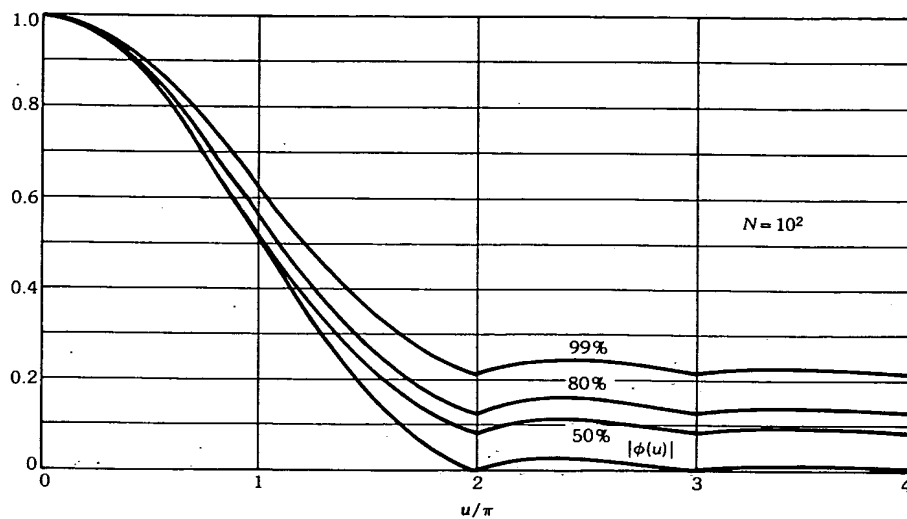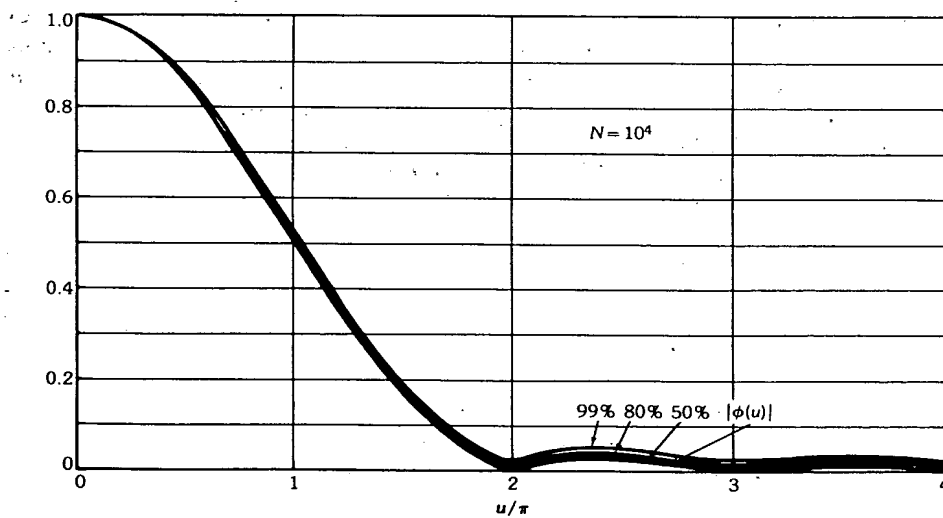

Fig. 5. Level curves of $|F(u)|$ for cumulative probability equal to 99 percent, 80 percent, and 50 percent with a cosine-square probability density function and uniform excitation, for $N = 10^4$. (*After Lo [12], © 1964 IEEE*)
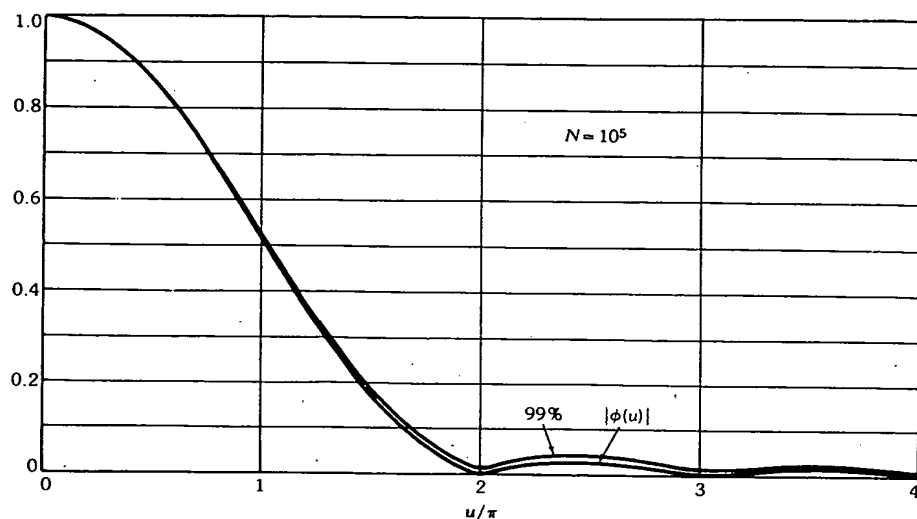
Fig. 6. Level curves of $|F(u)|$ for cumulative probability equal to 99 percent with a cosine-square probability density function and uniform excitation, for $N = 10^5$. (*After Lo [12]*, © *1964 IEEE*)

versus u with $\Pr\{|F(u)| < r_p\} = p$ percent. For $N \geq 10^4$, $|F(u)|$ is almost equal to $|\phi(u)|$ with 99 percent probability. But it should be emphasized that these curves are meaningful only for *each* value of u. In other words, the probability of obtaining the *entire* 99 percent level curve for all us in an interval is *not* 99 percent. In general, however, one is not interested in the exact pattern but rather the highest side lobe level. This is discussed next.

(*d*) The probability for a side lobe level less than r for $g(x) = 1/2$, $|x| < 1$, and u in the entire visible region (including the largest scan range) is

$$\Pr\{|F(u)| < r, |u| \in (u_f, 2\pi)\} \cong [1 - \exp(-Nr^2)]$$
$$\times \exp\{[-4\pi \sqrt{N} r \exp(-Nr^2)]$$
$$\times (a^2/12\pi)^{1/2}\} \tag{13}$$

where u_f is the first null (or the main beam null) of $\phi(u)$. Computer simulations [24] have shown that this formula gives accurate results even for an array with as few as eleven elements over an aperture of 5λ to 10λ. For large numbers of elements the formula assumes a simpler form:

$$\Pr\{|F(u)| < r, |u| \in (u_f, 2\pi)\} \cong [1 - 10^{-0.4343Nr^2}]^{[4a]} \tag{14}$$

where [4a] is the integer part of $4a$. This formula shows that the probability for achieving a certain side lobe level r is nearly zero as N is below a certain value and increases sharply as N increases to a certain critical value. After that the probability increases very slowly. Thus to ensure a good probability of success a sufficient

number of elements must be used for a desired side lobe level. For a 90 percent probability the required number N is plotted in Fig. 7 versus side lobe level in both ratio and decibel scale for various aperture dimensions $a = 10^q \lambda$. In this figure the graphs to the left of the dash-dot line are less accurate; here (13) should be used. It is of interest to see that for a 25-dB side lobe level the array needs about 4700 elements over $10^5 \lambda$ aperture with a half-power beamwidth of about 0.0005°, or $(5 \times 10^{-4})°$, and average element spacing of 20λ. If these same elements (4700) are spread over an aperture ten times larger, i.e., $10^6 \lambda$, the side lobe level increases only by about 0.5 dB but the beamwidth will be reduced by a factor of 10, i.e., to 0.000 05°, or $(5 \times 10^{-5})°$. Now the average element spacing becomes 200λ, and for this spacing an ordinary equally spaced array would have hundreds of grating lobes. Thus it is not necessary to use a large number of elements in order to achieve a narrow beam. In the case of a planar array the saving in the number of elements is even more dramatic. However, as will be seen later, this does not imply that the directivity can be increased in this manner. The common notion of associating a narrow beamwidth with high directivity is not always correct.

(e) The random variable u_0 defined by the smallest positive root of the following equation determines the half-power beamwidth $2\theta_0$:

$$|F(u_0)| = 1/\sqrt{2} \qquad (15)$$

where $F(u)$ is the random pattern function given by (4) and $u_0 = \pi a(\sin \theta_0 - \sin \alpha)$. Even for the deterministic problem the solution u_0 to the above problem cannot be obtained analytically. Since in practice one is interested only in large arrays with narrow beams an approximate distribution for u_0 can be found from the joint probability of $F(u)$ and $dF(u)/du$ for u in the neighborhood of the mean pattern half-power value u_1, i.e., $|\phi(u_1)| = 1/\sqrt{2}$. Details can be found in Lo [12]. For example, when $g(x) = \cos^2(\pi x/2)$ and $N = 10^4$ the half-power angle θ_0 will fall in $0.7244/a < \sin \theta_0 - \sin \alpha < 0.7377/a$ with 90 percent probability, where α is the scan angle. This implies that the half-power beamwidth deviates from its mean no more than ± 0.91 percent with 90 percent probability; in other words, it is almost certain in practice that the half-power beamwidth is equal to that of the mean pattern. This conclusion is generally true for most functions $g(x)$ of interest and, in fact, verified by Monte Carlo simulations and holey plate experiments to be discussed later.

(f) Since the element locations are drawn from a collection of random numbers, for each sample set of these numbers there is associated a sample radiation pattern and thus a sample directivity. It is of interest to know how the directivity is distributed probabilistically for all possible sets of the element arrangement. Using the Karhunen and Loeve theorem for the expansion of a random function [29], one can obtain the following approximate distribution for the norm $\|F(u) - \phi(u)\|$:

$$\Pr\{\|P(u) - \phi(u)\| < k \|\phi(u)\|\} = \Phi\left[\{(k^2\|g(x)\|^2/d_{av}) - 1\} \sqrt{\frac{a}{2}} \Big/ \|g(x)\| \right] \qquad (16)$$
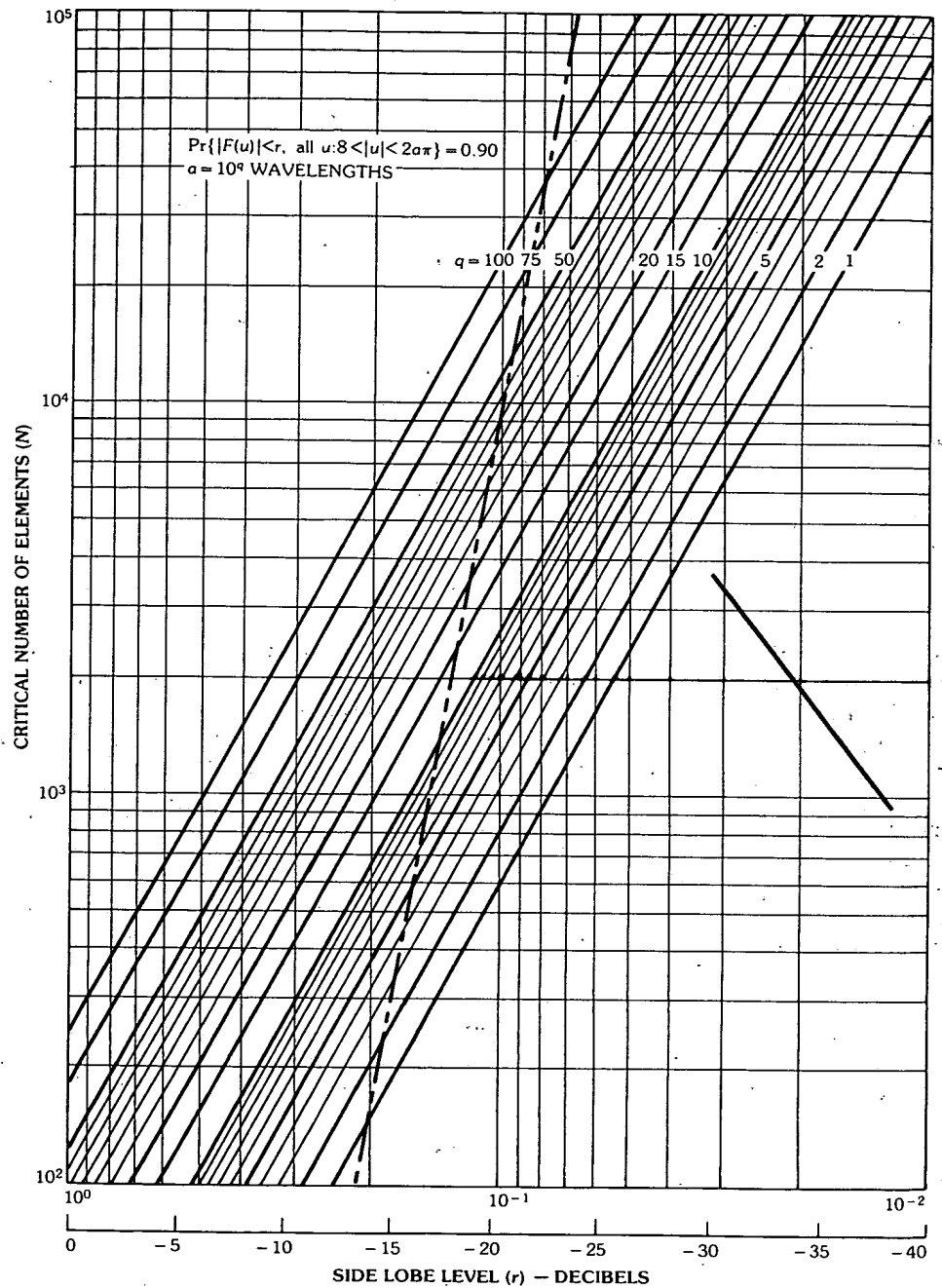
where

Fig. 7. Number of elements required as a function of the side lobe level for various values of $a = 10^q \lambda$ with a 90 percent probability. (*After Lo [12], © 1964 IEEE*)

$$\|F(u) - \phi(u)\|^2 = \int_{\substack{\text{visible} \\ \text{region}}} |F(u) - \phi(u)|^2 \, du$$

$$\|g(x)\|^2 = \int_{-1}^{1} |g(x)|^2 \, dx$$

d_{av} = average element spacing $\cong a/N$

k = a positive real number

$\Phi(\cdot)$ = standardized normal distribution function (i.e., one with zero mean and unit variance)

Because generally a is a very large number, if k^2 is slightly greater than $d_{\text{av}}/\|g\|^2$, the above probability is nearly unity, while if k^2 is slightly less than $d_{\text{av}}/\|g\|^2$, the above probability drops sharply to zero. From this result and the definition of directivity D associated with each sample pattern function, and the directivity D_0 associated with the mean pattern function $\phi(u)$, one can conclude that with probability nearly one

$$(D_0 - D) \, \text{dB} \leqq 20 \log(1 + \sqrt{d_{\text{av}}}/\|g(x)\|) \tag{17}$$

In other words, it is practically certain that D is lower than D_0 by a quantity no greater than $20 \log(1 + \sqrt{d_{\text{av}}}/\|g\|) \, \text{dB}$, which for large average element spacing equals $20 \log \sqrt{d_{\text{av}}}/\|g(x)\|$. The interpretation of this result can easily be understood if we consider two arrays of a different number of elements, say, N_1 and N_2. Let their corresponding directivities be D_1 and D_2, respectively; then the above results show that

$$(D_1 - D_2) \, \text{dB} \cong 10 \log(N_1/N_2) \tag{18}$$

with a probability nearly equal to 1. In other words it is practically certain that the directivity D is proportional to N, the number of elements. This result is in agreement with that obtained in Chapter 11. The reason why the probability is not exactly 100 percent is that there exist particular element arrangements, but with very small probabilities, for which D is not exactly equal to N, such as superdirectivity, as shown in Chapter 11.

(g) There is little difficulty in extending most of the above results to an array of higher dimensions. For example, consider a rectangular aperture of $ab\lambda^2$ in the xy plane with a probability density function $g(x, y)$ for the element locations which would produce a mean pattern with sufficiently low side lobe level as before. Then the relation between the total number of elements and the side lobe level is still approximately given by (14), except that [4a] is replaced by [16ab]. Assuming that $a = 10^q$ and $b = 10^p$, this relation is again shown by Fig. 7 except that q should be replaced by $(p + q)$, and 90 percent probability by 80 percent (approximately).

To give an example, the Benelux Cross antenna [30] is considered. This antenna consists of two perpendicular linear arrays each having an aperture of roughly $7 \times 10^3 \lambda \times 80\lambda$, or $ab \cong 10^6 \lambda^2$. From Fig. 7, with a -30-db side lobe level

and 90 percent chance of success, each arm requires only about 1.9×10^4 elements. But according to Christiansen and Hogbem [30], each arm would require 2×10^6 uniformly spaced dipoles. This is about 100 times larger than the former estimate. Moreover, if elements were randomly spread over a square aperture $10^4\lambda \times 10^4\lambda$, a total of only 2.3×10^4 elements would be needed to achieve a -30-dB side lobe level. This is very significant since the cross type telescope, being a multiplicative antenna system, will have a side lobe level of -15 dB in the two principal planes even if each arm is designed to have a -30-dB side lobe level. Of course, as already noted before, the directive gain of the randomly spaced array is perhaps 10 or 15 dB lower than that of the uniformly spaced array. Since the former has uniform amplitude weighting function while a uniformly spaced array must have a strongly tapered illumination in order to achieve a -30-dB side lobe level, then from a practical point of view (considering the feeding system and the aperture efficiency) the loss in directive gain may not be as much as indicated above.

Illustrative Examples

Suppose that it is desired to design a linear array whose array pattern will have approximately a half-power beamwidth of 1 minute of arc and a side lobe level of -18 dB. If $g(x)$ is chosen to be uniform, the near-in side lobe level would likely be -13 dB. To ensure that it is below -18 dB, one may, although not necessarily, let

$$g(x) = \cos^2(\pi x/2) \tag{19}$$

For this function the half-power beamwidth in degrees is approximately $83/a$ and, therefore, $a \cong 83 \times 60 \cong 5 \times 10^3(\lambda)$. From Fig. 7, N (the number of elements needed for a 90 percent probability of success) is approximately 800. The next step is to generate 800 random numbers, between $(0, 1)$ under the probability density function $g(x)$ given above, and these numbers, after scaled by the factor a, determine the actual element locations in the aperture. According to the theory this array when excited uniformly will have a 90 percent probability to yield a pattern with 1 minute of arc in half-power beamwidths and -18-dB side lobe level. Of course, before an investment is made for constructing this array it is prudent to first compute the pattern with the given set of element positions just found, since there is still a 10 percent chance of failure. In a sense the theory predicts that in about nine out of ten trials one should obtain the desired pattern. Hundreds of computer simulations have been made for many different arrays, and in almost all cases the desired properties as predicted by the theory were obtained in the very first trial. Since the *same* basic array theory is used for computing this pattern as for any conventional equally spaced array, there is no reason to doubt this array performance cannot be realized. In fact in this case, all elements being widely spaced, the mutual coupling will have a much less deleterious effect on the pattern. After the pattern properties are confirmed by the computations the array can then be constructed. From that step on, the array is as *deterministic* as any conventional array. This will be demonstrated in a holey plate experiment later.

For simplicity in pattern computation a symmetrical array has been considered for the example stated above. In this case the required number of elements becomes about 1000, somewhat more than that shown in Fig. 7, since there are in

effect only 500 random numbers [13]. These numbers were taken directly from Owen's table [31]. Since these numbers are uniformly distributed, the probability integral transformation [32] is then used to convert the set of numbers into another set which obeys the cosine-square law prescribed in (19). This is done by solving the following equation for x_n:

$$y_n = \int_0^{x_n} g(x)\, dx \tag{20}$$

where y_n is the uniformly distributed random number between 0 and 1, and x_n is the $g(x)$ distributed random number. This method is similar to that used to convert a set of uniform element spacings to a set of nonuniform element spacings in Fig. 1. With this transformation the distribution of the 500 random numbers taken from Owen's table is shown as dotted curves in Fig. 8. For comparison the exact cosine-square distribution is shown in solid line. The computed pattern for $0 \leq u/\pi \leq 19$ is shown as the solid curve in Fig. 9. Also shown are three other cases with $N = 100$, 300, and 600. It is clear that all four cases have almost identical main beams, but the side lobe level, as expected, increases as N decreases even for the small region of angle of observation shown in the figure. It is impractical to show the pattern for the entire visible range. Instead, a statistical distribution of $|F(u_i)/\sigma|^2$ for roughly 4×10^4 values of u_i uniformly spaced in the visible region is made for the case $N = 1000$ shown as the stepped sample curve in Fig. 10. The theory developed before predicts an χ^2 distribution which is also shown in the figure in a normalized scale. The agreement is nearly perfect. This implies that the theory, although it cannot predict the exact shape of the pattern curve, can predict quite accurately the *distribution* of the nearly 4×10^4 numbers of $\{|F(u_i)|\}$ actually computed. Unfortunately, a very accurate prediction of this distribution tells practically nothing about the side lobe level since if *one* of the numbers in the set $\{|F(u_i)|\}$ is changed to a very large value, it will have no effect on the distribution yet it alone will determine a high side lobe level. It is seen once again that the determination of side lobe level is a much more difficult problem. Using the approximate theory given earlier, however, one can predict the side lobe level as the aperture size a or visible region increases. This is shown in Fig. 11 for the four different cases along with the actually computed values for the sample arrays. In this figure the side lobe level in decibels is plotted against both a in wavelengths and the half-power beamwidth in minutes of arc. It is seen that even with as few as 300 uniformly excited elements one can obtain a half-power beamwidth of about 1 minute with a side lobe level of -13 dB. If the conventional design with a half-wavelength spacing is used, it would require 10^4 elements to produce the same beamwidth and side lobe level. The reduction in the number of elements is at a ratio of 100:3; in other words, 97 percent of the elements are saved. The directivity, however, being roughly proportional to N, cannot be obtained without paying the correct price. On the other hand, for the same number of elements as required for the directivity one can achieve a much narrower beam and lower side lobe level with a simple uniform excitation. As will be seen below, there are other significant advantages (such as absence of blind angles and a smaller deleterious effect due to phase errors in a digitalized phase system) for using this type of array.
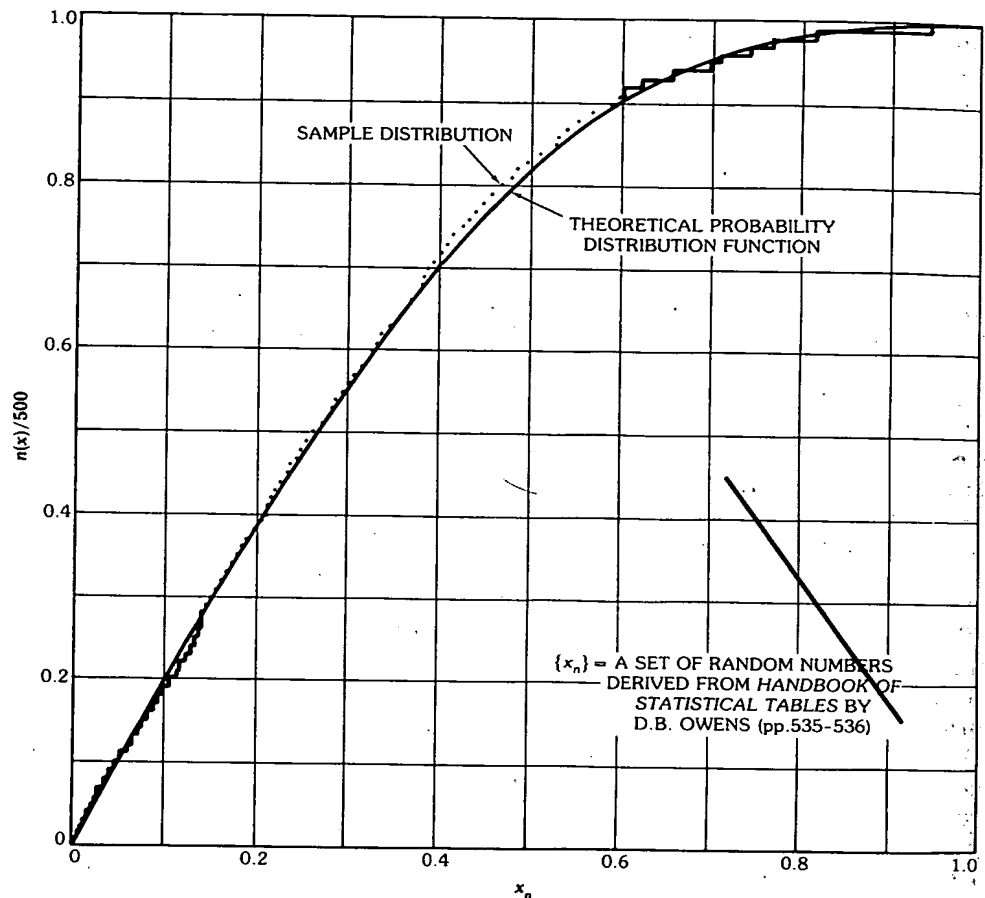
Fig. 8. Distribution of element positions $\{x_n\}$ for an assumed cosine-square density function. (*After Lo [13]*, © *1964 by the American Geophysical Union*)

The Mutual Coupling Effect and Blind Angles

In general, the mutual coupling in a phased array with randomly spaced elements is not a serious problem since for such an array elements are commonly many wavelengths apart from each other. However, it may be shown that even if array thinning is not the objective and elements are not spaced far apart, random spacings can still be used advantageously in some applications.

Rigorously speaking, the mutual coupling effect in a practical array is a difficult problem to analyze. The approximate methods commonly used, as discussed in other chapters, are two. The first is to consider a practical array as a truncated portion of a corresponding infinite array [33]. Only when the array is a periodic structure is this method applicable. For arrays with unequal or random element spacings one must resort to the second approach in which the mutual impedances between two elements at various spacings are determined first and their effect in an
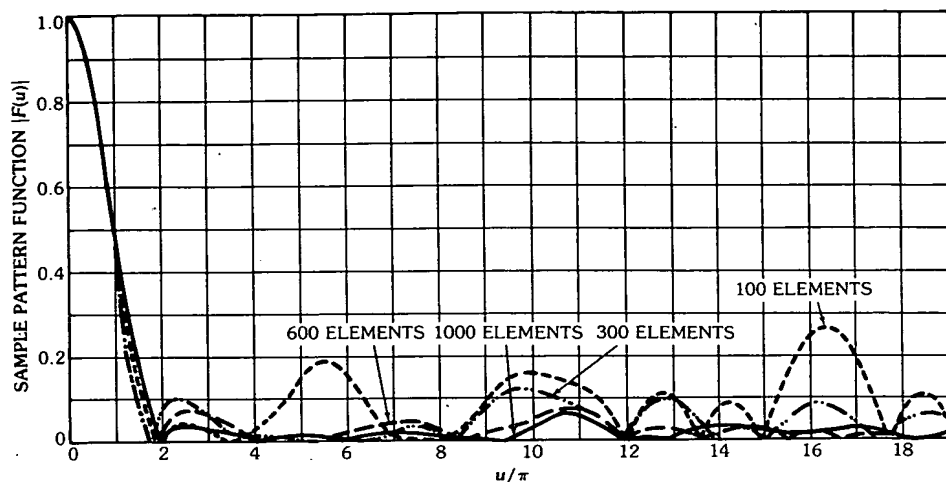
Fig. 9. Sample pattern functions for $0 \leqq u/\pi \leqq 19$ of four symmetrical arrays with $N = 100$, 300, 600, and 1000 elements, respectively. (*After Lo [13], © 1964 by the American Geophysical Union*)

array is then studied with a circuit treatment. In this approach it is assumed that the current or aperture field distributions on the two elements remain unchanged whether or not all other elements are present. This seems generally to be a valid assumption for elements of many types at not too close a spacing.

Let I_n be the actual feed current of the nth element in an array and $I_n^{(0)}$ be the current when all mutual couplings are absent. Then by circuit analysis,

$$I_n = I_n^{(0)} - \sum_{\substack{m=1 \\ m \neq n}}^{N} \frac{Z_{mn}}{Z_{11} + Z_0} I_m \qquad (21)$$

where

Z_{mn} = mutual impedance between the mth and nth elements

Z_{11} = self-impedance of the element at the feed terminals

Z_0 = generator or the feed-line impedance

For all the elements, (21) can be written as

$$\mathbf{I} = \mathbf{I}^{(0)} - \mathbf{CI} \quad \text{or} \quad \mathbf{I} = (\mathbf{E} + \mathbf{C})^{-1} \mathbf{I}^{(0)} \qquad (22)$$

where

$$\mathbf{I} = \begin{bmatrix} I_1 \\ \vdots \\ I_N \end{bmatrix}, \qquad \mathbf{I}^{(0)} = \begin{bmatrix} I_1^{(0)} \\ \vdots \\ I_N^{(0)} \end{bmatrix}$$
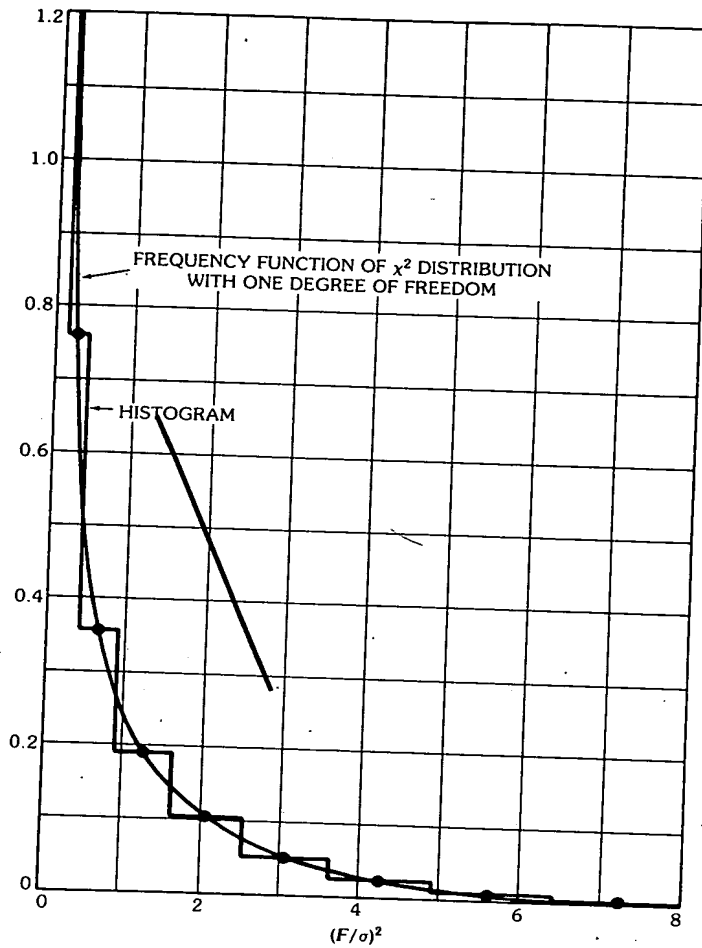
Fig. 10. Sample distribution of 4×10^4 points of the normalized pattern function squared $|F/\sigma|^2$, equally spaced in u/π from 0 to 10^4 (corresponding to $a = 10^4\lambda$) for $N = 1000$ as compared with the theoretical density function, namely the chi-square density function with one degree of freedom. (*After Lo [13], © 1964 by the American Geophysical Union*)

C is an $N \times N$ matrix with elements

$$C_{mn} = \frac{Z_{mn}}{Z_{11} + Z_0} \quad \text{and} \quad C_{mm} = 0$$

$\mathbf{E}$ = identity matrix

For uniform cophasal excitation $I_n^{(0)} = \exp(-jvx_n)$, the pattern function

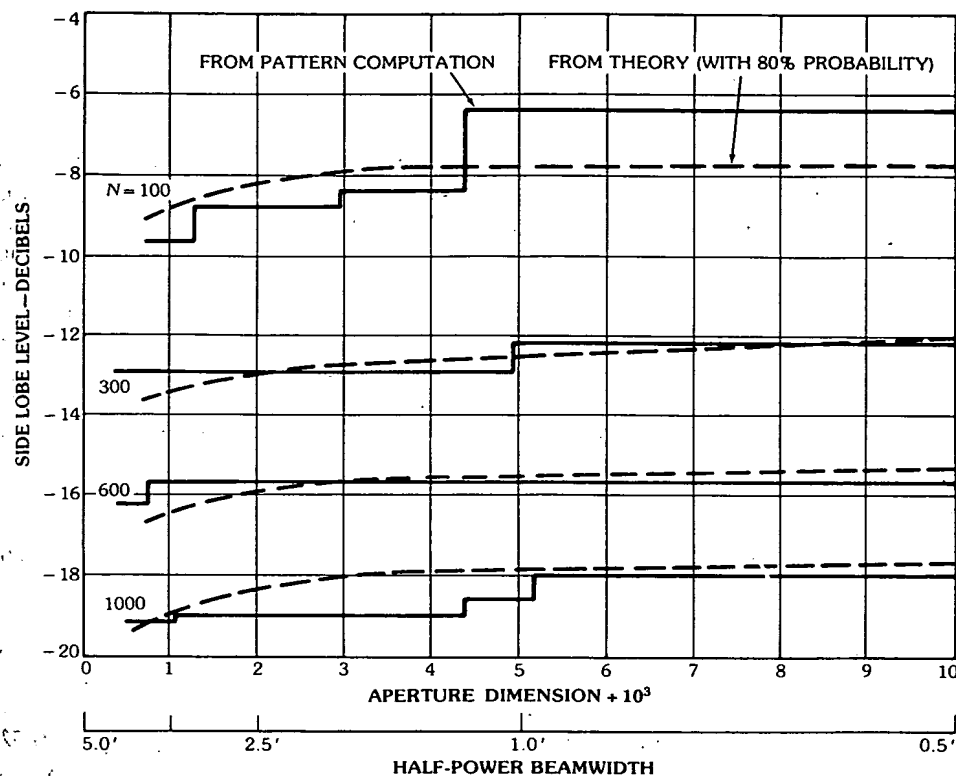$$F(u, v) = \frac{1}{N} \sum_{n=1}^{N} I_n \exp(jux_n) \tag{23}$$

Fig. 11. Side lobe level for four sample symmetrical arrays with $N = 100, 300, 600,$ and 1000 elements as a function of the aperture dimension in wavelengths, or the half-power beamwidth in minutes of arc. (*After Lo [13], © 1964 by the American Geophysical Union*)

where

$v = 2\pi \sin \alpha$

α = beam scan angle

$u = 2\pi \sin \theta$

θ = observation angle

x_n = nth element position in wavelengths

Except for the uninteresting case of close element spacing one may use the following approximation for (22),

$$I \cong (E - C) I^{(0)} \tag{24}$$

Then

$$F(u,v) = \frac{1}{N} \sum_{n=1}^{N} \exp[j(u-v)x_n] - \frac{1}{N} \sum_{n=1}^{N} \sum_{\substack{m=1 \\ m \neq n}}^{N} C_{mn} \exp[j(ux_n - vx_m)] \quad (25)$$

The first summation gives the pattern in the absence of mutual coupling and has been studied thus far, whereas the second, double summation is due to the coupling. The determination of Z_{mn}, or C_{mn}, is a boundary value problem depending on a particular type of antenna, which is not the subject matter of this chapter. At the present it is assumed that Z_{mn}, as a function of spacing, is known either analytically or experimentally. Its effect on the side lobe level distribution can then be found approximately by formulating the problem in terms of a diffusion equation for the probability function of the up-crossing of $|F(u,v)|$ at any given level η for u in any given region [24]. The equation is then solved numerically. To see the effect of mutual coupling on the side lobe level distribution, use has been made of the coupling coefficient

$$C_{mn} = \frac{0.11}{0.22 + |x_{mn}|} \exp(-j2.22\pi|x_{mn}|) \quad (26)$$

where $x_{mn} = x_m - x_n$, as determined experimentally by Lechtreck for two horn elements [34].

Fig. 12 shows the side lobe distributions for an array of 50 such elements uniformly distributed at random with three different average spacings: $d_{av} = 0.5\lambda$, 1.0λ, and 2.5λ. When the coupling is considered, the distributions are shown in solid curves, and when ignored, in dashed curves. As expected the coupling results in a higher side lobe level, but to a lesser degree for larger average spacing. Fig. 13 shows more clearly how the increase in side lobe level depends on the average spacings. In this case, $a = 500\lambda$ and $d_{av} = 0.5\lambda$, 1.0λ, 2.5λ, 5.0λ, and 10λ are considered. It is seen that when $d_{av} \geqq 2.5\lambda$ the coupling may be ignored. It may be noted that for $d_{av} = 2.5\lambda$ and $N = 200$, the increase in side lobe level is less than that shown in Fig. 12 for the same d_{av} and for $N = 50$. Thus even for the same average spacing, the effect of mutual coupling on side lobe level becomes less as N increases. This is also expected as the double summation in (25), consist of terms in random phase, contributes less and less as N increases, for the same reason that the side lobe level decreases when N increases even in the case of no coupling as shown in (14).

If $u = v$ in (25), one obtains the main beam maximum. For most antenna elements, if not spaced very closely, the phase of C_{mn} is nearly linear in spacing as shown in (26). Let

$$C_{mn} = |C_{mn}| \exp(j\beta|x_{mn}|), \qquad x_{mn} = x_m - x_n$$

Then the main beam magnitude as a function of scan angle α, or its corresponding value v, sometimes called the *array scan characteristics*, is
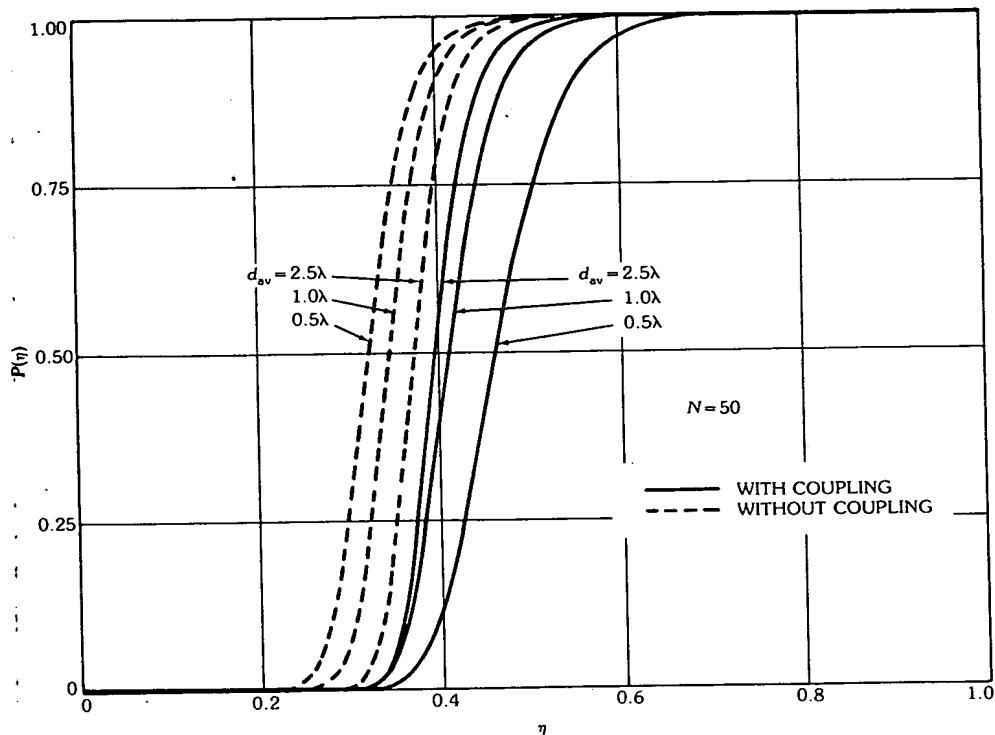
Fig. 12. Distribution of side lobe level for random arrays of 50 elements and average spacing $d_{av} = 0.5\lambda$, 1.0λ, and 2.5λ with and without mutual coupling. (*After Agrawal and Lo [24]*, © *1972 IEEE*)

$$F(v, v) = \frac{1}{N} \sum_{n=1}^{N} \left[1 - \sum_{\substack{n=1 \\ n \neq m}}^{N} |C_{mn}| \exp(-jvx_{mn} + j\beta|x_{mn}|) \right] \qquad (27)$$

The quantity in the square brackets is exactly the pattern function of the nth element with all other elements terminated in the match load Z_0. It may be called the *array element pattern*, namely, the pattern of an element in an array environment, which can be vastly different from that of an isolated element. The scan characteristic is therefore the average of all array element patterns. It is interesting to see that if $x_n = nd$ (i.e., uniform spacing), and if

$$(v \pm \beta)d = 2\pi p, \qquad p = 0, 1, 2, \ldots$$

the terms in the second sum of (27) will add up in phase to cause a sharp decrease in $F(v, v)$. For a very large array this sum could be as large as unity, thus resulting in the so-called blind angle phenomenon; namely, in that scan direction, v, the main beam maximum and therefore the total radiated power drop to nearly zero. In other words the array ceases to function as an antenna and all the power sent by
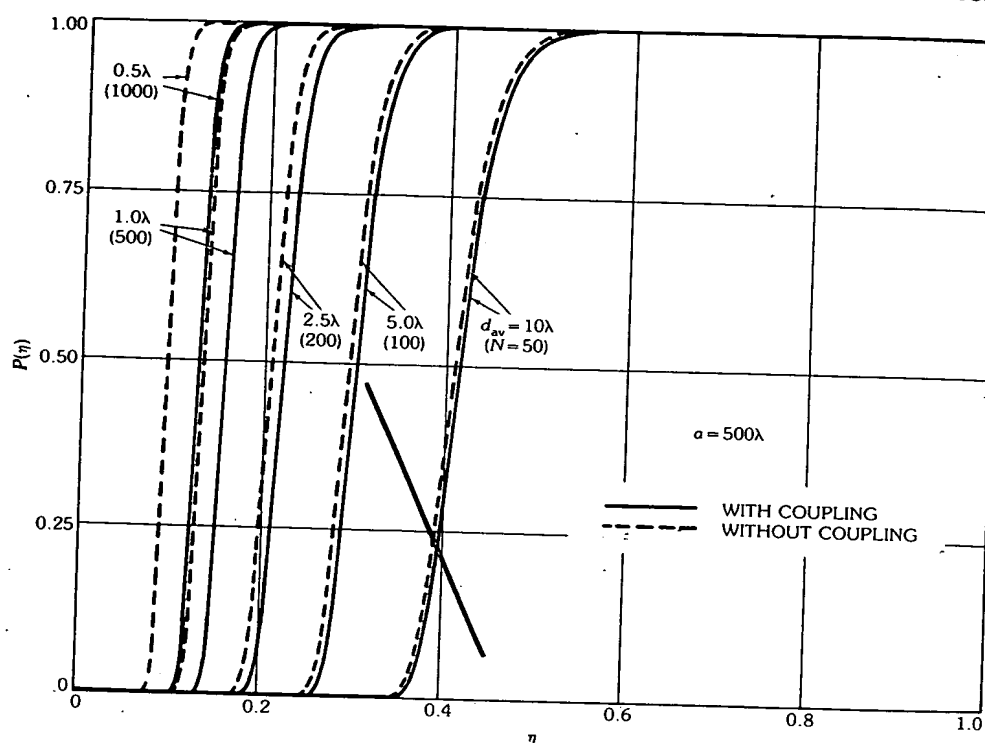
Fig. 13. Distribution of side lobe level for a 500λ aperture and 50, 100, 200, 500, and 1000 elements with and without mutual coupling. (*After Agrawal and Lo [24],* © *1972 IEEE*).

the exciting generator will be reflected, or the element impedance in the array becomes reactive. Now if $x_n \neq nd$ and $\{x_n\}$ is a set of random numbers, the in-phase condition for all the terms in the summation will be unlikely to occur. In fact, the larger the array (i.e., more elements), the smaller will be the sum and thus the smaller the drop of main beam magnitude. This conclusion is in exact opposition to that of a uniformly spaced array, a very gratifying result indeed.

The probability distribution of the main beam magnitude $F(v, v)$ can be determined approximately once the coupling coefficient C_{mn} for a given type of element to be used and the probability density function $g(x)$ for placing the elements are known. The readers may refer to Agrawal and Lo [24] for details. In the following only some typical results are given.

Let the *fluctuation* of the main beam magnitude be defined as

$$r = \max_{v \in [0, 2\pi]} F(v, v) - \min_{v \in [0, 2\pi]} F(v, v) \qquad (28)$$

When $g(x) = 1/2$ for $|x| \leq 1$ and 0 otherwise, C_{mn} is given by (26), $N = 50$, and $d_{av} = 0.5\lambda$, the probability for $r < \xi$ versus ξ can be computed and is plotted in Fig. 14. Also shown is the "experimental" result for 50 random sample arrays simulated by using the Monte Carlo method. The close agreement between the two results
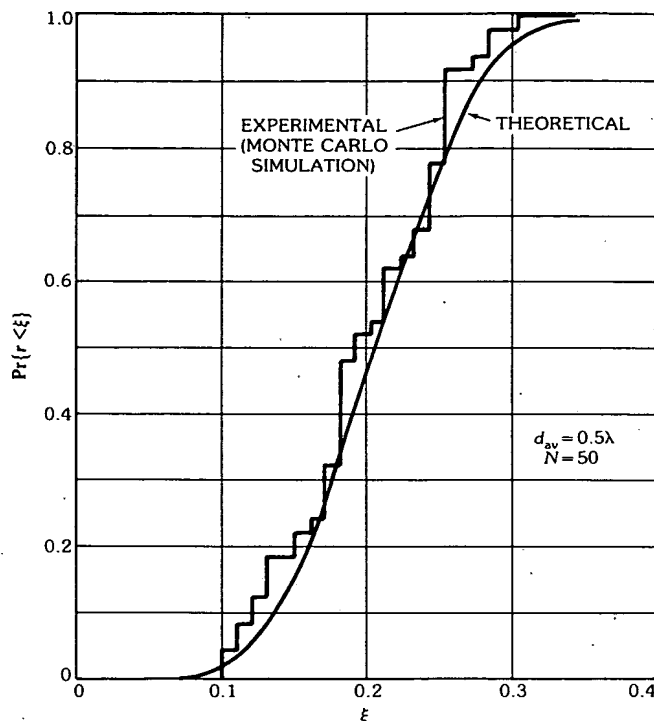
Fig. 14. Distribution of main beam amplitude fluctuation r over the entire scanning range for 50 elements and average spacing 0.5λ. (*After Agrawal and Lo [24], © 1972 IEEE*)

provides some confidence in the approximate theory. Fig. 15 shows the theoretical results for the same array except that $d_{av} = 0.5, 1.0, 2.5, 5,$ and 10λ. As expected, the larger the average spacing d_{av}, the smaller the coupling effect and the smaller the fluctuation of main beam magnitude over the scanning range.

The Holey Plate Experiment

Side Lobe Level and Half-Power Beamwidth—A physical experiment for a large array is a rather costly enterprise. Fortunately, the holey plate method as described by Stone at optical frequency [35] and by Skolnik at microwave frequency [36] provides a simple modeling technique. In this method the array is modeled by a large conducting plate perforated with small circular holes, each simulating an antenna element. The "holey" plate is illuminated by an incident plane wave from one side, and the field is measured from the other side for all directions. The pattern so obtained would be nearly the same as that of the actual array. The sketch in Fig. 16 shows the major components used. The holey plate is placed against a microwave lens which converts a spherical wave emitted from a reduced open waveguide at the focus into a plane wave. The assembly of these components is enclosed in a box made of absorbing material, and placed over a turntable.

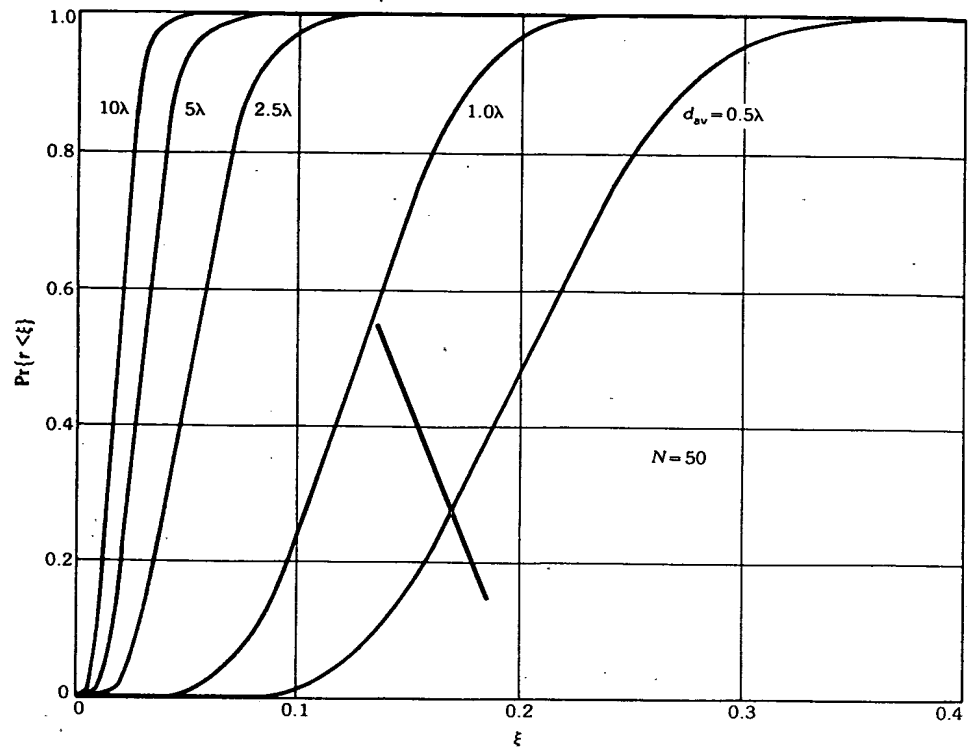In the actual setup the holey plate is used as a receiving array. Fig. 17 shows the

Fig. 15. Distribution of main beam amplitude fluctuation r over the entire scanning range for 50-element arrays with 0.5λ, 1.0λ, 2.5λ, 5λ, and 10λ average spacing. (*After Agrawal and Lo [24]*, © *1972 IEEE*)
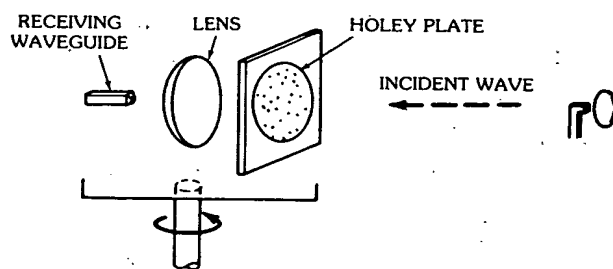

Fig. 16. Major components for the holey plate experiment. (*After Lo and Simcoe [23]*, © *1967 IEEE*)

physical experimental setup at 4 mm. The paraboloidal reflector at the far right is the transmitting antenna. The incident wave is diffracted by the holey plate and then focused on an open-ended waveguide on the left by a polystyrene lens. The receiving assembly, consisting of the plate, lens, and the open-ended waveguide, is
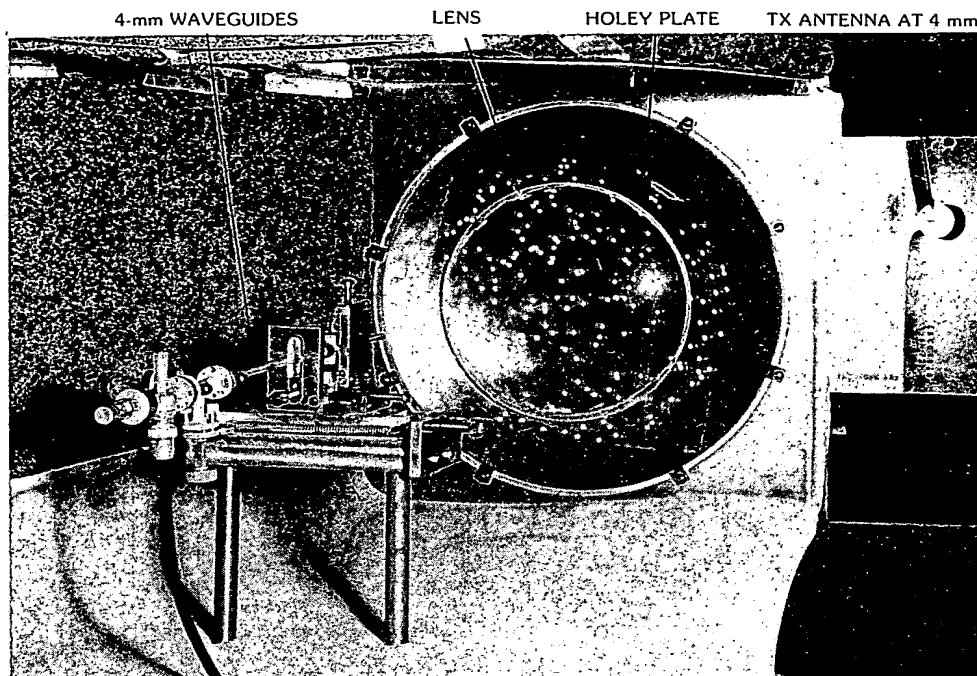
4-mm WAVEGUIDES   LENS   HOLEY PLATE   TX ANTENNA AT 4 mm

Fig. 17. Experimental setup for 4-mm waves. (*After Lo and Simcoe [23]*, © *1967 IEEE*)
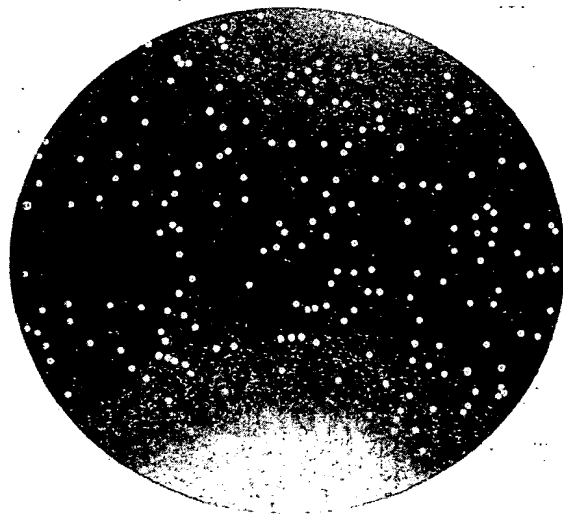

Fig. 18. Photo of the holey plate sample array, where the coordinates of elements are obtained from a set of uniformly distributed random numbers. (*After Lo and Simcoe [23]*, © *1967 IEEE*)

placed over a turntable. Except for the plate the assembly is enclosed with microwave-absorbing materials which are partially removed in order to show the details inside. In this picture the range has been reduced so that the transmitting antenna can also be shown. The holey plate contains 210 elements uniformly distributed at random over a circular aperture of about 56λ in diameter as shown in Fig. 18. Each element is a hole of about $\lambda/4$ in diameter. As is clear from this figure there exists no plane of symmetry and thus no principal plane. Therefore the measured patterns in a few planes cannot be used to infer the overall performance. It would be desirable to measure a three-dimensional pattern, but in this experiment a total of 90 cuts was taken (roughly twice as many as the highest spatial frequencies). A typical pattern with expanded main beam is shown in Fig. 19. The measured beams in all cuts are almost identical, with a half-power beamwidth ranging from $0.9°$ to $1.25°$ and a statistical mean of $1.04°$. The difference between this value and the theoretical mean of $1.05°$ is well within the experimental error.
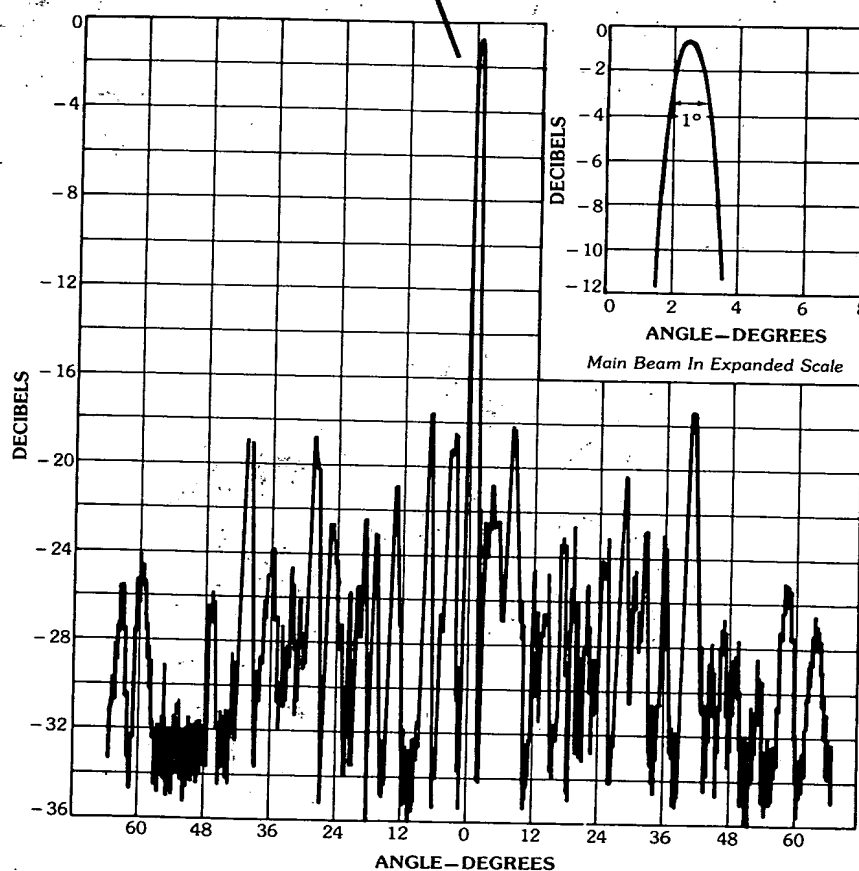

Main Beam In Expanded Scale

Fig. 19. A typical pattern in a plane cutting through the sample array as shown in Fig. 18. (*After Lo and Simcoe [23], © 1967 IEEE*)

The 90 measured patterns are statistically "identical" in the sense that all have nearly the same beam and a few high side lobes, ranging approximately from −18 dB to −13 dB. However, no two patterns are really identical in details. Fig. 20a shows the measured as well as the theoretically predicted distributions of the highest side lobe levels associated with the 90 patterns. The agreement is remarkable. To safeguard against the luck in this experiment, a second completely independently designed holey plate was also constructed and tested. The same close agreement was obtained as shown in Fig. 20b. Finally, it is worth noting again that if a conventional array design (i.e., using uniformly spaced elements) is used to produce the same beam and side lobe level, 10^4 elements would be required. This number is about 50 times what was used in the experiment. Obviously the
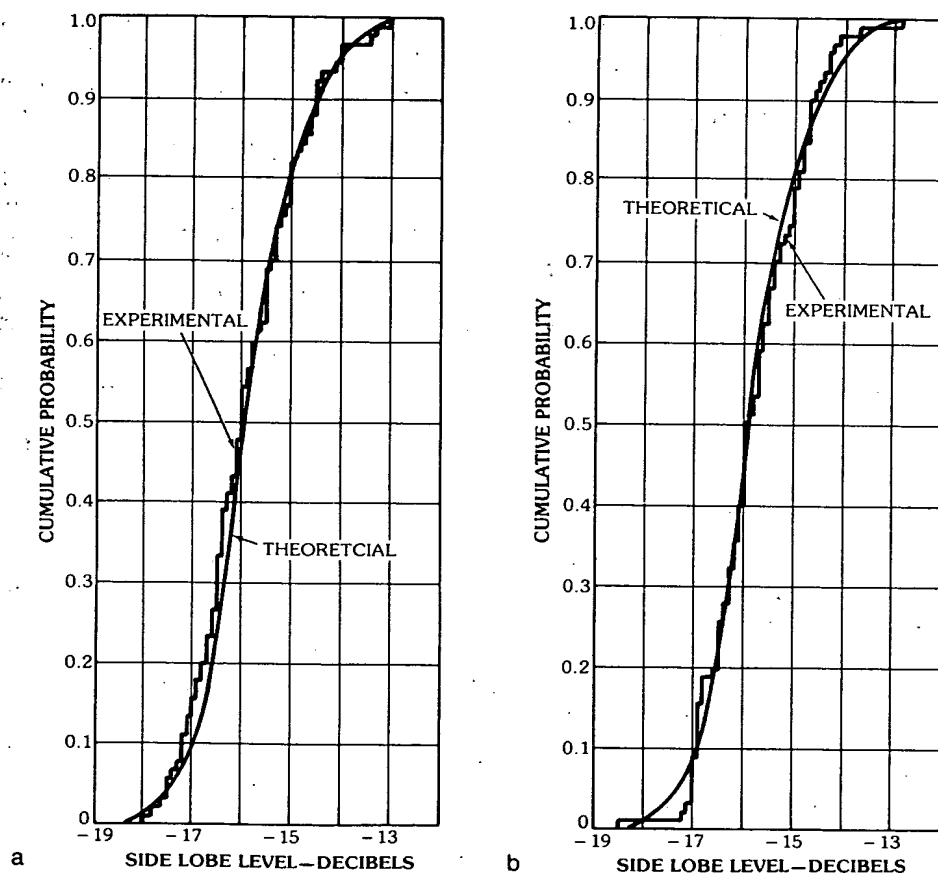

Fig. 20. Comparison of the theoretical and experimental distributions for the side lobe levels of linear arrays. (a) Experimental distribution obtained from a set of 90 pseudo-random linear arrays generated by the planar array 1. (b) Experimental distribution obtained from a set of 90 pseudo-random linear arrays generated by the planar array 2. (*After Lo and Simcoe [23], © 1967 IEEE*)

difference is by no means insignificant. Of course, the two designs would not have the same directivity. On the other hand, suppose that the desired directivity is less than 10^4, say 10^3. Then the random spacing approach will provide a design which uses not only 1/10 of the elements but also can yield a lower side lobe level and/or narrower beam. In other words, in this random design the required number of elements is determined not directly by the aperture size but rather by the desired directivity and side lobe level.

Scanning Characteristics—It is a simple matter to obtain cophasal excitation in a holey plate experiment. If the holey plate is rotated at an angle α with respect to the lens as shown in Fig. 21, all elements will automatically be excited cophasally to produce a beam at an angle α from the broadside. In Fig. 21 a linear uniformly spaced slot array (or grating), etched from a copper-clad substrate with relative permittivity $\epsilon_r = 4.25$, is placed in front of a lens. In this case if the receiving waveguide and the lens are held fixed while only the grating rotates, one obtains the scanning characteristics, namely, the main beam magnitude variation (or the scanning pattern) with the scan angle α. The measured scanning pattern for a linear array of 61 uniformly spaced slots when E is perpendicular to the slots is shown in Fig. 22. It is clearly shown that at about $\pm 18°$ the main beam magnitude drops sharply to -20 dB. These are the blind angles for this particular array. When the same 61 slots were rearranged to have random spacings but the same average spacing $d_{av} = 0.6\lambda$, the blind angles disappeared, as clearly seen in Fig. 22. Fig. 23 shows the superimposed measured main beams for another linear array of 45 slots, both uniformly spaced (Fig. 23a) and randomly spaced (Fig. 23b), all with the same average spacing $d_{av} = 0.6\lambda$. For this case the E vector is parallel to the slots and the blind angles appear at approximately $\pm 30°$ as shown in Fig. 23a when the slots are spaced uniformly and become absent in Fig. 23b when they are spaced at random.

Figs. 24a through 24c show the computed patterns for a single element in an array environment of 21 elements, i.e., $F(\nu, \nu)$ in (27), for the case of perpendicular polarization and uniform spacing. With the exception of the few edge elements, they all are almost identical with the scanning pattern shown in Fig. 22 so that the sharp drop at about $\pm 18°$ becomes cumulative, resulting in the blind angle [37]. From this, one expects that the larger the array, the deeper the drop. When spacings are random, however, the array element pattern is completely different from one element to another as shown in Fig. 25, thus resulting in a scanning pattern free from blind angles. For details and the theoretical analysis, readers are referred to Agrawal and Lo [24, 37].

Other Remarks

In most phased arrays quantized phases are used. For uniformly spaced elements the phase errors incurred in the elements are systematic and, as a result, not only the main beam magnitude may be reduced but the side lobe level raised also. In case of randomly spaced elements such deleterious effects can be reduced particularly for large arrays. Another method that can be used to achieve this goal in a similar manner is to deliberately add a small amount of random phase to each quantized level. However, this method is effective only when a large number of levels (or bits) is used in the system.
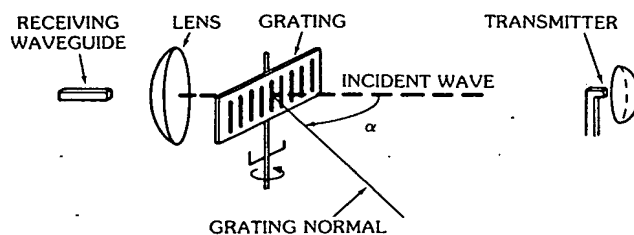
RECEIVING   LENS   GRATING   TRANSMITTER
WAVEGUIDE

INCIDENT WAVE

α

GRATING NORMAL

Fig. 21. Sketch of the experimental setup for measuring main beam magnitude fluctuation. (*After Agrawal and Lo [37]*)

$N = 61$ NUMBER OF SLITS
$T = 0.5$ mm GRATING PLATE THICKNESS
$W = 1.25$ mm SLIT WIDTH
$\lambda = 4.17$ mm WAVELENGTH
$E^i = $ PERPENDICULAR TO SLITS

RANDOM
GRATING
$d_{av} = 0.6\lambda$

UNIFORM
GRATING
$d = 0.6\lambda$
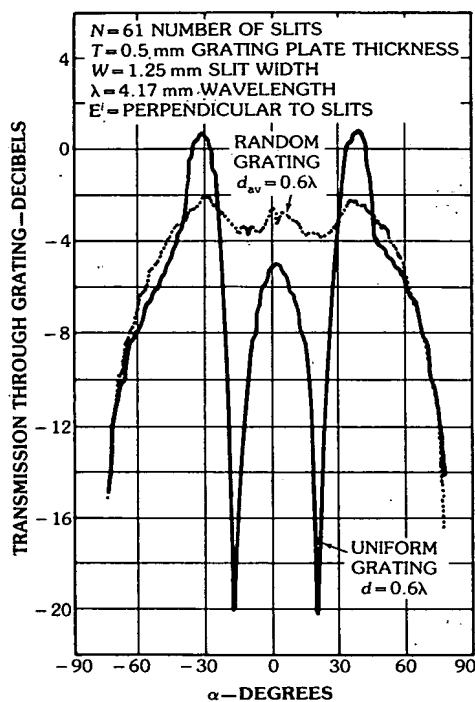
TRANSMISSION THROUGH GRATING—DECIBELS

α—DEGREES

Fig. 22. Measured transmitted power through uniform and random gratings versus orientation angle α (perpendicular polarization). (*After Agrawal and Lo [37]*)

For many conformal arrays, such as cylindrical and spherical arrays, even if the elements are placed in a regular manner (for example, equiangular spacings), their pattern functions cannot be simply expressed in terms of polynomials as for linear arrays. Thus there is, in general, no analytic advantage to considering a particular element arrangement. Commonly the patterns are computed numerically, and clearly for large arrays this brute force method is very costly. However, the contributions from all elements to a pattern in a plane have phases proportional to
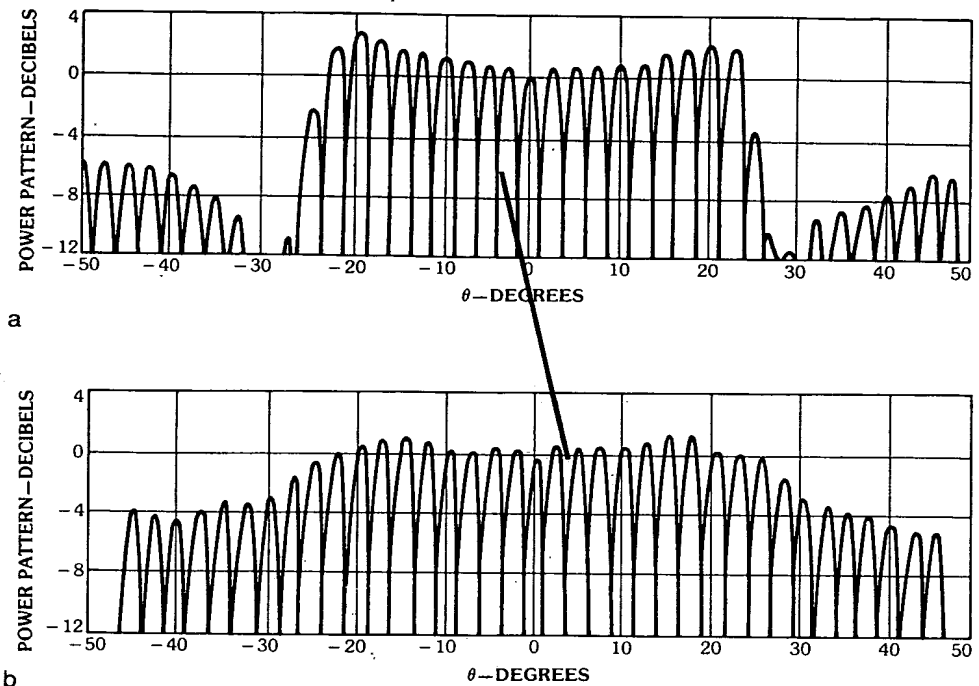
Fig. 23. Measured main beam patterns, superimposed for various scan angles α (parallel polarization). (*a*) Uniform array with $d = 0.6\lambda$, $N = 45$. (*b*) Random array with $d_{av} = 0.6\lambda$, $N = 45$. (*After Agrawal and Lo [37]*)

the projections of the element positions on that plane which are in general pseudo-random. For this reason a probabilistic approach to large cylindrical and spherical arrays has been studied [38].

With the advent of log-periodic antennas, extremely wide band antennas become a reality. This outstanding family of antennas, however, has its own limitations, namely, low directivity and wide beamwidth, since for each frequency only a limited portion of the antenna is active. To form an array with these elements for high directivity, one will be confronted with the difficulty that the physical element spacing increases with frequency, causing a serious grating lobe problem. To alleviate this difficulty random spacings of log-periodic elements, particularly for large arrays, should be used since such an array can tolerate large element spacings and is inherently frequency insensitive, as shown in this chapter.
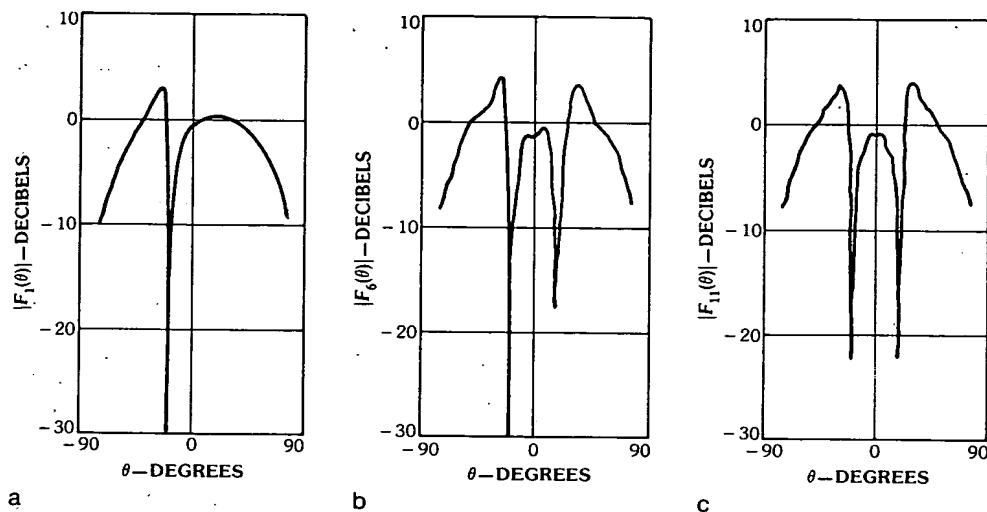
Fig. 24. Computed single-slit pattern $|F_k(\theta)|$ when only the kth element of a uniformly spaced array with 21 elements is excited, where $d = 0.6\lambda$, $\epsilon_r = 4.25$, $T = 0.5$ mm, $W = 1.25$ m, $\lambda = 4.17$ mm, and **E** is perpendicular to slit. (*a*) First-element pattern. (*b*) Sixth-element pattern. (*c*) Central-element pattern. (*After Agrawal and Lo [37]*)
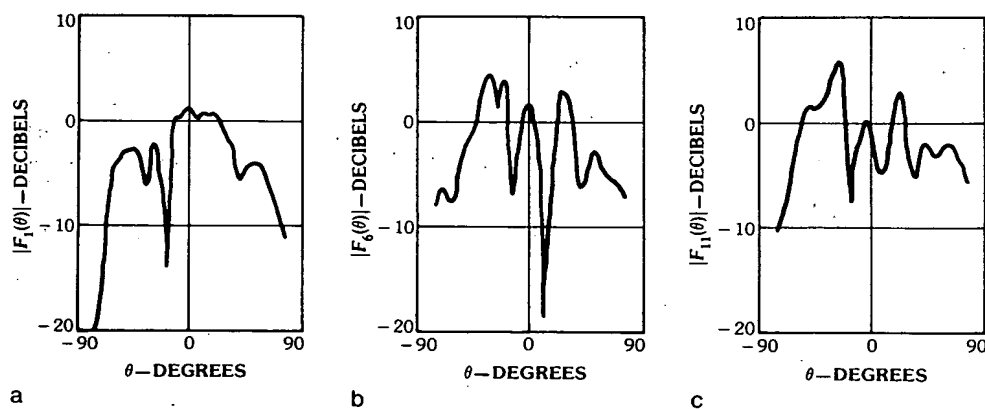

Fig. 25. Same as for Fig. 24 except that the 21 elements are randomly spaced with $d_{av} = 0.6\lambda$. (*a*) First-element pattern. (*b*) Sixth-element pattern. (*c*) Central-element pattern. (*After Agrawal and Lo [37]*)

5. References

[1]   H. Unz, "Linear arrays with arbitrarily distributed elements," *IRE Trans. Antennas Propag.*, vol. AP-8, pp. 222–223, March 1960.

[2]   D. D. King, R. F. Packard, and R. K. Thomas, "Unequally spaced broadband antenna arrays," *IRE Trans. Antennas Propag.*, vol. AP-8, pp. 380–385, July 1960.

[3] Y. T. Lo, "A nonuniform linear array system for the radio telescope at the University of Illinois," 1960 Spring URSI and IRE Joint Meeting, Washington, D.C., subsequently published in the *IRE Trans. Antennas Propag.*, vol. AP-9, pp. 9–16, January 1961, under the title, "The University of Illinois radio telescope," by G. W. Swenson and Y. T. Lo.

[4] A. L. Maffett, "Array factors with nonuniform spacing parameter," *IRE Trans. Antennas Propag.*, vol. AP-10, pp. 131–136, March 1962.

[5] M. G. Andreason, "Linear arrays with variable interelement spacings," *IRE Trans. Antennas Propag.*, vol. AP-10, pp. 137–143, March 1962.

[6] A. Ishimaru, "Theory of unequally spaced arrays," *IRE Trans. Antennas Propag.*, vol. AP-10, pp. 691–702, November 1962.

[7] J. L. Yen and Y. L. Chow, "On large nonuniformly spaced arrays," *Can. J. Phys.*, vol. 41, p. 1, January 1963.

[8] A. Ishimaru and Y. S. Chen, "Thinning and broadbanding antenna arrays by unequal spacings," *IEEE Trans. Antennas Propag.*, vol. AP-13, pp. 34–42, January 1965.

[9] G. Bernard and A. Ishimaru, *Tables on the Anger and Lommel-Weber Functions*, Seattle: University of Washington Press, 1962.

[10] Y. L. Chow and J. L. Yen, "Grating plateaux of planar nonuniformly spaced arrays," presented at the 1964 Fall URSI Meeting, Urbana, Il.

[11] M. I. Skolnik, G. Nemhauser, and J. W. Sherman, III, "Dynamic programming applied to unequally spaced arrays," *IEEE Trans. Antennas Propag.*, vol. AP-12, pp. 35–43, January 1964.

[12] Y. T. Lo, "On the theory of randomly spaced antenna arrays," *Tech. Rep. 1*, Antenna Lab., Dept. of Electr. Eng., Univ. of Illinois, Urbana, under NSF G 14894, 1962. Part of this report appeared in "A mathematical theory of antenna arrays with randomly spaced elements," *IEEE Trans. Antennas Propag.*, vol. AP-12, pp. 257–268, May 1964.

[13] Y. T. Lo, "A probabilistic approach to the problem of large antenna arrays," *Radio Sci.*, vol. 68D, pp. 1011–1019, September 1964.

[14] R. F. Harrington, "Side lobe reduction by nonuniform element spacing," *IRE Trans. Antennas Propag.*, vol. AP-9, pp. 187–192, March 1961.

[15] Y. V. Baklanov, V. L. Pokrovshi, and G. I. Surdotovich, "A theory of linear antennas with unequal spacing," *Radio Eng. Electron. Phys.*, no. 6, pp. 905–913, June 1962.

[16] S. J. Rabinowitz and R. F. Kolar, "Statistical design of space-tapered arrays," presented at the 1962 Twelfth Annual Symposium on USAF Antenna Res. and Dev. Prog., Univ. of Illinois, Urbana.

[17] M. I. Skolnik, J. W. Sherman, III, and F. C. Ogg, Jr., "Statistically designed density-tapered arrays," *IEEE Trans. Antennas Propag.*, vol. AP-12, pp. 408–417, July 1964.

[18] T. M. Maher and D. K. Cheng, "Random removal of radiators from large linear arrays," *IEEE Trans. Antennas Propag.*, vol. AP-11, pp. 106–111, March 1963.

[19] Y. T. Lo, "Side lobe level in nonuniformly spaced antenna arrays," *IEEE Trans. Antennas Propag. (Communications)*, vol. AP-11, p. 511, July 1963.

[20] Y. T. Lo, "High-resolution antenna arrays with elements at quantized random spacings," presented at the 1964 International Conference on Microwaves, Circuit Theory, and Information Theory, Tokyo.

[21] Y. L. Chow, "On grating plateaux of nonuniformly spaced arrays," *IEEE Trans. Antennas Propag.*, vol. AP-13, pp. 208–215, March 1965.

[22] Y. T. Lo and S. W. Lee, "A study of spaced-tapered arrays," *IEEE Trans. Antennas Propag.*, vol. AP-14, pp. 22–30, January 1966.

[23] Y. T. Lo and R. J. Simcoe, "An experiment on antenna arrays with randomly spaced elements," *IEEE Trans. Antennas Propag.*, vol. AP-15, pp. 231–235, March 1967.

[24] V. D. Agrawal and Y. T. Lo, "Mutual coupling in phased arrays of randomly spaced antennas," *IEEE Trans. Antennas Propag.*, vol. AP-20, pp. 288–295, May 1972.

[25] A. R. DiDonato and M. P. Jarnagin, "Integration of the general bivariate Gaussian distribution over an offset ellipse," *NWL Report 1710*, Naval Weapons Laboratory, Dahlgren, Va., 1960.

[26] S. O. Rice, "Mathematical analysis of random noise," *Bell Syst. Tech. J.*, vol. 24, p. 46, 1945.

[27] P. B. Patnaik, "The noncentral χ^2 and F distributions and their application," *Biometrica*, vol. 36, pp. 202–232, 1949.

[28] K. Pearson, *Tables of Incomplete Gamma Functions*, Department of Scientific and Industrial Research, Cambridge: Cambridge University Press, 1934.

[29] K. Karhunen, "Über lineare methoden in der wahrscheinlichkeits rechnung," *Ann. Acad. Sci. Fennicae*, ser. A, no. I, pp. 37–79, 1947.

[30] W. N. Christiansen and J. H. Hogbem, "A design for the Benelux Cross antenna," *BCAP Tech. Rep. No. 3*, Benelux Cross Antenna Project, Sterrewacht, Leiden, Netherlands.

[31] D. B. Owen, *Handbook of Statistical Tables*, pp. 535–536, Reading: Addison-Wesley Pub. Co., 1962.

[32] E. Parzen, *Modern Probability Theory and Its Applications*, New York: John Wiley & Sons, 1960.

[33] N. Amitay, V. Galindo, and C. P. Wu, *Theory and Analysis of Phased Array Antennas*, New York: Wiley-Interscience, 1972.

[34] L. W. Lechtreck, "Effects of coupling accumulation in antenna arrays," *IEEE Trans. Antennas Propag.*, vol. AP-16, pp. 31–37, January 1968.

[35] J. M. Stone, *Radiation and Optics*, New York: McGraw-Hill Book Co., pp. 146–152, 1963.

[36] M. I. Skolnik, "A method of modeling array antennas," *IEEE Trans. Antennas Propag.*, vol. AP-11, pp. 97–98, January 1963.

[37] V. D. Agrawal and Y. T. Lo, "Anomalies of dielectric-coated gratings," *Appl. Opt.*, vol. 11, pp. 1946–1951, September 1972.

[38] A. R. Panicali and Y. T. Lo, "A probabilistic approach to large circular and spherical arrays," *IEEE Trans. Antennas Propag.*, vol. AP-17, pp. 514–522, July 1969.

Chapter 18

Practical Aspects of Phased Array Design

Raymond Tang
Hughes Aircraft Company

CONTENTS

Raymond Tang is the manager of the Antenna Array Laboratory, Electromagnetic Laboratories, Surveillance and Sensor Systems Division, of Hughes Aircraft Company. He received the BSEE degree from the Polytechnic Institute of Brooklyn, and the MSEE degree from the University of Southern California.

During his 30 years at Hughes Aircraft Company Mr. Tang has been concerned with microwave antennas and components. He has participated in the design and development of various types of electronic scanning antennas, such as frequency-scan, phase-scan, and optically scanning lenses. In recent years he has been actively involved in the development of wideband phased arrays and limited-scan phased arrays. He has also been engaged in the development of diode and ferrite phase shifters, switches, and solid-state transmit/receive modules.

Mr. Tang holds 12 patents and has authored or coauthored 15 technical publications. He is a member of the IEEE, PGAP, PGMTT, PGED, and Eta Kappa Nu fraternity.

1. Introduction

The intent of this chapter is to provide the reader with a basic understanding of the practical aspects of phased array antenna design. The theory of phased arrays has been covered in the preceding chapters. In this chapter a treatment of the various design considerations and trade-offs is given, so that the antenna designer can arrive at an optimum antenna configuration in order to meet a given set of radar system requirements. The topics that will be covered are

(a) design specifications and procedure for phased array antennas
(b) selection criteria for array components
(c) effects of component errors on array performance

To establish a common basis of understanding, let us first define the basic components in a phased array antenna. As shown in Fig. 1, the phased array antenna consists of an array of radiating elements with each radiating element connected to a phase shifter. The phase shifters control the phase of the radiated signals at each element to form a beam at the desired direction θ_0. A beam-forming network, commonly called a *feed network*, is used to distribute the output signal from the transmitter to the radiating elements and to provide the required aperture distribution for beam shape and side lobe control. Phase shifter drivers provide the required control/bias currents and voltages for each phase shifter for steering the beam to the desired scan angle θ_0. The control signals (or phase words) for the drivers are calculated by the beam-steering computer and stored in the serial shift registers. When the beam is ready to be scanned, the beam-forming trigger signal causes the stored phase words in the serial shift registers to dump into the parallel latching registers, which in turn set the drivers and phase shifter for the desired scan angle. Using this type of phased array the radar is capable of performing the following functions:

1. Rapid and accurate beam scanning; typically the beam-switching time is 10 to 40 μs
2. Search and automatic target tracking over a hemispherical scan coverage by using four planar array faces
3. Perform multiple functions such as surveillance, multiple target tracking, target illumination and missile guidance, terrain following and avoidance, ground mapping, etc.
4. Pulse-to-pulse frequency and/or beam agility
5. Beam shaping and/or polarization flexibility
6. Low peak and average side lobe levels, typically −40 dB peak and −55 dB average
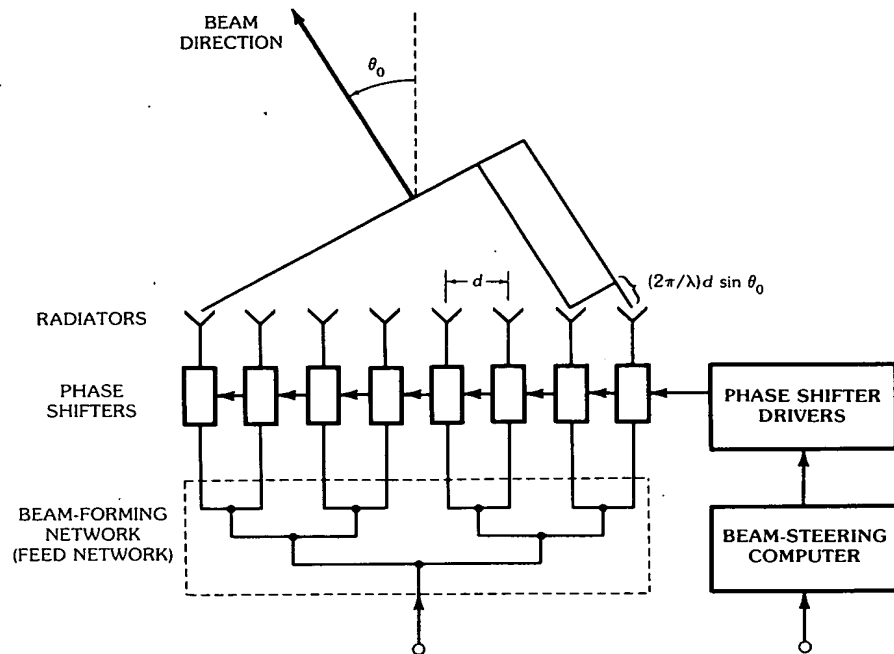
Fig. 1. Basic components of a phased array antenna.

7. High power transmission with multiple distributed transmitters
8. Electronic beam stabilization on moving platforms

With this simplified description of the basic functions of a phased array antenna, let us now proceed to the discussion of the design specifications of phased arrays.

2. Design Specification and Procedure of Phased Array Antennas

The design specifications of a phased array antenna are usually determined by the overall radar system requirements. These requirements are given in terms of radar performance requirements, physical requirements, operating environmental requirements, producibility, maintainability, and reliability requirements. A detailed listing of all the requirements, showing the breakdown of each category, is given in Chart 1.

The antenna engineers, working together with the system and mechanical design engineers, must perform a trade-off study of these requirements (as shown in Chart 1) in order to establish a set of antenna specifications that would satisfy all the radar system requirements at minimum cost. In other words, the antenna requirements must not be overspecified so that the cost would not be affordable. For example, the number of simultaneous beams, beam-switching speed, beamwidth, and total transmitted power can be traded against each other to simplify the

Chart 1. Design Requirements of Phased Array Antennas

1. Performance Requirements
   spatial scan coverage
   tunable and instantaneous bandwidth
   beamwidth
   peak and average side lobe level
   antenna gain
   polarization
   peak and average power
   beam-switching speed
   prime power
   number of simultaneous beams
   beam shape

2. Physical Requirements
   size
   weight
   transportability
   mobility—setup time and march time

3. Environmental Requirements
   operating temperature range
   shock and vibration loads
   humidity, salt, fog, and fungus
   overpressure

4. Producibility, Maintainability, and Reliability
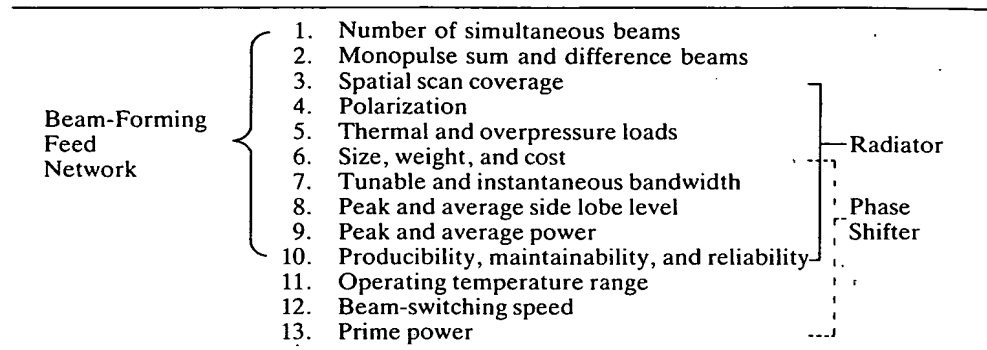
5. Cost (Affordability)

antenna requirements without sacrificing the required power aperture product for a given radar search mode. Once the antenna requirements are specified, the next step is to formulate and draw an overall antenna schematic diagram showing all the functional subassemblies of the antenna system. The subsequent step is to select the array components for the various functional subassemblies that would best meet the system requirements in terms of performance and cost. Following the component selection, the next step is to perform an error analysis to determine the allowable tolerances of these components that would meet the antenna performance requirements. These tolerance requirements are then used as the performance and physical specifications for the design, development, fabrication, and acceptance testing of these components. Detailed discussions on the selection criteria of array components and error analysis follow in Sections 3 and 4.

3. Selection Criteria of Array Components

The three major components of a phased array antenna are the radiators, phase shifters, and beam-forming feed network. Some of the commonly used criteria in selecting these components for a given phased array application are shown in Chart 2.

The requirements in Chart 2 influence the selection of array components in different ways. For example, the selection of the type of radiator is mainly

Chart 2. Selection Criteria of Array Components

Beam-Forming Feed Network
{
1. Number of simultaneous beams
2. Monopulse sum and difference beams
3. Spatial scan coverage
4. Polarization
5. Thermal and overpressure loads
6. Size, weight, and cost
7. Tunable and instantaneous bandwidth
8. Peak and average side lobe level
9. Peak and average power
10. Producibility, maintainability, and reliability
11. Operating temperature range
12. Beam-switching speed
13. Prime power

— Radiator
Phase Shifter

determined by the requirements of items 3 through 10, whereas the selection of the type of phase shifter is mainly determined by the requirements of items 6 through 13, and the selection of feed network is determined by items 1 through 10. As shown in Chart 2, some of the requirements are unique to only one of the components while the others affect two or all three components. For example, the requirements of beam-switching speed, operating temperature range, and prime power affect only the phase shifter selection, whereas the frequency bandwidth, side lobe, and power level requirements affect all three components. In general, there are many combinations of antenna component specifications that can result in the same overall system performance. These nonunique component requirements allow the antenna designer to perform trade-offs in selecting the component to arrive at an optimum design in terms of meeting performance requirements at minimum cost. A detailed discussion of the various trade-offs available in component selection is given in the following sections.

Radiator Selection

Types of Radiators—Before we begin the discussion on radiator selection, let us first review the various types of radiators that are commonly used in phased arrays. The basic types of phased array radiators are listed below:

1. Open-ended waveguide radiators
2. Dipole radiators
3. Waveguide slot radiators
4. Disk and patch radiators

The open-ended waveguide radiator comes in two basic forms, namely, the rectangular and the circular waveguide radiators. The rectangular waveguide radiator is usually used for linear polarization applications, whereas the circular waveguide radiator is frequently used for dual linear or circular polarization applications. The rectangular waveguide radiator can be packaged into very close spacing in the E-plane of the waveguide (less than 0.5λ) by using reduced height waveguide, thus allowing a very large scan coverage in the E-plane. The H-plane scan is restricted by the width of the guide as determined by the desired ratio of the operating frequency to the cutoff frequency. The rectangular waveguide radiator,

however, can be packaged into an equilateral triangular element lattice arrange-
ment in order to provide conical scan coverage as in the case of the circular wave-
guide radiators, thus allowing an increase in H-plane scan coverage. The various
possible lattice arrangements for both the rectangular and circular waveguide
radiators are shown in Fig. 2. The dimension d in Fig. 2 is usually in the order of
one-half wavelength at the high end of the operating frequency band. For all cases
of lattice arrangements the spacing between the elements can be reduced by
dielectrically loading and/or ridge loading the waveguides.

The two common types of dipole radiators are the microstrip dipole [1, 2] and
the coaxial dipole as shown in Fig. 3. In the case of the microstrip dipole the dipole
wings are either etched or printed on a dielectric substrate, such as a copper-clad
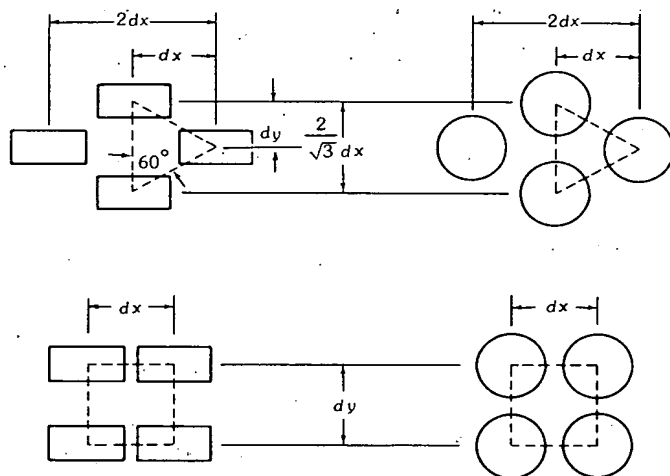Teflon-fiberglass board, or on an alumina (Al_2O_3) substrate. These dipole wings

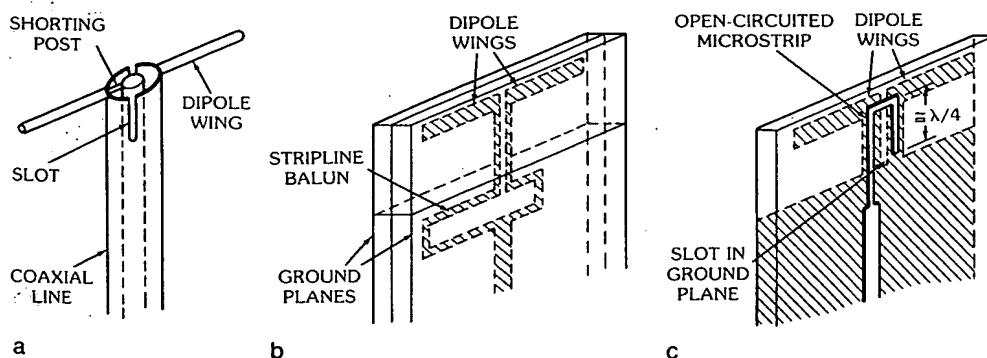**Fig. 2.** Lattice arrangements of waveguide radiators.

Fig. 3. Common types of dipole radiators. (*a*) Coaxial dipole. (*b*) Stripline dipole.
(*c*) Microstrip dipole.

are excited by means of a microstrip balun. In the case of the coaxial dipole the dipole wings are excited by means of a slotted coaxial transmission line as shown in Fig. 3. These dipole radiators can be packaged in a large two-dimensional array just as in the case of the rectangular waveguide radiators.

.There are many different types of slot radiators. In the case of slots excited by waveguide transmission lines, there are shunt slots [3] which are cut along and parallel to the centerline of the broadwall of the waveguide and series inclined [4] as well as noninclined slots [5] which are cut along the sidewall of the waveguide (see Fig. 4). The noninclined slot, which is a magnetically coupled transverse slot [5], does not have cross polarization as in the case of the inclined slot. There are also slot radiators which are etched on the ground plane side of a microstrip transmission line. The operating bandwidth of the slot radiators, as in the case of the dipole radiators, is less than that of the open-ended waveguide radiators.

The disk and patch radiators are not commonly used in ground-based or shipboard applications. These radiators are more commonly used in conformal arrays for airborne or missile applications where the depth of the array is of cardinal importance. The two common types are the microstrip excited-patch radiator [6,7] and the coaxial excited-disk radiator [8] as shown in Fig. 5. The coaxial excited-disk radiator has much larger bandwidth than that of the microstrip excited-patch radiator.

Selection Considerations of Radiators—With the knowledge of the various types of available radiators, let us now proceed to a discussion on how to select a radiator for a given application. In general, the radiator must be selected on the basis of meeting all the antenna performance, physical packaging, and environmental requirements at minimum cost. Some of these requirements and the corresponding selection considerations are given in Chart 3.

The allowable area per element requirement is determined by choosing the proper element spacing and lattice to avoid the formation of grating lobes over the entire volumetric scan coverage. The element lattice is usually chosen to maximize
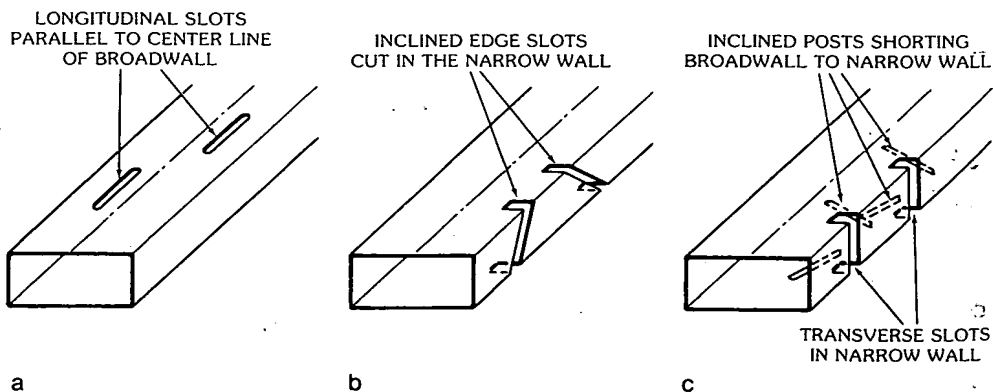

Fig. 4. Various types of slot radiators. (a) Broadwall shunt slots. (b) Inclined edge slots. (c) Magnetically coupled transverse slots.
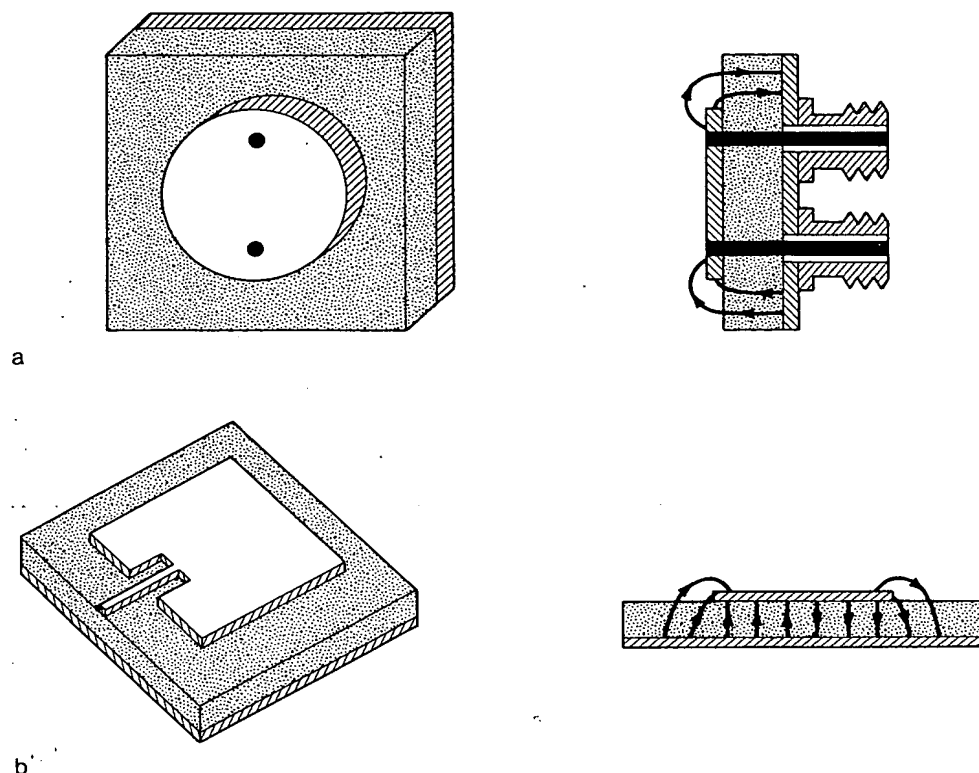
a

b

Fig. 5. Microstrip radiators. (*a*) Coaxial excited-disk radiator. (*After Byron [8]; reprinted by permission, © 1972 Artech House, Inc.*) (*b*) Microstrip excited-patch radiator. (*After Carver and Mink [1], © 1960 IEEE*)

the allowable area per element corresponding to the required scan coverage. For example, a triangular lattice should be used for a conical scan coverage and a rectangular lattice for a rectangular scan coverage. The grating lobe locations for a rectangular lattice are given by

$$\sin\theta\,\cos\phi - \sin\theta_0\,\cos\phi_0 = \pm\frac{\lambda}{d_x}p \qquad (1a)$$

$$\sin\theta\,\sin\phi - \sin\theta_0\,\sin\phi_0 = \pm\frac{\lambda}{d_y}q \qquad (1b)$$

where

θ_0, ϕ_0 = the scan direction of the main beam

d_x, d_y = element spacing along the x and y axis

$p, q = 0, 1, 2, \ldots$

Chart 3. Selection Considerations of Radiators

Design Requirements	Selection Considerations
Allowable area per element element spacing lattice operating frequency	Dipoles, disk, and patch radiators for X-band or lower. Waveguide and slot radiators for S-band or higher
Aperture impedance matching scan coverage frequency bandwidth	Dipoles and waveguides for 10- to 25-percent bandwidth. Waveguides for 10-percent to octave bandwidth
Polarization linear or circular single or dual	Dipole and rectangular waveguide for linear. Cross dipole and circular waveguide for dual linear or dual circular
Power-handling capacity peak and average	Dipole and waveguide for 1 kW or less. Waveguide for 1 kW or more
Environmental thermal, shock, vibration, etc.	Dipole and waveguide for non-nuclear hardened. Waveguide for nuclear hardened
Cost, reliability, and producibility	Dipoles for integrated subarray modular construction

For a triangular lattice the grating lobes are located at

$$\sin \theta \cos \phi - \sin \theta_0 \cos \phi_0 = \pm \frac{\lambda}{2d_x} p \qquad (2a)$$

$$\sin \theta \sin \phi - \sin \theta_0 \sin \phi_0 = \pm \frac{\lambda}{2d_y} q \qquad (2b)$$

where $p + q$ is even.

In order to prevent the grating lobe formation the maximum projected element spacing d along a given scan plane must satisfy the following formula:

$$\frac{d}{\lambda} \leqq \frac{1}{1 + \sin \theta_{max}} \qquad (3)$$

For a conical scan coverage of a 60° half-angle cone the maximum allowable area per element is approximately $0.3\lambda^2$ as shown in Fig. 2. Once the area per element is established, a radiator must be selected to fit within that area. Since the element spacing is directly proportional to the wavelength of the operating frequency, the dipole radiators are usually used for X-band or lower frequencies and waveguide/slot radiators are used for S-band or higher frequencies. Another requirement for radiator selection is aperture impedance matching over the required scan coverage and operating frequency bandwidth. For a 60° half-angle cone coverage the dipole and waveguide radiators can be reasonably well matched over a 10-percent bandwidth, whereas waveguide radiators [9] can be matched over almost an octave bandwidth. In general, some of the other considerations in radiator selection for meeting the requirements of polarization, power-handling capacity, environment, cost, etc., are given in Chart 3.

Development Procedure of Phased Array Radiators—Once the radiator selection is made in accordance with the requirements of Chart 3, the usual step-by-step procedure to develop this radiator in a two-dimensional array environment is given below:

Step 1

Select an element spacing and lattice that does not formulate grating lobes or surface-wave resonances over the required scan coverage and the operating frequency band.

Step 2

Formulate an analytical model of the radiating aperture and optimize the performance by varying the design parameters, such as element dimensions.

Step 3

Perform aperture matching, such as by using an inductive iris or a dielectric plug in the opening of the waveguide radiator, metallic fences around dipole radiators, or using dielectric sheets in front of the radiating aperture.

Step 4

Using the analytical results from steps 2 and 3, fabricate waveguide simulators to measure and verify the radiation impedance at discrete scan angles.

Step 5

Fabricate a small test array (usually 9×9 elements) and measure the active element pattern of the central element over the required frequency band. This active element pattern is defined as the pattern of an element with all the neighboring elements terminated into matched loads. It describes the variation in array gain G (including aperture mismatch) as a function of beam scan angle:

$$G = \frac{4\pi A}{\lambda^2}\, \eta \cos\theta \, (1 - |\Gamma(\theta)|^2) \tag{4}$$

where

A = area of element multiplied by the total number of elements in the array antenna

η = aperture efficiency corresponding to the amplitude distribution across the array aperture, with $\eta = 1$ for uniform amplitude distribution

θ = beam scan angle

$|\Gamma(\theta)|$ = magnitude of reflection coefficient at scan angle θ

The net gain of the antenna is given by the above gain minus all the other ohmic losses and mismatch losses, such as the phase shifter loss, beam-forming feed network loss, etc.

Step 6

Establish the performance characteristics of the final radiator design by combining the measured impedances of step 4 with the measured active element patterns of step 5.

Phase Shifter Selection

The selection criteria of a phase shifter for a particular phased array application are listed below:

1. Operating frequency and bandwidth (tunable and instantaneous)
2. Peak and average rf power
3. Insertion loss
4. Switching time (reciprocal and nonreciprocal)
5. Drive power
6. Size and weight
7. Phase quantization error
8. Cost and producibility

Some of these criteria are established by radar requirements, while the others are used to compare the relative merits of various phase shifter types. Among all the above criteria the six most often used criteria for selecting a particular phase shifter are the operating frequency, peak and average rf power, switching time, size, weight, and cost. The cost is an important consideration since the phase shifters contribute to one-third of the cost of most phased arrays. The other two-thirds of the total cost are contributed almost equally by the phase shifter drivers and the beam-forming feed network plus the radiators. A more detailed discussion on the selection criteria of the phase shifters will be given after the various available phase shifter types are described.

Phase Shifter Types—The two types of commonly used phase shifters are the semiconductor diode phase shifters [10,11,12] and the ferrite phase shifters [10,11,12]. It is not the intention here to describe the theory of operation of these phase shifters since this subject is well covered elsewhere. This section will, however, describe in detail the performance and physical characteristics of these phase shifters so that a comparison can be made to select the proper phase shifter for a particular radar application. The diode phase shifters are generally digital phase shifters, i.e., the phase states of the phase shifter are in discrete binary phase increments. Fig. 6 shows the binary phase states of a 4-bit diode phase shifter. The
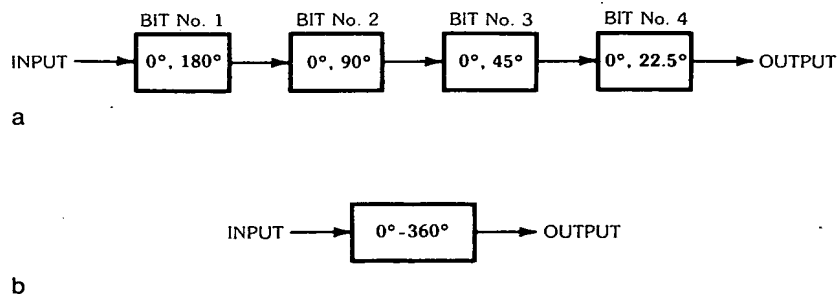

a

b

Fig. 6. Basic types of electronic phase shifters. (*a*) Semiconductor diode phase shifter (digital). (*b*) Ferrite phase shifter (digital or analog).

diode phase shifter uses pin diodes to provide phase shifting either by switching in different line length across a transmission line or by changing from inductive to capacitive loading across the transmission line. Typical phase shifter circuits using pin diodes are shown in Fig. 7. There are analog diode phase shifters [13, 14] containing either varactor diodes or pin diodes. However, these analog diode phase
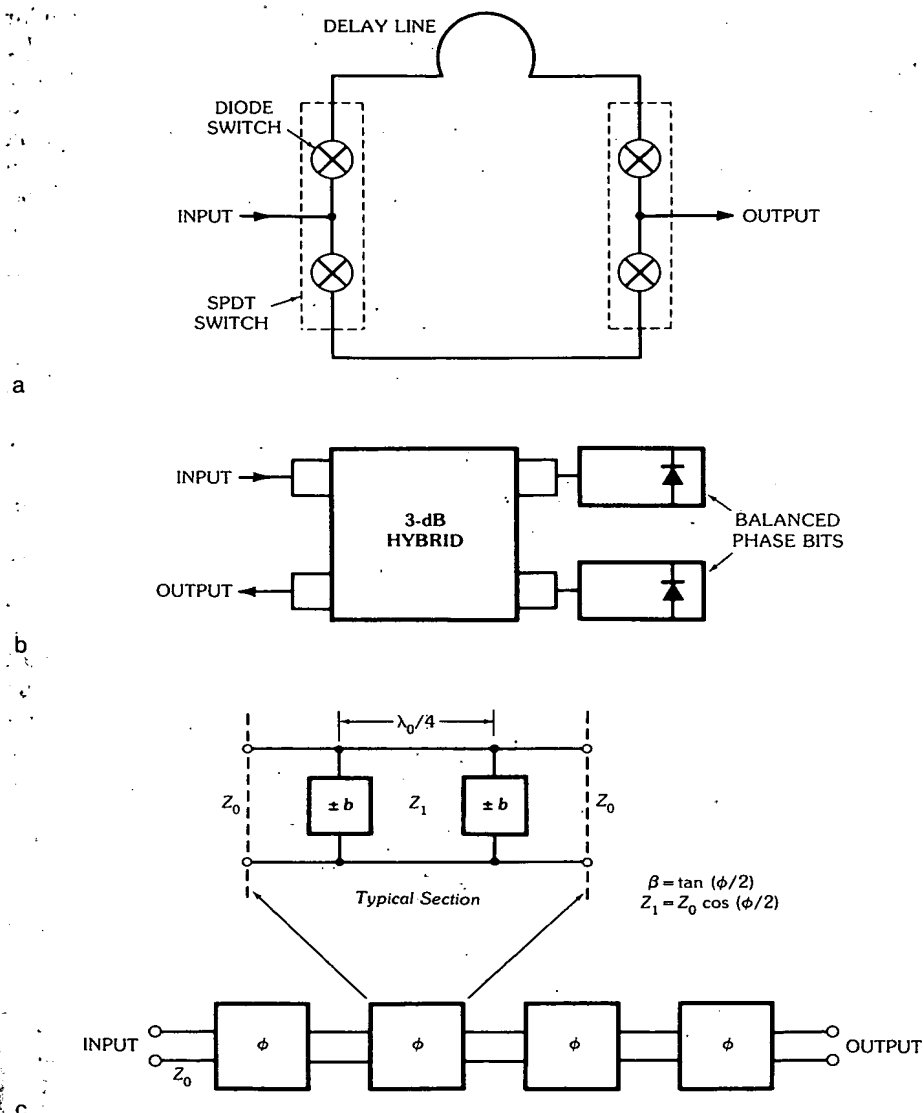
$$\beta = \tan (\phi/2)$$
$$Z_1 = Z_0 \cos (\phi/2)$$

Fig. 7. Circuit designs for diode phase shifter. (*a*) Switched-line phase bit. (*b*) Hybrid-coupled phase bit. (*c*) Loaded-line phase bit. (*After Stark [10],* © *1984; reprinted with permission of McGraw-Hill Book Company*)

shifters are extremely low power devices, typically in the milliwatts range. On the other hand, the ferrite phase shifters can be either digital or analog devices as illustrated in Fig. 8. In general, the two types of commonly used ferrite phase shifters are the nonreciprocal, toroidal ferrite phase shifter [15, 16] and the reciprocal, dual-mode ferrite phase shifter [17, 18]. Fig. 8 shows the basic configurations of these two types of ferrite phase shifters. The toroidal ferrite phase shifter employs the use of a toroidal shaped ferrite bar placed in a rectangular waveguide. A drive wire is inserted longitudinally through the center core of the toroid to provide transverse magnetization in the toroid. Phase shifting is achieved by varying the current in the drive wire, hence varying the biasing magnetic field in the toroid. This phase shifter can operate as an analog device by using a long toroid and varying the phase shift by means of changing the holding current in the drive wire. It can also operate as a digital device by magnetically latching (no
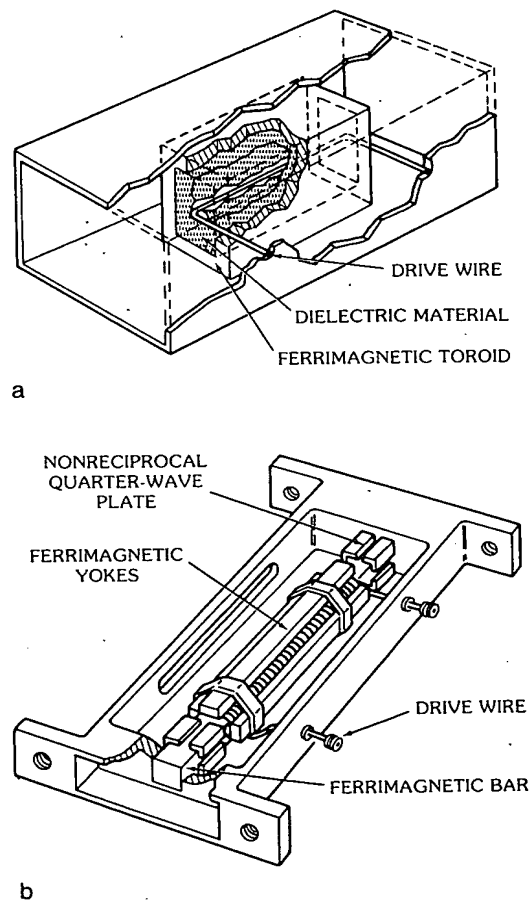
a

b

Fig. 8. Basic ferrite phase shifters. (a) Nonreciprocal twin-slab toroidal type. (b) Reciprocal dual-mode type. (*After Tang and Burns [11]*)

holding current) the toroid to the various minor hysteresis loops. The amount of phase shift is determined by the product of the magnitude and the time duration of the voltage pulse. In applications where fast switching speed is required, the long toroid can be split into smaller sections with the length of each section corresponding to a binary phase bit. In this case each section is magnetized into saturation and is quickly switchable since the volume of ferrite material for each section is significantly smaller. This type of phase shifter is nonreciprocal; hence the phase shift must be reset between the transmit and receive modes of the radar. The dual-mode ferrite phase shifter, however, is reciprocal, and it does not require resetting between transmit and receive. This phase shifter consists of a long metallized ferrite bar in between two nonreciprocal quarter-wave plates. The quarter-wave plate at each end of the ferrite bar converts the incident linearly polarized electric field into a circularly polarized field. This circularly polarized field interacts with the longitudinally magnetized biasing field in the ferrite bar to produce Faraday rotation, resulting in a net phase shift of the wave propagating through the ferrite bar. The amount of phase shift is controlled by the magnitude of the biasing field in the ferrite bar. This device can be used as a digital or analog phase shifter as in the case of the nonreciprocal toroidal phase shifter. However, the switching time of this phase shifter is much longer (50 µs compared with 10 µs for the toroidal phase shifter) due to the eddy current effects of the metal wall around the ferrite bar. There are other types of reciprocal ferrite phase shifters such as the Reggia-Spencer phase shifter [19] and Fox phase shifter [20]. The details of these phase shifters can be found in the references.

Performance Characteristics of Phase Shifters—A comparison of the general characteristics of diode and ferrite phase shifters is shown in Table 1. As shown in this table, most of the diode phase shifters that have been built operate over the frequency range of uhf to X-band, whereas the ferrite phase shifters have been built to operate over the frequency range of S-band to W-band. Ferrite phase shifters of the reciprocal, dual-mode type have been built at 95 GHz with insertion loss of approximately 2.5 dB for 360° of phase shift. The insertion loss of the diode phase shifter varies typically from 0.5 dB at L-band to 1.4 dB at X-band. On the other hand, the insertion loss of the ferrite phase shifter varies typically from 0.6 dB at S-band to approximately 1.0 dB at X-band. The insertion loss of the

Table 1. General Characteristics of Diode and Ferrite Phase Shifters

Parameter	Diode (Digital)	Remanent Ferrite (Analog and Digital)
Frequency	Uhf to X-band	S- to W-band
Insertion loss/2π	0.5 to 1.4 dB	0.6 to 2.5 dB
Temperature sensitivity	Negligible	<0.03 to 0.3%/°C
Peak power	$\leqq 8$ kW	$\leqq 100$ kW
Average power	$\leqq 300$ W	$\leqq 800$ W
Bandwidth	10% to 25%	10% to octave
Switching speed	10 ns to 30 µs	1 to 50 µs
Control power	0.1 W to 0.5 W	20–800 µJ

ferrite phase shifter goes up to approximately 1.4 dB at 30 GHz. A comparison of the insertion loss of the diode and ferrite phase shifters as a function of frequency is shown in Fig. 9. At L-band frequencies or below, the diode phase shifters are used because of their low insertion loss and lower cost. At S-band frequencies the insertion loss of the diode phase shifter is quite comparable to that of the ferrite phase shifter. For example, the insertion loss of the ferrite phase shifter is approximately 0.2 to 0.3 dB lower. Above S-band, however, the disparity in insertion loss becomes significantly more in favor of the ferrite phase shifter. The temperature sensitivity of the diode phase shifter is nil compared to 0.03%/°C to 0.3%/°C for the ferrite phase shifter, depending on the type of ferrite material used. The peak and average power handling capacity of most of the diode phase shifters is approximately 8 kW and 300 W, respectively, compared with 100 kW and 800 W, respectively, for the ferrite phase shifter. The bandwidth of most of the diode phase shifters is typically 10 percent. However, an octave bandwidth can be achieved by using Schiffman coupled circuits [21]. In the case of the ferrite phase shifter an octave bandwidth can also be achieved by using multiple stages of ridge-loaded waveguide transformers. The switching speed of the diode phase shifter varies from 0.5 ns to approximately 30 μs depending on the capacitance of the diode and the type of driver used to switch the diode from forward bias to reverse bias. Typically, the switching speed is approximately 30 μs, using a simple resistive pull-up type of driver circuit. However, the switching speed can be reduced to 10 μs or less when an active pull-up circuit is used. The switching speed for the ferrite phase shifter varies from 1 μs for the individual toroidal bit type to about 50 μs for the long Faraday rotator type. The required control power for the diode phase shifter varies from 0.1 to 0.5 W depending on the amount of forward bias current needed to set the quiescent state of each bit to the constant resistance region of diode I-V characteristics. Forward bias currents can be reduced from the above settings at the expense of a slight increase in insertion loss. The required control energy for the ferrite phase shifter varies from 20 to 800 μJ, depending on the speed with which the phase shifter has to be switched.
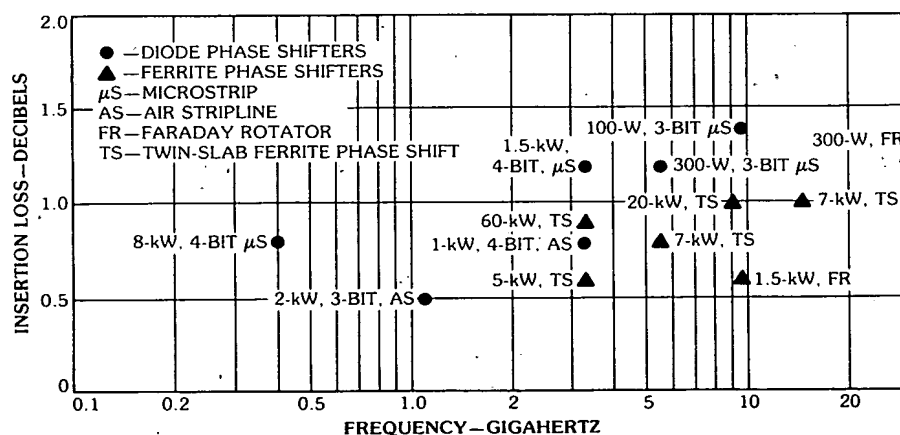

Fig. 9. Insertion loss of diode and ferrite phase shifters. (*After Tang and Burns [11]*)

General Observations in Selecting Phase Shifter Type—Above S-band and at peak power level of 2 kW or more per element, ferrite phase shifters are preferred due to their lower insertion loss. However, in situations where the required rf power is low (less than 2 kW) and size and weight constraints dictate a compact and lightweight package, diode phase shifters are preferred due to their simplicity in construction and lower production cost. For example, cost can be minimized by combining several dipole radiators, diode phase shifters, feed networks, drivers, and logic circuits on a common alumina substrate as an integral subarray module.

Beam-Forming Feed Network Selection

Among all the selection criteria, as stated in Chart 2, the most influential criteria in the selection of a beam-forming feed network for a particular radar application are the following:

1. Number of simultaneous beams
2. Monopulse sum and difference beams
3. Peak and average side lobe level
4. Tunable and instantaneous bandwidth
5. Peak and average power
6. Size, weight, and cost

For most applications the above criteria can be narrowed down from the multitude of possible design choices to a few practical design selections. For example, if a large number of multiple simultaneous beams are required, the possible design choices for the beam-forming feed network would be either a multiple-beam optical feed (such as the circular pillbox feed, Rotman lens feed, etc.) or a constrained matrix feed (such as the Butler or Blass matrix feed). Once the choices are narrowed down to only a few possible design approaches, a comparison of these approaches can then be made in terms of side lobe performance, bandwidth, size, weight, and cost in order to determine the optimum design approach. In order to select the optimum feed for a particular application it is necessary for the antenna designer to have a broad and comprehensive knowledge of the various types of available beam-forming feed networks. This subsection summarizes some of the basic types of beam-forming feed networks and their performance capabilities and limitations. A detailed discussion of the various feed network designs is given in Chapter 19, on beam-forming feed networks.

In general, all the beam-forming feed networks can be classified into the following three basic categories:

Category 1—Space feeds:
                transmission type
                reflection type
Category 2—Constrained feeds:
                series feed
                parallel feed
Category 3—Hybrid feeds (a combination of space and constrained feeds)

Space Feeds—In the category of space feeds there are two basic types, namely, the transmission type [22] and the reflection type [23]. In the case of the transmission

type the array elements and phase shifters are connected to an array of pickup elements, which are in turn illuminated by a feed horn located at a given focal distance away from the aperture of the pickup array (see Fig. 10). The ratio of the focal distance to the diameter of the radiating aperture varies nominally from 1/2 to 1. The array of pickup elements in conjunction with the phase shifters and the radiating elements forms an electronic scanning feedthrough lens (transmission lens). The phase shifters are set to provide the required phase increments between the radiating elements for beam scanning and for correcting the phase error introduced by the spherical phase front from the feed horn. When digital phase shifters (constant phase with frequency type) are used in the lens this spherical phase front correction approach can suppress the peak error side lobe introduced by the phase quantization error of the digital phase shifter. A detailed discussion of the effect of phase quantization error on array performance is given by Miller [24]. The tunable and instantaneous bandwidths of this space-fed antenna are typically 10 percent and 40 MHz, respectively. When the time-delay type of phase shifters are used, this antenna system has extremely wide instantaneous bandwidth limited only by the performance of the components. An instantaneous bandwidth of 1000 MHz is achievable. Monopulse sum and difference beams can be formed by using a cluster of feed horns at the focal point. For example, a cluster of 2×2 feed horns combined with magic tees can provide a sum beam, an elevation difference beam, and an azimuth difference beam as shown in Fig. 10. Multiple simultaneous beams can also be formed by using feed horns displaced from the focal point. The number of multiple beams that can be formed, however, is limited by the spherical aberration effects. Various methods of correcting the spherical aberration are treated by Rotman and Turner [25]. Since the signal distribution from the feed horns to the elements is through free space, this space feed is probably the simplest
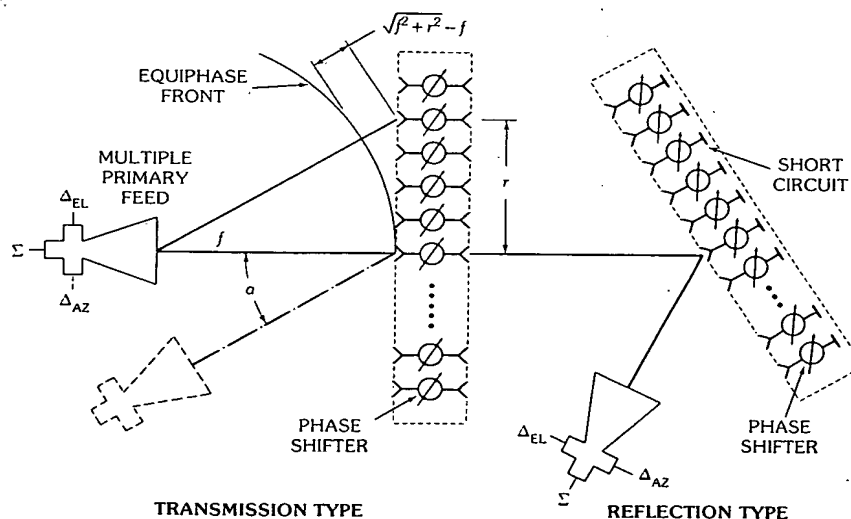

Fig. 10. Space feed systems. (*After Cheston and Frank*, Array Antennas *[22]* TG-956, *JHU/APL, Laurel, MD, March 1968*)

way to form multiple simultaneous beams. In the case of the reflection type of space feed (see Fig. 10), the concept is the same as that of the transmission type except a short is placed behind each phase shifter so that the signals are reflected and reradiated from the pickup elements. Since the signal travels back and forth through the phase shifters twice, the amount of required phase shift at each element is half of that of the transmission case for the same scan angle. However, the peak power requirement for the phase shifter is quadrupled because of the standing wave. In order to minimize the blockage effect of the feed horn, the feed horn has to be offset with respect to the axis of the reflective lens.

Space feeds have several disadvantages. One of them is the large physical volume required by the space feed. Another is the multiple reflection effects between the mismatches of the two lens apertures as a function of beam scan angle. This effect can be minimized by performing the best impedance matching possible for the two apertures over the required scan coverage and frequency band. A less obvious problem with space feeds is the difficulty of connecting control wires of the phase shifters in the lens because of the lack of access from the front or the back of the lens. The only access is through the peripheral edge of the lens.

Constrained Feeds—In the category of the constrained feeds there are two basic types, namely, the series feeds and the parallel feeds. By definition the radiating elements are fed serially in a series feed, while they are fed in parallel in a parallel feed. Typical examples of the series feed are shown in Fig. 11. The basic form of a series feed is shown in Fig. 11a. The input signal is fed from one end of the feed and the other end is terminated into a matched load. The input signal is then coupled serially through directional couplers to the phase shifters and radiating elements. Since the transmission line length increases from the input to the following radiating elements, there is a progressive phase change between the radiating elements with frequency variations; thus the beam scans with frequency change. The amount of beam squint with frequency is given by

$$\text{beam squint} = \frac{\Delta f}{f} \frac{1}{\cos \theta_0} \tag{5}$$

where Δf is the amount of frequency change and θ_0 is the nominal scan angle. A detailed discussion of the bandwidth limitations of series and parallel feeds is given by Frank [26]. The beam squint, however, can be brought back to the original position by resetting the phase shifters at each radiating element. One of the problems with this type of series feed is that the mismatches from the radiating elements, phase shifters, and couplers can all add up in phase at the frequencies when the path length between the elements is a multiple of a half-wavelength. In order to provide sum and difference beams for monopulse tracking the feed input is moved from the end to the center of the series feed as shown in Fig. 11b. The two halves of the feed are fed by a magic tee so that the sum port of the magic tee provides in-phase excitation of the two halves and the difference port provides out-of-phase excitation to generate a difference beam. Since the same coupling coefficients of the couplers are used for both the in-phase and the out-of-phase excitations, the side lobes for the sum and difference beams cannot be op-
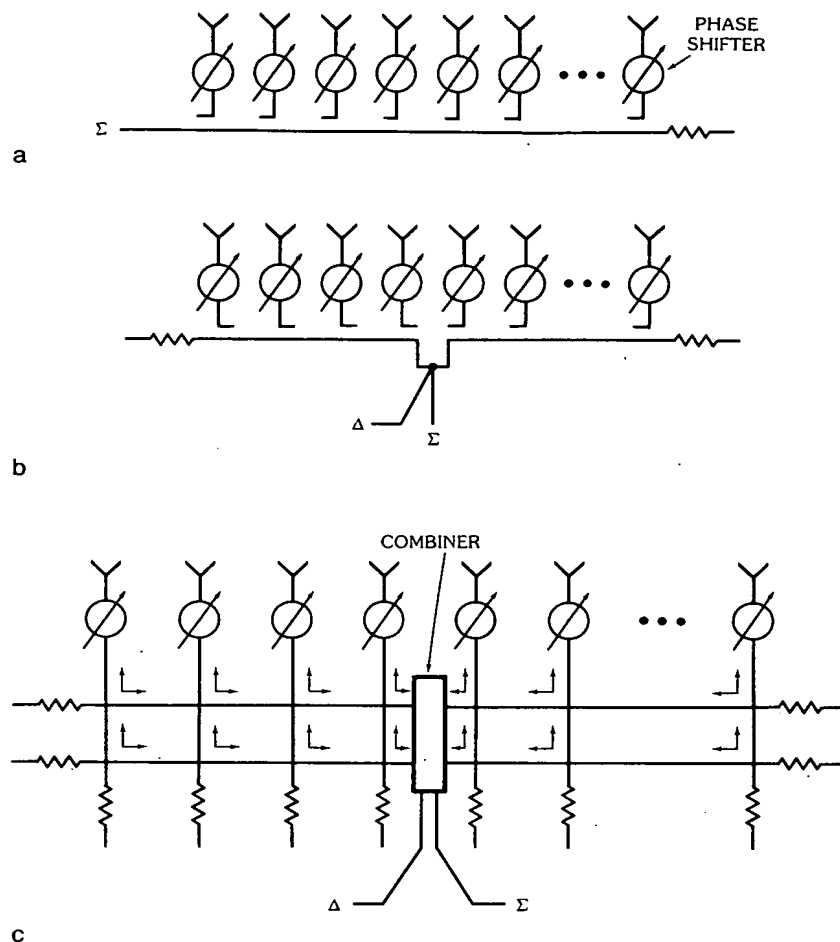
Fig. 11. Constrained feeds (series feed networks). (*a*) End feed. (*b*) Center feed. (*c*) Center fed with separately optimized sum and difference channels. (*d*) Equal path length feed. (*e*) Series phase shifters. (*After Cheston and Frank,* Array Antennas *[22], TG-956, JHU/APL, Laurel, MD, March 1968*)

timized simultaneously. For low side lobes the sum beam requires an even distribution, such as the Taylor distribution [27], and the difference beam requires an odd distribution, such as the Bayliss distribution [28]. In order to achieve low side lobes for both sum and difference beams a center-fed dual series feed (see Fig. 11c) is used. The excitations of the two parallel series feeds are adjusted to optimize the side lobes for both the sum and the difference beams. A detailed description of the dual series feed is given by Lopez [29]. At broadside beam position the two halves of the center-fed series feed scan in opposite directions with frequency. This results in a beam broadening with no change in direction. If the two halves scan too
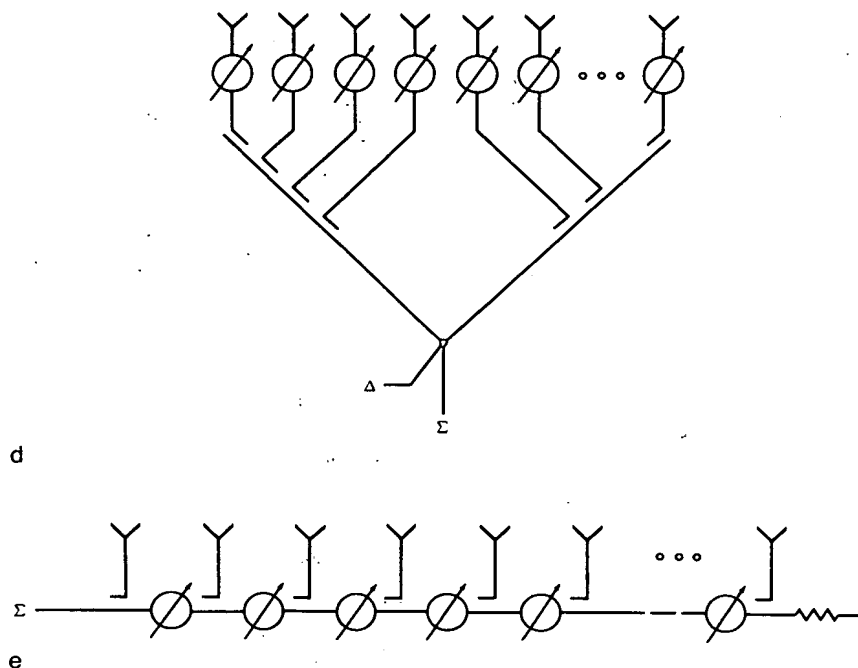
d

e

Fig. 11, *continued.*

far apart, it could even result in a splitting of the beam. Therefore the bandwidth of the center-fed series feed is significantly worse than that of the parallel feed. However, at large scan angles such as 60° from broadside the bandwidth of the center-fed series feed is quite comparable to that of a parallel feed (see Frank [26]). In order to broaden the bandwidth at broadside for a center-fed array the path length from the feed input to the radiating elements can be made equal as shown in Fig. 11d. In this case the bandwidth is only limited by the in-phase addition of the mismatches of the couplers. For a series-fed array the phase shifters can be also inserted serially between the couplers along the series feed line as shown in Fig. 11e. In this design the amount of required phase shift for each phase shifter is greatly reduced compared with that of the phase shifters at the radiating elements. However, the insertion losses of these serial phase shifters are additive, resulting in a reduction in array gain and an increase in side lobe level from the asymmetrical amplitude distribution.

Typical examples of the parallel feeds are shown in Fig. 12. The basic form of a parallel feed is shown in Fig. 12a. In this basic form the input signal is divided in a corporate tree fashion to all the radiating elements. The path lengths from the input to each output are made equal. The bandwidth at broadside is ideally infinite, except for the practical limitations of such components as the couplers, phase shifters, and radiators. When the beam is scanned away from broadside the beam scans with frequency. The amount of beam squint with frequency is given by
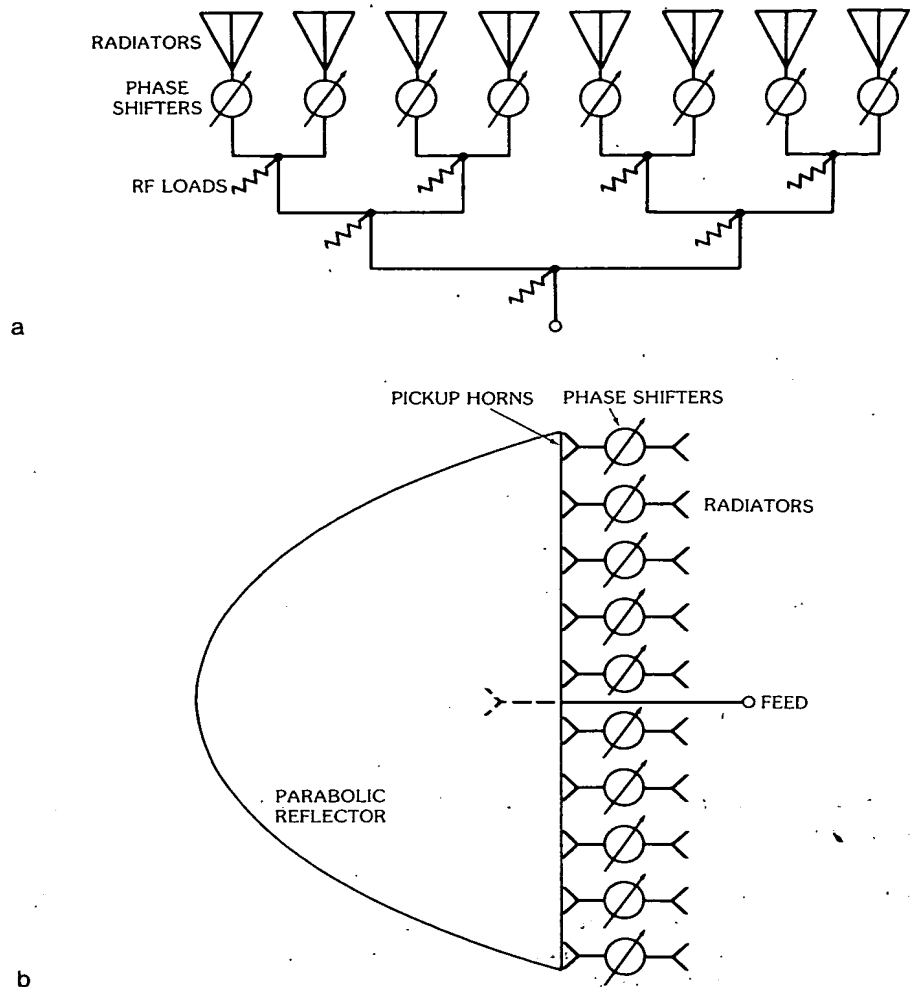
RADIATORS

PHASE
SHIFTERS

RF LOADS

a

PICKUP HORNS   PHASE SHIFTERS

RADIATORS

FEED

PARABOLIC
REFLECTOR

b

Fig. 12. Constrained feeds (parallel feed networks). (a) Corporate feed. (b) Pillbox feed. (After Rotman [34], © 1958 IEEE) (c) Butler matrix feed (multiple beams). (After Butler and Lowe [30]) (d) Time-delay matrix feed (multiple beams). (After Blass [31], © 1960 IEEE)

$$\text{beam squint} = \frac{\Delta f}{f} \tan \theta_0 \qquad (6)$$

The bandwidth at 60° scan (see Frank [26]) is given by

$$\text{percent bandwidth} = \text{beamwidth in degrees}$$

When magic tees or hybrid couplers are used at each level of the corporate feed the mismatches from the radiating elements are reasonably well isolated from each other. Hence the parallel corporate feed does not have the additive effect as in the
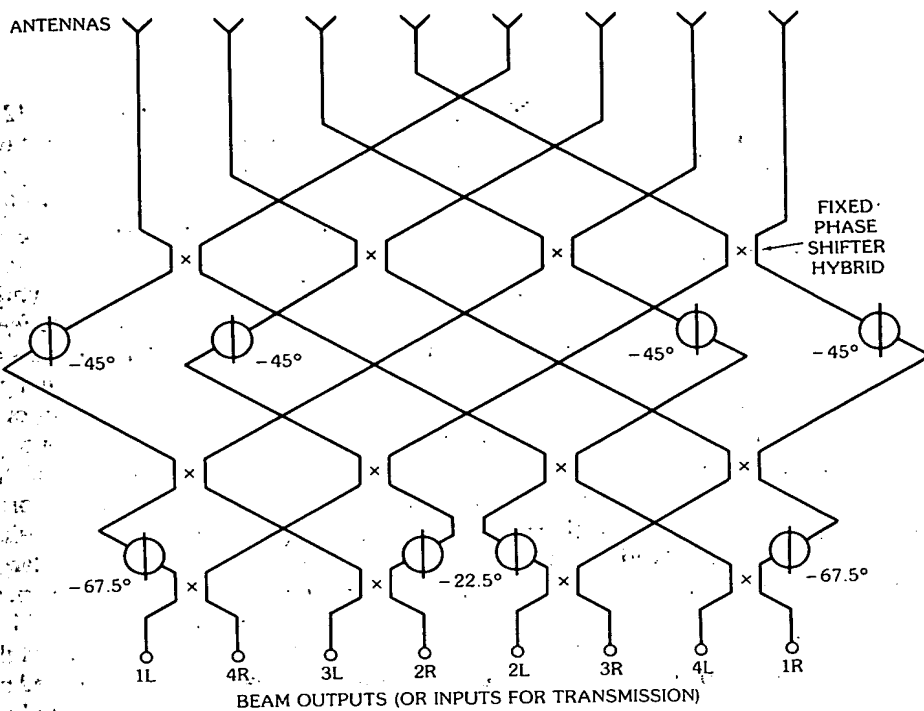
ANTENNAS

FIXED
PHASE
SHIFTER
HYBRID

−45° −45° −45° −45°

−67.5° −22.5° −67.5°

1L   4R   3L   2R   2L   3R   4L   1R

BEAM OUTPUTS (OR INPUTS FOR TRANSMISSION)

$\Delta\theta$

z

D

1
RADIAN

$\Delta\theta$

BEAM 2
BEAM 1
BEAM 0 (BROADSIDE)
BEAM −1
BEAM −2
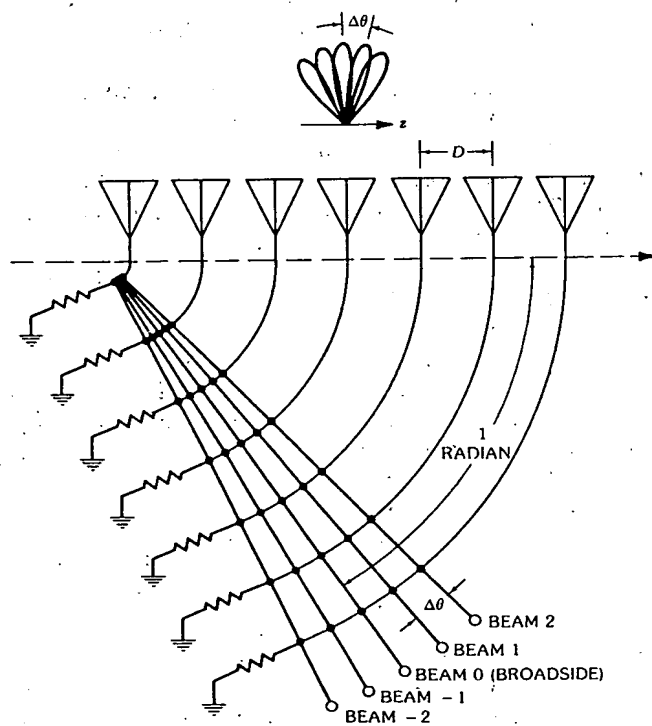
Fig. 12, *continued*.

case of the series feed. An optical form of the corporate feed is shown in Fig. 12b. In this optical configuration the input feed horn illuminates a parabolic reflector, which in turn produces a reflected plane wave illuminating the pickup horns located at the aperture of the reflector. The signals received by the pickup horns are fed into the phase shifters and radiating elements the same way as the corporate feed. The fact that the power distribution from the feed input to the radiating elements is accomplished optically with the parabolic reflector, instead of with the hybrid couplers as in the case of the corporate feed, enhances the bandwidth of the feed system. However, the freedom in controlling the amplitude taper of the signals at the radiating elements is restricted to those provided by the primary illumination pattern of the feed horn. Typically the amplitude distribution is of the form of a truncated $\cos^n x$ distribution, where n is an integer greater than 1. This form of amplitude taper is achieved by using multiple feed horns at the focal point of the reflector. For example, a cosine distribution is achieved by using two feed horns displaced symmetrically on both sides of the focal point. Higher-order cosine distributions can be achieved by employing three or more feed horns. When a large number of feed horns are used to generate the desired amplitude taper, the aperture blockage effect caused by the feed horns can be circumvented by using a folded pillbox feed. The feed horns are placed at one level of the folded pillbox feed, while the pickup horns are placed at the next level. Multiple beams can also be formed by using multiple-feed horns. The number of multiple beams, however, is limited by the defocusing effect of the parabolic reflector. Typically, scanned beams can be formed to approximately two beamwidths from either side of the focal beam (broadside beam). In order to form more simultaneous beams the shape of the reflector must be changed from a parabolic to a circular configuration, and the feed horns must be arranged along a circular arc, concentric to the reflector surface. For this case the f/D ratio is nominally 1/2. Due to the circular symmetry the radiation patterns of the feed horns are essentially identical except for the edge or truncation effect of the reflector. The radiation patterns, however, are deteriorated slightly by the spherical aberration effect of the circular reflector.

Multiple simultaneous beams can also be formed by using constrained parallel feeds such as the Butler matrix feed [30] and the Blass matrix feed [31]. The Butler matrix feed, as shown in Fig. 12c, consists of layers of 90° hybrids (3-dB couplers) interconnected with transmission lines and fixed phase shifters. The maximum number of simultaneous beams that are formed by the Butler matrix feed is equal to the total number of radiating elements in the array. For example, an eight-element array has eight simultaneous beams. All the beams are orthogonal to each other, and they cover the entire radiation space from one end-fire direction to the opposite end-fire direction. Due to the drop-off in the active element pattern of the radiating elements the beams close to end-fire directions are generally not used. The amplitude distribution across the radiating elements corresponding to any beam position is uniform; hence the crossover point of the adjacent beams is approximately 4 dB for orthogonal beams. The beam-pointing direction and the beamwidth change with frequency so that the orthogonality is maintained. Due to the large number of components required in the matrix feed for a large array and the complexity of packaging these components, the practical usage of the Butler matrix feed is generally limited to a sixteen-element array.

. In order to prevent the beam from scanning with frequency a time-delay matrix feed of the form shown in Fig. 12d can be used. This time-delay matrix feed is a special form of the Blass matrix feed [31]. For the broadside beam (beam 0 in Fig. 12d) all the path lengths from the input to the radiating elements are equal. For all the scanned beams the difference in path lengths between two adjacent feed lines from the beam input terminal to the radiating elements is exactly equal to the required time delay between these elements for that particular scan angle. Hence this time-delay matrix feed has extremely wide bandwidth, and it is only limited by the bandwidth of the couplers in the feed. One of the practical design problems of this time-delay matrix feed is the coupling between the feed lines. The amount of coupling is determined by the crossover level of the corresponding beams and the directivity of the couplers. High crossover level between beams (higher than the level corresponding to orthogonal beams) appears as a cross-coupling loss which in turn degrades the antenna gain. Poor directivity in the couplers causes circulating power between feed lines, which produces amplitude and phase errors at the radiating elements. In order to minimize amplitude and phase errors it is imperative that the beams are spaced as closely to the orthogonal condition as possible, and the directivity of the couplers is as high as possible.

. Independently controlled sum and difference beams for monopulse tracking can be formed in a parallel constrained feed as shown in Fig. 13. The signals from symmetrical pairs of radiating elements located diametrically opposite from the centerline are combined in 180° hybrids (magic tees) to form in-phase and out-of-phase signals. The in-phase signals are combined in a feed network with the proper amplitude weighting to form a sum beam. The out-of-phase signals from the magic
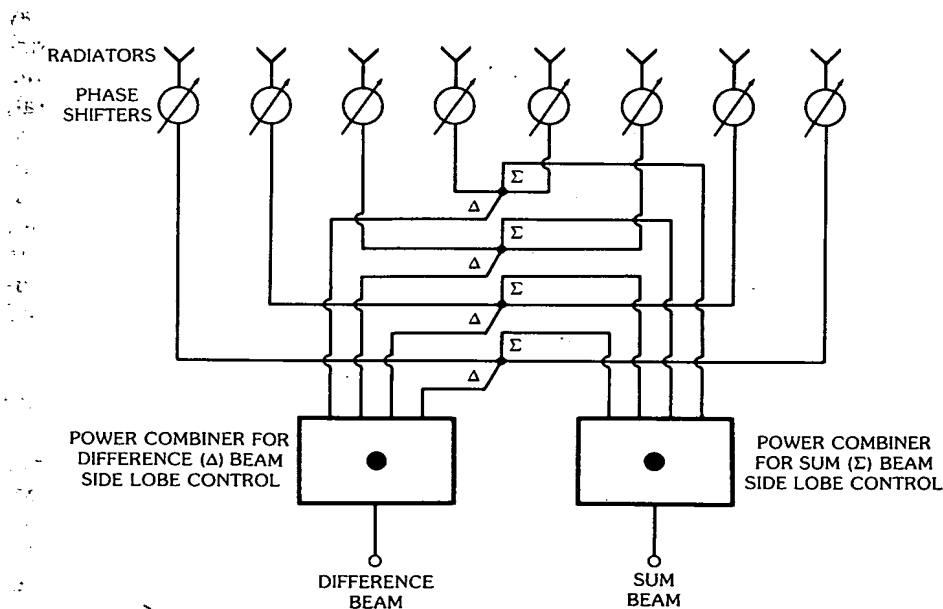

Fig. 13. Constrained monopulse feed with independently controllable sum and difference beam side lobes. (*After Tang and Burns [11]*)

tees are combined in a separate feed network to form a difference beam. Different amplitude distributions, such as the Taylor distribution for the sum beam feed network and the Bayliss distribution for the difference beam feed network, can be used to independently control the side lobes of both beams. When the lengths of the transmission lines from the input to the radiating elements are made equal, the bandwidth of this monopulse feed network is the same as that of a corporate feed.

General Observations in Selecting Beam-Forming Feeds—In general, the series feeds are more frequency sensitive than the parallel feeds; hence the series feeds are more bandwidth limited. Furthermore, the mismatches from the couplers in a series feed are additive when the transmission lines between the couplers are integer multiples of a half-wavelength. However, the lengths of transmission lines between the couplers in a parallel feed are nonuniform so that the mismatches do not add in phase. Also, the mismatches from the couplers can be isolated by the magic tees in order to prevent the reflected signal from circulating in the feed network and, as a result, cause high-power breakdown problems. In order to avoid the resonance problem in the series feed the length of transmission line in the series feed is chosen to avoid resonance over the operating band. One advantage of the series feed is that it is physically more compact than the parallel feed; hence it is more useful for applications where antenna volume is of prime importance.

4. Effect of Component Errors on Array Performance

One of the most important considerations in the design of a phased array antenna is the effect of errors in the array components on the antenna performance. These errors are mainly caused by the manufacturing tolerances of the components and the batch-to-batch variations in material consistency. In general, all the errors can be identified and grouped into two basic types: namely, the systematic type of error and the random type of error. The systematic errors are deterministic errors resulting from some inherent characteristics of the components. For example, the use of quadrature couplers in a beam-forming network results in fixed 90° errors across the outputs of the feed network. These phase errors can be trimmed out by storing the required phase correction terms in the programmable read-only memories (PROMs) of the beam-steering computer, and then by correcting these errors with the phase shifters at the radiating elements. The net required setting of the phase shifter is the sum of the phase correction term and the incremental beam-steering phase term. Any systematic type of amplitude error can also be trimmed out by fine-tuning the power split ratios of the couplers. The random errors, on the other hand, are not deterministic, and they are not correlated from element to element. Therefore, it would not be practical to correct the error at each element with the phase shifter since they are all different. These random errors can be minimized by controlling the manufacturing tolerances of the components. Therefore, in the remainder of this section, we will address the effects of random errors on antenna performance.

Before we can analyze the effect of random errors on array performance the following assumptions relating to the characteristics of these errors are made:

1. Errors in each radiating element are statistically independent from those in all the other elements.
2. Errors in all elements possess the same statistic.

Based on the above assumptions the array performance can be calculated in terms of the net rms amplitude and phase errors at each element of a large two-dimensional array. The net rms error at each element is determined by statistically summing all the contributions from the various components to that element using the central limit theorem. Detailed treatments of the error effects on array performance were done by Ruze [32], Allen [33], Miller [24], etc. They have expressed the array performance in terms of the rms error as follows:

1. The rms side lobe power, $\bar{p}$, is

$$\bar{p} = \frac{\sigma^2}{\eta N} \tag{7}$$

where

$\sigma^2 = \sigma_a^2 + \sigma_p^2$

σ_a = rms amplitude error

σ_p = rms phase error in radians

η = aperture efficiency, which is less than or equal to 1

N = total number of elements

2. The peak side lobe level,* p_{pk}, is

$$p_{pk} = |S_0| + 2\sigma/\sqrt{\eta N} \tag{8}$$

where S_0 is the amplitude of the design side lobe without errors.

3. The reduction in antenna gain is

$$\frac{G}{G_0} = \frac{1}{1 + (3\pi/4)(d/\lambda)^2\sigma^2} \tag{9}$$

where

d/λ = element spacing in wavelengths

G_0 = antenna gain with the absence of errors

4. The beam-pointing error is

$$\frac{\delta_\psi}{\Delta\theta_{rad}} = \sqrt{\frac{3}{N}} \frac{\sigma}{0.88\pi} \tag{10}$$

---

*Estimate is based on power not to be exceeded with 98-percent probability.

where

δ_ψ = rms beam-pointing error in radians

$\Delta\theta_{rad}$ = beamwidth in radians

The above formulas can be used in conjunction with actual radiation pattern calculations to estimate the allowable error budgets for the array components in meeting a given set of array performance specifications. Conversely, if the amplitude and phase errors of the components are known, then the array performance can be estimated by the above formulas. An example which illustrates the effects of errors on the array performance is given below. This example is for the case of an array of 2000 elements with element spacing d of 0.5λ. The error-free side lobe level $(p_{pk})_0$ is asumed to be -40 dB; correspondingly, the aperture efficiency η is equal to 0.64. Assuming the composite rms amplitude error σ_a and the rms phase error σ_p are 0.5 dB and 4°, respectively, then the net rms error σ is given by

$$\sigma^2 = \sigma_a^2 + \sigma_p^2 = 0.0035 + 0.0049 = 0.0084$$

The average side lobe level of the array with errors is given by

$$\bar{p} = \frac{\sigma^2}{\eta N} = 6.6 \times 10^{-6} \quad \text{or} \quad -51.8 \text{ dB}$$

The peak side lobe level p_{pk} is obtained from $p_{pk} = |S_{pk}|^2$, where

$$S_{pk} = S_0 + \frac{2\sigma}{\sqrt{\eta N}} = 0.01 + 0.005 = 0.015$$

so that

$$p_{pk} = -36.5 \text{ dB}$$

The gain reduction is given by

$$\frac{G}{G_0} = \frac{1}{1 + (3\pi/4)(d/\lambda)^2\sigma^2} = 0.995 \quad \text{or} \quad -0.02 \text{ dB}$$

The beam-pointing error is given by

$$\frac{\delta_\psi}{\Delta\theta_{rad}} = \sqrt{\frac{3}{N}} \frac{\sigma}{0.88\pi} = 0.001\,28 \quad \text{or} \quad \delta_\psi = \Delta\theta_{rad}/800$$

5. References

[1] K. R. Carver and J. W. Mink, "Microstrip antenna technology," *IEEE Trans. Antennas Propag.*, vol. AP-29, no. 1, pp. 2–24, January 1981.

[2] R. J. Mailloux, J. F. McIlvenna, and N. P. Kernweis, "Microstrip array technology," *IEEE Trans. Antennas Propag.*, vol. AP-29, no. 1, pp. 25–37, January 1981.

[3] R. J. Stegen, "Longitudinal shunt slot characteristics," *Tech. Memo. No. 261*, Hughes Aircraft Company, 1951.

[4] A. F. Stevenson, "Theory of slots in rectangular waveguide," *J. Appl. Phys.*, no. 19, pp. 24–38, 1948.

[5] J. S. Ajioka, "Frequency-scan antennas," *Antenna Engineering Handbook*, 2nd ed., ed. by R. C. Johnson, New York: McGraw-Hill Book Co., 1984, pp. 19-1–19-30.

[6] R. S. Munson, "Microstrip antennas," *Antenna Engineering Handbook*, 2nd ed., ed. by R. C. Johnson, New York: McGraw-Hill Book Co., 1984, pp. 7-1–7-28.

[7] J. Q. Howell, "Microstrip antennas," in *Dig. Intl. Symp. Antennas Propag. Soc.*, pp. 177–180, Williamsburg, Virginia, December 1972.

[8] E. V. Byron, "A new flush-mounted antenna element for phased array application," in *Proc. 1970 Phased Array Antenna Symp.*, pp. 187–192, Polytechnic Institute of Brooklyn, June 1970. Reprinted in *Phased Array Antennas*, ed. by A. A. Oliner and G. H. Knittel, Dedham: Artech House, 1972.

[9] C. C. Chen, "Broadband impedance matching of rectangular waveguide phased arrays," *IEEE Trans. Antennas Propag.*, vol. AP-21, pp. 298–302, May 1973.

[10] L. Stark, R. W. Burns, and W. P. Clark, "Phase shifters for arrays," *Radar Handbook*, ed. by M. I. Skolnick, New York: McGraw-Hill Book Co., 1970, pp. 12-1–12-65.

[11] R. Tang and R. W. Burns, "Phased arrays," *Antenna Engineering Handbook*, 2nd ed., ed. by R. C. Johnson, New York: McGraw-Hill Book Co., 1984, pp. 20-1–20-67.

[12] D. H. Temme, "Diode and ferrite phaser technology," in *Proc. Phased Array Antenna Symp.*, 1970, pp. 212–218, reprinted in *Phased Array Antennas*, ed. by A. A. Oliner and G. H. Knittel, Dedham: Artech House, 1972.

[13] C. A. Liecht and G. W. Epprechi, "Controlled wideband differential phase shifters using varactor diodes," *IEEE Trans. Microwave Theory Tech.*, vol. MTT-15, pp. 586–589, October 1967.

[14] J. F. White, "Figure of merit for varactor reflection type phase shifters," *NEREM Rec.*, pp. 206–207, November 1965.

[15] W. J. Ince et al., "The use of manganese-doped iron garnets and high dielectric constant loading for microwave latching ferrite phasers," *G-MTT Dig.*, pp. 327–331, 1970.

[16] D. H. Temme et al., "A low cost latching ferrite phaser fabrication technique," *G-MTT Dig.*, pp. 88–96, 1969.

[17] R. G. Roberts, "An X-band reciprocal latching Faraday rotator phase shifter," *G-MTT Dig.*, pp. 341–345, 1970.

[18] C. R. Boyd, Jr., "A dual-mode latching reciprocal ferrite phase shifter," *G-MTT Dig.*, pp. 337–340, 1970.

[19] F. Reggia and E. G. Spencer, "A new technique in ferrite phase shifting for beam scanning of microwave antennas," *Proc. IRE*, vol. 45, pp. 1510–1517, November 1957.

[20] A. G. Fox, "An adjustable waveguide phase changer," *Proc. IRE*, vol. 35, pp. 1489–1498, December 1947.

[21] B. M. Schiffman, "A new class of broadband microwave 90-degree phase shifters," *PGMTT-MTT-6*, pp. 232–237, 1958.

[22] T. C. Cheston and J. Frank, "Array antennas," *Tech. Memo. TG-956*, The Johns Hopkins University Applied Physics Laboratory, March 1968.

[23] R. Tang, R. W. Burns, and N. S. Wong, "Phased array antenna for airborne application," *Microwave J.*, vol. 14, no. 1, pp. 31–38, January 1971.

[24] C. J. Miller, "Minimizing the effects of phase quantization errors in an electronically

scanned array," *Proc. 1964 Symp. Electronically Scanned Array Techniques and Applications*, RADC-TDR-64-225, vol. 1, pp. 17–38.

[25] W. Rotman and R. F. Turner, "Wide angle microwave lens for line source," *IEEE Trans. Antennas Propag.*, pp. 623–632, November 1963.

[26] J. Frank, "Bandwidth criteria for phased array antennas," *Proc. Phased Array Antenna Symp.*, pp. 243–253, Polytechnic Institute of Brooklyn, June 1970. Reprinted in *Phased Array Antennas*, ed. by A. A. Oliner and G. H. Knittel, Dedham: Artech House, 1972.

[27] T. T. Taylor, "Design of line-source antennas for narrow beamwidth and low side-lobes," *IRE Trans. Antennas Propag.*, vol. AP-3, pp. 16–28, 1955.

[28] E. T. Bayliss, "Design of monopulse antenna difference patterns with low sidelobes," *Bell Syst. Tech. J.*, pp. 623–650, May–June 1968.

[29] A. R. Lopez, "Monopulse networks for series feeding an antenna," *IEEE Trans. Antennas Propag.*, vol. AP-16, pp. 436–440, June 1968.

[30] J. Butler and R. Lowe, "Beamforming matrix simplifies design of electronically scanned antennas," *Electron. Des.*, vol. 9, no. 7, pp. 170–173, April 1961.

[31] J. Blass, "The multi-directional antennas: a new approach to stacked beams," *IRE Conv. Proc.*, vol. 8, pt. 1, pp. 48–51, 1960.

[32] J. Ruze, "Physical limitations on antennas," *Tech. Rep. No. 248*, Massachusetts Institute of Technology, October 30, 1952.

[33] J. L. Allen, "The theory of array antennas," *Tech. Rep. No. 323*, Lincoln Lab, Massachusetts Institute of Technology, July 25, 1963.

[34] W. Rotman, "Wide-angle scanning with microwave double-layer pillboxes," *IRE Trans. Antennas Propag.*, vol. AP-6, pp. 96–105, January 1958.

Chapter 19

Beam-Forming Feeds

J. S. Ajioka
Hughes Aircraft Company

J. L. McFarland
(Late) Hughes Aircraft Company

CONTENTS

James S. Ajioka was born in Thornton, Idaho. He received the BS and MS degrees in electrical engineering from the University of Utah in 1949 and 1951, respectively.

From 1949 to 1955 he was a group leader and project engineer in the Antenna Design Section of the Navy Electronics Laboratory. In 1955 he joined Hughes Aircraft Company, where he is manager of the Electromagnetics Laboratories, Hughes Ground Systems Group, in Fullerton, California. He has been active in the design and development of electronically scanning arrays, waveguide slot arrays, geodesic antennas, and wide-angle multiple-beam optical antenna systems, and also low-noise high-efficiency feeds, broadband multioctave multiplexing feeds for reflectors and lenses, and millimeter-wave phased arrays.

Mr. Ajioka has more than 20 patents awarded and several are pending. He has presented and published numerous papers on antenna and microwave systems and has contributed to several books. He has also won awards for outstanding achievements in antenna engineering. Mr. Ajioka is a Fellow of the IEEE.

Jerry L. McFarland was born in Iraan, Texas. He received the BS and MS degrees in electrical engineering, with the latter being from the University of Southern California, Los Angeles.

From 1958 to 1964 he was a staff engineer with Hughes Aircraft Company involved with the development of frequency scanning antennas and research on multiple-beam geodesic lenses. From 1964 to 1972 he was engaged in similar work with Autonetics, a division of Rockwell International. In 1972 he became the technical director of EMP, Chatsworth, California, developing antennas and single-axis trackers. In 1977 he joined Lockheed Missiles and Space Company, where he was concerned with adaptive arrays and multiple-beam antennas. He rejoined Hughes Aircraft Company, Fullerton, California, in 1982 as a senior scientist and was most recently involved in antenna development and investigation of nonconventional slot radiators.

Mr. McFarland's untimely death is a great loss to his profession and to all his friends and associates.

1. Introduction

When phased arrays were relatively simple, antenna subassemblies were easy to identify as feed networks, phasors, and radiating aperture. Modern phased arrays, however, have become quite complex, with a wide variety of designs and physical implementations depending on the particular application. With simple phased arrays the feed network was a passive network of branching transmission lines to distribute the power from a single transmitter to each of the radiating elements in the array via the phasors, and, conversely on receive, it combined the power received by each of the radiating elements to the input to a single receiver. Modern phased arrays may have multiple distributed transmitters, multiple distributed preamplifiers, multiple duplexing switches, and multiple simultaneous beam ports, each with its own final receiver. In addition, adaptive arrays may have adaptive control loops distributed throughout the feeding network with a significant amount of signal processing done within the antenna. For these reasons, general categories and general definitions become somewhat ambiguous. However, since generality is necessary to discuss phased arrays in general, an attempt is made to organize feed systems into general categories, and the reader should be aware of the shortcomings.

2. Constrained Feeds (Transmission-Line Networks)

The simplest method of feeding an array is to use simple passive transmission-line networks which take the transmitter power from a single source, or possibly multiple sources, and to distribute the power to each radiating element via transmission lines and associated passive microwave devices, such as hybrids, magic-Ts, or directional couplers, etc. The network itself is usually a combination of directional couplers, hybrids, and/or Ts in waveguide, coax, stripline, or microstrip. Printed-circuit techniques are popular for some of the approaches to be discussed. Fig. 1 is a simplified diagram of a constrained feed showing the basic subassemblies. In the case of multiple beams, there would be more than one input and more than one beam. In the following sections the series-fed, parallel-fed, time-delay-fed, and multiple-beam matrix-fed approaches are discussed.

Series Feed Networks

The simplest power distribution feed is an end-fed transmission line in which power is coupled off at (usually) periodic intervals to the radiating elements as shown schematically in Fig. 2. Although the series feed is simple, low cost, and packages easily, it has a drawback in that it "frequency scans" because there is an interelement progressive phase delay equal to $k_g d$, which is proportional to frequency, where $k_g = 2\pi/\lambda_g = \omega/v_g$ is the wave number of the feeding transmission line and d is the line length between branch line couplers. Although the phase
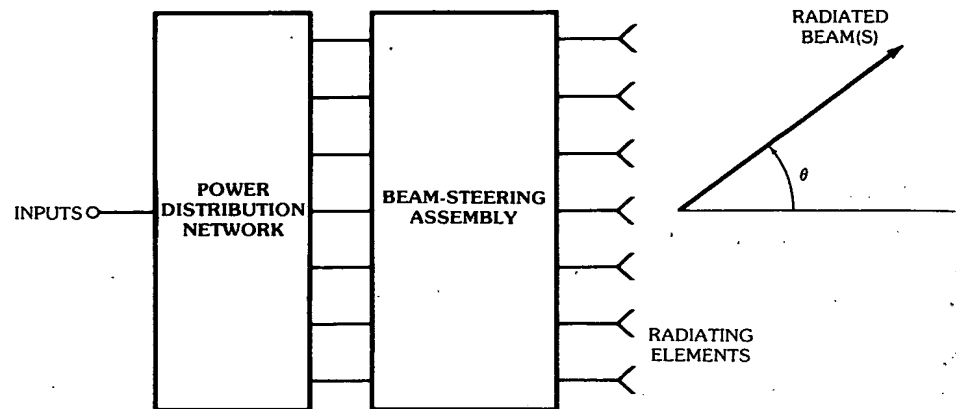
19-3

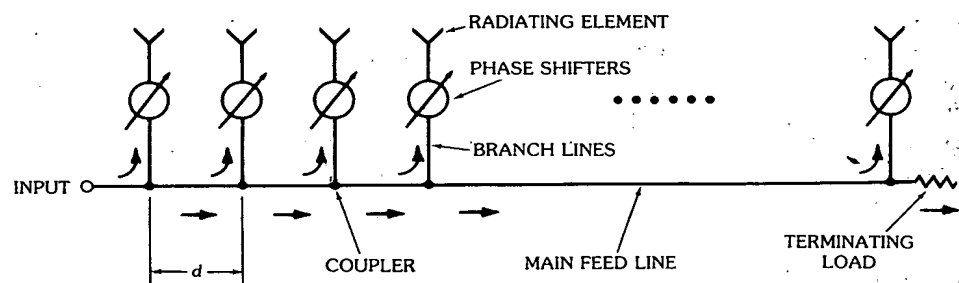Fig. 1. Constrained feed approach.

Fig. 2. Schematic diagram of a series feed.

shifters are usually reset for each frequency change, the instantaneous or signal bandwidth is degraded because the antenna beams corresponding to each of the frequency components in a narrow pulse will be pointing in slightly different directions in space. Thus the composite antenna beam is "smeared out" in angular space, thereby broadening the effective beamwidth to reduce the antenna gain and angular resolution.

There are many coupler designs that can couple the desired amount of power from the main feed line to the branch lines. The couplers can be nondirective three-port reactive couplers, such as pure series or pure shunt couplers, nondirective matched couplers, or directive four-port couplers. Nondirective couplers are simple and inexpensive to fabricate. Pure series or shunt couplers are the simplest but are inherently mismatched. For arrays with a large number of elements (on the order of 50 or more elements) the individual reflections due to coupler mismatch are quite small because the coupling is very loose. For large arrays the maximum voltage coupling coefficient is on the order of 0.1. These coupler mismatch reflections, for the most part, add randomly in phase at the input to give a low feed input vswr except at or very near the resonant frequency, that is, the frequency corresponding

to a broadside beam. At the resonant frequency the couplers are an integral number of wavelengths apart (or half-wavelengths if the phase of the couplers is alternately 0° and 180°) and all the reflections add in phase to result in a very high input vswr. For purely series couplers the impedances add, and for purely shunt couplers the admittances add. The input vswr versus frequency curve shows high resonance for large arrays, and the width of the vswr versus frequency curve is inversely proportional to the number of elements in the array. In short, the input vswr versus frequency curve resembles an antenna pattern in all respects except the independent variable is frequency instead of spatial angle. That is, tapered aperture distributions result in lower side lobes and broader beamwidth in antenna patterns, and tapered coupling coefficients result in lower side lobes and broader resonance bandwidths in the vswr curve.

Because of the high vswr at resonance the resonant frequency is usually designed to be out of the operating frequency range when simple nondirective couplers are used. Matched nondirective couplers have been designed in waveguide that allow operation at the resonant frequency [1]. Although they are more complex, more costly, and, in general, more difficult to package, directional couplers have superior performance because they are inherently matched at all four ports.

In designs using nondirective couplers the reflections from the couplers can couple into the preceding branch arms and cause spurious side lobes in the antenna pattern; hence they are called *reflection lobes*. In particular, a reflection from a poorly matched terminating load will cause a reflected beam in the conjugate direction from broadside as the desired beam. Reflections from mismatches in the branch lines, such as reflections from the input end of the phase shifters or connectors on the feed side of the phase shifter, will usually reflect specularly as a whole and the reflected wave reflects back into the feed main line and will be phased such that it will be dissipated in the terminating load of the series feed.

Parallel Feed Networks

The simplest parallel feed network consisting of branching transmission lines is commonly known as a corporate feed (see Fig. 3). Since the path lengths from the feed point to the radiating elements are equal, there is no progressive phase delay between radiating elements, and hence no frequency scan, so that the instantaneous bandwidth is much greater. If the corporate feed were made up nondispersive TEM transmission line, the feed itself would be true time delay and would, in principle, have unlimited bandwidth.

The power dividing branch points of the feed are usually matched four-port hybrid junctions instead of reactive three-port T junctions. Since a matched four-port junction is impedance matched in all four ports, spurious reflections from connectors, phase shifters, radiating apertures, etc., will not be scattered from the various junctions back into the radiating aperture to cause undesired side lobes and other antenna pattern degradation. Instead, these spurious reflections are absorbed in the terminating loads of the hybrids. Also, multiple reflections among the junctions can cause high resonance effects that can lead to high-power breakdown in the feed network. The use of directional couplers helps alleviate this potential problem.

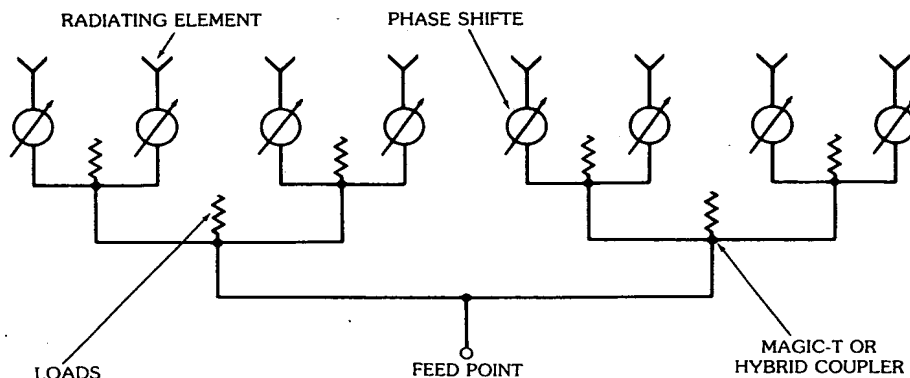As with the use of directional couplers in the series feed, the unused terminal

RADIATING ELEMENT   PHASE SHIFTE

LOADS   FEED POINT   MAGIC-T OR
HYBRID COUPLER

Fig. 3. Diagram of a corporate feed, phase shifters, and radiating elements.

(the port that is normally terminated in a matched load) can be used to form a multitude of auxiliary antennas such as side lobe blanking and coherent side lobe cancellation antennas [2].

Again, as in the series feed, when a plane wave is incident on the antenna from the direction of the main beam, most of the receive power arrives at the input port of the feed and very little power ends up in the terminating loads. In an ideally lossless feed network, that portion of the power in the incident plane wave which ends up in the terminating loads accounts for the fact that the aperture efficiency η is less than unity for aperture distributions other than uniform. For uniform aperture distributions none of the received power is dissipated in the terminating loads. For tapered aperture distributions most of the received power that does not arrive at the feed input is dissipated in the terminating loads of the junctions that have the highest power split ratios which are near the edges of the aperture. With reactive three-port power splitters the receive power that is not received at the input port of the feed is reflected back into free space and can result in a high radar cross section. In any case in which matched four-port junctions are used in the feed, the radar cross section of the ideal impedance-matched aperture antenna is zero. Of course it is assumed that the incident radar wave has the same polarization and frequency as the antenna. That is, all the energy incident in the direction of the main beam of the antenna is absorbed at the antenna input (receiver or duplexer load)—none of it is reflected back into space. For plane waves incident on the antenna from any other direction than in the main beam, the incident power nearly all (except for the small amount of energy associated with side lobes of the antenna pattern) ends up in the terminating or "unused" ports of the hybrid junctions. That small amount of incident power (if there is any) associated with the side lobe in that direction ends up at the input port of the antenna feed. Hence the unused ports of the hybrid junctions can be combined in various ways to create a large variety of antenna pattern shapes outside the region of the main beam of the main antenna. Such patterns can be used as auxiliary antennas such as for coherent side lobe cancellation or for communications outside the region of the main beam of the main antenna. All these auxiliary antenna patterns would have essentially a null in the direction of the main beam of the main antenna [2].

True Time-Delay Feeds

A true time-delay antenna is in which that the time delay from an incoming wavefront to a feed point is the same for every path from the wavefront via each of the radiating elements, phase shifters, etc., to the feed point. This is illustrated in Fig. 4. The equal time delay ensures that signals via all paths add in phase at the feed point for every frequency component in the pulse. In a non-true-time-delay antenna the time delays for the various paths may differ by an integral number of rf cycles of the center frequency in the pulse. In general, other frequencies in the pulse do not add exactly in phase at the feed point. Hence there is a reduction in the peak of the received pulse and the pulse is smeared out or broadened in time. From the transmit point of view the interelement phase shift ψ is correct only at the center frequency to have its main beam point in the desired direction in space. Antenna patterns corresponding to other frequencies in the pulse will be scanned off from the desired direction according to the expression $\sin \theta = c\psi/\omega d$, which shows that the beam-pointing angle θ depends on the frequency ω since ψ is constant. The antenna is a bandpass filter in that the frequency spectrum of the
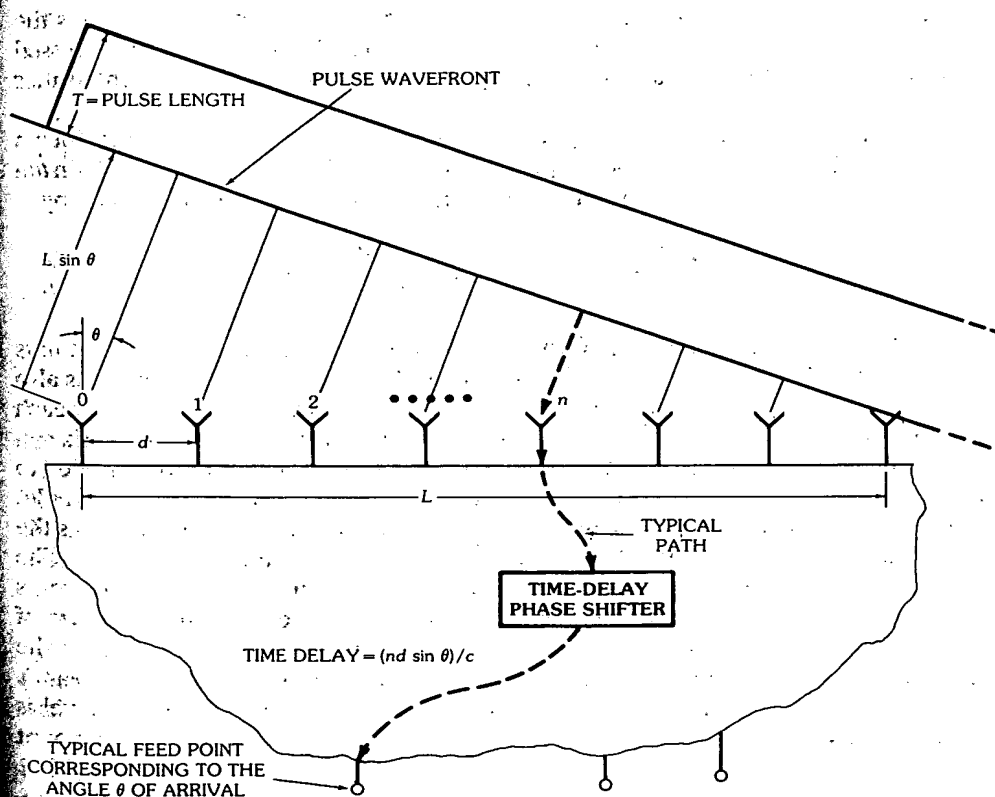
Fig. 4. Schematic diagram of true-time-delay antenna using time-delay phase shifters. (*Courtesy Hughes Aircraft Co., Fullerton, Calif.*)

pulse radiating toward a target is modified. The frequency component corre-sponding to the center frequency of the pulse is weighted most heavily because its corresponding antenna pattern is, by design, pointing in the direction of the target, whereas the other frequency components in the short pulse have their antenna patterns scanned off from the direction of the target; hence their weighting is reduced by the amount that their antenna patterns are scanned off. By the principle of reciprocity this spectral transformation on receive is the same as that previously discussed for transmit.

In a true time-delay array the interelement phase shift ψ must not be constant but must be proportional to frequency so that all frequency components in the pulse will have their corresponding antenna patterns all pointing in the same direction.

Examples of true time-delay feeding techniques include the use of the circular folded pillbox covered in Section 3, under "Pillbox," and the Meyer geodesic lens covered in Section 3, under "Meyer Lens," and in Section 6, under "Hughes Matrix-Fed Meyer Geodesic Lens," among others.

Multiple-Beam Matrix Feeds

Butler Matrix—Probably the most widely known multiple-beam matrix feed is the Butler matrix. It is well documented in the literature [3–8] and will be discussed only briefly here. Fig. 5 is a schematic representation of an eight-element Butler matrix.

The Butler matrix has N outputs (aperture elements) and N inputs (beam ports). Unit excitation at the beam ports results in N orthogonally spaced $\sin u/u$ type patterns.* The aperture distribution $B(n)$ is related to the beam inputs by

$$B_{nm} = \frac{\exp j\{[n - (N + 1)/2][m - (N + 1)/2]2\pi/N\}}{\sqrt{N}}$$

where B_{nm} is the field amplitude of the nth aperture element when beam port m is excited with unit amplitude and N is the number of aperture elements, which is also the number of beam ports. In the above form of B_{nm}, the phase distribution for each beam is symmetrical about the center of the aperture array. Any Butler matrix can be put into this form because an arbitrary aperture phase gradient can be applied to the aperture. This merely causes the whole beam cluster to scan as a whole, retaining the same beam spacing in $\sin \theta$ space. The quantity that is invariant is the difference in phase gradients between adjacent beams, which is always $2\pi/N$. The aperture amplitude distribution is uniform for all beams with $(\sin u)/u$ type patterns and each beam derives full 100-percent directivity from the projected aperture of the common array. The beams cross over at $E = 2/\pi$ or 3.92 dB down from the beam peaks and the peak of any beam peak falls on the nulls of all other beams. The beams are orthogonal and there is no beam coupling. The crossover level is independent of frequency; hence the beams must frequency scan by an amount

---

*More accurately, for discrete arrays it is $(\sin n\psi)/n \sin \psi$, where $\psi = (\pi d/\lambda)\sin \theta$, which is the counterpart for $(\sin u)/u$ for continuous distributions.
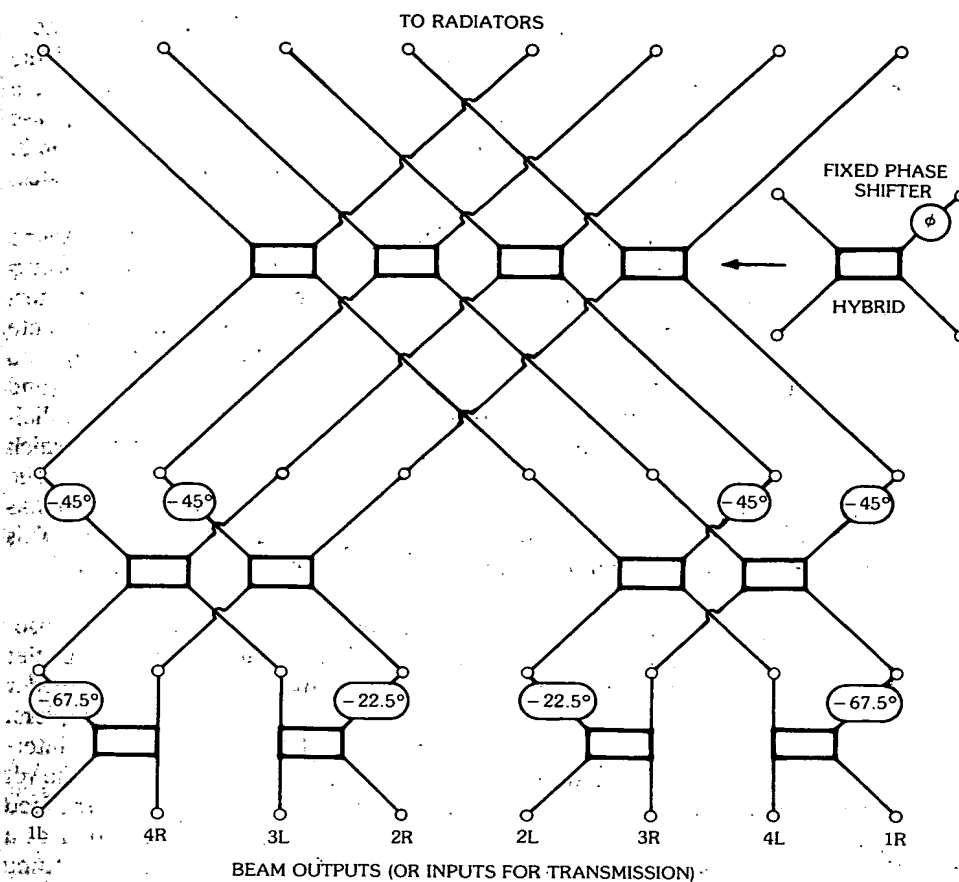
Fig. 5. Eight-port Butler matrix. (*Courtesy Hughes Aircraft Co., Fullerton, Calif.*)

proportional to their separation from broadside in order to retain orthogonality and a fixed crossover level. For large arrays the beams span an angular coverage of $2\sin^{-1}(\lambda/2d)$, where d is the element spacing and λ is the free-space wavelength. For $d > \lambda/2$, grating lobes will fill in the region near end-fire, and for $d < \lambda/2$, some beams will be in imaginary space. In all cases all of visible space is covered.

As exemplified by Fig. 5, numerous hybrid junctions and fixed phase shifters must be cascaded to generate a Butler matrix. Specifically [5], the number of hybrids is equal to $(N/2)\log_2 N$ and the number of fixed phase shifters is equal to $(N/2)\log_2(N - 1)$. Moody [8] gives a systematic design procedure for generating such matrices.

It should be mentioned that the multiple-beam matrices of the type described in [5] (and most others in the literature) use all 90° 3-dB or all 180° 3-dB couplers. In these matrices the number of elements/beams is a power of 2 and requires fixed phase shifts. However, since any fixed phase shift can be generated by a combination of 90° and 180° hybrids, matrices without separate fixed phase shifters

can be designed. Jones and Van Blaricum [7] give a design procedure for these matrices. In general, the hybrids are not necessarily a 3-dB power split and the number of elements/beams is not necessarily a power of 2. An example of a multiple-beam matrix that uses both 90° and 180° hybrids with no fixed phase shifters is the one used to feed the radial transmission line described in Section 3. The preceding expression for B_{nm} is general and is applicable to all lossless multiple-beam matrices.

There are numerous applications of the Butler matrix, not only as an antenna itself, or as an antenna feed, but as a multimode generator. When the outputs are placed on a circle, modes of the form $e^{\pm jm\phi}$ are generated (m = integer, ϕ = circumferential angle). Due to the unitary nature of this matrix, a complete set of orthogonal modes is created. Most of the time the number of beams required is much less than the number of elements; consequently the full capability (and associated complexity) of a Butler matrix is not needed. A later section on parallel-plate optics using a multimode radial transmission line describes a scheme in which the number of elements and the number of beams are totally independent. The next section describes a multiple-beam transmission-line matrix that also has independence between the number of elements and the number of beams. This scheme also allows arbitrary beam spacing. Also see Hansen [4], vol. 3, ch. 3.

Blass Matrix—Another multiple-beam matrix invented by J. Blass [9] that uses serially coupled transmission lines instead of the parallel coupled lines of the Butler matrix is briefly described here (see Fig. 6). This configuration uses one feeder line for each beam with branch guides coupled serially by directional couplers. The transmission lines may be waveguide, coax, or stripline. For a specified inter-element spacing d, the beam position in space is determined by two things: the tilt angle of the feed line and the propagation constants of the branch lines and the feed line in question (may be all the same or all different). Each feed line produces a linear (ideal) phase gradient at the array aperture and forms a frequency scanning beam in space. By proper choice of the feed line tilt angles, propagation constants, and coupling distributions, multiple beams can be generated in space having whatever crossover value the designer chooses. These multiple beams, in general, may not be precisely orthogonal over a large frequency band but can be designed to be nearly so from a loss point of view. All the beams frequency scan together. For a small number of beams (two or so) this array works quite well. For a large number of beams, or for very low side lobes, care must be taken to account for the phase and amplitude changes that occur in the transmission coefficient as the wave passes by a multiplicity of nonideal directional couplers. The larger the number of beams, the more difficult this becomes. As can be seen from Fig. 6, feed line 1 produces a branch guide field that does not have to pass by any other couplers, while beam M must pass by $M - 1$ other couplers before entering free space; hence perturbations are present in feed line M that are not there for feed line 1. These perturbations will manifest themselves to some degree in the form of radiation pattern degradation and/or excessive power dissipated in the terminating loads. These properties are manifestations of the fact that ideal beam orthogonality is not guaranteed as in the Butler matrix or radial line approaches. It is conceivable that orthogonality could be forced by a design procedure similar to the Gram-Schmidt procedure [10], but in
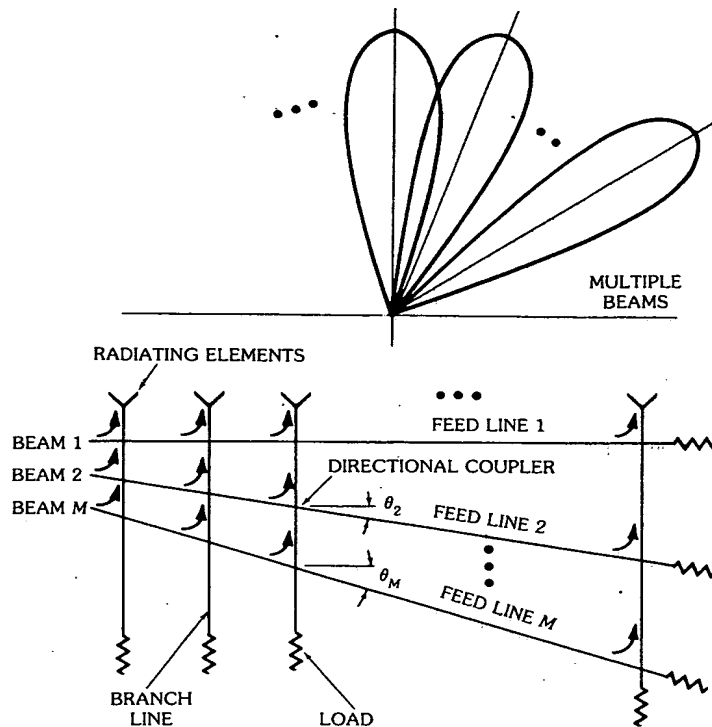
Fig. 6. Multiple-beam Blass matrix. (*After Butler and Lowe [3], © 1961; reprinted with permission of Hayden Publishing Co.*)

doing so, some of the advantages of the Blass matrix, such as simplicity and arbitrary beam spacing, could be restricted. However, this allows arbitrary beam spacing.

Various derivatives of the Blass matrix are also given in Hansen [4], including a true time-delay version of this matrix. The reader is referred to this reference for more details.

Two-Dimensional, Isosceles, Triangularly Spaced, Multiple-Beam Matrix—This class of two-dimensional multiple-beam matrices introduced by Chadwick and Glass has been extensively investigated by Chadwick, McFarland, Charitat, Gee, and Hung of the Lockheed Missile and Space Company [11, 12]. The analysis of this relatively new class of two-dimensional multiple-beam matrices is quite involved and, compared with other topics of this handbook, the required length of a self-contained explanation would not be justified. For this reason, only an acknowledgment that such an antenna technique does exist and a discussion of its possible advantage over the more established techniques are given. For further information the reader is referred to the references cited.

The Butler matrix multiple-beam antenna is one-dimensional and applies to multiple-beam linear arrays. A two-dimensional array is made by an array of these

linear arrays. The Butler matrix is a special case of the triangularly spaced array in which the triangle collapses into a line. This two-dimensional matrix forms a family of lossless, isosceles, triangularly spaced, orthogonal beams.

This two-dimensional matrix offers more freedom for the designer to choose the number of elements (beams) with a variety of array shapes. These shapes are derived from the basic triangle and include such shapes as irregular hexagons, V shapes, Z shapes, hourglass shapes, and parallelograms. Since there is a one-to-one correspondence between array space and beam space, a variety of beam coverage geometries are available. This may be advantageous where irregular beam coverage is desired, such as the coverage of certain geographical areas on earth from a spacecraft antenna. A desired beam coverage might be approximated by one of the allowed beam coverage shapes. Butler matrices achieve an irregular coverage by terminating the beam ports corresponding to beams that fall outside the desired coverage area. This is wasteful in that the total number of components in the matrix is greater than for a matrix that utilizes all the available beams. Due to the variety of beam coverage shapes available, the relative number of "wasted" beams should be smaller for this two-dimensional matrix array.

Multimode Element Array Technique

For electronically scanning antennas with requirements of high directivity and high gain but with limited field of view (typically on the order of 10°), it is very wasteful to have radiating elements with phase shifters at half-wavelength intervals over the entire radiating aperture. The limited scan requirement allows a reduction in these devices (which may include power amplifiers and low-noise amplifiers in an active array) in proportion to the limited solid angle of scan. Limited-scan antennas are designed to minimize the number of these costly devices with minimal degradation of antenna performance. Constrained feeding techniques using large directive elements spaced much greater than at $\lambda/2$ intervals are discussed in this section. Limited-scan techniques using optical type devices are described in Section 4 on unconstrained optical feeds and in Section 5 on optical transform feeds.

The use of large directive elements (e.g., waveguide horns) in a phased array usually results in high grating lobe levels as scanning is performed; however, for limited-scan, Mailloux and Forbes [13, 14] have found that by properly exciting waveguide flared horns with not only the dominant LSE_{10} mode but with controlled higher-order odd modes as well, the grating lobe that would ordinarily be the worst can be suppressed. For example, consider first that array scanning is to be performed in the E-plane only, with elements as depicted by Fig. 7. The array factor will be scanned by controlling the phase shifter labeled η, while the odd-mode amplitude control will utilize the phase shifter labeled $\eta + \Delta$. An example of far-field radiation patterns for the LSE_{10} and LSE_{11} modes is shown in Fig. 8. This particular example is predicated on forming a null at $\eta = -0.75$. This null location would correspond to a grating lobe position for a positive main beam scan angle. The null location can be controlled by an appropriate linear combination of these two modes. By linearly combining the two modes, a scanned element pattern that suppresses the worst grating lobe can be achieved. An example of this is given by Fig. 9 for waveguide horns that are 2.9λ by 2.9λ on a side. Also shown, for reference purposes, is the element pattern produced by the dominant LSE_{10} mode only.

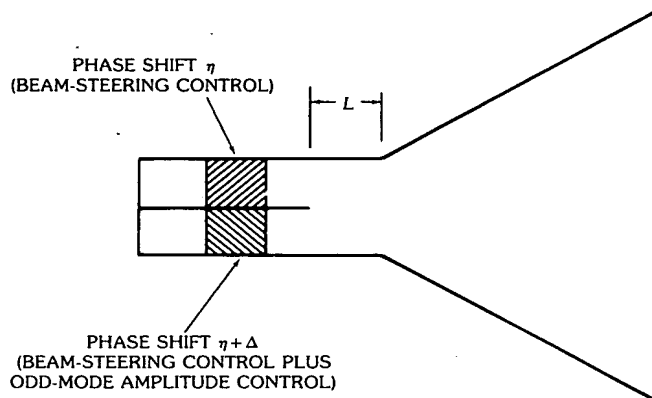Fig. 10 is a photograph of an experimental eight-element array taken from

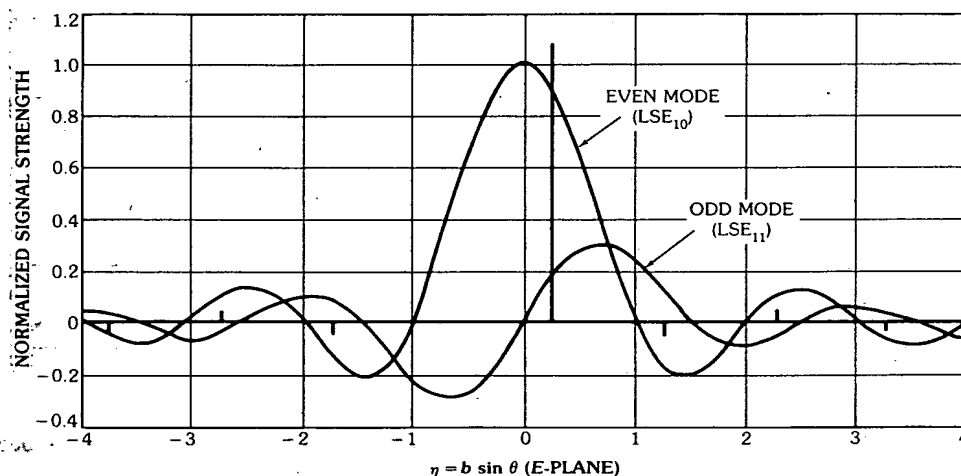**Fig. 7.** Even/odd-mode power divider circuit for E-plane scanning. (*After Mailloux [13]*)

Fig. 8. E-plane field patterns for LSE_{10} and LSE_{11} waveguide modes. (*After Mailloux [13]*)

Mailloux [13]. It is designed for E-plane scan of $\pm 12°$. The amplitude distribution is such that the center four are uniform, the second element in from each end is -3 dB, and the outer elements are -6 dB. Examples of the measured far-field patterns are given in Figs. 11 and 12, where for comparison the latter also shows the calculated pattern without odd-mode control. Without odd mode control, the highest grating lobe for 12° scan of the main beam would be about 4 dB higher than the main beam. With odd-mode control, however, this grating lobe is suppressed by about 20 dB for $\pm 12°$ scan.

For odd-mode control in both planes the configuration shown by Fig. 13 can be used [14]. This configuration would allow large directive elements to be used in both dimensions, while suppressing the offending grating lobe ordinarily encountered. For more details the reader is referred to Mailloux and Forbes [13, 14].
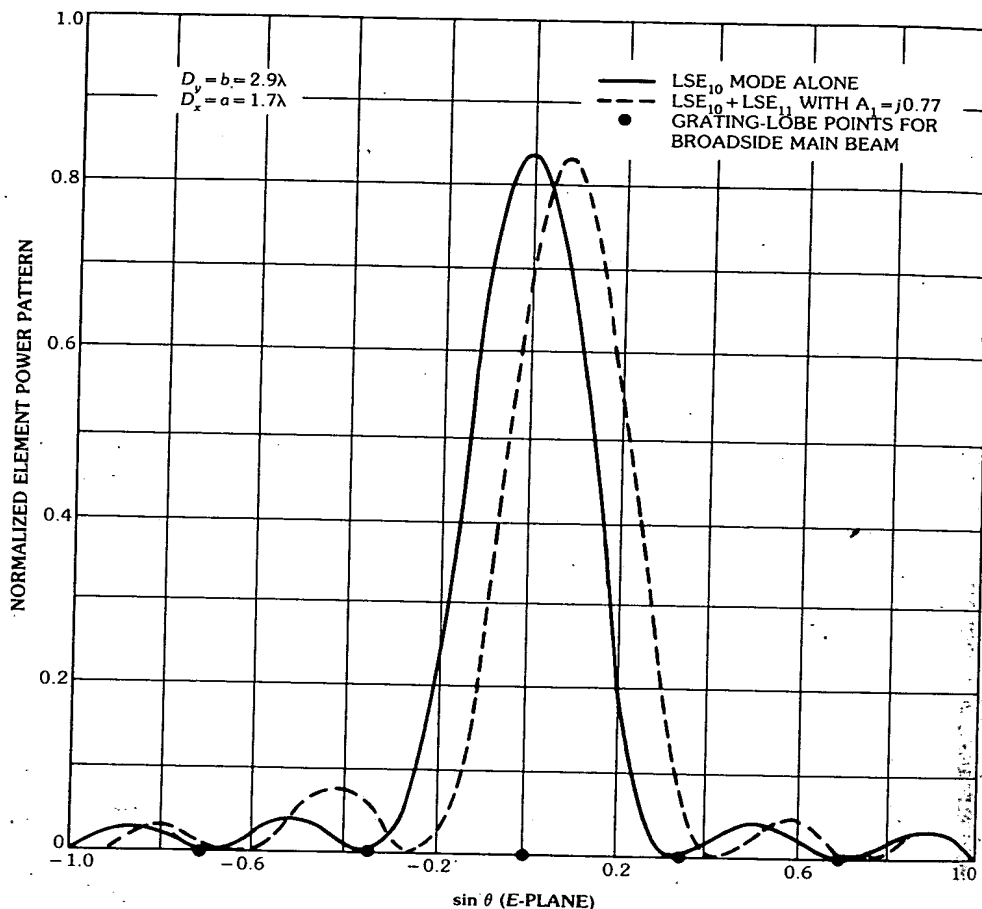
Fig. 9. Array element patterns of fundamental mode ($A_1 = 0$) and of fundamental mode with odd mode ($A_1 = j0.77$), with 2.9λ element separation in the E-plane.

3. Semiconstrained Feeds (Parallel-Plate Optics)

Feed systems that are constrained in one dimension but are not constrained in the other dimension are used because of simplicity, low cost, low loss, and high power handling capability. The volume occupied, however, is generally greater than that for fully constrained feeds. These feeds utilize propagation in the quasi-TEM mode between closely spaced (less than $\lambda/2$) parallel metallic surfaces. The surfaces need not be planar but can also be singly or doubly curved as long as the spacing between the surfaces is small in terms of wavelength and the radii of curvature are large with respect to the wavelength. Under these conditions the wave is considered to be propagating on the mean surface. In the dimension of the mean surface the wave is essentially unbounded and is not constrained by guiding structures. The rf power "radiates" from the primary feed along the mean surface to a pickup array that, in turn, feeds the radiating elements of the antenna. Hence
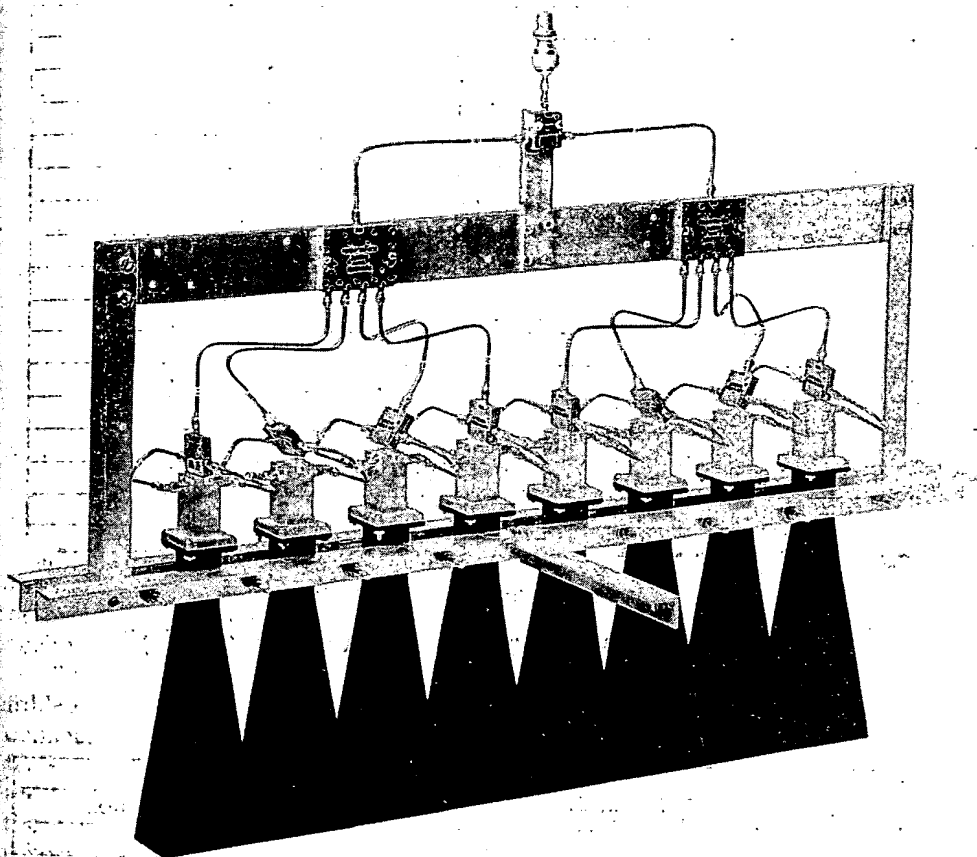
Fig. 10. Prototype array for E-plane scan ($W = 3.01$). (*After Mailloux [13]*)

the aperture distribution of the antenna array is determined by the radiation pattern of the primary feed and the geometric properties of the mean surface. If the mean surface is planar, the aperture illumination is determined by the feed pattern in the usual sense. However, if the mean surface is doubly curved or if the index of refraction is a function of position, the feed pattern is modified, as will be discussed later.

Under the restrictions of closely spaced surfaces and other dimensions large compared with the wavelength, the laws of geometric optics are quite valid on the mean surface. That is, Fermat's principle stating that the path of a ray in geometric optics is stationary applies. Stated mathematically,

$$\delta \int_{\text{ray path}} n\, ds = 0$$

where n is the index of refraction of the medium between the surfaces. The index of refraction may vary as a function of position on the mean surface. This is the same
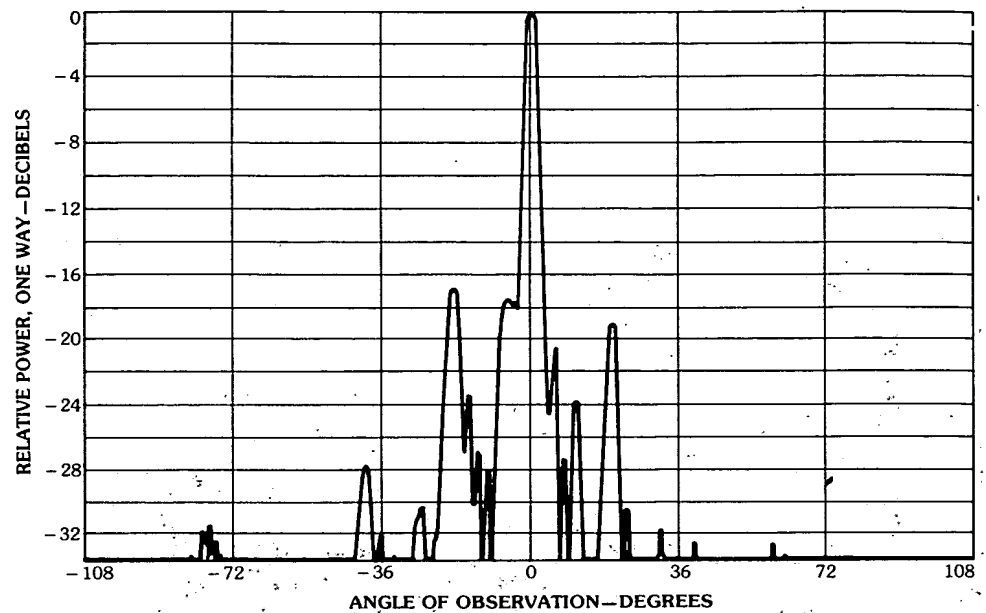
Fig. 11. Array radiation patterns (broadside). (*After Mailloux [13]*)
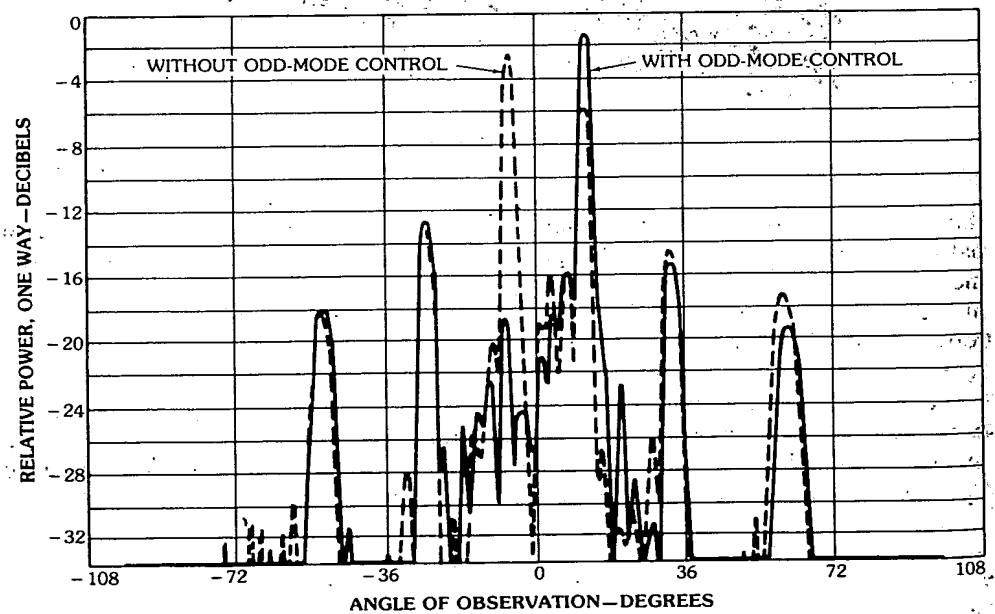
Fig. 12. Array radiation patterns (12° scan). (*After Mailloux [13]*)

PHASE SHIFT $\eta + \Delta_E$
(BEAM STEERING PLUS ODD-
MODE CONTROL E-PLANE)

PHASE SHIFT $\eta + \Delta_E + \Delta_H$
(BEAM STEERING PLUS ODD-
MODE CONTROL E AND H)

PHASE SHIFT η
(BEAM STEERING)

PHASE SHIFT $\eta + \Delta_H$
(BEAM STEERING PLUS ODD-
MODE CONTROL H-PLANE)
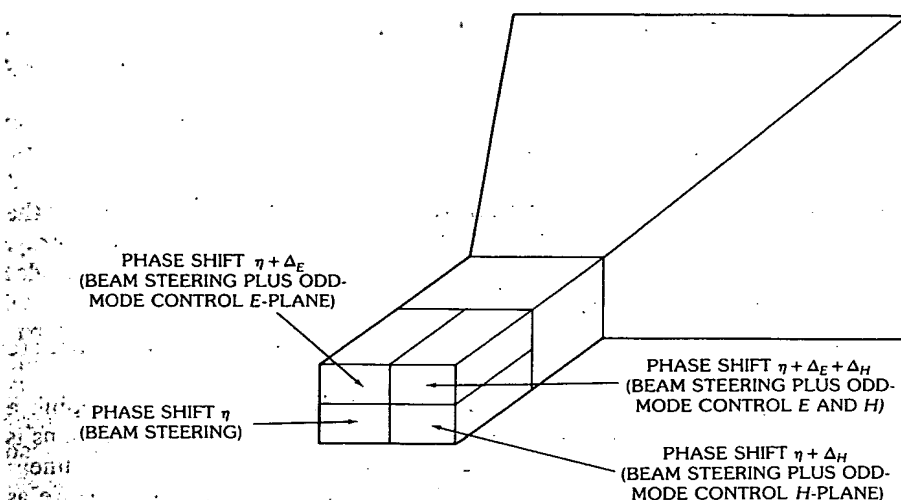
Fig. 13. Four-mode horn and power divider circuit. (*After Mailloux [13]*)

as saying that the time of transit of a ray between two points on the mean surface is an extremum (usually a minimum) and the rays are geodesics [15]. For this reason such feeds are generally called *geodesic feeds* or *lenses*.

The simplest and probably the earliest geodesic feed for phased arrays is the folded or two-layered pillbox [16–19]. It consists of two parallel-plate regions connected by a 180° bend that is parabolic in the plane of the plates. A point source feed is located in one layer. A cylindrical wave radiated from the feed goes around the 180° bend to enter the second layer, where it is collimated into a plane wave by the parabolic shape of the bend. The bend may be abrupt [16, 17], circular, or mitered [19].

The mean surface of geodesic lenses may be planar, singly curved, doubly curved, or composite. For planar surfaces the geodesics are straight lines. For singly curved (cylindrical) surfaces the geodesics are straight lines on the developed (flattened into a plane without stretching or tearing) surface. Doubly curved surfaces cannot be flattened into a plane without stretching or tearing the surface. The geodesics on doubly curved surfaces are the curves that a tightly stretched string would take with the string constrained to stay on the surface everywhere. Mathematically the geodesic is an extremum, which is the shortest or the longest path length on the surface between two points. As a simple example the shortest arc of a great circle through two points on a sphere is a geodesic, as is the longest arc of the same great circle through the points. Usually the geodesics of interest are the shortest paths between two points.

If two surfaces intersect* along a line, a geodesic (ray) across the intersection obeys Snell's laws of reflection and transmission, namely,

---

*Of course, any arbitrary "cut" in a geodesic surface can be considered as an intersection but most often the intersection is between two portions that are each developable.

(1) . The angle of reflection is equal to the angle of incidence, $\theta_r = \theta_i$.

(2)   The angle of refraction (transmission) is related to the angle of incidence by

$$\frac{\sin \theta_t}{\sin \theta_i} = \frac{\sqrt{\epsilon_i}}{\sqrt{\epsilon_t}} = \frac{n_i}{n_t}$$

where ϵ_i is the relative dielectric constant in the parallel-plate region of the incident ray and ϵ_t is that in the region of the transmitted (refracted) ray. The terms n_i and n_t are the corresponding indexes of refraction. All angles are measured from the common normal.

As will be discussed later, there are many practical geodesic lens surfaces that are composites of developable surfaces.

The parallel-plate Luneburg lens is not applicable for efficiently feeding a linear array. This is clearly evident from Fig. 14. Although the Luneburg lens is perfectly focused for all scan angles, it is very inefficient for feeding a fixed linear array because the illumination scans or translates off the linear array aperture as
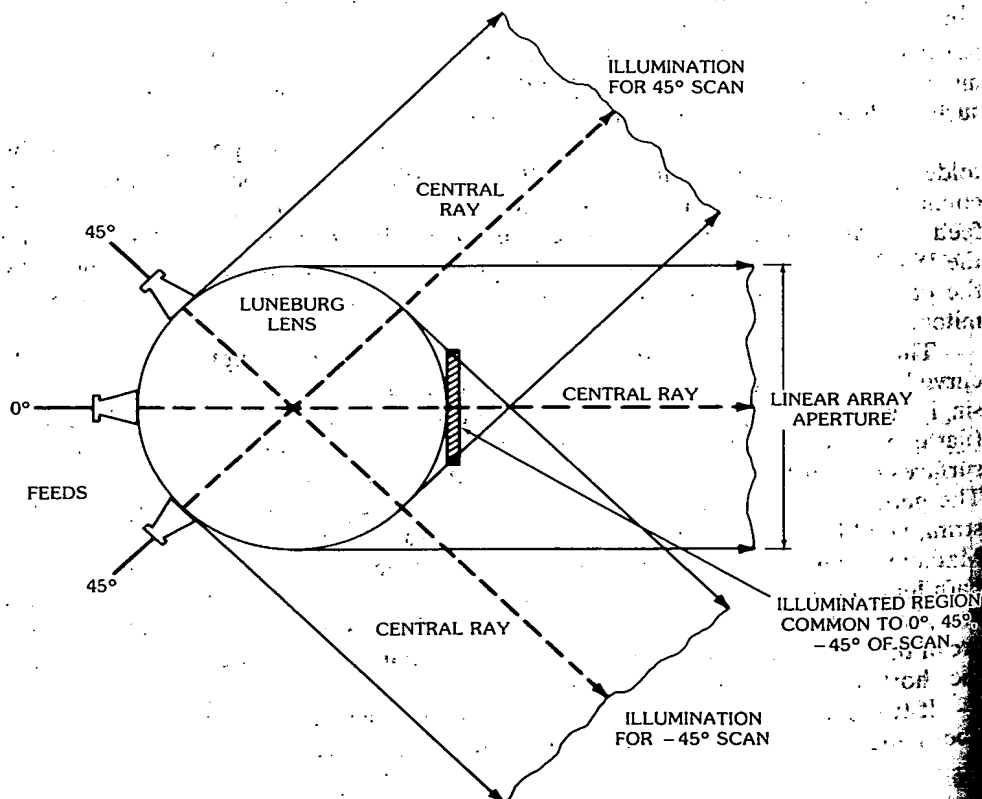
Fig. 14. Luneburg lens illuminating a linear array. (*Courtesy Hughes Aircraft Co., Fullerton, Calif.*)

the beam is scanned. The darkened portion of the linear array is all that is common for angles of scan out to ±45°. The amount of feed spillover and illumination asymmetry that results with beam scan is intolerable. Note that the central ray does not pass through the center of the linear array for scanned off beams. This results in asymmetric array illumination for tapered distributions. The circular pillbox and Meyer lens (these lenses are discussed later) do not suffer this shortcoming, as can be seen in Fig. 15, which shows that for the Meyer lens (the same is true for the circular folded pillbox) the central ray for all beams passes through the center of the linear array, i.e., the illumination does not translate across the linear array aperture. It should be mentioned that since the projected aperture of the linear array decreases as the cosine of the angle of scan, to keep the illumination efficiency from degrading, the feed illumination pattern should be made more directive according to the secant of the scan angles. This requires larger feeds as the scan increases. Fortunately, there is just enough space to do this (in terms of beamwidths of scan) because the radiated beamwidth also increases as the secant of the scan angle. This effect is true for *all* optical type feeding techniques for linear or planar arrays.

Pillbox

Fig. 16 shows a sketch of a parabolic folded pillbox [16–19]. This device has been used since the early 1950s for IFF and air traffic control antennas and as a feed for phased arrays.

The input primary feed is usually an open-ended waveguide, or two of them side by side for monopulse operation. Sometimes electric probes fed by coaxial lines backed by a quarter-wave short or cavity are used for the primary feed. The primary feed radiates in the region between a pair of parallel plates, as depicted by Fig. 16. The phase center of the primary feed is located at the focus of the parabola. The field then propagates in the TEM parallel-plate mode to the 180° bend. The bend is designed such that the "reflected" (or more accurately, transmitted around
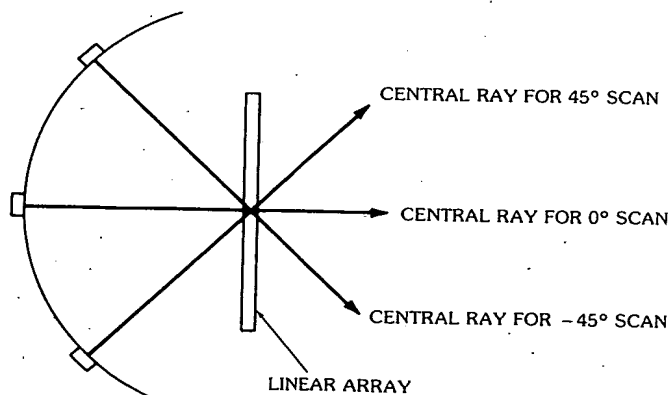

CENTRAL RAY FOR 45° SCAN

CENTRAL RAY FOR 0° SCAN

CENTRAL RAY FOR −45° SCAN

LINEAR ARRAY

Fig. 15. Meyer lens illuminating a linear array. (*Courtesy Hughes Aircraft Co., Fullerton, Calif*).
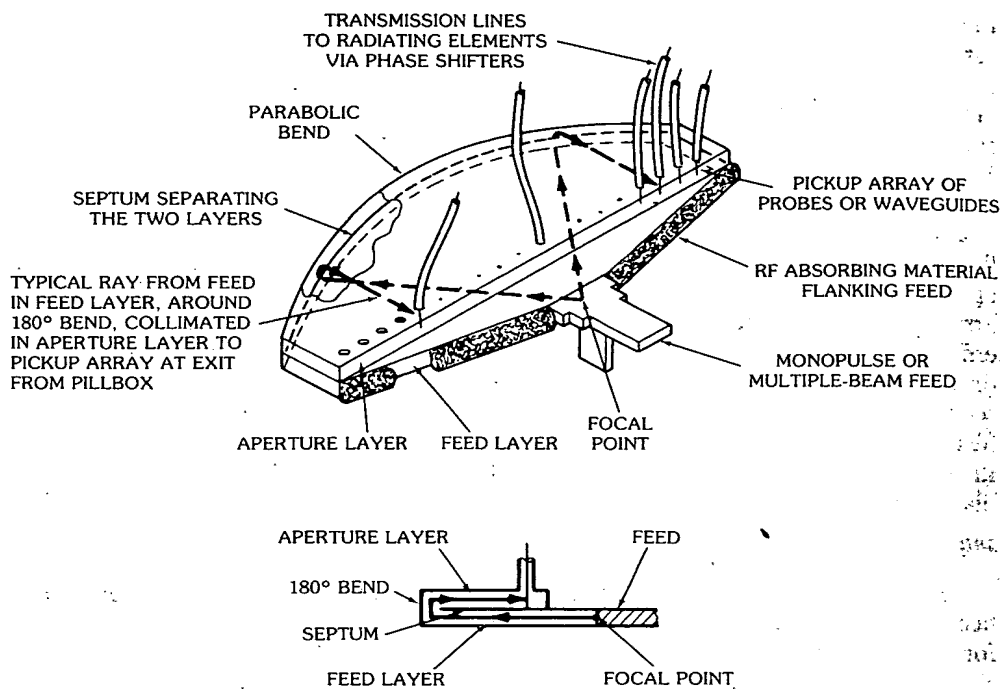
Fig. 16. Folded pillbox feed for phased array. (*Courtesy Hughes Aircraft Co., Fullerton, Calif.*)

the bend) field emerges between the upper set (ideally) of TEM parallel plates, and is collimated because of the parabolic shape. The output is located in the upper set of parallel plates at any convenient terminal plane. The output is transitioned to coax waveguide or stripline, thus forming the pickup array. Radio-frequency absorbing material should be used in the lower set of parallel plates to absorb any reflected power that did not go around the 180° bend [18]. This is especially important if low side lobes are required. Using the parabolic folded pillbox, low side lobe radiation patterns (e.g., 30 dB or better) are fairly straightforward to obtain [18]. Moreover, the loss through the structure is very low, being less than an equal path length run of waveguide of the same height as the parallel-plate separation.

The reason this device has been used so extensively throughout industry is because of its high performance, simplicity, and form factor. Its flat, thin profile usually makes it easy to package (e.g., on the back side of a planar array). In any application where a parallel-fed corporate feed is required, the parabolic folded pillbox can be used instead. Moreover, monopulse operation is simple to implement in the pillbox by feeding it with a dual feed and a magic-T or with a multimode feed with independent sum and difference modes. It is much less complicated (mechanically) than the corporate feed and does not require the multiplicity of components (hybrid junctions or directional couplers, bends, etc.) inherent in the corporate feed.

If wide-angle-coverage multiple beams are desired, the circular folded pillbox [19] can be used instead of the parabolic folded pillbox. Fig. 17 is a photograph of a 29-beam circular folded pillbox at X-band. Its principle of operation is similar to that of the parabolic folded pillbox, except that a circular arc is used at the 180° bend rather than a parabolic arc, and the feed locus is a circle whose radius is slightly greater than half the radius of the circular reflector (at the 180° bend). Without dielectric loading, the usable portion of the output aperture is restricted to about one-half the diameter, or slightly greater. The reason for this is that spherical aberration produces phase errors that limit the usable portion of the aperture. Most of the phase errors at the aperture can be corrected by trimming the line lengths at the output aperture, similar to a Schmidt correction in optics. The spherical aberration for the scanned beams resembles the spherical aberration for the on-axis beam; hence the spherical aberration that is common to all beams can be removed at the output aperture by line length adjustment.

For example, consider a design that forms multiple beams over a 90° sector ($\pm 45°$). Fig. 18 shows the calculated spherical aberration for scanned beams over $\pm 45°$. The curves all resemble each other, grossly speaking; consequently the mean value of the spherical aberration can be removed. The long and short dashed curve is the mean value, or compensation curve. The negative of this curve is inserted at the aperture by line length adjustments in the pickup array. The maximum phase error after compensation is shown dashed. The spherical aberration has been reduced by a factor of about 5 or 6. This factor depends on the total field of view over which multiple beams are formed, and the allowable degree of spherical aberration (after compensation) that can be tolerated.

With partial dielectric loading of the entrance layer the optics can be modified such that nearly 80 percent of the output diameter is usable aperture. For example, the pillbox in Fig. 17 uses Rexolite 1422 loading ($\epsilon_r = 2.56$) between the feed arc and 0.8R in the entrance layer and gives respectable phase error over 80 percent of D. The extreme scanned beams suffered from what appeared to be residual spherical aberration phase error, indicating that the use of 80 percent of D is
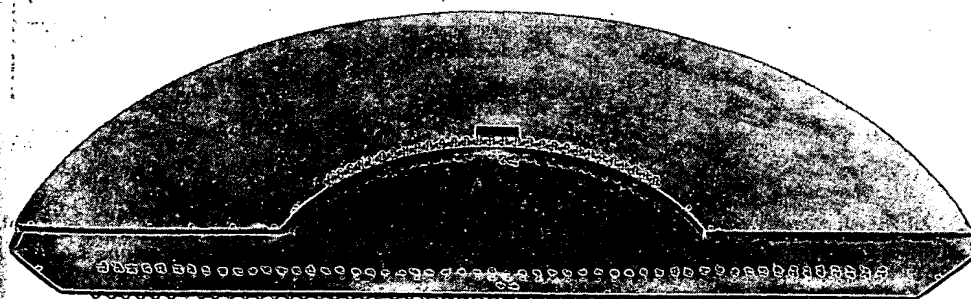

Fig. 17. Circular, folded, multiple-beam pillbox, shown with 12-in (30.48-cm) ruler. (*Courtesy North American Rockwell*)
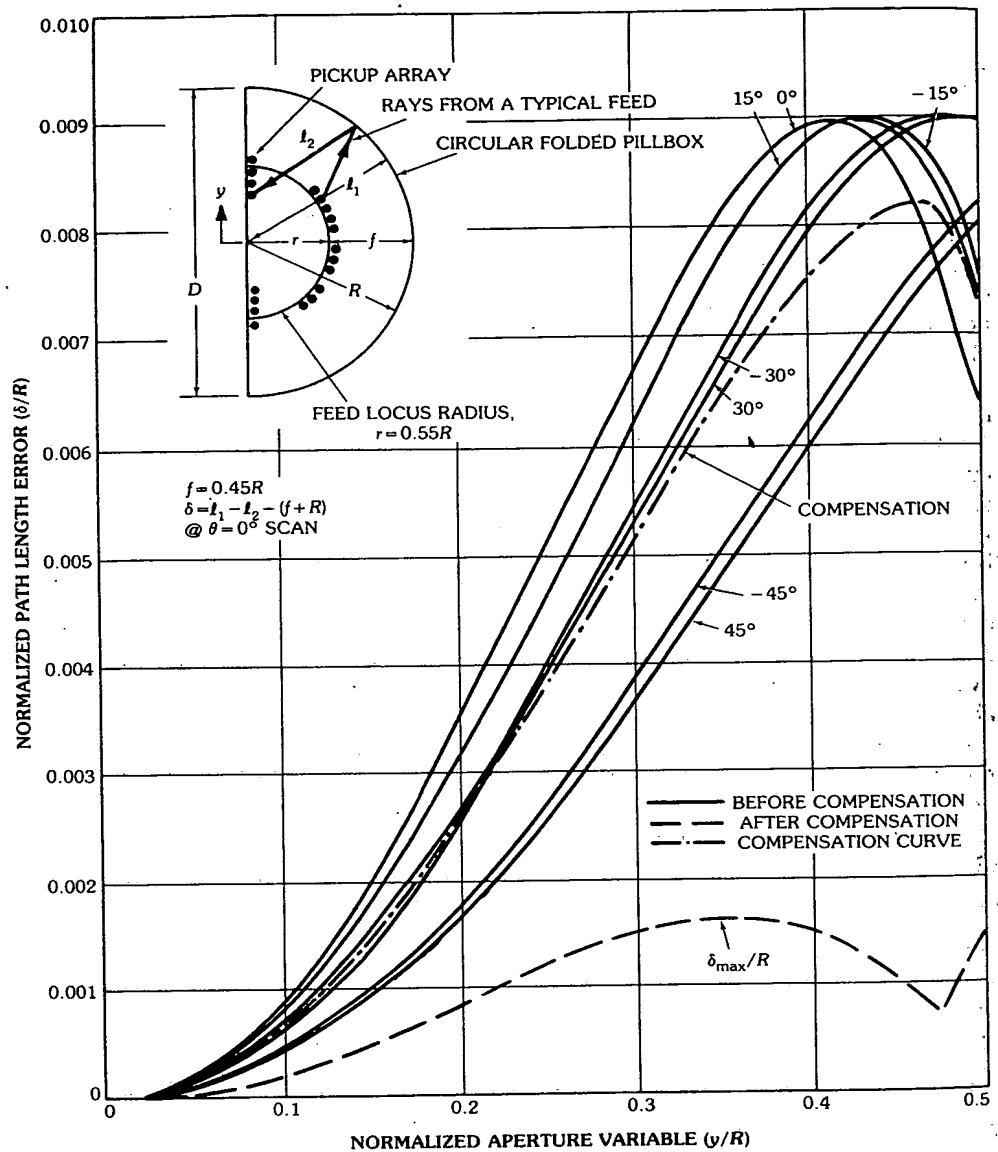
Fig. 18. Path length error versus aperture variable before compensation, and maximum path length error after compensation. (*Courtesy Hughes Aircraft Co., Fullerton, Calif.*)

probably a little too much. There was no mechanism for focusing (i.e., feed probe positions were not adjustable). In this design electric probes are used as feeds, which yields a very nearly uniform amplitude distribution at the aperture, with beam crossover levels of about 4 dB and side lobe levels consistent with a uniform amplitude distribution (13 dB) for most of the beams. The crossover level varies

with frequency consistent with the beamwidths' dependence on frequency. The 29-beam peak positions remain fixed in space independent of frequency. If waveguides were used as feeds with focusing (radial feed position adjustability) capability, improved performance would undoubtedly be realized.

Radial Transmission Line

This section describes a simple, inexpensive, and ideally lossless multiple-beam-forming device whose cost and complexity do not increase rapidly with the number of radiating elements [20-22].

In physical appearance it resembles a constrained lens using parallel-plate optics. From the microwave circuit point of view it is similar to the Butler hybrid matrix but it differs in that the number of beams does not have a definite mathematical relationship with the number of radiating elements. The number of elements is arbitrary, in contrast with the Butler matrix in which the number of beams equals the number of elements. In practice the number of beams is quite limited in the radial transmission-line scheme but the number of radiating elements can be increased arbitrarily with little extra complexity and at a cost that varies only linearly with the number of elements.

Consider a parallel-plate radial transmission line terminated on its periphery by an array of "pickup" probes connected to the radiating elements of a linear array with equal lengths of transmission line as shown in Fig. 19. Suppose that besides the TEM mode, higher-order cylindrical modes with circumferential phase variation could be excited in the radial line. The circumferential variation of these modes can be characterized by $A_m \exp(jm\phi)$, where A_m is the amplitude of the mth mode and m is an integer (positive or negative). Because of the orthogonality properties of the modes they do not couple. By virtue of equal line length connection between the circumferentially dispersed pickup probes and the elements of the linear array,
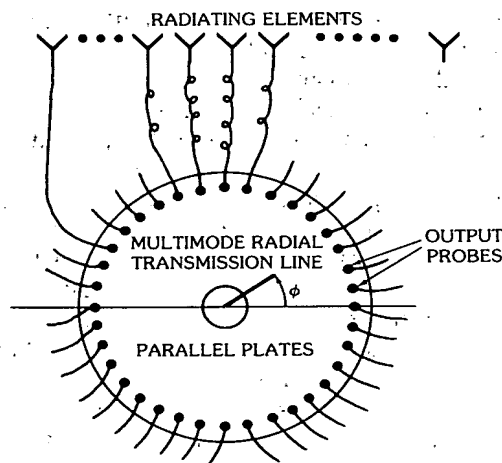

Fig. 19. Radial-transmission-line multiple-beam-forming network. (*Courtesy Hughes Aircraft Co., Fullerton, Calif.*)

the circumferential phase variation $\exp(jm\phi)$ is transformed to a linear progressive phase $\exp(j2m\pi x/L)$, where L is the length of the array and x is the aperture variable ($\phi = 0$ corresponds to $x = 0$ and $\phi = 2\pi$ corresponds to $x = L$). Thus there is a beam for each value of m. Positive and negative values of m correspond to left and right beams, respectively. For $m = 0$, there is a beam at broadside. The amplitude distribution for each of the beams is uniform and the far-field pattern is given by

$$E(\psi) = \frac{\sin(N\psi/2)}{N\sin(\psi/2)}$$

where

$N =$ number of elements in the array

$\psi = 2\pi d/\lambda \sin(\theta - \alpha)$

$\theta =$ angle of beam from broadside

$d = L/(N - 1)$, interelement spacing

$\alpha = 2m\pi/N$, interelement phase shift for the mth beam

This is exactly the same as a Butler matrix array of N elements with m beams being used.

The $m = 0$ mode can be excited at the center of the radial transmission line with a circular waveguide operating in the TM_{01} or with a coaxial TEM mode as shown in Fig. 20. The method of Fig. 20 also generates the $m = \pm1$ modes. The peak power-handling capability is limited by the E-plane magic-T. Fig. 21 shows a very high power transition using a multimode turnstile junction to excite these modes. The TE_{11} excitation results in a $\cos\phi$ circumferential variation. An orthogonal TE_{11} mode phased $90°$ will give a $j\sin\phi$ circumferential variation. Hence, by adding or subtracting the two orthogonal TE_{11} modes, the $\exp(\pm j\phi)$ circumferential variation in the radial transmission line is achieved. In other words, an excitation of right and left circular polarizations in the circular waveguide feed will result in a right and a left antenna beam. Orthogonal TE_{12} modes as shown in Fig. 22 will excite $\exp(\pm2j\phi)$ modes in the radial transmission line. In this figure the solid lines represent the field configuration of the TE_{21} mode ($\cos2\phi$ circumferential variation). The dashed lines represent the field configuration of the orthogonal TE_{21} mode ($\sin2\phi$ variation). By combining them in a $90°$ phase relationship, $\exp(j2\phi)$ and $\exp(-j2\phi)$ modes are created. The radial line can be fed with a multimode turnstile type junction fed by hybrid circuitry as in Fig. 21a. A photograph of an S-band radial line fed by this method is shown in Fig. 21b. This hybrid-fed waveguide method of excitation of higher-order modes in the radial transmission line has the advantage of simplicity, low loss, and high power handling capability. For more beams, feeding at essentially one point becomes impractical. For a greater number of beams a circular array of probes with less than half-wave spacing fed with a Butler matrix would probably be the most efficient. The obvious question may be raised as to why not dispose of the radial line and just use the
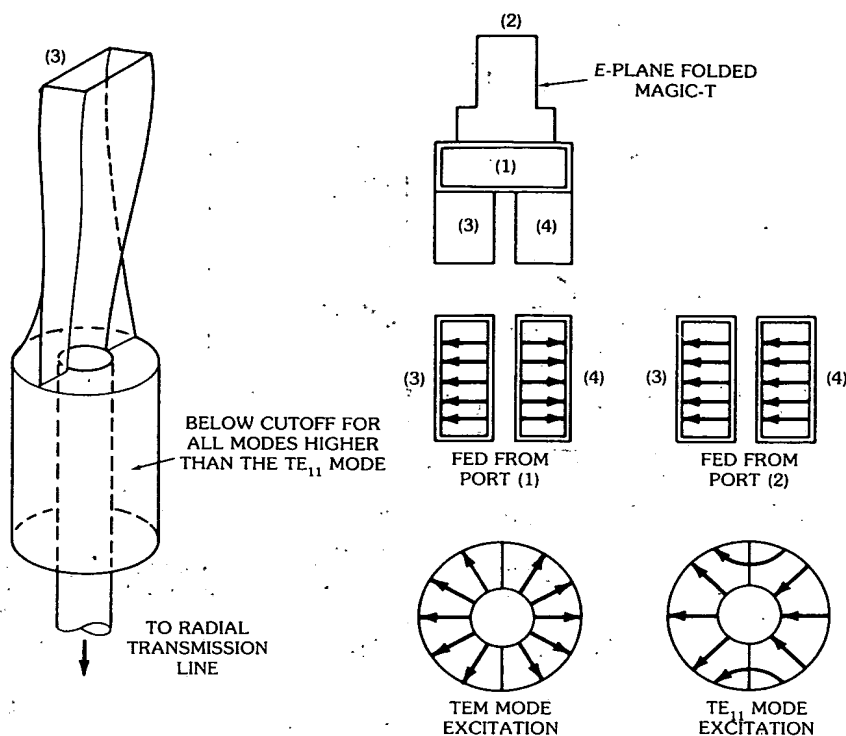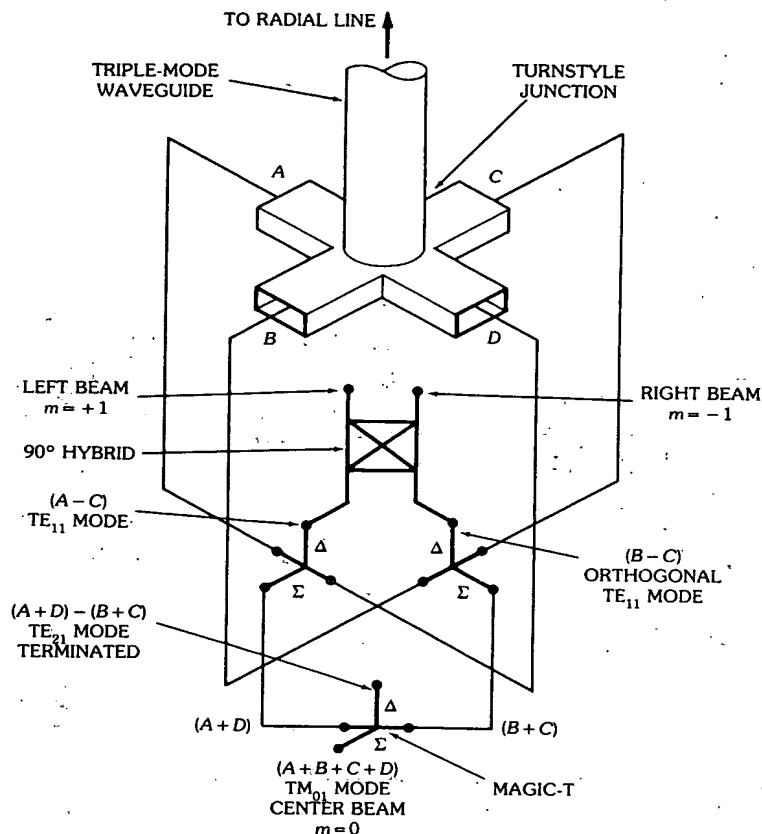
Fig. 20. Operation of high-power, dual-mode feed for radial transmission line. (*Courtesy Hughes Aircraft Co., Fullerton, Calif.*)

Butler matrix [3, 5]. The advantage of using the radial line is that regardless of the number of beams the number of outputs from the radial line can be increased to any arbitrary number by merely enlarging the diameter of the radial line to accommodate a larger number of output elements. In many systems applications requiring large arrays the number of simultaneous beams required is often much less than the number of radiating elements. For example, many phased-array systems may require only two beams for monopulse capability with beam steering achieved with ferrite or diode phase shifters. Obviously in this extreme case a radial line feed would be much simpler and much less expensive than a Butler matrix. In other applications a relatively small multiple-beam cluster that can be scanned in synchronism may satisfy the system requirements.

As an example of a possible application of the multimode radial line beam-forming network, suppose that on transmit a uniform distribution is desired and on receive a 30-dB side lobe tapered aperture distribution is desired with monopulse capability. A feeding arrangement that is still different from those of Figs. 20 and 21 is shown in Fig. 23 and is used for this example. The radial transmission line has a coaxial input (excites $m = 0$ mode) and a dual orthogonal-mode (TE$_{11}$ mode and orthogonal TE$_{11}$ mode) waveguide input which can excite the $m = \pm 1$ mode. On transmit the coaxial line input only is used, resulting in a uniform aperture

TO RADIAL LINE

TRIPLE-MODE
WAVEGUIDE

TURNSTYLE
JUNCTION

A   C

B   D

LEFT BEAM
$m = +1$

RIGHT BEAM
$m = -1$

90° HYBRID

$(A - C)$
TE_{11} MODE

$(B - C)$
ORTHOGONAL
TE_{11} MODE

$(A + D) - (B + C)$
TE_{21} MODE
TERMINATED

$(A + D)$ $(B + C)$

$(A + B + C + D)$
TM_{01} MODE
CENTER BEAM
$m = 0$

MAGIC-T

a

Fig. 21. Turnstyle junction and antenna. (*a*) High-power turnstyle junction to generate three beams. (*b*) Multiple-beam antenna using a multimode radial transmission line fed by a hybrid turnstyle junction. (*Courtesy Hughes Aircraft Co., Fullerton, Calif.*)

distribution on transmit. On receive, the $m = 0$ (uniform) mode and the $m = 1$ ($\cos \phi$) mode are combined in the power ratio of 2 to 1 to form a voltage distribution of $1 + \cos \phi$, which is equal to $2 \cos^2 (\phi/2)$, which is theoretically a -32-dB side lobe level distribution. This creates the low side lobe "sum" monopulse pattern. By changing the power division ratio a more efficient and lower side lobe cosine squared on a pedestal distribution is easily achieved. The "difference" monopulse pattern is taken from the orthogonal TE_{11} mode port, which gives a $\sin \phi$ aperture distribution which results in a difference pattern with good side lobe characteristics because there is no abrupt discontinuity in the aperture distribution, as in the case of split aperture phase monopulse schemes.

A technique for a larger number of beams uses a small circular array of probes concentric with the center of the radial line, which are properly phased to generate the different modes. A seven-beam system was designed and tested [22]. This feed system utilized a hybrid network of 90° and 180° 3-dB couplers. A Butler matrix of

b
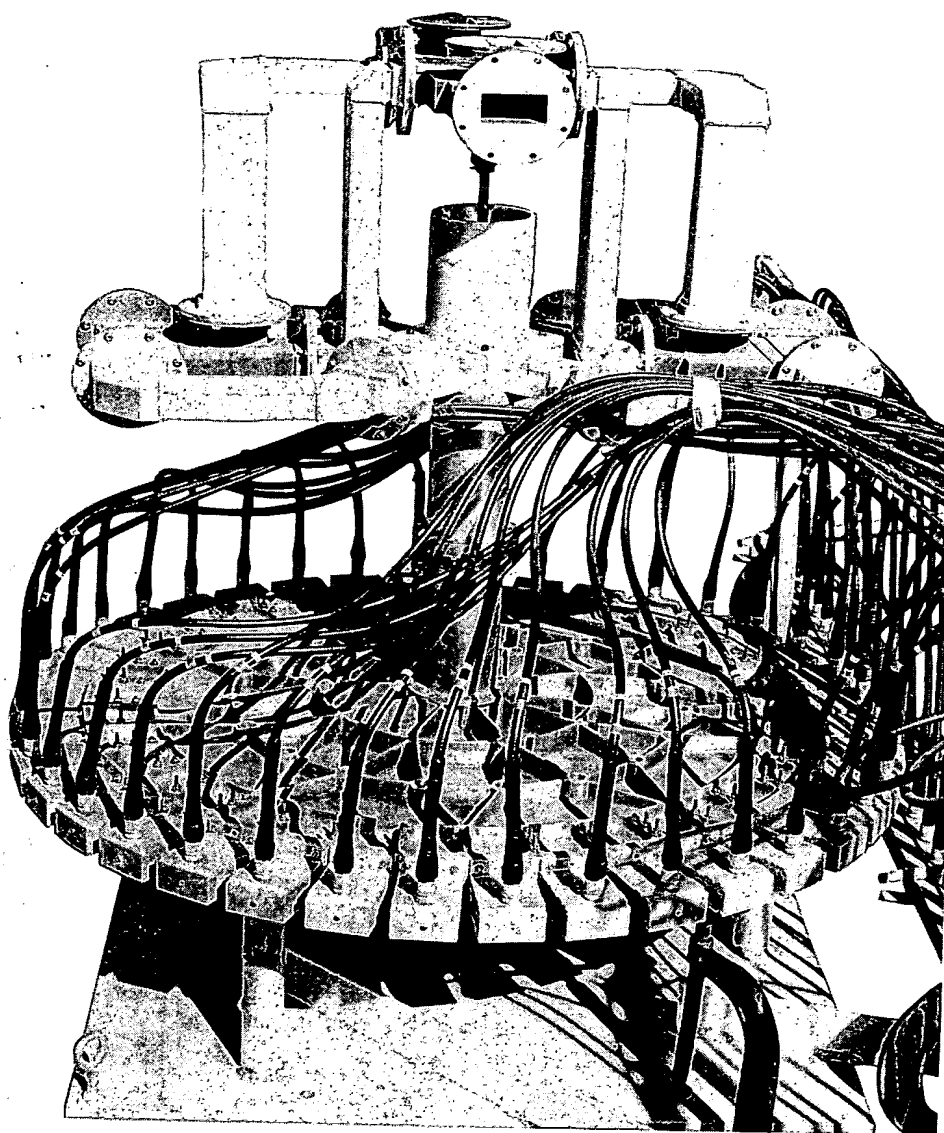
Fig. 21, *continued.*

the type shown in Fig. 5 could have been used just as well. It is interesting to note that, as mentioned in Section 2, the matrix in Fig. 24 does not require fixed phase shifters, in contrast to that of Fig. 5. Fig. 24 is a schematic diagram of the net-work; the 180° (magic-T) is designated by the letter T and the 90° coupler by the letter H. The phase progression around the circular array for each antenna
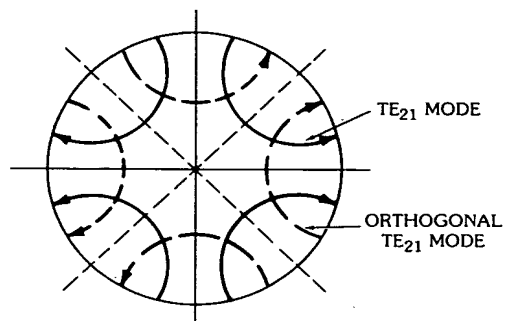
Fig. 22. Waveguide excitation of $m = 2$ modes. (*Courtesy Hughes Aircraft Co., Fullerton, Calif.*)
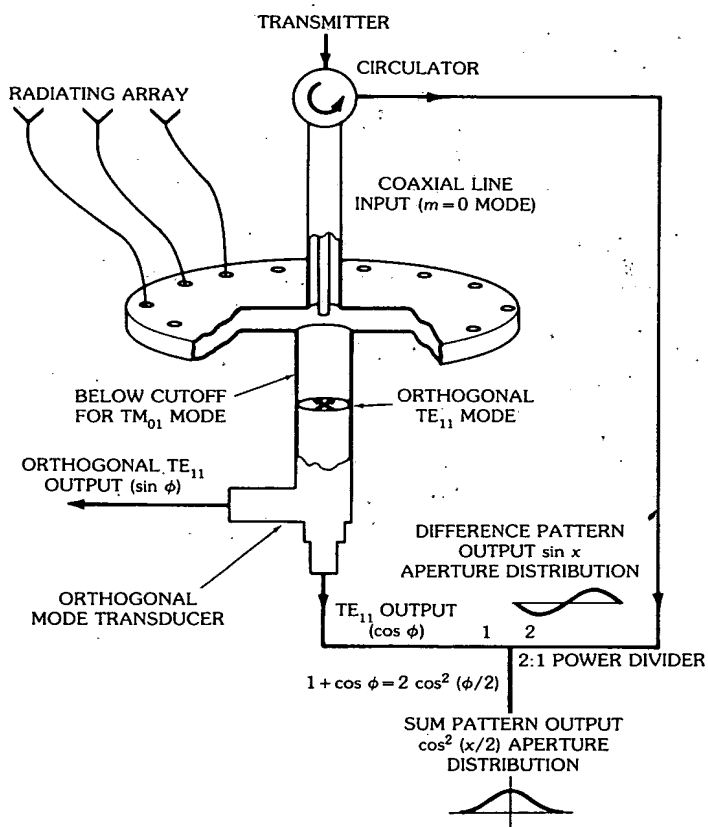
Fig. 23. Arrangement to achieve uniform aperture distribution on transmit and cosine-squared distribution on receive with monopulse capability. (*Courtesy Hughes Aircraft Co., Fullerton, Calif.*)
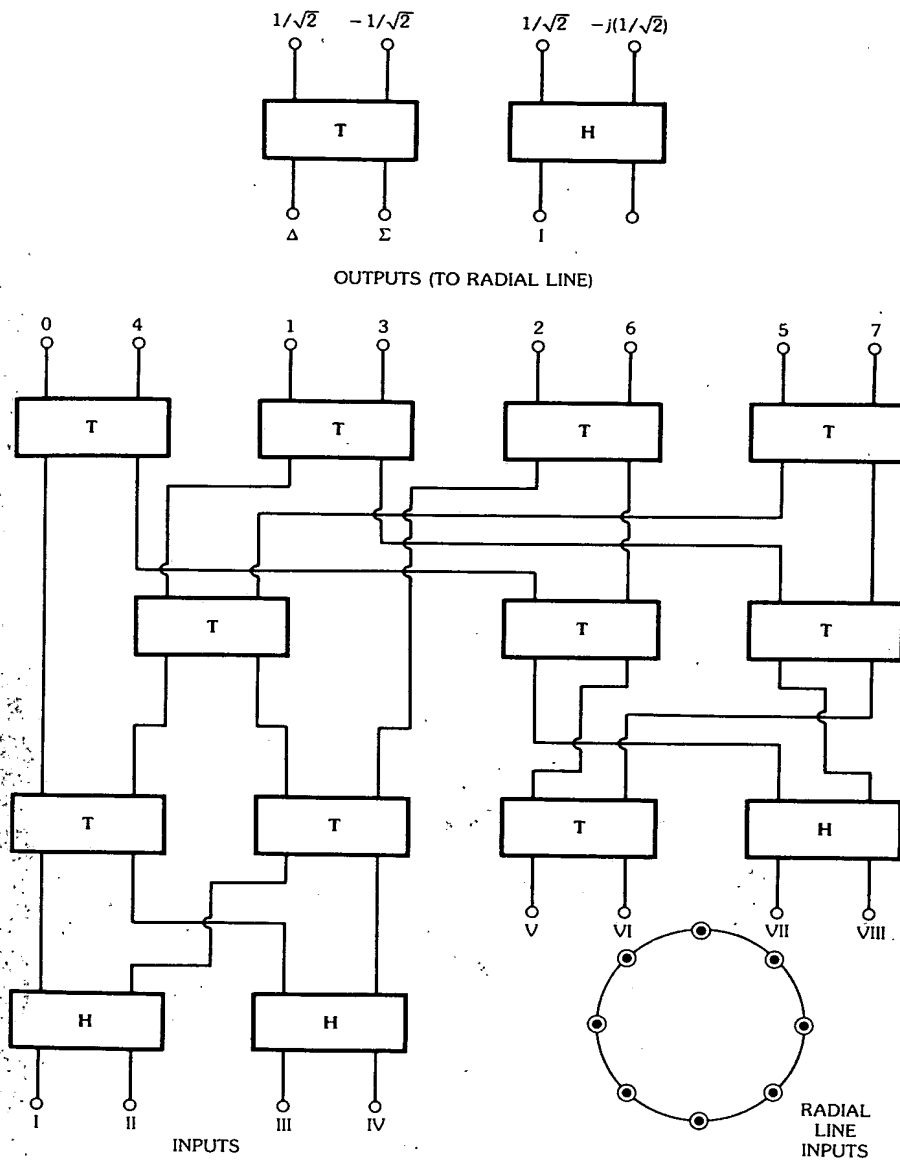
Fig. 24. Block diagram of feed circuitry. (*Courtesy Hughes Aircraft Co., Fullerton, Calif.*)

beam (mode) is given in Table 1. Note that input V, which corresponds to output phases that are alternately 0° and 180°, gives rise to a split end-fire beam that results in two actual opposing end-fire beams. This input is not used and is terminated in a matched load. Fig. 25 is a photograph of the stripline network. Because of the finite number of probes the $\exp(\pm jm\phi)$ variation is only discretely approximated, and if the probe separation is too great, undesirable higher-order modes are also

Table 1. Phase Progression Around Circular Array for Each Antenna Beam

	Outputs							
Input	0	1	2	3	4	5	6	7
I	0°	135°	270°	45°	180°	315°	90°	225°
II	0°	225°	90°	315°	180°	45°	270°	135°
III	0°	45°	90°	135°	180°	225°	270°	315°
IV	0°	315°	270°	225°	·180°	135°	90°	45°
V	0°	180°	0°	180°	0°	180°	0°	180°
VI	0°	0°	0°	0°	0°	0°	0°	0°
VII	0°	90°	180°	270°	0°	90°	180°	270°
VIII	0°	270°	180°	90°	0°	270°	180°	90°

Radial Transmission-Line Modes Corresponding to Each Input			
Input I	$m = +3$	Input V	(terminated)
Input II	$m = -3$	Input VI	$m = 0$
Input III	$m = +1$	Input VII	$m = +2$
Input IV	$m = -1$	Input VIII	$m = -2$
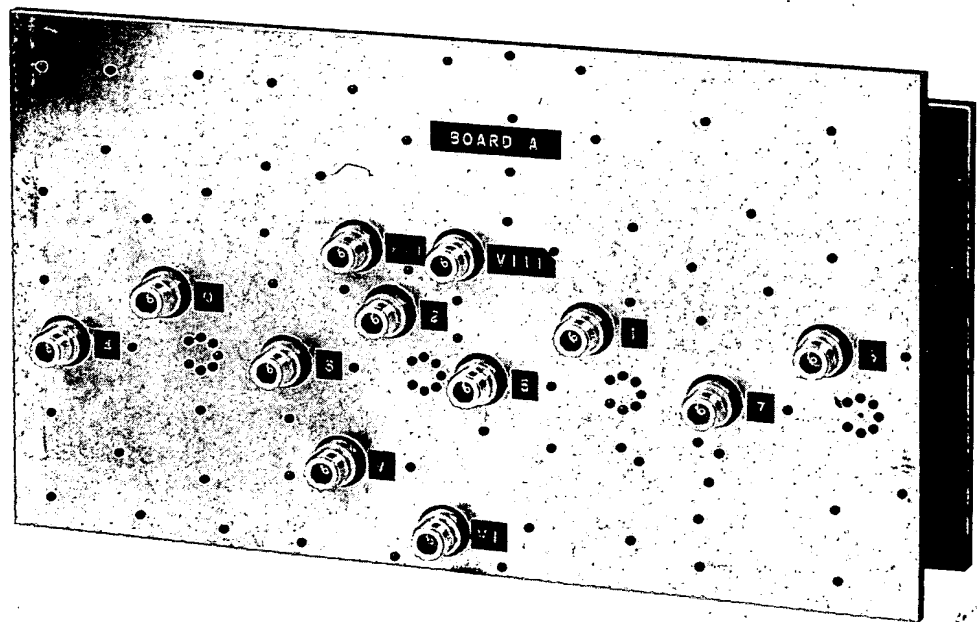
Fig. 25. Stripline hybrid-feed network. (*Courtesy Hughes Aircraft Co., Fullerton, Calif.*)

generated. However, if the feed probe spacing is somewhat closer than $\lambda/2$, the undesirable higher-order modes are "below cutoff." This corresponds to $n > kR_0$ in the cylindrical modal expansion, where n is any undesired higher-order mode number ($n > m$), R_0 is the radius of the circular array of probes, and k is $2\pi/\lambda$. In

this case the higher-order modes are "below" cutoff and do not radiate from the feed circle. The undesired higher-order modes, if they did radiate, would result in extraneous beams in directions corresponding to these modes which can also be identified as grating lobes from the linear array due to the periodic amplitude ripple in the aperture distribution. With a $\lambda/2$ probe spacing, the undesired higher-order modes were not sufficiently suppressed; hence a $3\lambda/8$ spacing was used in the experimental model. It should be emphasized that by higher-order modes we mean modes that are higher than the desired modes intentionally generated by the feed. A photograph of the experimental model including the hybrid feed network, the radial line, and the linear array is shown in Fig. 26. The radial line outputs are waveguides and the linear array consists of open-ended waveguide elements with a common horn.

Fig. 27 gives the measured patterns of the seven beams superposed. The patterns were taken without individual tuning or gain adjustment of the different beams. Hence the patterns as recorded indicate the relative gains of the separate beams including impedance-mismatch, circuit, and scan losses. As with the waveguide method of excitation the patterns agree quite well with the theoretical patterns. The vswr was less than 1.3 for all beams. To verify the beam-combining technique to produce tapered aperture distributions, three beams were combined to give a cosine-squared function on a pedestal aperture distribution. Fig. 28 is a typical antenna pattern which shows that low side lobe distributions are achievable. Also, as with other multiple-beam antennas, sector beams and other shaped
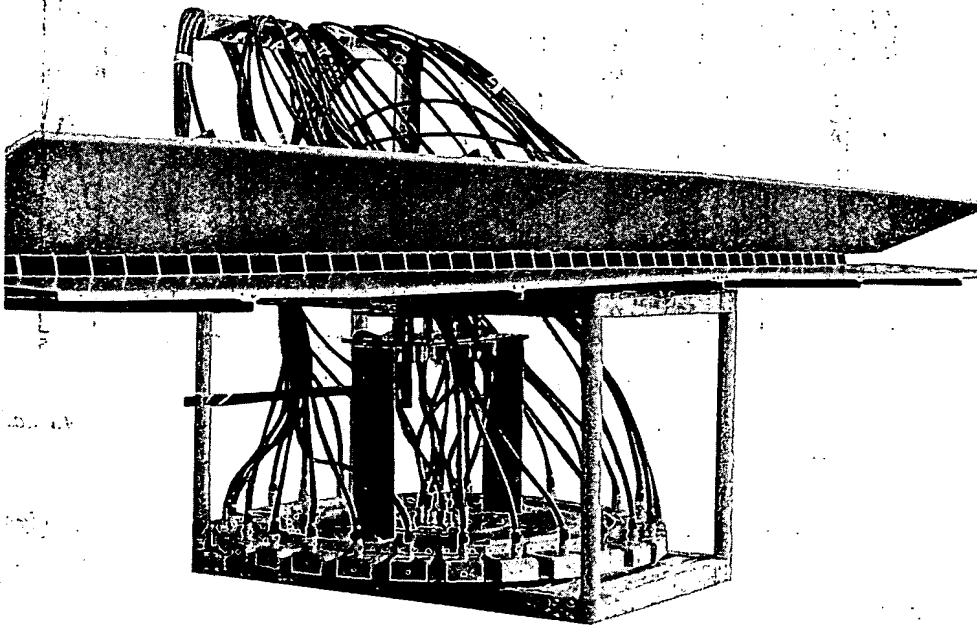

Fig. 26. Experimental model of seven-beam antenna. (*Courtesy Hughes Aircraft Co., Fullerton, Calif.*)
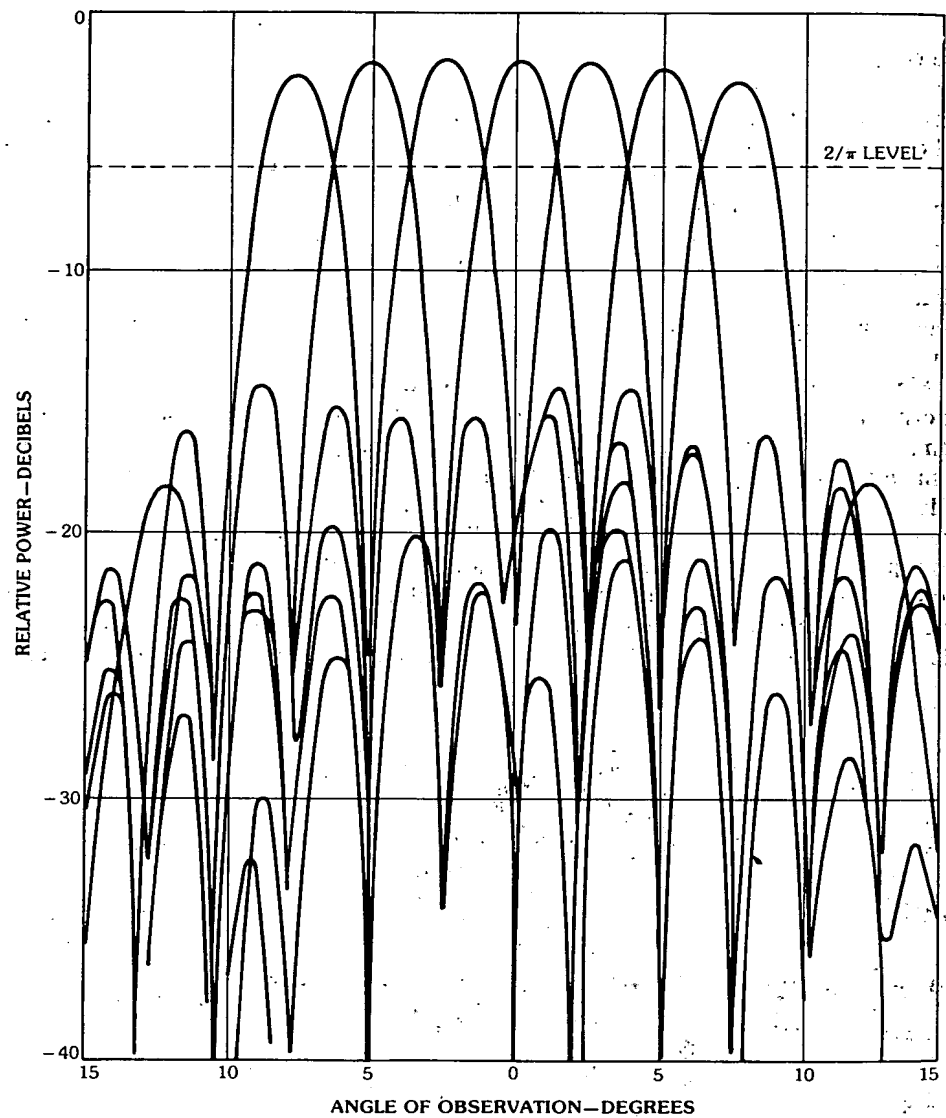
Fig. 27. Measured patterns from the seven-beam antenna system. (*Courtesy Hughes Aircraft Co., Fullerton, Calif.*)

patterns are achievable by combination of beams in the proper relative amplitudes and phases.

Meyer Lens

The principle of the Meyer lens is easily seen by considering a point-source feed radiating in the region between parallel plates as shown in Fig. 29a. The phase
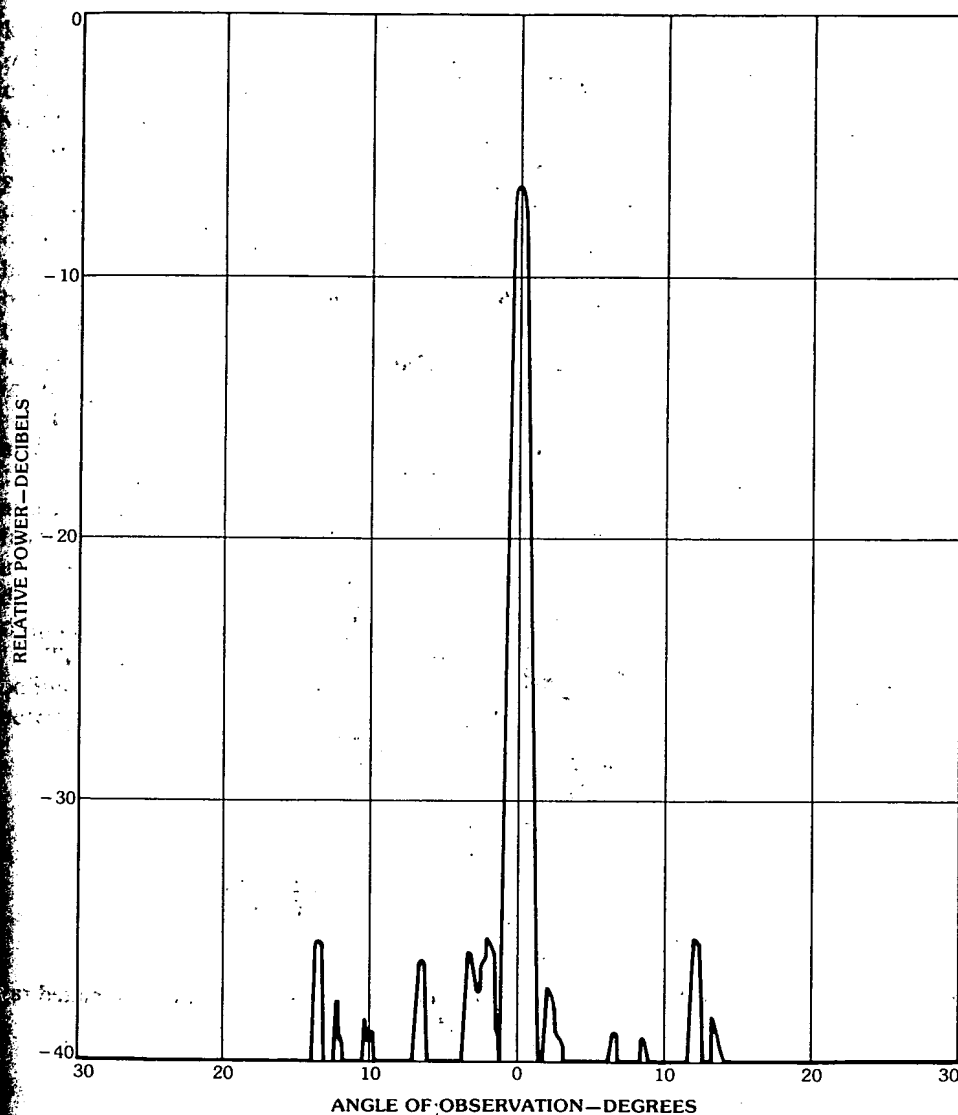
Fig. 28. Measured pattern of cosine-squared function on a pedestal distribution. (*Courtesy Hughes Aircraft Co., Fullerton, Calif.*)

front in the parallel plates is circular and the rays are radial from the feed. The circular phase front can be made linear to collimate the rays by simply curving the parallel plates in the form of a cylinder and putting a 90° bend at the base of the cylinder to direct the collimated rays normal to the axis of the cylinder as shown in Fig. 29b. The Meyer concept is more general in that the bend angle need not be 90° but is arbitrary. The shape of the curve of the cylinder for perfect focus from a

a

b
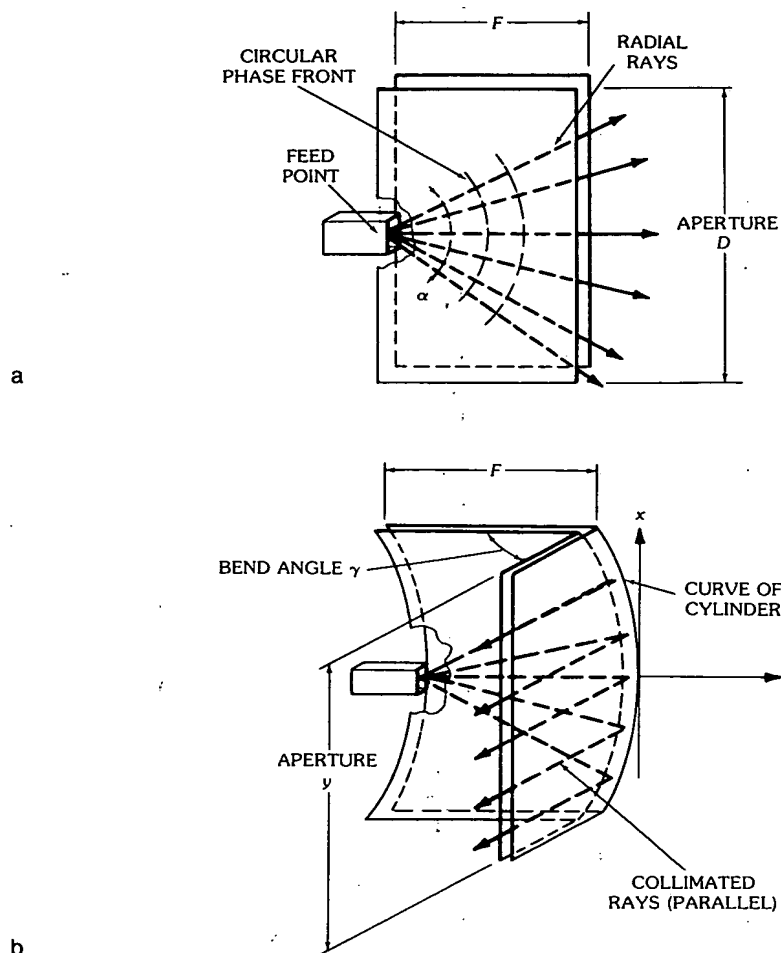
Fig. 29. Principle of the Meyer lens. (*a*) For circular phase front. (*b*) For collimated rays. (*Courtesy Hughes Aircraft Co., Fullerton, Calif.*)

given point-source feed is a catenary [23] given by

$$\frac{y}{\delta} = \cosh\!\left(\frac{x}{\delta}\right) - 1, \qquad \delta = f(\sec\phi + \tan\phi), \qquad \gamma = \frac{\pi}{2} - \phi$$

where γ is the angle of the bend. If the feed is moved laterally and rotated about its phase center to maintain the proper illumination of the common aperture, the beam will scan from that of the original beam by an amount proportional to lateral displacement, just as with a parabolic antenna. In general, as with all optical devices, the wide-angle scan capability improves with larger F/D, or more precisely the smaller the feed subtending angle α. By making the bend angle γ larger

keeping the aperture size D the same, the F/D ratio is made larger, the feed angle α is smaller, and the wide-angle scannability is improved. As with all optical devices, however, the feed must be larger and the whole structure less compact by virtue of larger F.

It is interesting to note that if the bend angle γ is made 0°, the catenary degenerates into a parabola and the Meyer lens becomes the familiar folded pillbox described in Section 3, under the heading "Pillbox." For bend angles on the order of 90° or greater the catenary curve is a much better fit to a circle than is a parabola; hence the Meyer lens designed with a nonperfectly focusing circular cylinder has better aperture phase characteristics than a circular pillbox with the same F/D. Due to their circular geometry both have unlimited scannability. A modified 360° Meyer lens with dielectric loading can be used to feed a cylindrical array. This is discussed in the last part of Section 6.

The circular Meyer lens [24] is depicted by Figs. 30 and 31 in its undeveloped and developed states, respectively.

A feed may be placed and properly oriented at any point along the feed circle, and the beam radiated from the lens will point in the direction of a principal ray from the feed point through the center of the lens. The analysis may be more easily understood by developing the lens onto a flat surface, as in Fig. 31. In the developed lens all the geodesic paths become straight lines, making analysis very simple.

Two developed* surfaces can be connected together by joining corresponding points of the two surfaces with equal lengths of TEM cable. In this case Snell's laws become
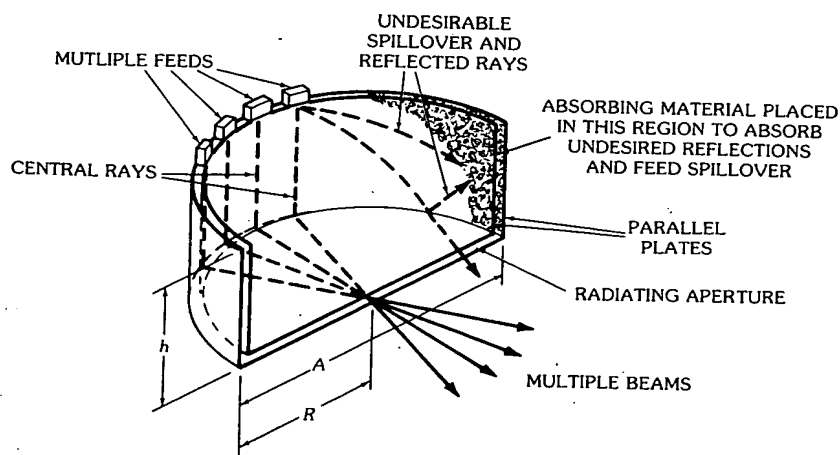

Fig. 30. Schematic diagram of undeveloped multiple-beam geodesic line source. (*Courtesy Hughes Aircraft Co., Fullerton, Calif.*)

---

*The joining surfaces need not, in general, be developable or even be physically joinable but in most practical cases the parts are separated at an intersection in the undeveloped configuration.
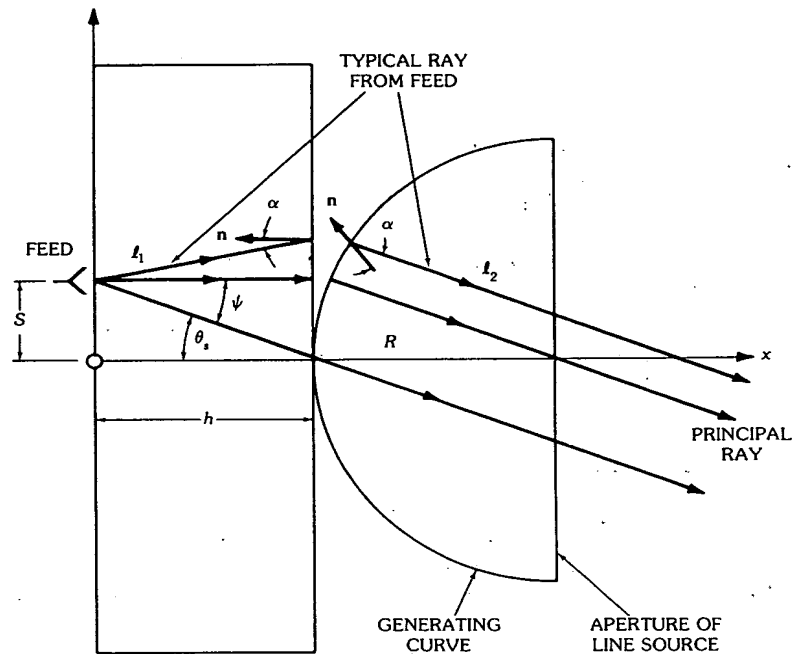
Fig. 31. Developed geodesic lens. (*Courtesy Hughes Aircraft Co., Fullerton, Calif.*)

$$\alpha_i = \alpha_r$$

$$\frac{\sin \alpha_t}{\sin \alpha_i} = \frac{\sqrt{\epsilon_1}\,ds_1}{\sqrt{\epsilon_2}\,ds_2} = \frac{n_1 ds_1}{n_2 ds_2}$$

where

α_i = the angle of incidence

α_r = the angle of reflection

α_t = the angle of transmission (refraction)

ϵ_1, ϵ_2 = the relative dielectric constants of regions 1 and 2, respectively

n_1, n_2 = corresponding indexes of refraction

ds_1, ds_2 = the local spacing of connecting points of regions 1 and 2, respectively

It can be seen from these relationships that the relative spacings ds_1 and ds_2 of the connecting points have the same effects as the relative index of refraction, n_1 and n_2.

An obvious further generalization can be made to make the cable lengths not necessarily equal. Then the differential line length $d\ell$ between adjacent lines times the index of refraction $\sqrt{\epsilon_3}$ in the cables must be added to give the relation

$$\sqrt{\epsilon_1}\, ds_1 \sin \alpha_1 = \sqrt{\epsilon_2}\, ds_2 \sin \alpha_2 + \sqrt{\epsilon_2}\, d\ell$$

The law of reflection remains essentially the same with the assumption that the major portion of the reflected energy is due to the parallel plate–to-cable transition mismatch.

Rotman and Turner [25] used these concepts to design wide-angle multiple-beam lenses using planar parallel plates interconnected by cables. Consequently, these types of lenses are known as *Rotman lenses*. Excerpts from a paper by Rotman and Turner are given in the next section.

In Fig. 31 the beam direction is determined by the principal ray which passes through the center of the aperture. The phase across the aperture may be found by comparing the geodesic path length $\ell = \ell_1 + \ell_2$ for any ray to the principal ray of path length $h + R$.

This type of lens is not perfectly focusing, that is, it will not provide a perfectly plane phase front over the entire aperture. It does, however, provide a reasonably flat phase front over approximately 70 to 80 percent of the aperture. The spherical aberration of this lens is similar to that of the circular folded pillbox covered earlier, but smaller as explained before, allowing more usable aperture.

For phasing a linear array, a pickup array is located at the output aperture which could be waveguide, coax, or stripline. The line lengths at the pickup array would be adjusted to remove the portion of the spherical aberration that is common to all beam positions in exactly the same fashion as discussed previously for the circular folded pillbox.

A multiplicity of feeds located on the circular feed arc is used to create multiple simultaneous beams. The pointing angles of the multiple beams are frequency independent, which implies that the crossover level is frequency dependent, since the beamwidths depend on frequency.

The main advantage of this lens over the circular folded pillbox is that it has more usable aperture. Its main disadvantage is its form factor (in its undeveloped form), which could represent a packaging problem for some applications. However, the circular portion of this lens could be folded, thereby halving its height. It could also be folded more than once to decrease its height even more, but there is certainly a point of diminishing returns.

Radio-frequency absorbing material should be placed in the curved plates at places that do not interfere with the principal optical paths of any feed. This is to absorb any reflected power that does not go around the 90° bend. Materials such as synthane (linen base phenolic) can be used as structural members to hold the plate separation fixed while also acting as rf absorbers. The loss through the Meyer lens is very low, similar to that of the folded pillbox.

Rotman and Turner Line Source Microwave Lens

The Rotman and Turner lens [25] is a parallel-plate constrained lens consisting of a focal arc on which multiple feeds are placed (see Figs. 32 and 33), a set of parallel plates whose plate separation is less than $\lambda/2$ into which the feeds radiate, a pickup array along a surface designated Σ_1 in Fig. 32, a set of interconnecting cables of variable line lengths, and a radiating array designated Σ_2 along a straight line. Fig. 33 illustrates the physical configuration. Four independent conditions are

Fig. 32. Microwave lens parameters. (*After Rotman and Turner [25], © 1963 IEEE*)

Fig. 33. Parallel-plate microwave lens. (*After Rotman and Turner [25], © 1963 IEEE*)

imposed on the lens system to uniquely determine its configuration: the four conditions imposed are a straight front face, two symmetrical off-axis focal points, and an on-axis focal point. This lens is similar to Ruze's [26] lens except that an additional degree of freedom is available (that is, $y \neq N$, see Fig. 33) which will manifest itself in improved performance for very large apertures. In Ruze's design the lens has two perfect off-axis symmetrical focal points and an on-axis focal point for which the second, but not higher-order, phase deviation is zero. One hundred beamwidths of scan are possible. For these no-second-order lenses, both the front and back lens contours are curved. Ruze [26] also discusses a straight front-face design that has two perfect symmetrical off-axis foci and one highly corrected on-axis focal point. For very large apertures there is some degree of residual higher-order coma aberration in the design.

Rotman and Turner use the generalized lens design principles developed by Gent [27] and others and impose the four previously mentioned conditions to arrive at their configuration.

The following three equations condition perfect focusing at the three* foci using a straight radiating face (see Fig. 32):

$$\overline{(F_1 P)} + W + N \sin \alpha = F + W_0 \tag{1}$$

$$\overline{(F_2 P)} + W - N \sin \alpha = F + W_0 \tag{2}$$

and

$$\overline{(GP)} + W = G + W_0 \tag{3}$$

where

$$\overline{(F_1 P)}^2 = F^2 + X^2 + Y^2 + 2FX \cos \alpha - 2FY \sin \alpha, \tag{4}$$

$$\overline{(F_2 P)}^2 = F^2 + X^2 + Y^2 + 2FX \cos \alpha + 2FY \sin \alpha \tag{5}$$

and

$$\overline{(GP)}^2 = (G + X)^2 + Y^2 \tag{6}$$

A set of parameters is normalized relative to the focal length F:

$$\eta = N/F, \qquad x = X/F, \qquad y = Y/F \tag{7}$$

$$\omega = \frac{W - W_0}{F}, \qquad g = G/F \tag{8}$$

Also,

---

*Very recently a quadrufocal bootlace lens has been reported by Rappaport and Zaghloul [28].

$$a_0 = \cos \alpha \qquad b_0 = \sin \alpha \cdot \tag{9}$$

After normalizing and using definition (9), Equations 4, 5, and 6 can be combined with (7):

$$\frac{\overline{(F_1 P)}^2}{F^2} = 1 + x^2 + y^2 + 2a_0 x - 2b_0 y \tag{10}$$

$$\frac{\overline{(F_2 P)}^2}{F^2} = 1 + x^2 + y^2 + 2a_0 x + 2b_0 y \tag{11}$$

$$\frac{\overline{(GP)}^2}{F^2} = (g + x)^2 + y^2 \tag{12}$$

The normalized forms of (1) and (10) are combined to yield

$$\begin{aligned}
\frac{\overline{(F_1 P)}^2}{F^2} &= (1 - \omega - b_0 \eta)^2 \\
&= 1 + \omega^2 + b_0^2 \eta^2 + 2b_0 \omega \eta - 2\omega - 2b_0 \eta \\
&= 1 + x^2 + y^2 + 2a_0 x - 2b_0 y
\end{aligned} \tag{13}$$

Since the off-axis focal points are located symmetrically about the center axis, the lens contours must also be symmetrical. Therefore, (13) remains unchanged and can be separated into two independent equations if η is replaced by $-\eta$ and y by $-y$. One equation contains only odd powers of y and η while the other contains the even powers. Thus,

$$-2b_0 \eta + 2b_0 \omega \eta = -2b_0 y \tag{14}$$

or

$$y = \eta(1 - \omega) \tag{15}$$

Also,

$$x^2 + y^2 + 2a_0 x = \omega^2 + b_0^2 \eta^2 - 2\omega \tag{16}$$

Equations 3 and 6 relating to on-axis focus together with definitions (8) and (9) are similarly combined to give

$$\frac{\overline{(GP)}^2}{F^2} = (g - \omega)^2 = (g + x)^2 + y^2 \tag{17}$$

or

$$x^2 + y^2 + 2gx = \omega^2 - 2g\omega \tag{18}$$

After algebraic manipulation, (15), (16), and (18) give the following relations between ω and η:

$$a\omega^2 + b\omega + c = 0 \tag{19}$$

where

$$a = \left[1 - \eta^2 - \left(\frac{g-1}{g-a_0}\right)^2\right] \tag{20}$$

$$b = \left[2g\left(\frac{g-1}{g-a_0}\right) - \frac{(g-1)}{(g-a_0)^2}b_0^2\eta^2 + 2\eta^2\right] \tag{21}$$

and

$$c = \left[\frac{gb_0^2\eta^2}{g-a_0} - \frac{b_0^4\eta^4}{4(g-a_0)^2} - \eta^2\right] \tag{22}$$

For a fixed set of values of the design parameters α and g, ω can be computed as a function of η from (19). These values of ω and η are then substituted into (14) and (18) to give x and y, which completes the solution of the lens design.

Choosing $\alpha = 30°$, Figs. 34a, 34b, and 34c show the computed lens shape and mapping function $\eta(y)$, as well as the feed locus, for values of $g = 1.10$, 1, 1.137, respectively. The corresponding path length errors $\Delta\ell$ for scan angles of 5°, 10°, 20°, 30° are given in Fig. 35, illustrating the extremely small degree of error over these scan angles.

Fig. 36 illustrates the hardware implementation of this technique, while Figs. 37a, 37b, and 37c illustrate the measured scanned radiation patterns.

According to Rotman and Turner's calculations this type of antenna design is capable of scanning 800 beamwidths of scan without appreciable degradation. For further details, the reader is referred to Rotman and Turner [25].*

Rinehart-Luneburg Lens

Up to this point, this section has dealt with the feeding of linear or planar phased arrays. Although the Rinehart-Luneburg lens is not particularly applicable to the feeding of linear or planar phased arrays, which is the subject of Section 2, under "Multiple-Beam Matrix Feeds," it is introduced here because it is a parallel-plate device. It is applicable for feeding circular or cylindrical arrays and is discussed more fully for that application in Section 6.

The Rinehart [29] geodesic lens is an analog of the nonuniform index of

---

*The reader should be warned that there are some typographical errors in some of the equations in [25]. The most important error is in the expressions for b (Equation 21 of this chapter). The term $-2g$ is missing in the corresponding equation (12) in [25].
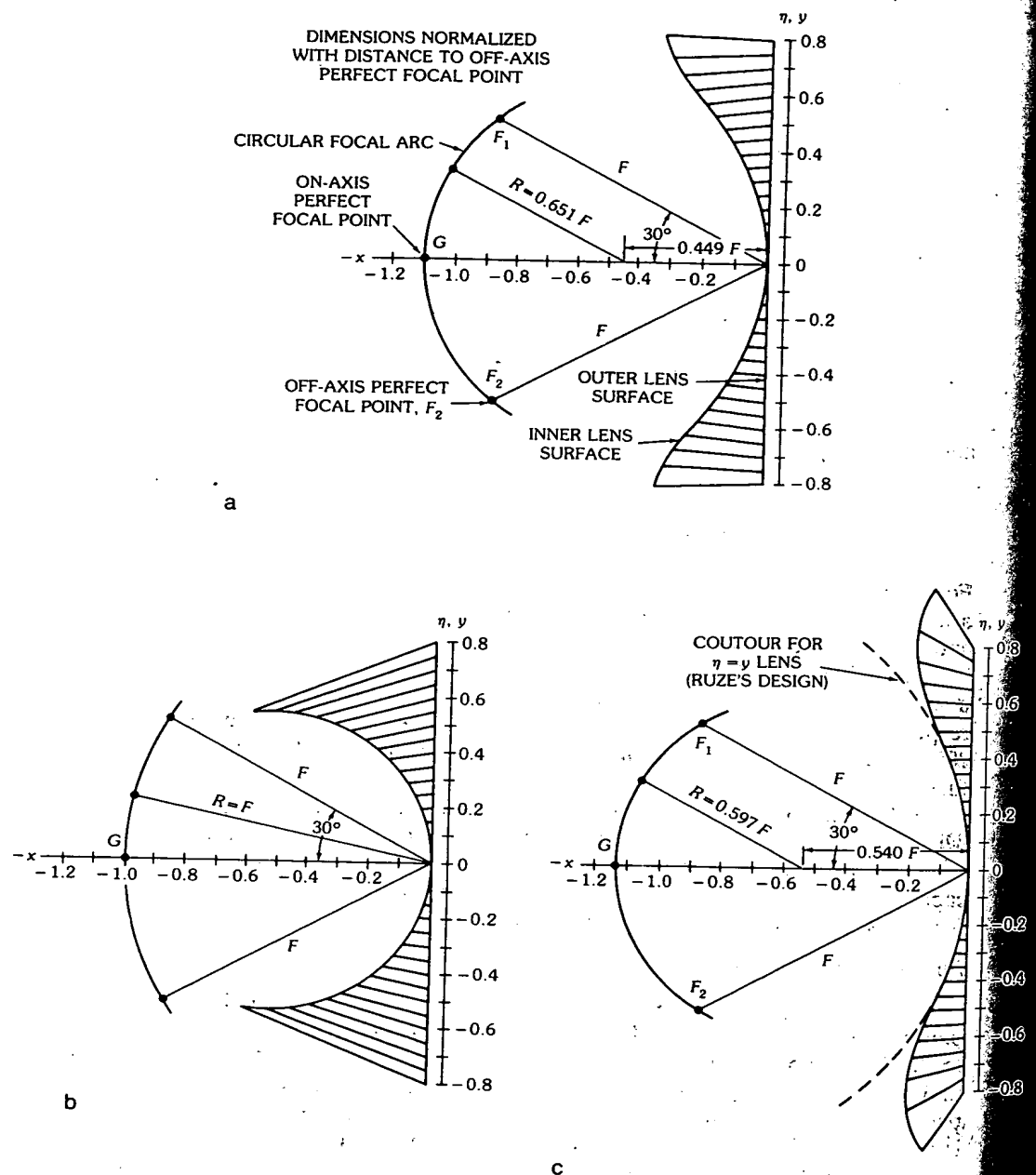
a

b

c

Fig. 34. Microwave lens contours. (*a*) With $g = 1.10$. (*b*) With $g = 1$. (*c*) With $g = 1.137$. (*After Rotman and Turner [25], © 1963 IEEE*)
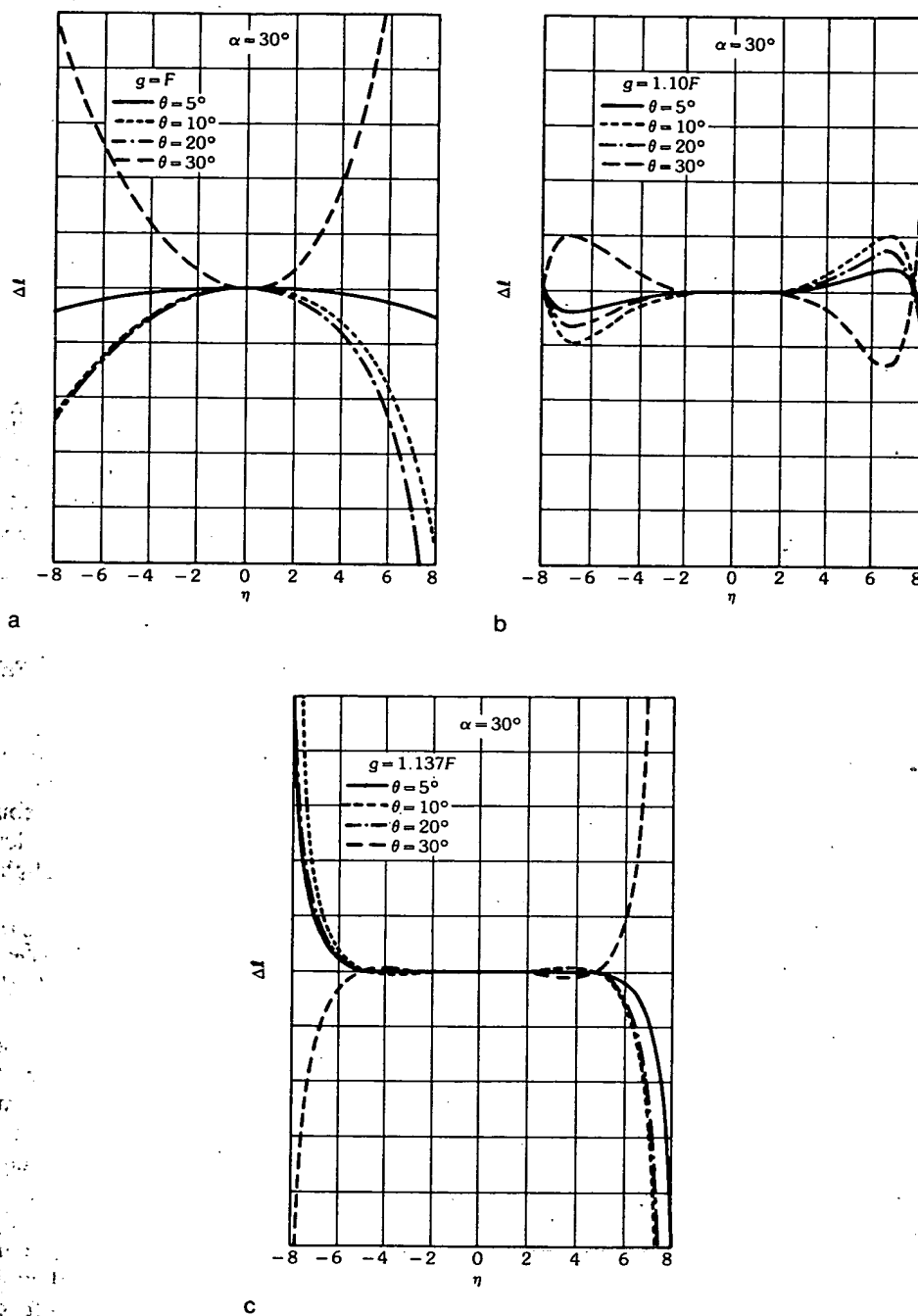
Fig. 35. Path length errors in a microwave lens. (*a*) With $g = 1.00$. (*b*) With $g = 1.10$. (*c*) . With $g = 1.137$. (*After Rotman and Turner [25],* © *1963 IEEE*)
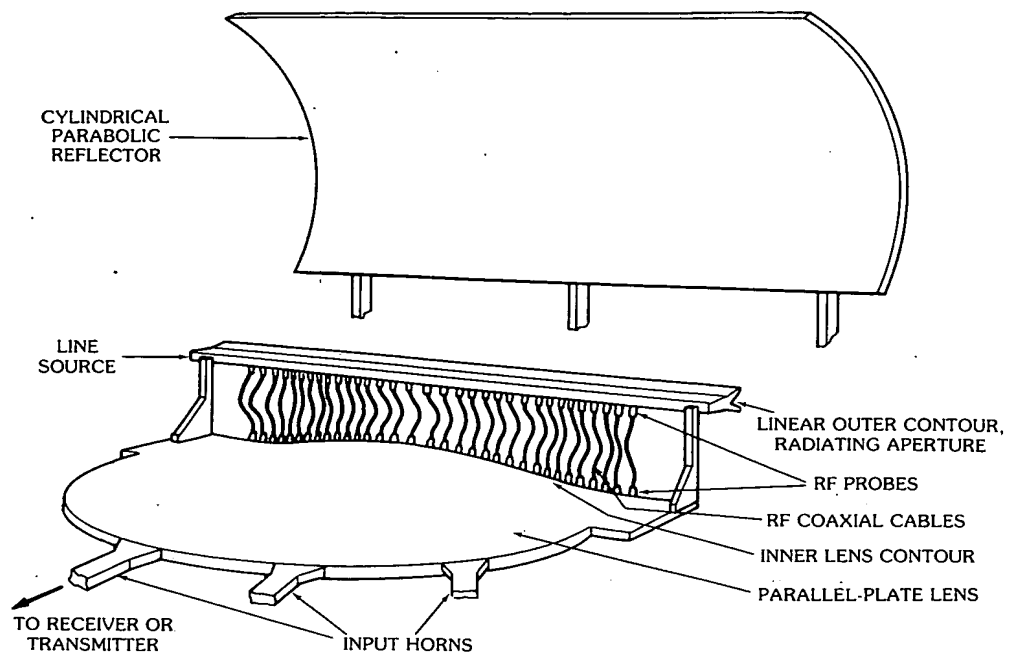
Fig. 36. Parallel-plate lens and reflector. (*After Rotman and Turner [25],* © *1963 IEEE*)

refraction spherical lens due to R. K. Luneburg [30]. Because of its shape it is commonly referred to as the "tin-hat" Rinehart lens.

Figs. 38 and 39 illustrate two versions of the geodesic analog of the Luneburg lens, commonly referred to as the tin-hat or Rinehart and flat-plate Luneburg lens, respectively. Both of these operate in the TEM mode. The electrical parallel-plate separation is less than $\lambda/2$ for both lenses.

The tin-hat derives its focusing properties from the physical length that the rays must traverse in propagating from the feed point to the linear aperture as depicted. The feed is usually an open-ended waveguide or waveguide horn, although other types may be used.

The main advantages of the tin-hat are that it contains no dielectric materials, is very simple in construction, and is perfectly focusing over 360°. Moreover, it is very low loss. Since it operates in the TEM mode it is fairly forgiving of small perturbations in shape because slight feed defocusing can partially correct for slowly varying errors. The amplitude transformation that occurs through this lens is such that an inverse taper occurs, e.g., a primary feed with a $\cos\theta$ power pattern transforms into a uniform distribution on emerging from the lens, as illustrated by the bunching of rays near the edges of the output aperture in Fig. 38. Consequently a high gain factor is realizable; however, because of this phenomenon, ultralow side lobes may be difficult to achieve with a simple feed, and a highly directive feed is required to produce very low side lobes.

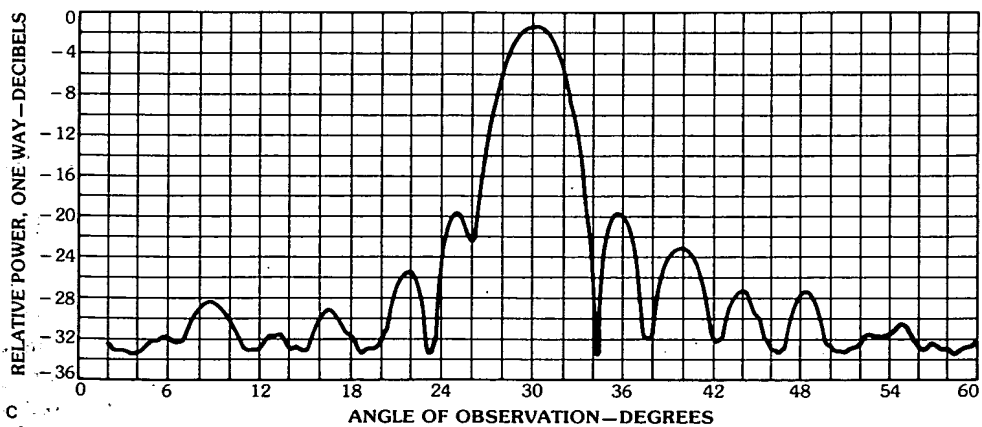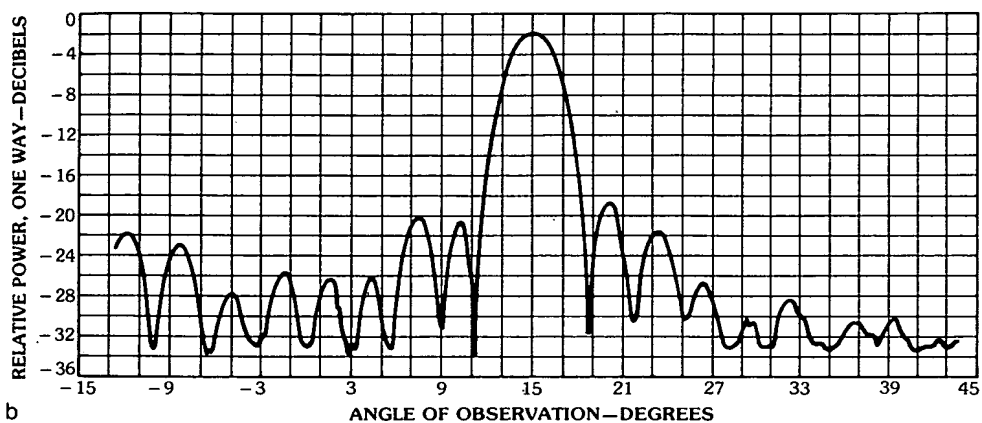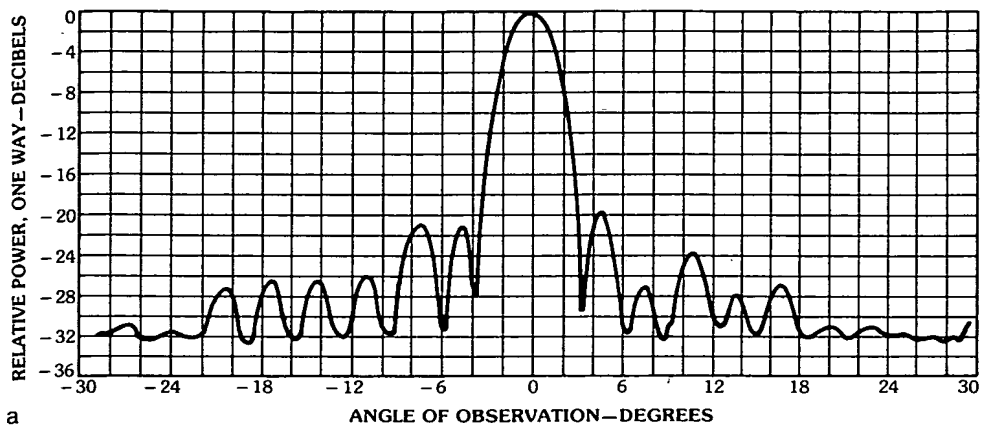The bandwidth capability of the tin-hat and flat-plate Luneburg lens is

Fig. 37. Radiation patterns of microwave lens antenna. (*a*) For $\theta = 0°$ (on axis). (*b*) For $\theta = 15°$. (*c*) For $\theta = 30°$. (*After Rotman and Turner [25], © 1963 IEEE*)
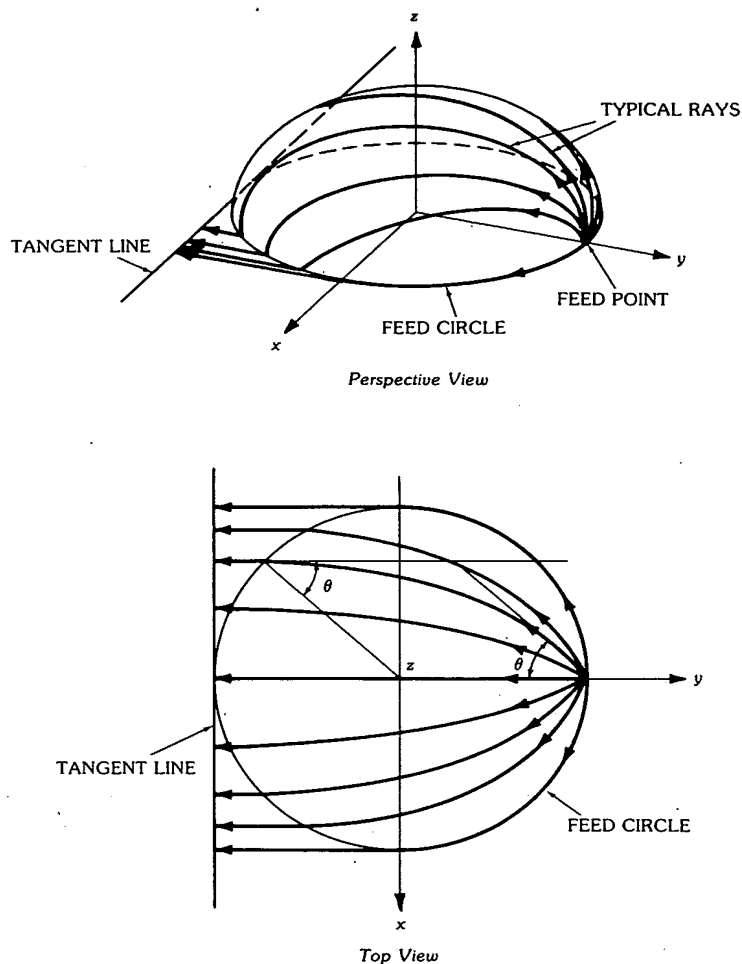
19-45

Perspective View

Top View

Fig. 38. Paths taken by rays on mean surface of geodesic Rinehart lens.

essentially limited only by the bandwidth of the components used in conjunction with them, since the lens is a true time-delay device.

The main advantage of the flat-plate Luneburg lens lies in its form factor, i.e., being flat, it is relatively easy to package.

If either of these lenses is to form multiple simultaneous beams over 360°, then switchable circulators would have to be used, one for each element. The reason for this is that each element in the pickup array around its periphery has to act as a feed as well as a transfer element. Fig. 40 illustrates this situation. The radiating array would have to be on the same radius as the pickup array to retain the correct phase distribution. The two arrays are depicted as lying on different radii for clarity only.

If 360° coverage is needed, but not simultaneously, then diode switches could be used rather than circulators. The reason for this is because, at any given

Top View

CONDUCTING PLATES   DIELECTRIC

FEED

Side View
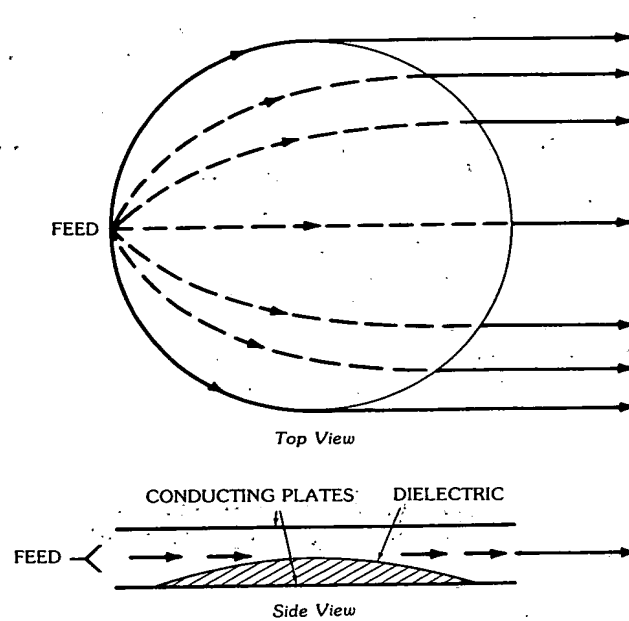
Fig. 39. Flat-plate Luneburg TEM-mode lens.

R_3

R_2 F_2 F_3 R_4, RADIATING ELEMENT, TYPICAL

CIRCULATOR
(SWITCHABLE BETWEEN
TRANSMIT AND RECEIVE)

F_1 F_4, FEED INPUT, TYPICAL

R_1 LENS R_5

F_8 F_5

PICKUP ARRAY

R_8 F_7 F_6 R_6

R_7
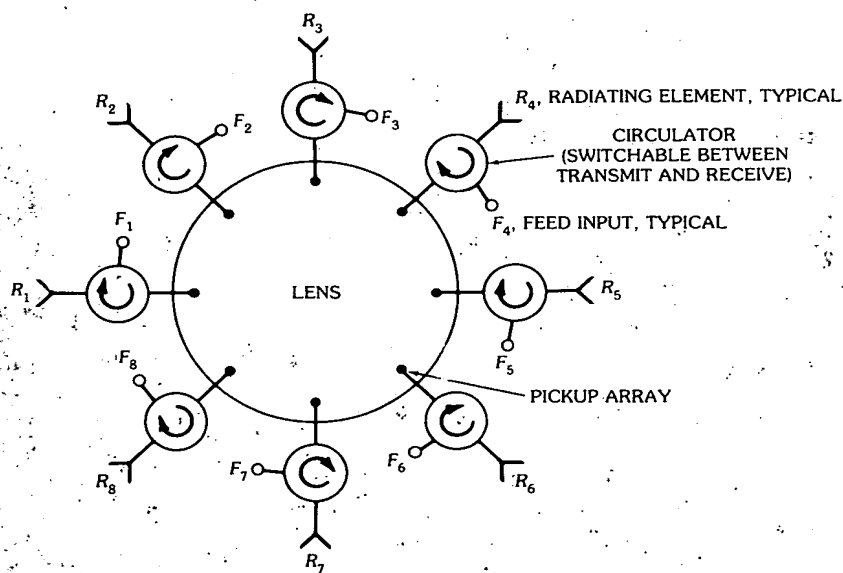
Fig. 40. Flat-plate Luneburg or Rinehart lens for simultaneous beams over 360°. (*Courtesy Hughes Aircraft Co., Fullerton, Calif.*)

moment, each element either acts as a feed or as a transfer element but not simultaneously. Fig. 41 is a photograph of a cylindrical array of line sources fed by a Rinehart geodesic lens.

There are some limited-scan applications whereby these lenses are used to phase a line source. In that case the planar output parallel plates must be extended to form a line source. (See Fig. 19.) The output amplitude distribution moves with scan, however, and the physical length of the line source is longer than its active length.

There are numerous derivatives of these lenses, among them the TE_{10} mode Luneburg that uses the TE_{10} mode between nearly parallel plates. The central plate spacing is greater than at the periphery. Dielectric is usually used to fill the separation between plates to structurally act as plate separators. The bandwidth is much less than its TEM mode counterpart because the ideal plate spacing for the
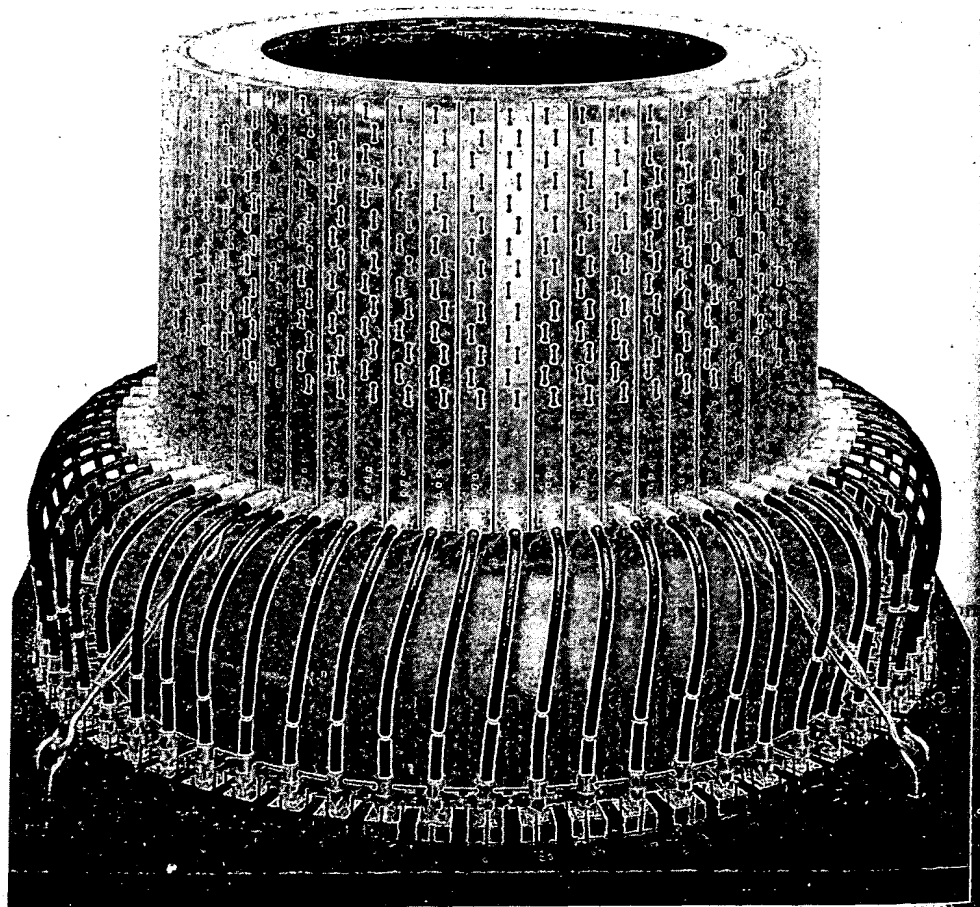
Fig. 41. Cylindrical array fed by a Rinehart geodesic lens. (*Courtesy Hughes Aircraft Co., Fullerton, Calif.*)

TE_{10} mode lens depends on wavelength. Since the correct spacing can be specified only at center frequency, it results in a design that is correct only at the center frequency. The actual bandwidth is a function of the size.

The folded Luneburg lens is, in principle, geodesically the same as the nonfolded one. It resembles a convex dome with a concave dent in the top. From a practical point of view the problem that arises is that of reflections occurring at the points where the slope changes. A mitered bend could probably be used to impedance-match the rays for certain angles of incidence; however, it is doubtful that such a design would work well for all the angles of incidence that the lens requires (up to grazing angles of incidence). Using a smooth bend in the region where the slope changes could be attempted but this changes the geodesics. Little or no information is available to draw definite conclusions regarding the folded Luneburg.

DuFort-Uyeda Lens

DuFort and Uyeda [31] reported a modified Rinehart metal dome antenna with a dielectric ring lens at the output for decreased beamwidth in the elevation plane. The ring lens provides beam collimation in the plane perpendicular to the azimuth scan plane and results in a much smaller antenna than a conventional Rinehart lens fitted with an E-plane flared horn.

Even for moderate directivity in the plane perpendicular to the plane of the multiple beams, the length of a low-phase-error, low-flare-angle horn is quite an appreciable fraction of the radius of the dome. This added radius does not contribute to the effective aperture in the azimuth plane which, of course, is equal to the diameter of the dome only. If a shorter horn with a larger flare angle were used, a dielectric lens would be required to collimate the circular phase front of the horn. With dielectric in the toroidal horn it becomes clear by tracing a few rays that the Rinehart lens will no longer focus in the azimuthal plane. The DuFort-Uyeda lens focuses perfectly in the azimuthal plane with an effective aperture equal to the total diameter of the dome and dielectric ring-horn while achieving directivity in the perpendicular plane.

An experimental model was built and tested at K_a-band (26.5 to 40 GHz). It provided a 1.7° by 10.7° beam at 40 GHz. Pattern and gain data show excellent performance.

Fig. 42 shows the top view and cross section of the experimental model. Fig. 43 is a photograph of the experimental model. Fig. 44 shows a typical beam measured at 32 GHz using reduced-height WR28 waveguides for feeds. Fig. 45 depicts an H-plane multiple-beam overlay of five contiguous beams measured at 32 GHz. Fig. 46 shows a lower side lobe pattern measured at 32 GHz using a 3/4-inch (1.905-cm) H-plane flared horn for the feed.

Aperture efficiencies of between 60 and 72 percent were obtained over the 26.5- to 40-GHz band. Uniform multiple beams of similar gain and pattern behavior can be generated over a 90° sector [31].

4. Unconstrained (Optical) Feeds

An *unconstrained feed* is one in which free space exists between the feed(s) and the radiating aperture. The rf power distribution from feed to aperture is achieved
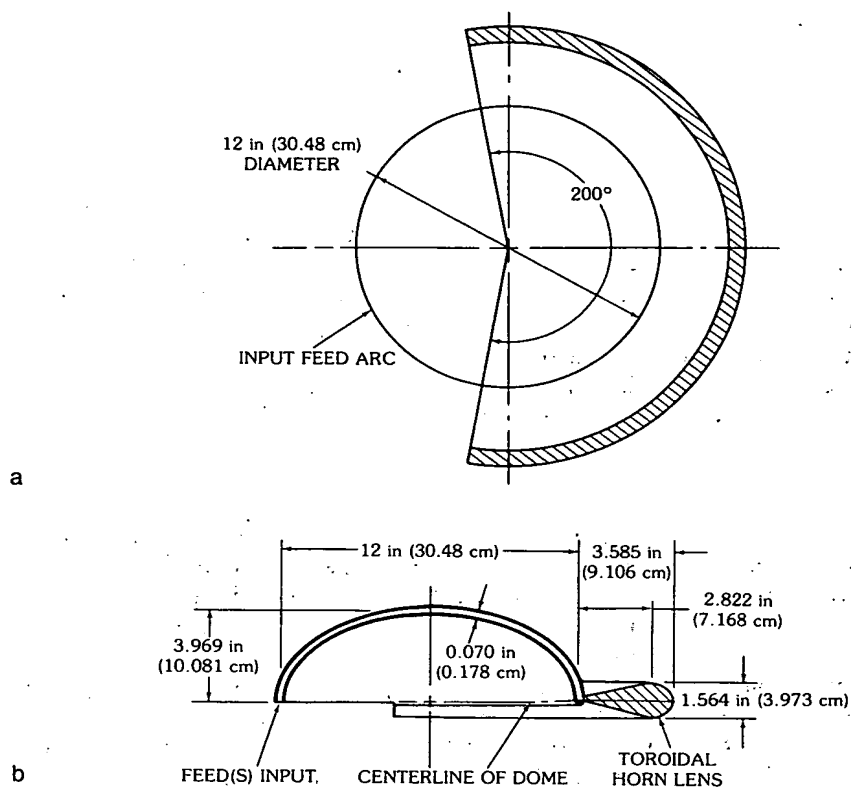
a

b

12 in (30.48 cm)
DIAMETER

200°

INPUT FEED ARC

12 in (30.48 cm)

3.585 in
(9.106 cm)

2.822 in
(7.168 cm)

3.969 in
(10.081 cm)

0.070 in
(0.178 cm)

1.564 in (3.973 cm)

FEED(S) INPUT.   CENTERLINE OF DOME

TOROIDAL
HORN LENS

Fig. 42. Design for K_a-band geodesic dome and lens aperture. (*a*) Top view. (*b*) Cross section. (*Courtesy Hughes Aircraft Co., Fullerton, Calif.*)
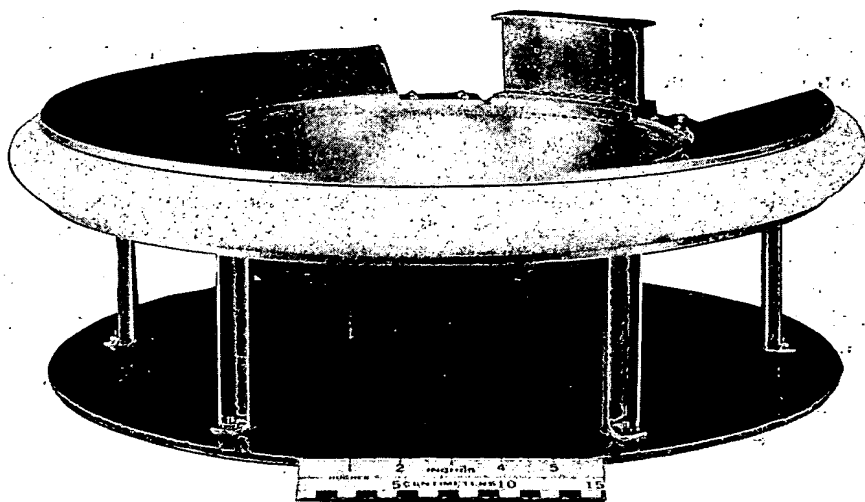

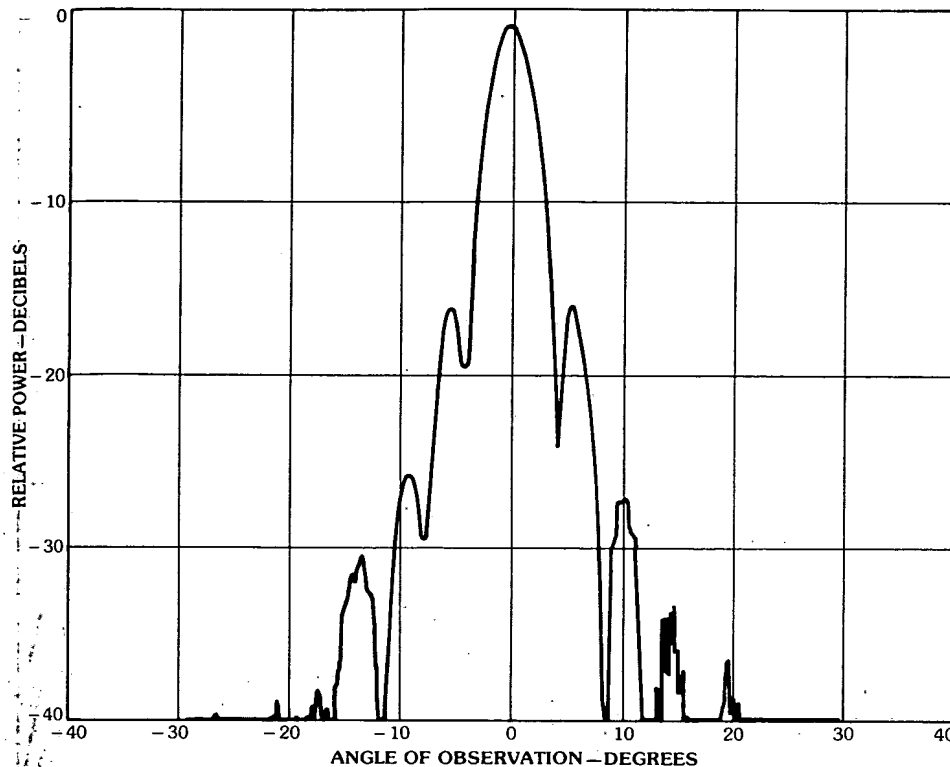**Fig. 43.** Experimental model DuFort-Uyeda lens. (*Courtesy Hughes Aircraft Co., Fullerton, Calif.*)

19-50

Fig. 44. *E*-plane pattern measurement with WR28 reduced-height waveguide feed at 32 GHz. (*Courtesy Hughes Aircraft Co., Fullerton, Calif.*)

by unconstrained radiation from the feed to the aperture. Hence the aperture distribution is essentially determined by the radiation pattern of the feed. Fig. 47 illustrates such a feed in its most general form. For example, the feed could be a one- or two-dimensional array of radiating elements while the beamformer which collimates the beams could be a reflector(s) or lens which could limit the FOV (field of view) to a relatively narrow sector of space because of off-axis aberrations. As another example the feed could be a simple monopulse feed and the beamformer could be a two-dimensional, nominally half-wavelength-spaced pickup array and radiating array with a phase shifter between a pickup element and a radiating element. In the latter case the FOV is limited only by the wide angle of aperture matching and grating lobe formation (see Chapter 13). A FOV of, say, 90° to 120° cone or greater can be achieved with proper aperture design. For a specified gain (or beamwidth) one would probably use entirely different techniques for achieving a large FOV as opposed to a narrow FOV, or limited scan. In general, the larger the FOV, the greater the complexity and cost of the antenna system. Also, the greater the instantaneous bandwidth, the greater the complexity and cost. Trade-offs can be made between FOV and instantaneous bandwidths.

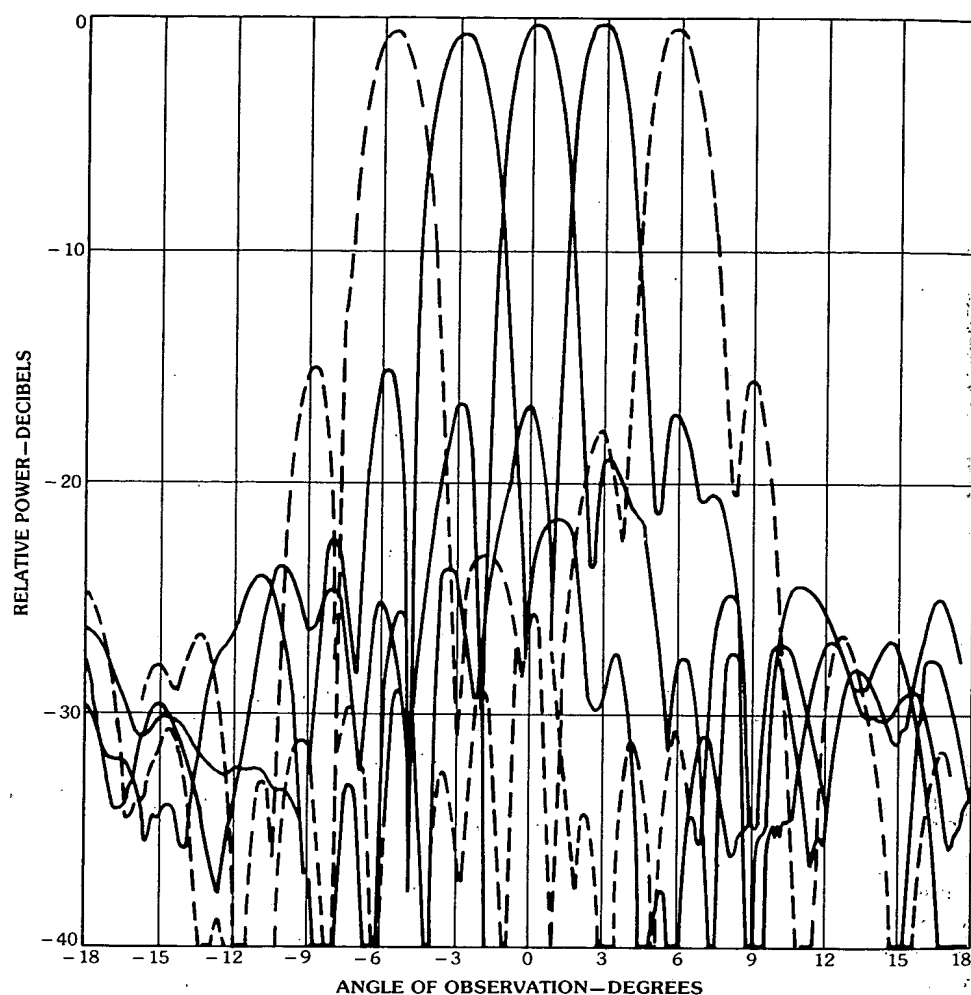Any attempt to categorize the various unconstrained-feed approaches is

Fig. 45. *H*-plane multiple-beam overlay of five contiguous beams measured at 32 GHz with WR28 reduced-height feeds. (*Courtesy Hughes Aircraft Co., Fullerton, Calif.*)

difficult because there are overlaps in the categories. Nevertheless, a review of the various techniques suggests four categories for the purpose of discussion. These are the following:

1. Wide FOV (0° to 360° phase shifters, nominally half-wavelength-spaced elements
2. Limited scan (0° to 360° phase shifters and optics with aperture magnification)
3. Subarray or partial time delay using overlapping or non-overlapping subarrays, 0° to 360° phase shifters, and time delay at the subarray level. *Note*: Totally constrained limited-scan techniques are discussed in Section 3 of Chapter 13,
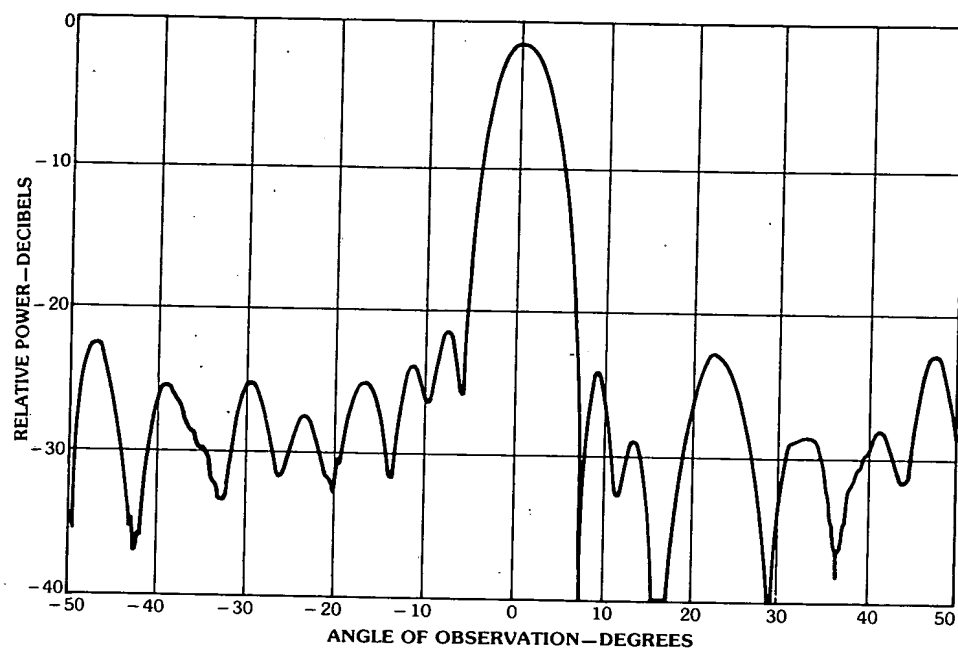
Fig. 46. Low side lobe *H*-plane pattern measured at 32 GHz with 0.75-in (1.905-cm) *H*-plane flared horn. (*Courtesy Hughes Aircraft Co., Fullerton, Calif.*)
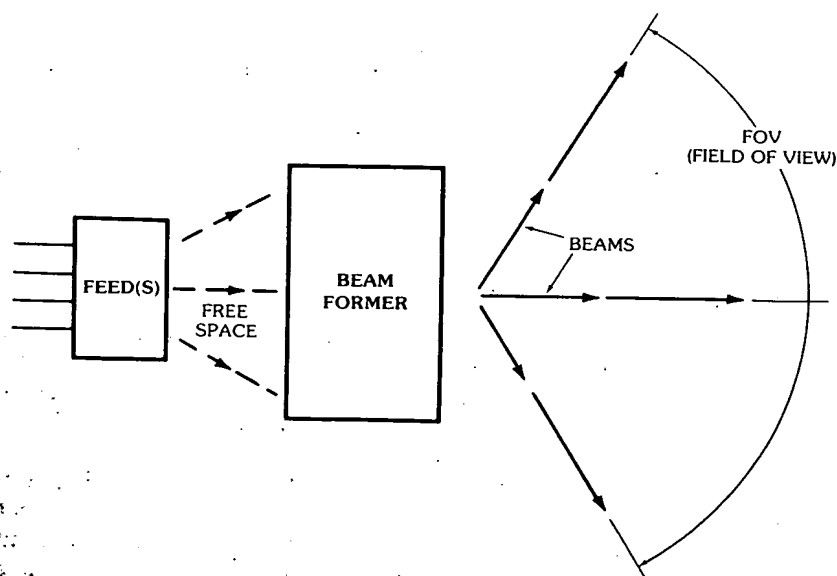
Fig. 47. Unconstrained feed. (*Courtesy Hughes Aircraft Co., Fullerton, Calif.*)
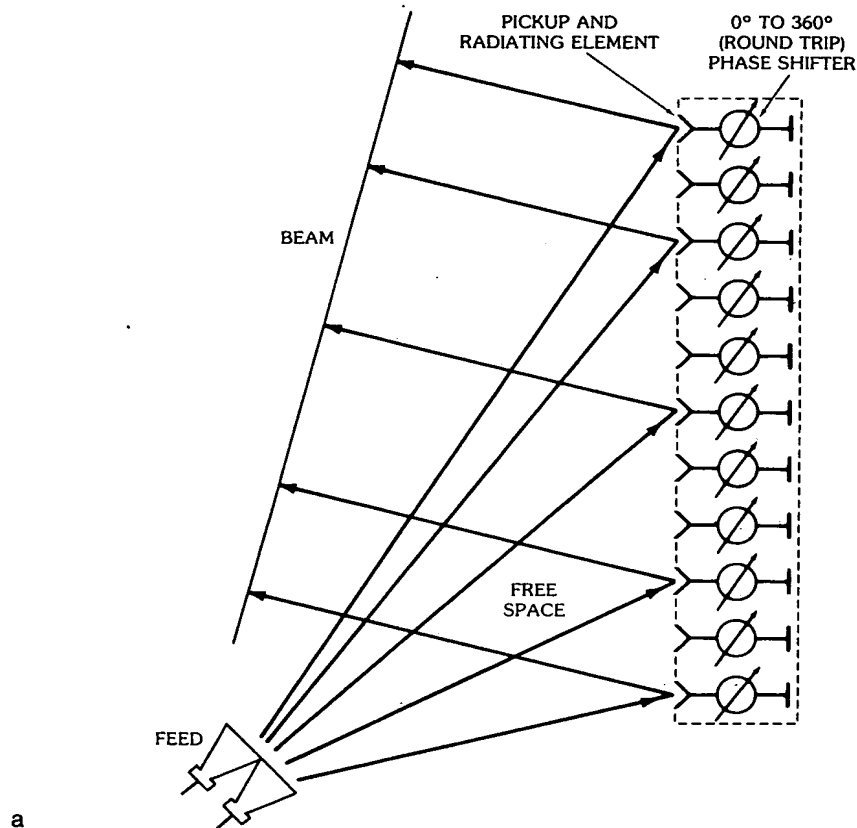
PICKUP AND   0° TO 360°
RADIATING ELEMENT   (ROUND TRIP)
                    PHASE SHIFTER

BEAM

FREE
SPACE

FEED

a

Fig. 48. Space-fed reflectarray. (*a*) Offset-fed. (*b*) Center-fed. (*Courtesy Hughes Aircraft Co., Fullerton, Calif.*)

under the heading "Array Organization: Subarrays and Broadband Feeds," and also in Section 2 of this chapter.

4. True time delay (true time-delay phasing of all elements)

Wide Field of View (Nontrue Time Delay)

The wide field of view technique implies a space-fed two-dimensional array of nominally half-wavelength-spaced elements. The offset-fed and center-fed reflectarray of Fig. 48 depicts examples of this approach [32]. In these cases the feed would typically be a four-horn monopulse feed (only two shown). Offset feeding offers less aperture blockage but causes an asymmetry in the illumination. The spherical wavefront incident on the array is converted to a scanned beam by 0° to 360° type phase shifters. Center feeding eliminates the illumination asymmetry but presents aperture blockage which would cause some side lobe level degradation. Many systems do not require ultralow side lobe levels, and this feed approach offers a straightforward solution. The Raytheon MTR Radar and Radome Antenna
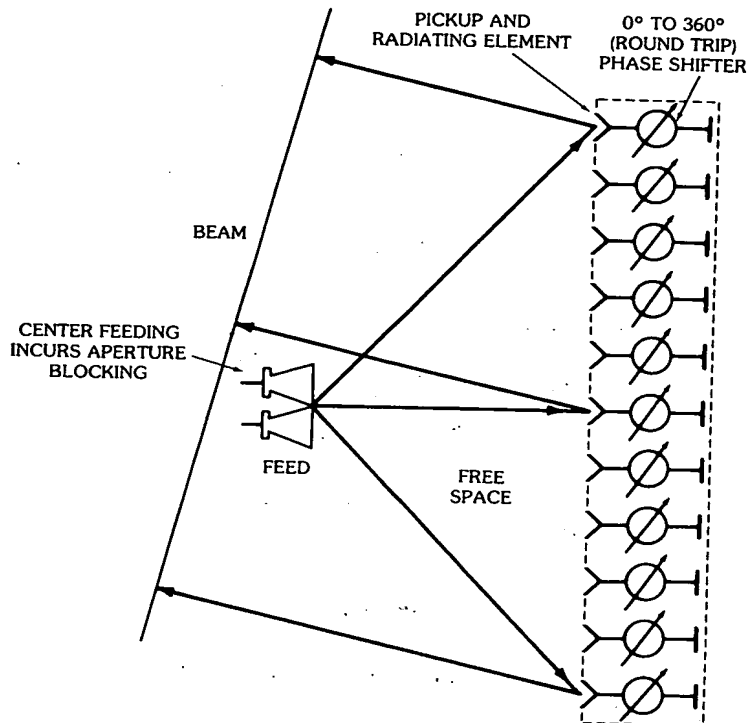
PICKUP AND RADIATING ELEMENT

0° TO 360° (ROUND TRIP) PHASE SHIFTER

BEAM

CENTER FEEDING INCURS APERTURE BLOCKING

FEED

FREE SPACE

Fig. 48, *continued.*

and RF Circuitry (RARF) array are examples of the center-fed reflectarray [32]. In the case of the RARF array six waveguides (monopulse sum and two difference channels for two orthogonal polarizations) are routed to the feed in order to achieve polarization agility. Other examples are the NRL S-band Reflect Array Radar (RAR) developed by Blass Antenna Electronics Company [32] and the Hughes Aircraft Company Electronically Scanning Airborne Intercept Radar Antenna (ESAIRA).

Aperture blockage is eliminated entirely using a space-fed feed through lens array as depicted in Fig. 49. Since no aperture blockage is presented, the feed could be as large and complex as desired, without degraded side lobe level effects. There are numerous advantages to this feeding scheme. The Raytheon Sam-D Radar uses this approach [32]. It enables a space-duplexing feature to be employed; that is, on transmit the phase shifters are set to focus on the transmit feed, and on receive the phase shifters are set to focus on a separate receive feed. Moreover, two transmitter feeds could be employed using two transmitters for redundancy, where different phase shifter settings are used, depending on which transmitter is being used [32]. (The offset-fed reflectarray could also have this feature without increased aperture blockage.) Since there is room available, optimized sum and difference aperture illuminations could be realized by a sophisticated monopulse feed design. A multiple stack of vertical feed horns could be combined for elevation beam
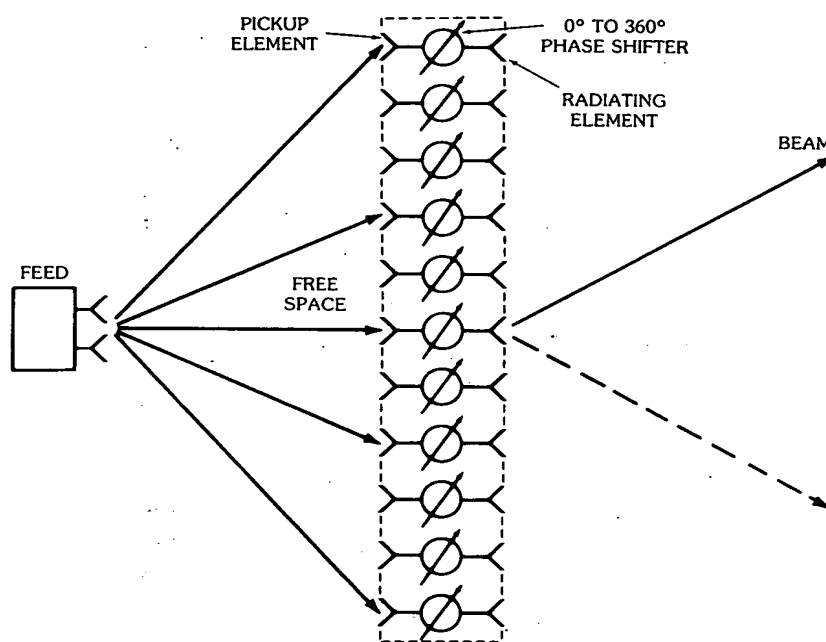
Fig. 49. Space-fed feedthrough lens array. (*After Patton [34]*, © *1972; reprinted with permission of Artech House*)

shaping, and azimuth patterns could be generated by using multimode sum and difference extraction of each horn in the azimuth plane [32].

Although Fig. 49 depicts the space-fed feed through array with both faces flat, they need not be.

The sperry HAPDAR radar uses a curved pickup face and flat radiating face, with phase shifters in the transmission lines between faces. This structure is called TACOL, for thinned aperture computed lens [32,33]. The feed is a five-horn cluster that provides independent control over the sum and difference illumina-tions, using an F/D ratio of 1. All five horns are used for the sum pattern but only the outer four are used for the difference patterns. In this way, low side lobe sum and acceptable difference patterns are realized.

Limited Scan

High-gain antennas with wide field of view and/or wide instantaneous bandwidths are very costly due to the large number of active devices. For phased arrays a phase shifter and driver are required for each radiating element, which may total to many thousands for a high-gain array. For multiple-beam antennas with beam switching, a similar number of switching elements and drivers are required. In many radar applications wide field of view is not required although high angular resolution and high gain are. Examples of such limited-scan applica-tions are the airport precision-approach radar, weapon-locating radars, and earth-coverage antennas for synchronous satellites.

It is the objective of limited-scan antenna design to take advantage of this

limited field of view to design an antenna with the fewest number of active devices but retain the narrow beamwidth and high gain. To achieve high gain and narrow beamwidth requires a large antenna aperture, and a large field of view requires a phase shifter and drivers for every nominally half-wavelength-spaced radiating element. Hence high gain and large FOV result in an extremely costly antenna system. By restricting the FOV the cost can be greatly reduced.

Limited-scan antennas can employ optical (unconstrained) feeds, totally constrained feeds, or combinations of these. In this section on unconstrained feeds, only those antennas employing optical techniques are discussed. Limited-scan techniques using totally constrained feeds in which elements of an array are grouped together to form identical subarrays with a phase shifter per subarray are discussed in Chapter 13, Section 3, on array organization.

Optically Fed Aperiodic Array—An array of large equal-size directive elements (e.g., a nonscanning subarray) whose element pattern is tailored to the required FOV could be considered, using a phase shifter for each large element or subarray. For regular element spacing, however, this approach produces excessively high grating lobes as the beam is scanned, which would not meet most system requirements. The grating lobes result from the fact that radiation from periodic widely spaced elements add in phase at angles in space other than the desired direction of the main beam. If the periodicity is broken up, the energy concentrated in the grating lobes is smeared out "randomly" in all directions, resulting in lower peak values. The overall antenna gain, however, is not improved since it is only a redistribution of the grating lobe energy. In most cases there is a slight though usually negligible reduction in gain.

One method of minimizing the grating lobe problem, while still using large directive elements, is given by Patton [13, 34]. In this approach he uses concentric rings of equal-area subarray elements, as shown in Fig. 50 (depicted for only a few subarrays). Fig. 51 depicts a large number of subarrays of equal area. The subarrays are dual-polarized dipoles above a ground plane. Each polarization is summed (in phase) within each subarray. Thus each subarray has two outputs— one for each polarization. Fig. 52 illustrates how the concentric ring array is fed. For each subarray pair of cables there is a corresponding pair of terminals (one for each polarization) located on the surface of a partial sphere. The cables must track in phase over the frequency band of the system. The feed is located at the center of the spherical cap. The output final aperture distribution is thus determined by the primary Σ and Δ patterns produced by the primary feed. Since dual-polarized elements are used, the final radiated polarization is determined solely by the polarization of the primary feed. There are phase shifters in every semirigid coaxial line between the concentric ring array and the spherical cap.

By using this technique the periodicity of the usual array factor (for regular spacing) is broken up; consequently, grating lobes are suppressed. The degree of suppression is determined by the total number of subarrays used. Patton [34] shows calculated data for 10 ft and 30 ft diameter (3.0 and 9.1 m) arrays at C-band using a ±5° FOV. For the 30 ft diameter case, using 1000 subarrays, the vestigial grating lobe is suppressed to about −21 dB for maximum scan of ±5°. The 10 ft diameter case (100 subarrays) corresponds to −15-dB suppression at ±5° scan.

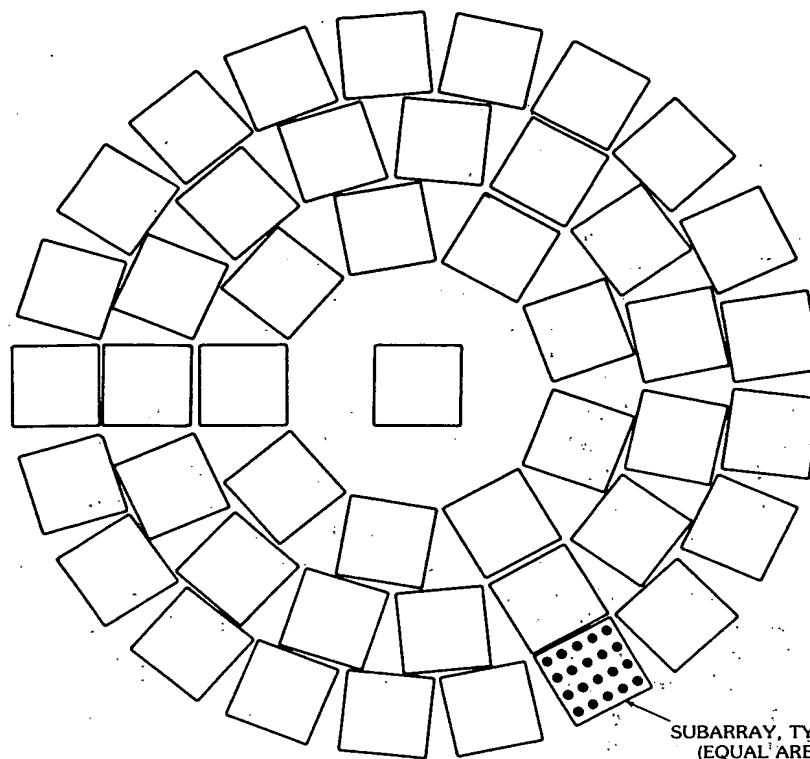Predicted and measured loss, including illumination taper (10-dB tapered

Fig. 50. Concentric ring array of equal-area subarrays. (*After Patton [34]*, © *1972; reprinted, with permission of Artech House*)

Gaussian) for the 10 ft diameter model are 5.94 dB and 5.58 dB, respectively, at midband. Measured first side lobes were about −15 dB, due to effective aperture blockage. The gain decreased with scan by about 2.5 dB at ±5° from broadside.

The primary feed is a multimode monopulse feed, dual polarized for the sum channel, and horizontally polarized only for the difference. Conventional reflector feed techniques for achieving dual monopulse, dual polarization, for both Σ and Δ channels are applicable here; moreover, techniques for achieving independent control over the Σ and Δ patterns can also be used. Since there is room available, a more complex feeding structure could be considered for any additional advantages that may be realized.

Phased Array with Paraboloid—Fig. 53 depicts a paraboloidal reflector fed by a phased reflectarray, after Winter [35]. The reflectarray radiating face is not located at the focus, but is shifted toward the vertex of the paraboloid. Conceptually viewed on receive, the idea is to place the reflectarray aperture in the region forward of the focus, pick up the converging field, and phase-shift it to refocus on the primary feed(s). Geometrical optics was used to determine the phase shifter values, as a function of scan angle θ_s. As θ_s varies, the converging field
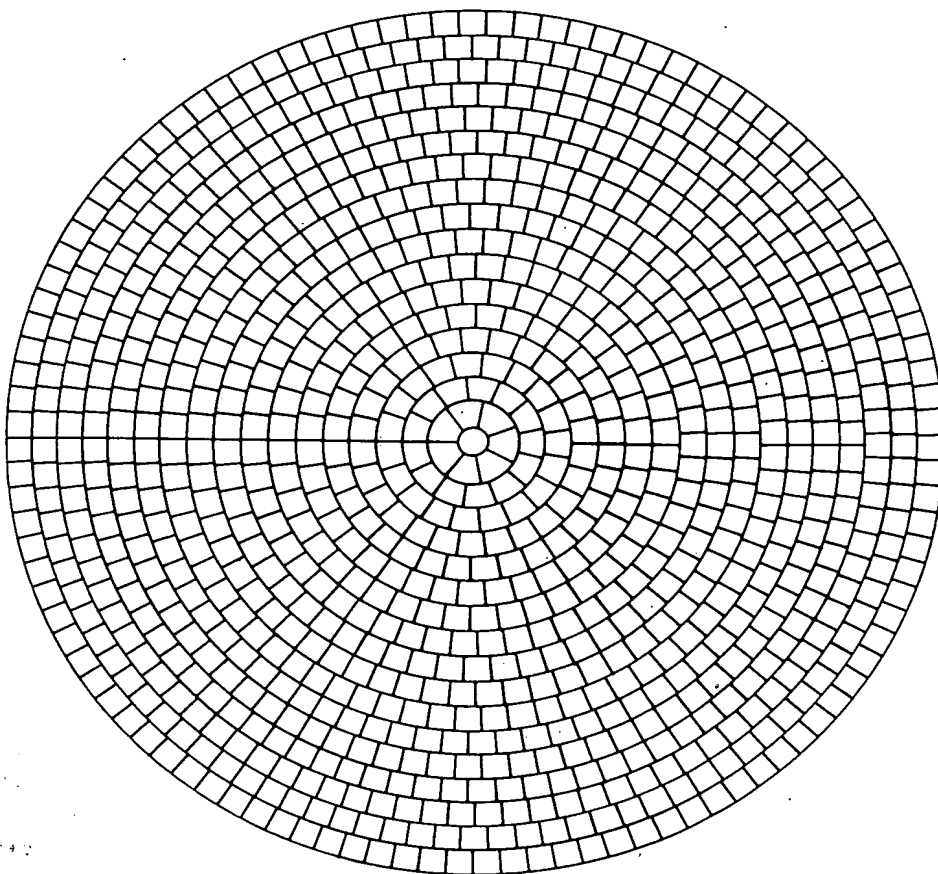
Fig. 51. Aperiodic array for limited scan. (*After Patton [34], © 1972; reprinted with permission of Artech House*)

moves, but for small enough θ_s, most of the reflected power will still be incident on the reflectarray face. Thus one can still change the phase of the converging field to refocus on the primary feed. Note that only the phase is controllable, not amplitude. As θ_s gets larger, only part of the reflected incident field is intercepted by the radiating aperture of the reflectarray antenna; hence, spillover occurs (on receive), causing irretrievable loss. Furthermore, for large θ_s, the effects of aberrations are to cause the reflectarray amplitude distribution to become skewed, introducing both an even and an odd part. The simple primary feed horn couples only to the even part, and the energy in the odd part is lost. Ideally, a horn containing an odd-mode component as well as the even mode, or a small array with the proper amounts of even and odd parts, could be employed to regain that lost energy. For maximum gain, one would use a simple feed designed to produce an illumination across the reflectarray face that best fits the even part of the received converging illumination across the reflectarray face over some specified range of
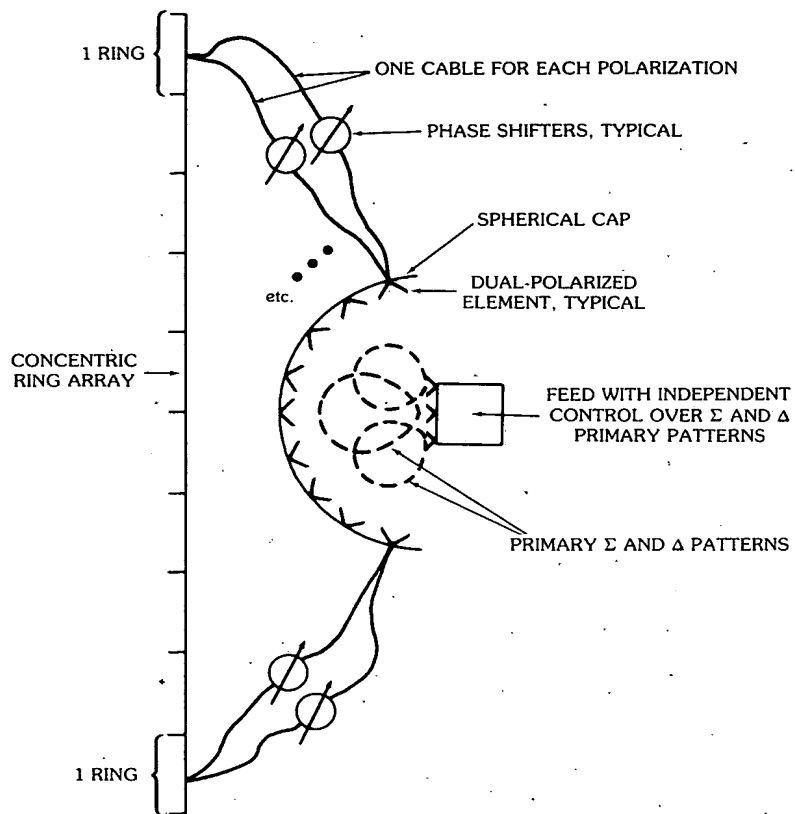
Fig. 52. Concentric ring array showing feed mechanization and power transfer for each polarization. (*After Patton [34], © 1972; reprinted with permission of Artech House*)

scan angles $\pm\theta_s$. This would produce the best amplitude fit that is achievable using a simple primary feed.

Viewing the process on transmit, the primary feed and reflectarray could be designed to illuminate the entire reflector* for a broadside beam; however, as scanning is performed, because of the optics of the system, only a portion of the reflector can be illuminated correctly to form a beam in an arbitrary given direction. Thus the illuminated portion of the reflector moves with scan, which diminishes the efficiency of the antenna system. The aperture blockage presented by the relatively large reflectarray causes a further reduction in efficiency, as well as increased side lobe levels. One of Winter's [35] experimental models used a 988-element reflectarray and simple feed horn and achieved eight beamwidths of scan with 15-dB side lobes in the H-plane and 10 dB in the E-plane. The reflector was

---

*In Winter's experiment 80 inches (203 cm) of the 96-inch (244-cm) diameter was used for a broadside beam.
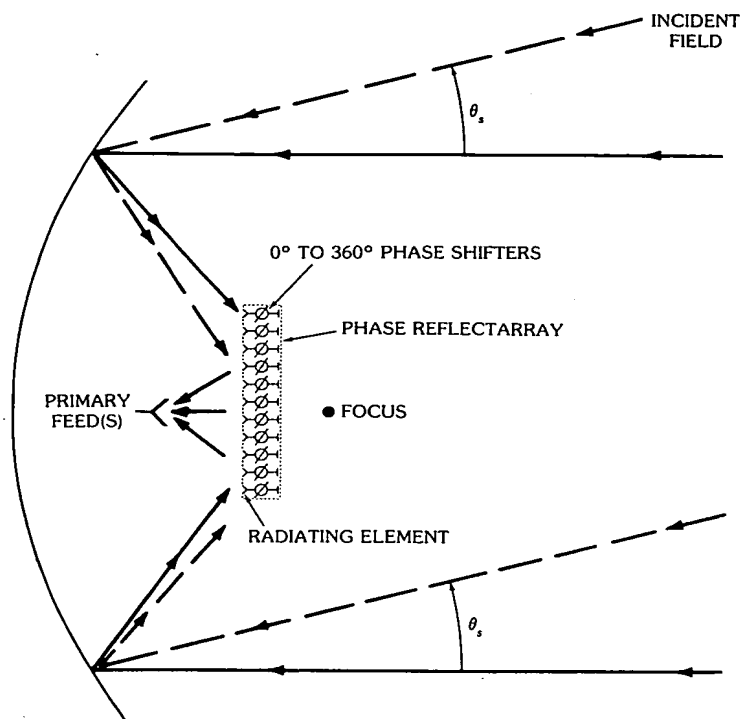
INCIDENT
FIELD

θ_s

0° TO 360° PHASE SHIFTERS

PHASE REFLECTARRAY

PRIMARY
FEED(S)

● FOCUS

RADIATING ELEMENT

θ_s

Fig. 53. Winter's approach, using phased array with paraboloid. (*After Winter [35],* © *1968 IEEE*).

8 ft (244 cm) in diameter with a 51-inch (130-cm) focal length, offset fed as shown in Fig. 54. His results show that it is feasible to utilize a phased array in conjunction with a reflector to achieve a limited degree of scan. The high blockage presented by the phased array could be circumvented by using the phased array in conjunction with a transmission type feedthrough lens, or by offset-feeding to a greater degree. By using a more complex primary feeding arrangement, such as a small active array that is commanded to change with scan, more control over the amplitude would be possible. Thus the radiation characteristics would be expected to improve, provided the design is not blockage limited, as appears to be the case in Winter's experiment.

Offset Phased Array with Hyperbolic Reflector—By moving the phased array out of the FOV of the reflector the aperture blockage would be eliminated and improved radiation characteristics obtained. The GCA System TPN-19 uses such an approach [36], utilizing 824 phase shifters in conjunction with a 9- × 11½-ft (2.74- × 3.5-m) hyperbolic main reflector. Improved side lobe levels of 22 to 24 dB were obtained. The aperture efficiency was 30 percent at broadside and dropped 3½ dB over ±10 beamwidths (elevation) by ±7.15 (azimuth) beamwidths of scan. Azimuth and elevation beamwidths are 1.4° by 0.75°, respectively. The illumination
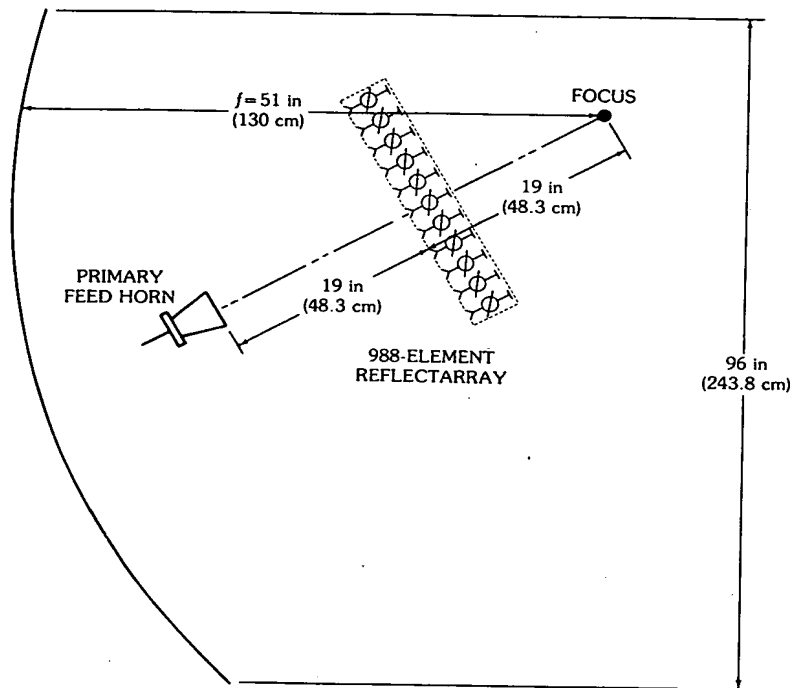
Fig. 54. Winter's experimental model. (*After Winter [35]*, © *1968 IEEE*)

moves over the surface of the reflector as scanning is performed; hence the aperture efficiency is low at the extreme scanned beam positions. The system operates at *X*-band over a 2-percent bandwidth, with an on-axis gain of 42.5 dB.

Near-Field Cassegrain System—Fig. 55 depicts the near-field Cassegrain antenna system. A typical application of this system would have a limited field of view (LFOV) of 5° to 10°, and a very large electrical aperture, e.g., $D/\lambda > 250$. It is composed of two confocal paraboloids with $f/d = F/D$, and is fed by a planar two-dimensional phased array of 0° to 360° type phase shifters. Since the subreflector is in the near field of the phased array, the rays remain collimated from the phased array to the subreflector such that there is no space attenuation. The optics of this system are such that the amplitude distribution emerging from the main reflector is the same as the amplitude distribution across the phased-array feed. In particular, a uniform amplitude distribution over the phased-array feed transforms into a uniform amplitude distribution emerging from the main dish. There is, however, a relatively large blockage by the subreflector or by the effective blockage, (d_e) presented by the phased-array feed. Minimum blockage occurs when these two blockages are equal. A typical design [36] would have d/D ratios between 0.25 for $D/\lambda = 400$ and 0.35 for $D/\lambda = 250$. (Also see reference 37.)

The near-field Cassegrain system can be considered as the limiting case of the standard Cassegrain system as the feed point focus of the hyperboloid recedes to
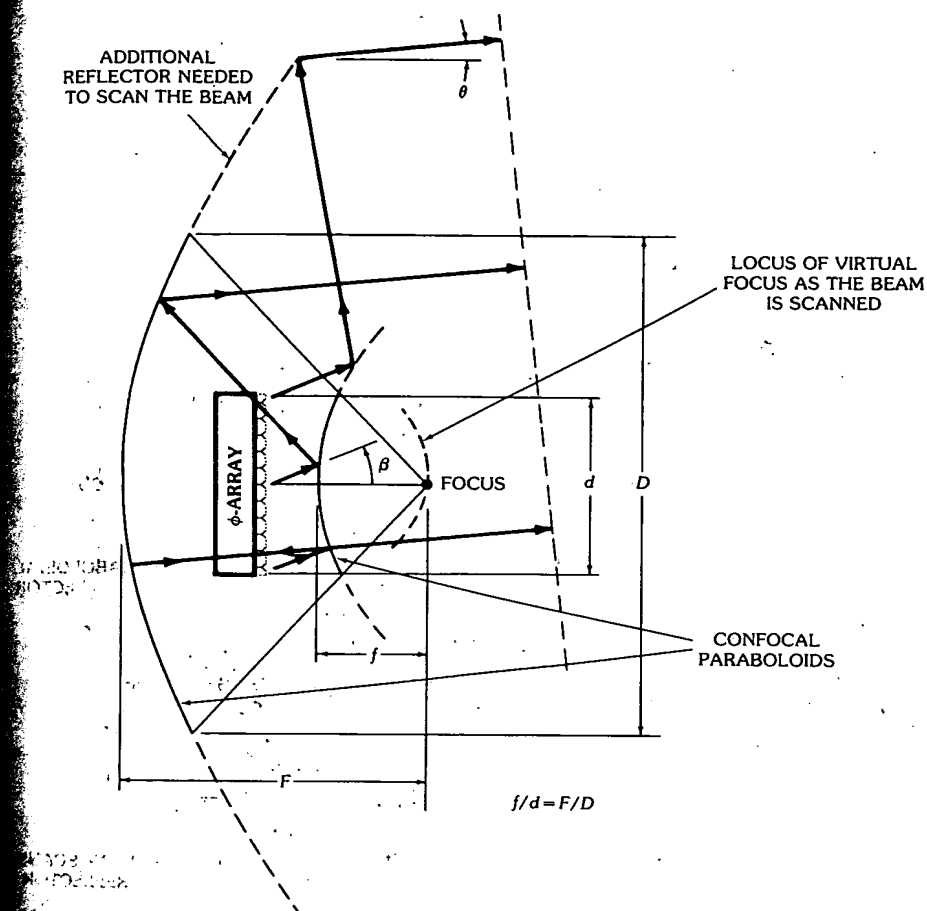
Fig. 55. Near-field Cassegrain system. (*Courtesy Hughes Aircraft Co., Fullerton, Calif.*)

infinity, when the hyperboloid subreflector becomes paraboloidal. The main-beam scan angle θ is related to the angle β by $\tan\beta = (D/d)\tan\theta$. The remotely located primary feed (at infinity) is replaced by the phased-array feed near the vertex of the main reflector with a linear phase gradient to produce rays making an angle β with respect to the z axis, which scans the main beam by the angle θ. Only linear phase gradients are required to scan the main beam; thus one has the advantage of row and column beam steering. A major disadvantage of this scheme is that the illuminated portion of the large reflector moves with beam scan, which causes inefficient usage of the large reflector aperture. This is illustrated in Fig. 55.

Lincoln Lab's Offset-Fed Gregorian System—Fig. 56 depicts a cross-sectional view of the Lincoln Lab's offset-fed Gregorian antenna system. The main reflector is a paraboloid and the subreflector is also a paraboloid with a common focus. Fig. 57
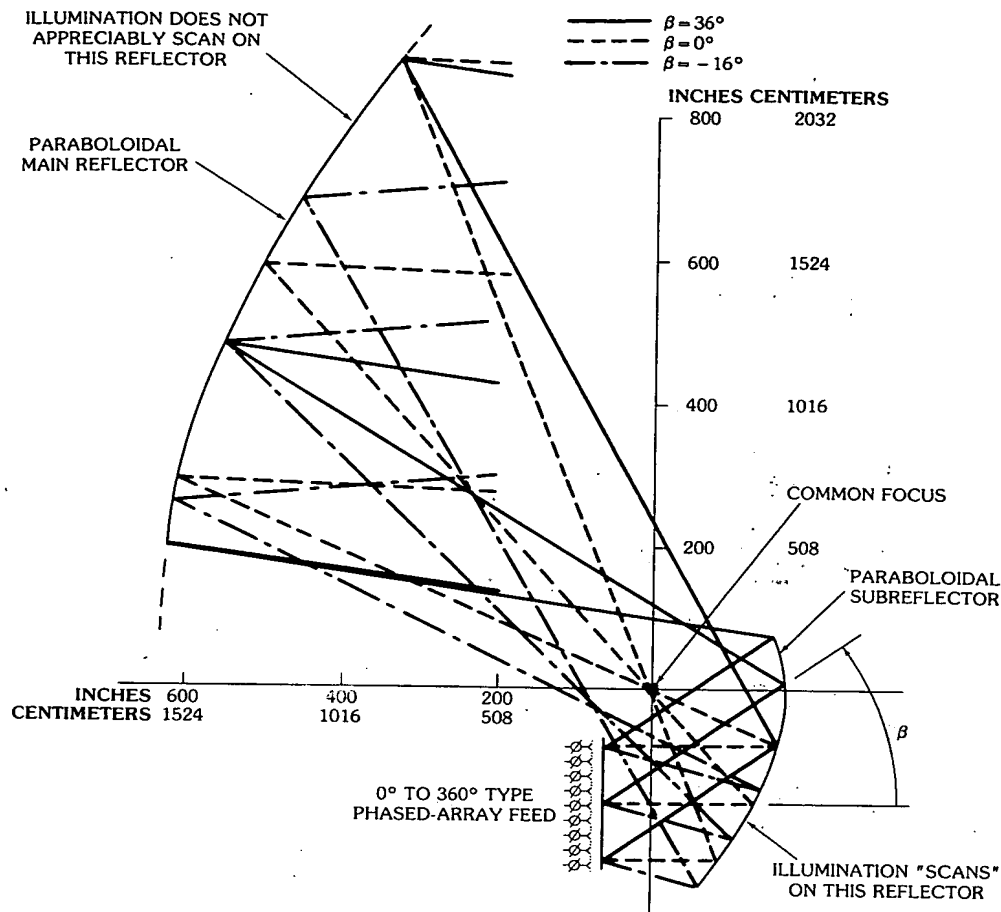
Fig. 56. Preliminary design of an offset-fed Gregorian system and ray tracing for three scan angles. (*After Interim Report [38]*)

shows an artist's concept of such a system. The primary feed for this system is a planar two-dimensional phased array using 0° to 360° type phase shifters. The basic idea here is to use two offset-fed paraboloids in such a way that the off-axis aberrations tend to cancel each other. If this could be achieved, then a small, truncated plane wave leaving the relatively small phased-array feed would be converted to a large, truncated plane wave emerging from the large main reflector. Fig. 56 illustrates ray tracings [38] for three angles β of scan for the phased array. (Also see references 39 and 40.) Although not perfectly parallel, the corresponding rays leaving the main reflector remain nearly collimated, where the scan in terms of beamwidths for the system as a whole would be about the same as the scan in terms of beamwidths for the phased-array feed alone. As can be seen from the ray tracings most of the main reflector is utilized as aperture for all β scan angles; consequently, the efficiency of this system is good for all scan angles. Mailloux and
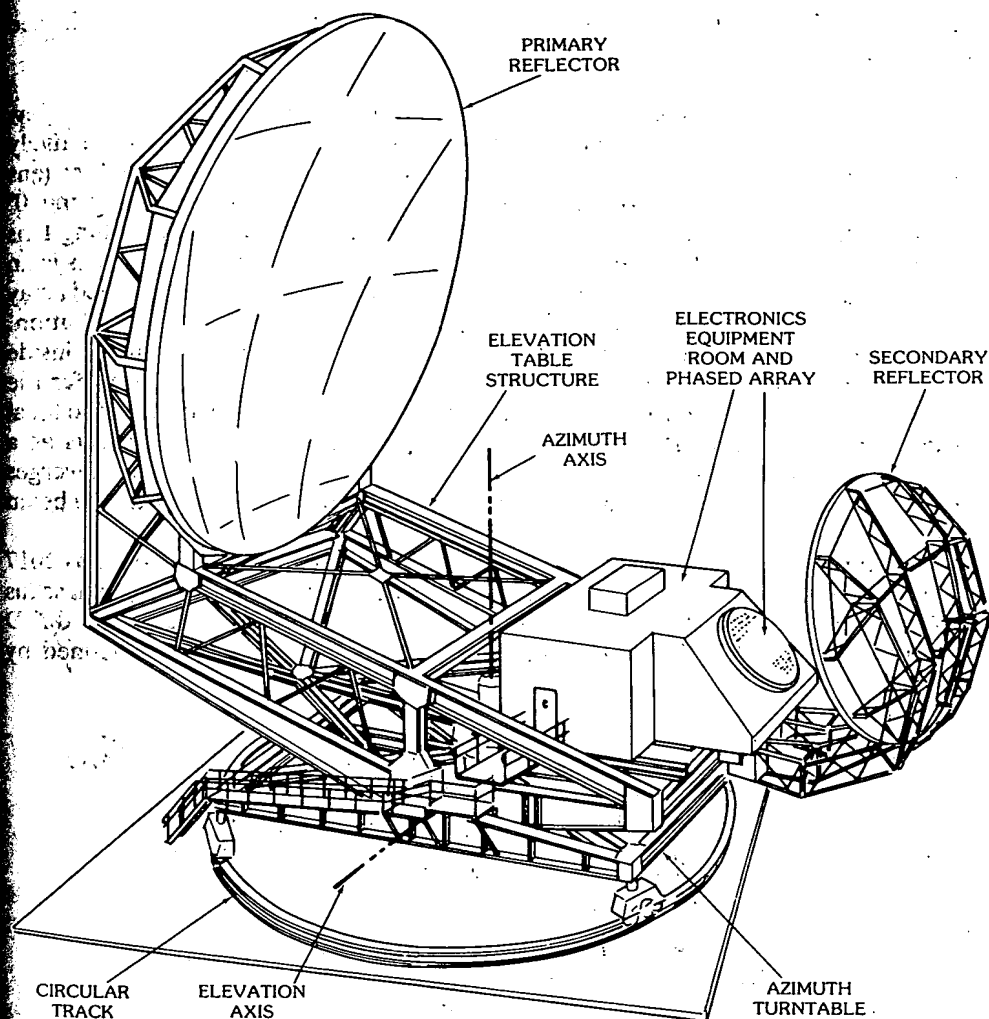
Fig. 57. Physical configuration of the antenna. (*Courtesy Hughes Aircraft Co., Fullerton, Calif.*)

Blacksmith [36] cite an example of a ½°-beamwidth system being scanned 14 beamwidths using a $45\lambda \times 45\lambda$ phased-array feed. Side lobe levels were -15 to -17 dB for all scan angles. The generalized [36] F/D ratio was 1.5.

A study [41, 42] to develop a computer program that determines the optimum main reflector and subreflector contours for maximum gain for a given scan range showed that appreciable improvement over the confocal paraboloidal system is possible. For details the reader is referred to references 41 and 42.

Improved performance can be obtained by matching the caustics of the main reflector and the subreflector, arriving at a configuration in which the smaller

parabola of Fig. 56 is rotated in a clockwise direction by 45°. For more details, see Sletten [43].

Raytheon Dual-Lens Limited-Scan Concept—Fig. 58 depicts a cross-sectional view of the Raytheon dual-lens, limited-scan concept [44]. It is composed of a relatively large, constrained-aperture lens fed by a relatively small, constrained matching lens which in turn is fed by a two-dimensional planar phased-array feed using 0° to 360° type phase shifters. The contour of the output face of the matching lens corresponds to the focal surface of the aperture lens. The main aperture lens is an equal path length lens with a two-point correction (0°, ±10°). The planar feed array uses 437 radiating elements with a 23-dB tapered Gaussian amplitude distribution. The phase shifters are set to focus the array output to a small spot on the inside surface of the matching lens. The function of the matching lens is to transfer the focused field to the output face of the matching lens which is, by design, the focal surface of the main aperture lens. The transferred focused field then acts as a primary feed on the focal surface of the aperture lens, that is, the field diverges from the focused spot, illuminating the main aperture lens to form a scanned beam in space.

The inner surface of the matching lens is elliptical in shape and contains 2617 elements. The main aperture lens is 65 wavelengths in diameter. This system scans an FOV of ±10° with a 1.2° beamwidth for all angles of scan. The generalized F/D ratio [36] is about 1.7. Using this technique, the element-use factor (defined by
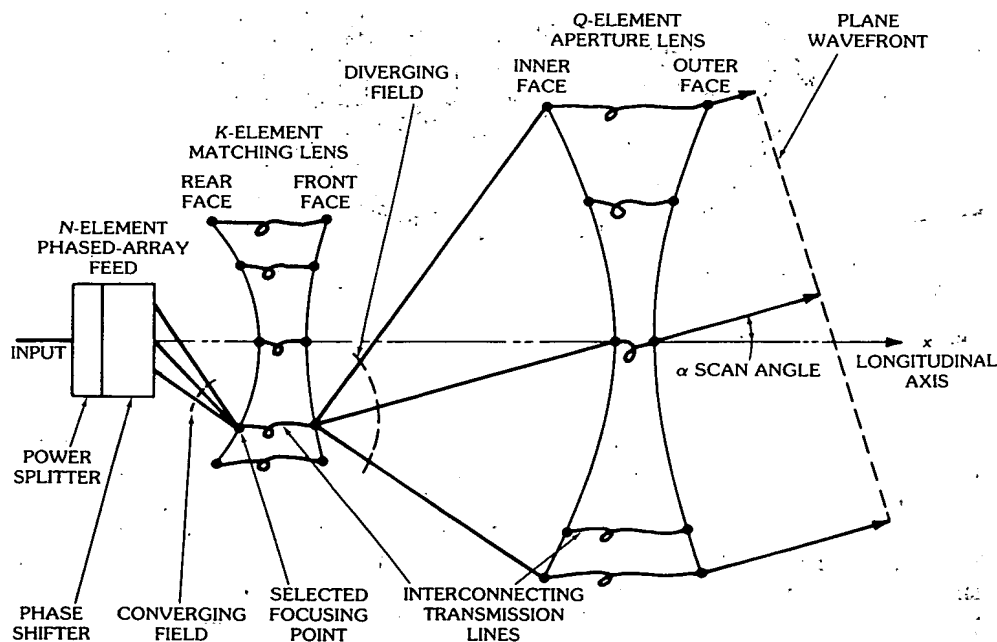

Fig. 58. Dual-lens, limited-scan concept. (*After C. H. Tang, Raytheon Co.*)

Patton [34]) is very good (about 1.5) because of the highly efficient use of the main aperture lens.

Hughes Reflector-Lens Limited-Scan Concept—Fig. 59 shows a multiple-beam constrained lens feeding an offset parabolic reflector. Ideally, points from the feed array are mapped to points on the aperture of the reflector. These points are conjugate focii of the overall optical system as shown by ray tracing, say, from feed point A to aperture point A'. Other points, such as B to B', are likewise mapped. This mapping is not perfect due to the optical aberrations of the system but is adequate for ±10° field of view. It is well known [45] that the focal spot of con-

REFLECTOR

B', FOCUS FOR FIELD B

FAR-FIELD
SECTOR-SHAPED
PATTERN OF
SUBAPERTURE

$\theta_{SA} \equiv$ SECTOR WIDTH

A', FOCUS FOR FEED A

FOCAL-SPOT DISTRIBUTION =.
SUBAPERTURE DISTRIBUTION
AND RESEMBLES (sin u)/u

PASSIVE
SPHERICAL
LENS

PRIMARY ARRAY
OF FEED ELEMENTS

A

B
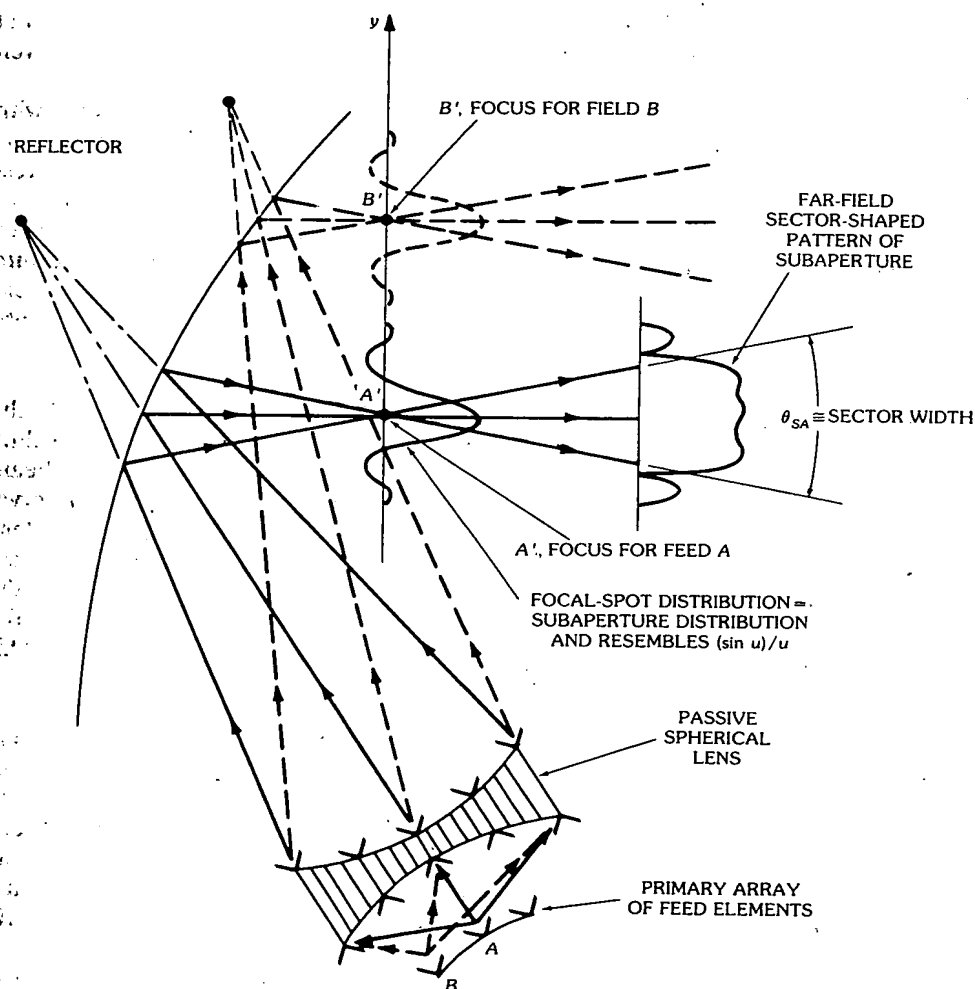
Fig. 59. Idealized geometrical mapping of rays from feed to final aperture. (*Courtesy Hughes Aircraft Co., Fullerton, Calif.*)

verging or diverging waves uniform over a sector has a focal plane distribution like $J_1(u)/u$ for spherical waves and like $(\sin u)/u$ for cylindrical waves. These distributions form overlapping $(\sin u)/u$-like subapertures that can be made orthogonal, or nearly so, by the proper amount of overlap, which is controlled by primary feed spacing along the feed arc. To be truly orthogonal, $(\sin x)/x$ distributions must be all of equal width and crossover such that the peak of any one distribution occurs at the nulls of all others. Proper radial positioning of the feed is made so that the conjugate focal point falls on the aperture plane. The $(\sin u)/u$-like subaperture distributions give rise to sector-shaped far-field patterns whose width is approximately that of the geometrical angle subtended by the rays focused at the aperture, as shown in Fig. 59.

An experimental two-dimensional parallel-plate model was built and tested [46]. An artist's concept is shown in Fig. 60 and a photograph of the experimental model is shown in Fig. 61. Calculated and measured subaperture patterns are given in Fig. 62.

Now consider the primary feeds fed by a Butler matrix (or equivalent) with intervening phase shifters. This allows multiple simultaneous beams that can be scanned in unison by the phase shifters. This is possible because a linear progressive phase across the array of lens feed elements will cause a corresponding progressive phase across the subapertures by virtue of the one-to-one correspondence explained previously. The beam can be scanned within the limits of the subaperture pattern (approximately $\pm 10°$). Fig. 63 shows representative patterns both measured and calculated for beam scans of $0°$, $-5°$, and $-9°$—all within the subaperture pattern of $10°$.

Partial-Time-Delay Systems—One of the earlier partial-time-delay systems is the MUBIS (multiple-beam interval scanner) proposed by Rotman and Franchi.* Widely spaced (several beamwidths) true-time-delay beams from a multiple-beam lens or from a true-time-delay network are synchronously scanned in the interval between the true-time-delay beams by means of $0°-360°$ phase shifters in the lens aperture. The system has true time delay at the true-time-delay (phase shifters set to zero) beam positions and almost true time delay if a small amount about the true-time-delay angles is scanned. Thus the field of view is increased by the number of time-delay beams for a given required instantaneous bandwidth. This technique is fully described in Chapter 13.

Completely Overlapped Space-Fed Subarray Antenna System—The completely overlapped space-fed subarray antenna system developed at Hughes Aircraft Company [47, 48] is illustrated in Fig. 64. It is composed of a planar feedthrough lens with $0°$ to $360°$ type phase shifters in every element. It is fed by a planar-feed array, which in turn is fed by a Butler or Blass multiple-beam matrix. Time-delay type phase shifters are placed at the inputs to the Butler or Blass matrix with a corporate summing feed network. The subarray inputs to the matrix form uniform

---

*See Chapter 13, Section 3, under the heading "Broadband Array Feeds With Time-Delayed Offset Beams."
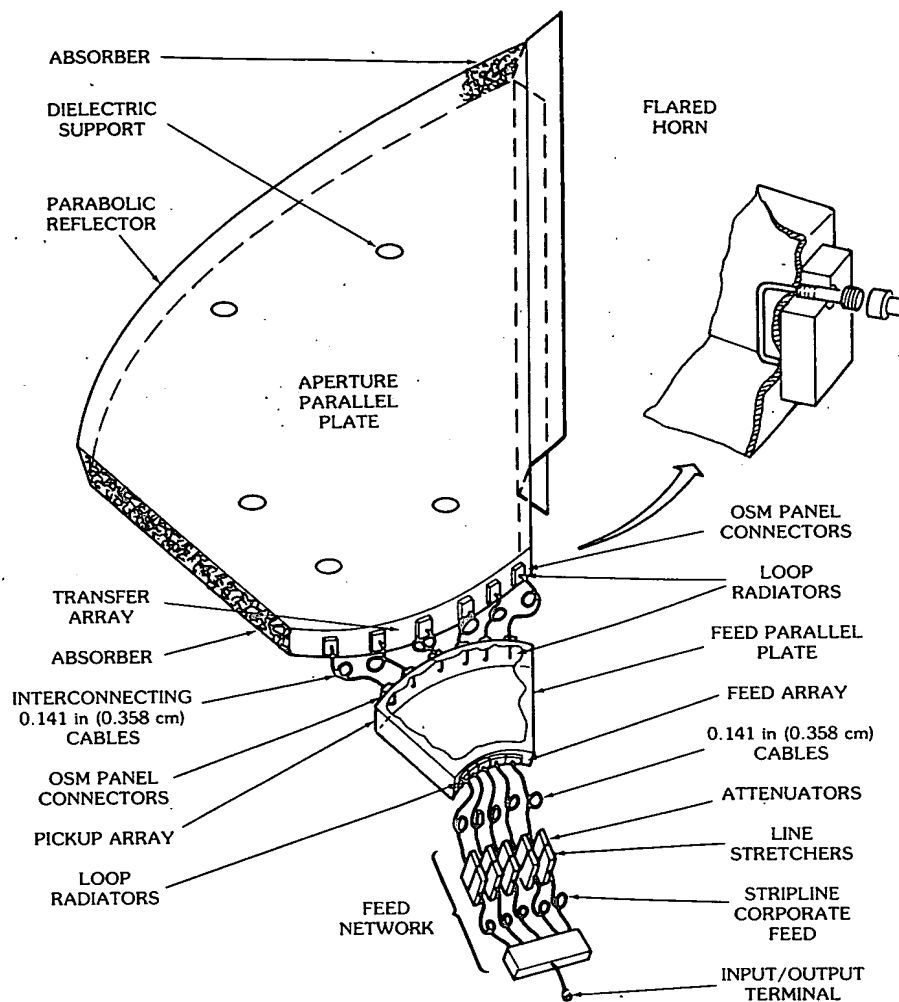
Fig. 60. Artist's concept of the experimental reflector-lens, limited-scan antenna.

distributions at the output of the feed array, which in turn form an orthogonal set of $(\sin u)/u$ type primary radiation patterns that illuminate the pickup array. Except for the slight amount of inverse distance-squared power decay, the emerging distributions from the radiating array form a near-orthogonal set of amplitude subarray distributions which completely overlap each other over the entire radiating aperture face as shown in Fig. 64. The subarray far-field radiation patterns form near-rectangular patterns superimposed in space but whose phase centers are displaced across the face of the radiating aperture. In order to minimize gain loss as a function of scan and to apply grating lobes over a wide range of scan angles and wide bandwidth, the ideal subarray pattern would be rectangular in shape but narrower than the angular separation between the first grating lobes [47].
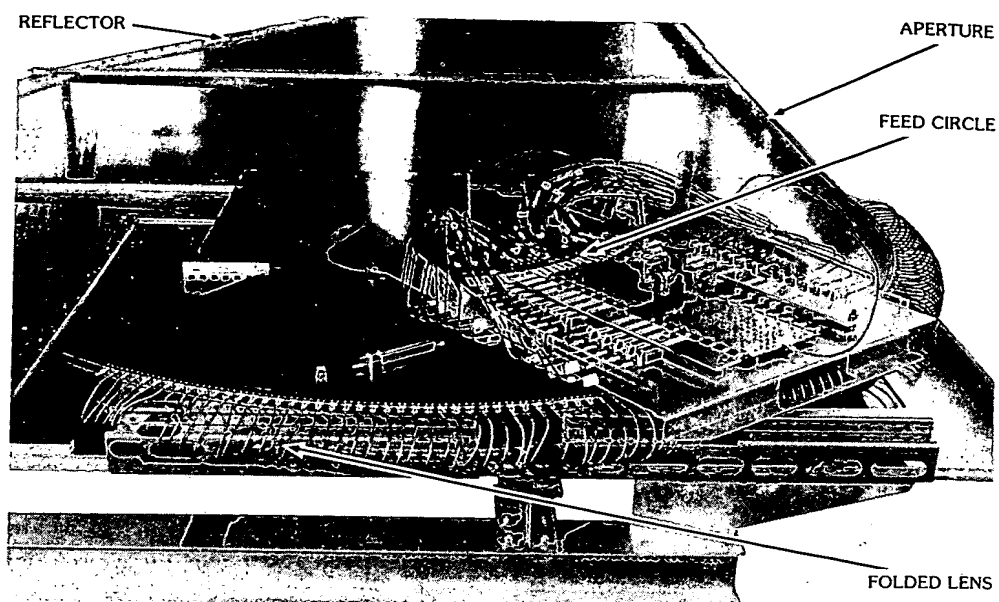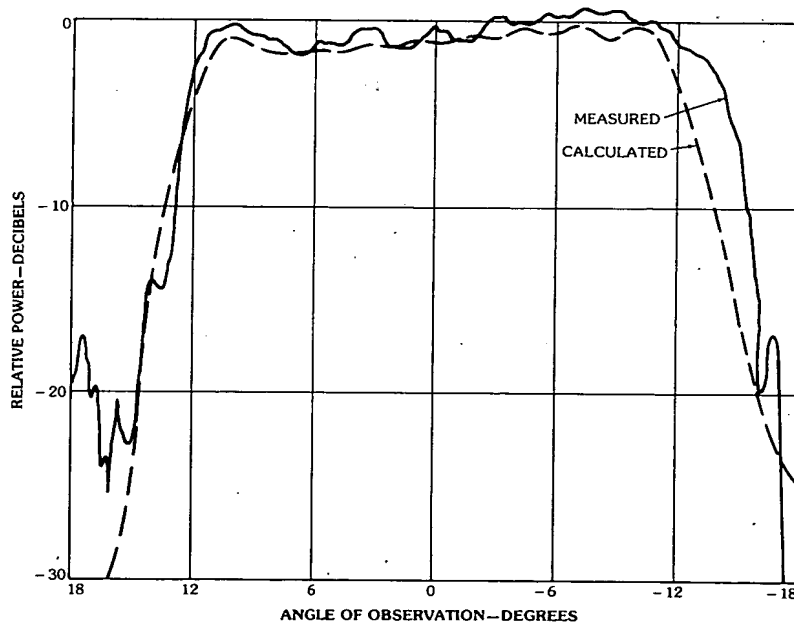
Fig. 61. Reflector-lens, limited-scan antenna, showing lens assembly. (*Courtesy Hughes Aircraft Co., Fullerton, Calif.*)

a

Fig. 62. Subaperture far-field patterns. (*a*) Subaperture centered at $y = 0$. (*b*) Subaperture centered at $y = -11.5\lambda$. (*c*) Subaperture centered at $y = -23\lambda$. (*Courtesy Hughes Aircraft Co., Fullerton, Calif.*)
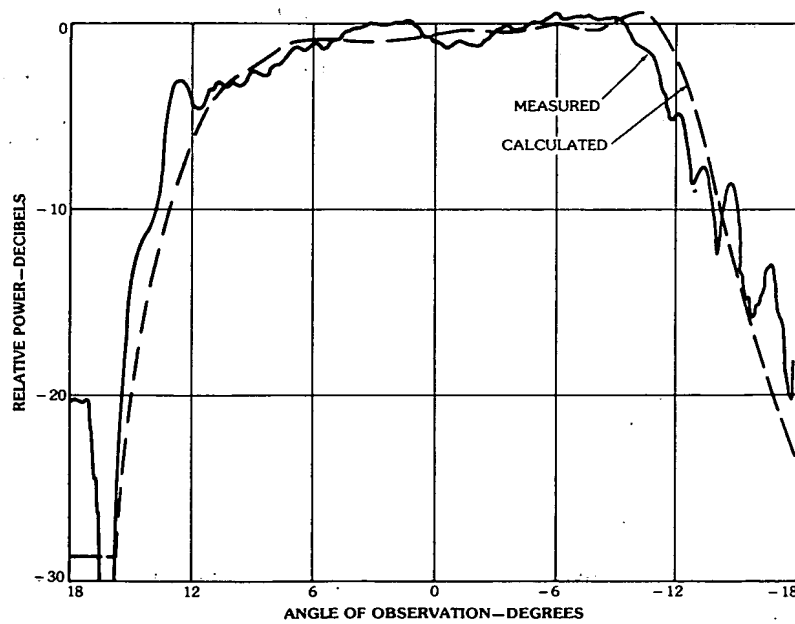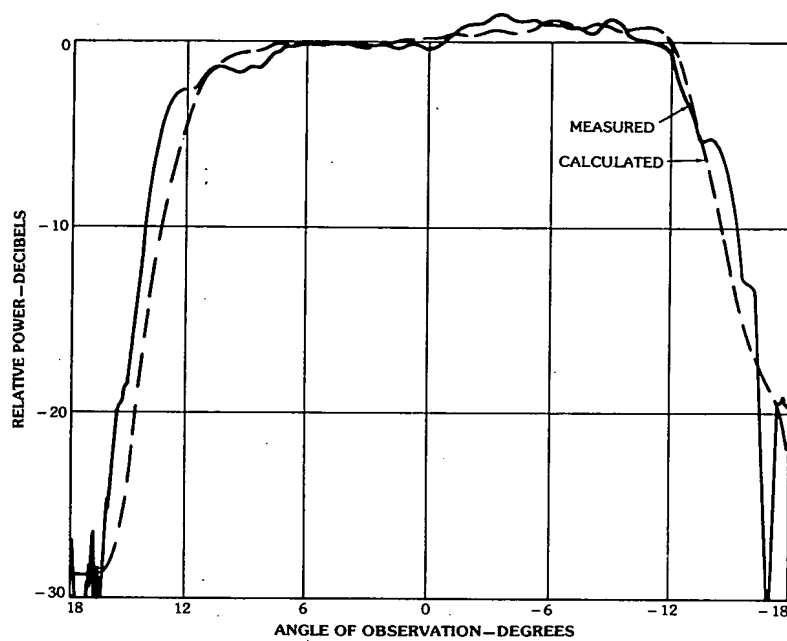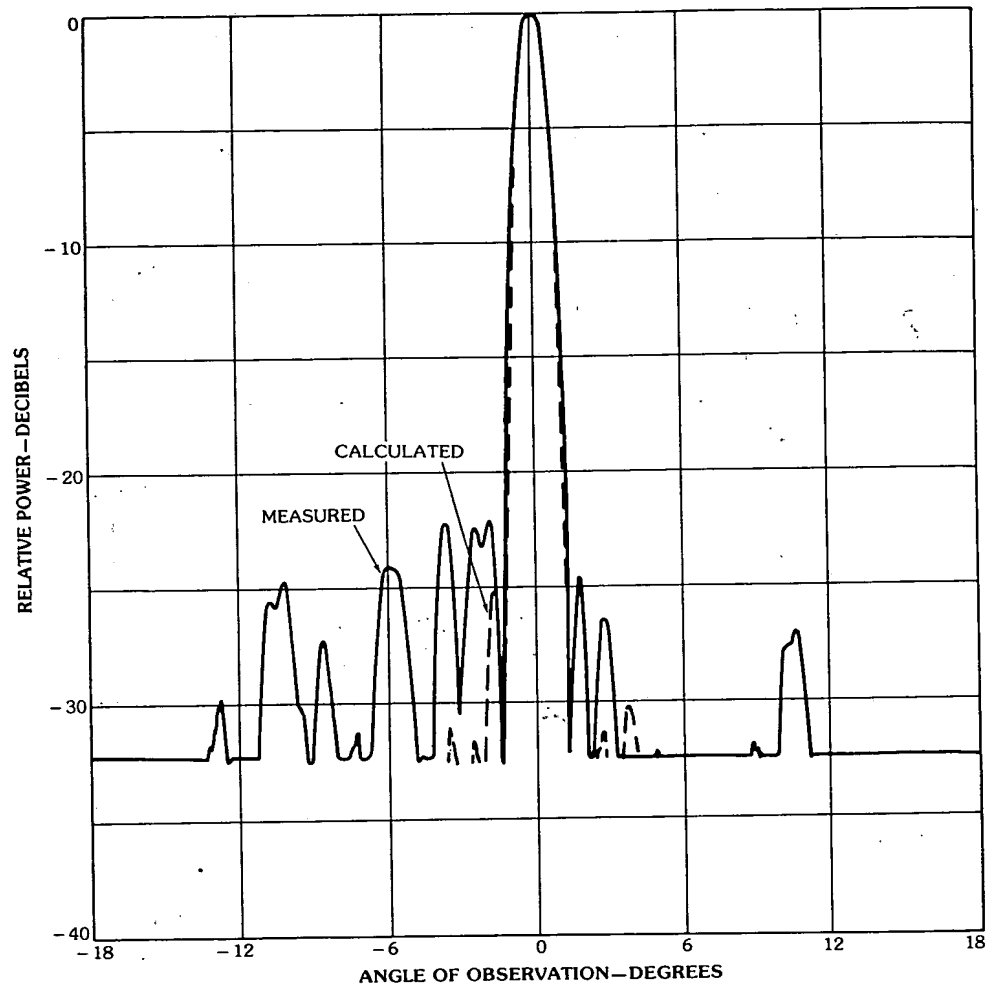
19-70

Fig. 62, *continued.*

Fig. 63. Representative patterns for various beam scans at $f = 9.5$ GHz. (a) For a beam scan of 0°. (b) For a beam scan of $-5°$. (c) For a beam scan of $-9°$. (*Courtesy Hughes Aircraft Co., Fullerton, Calif.*)

Fig. 65 depicts the effect of scanning the ideal subarray pattern with respect to the array pattern. This ideal subarray pattern results in no gain reduction as the main beam is scanned within the subarray pattern and has complete grating lobe suppression outside the subarray pattern. The completely overlapped space-fed subarray technique achieves a close approximation to the ideal subarray pattern. The amplitude distribution over the radiating aperture for each subarray input terminal is a discrete truncated $(\sin x)/x$ function which gives an approximate rectangular subarray pattern.
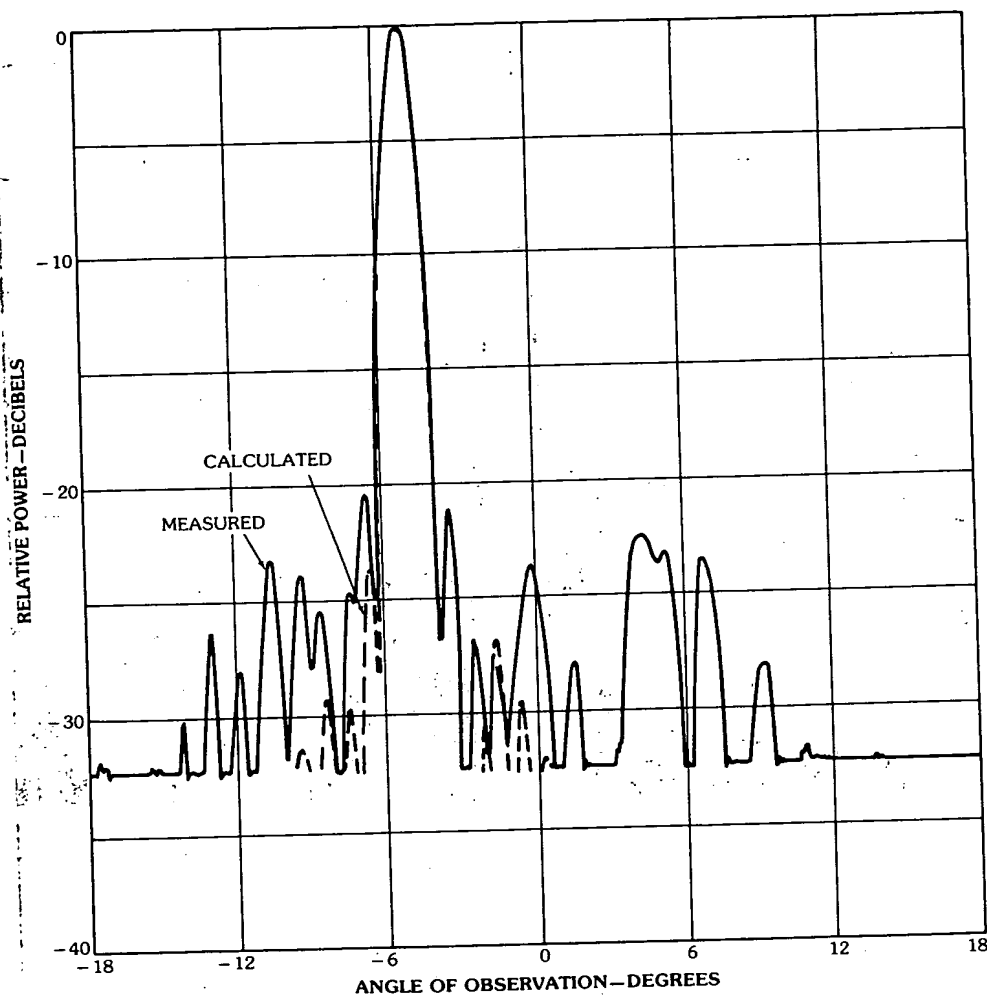
Fig. 63, *continued.*

Completely overlapped subarrays using transform networks are described in
.Chapter 13.

.DuFort's Optical Technique—DuFort's optical technique [49] for broadbanding
:a phased array is illustrated in Fig. 66. It is composed of a relatively large feed-
:through aperture lens with 0° to 360° type phase shifters, an intermediate passive
:lens with fixed phase shifters and fixed time. delayers, a small feed array with
variable phase shifters and variable time delayers, and a summing network.

The aperture lens and the feed lens have a common focus, with a magnification
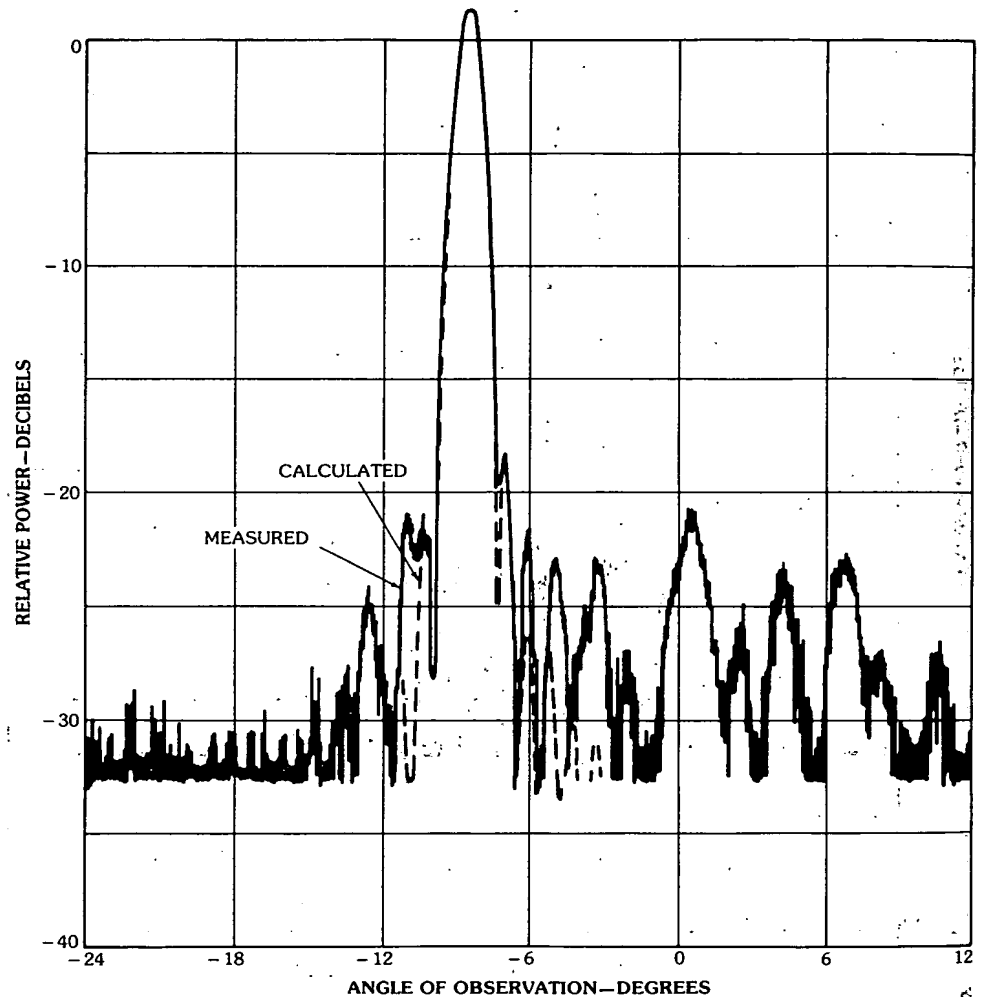$m = F/f$.

Fig. 63, *continued.*

The feed array is located at a distance h behind the confocal feed lens as shown.

The operation of this lens technique is as follows: A plane wave is incident on the lens aperture* x_1, making some general angle θ_0 with respect to the aperture lens normal. The 0° to 360° type phase shifters in the aperture lens are set such that at center frequency the received rays are focused to the center-frequency focal point as shown. These focused rays then diverge and are incident as a spherical

---
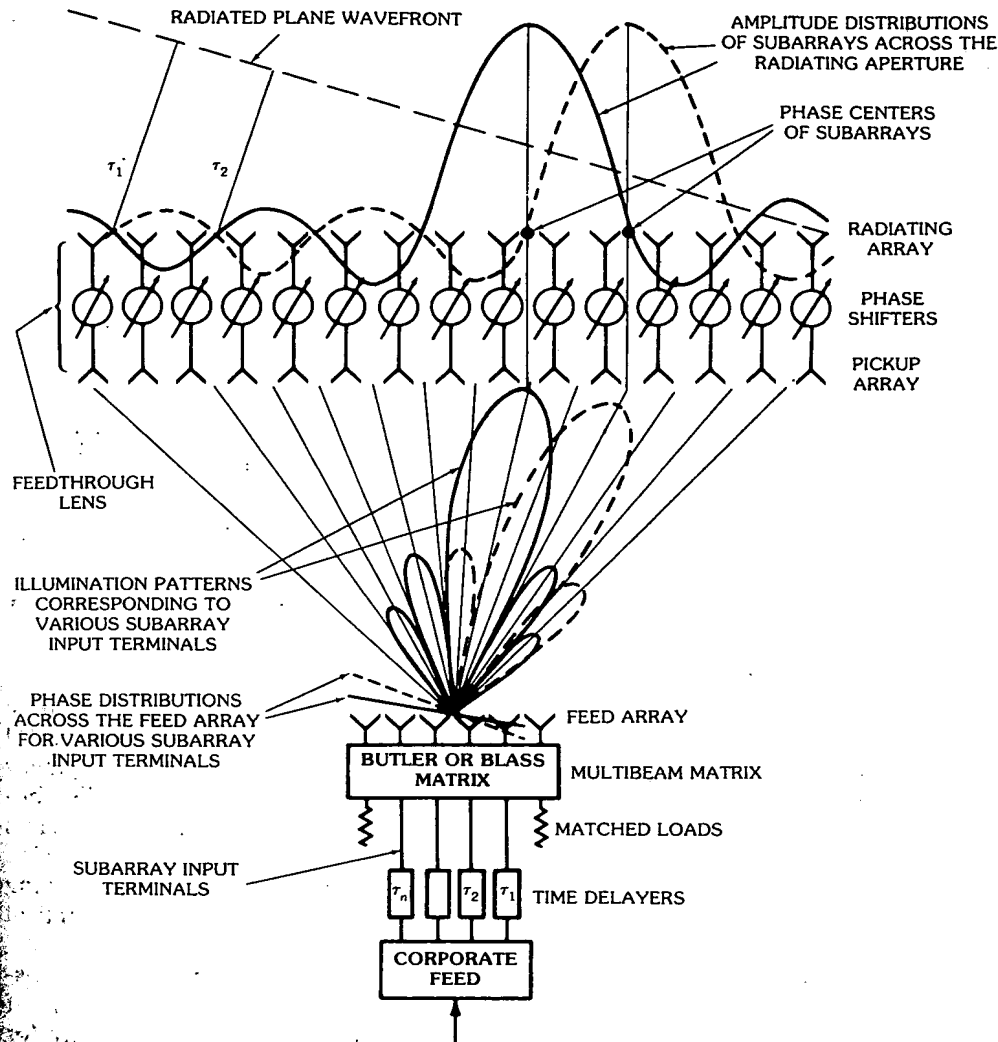
*Note that x_1 is an axis or aperture, not a specific point.

RADIATED PLANE WAVEFRONT

AMPLITUDE DISTRIBUTIONS
OF SUBARRAYS ACROSS THE
RADIATING APERTURE

PHASE CENTERS
OF SUBARRAYS

τ_1 τ_2

RADIATING
ARRAY

PHASE
SHIFTERS

PICKUP
ARRAY

FEEDTHROUGH
LENS

ILLUMINATION PATTERNS
CORRESPONDING TO
VARIOUS SUBARRAY
INPUT TERMINALS

PHASE DISTRIBUTIONS
ACROSS THE FEED ARRAY
FOR VARIOUS SUBARRAY
INPUT TERMINALS

FEED ARRAY

BUTLER OR BLASS
MATRIX

MULTIBEAM MATRIX

MATCHED LOADS

SUBARRAY INPUT
TERMINALS

τ_n τ_2 τ_1 TIME DELAYERS

CORPORATE
FEED

Fig. 64. Completely overlapped subarray pattern antenna system. (*After Tang [47]*)

phase front on the confocal feed lens. The fixed phase shifters and fixed time delayers in the confocal feed lens are such that the divergent incident rays are collimated and normal to the feed lens aperture or the x_2 axis. The feed array then receives these normally incident rays and coherently sums them through the appropriate settings of variable phase shifters and variable time delayers. Off the center frequency the aperture-lens phase shifter settings cause the received plane wave to be defocused from the center-frequency focal point and shifted laterally to an off-frequency focal region.

The divergent rays incident on the confocal feed lens are displaced along the x_2
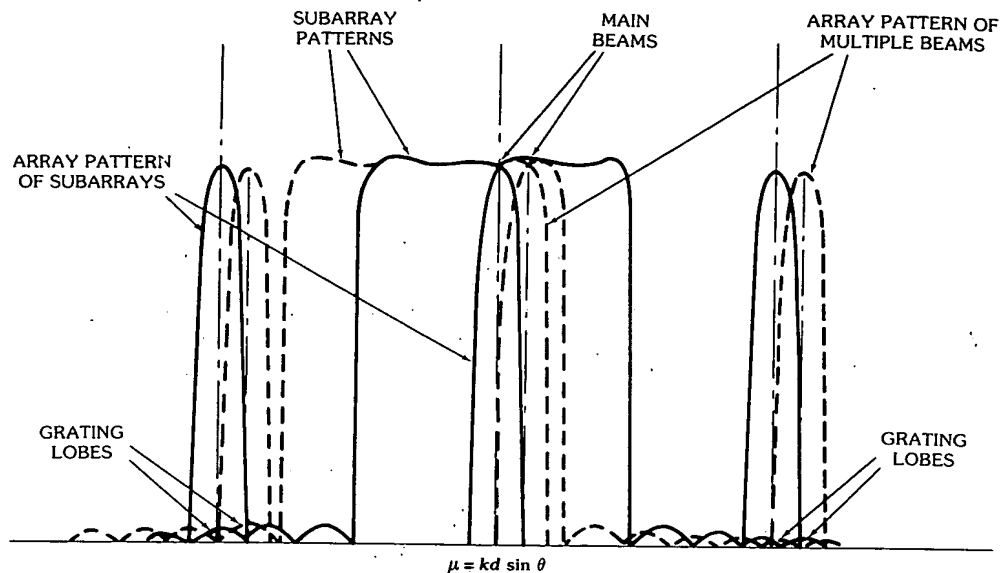
Fig. 65. Effect of scanning the ideal "rectangular" subarray pattern with respect to the array pattern. (*Courtesy Hughes Aircraft Co., Fullerton, Calif.*)

axis; however, by a judicious choice of the fixed phase shifters and fixed time delayers in the confocal feed lens, the displaced rays emerge from the x_2 axis still focused to the feed array aperture, to the first order in fractional frequency bandwidth. This design thus preserves the even-amplitude aperture lens distribution and minimizes the spillover loss. DuFort analyzes several cases and compares the results with the results one would obtain using a discrete subarray approach. He concludes that this optical approach provides less gain than the corresponding discrete subarray system, but that the side lobe performance of the optical approach is substantially better.

For example, a sample case has been calculated for cosine amplitude distribution, $F/D = 1/\sqrt{2}$, using eleven time delayers, at the extreme scan angle of 50° and at a frequency 5 percent above center frequency. The radiation pattern for the optical case is given by Fig. 67. The normalized gain is down about 1.7 dB from the maximum value of 0.816 due to cosine tapering. The far-out side lobe level is −18.5 dB, with other side lobes mostly below −25 dB. Spillover loss is only 1.1 percent. The gain loss is due to off-axis phase error that causes beam broadening. The corresponding case for the discrete subarray is shown in Fig. 68. The main beam is narrower than the optical case and the gain is down only 0.7 dB, but the grating lobe level is up to −9.9 dB, with several above −20 dB.

For more details the reader is referred to DuFort [49].

Wide Field of View True-Time-Delay Antenna Systems

Most unconstrained feeds that offer true-time-delay performance are optical in nature. The transit time between the incident wavefront, from any angle within the
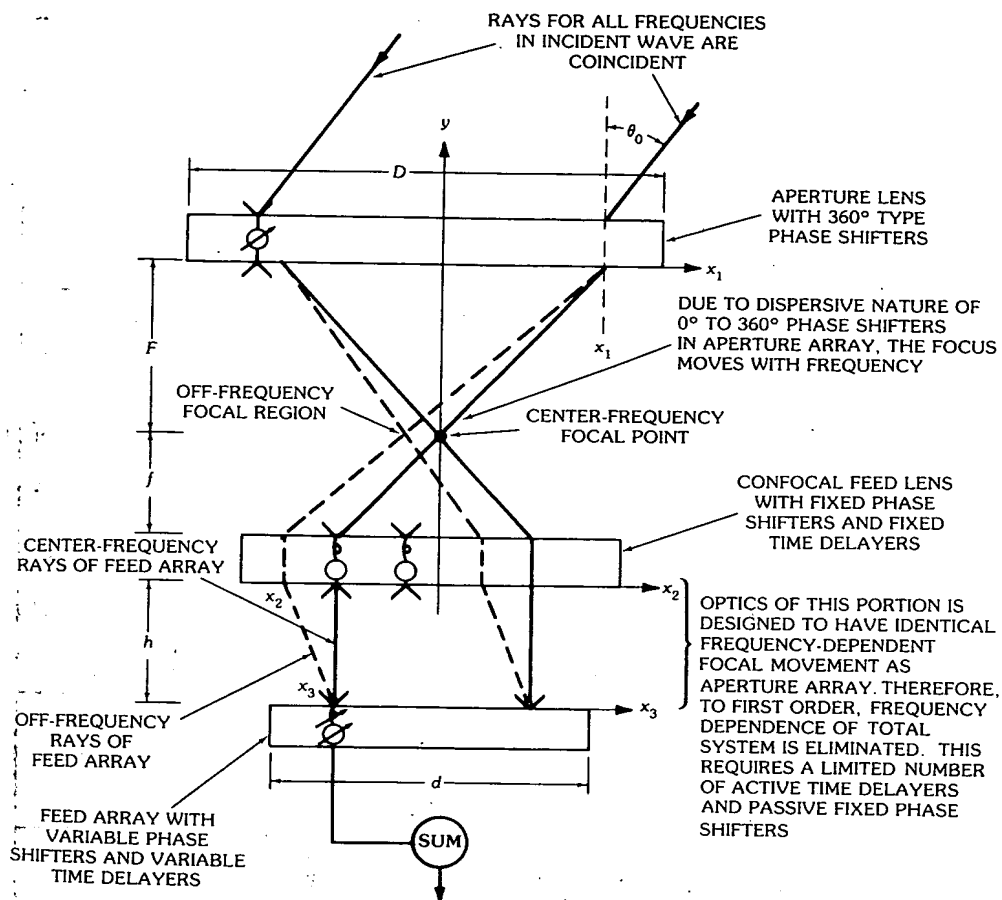
RAYS FOR ALL FREQUENCIES
IN INCIDENT WAVE ARE
COINCIDENT

θ_0

D

y

APERTURE LENS
WITH 360° TYPE
PHASE SHIFTERS

x_1

F

x_1

DUE TO DISPERSIVE NATURE OF
0° TO 360° PHASE SHIFTERS
IN APERTURE ARRAY, THE FOCUS
MOVES WITH FREQUENCY

OFF-FREQUENCY
FOCAL REGION

CENTER-FREQUENCY
FOCAL POINT

f

CONFOCAL FEED LENS
WITH FIXED PHASE
SHIFTERS AND FIXED
TIME DELAYERS

CENTER-FREQUENCY
RAYS OF FEED ARRAY

x_2

x_2

h

OPTICS OF THIS PORTION IS
DESIGNED TO HAVE IDENTICAL
FREQUENCY-DEPENDENT
FOCAL MOVEMENT AS
APERTURE ARRAY. THEREFORE,
TO FIRST ORDER, FREQUENCY
DEPENDENCE OF TOTAL
SYSTEM IS ELIMINATED. THIS
REQUIRES A LIMITED NUMBER
OF ACTIVE TIME DELAYERS
AND PASSIVE FIXED PHASE
SHIFTERS

x_3

x_3

OFF-FREQUENCY
RAYS OF
FEED ARRAY

d

FEED ARRAY WITH
VARIABLE PHASE
SHIFTERS AND VARIABLE
TIME DELAYERS

SUM

Fig. 66. Components of optical broadband phased array. (*Courtesy Hughes Aircraft Co., Fullerton, Calif.*)

FOV, to the corresponding collecting feed is a constant, regardless of the actual path that is taken for any given ray. Consequently, an extremely short time pulse, approaching a delta function, could, in principle, be transmitted or received by such an antenna system without distortion or spreading in the time domain. In practice, however, the instantaneous bandwidth is determined by the components that are used in devising such a system. If waveguides are used, or other types of elements, they will not possess infinite bandwidth when impedance matching or grating lobe phenomena are addressed. If a switching matrix is used to switch between beams, it will function only over some finite bandwidth. Thus the instantaneous bandwidth limitation of a true-time-delay system will not be established by the optics of the system but rather by the bandwidth of the components used in implementing it. For example, all parabolic reflector systems and dielectric lenses that are not zoned are true-time-delay antenna systems. Their
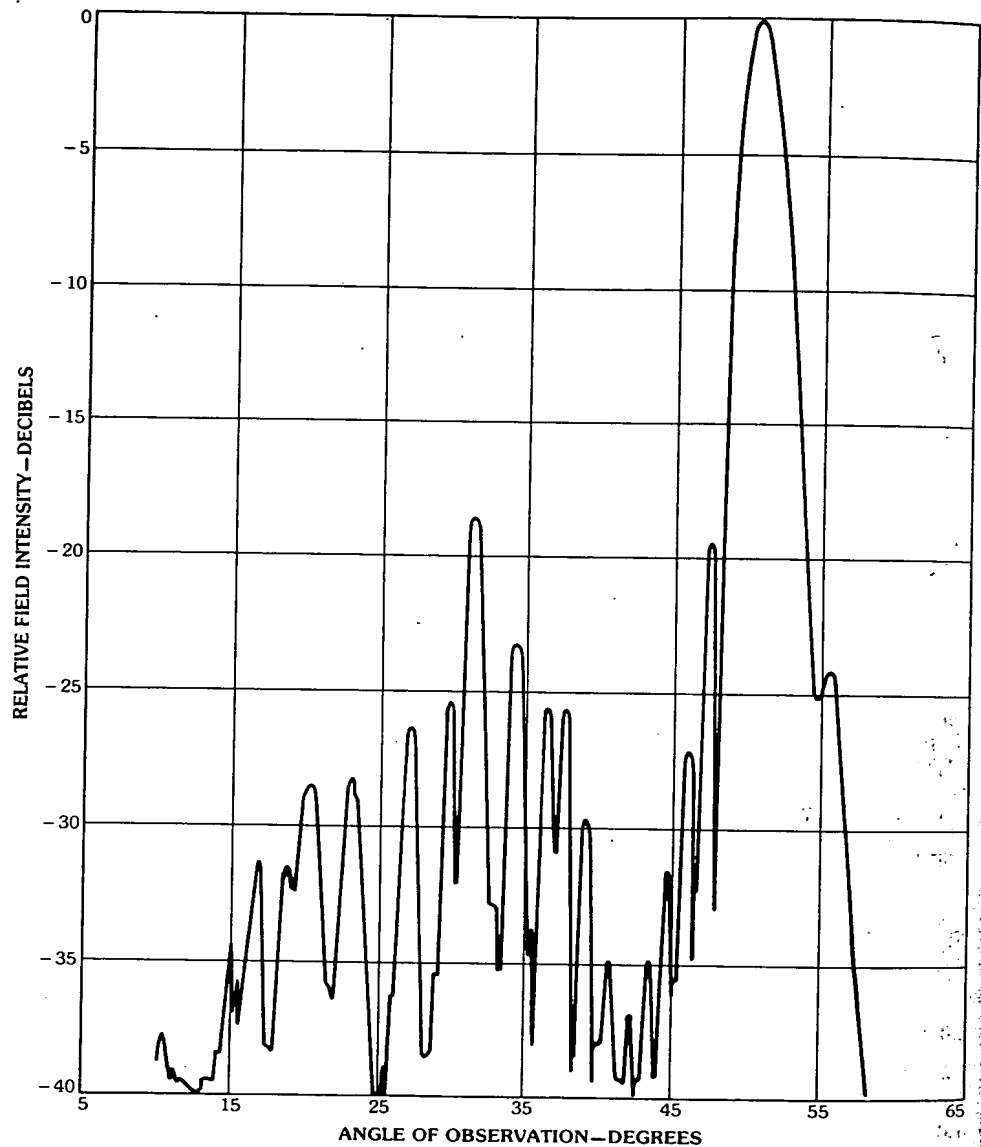
Fig. 67. Optical system radiation pattern. (*Courtesy Hughes Aircraft Co., Fullerton, Calif.*)

bandwidth, both instantaneous and tunable, is determined by the bandwidth of the feed system, or, perhaps to some extent in the case of dielectric lenses, the bandwidth may be determined by the impedance-matching transformers on the lens surfaces, as well as the primary feed(s).

Conventional monopulse feeds for conventional reflectors and lenses are well documented in the literature and will not be covered here, since most of these
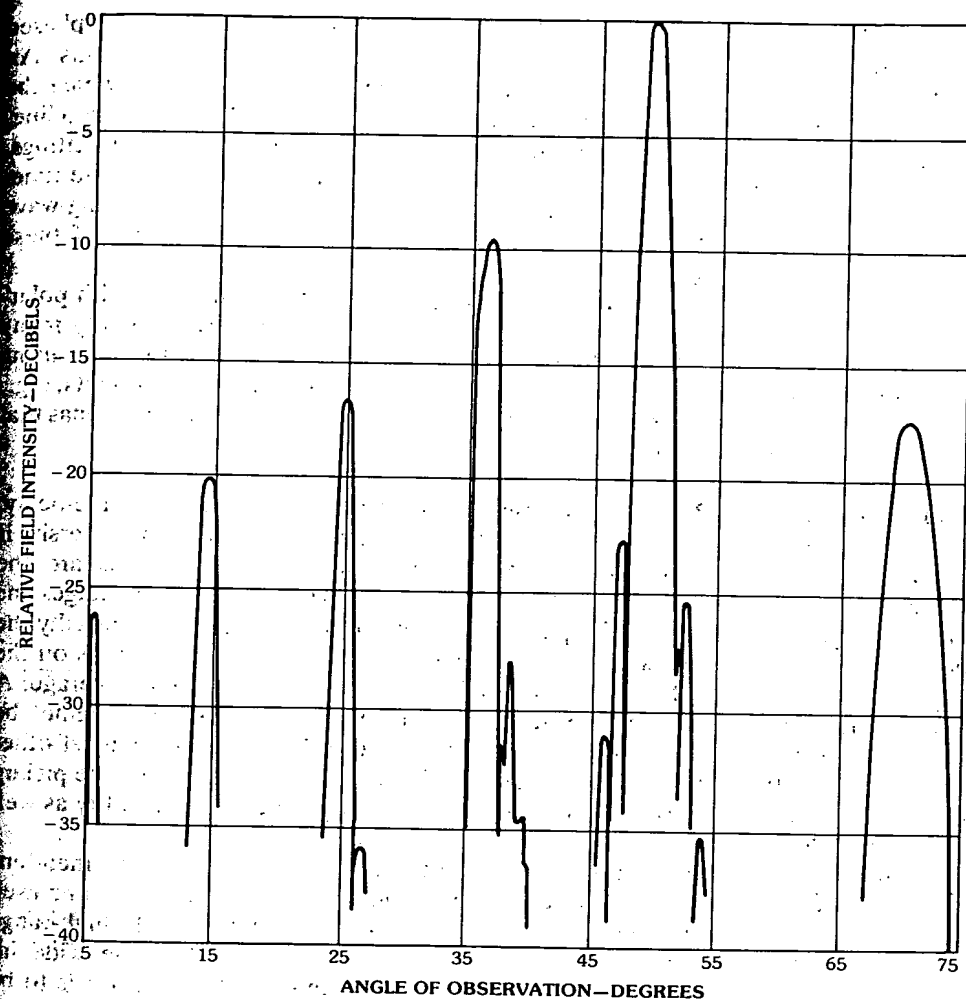
Fig. 68. Discrete subarray radiation pattern. (*Courtesy Hughes Aircraft Co., Fullerton, Calif.*)

antenna systems do not offer wide-angle performance. The purpose of this subsection is to consider and illustrate some true-time-delay approaches that can be used to feed and phase a planar array over a wide angular FOV, e.g., a 90° to 120° conical FOV. Since this section is on unconstrained feeds it may seem out of place to discuss systems that are partially constrained; however, if free space exists between the feeds and the final aperture, then they are considered unconstrained in this context.

True-time-delay antennas can be further subdivided into those that have simultaneous multiple-beam capability and those that do not. Simultaneous multiple-beam capability is important for high-data-rate systems. An example of a

true-time-delay system without simultaneous multiple-beam capability is a phased array with true-time-delay phase shifters for each of the radiating elements. An example of a true-time-delay phase shifter is a digital phase shifter in which the phase shift is achieved by switching in the proper length of TEM transmission line. In this example there is only one beam for a given set of phase shifter settings. Examples of antennas with simultaneous multiple beams which are not true-time-delay system are the Maxson (Blass)* tilt transmission-line-fed traveling-wave array [9] and the Butler hybrid-matrix multiple-beam array [3]. Both of these produce multiple beams in only one plane.

True-time-delay, high-gain, simultaneous-multiple-beam antennas with polarization diversity are necessarily quite complex because they are in reality many antennas sharing a common radiating aperture. The advantages of this over using many separate antennas is obvious because so many of the costly components, e.g., transmit/receive modules of an active array, are shared by each of the antennas that make up the multiple-beam antenna system.

Wide-Angle Multiple-Beam Constrained Lens—The design of a true-time-delay, simultaneous-multiple-beam, constrained-lens system with polarization diversity is described here. Other antenna systems that achieve the same goals are the Luneburg lens and spherical reflector systems. Each system has its advantages and disadvantages, depending on the particular application in which cost is usually the determining factor. Studies have shown that the optimum choice depends on the desired beamwidth, the frequency band of operation, and the desired coverage. A general statement as to the superiority of one method over another cannot be made. The system described here, however, has one advantage over most other systems in that the beam-positioning (feed) elements are separate from the pickup or transfer elements. This facilitates component design and packageability as well as offering electrical advantages.

The true-time-delay, multiple-beam, spherically symmetrical, constrained-lens antenna described here can be used as a radiating antenna by itself or can be used as a phasing device for a multiple-beam planar array. For extremely high-range resolution a true-time-delay system is required to accommodate the wide instantaneous frequency spectrum of extremely short pulses. If the device is to be used as a phasing device for a planar array as shown in Fig. 69, it should illuminate the array aperture with the same amplitude distribution for all beam positions. That is, the illuminated portion of the aperture should not scan as the beam is scanned. Concentric (spherical) lenses or reflector systems, such as the hemispherical reflector system shown in Fig. 69, automatically satisfy the nonscanning-aperture requirement because the central ray for every beam passes through the center of the aperture.

Concentric systems have inherent wide-scan capability because they are spherically symmetrical, and hence the beam-forming device, by itself, has phase errors independent of scan angle. However, when the latter is used as a phasing

---

*The Maxson or Blass array can be made true time delay but in doing so, much of its appealing simplicity, low cost, and compact packaging is sacrificed. See Hansen [4], vol. 3, p. 254.
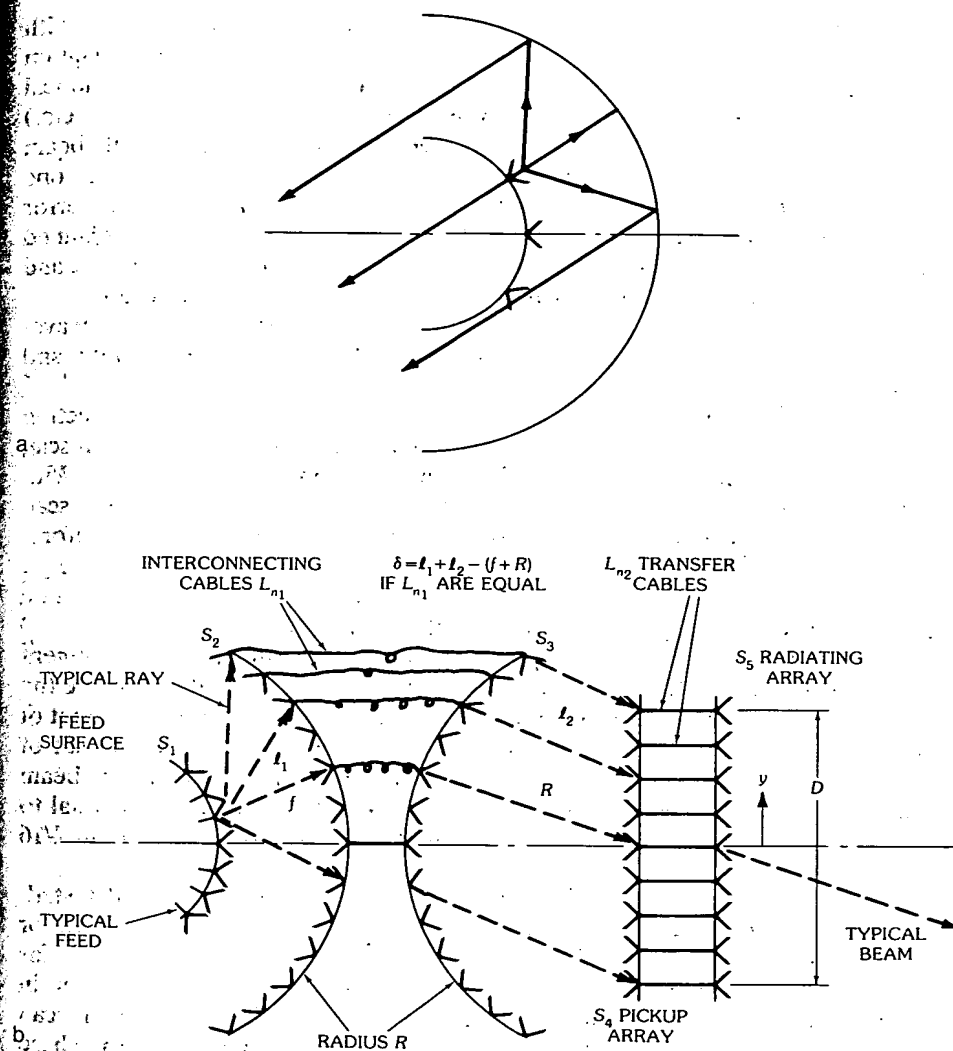
Fig. 69: Hemispherical reflector and lens counterpart: (a) Reflector. (b) Lens. (Courtesy Hughes Aircraft Co., Fullerton, Calif.)

device for a planar array the phase errors may actually decrease as the beam is scanned off broadside. The reason for this is that only the central portion of the phase front is intercepted by the planar array. This is true to the extent that phase errors at one plane can be projected to phase errors at another plane.

A hemsipherical lens [50] developed at Huges Aircraft Company, Fullerton, California, is the transmission (lens) counterpart to a hemspherical reflector system, as shown in Fig. 69a. If the current distribution on the reflector of the hemisphere were transferred via pickup elements with equal line lengths to an

identical transfer array, the radiation of the transfer array would be identical with that from the reflector as indicated in the schematic diagram, Fig. 69b. The diagram shows such a lens used as a phasing device for a planar array. Because of spherical symmetry the basic lens has virtually only even (e.g., quadratic, quadric, etc.) phase errors. These even phase errors can be corrected exactly for any single beam position by adjustment of line lengths L_{n_1} or L_{n_2}. By doing this, however, one causes the system to deviate from being spherically symmetrical and the phase error now depends on scan position. In fact, odd phase errors may now arise for scanned beams. By line length adjustment, however, the total phase errors, both odd and even, can be made considerably less than that for the uncompensated lens.

The optimum parameter values depend on the size of the antenna in wavelengths and the desired amount of maximum scan. For narrow beamwidths and large maximum scan angle, S_1, S_2, and S_3 should be spherical.

If an angular correspondence between feed position angle and beam direction is desired, S_4 and S_5 should have the same size. That is, the ratio of the beam scan angle to feed position angle is the ratio of the linear dimensions of S_4 and S_5. With no line length phase compensation the path length error curves in the plane of scan for various scan angles are given in Fig. 70 (for a typical f/R). As mentioned before, because of spherical symmetry the aperture phase errors are essentially even (e.g., quadratic quadric) for all scan angles. A similar set of phase error curves can be calculated in the plane perpendicular to the plane of scan.

The common portion of the even phase errors can be removed by adjustment of the output line lengths L_{n_2}, e.g., the line lengths L_{n_2} are adjusted to remove the path length labeled "compensation curve" shown in Fig. 70; it also shows a plot of maximum path length error after line length compensation for a typical set of parameters. To illustrate the relative sizes involved, for a 70λ aperture (1° beam for typically tapered distribution), the diameter of the radiating array is equal to the radius of the lens sphere and the maximum phase error would be about $\lambda/16$ for beam scan to $\pm 45°$.

An experimental model of such a beam-forming lens was built and tested. Figs. 71a and 71b are photographs of this model. Antenna patterns were taken for scan in vertical, horizontal, and 45° planes. Fig. 72a shows typical patterns for various scan angles in the plane of scan. Fig. 72b shows typical patterns taken in planes normal to the plane of scan. Fig. 72c shows patterns for 45° diagonal scan over a range of frequencies covering approximately a 40-percent bandwidth. These test results establish the feasibility of this type of three-dimensional, multiple beam-forming device.

Below is a summary of the properties of the lens:

1. Wide angular coverage
2. Simultaneous multiple true-time-delay beams
3. Nonscanning aperture, hence efficient as phasing device for planar array
4. Polarization diversity capability. With dual-polarized lens elements the polarization is determined solely by the polarization of the feed
5. The number of beams and beam positions are independent of the number and locations of the transfer or pickup elements of the lens since these elements are not used for a dual purpose of feed and transfer or pickup elements
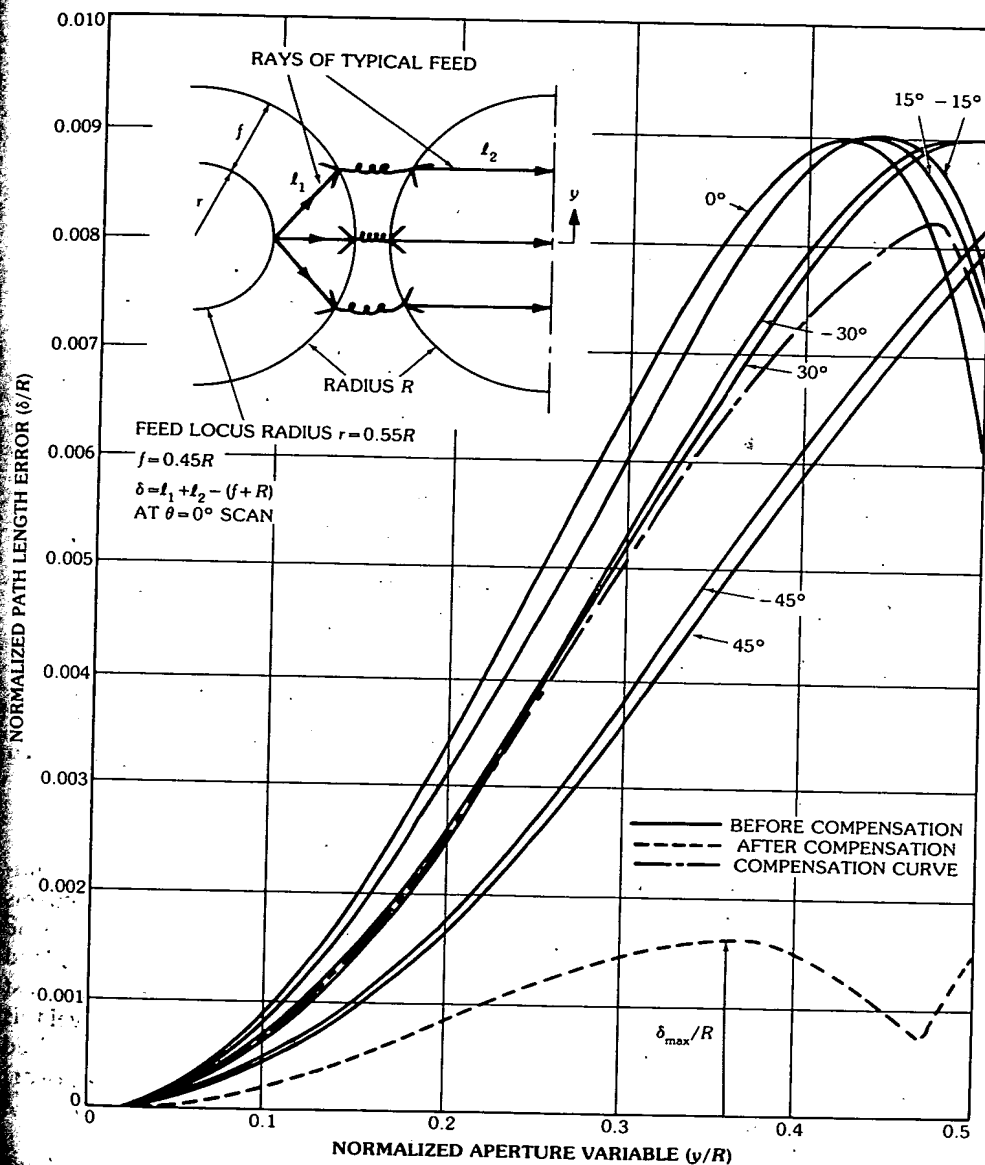
Fig. 70. Path length error versus aperture variable before compensation, and maximum path length error after compensation. (*Courtesy Hughes Aircraft Co., Fullerton, Calif.*)

A consequence of the property stated above is that the beams can be placed in any desired manner in space by proper placement of feeds on surface S_1 of Fig. 69b. For example, if the device is used to phase a planar array, the feeds can and should have variable spacing to keep a constant "crossover level" between adjacent beams since the radiated beam broadens as the beam is scanned off broadside to the

TYPICAL ARRAY ELEMENT
(DIPOLE IN CAVITY)

a
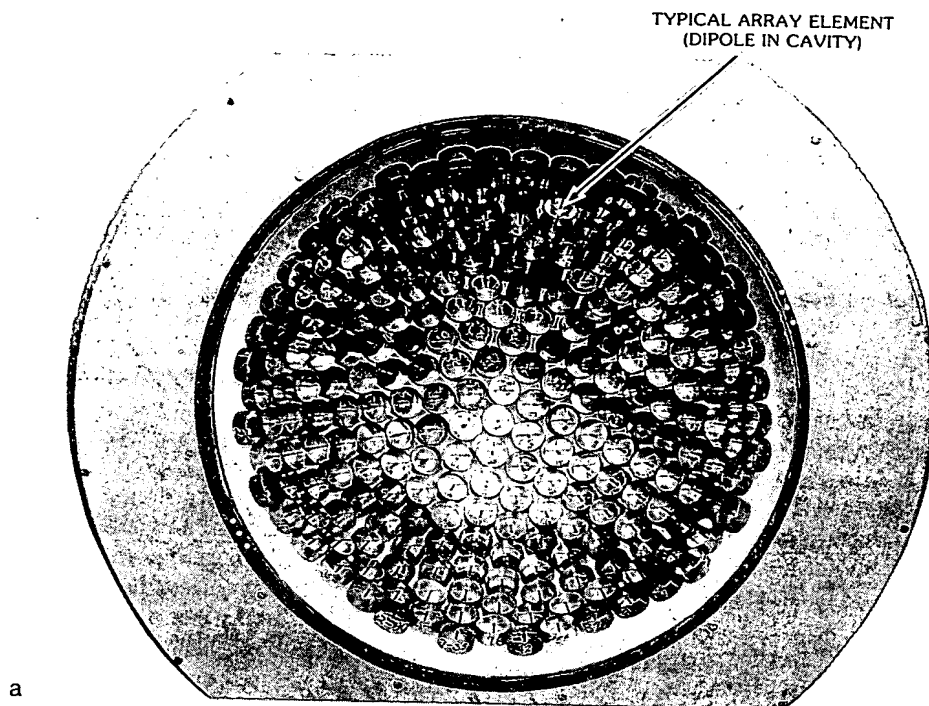
Fig. 71. Beam-forming lens. (*a*) Front view of lens. (*b*) Side view of partially interconnected lens. (*Courtesy Hughes Aircraft Co., Fullerton, Calif.*)

planar array. This capability of arbitrary beam positioning facilitates the implementation and computation of monopulse operation between adjacent beams for increased angular accuracy. Since the projected aperture decreases as the cosine of the scan angle, the feed directivity must increase in like manner to keep the feed spillover loss a constant. Thus the feed directivity (hence the feed aperture) must increase as the secant of the scan angle, and for a constant beam crossover level this is just the amount of space available for the feed. Thus the independence of feed and lens element allows the antenna efficiency to be the same (equal feed spillover) for all beam positions.

For the detailed design procedure see McFarland and Ajioka [50].

Modifications of the Basic Lens—Two modifications of the basic lens have been studied in an attempt to improve the aperture efficiency or to increase the usable portion of the approximate plane wave. The first scheme is similar to a Cassegrain technique, as illustrated in Fig. 73a.

This scheme slightly increases the usable portion D of the S_3 surface diameter $2R$, as is shown by Fig. 73b, where it is compared with the basic lens. However, it has the disadvantage of using the radiators covering surface S_2 for the dual purpose of acting as feeds and transfer radiators. To accomplish this function would require the appropriate circuitry in the interconnecting cables L_{n_1}.
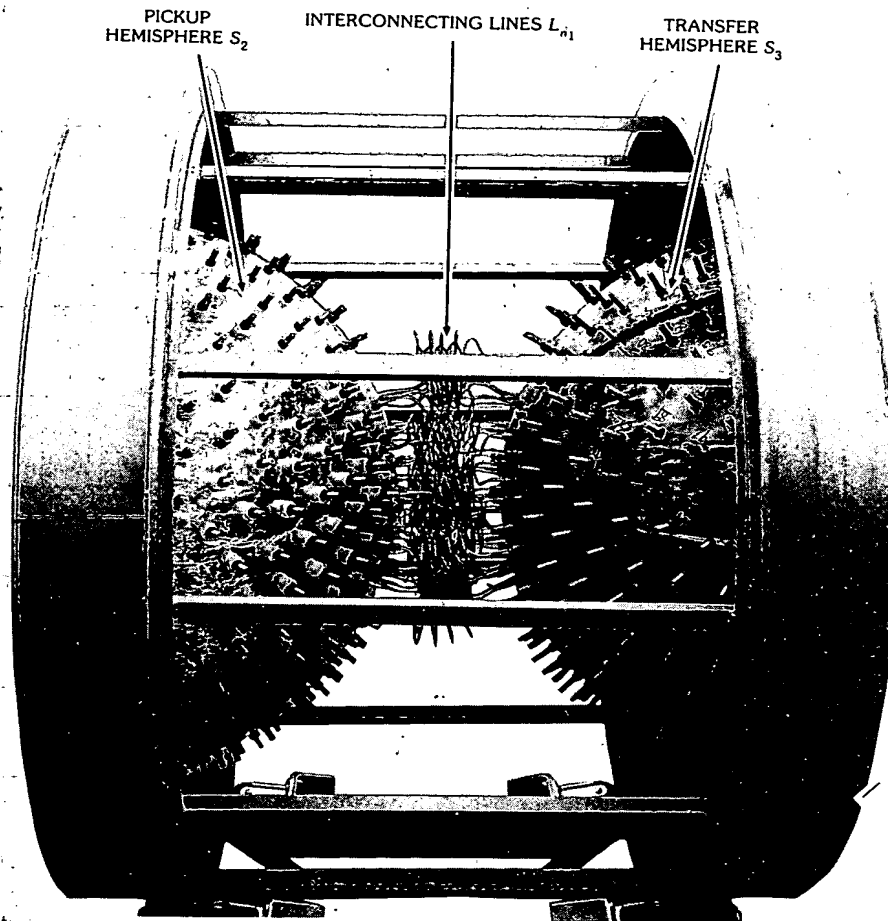
Fig. 71, *continued*.

The second scheme is similar to a Mangin Mirror, as shown in Fig. 74. It uses a constant concentric dielectric correcting lens at the feed side of the basic lens.

This scheme appreciably increases the usable portion D of the S_3 surface diameter $2R$, as is shown by Fig. 73b, where it is compared with the basic lens. This modification retains all of the merits of the basic lens while considerably improving the output phase.

A similar design procedure can be followed in designing the modified versions of the lens as has been used for the basic lens.

High-Resolution Hemispherical Reflector Antenna (HIHAT)—The HIHAT multiple-beam antenna system was invented [51] at Hughes Aircraft Company in the early 1960s by Louis Stark of the Ground Systems Group. Fig. 75 illustrates the
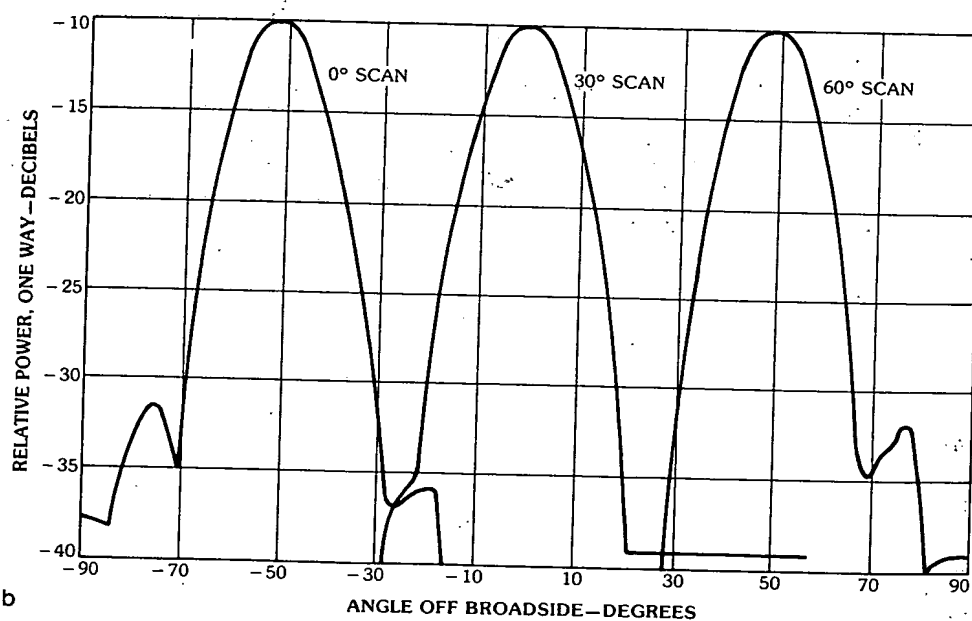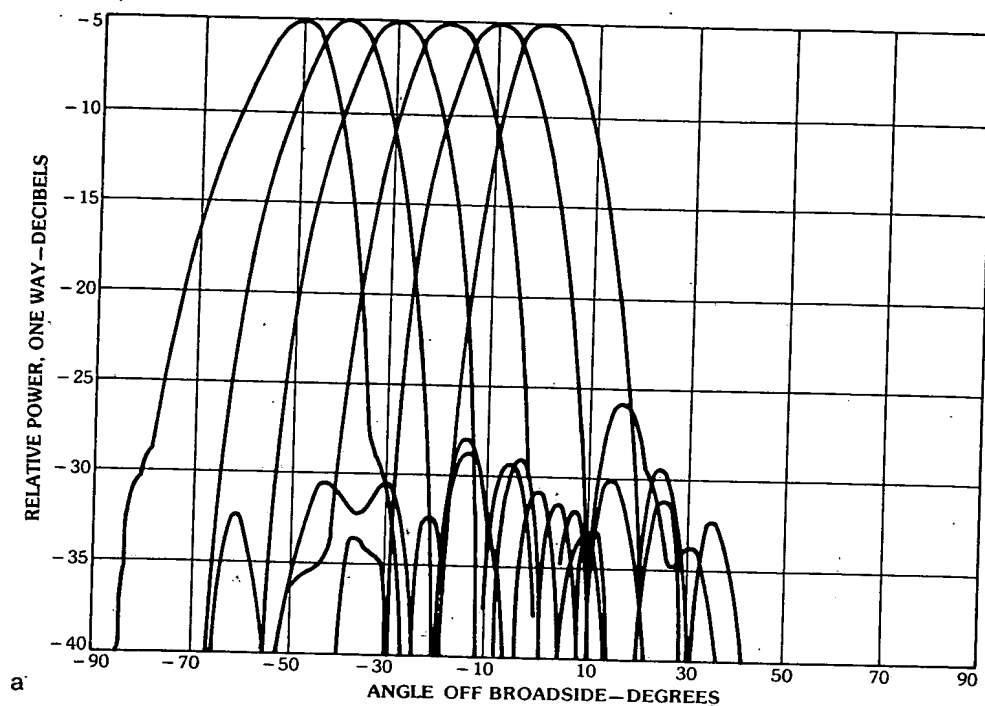
Fig. 72. Typical beam-forming lens antenna patterns. (*a*) In plane of scan, showing wide-scan capability. (*b*) Normal to plane of scan for various scan angles. (*c*) Over frequency range (beam scanned 45° in diagonal plane). (*Courtesy Hughes Aircraft Co., Fullerton, Calif.*)
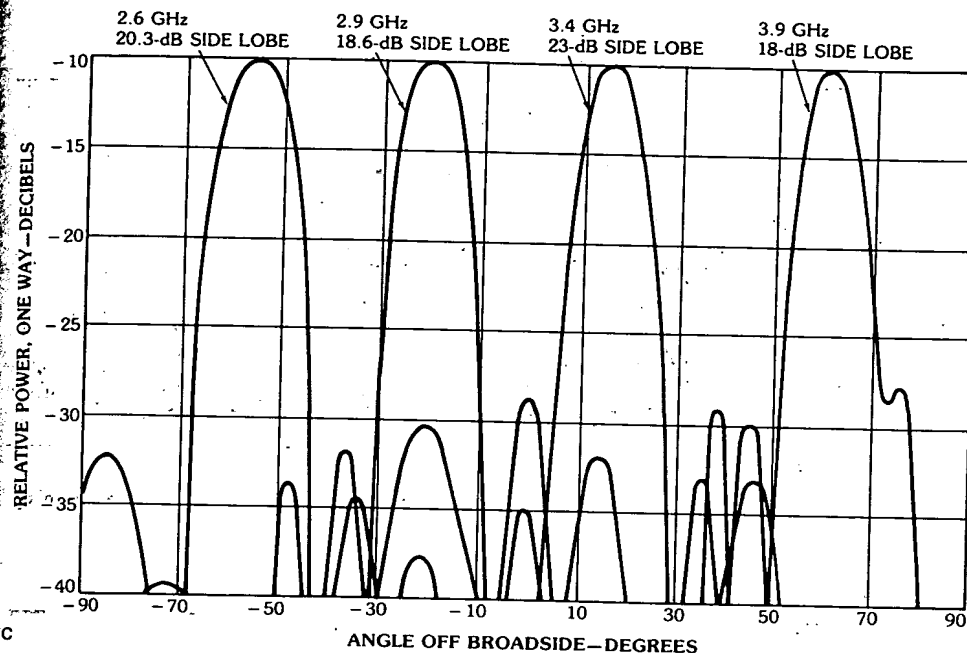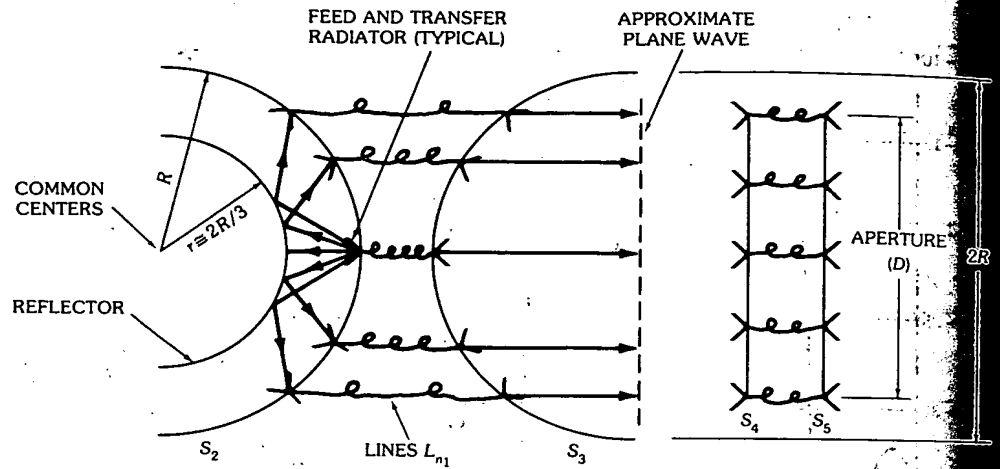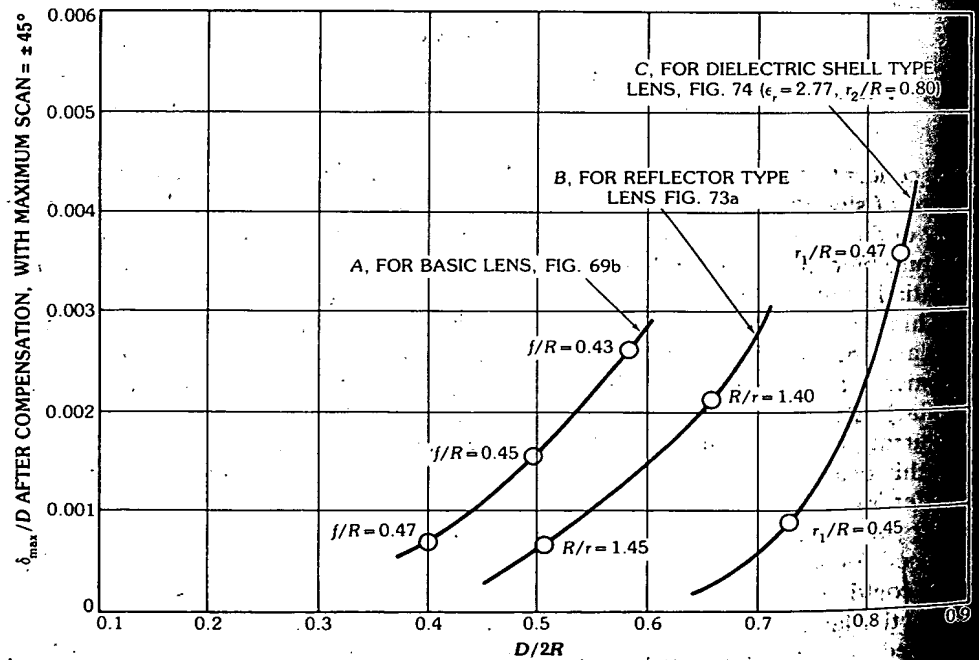
19-86

2.6 GHz
20.3-dB SIDE LOBE

2.9 GHz
18.6-dB SIDE LOBE

3.4 GHz
23-dB SIDE LOBE

3.9 GHz
18-dB SIDE LOBE

c

Fig. 72, *continued.*

basic concept. A spherical reflector is fed by a concentric array of feeds located on a sphere of slightly greater than half that of the spherical reflector. This concentric array of duplexing feeds is dual circularly polarized. This novel feature enables the aperture blockage that would ordinarily be presented by the feed array to become essentially "invisible"; thus a given feed or feed cluster is selected by a beam-switching matrix to be excited as a circularly polarized primary feed, e.g., right circular. The primary feed(s) illuminates a portion of the spherical reflector and becomes nearly collimated with the opposite sense circular polarization (e.g., left circular) after reflection off the spherical reflector. The dualpolarized duplexing feed array picks up the nearly collimated rays in the left circularly polarized channel (for this example) and transfers the nearly collimated wavefront to a spherical transfer array. The spherical transfer array is designed to have its radiators' phase centers lie on the same radius sphere as for the duplexing array. Equal line lengths are used for this transfer. From the spherical transfer array, radiation into free space could take place, or it could be used to phase a planar array, as shown in Fig. 76. In the latter case the common portion of the spherical aberration could be removed prior to radiation into free space, thereby improving the flatness of the radiated phase front. This technique was discussed in the previous section and is applicable here. Excellent radiation patterns are obtainable since the central portion of the reflected phase front is highly correctable by using variable line lengths between the pickup and radiating planar array. Fig. 77 shows typical measured Σ and Δ patterns using two adjacent feeds for primary illumination.

a

FEED AND TRANSFER
RADIATOR (TYPICAL)

APPROXIMATE
PLANE WAVE

COMMON
CENTERS

REFLECTOR

R

$r \cong 2R/3$

APERTURE
(D)

$2R$

S_2

LINES L_{n_1}

S_3

S_4 S_5

Note: S_4, in reality, is located at the diameter of S_3

b

C, FOR DIELECTRIC SHELL TYPE
LENS, FIG. 74 ($\epsilon_r = 2.77$, $r_2/R = 0.80$)

B, FOR REFLECTOR TYPE
LENS FIG. 73a

A, FOR BASIC LENS, FIG. 69b

$f/R = 0.43$

$r_1/R = 0.47$

$R/r = 1.40$

$f/R = 0.45$

$f/R = 0.47$

$R/r = 1.45$

$r_1/R = 0.45$

δ_{max}/D AFTER COMPENSATION, WITH MAXIMUM SCAN $= \pm 45°$

0.006
0.005
0.004
0.003
0.002
0.001
0

0.1 0.2 0.3 0.4 0.5 0.6 0.7 0.8 0.9

$D/2R$

Fig. 73. Cassegrain modification of basic lens. (*a*) Cassegrain reflector type variation of basic lens. (*b*) Normalized maximum path length error, after compensation, versus usable portion of the output hemisphere diameter as radiating aperture. (*Courtesy Hughes Aircraft Co., Fullerton, Calif.*)
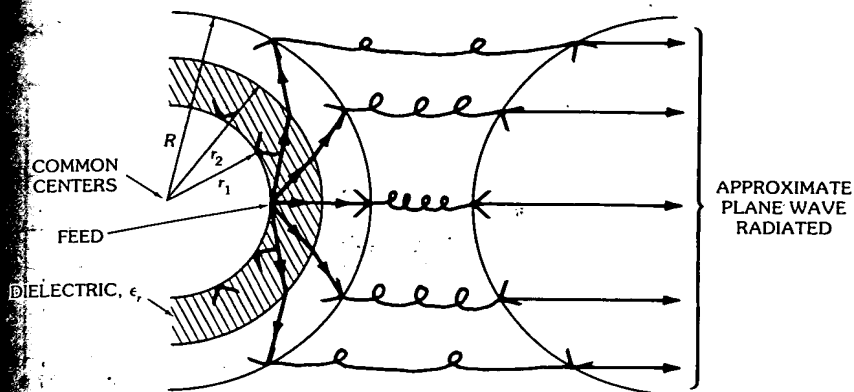
Fig. 74. Dielectric-loaded variation of basic lens. (*Courtesy Hughes Aircraft Co., Fullerton, Calif.*)
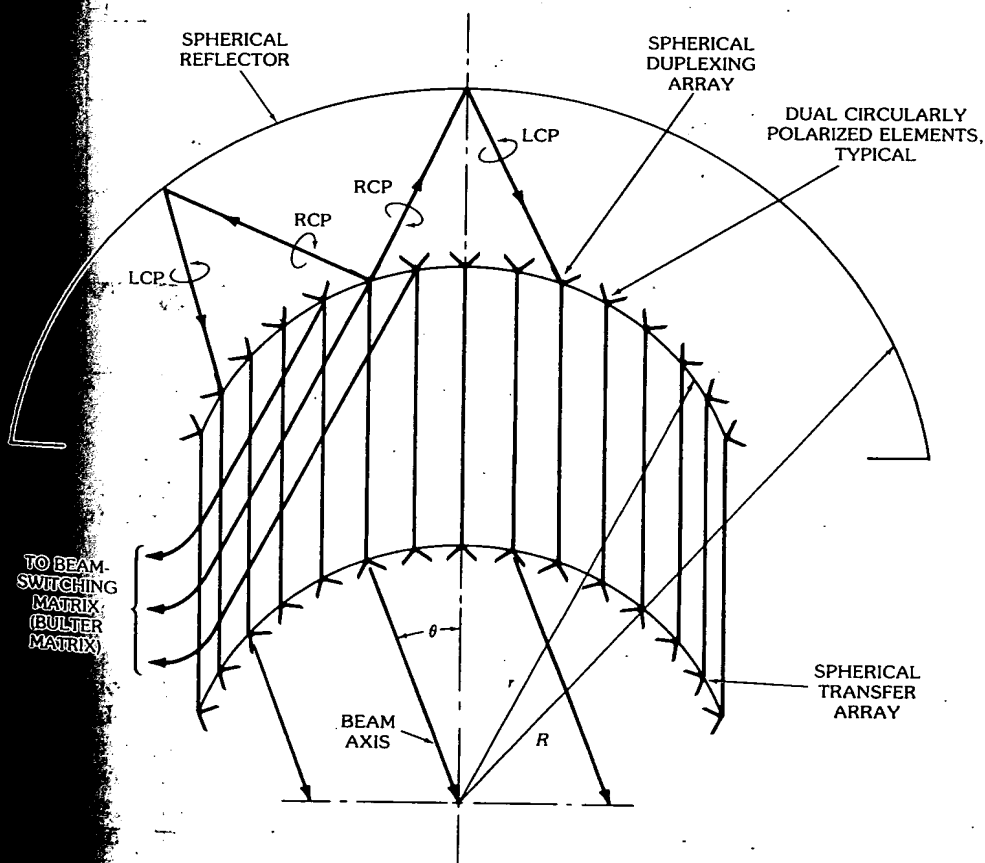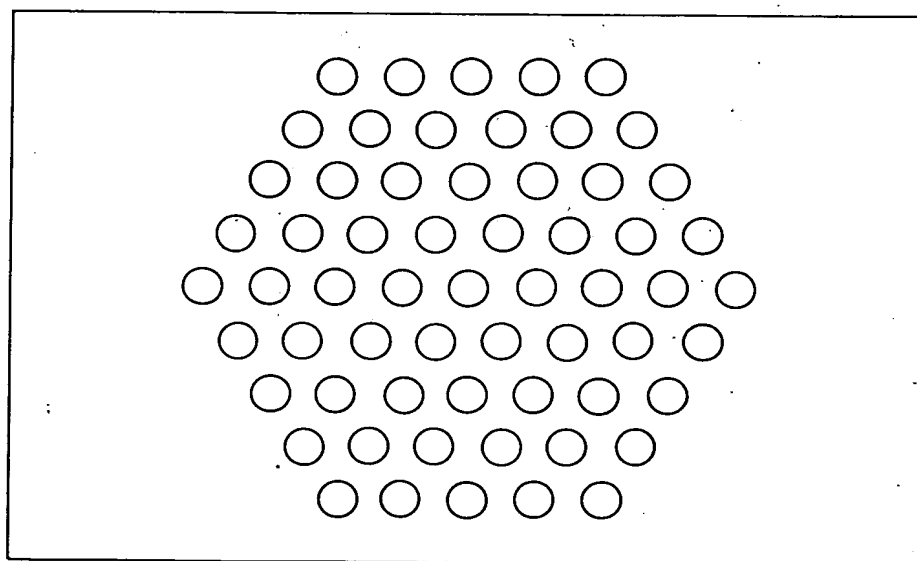

Fig. 75. The HIHAT antenna as a multiple-beam device. (*Courtesy Hughes Aircraft Co., Fullerton, Calif.*)
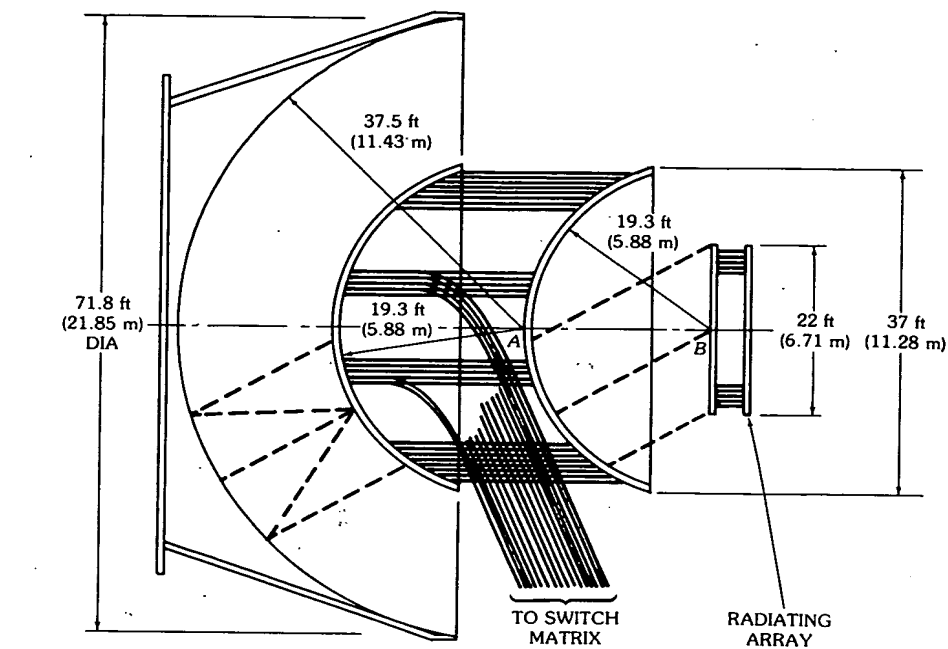
Fig. 76. The HIHAT used to phase a planar array. (*a*) System setup. (*b*) Radiating array. (*Courtesy Hughes Aircraft Co., Fullerton, Calif.*)
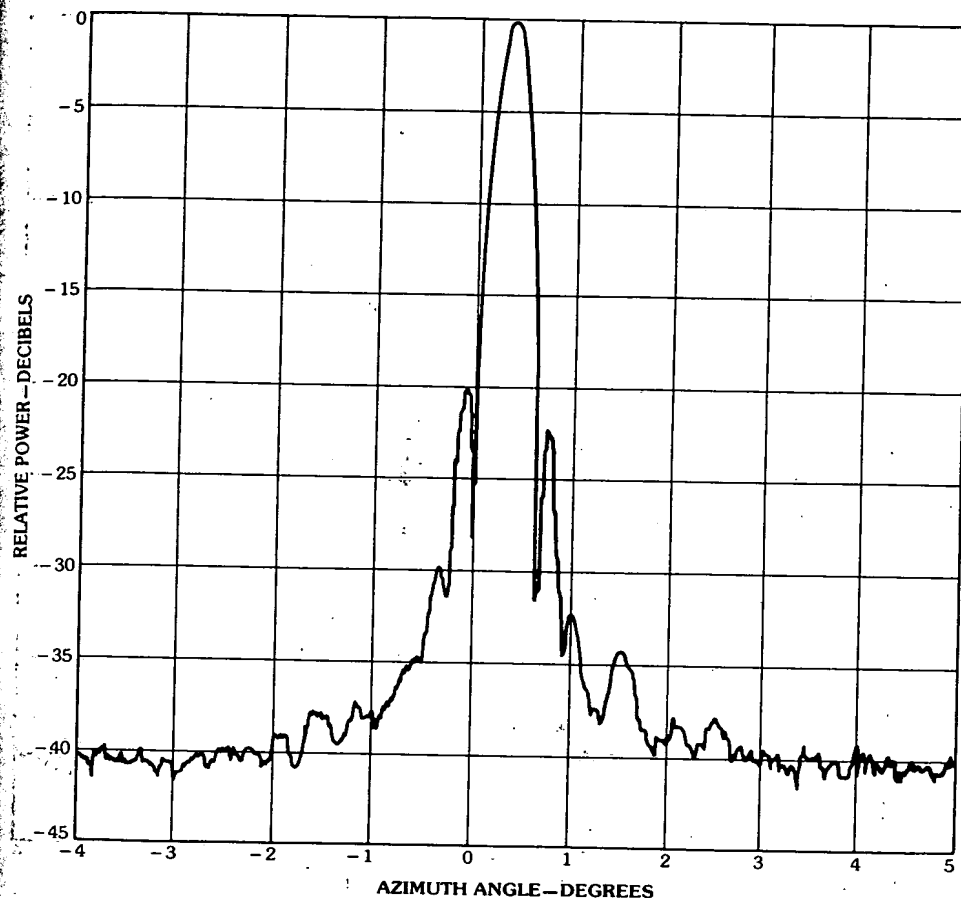
AZIMUTH ANGLE—DEGREES

Fig. 77. Typical measured Σ and Δ patterns using two adjacent feeds (in the plane of scan). (a) Σ pattern. (b) Δ pattern. (*Courtesy Hughes Aircraft Co., Fullerton, Calif.*)

5. Optical Transform Feeds

In certain feed systems the input to the feed and the resulting aperture distribution of the array are related by one or more Fourier transforms. This has been evident in many of the limited-scan techniques that were described in Section 4. These feeds are called *transform feeds* [47, 49, 52]. As stated earlier it is prohibitively expensive to have active elements, such as phase shifters,* power amplifiers, low-noise amplifiers, or adaptive control loops, for every radiating element in a large phased array. But if we back down to having active elements only

---

*For broad instantaneous bandwidths, true-time-delay phase shifters may be required.
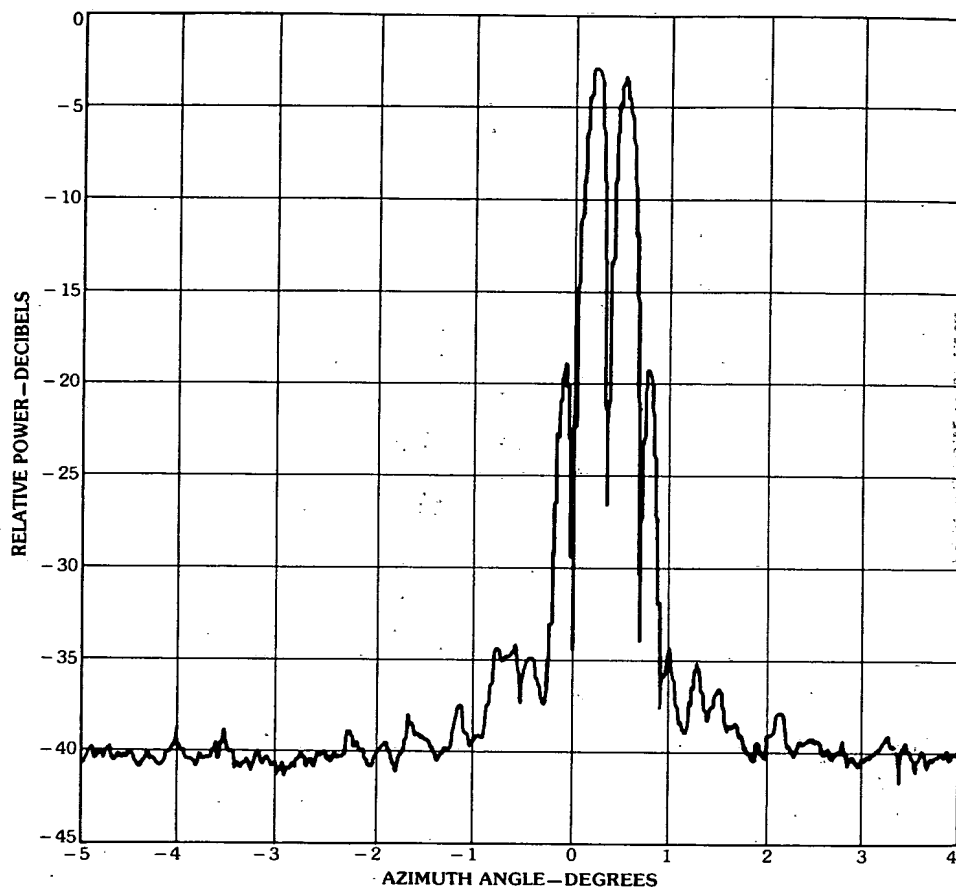
b

Fig. 77, *continued.*

at one feed point of the antenna, we do not have an electronically steerable antenna at all. It is therefore necessary for us to back down to an intermediate level where the number of devices becomes affordable. In doing so, a certain amount of performance must be sacrificed, i.e., the amount of scan coverage is reduced by the ratio of the number of active elements used to the number of active elements required to scan the larger field of view.

Two basic concepts of transform feeds that involve several Fourier transforms are depicted in Figs. 78 and 79. The first concept is a fully constrained feed that uses a small Butler matrix to feed a large Butler matrix whose outputs feed the radiating elements of the antenna. The second concept is an example of optical Fourier transformers in which a large lens is fed by a small lens. The active elements (e.g., phase shifters) are placed in a small phased array that feeds or illuminates the small
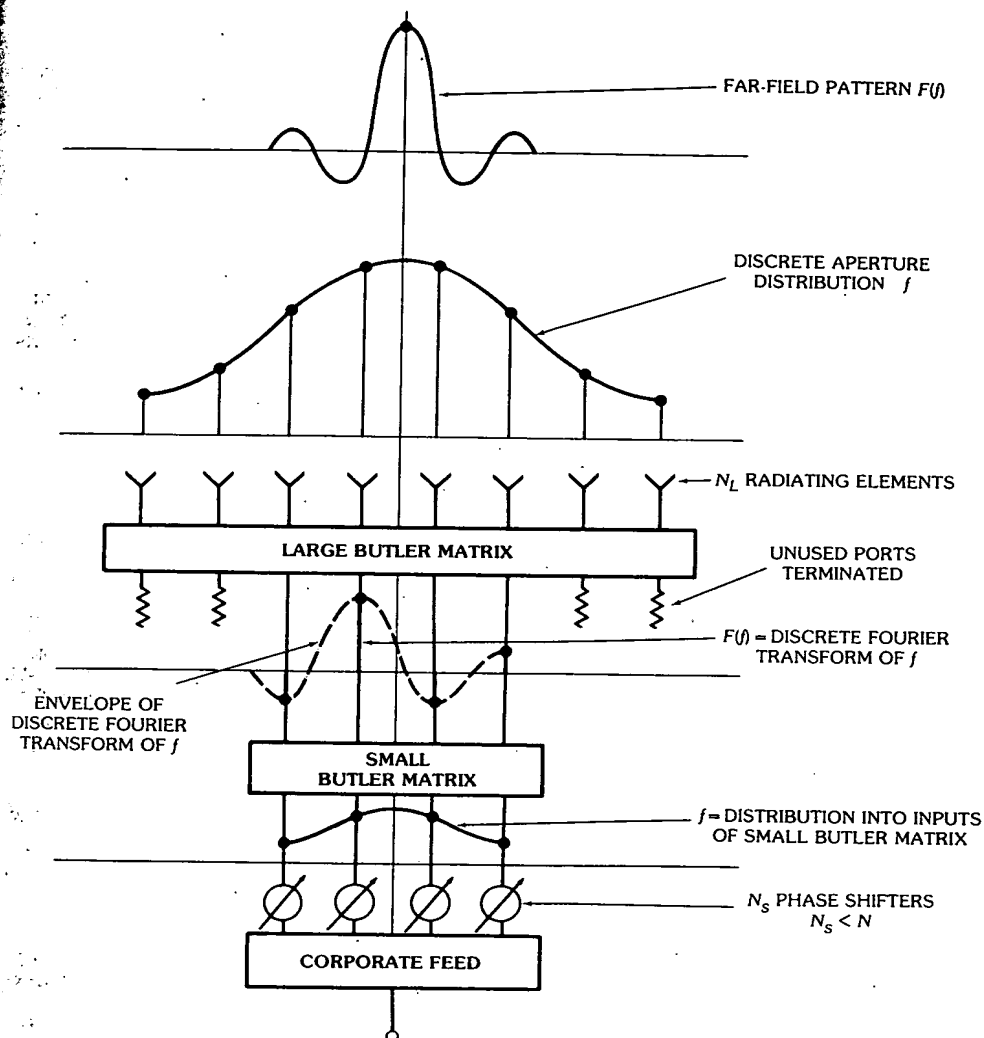
FAR-FIELD PATTERN $F(t)$

DISCRETE APERTURE
DISTRIBUTION f

N_L RADIATING ELEMENTS

LARGE BUTLER MATRIX

UNUSED PORTS
TERMINATED

$F(t)$ = DISCRETE FOURIER
TRANSFORM OF f

ENVELOPE OF
DISCRETE FOURIER
TRANSFORM OF f

SMALL
BUTLER MATRIX

f = DISTRIBUTION INTO INPUTS
OF SMALL BUTLER MATRIX

N_S PHASE SHIFTERS
$N_S < N$

CORPORATE FEED

Fig. 78. Example of constrained transform feed. (*Courtesy Hughes Aircraft Co., Fullerton, Calif.*)

matrix or optical device. Figs. 78 and 79 are conceptual schemes only and may not represent practical antenna systems. For practical transform antennas refer to Section 4 and the quoted literature.

The ideal Butler matrix is a perfect discrete Fourier transformer. A reflector or lens that focuses a plane wavefront to a point is also a Fourier transformer, but not perfect. The Butler matrix will be briefly discussed, while the optical transformers will be discussed in greater length because of their imperfections.
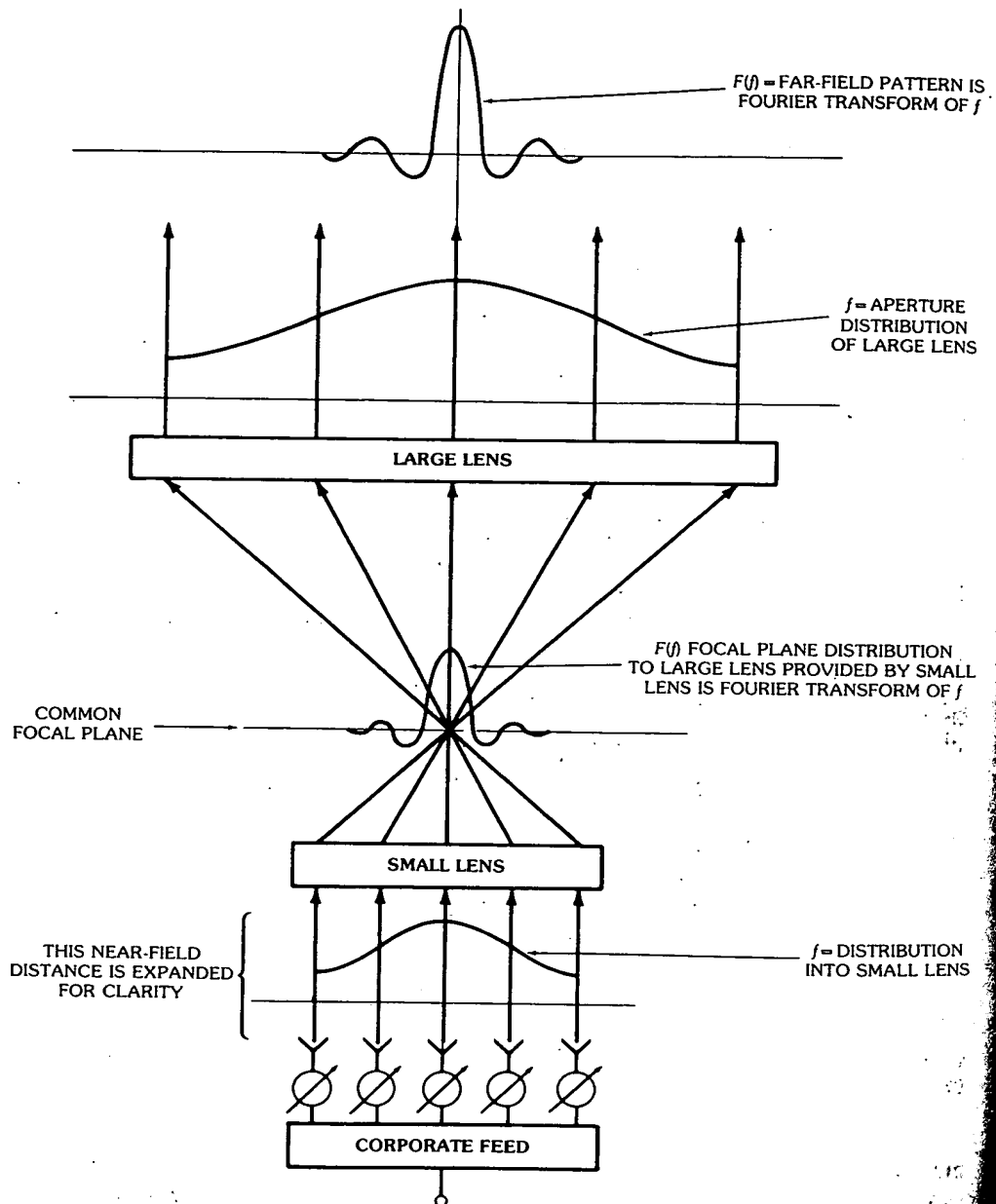
$F(f) =$ FAR-FIELD PATTERN IS
FOURIER TRANSFORM OF f

$f =$ APERTURE
DISTRIBUTION
OF LARGE LENS

LARGE LENS

$F(f)$ FOCAL PLANE DISTRIBUTION
TO LARGE LENS PROVIDED BY SMALL
LENS IS FOURIER TRANSFORM OF f

COMMON
FOCAL PLANE

SMALL LENS

THIS NEAR-FIELD
DISTANCE IS EXPANDED
FOR CLARITY

$f =$ DISTRIBUTION
INTO SMALL LENS

CORPORATE FEED

Fig. 79. Example of optical transform feed. (*Courtesy Hughes Aircraft Co., Fullerton, Calif.*)

Butler Matrix as a Fourier Transformer

The inputs and outputs of an N-element Butler matrix are related by (Section 2)

$$g_{nm} = \frac{\exp j\{(2\pi/N)[n - (N + 1)/2][m - (N + 1)/2]\}}{\sqrt{N}}$$

referenced to the center of the array, $(N + 1)/2$ spaces, where g_{nm} is the field amplitude at the nth output element due to unit excitation at the mth input or beam port. That is, a delta-function input (each port is a discrete delta function) results in a plane wave (linear progressive phase) over all the outputs. By the principle of superposition an arbitrary input distribution $f(m)$ will result in a superposition of discrete plane waves weighted by $f(m)$, resulting in the Fourier transform

$$g(n) = \frac{1}{\sqrt{N}} \sum_{m}^{N} f(m) \exp j\{(2\pi/N)[n - (N + 1)/2][m - (N + 1)/2]\}$$

Fig. 78 illustrates the use of Butler matrices in a transform feed application. The figure is self-explanatory.

Optical Devices as Fourier Transformers

Fig. 79 is an idealized optical analog to the matrix method of Fig. 78. With idealized assumptions to be discussed shortly, Fig. 79 is self-explanatory. Refer to Fig. 80 for the following discussion.

For purposes of discussion consider a wide-angle lens or reflector that will focus over a relatively large region of the focal plane (see Section 4, under "Wide-Angle Multiple-Beam Constrained Lens"). A point-source feed at some point on the focal plane will radiate a spherical wave that will be collimated into a continuous plane wave over the aperture of the lens. Then, just as in the Butler matrix, a point-feed (delta function) input will result in a plane wave output. Again, by the principle of superposition, any focal plane distribution can be generated by a superposition of point feeds over the usable portion of the focal plane.* Again, we have an expansion into plane waves radiating in different directions in space. In general, any device that can focus electromagnetic energy from one point to another is a Fourier transformer. Usually one of the points is infinity.

It should be mentioned that the focal region field is planar on the focal plane [45]. A beam waveguide is an example where both focii are finite. A Gaussian distribution where f and $F(f)$ are identical is used in this application.

Roughly speaking, the primary feed pattern that illuminates a lens or reflector is the Fourier transform of the feed aperture distribution. After collimation this primary feed pattern becomes the aperture distribution of the lens or reflector. Now the Fourier transform of this aperture distribution is the far-field pattern of the lens or reflector. Thus, for real, even feed distributions, the far-field pattern should be identical in shape with the aperture distribution of the primary feed. It is

---

*The term "usable portion" means that off-focal point aberrations are tolerable over that region.

FAR-FIELD
PATTERN OF LENS
(RESEMBLES FEED
APERTURE DISTRIBUTION)

LENS APERTURE
DISTRIBUTION AFTER
MODIFICATION

TRUNCATION
OF ILLUMINATION
FUNCTION

ABBE LENS

PRIMARY FEED PATTERN
ILLUMINATING THE LENS

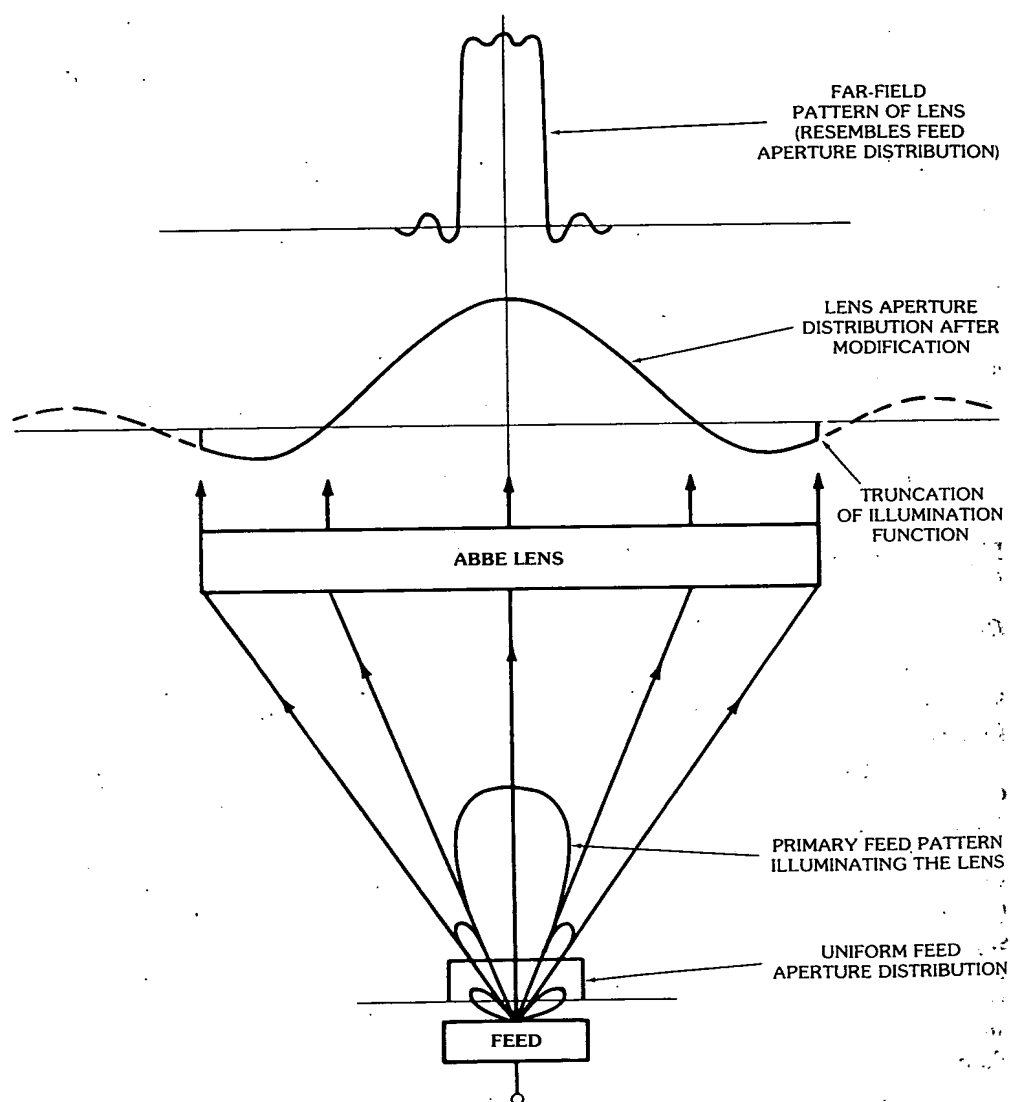UNIFORM FEED
APERTURE DISTRIBUTION

FEED

Fig. 80. Lens configuration used for discussion. (*Courtesy Hughes Aircraft Co., Fullerton, Calif.*)

assumed that the lens or reflector is in the far field of the feed, the feed spillover effects are negligible, and the amplitude modification due to the $1/r^2$ spreading of the rays and the modification of the amplitude due to the lens configuration are also negligible. The latter two assumptions are the most significant. Since all the radiation from the primary feed is not intercepted by the finite lens, the primary illumination function is truncated. The effect of this truncation is discussed later.

The other major effect is the $1/r^2$ effect and the modification of amplitude of the illumination function by the lens design. Depending on the lens configuration the net result may be an additional taper to the incident illumination, or it may add an additional inverse taper. For example, a parabolic reflector or a hyperbolic dielectric lens with one flat face will give an additional tapering effect, while an elliptical dielectric lens with a spherical inner surface results in an inverse tapering effect. Lenses obeying the Abbe sine condition have an inverse tapering effect in power that varies as the secant of the angle between the axis of the lens and a general ray from the focal point. The Abbe sine condition states that the distance of a collimated exit ray from the axis of the lens is proportional to the sine of the angle θ that the corresponding ray from the focal point makes with the lens axis. This results in a modifying factor $k\sqrt{\sec\theta}$ to the illumination function.

To help one get a "feel" for the aforementioned effects a special case of a uniform feed distribution is calculated. This is a relatively stringent test because highly tapered distributions would be less affected by feed pattern truncation due to the low amplitude at the point of truncation. Aside from these effects the uniform feed distribution should give a uniform (sector-shaped) far-field pattern from the lens. Fig. 81 shows a calculated far-field pattern from a lens that satisfies the Abbe
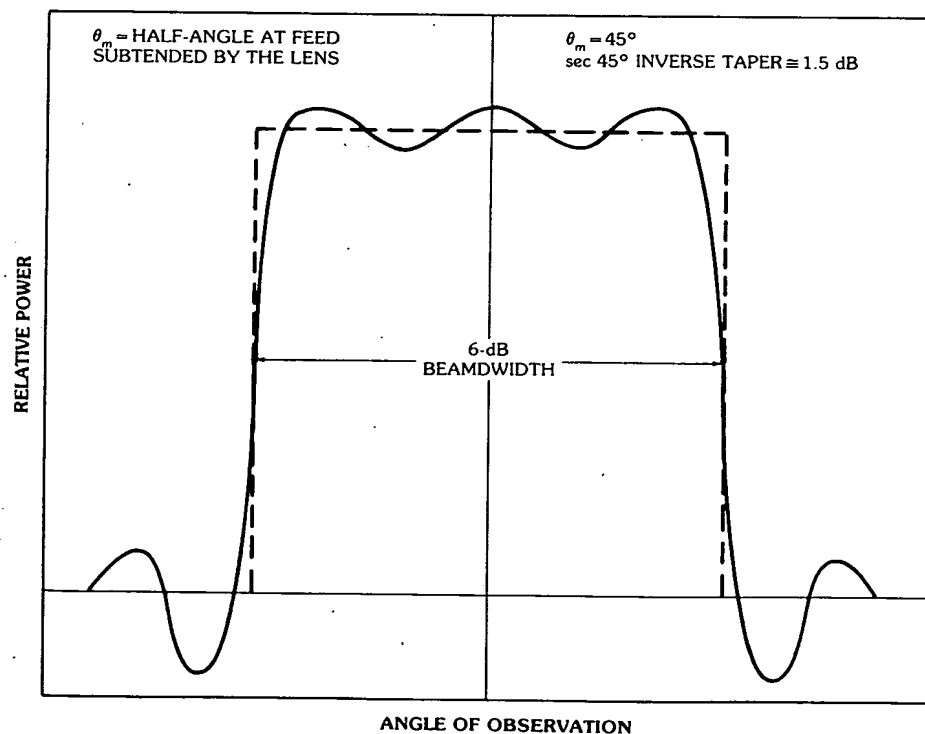
Fig. 81. Far-field pattern of a lens obeying the Abbe sine condition when the primary feed pattern is truncated to the peaks of the first side lobes of the primary pattern. (*Courtesy Hughes Aircraft Co., Fullerton, Calif.*)

sine condition. The lens truncated the $(\sin u)/u$ type primary feed pattern at the peaks of the first side lobes. This is a rather severe truncation. One would expect that at least several side lobes of the illuminating function would have to be included. However, it is seen that, even so, the resulting far-field pattern does resemble a sector-shape pattern with small ripples. In this case the inverse tapering effect of the Abbe lens was 1.5 dB. It has also been shown that the sector shape and width are nearly frequency independent. This is also a consequence of the Fourier transform. At a higher frequency the primary pattern is more directive, which effectively illuminates less of the lens aperture, thereby causing the final far-field pattern to broaden to compensate for the narrowing of the pattern due to the increase in frequency.

A three-dimensional case was both measured and calculated. A circular aperture feed with uniform aperture distribution was used to feed a lens. The far-field pattern of the lens was measured and calculated by the Fourier transform methods. A comparison of the measured and calculated far-field patterns is shown in Fig. 82. It can be seen that the expected sector shape was obtained and the measured and calculated patterns show excellent agreement.

This example, both measured and calculated parts, lends justification to the concept of an optical type antenna as a Fourier transformer.

6. Cylindrical Array Feeds

Numerous techniques have been conceived for the scanning of a cylindrical array [53–56]. The application of such an array may be for air traffic control, radar, and other uses requiring 360° of azimuthal coverage. Electronic scanning may be required in azimuth only, with perhaps some particular beam shape in elevation, or electronic scanning may be required in both planes with or without special elevation (and perhaps azimuth) beam shaping. Each particular system has its own set of requirements.

For the purpose of discussion, consider that the antenna is composed of a cylindrical array of identical line sources parallel to the z axis, as depicted by Fig. 83. The line sources may have phase shifters behind every element, or they may be passively fed with an azimuthal beam-forming network or lens. For good radiation patterns it is apparent that only a portion (180° sector or less) of the total number of line sources should be fed (and phased) for any given azimuthal beam direction. Consequently, some means must be devised to position a given amplitude distribution around the circumference of the array as a function of the desired azimuth direction of the main beam. The main differences between the various concepts are the techniques for generating and positioning this excitation.

Before proceeding further some terms should be defined, and assumptions stated. The term $P(R, \theta, \phi)$ represents the spherical coordinates of the point of observation in the far field (Fig. 83b). The term $P'(a, \phi'_n, z'_p)$ represents the cylindrical coordinates on a cylinder of radius a of a typical radiating element. The terms n and p are integers associated with (ϕ'_n, z'_p), using the notation of [53], except for the angle θ. It is assumed that the element is impedance matched for wide-angle scanning and the interelement spacing in both directions is close enough
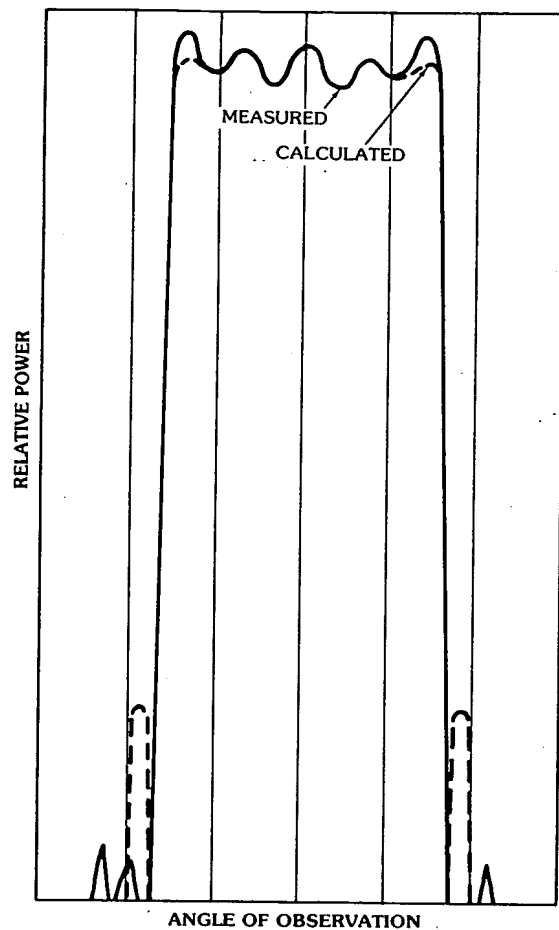
Fig. 82. Measured and calculated far-field patterns from a lens with a circular aperture feed with a uniform distribution. (*Courtesy Hughes Aircraft Co., Fullerton, Calif.*)

(near $\lambda/2$) to produce an ideal element factor $\sqrt{\cos\gamma}$, where γ is the angle between the normal to the array and the point of observation.
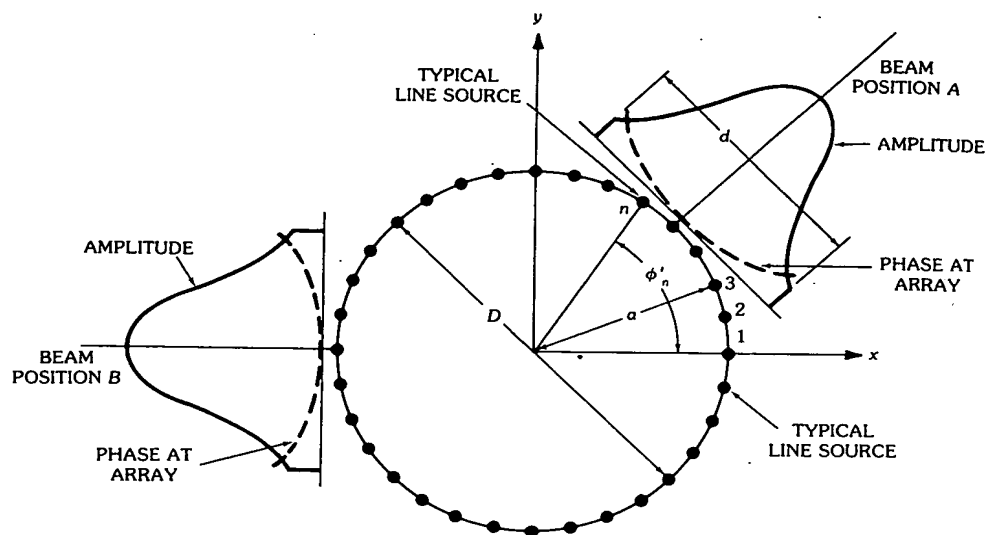
The far-field pattern is related to the surface illumination by

$$E(\theta,\phi) = \iint \varepsilon(\phi',z') \frac{e^{-jkR}}{R} \sqrt{\cos\gamma}\, d\phi'\, dz' \tag{23}$$

Let the complex array illumination function be

$$\varepsilon(\phi_n, z_p') = \ell(\phi_n')f(z_p') \tag{24}$$

Then the far field for the array is given [54] by

a
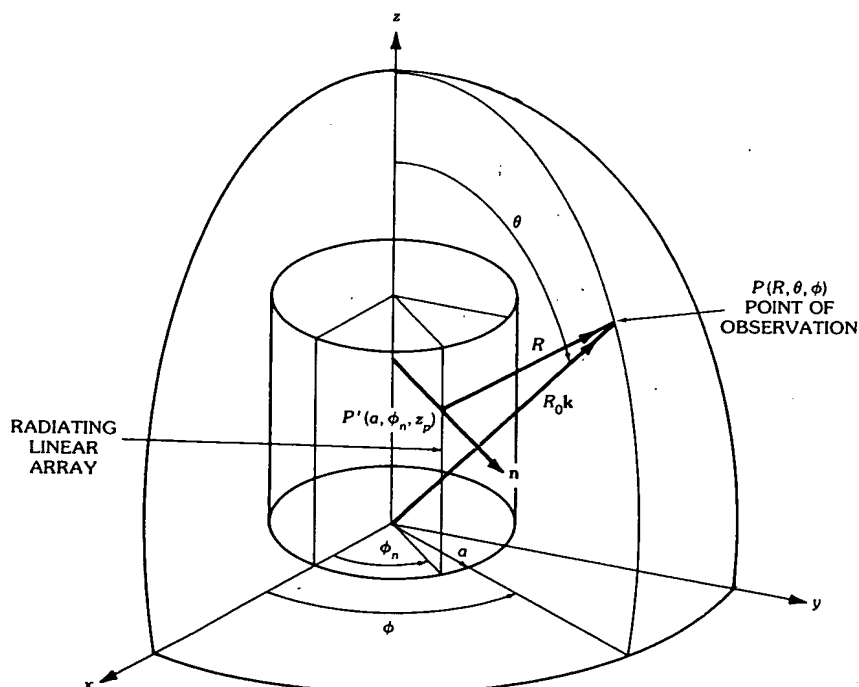
b

Fig. 83. Antenna as a cylindrical array of line sources. (*a*) Cylindrical array plan view. (*b*) Cylindrical array oblique view. (*Courtesy Hughes Aircraft Co., Fullerton, Calif.*)

$$E(\theta) = \sqrt{\cos\theta} \sum_p f(z_p') e^{jkz_p'\cos\theta} \sum_n \ell(\phi_n') \sqrt{\cos(\phi - \phi_n')} e^{jka\sin\theta\sqrt{\cos(\phi - \phi_n')}} \quad (25)$$

or :

$$E(\theta, \phi) = L(\theta) R(\theta, \phi) \quad (26)$$

where

$$L(\theta) = \sqrt{\cos\theta} \sum_p f(z_p') e^{jkz_p'\cos\theta} \quad (27)$$

and

$$R(\theta, \phi) = \sum_n \ell(\phi_n') \sqrt{\cos(\phi - \phi_n')} e^{jka\sin\theta\cos(\phi - \phi_n')} \quad (28)$$

Thus the required array excitation to generate a main beam at (θ_m, ϕ_m) is given by

$$|f(z_p')||\ell(\phi_n')| e^{-jk[z_p'\cos\theta_m + a\sin\theta_m\cos(\phi_m - \phi_n')]} \quad (29)$$

Various techniques for generating this cylindrical array excitation will be discussed briefly. For purposes of clarity some of the diagrams to follow show the use of only eight-array elements.

Matrix-Fed Cylindrical Arrays

The various matrix-fed arrays can be readily understood by use of the following tutorial model.

Consider two back-to-back Butler matrices with controllable phase shifters in between them as shown in Fig. 84a. If an input port a_n of Butler matrix A is excited with any amplitude and phase, a corresponding port b_n of Butler matrix B will be excited with equal amplitude and phase when the phase shifters are all set equal. If the a_ns are weighted in amplitude and phase to any desired distribution, a corresponding distribution is achieved at the outputs b_n. Now if a linear phase distribution with a total phase of $m2\pi$ (m an integer) is applied across the array of phase shifters, the entire distribution over b_n will translate across the output in increments of one element spacing for each successive value of m. The translation of the output distribution by an increment less than one element spacing requires a total phase that is a nonintegral multiple K of 2π. That is, $|m| < |K| < |m| + 1$. In these cases there is no longer a one-to-one correspondence between an input port excitation and an output port excitation. Instead, if one input port is excited, not one but all output ports are excited to some extent. However, as would be expected the two adjacent ports corresponding to phases of $m2\pi$ and $(m + 1)2\pi$ are excited most strongly since they straddle the "phantom" element corresponding to the phase of $K2\pi$. In fact, the output distribution is a discrete sampling of a sharp $(\sin x)/x$ distribution as shown in Fig. 84b. The width of the "main lobe" of the
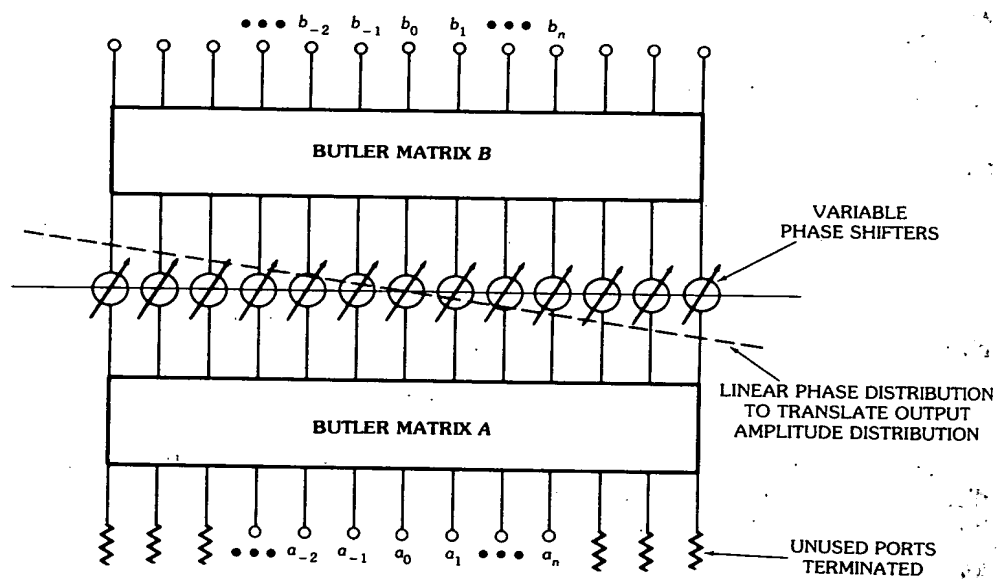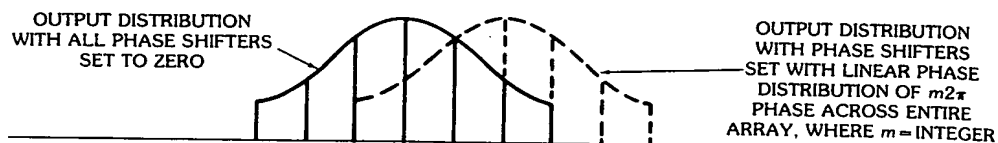
a
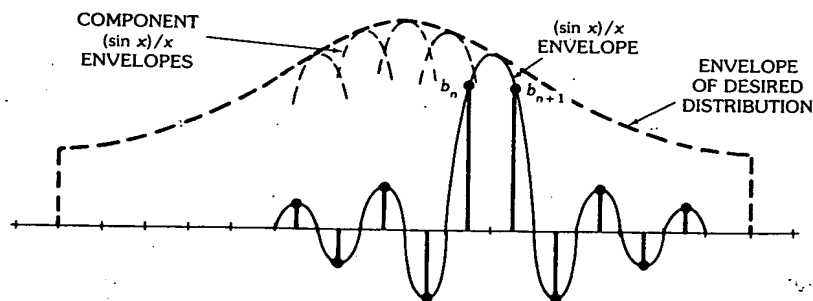
b

Fig. 84. Back-to-back Butler matrix feeding technique. (*a*) Tutorial model of matrix feeding. (*b*) Output excitation when only one input is excited and linear phase across bank of phase shifters is not an integral multiple of 2π. (*Courtesy Hughes Aircraft Co., Fullerton, Calif.*)

envelope $(\sin x)/x$ is two elements and the side lobe width is one element. The output distribution corresponding to phases of integral multiples of 2π consists of discrete values identical with those at the input to the first Butler matrix A because of the one-to-one correspondence between a_ns and b_ns. This is consistent with the sampled $(\sin x)/x$ output in these special cases; the sampling points are all at the nulls of the $(\sin x)/x$ function except at the peak of the main lobe, hence only that element is excited. For intermediate cases corresponding to nonintegral multiples of 2π, the output distribution is a superposition of sampled $(\sin x)/x$ functions of the kind just described. The net result is that the envelope of this output distribution is almost identical with that of the envelope of the designed output distribution, which is identical with the input distribution of matrix A.

Now, if the output ports b_n are connected by equal line lengths to a similar number of elements arranged uniformly along a circle of radius R, linear phase shifter adjustments will cause the distribution over the b_ns to move along the periphery of the circular array. If the phase distribution is such as to radiate a plane wavefront from the circular array, a directive beam is formed from the circular array that can be steered by means of changing the linear progressive phase of the phase shifters. It is obvious that this peripherally scanned distribution should not extend more than a semicircle because elements to the rear should not be excited. The input ports corresponding to these rearward-looking elements are shown terminated in Fig. 84a. In practice, less than 180° of the circular (or cylindrical) array is excited for one beam direction because of active element patterns, local grating lobe formation, and aperture matching problems associated with the edge elements that are locally phased for near end-fire. Also, for intermediate phasing, the elements near the edge of the active portion of the cylinder may have their corresponding sampled $(\sin x)/x$ lobes to the rear that are greater than desired for low side lobe and rear lobe patterns.

Collimation of the beam from the circular array requires a phase distribution of $\phi_n = kR(1 - \cos n\Delta\theta)$, where $\Delta\theta$ is the angle subtended by one-element spacing, R is the radius of the cylinder, and $k = 2\pi/\lambda$. This phase is easily incorporated in the weighting of the a_ns.

It is interesting to note that the amount of beam scan in terms of antenna beamwidths for each 2π of total phase change is equal to one beamwidth if the element spacing Δs is $\lambda/2$:

$$\Delta s = R\,\Delta\theta = \frac{\lambda}{2}, \qquad \Delta\theta = \frac{\lambda}{2R}$$

This is also the beamwidth for a uniform array of aperture $2R$.

The foregoing serves as a tutorial basis for describing some of the feeding techniques for cylindrical arrays to be discussed.

Sheleg Method—In the preceding discussion it is readily seen that the output of the first Butler matrix A (input to the bank of phase shifters) has an amplitude and phase distribution that is fixed (independent of beam steering); therefore it can be replaced by a passive feed network that produces that same distribution. This reduces to the Sheleg approach. A simplified schematic diagram of the approach

for an eight-element array is shown in Fig. 85. Sheleg arrived at this solution from a different point of view. He expressed the far-field pattern in cylindrical modes in the form

$$E(\phi) = \sum_{-N}^{N} C_m e^{jm\phi}$$

where the number of elements is $2N$, and

$$C_m = 2\pi K j^m I_m J_m(ka)$$
$$K = \text{constant}$$

Sheleg made the observation that it is not necessary or even desirable to use all the m modes of the Butler matrix. This concurs with the foregoing tutorial discussion in that modes that excite elements to the rearward direction of the cylinder should not be used. As stated earlier, in practice less than half the number of available modes should be used to avoid local end-fire radiation at the extremes of the active semicircle. The Sheleg scheme is depicted for an eight-element array in Fig. 85.

This technique can be used to produce uniform or tapered illuminations for the cylindrical array. Sheleg gives computed and measured results for uniform, cosine, and cosine-squared array distributions with quite close correlation between

FEED POINTS TO ELEVATION ARRAY = N (REQUIRED)
VARIABLE PHASE SHIFTERS = N (EXPENSIVE)
FIXED PHASE SHIFTERS = N (INEXPENSIVE)
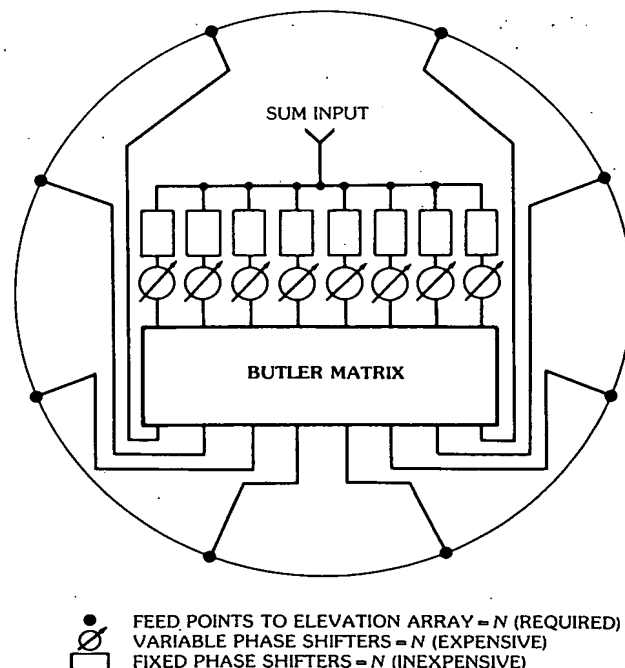
Fig. 85. Sheleg's approach. (*Courtesy Hughes Aircraft Co., Fullerton, Calif.*)

measurement and theory except in the remote side lobe region. He shows the patterns as a function of the number of modes used. Up to a point the patterns improve as more modes are used; then, beyond this point, the radiation pattern degrades somewhat. This has been explained by use of the tutorial model previously discussed.

For uniform distribution the azimuth pattern shape as a function of azimuth scanning of the main beam is shown to be reasonably invariant, i.e., it makes little difference whether the peak of the array distribution falls on an element, midway between two elements, or any fractional part thereof. This is also explained by use of the tutorial model. For more details the reader is referred to Sheleg's paper [56].

Wheeler Lab Approach—Fig. 86 depicts the Wheeler Lab approach [53,54] to feeding a cylindrical array. It consists of a power divider followed by fixed phase shifts, variable phase shifters, a sequencing switch, an array of diode switches, and the radiating array.

This technique utilizes a *switching network* to step the amplitude distribution around the cylindrical array in coarse steps equal to the interelement angular spacing. The phase and amplitude distribution are established by the power divider and a set of fixed and variable phase shifters. *The variable phase shifters provide fine steering.*


●   FEED POINTS TO ELEVATION ARRAY = N (REQUIRED)
∅   VARIABLE PHASE SHIFTERS ≅ N/2 (EXPENSIVE, ACTIVE)
○   DIODE SWITCH ≅ N/2 (EXPENSIVE, ACTIVE)
□   FIXED PHASE SHIFTER ≅ N/2 (INEXPENSIVE, PASSIVE)
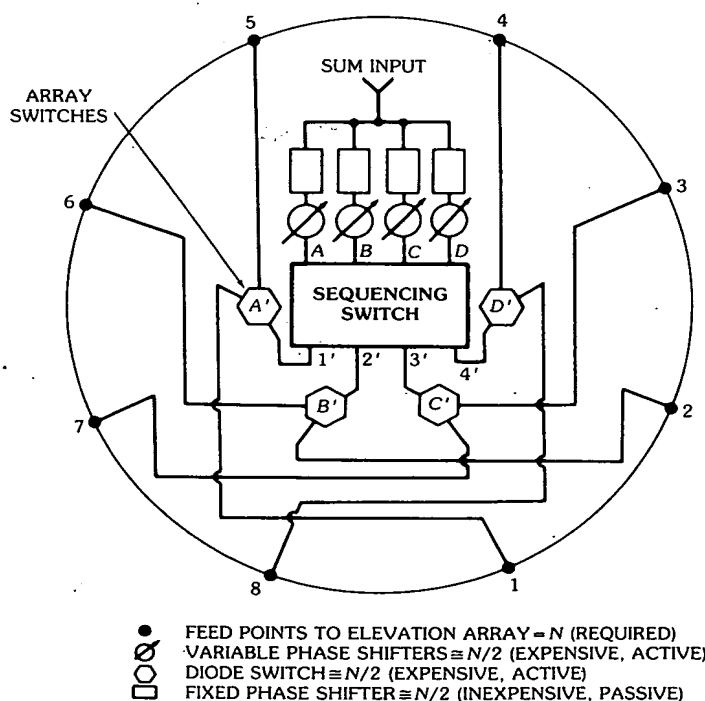
Fig. 86. Wheeler Lab approach. (*Courtesy Hughes Aircraft Co., Fullerton, Calif.*)

In this technique the ratio of the total number of azimuth elements to the number of active elements used at any beam position must be an integer.

In Fig. 86 the number of elements used at a given time is four since the corporate feed is shown as having four outputs. The desired output amplitude and phase distribution is designated A, B, C, D. For a given state of the sequencing switch, for example, elements $1, 2, 3, 4$ are excited with the complex amplitude A, B, C, D, respectively. Now suppose it is desired to move the distribution by one element, say, elements $2, 3, 4, 5$. With no sequencing switch the output amplitude distribution would be B, C, D, A, which is not the desired distribution. The sequencing switch reswitches the distribution back to A, B, C, D, the desired output. The same technique will allow the desired distribution, A, B, C, D, to be positioned all the way around the array in steps of one element at a time.

For the example shown, the sequencing switch would consist of four dpdt pin diode switches, as depicted by Fig. 87a. The complex inputs to the sequencing switch are labeled A, B, C, D. The outputs of the sequencing switch are labeled $1', 2', 3', 4'$. Each of the four pin diode switches has two possible states, labeled a or

a
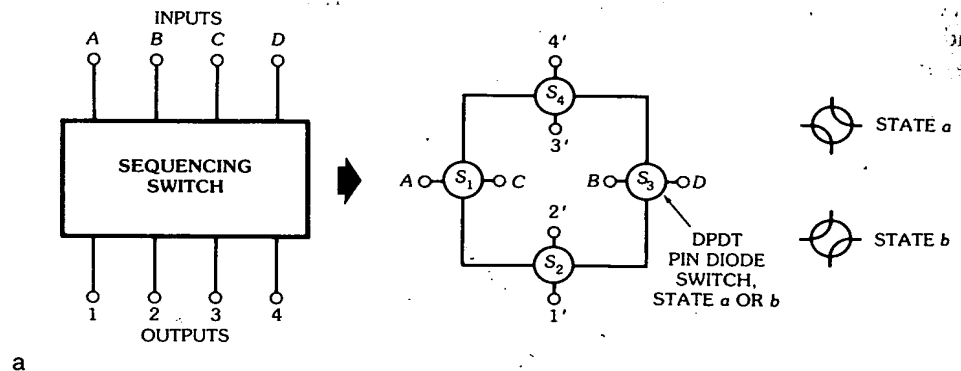
Arrangement	Sequencing Switch Outputs				Pin Diode Switching States			
	(Normal)							
	1'	2'	3'	4'	S_1	S_2	S_3	S_4
1	A	B	C	D	a	a	a	a
2	B	C	D	A	b	b	a	b
3	C	D	A	B	b	a	b	a
4	D	A	B	C	a	b	b	b
(Inverted)								
5	D	C	B	A	b	b	b	b
6	A	D	C	B	a	a	b	a
7	B	A	D	C	a	b	a	b
8	C	B	A	D	b	a	a	a

b

Fig. 87. Sequencing switch circuit and logic. (a) Sequencing switch circuit. (*Courtesy Hughes Aircraft Co., Fullerton, Calif.*) (b) Logic of switch circuit.

b. The table of Fig. 87b shows four normal combinations and four inverted combinations of complex distributions emerging from the output of the sequencing switch, along with their corresponding switching states for the four dpdt switches labeled S_1, S_2, S_3, S_4. By using the inverted as well as the normal arrangements, beam positions mirror-imaged about the center line of the active cylindrical array normal are generated; consequently the number of phase states required by the phase shifters is halved. The switches labeled array switches in Fig. 86 have a single input with one of two possible outputs, depending on which radiating elements are to be excited.

For fine beam steering, for beam positions corresponding to that between elements for example, the variable phase shifters are used while the elements excited remain fixed at the same position as for a beam position corresponding to an angle through an element.

The power divider as depicted in Fig. 86 shows only a sum input. In actuality, both a sum and a difference port would typically be available by appropriate design of the power divider network.

Hughes Phased-Lens–Fed Approach—This technique utilizes a rotationally symmetric lens such as a Luneburg or Rinehart lens to perform the azimuth beam forming, a switching system to select lens feed points for coarse steering, and phase shifters at each lens output to the cylindrical array to do the fine steering. Fig. 88 schematically depicts this approach.

The sum (and difference, not shown) input is power-divided by the number of lens probes to be fed simultaneously, forming the lens primary feed illumination, two for the example of Fig. 88. Suppose lens probes 1 and 2 are chosen to form a beam diametrically opposite to the position lying between probes 1 and 2. Then switch *A* would select probe position 1 while switch *B* would select position 2. All the probes dispersed over the arc labeled 4, 5, 6, 7 would then pick up the focused field and switches labeled *D, C, J, I* would switch the fields to the elements labeled 4, 5, 6, 7 via phase shifters behind each element. The coarse beam position is determined by choosing which probes to excite. The fine beam steering is accomplished by the phase shifters behind each element.

The number of actively excited probes for a given beam position must divide integrally into the total number of elements; that is, the ratio of the total number of azimuth elements to the number of simultaneously excited lens probes must be an integer.

For example, if three probes needed to be excited simultaneously to achieve the desired primary lens feed distribution, then the total number of elements must be a multiple of three. If nine elements were chosen to satisfy this requirement, then the sum (and difference) input would have to be divided into three outputs followed by three switches each with three positions, rather than four as depicted in Fig. 88.

The lens probes are seen to have to perform the dual function of not only acting as primary feed elements but as transfer elements as well.

Matrix-Fed Conventional Lens Approach—For coarse beam stepping this technique is identical with the phased lens–fed approach described previously. For
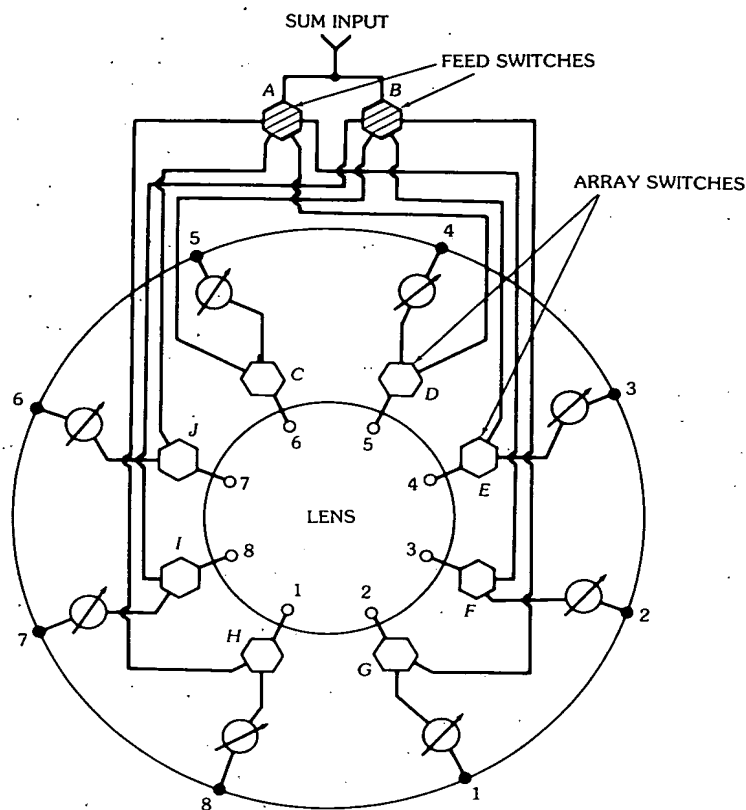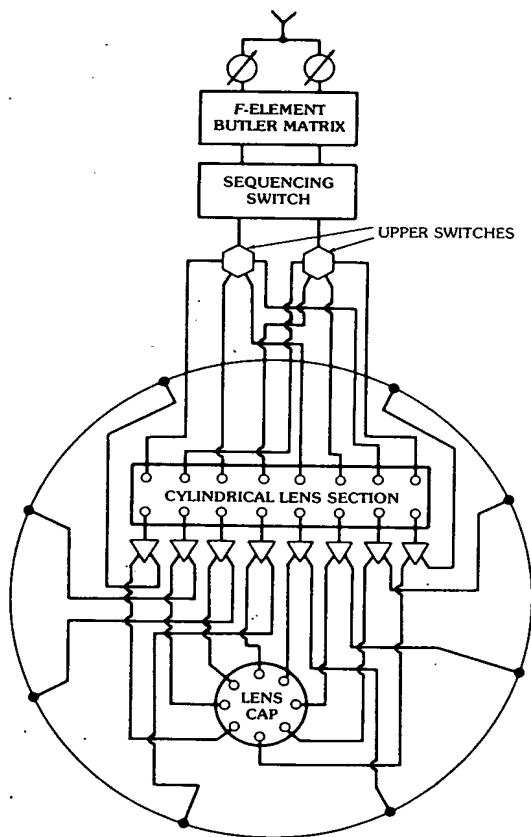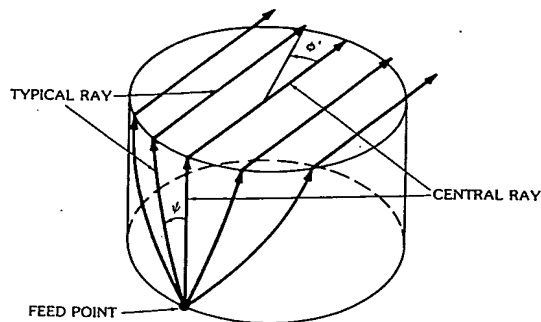
FEED POINT TO ELEVATION ARRAY = N (REQUIRED)
VARIABLE PHASE SHIFTERS = N (ACTIVE, EXPENSIVE)
DIODE SWITCH = N (2:1) (ACTIVE, EXPENSIVE)
DIODE NETWORK = F (A:1) (ACTIVE, EXPENSIVE)
LENS FEED PROBE = N (INEXPENSIVE, PASSIVE)
N = TOTAL NUMBER OF RADIATING ELEMENTS
F = NUMBER OF LENS ELEMENTS USED TO FORM FEED PATTERNS OF LENS
A = NUMBER OF ACTIVE RADIATING ELEMENTS A < N/2

Fig. 88. Phased-lens–fed approach. (*Courtesy Hughes Aircraft Co., Fullerton, Calif.*).

fine steering a "Sheleg" technique is used on a relatively small feed array using an
F-element Butler matrix and F variable phase shifters, where F is the small number
of lens elements used to form the desired feed pattern. The feed distribution is
translated as described before in Fig. 84a, which translates the phase center of the
feed for fine steering.

Hughes Matrix-Fed Meyer Geodesic Lens—This technique [54, 57] is a variation of
the matrix-fed conventional lens approach discussed in the previous section but
utilizes a modified Meyer geodesic lens (figure of revolution) for the beam forming
to eliminate active switches and uses passive diplexers or circulators instead. The

Fig. 89. Meyer geodesic lens. (*a*) Basic Meyer lens. (*b*) Matrix feed. (*Courtesy Hughes Aircraft Co., Fullerton, Calif.*)

basic Meyer lens for 360° coverage showing typical ray paths from a feed point is given pictorially in Fig. 89a.

The matrix feed is depicted in Fig. 89b. The sum-and-difference corporate power divider, input phase shifters to the Butler matrix, the amplitude sequencing switch, and feed switches are identical to those of the conventional lens above. The remainder of this approach includes passive diplexers, a cylindrical portion of the Meyer lens, a lens cap, and the radiating elements. A somewhat more physical depiction of this approach is illustrated in Fig. 90.

The cylindrical portion of the lens may be as shown in Fig. 90 or it may be folded, since folding does not change the geodesic paths. The rf paths on transmit and receive are depicted in Fig. 91, showing the folding of the cylindrical portion of the lens. A schematic of the diplexer/circulator is given in Fig. 92. A functional diagram showing transmit and receive signal flow in the diplexer/circulator is shown in Fig. 93.

The Meyer lens, as usually used (discussed in Section 3) phases a line source; however, by completing the cylindrical portion to 360°, it can be used to phase a cylindrical array. It is then possible to feed the lens at any point on the 360° feed circle, and the output of the lens may be taken along the circumference of the circular cap. Furthermore, if the lens cap is dielectrically loaded, it can be smaller
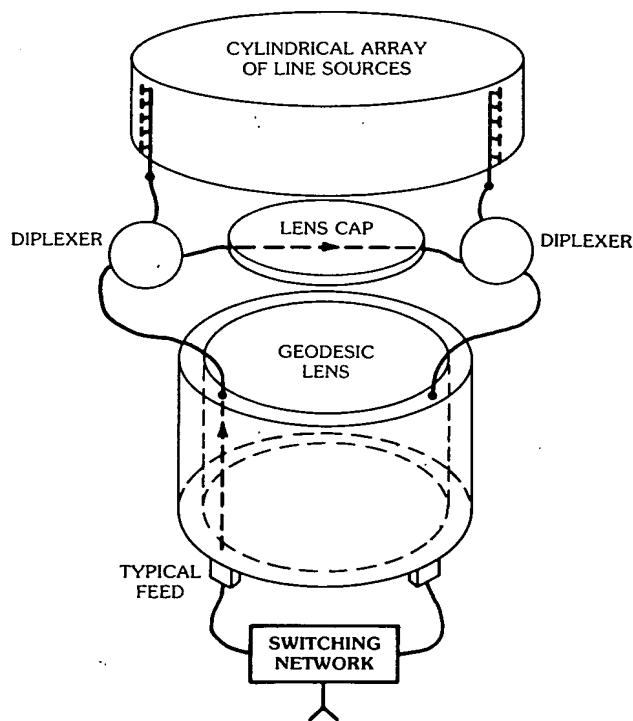

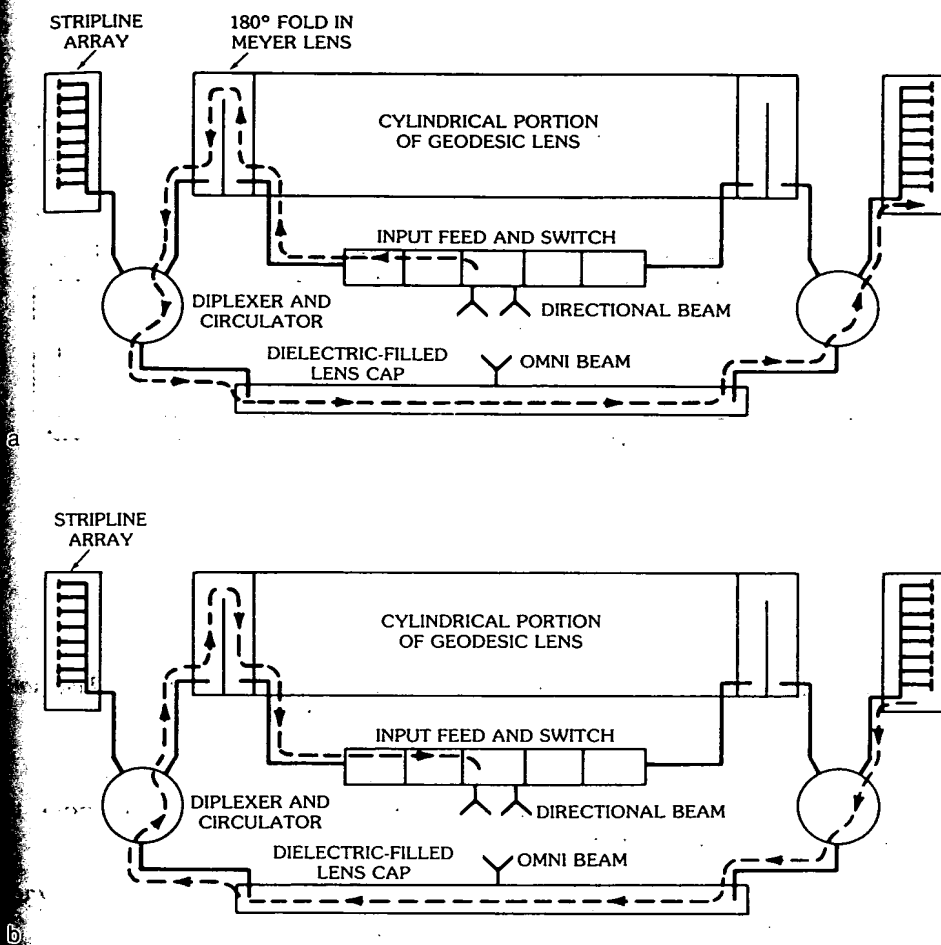**Fig. 90.** Meyer system configuration. (*Courtesy Hughes Aircraft Co., Fullerton, Calif.*)

Fig. 91. Functional block diagram showing rf paths of Meyer lens. (*a*) Directional-beam signal flow. (*b*) Receive signal flow. (*Courtesy Hughes Aircraft Co., Fullerton, Calif.*)

by the square root of the relative dielectric constant. This allows for easier packaging of the associated components.

A brief analysis of the dielectrically loaded lens is given and experimental results are presented. Since the cylinder is a singly curved surface, the cylinder and flat circular portion can be developed, or broken apart and flattened for the sake of easy analysis. Refer to Fig. 94. The geodesics all become straight lines in the developed case. As in Fig. 94 equal lengths of transmission line are used for the rf connection between the developed cylinder and the cap, where the arc length s is preserved, or is linearly mapped onto the lens cap through some proportionality constant α. The choice of α determines the physical size of the lens cap and the necessary dielectric loading ϵ_2 to correctly phase the radiating elements. The same is true between the cap and the radiating elements, but the mapping here preserves
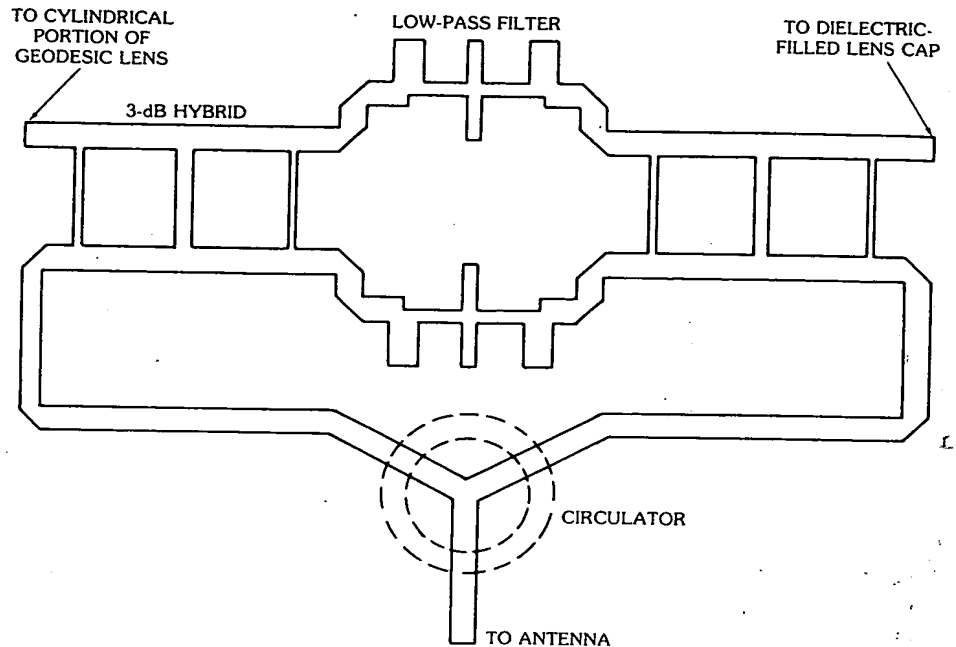
Fig. 92. Schematic of diplexer/circulator circuit. (*Courtesy Hughes Aircraft Co., Fullerton, Calif.*)

the angle designated ϕ'. The electrical path length $L(\phi')$ from the feed point to the plane wavefront in space is given by geometrical optics:

$$L(\phi') = \ell_1\sqrt{\epsilon_1} + \ell_2\sqrt{\epsilon_2} + \ell_3 \tag{30}$$

The reference path length through the center is ℓ_0, given by

$$\ell_0 = h\sqrt{\epsilon_1} + 2b\sqrt{\epsilon_2} \tag{31}$$

Thus the electrical path length error δ is given by

$$\delta = L(\phi') - \ell_0 \tag{32}$$

The output phase error $\Phi(\phi')$ is then

$$\Phi(\phi') = k\delta(\phi') \tag{33}$$

Snell's law is obeyed because of equal line lengths; thus

$$\frac{\sin \gamma}{\sin \psi} = \frac{n_1}{an_2} \tag{34}$$
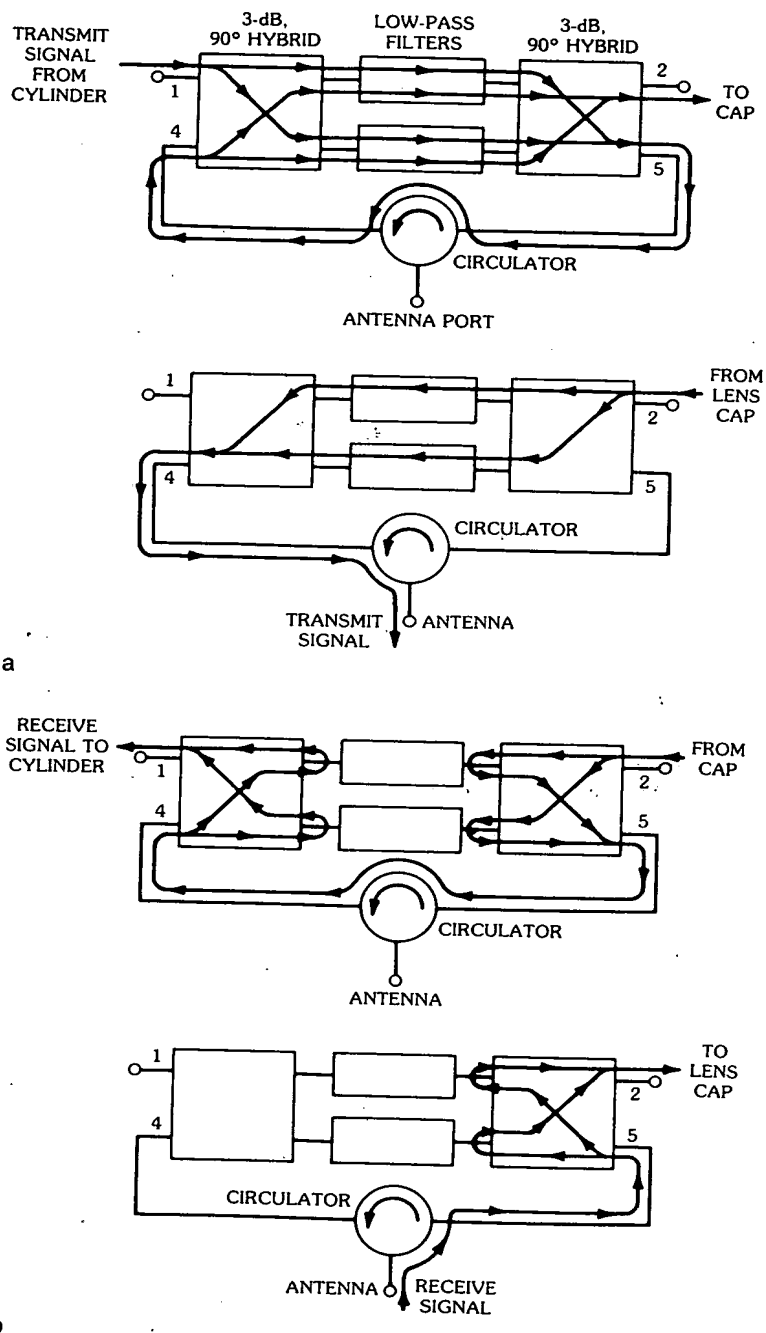
Fig. 93. Functional diagram of diplexer/circulator, showing signal flow. (*a*) Transmit signal paths. (*b*) Receive signal paths. (*Courtesy Hughes Aircraft Co., Fullerton, Calif.*)
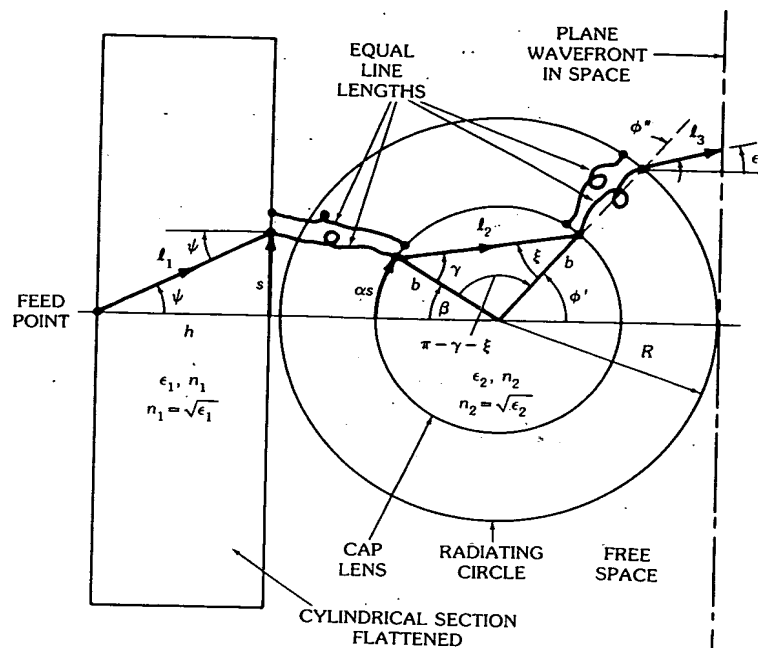
Fig. 94. Developed full cylindrical lens. (*Courtesy Hughes Aircraft Co., Fullerton, Calif.*)

The following relations can be seen from Fig. 94:

$$\ell_1 = h \sec \psi \tag{35}$$

$$s = h \tan \psi \tag{36}$$

$$\alpha s = b\beta \tag{37}$$

Thus

$$\beta = \frac{\alpha}{b} h \tan \psi \tag{38}$$

From the law of sines,

$$\frac{b}{\sin \gamma} = \frac{b}{\sin \xi} = \frac{\ell_2}{\sin(\gamma + \xi)} \tag{39}$$

Thus
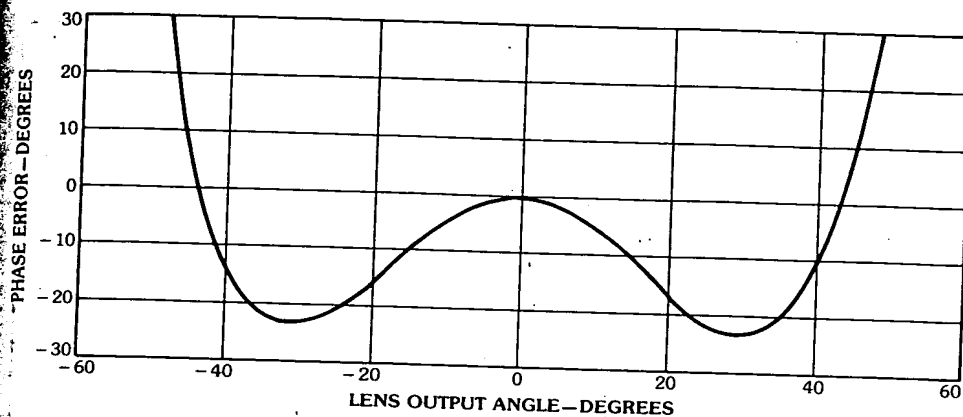
Fig. 95. Phase error at output of geodesic lens. (*Courtesy Hughes Aircraft Co., Fullerton, Calif.*)
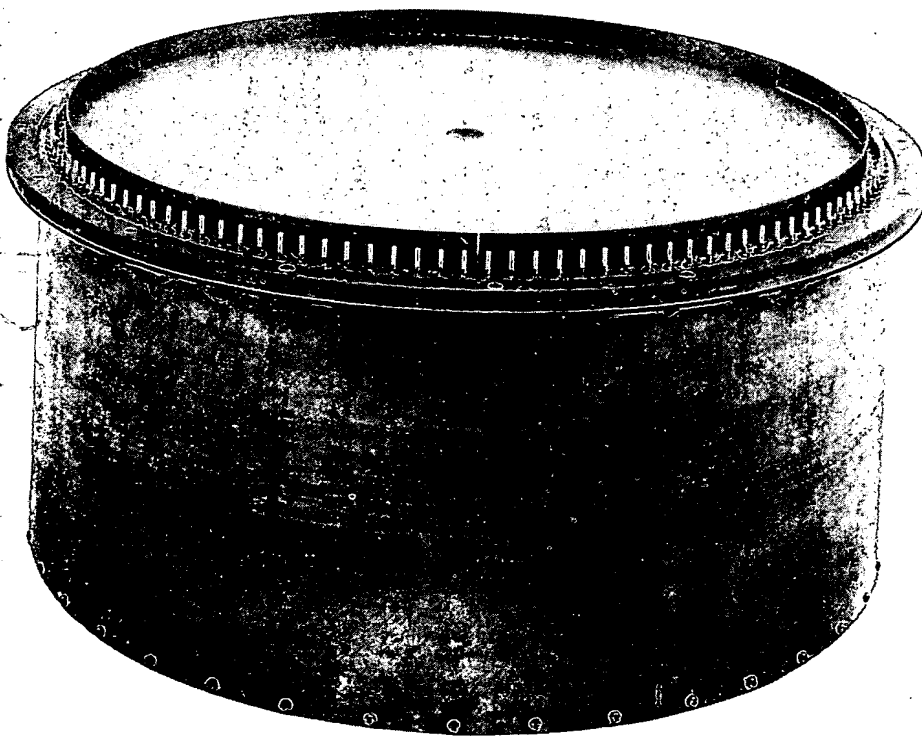
Fig. 96. Geodesic lens and patterns. (*a*) Modified Meyer lens. (*b*) Pattern (eight adjacent beams). (*c*) Sum pattern. (*d*) Expanded sum and difference pattern. (*Courtesy Hughes Aircraft Co., Fullerton, Calif.*)
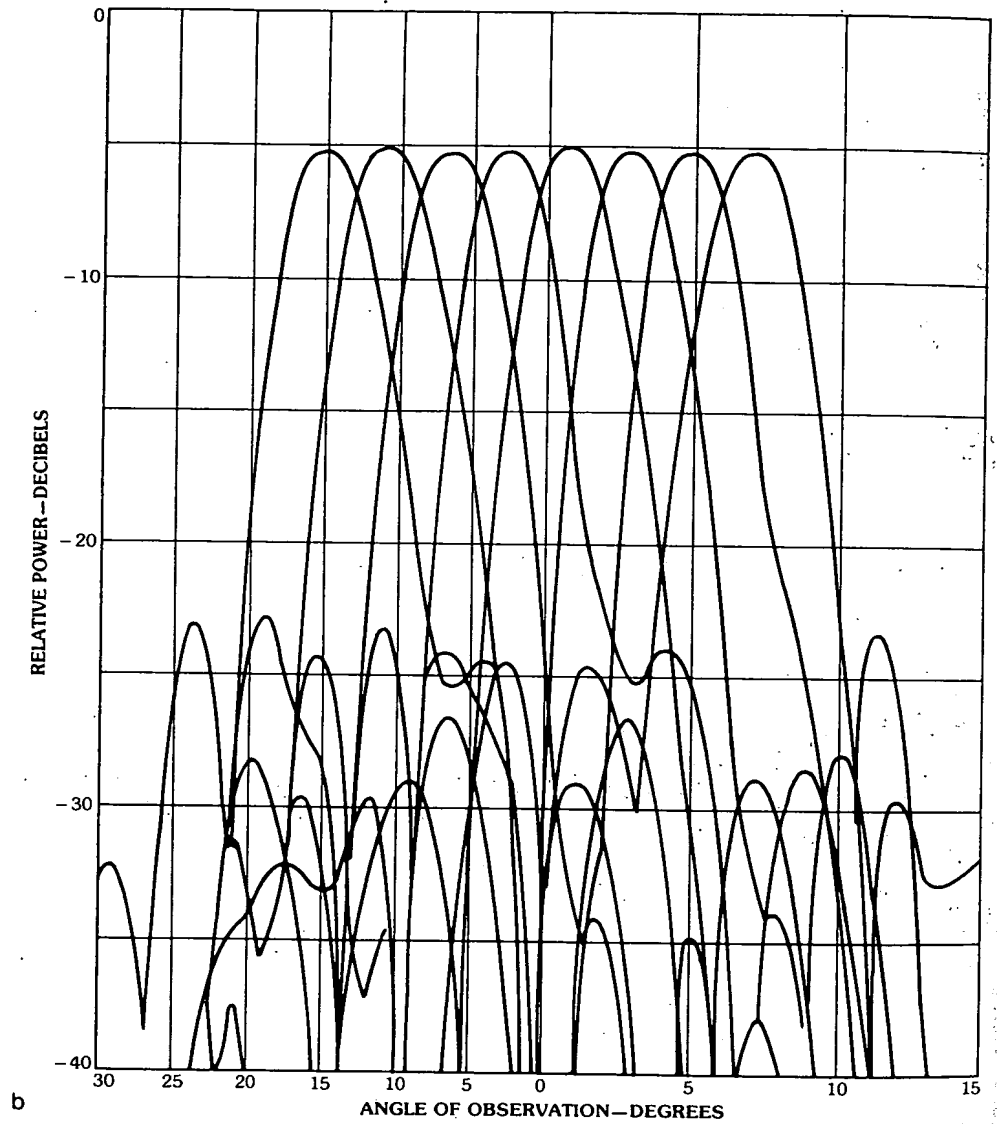
Fig. 96, *continued.*

$$\xi = \gamma \tag{40}$$

$$\ell_2 = \frac{b \sin 2\gamma}{\sin \gamma} = 2b \cos \gamma \tag{41}$$

From geometry it follows that

RELATIVE POWER—DECIBELS
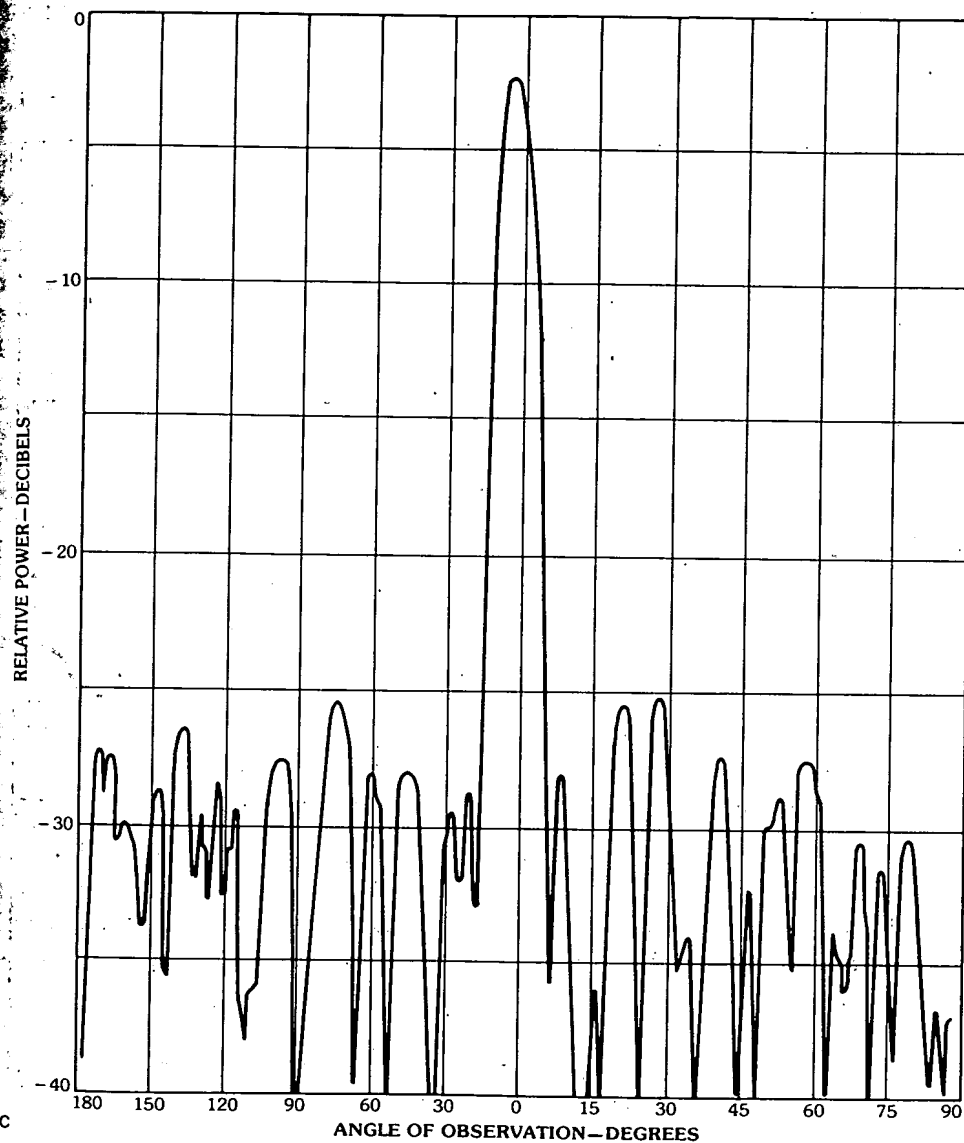
ANGLE OF OBSERVATION—DEGREES

Fig. 96, *continued.*

$$\phi' = 2\gamma - \beta \tag{42}$$

Again using Snell's law, it follows that
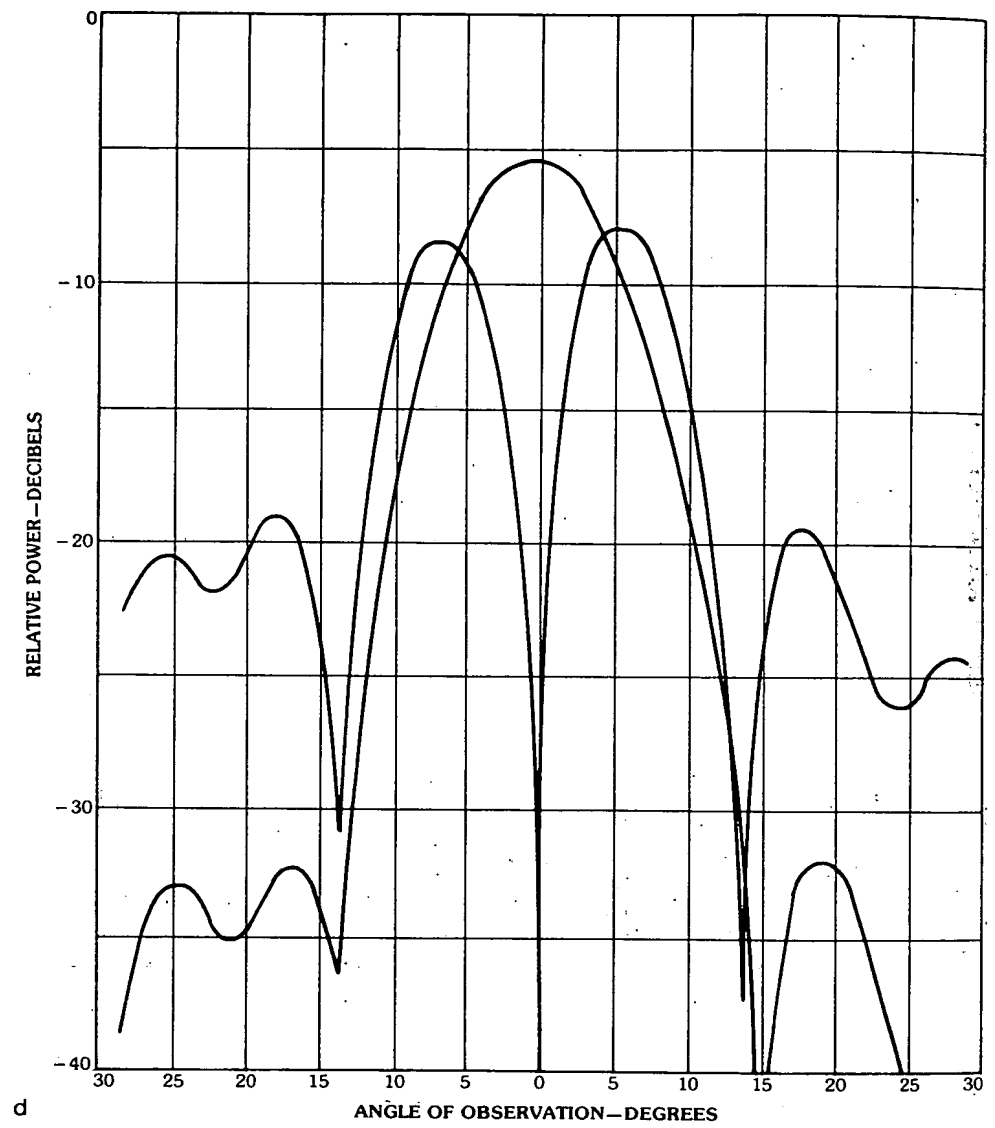
$$\frac{\sin \phi''}{\sin \xi} = \frac{bn_2}{R} \tag{43}$$

RELATIVE POWER—DECIBELS

ANGLE OF OBSERVATION—DEGREES

d

Fig. 96, *continued.*

From geometry,

$$\epsilon = \phi'' - \phi' \tag{44}$$

$$\ell_3 = R(1 - \cos\phi')\sec\epsilon \tag{45}$$

$$y = R\sin\phi' + R(1 - \cos\phi')\tan\epsilon \tag{46}$$

Relations 34 through 46 then enable one to compute the path length error for all the rays, evaluated on the hypothetical plane wavefront in space. The parameters h/b, a, b/R, n_1, and n_2 are selected to minimize the overall path length error, as well as to establish physical sizes.

For example, Fig. 95 is the calculated phase error for a 256-element array, illustrating that the spherical aberration phase error is less than $\pm20°$ over a $\pm45°$ sector. Thus over 70 percent of the cylindrical array diameter is nearly perfectly phased. Moreover, the associated amplitude distribution falls off rapidly beyond $\pm45°$. Consequently, a low-azimuth side lobe distribution is realizable using this technique. A high degree of amplitude distribution control is inherent, for both the sum and difference distributions independently, since an eight-element array of probes was used, each of which is amplitude controllable.

To demonstrate the feasibility of this approach, a 128-element array was constructed and tested at X-band. The beamwidth of the model was 5°. Fig. 96a shows the actual model. In the interest of time and funding, the lens was fabricated in one piece rather than connecting the cap and cylinder with cables; however, the array was coupled to the lens by coaxial probes.

The measured patterns of this model are shown in Figs. 96b through 96d. Fig. 96b shows several adjacent beams superposed. Fig. 96c shows a typical sum pattern; and Fig. 96d shows expanded sum and difference patterns. For economy of cost and time the feed used was a simple dual open-ended waveguide. Time did not allow an array-type feed which would have given more precise illumination with independent control over the sum and difference illuminations. Had an array-type feed been used, better patterns would have resulted, especially for the difference pattern.

Acknowledgments

The authors of this chapter gratefully acknowledge their colleagues in the Electromagnetics Laboratories of Hughes Aircraft Company, Fullerton, California, for their consultation and constructive criticism and especially Mrs. Lynda Schenet for typing, revising, and editing many cycles of the manuscript.

7. References

[1] L. A. Gustafson, "S-band two-dimensional slot array," *Tech. Memo 462*, Hughes Aircraft Company, Culver City, California, March 1957.

[2] R. M. Brown, "Performance of an antenna sharing the aperture of a frequency scanned array," *Rep. 8226*, Naval Research Lab, Washington, DC, May 1978.

[3] J. Butler and R. Lowe, "Beam forming matrix simplifies design of electronically scanned antenna," *Electron. Design*, vol. 9, no. 8, pp. 170–173, April 12, 1961.

[4] R. C. Hansen, *Microwave Scanning Antennas*, vols. 1, 2, 3, Array Systems, New York: Academic Press, 1966.

[5] W. P. Delaney, "An rf multiple beam forming technique," *IRE Trans. Mil. Electron.*, pp. 179–186, April 1962.

[6] J. P. Shelton and K. S. Kelleher, "Multiple beams from linear arrays," *IRE Trans.*, vol. AP-9, pp. 154–161, March 1961.

[7] W. R. Jones and G. F. Van Blaricum, "Multiple-beam forming hybrid networks,"

Hughes Aircraft Co., Ground Systems Group, *Tech. Memo. No. TP71-14-2*, April 7, 1970.

[8]   H. J. Moody, "The systematic design of the Butler matrix," *IEEE Trans. Antennas Propag.*, vol. AP-12, pp. 786–788, November 1964.

[9]   J. Blass, "The multidirectional antenna: a new approach to stacked beams," *1960 IRE Conv. Rec.*, pt. 1, pp. 48–50, 1960.

[10] J. Matthews and R. L. Walker, *Mathematical Methods of Physics*, 2nd ed., Menlo Park: Benjamin-Cummings, pp. 152–153, 1970.

[11] G. G. Chadwick, W. Gee, P. T. Lam, and J. L. McFarland, "An algebraic synthesis method for RN^2 multi-beam matrix network," internal publication of Lockheed Missile and Space Co., Sunnyvale, Calif., 94086. Also in *Proc. 1981 Antenna Appl. Symp.*, Allerton Park, Univ. of Illinois, September 23, 1981.

[12] J. L. McFarland, "The RN^2 multiple beam array family and beam forming matrix," *Proc. 1981 Antenna Appl. Symp.*, Allerton Park, Univ. of Illinois, September 23–25, 1981.

[13] R. J. Mailloux, "Array techniques for limited-scan applications," *Phys. Sci. Res. Papers, No. 503*, AFCRL-72-0421, Air Force Cambridge Research Laboratories, July 19, 1972.

[14] R. J. Mailloux and G. R. Forbes, "Experimental studies of a multiple mode array technique for limited-scan applications," *Phys. Sci. Res. Papers, No. 575*, AFCRL-TR-73-0686, Air Force Cambridge Research Laboratories, November 6, 1973.

[15] G. T. DiFrancia, "A family of perfect configuration lenses of revolution," *Optica Acta*, vol. 1, no. 4, pp. 157–163, February 1955.

[16] L. J. Chu and M. A. Taggart, "Pillbox antenna," US Patent No. 2,688,546, May 12, 1945.

[17] M. A. Taggart and E. C. Fine, "Parallel-plate bends," *MIT Radiation Lab Rep. 760*, September 5, 1945.

[18] J. S. Ajioka, "The development of an integral mkx iff antenna for low-frequency radar," *Rep. No. 534*, US Navy Electronic Lab, San Diego, January 1955.

[19] W. Rotman, "A study of microwave double-layer pillboxes," *AFCRC-TR-54-102*, Air Force Cambridge Research Center, Cambridge, Massachusetts, July 1954.

[20] J. S. Ajioka, "A multiple beam forming network using a multimode radial transmission line," *1963 NEREM Conv. Rec.*

[21] J. S. Ajioka, "A multiple beam forming antenna apparatus," US Patent No. 3,290,682, December 6, 1966.

[22] J. S. Ajioka and H. A. Uyeda, "Experimental performance of a multimode radial transmission line beam-forming network," *Microwave J.*, pp. 53–56, December 1968.

[23] J. L. McFarland, "Catenary geodesic lens antenna," US Patent No. 3,383,691, assigned to Hughes Aircraft Co., May 14, 1968.

[24] S. B. Meyer, "Parallel-plate optics for rapid scanning," *J. Appl. Phys.*, vol. 18, pp. 221–229, 1947.

[25] W. Rotman and R. F. Turner, "Wide-angle microwave lens for line source applications," *IEEE Trans. Antennas Propag.*, pp. 623–632, November 1963.

[26] J. Ruze, "Wide-angle metal plate optics," *Proc. IRE*, vol. 38, pp. 53–58, January 1950.

[27] H. Gent, "The bootlace aerial," *Royal Radar Establishment J.*, pp. 47–57, October 1957.

[28] C. M. Rappaport and A. I. Zaghoul, "Optimized three-dimensional lenses for two-dimensional scanning," *IEEE AP-S 1984 Symp. Dig.*, vol. II, June 25–29, 1984.

[29] R. F. Rinehart, "A solution of the problem of rapid scanning for radar antennae," *J. Appl. Phys.*, vol. 19, September 1948.

[30] R. K. Luneburg, *Mathematical Theory of Optics*, Providence: Brown University, pp. 189–213, 1944.

[31] E. C. DuFort and H. A. Uyeda, "A wide-angle scanning optical antenna," *IEEE Trans. Antennas Propag.*, vol. AP-31, no. 1, p. 60, January 1983.

[32] R. T. Hill, "Phased array feed systems," in *Phased Array Antennas*, ed. by A. A.

Oliner and G. H. Knittel, Dedham: Artech House, pp. 197–211, April 1972.

[33] J. R. Kahrilas, "HAPDAR—an operational phased array radar," *Proc. IEEE*, November 1968.

[34] W. T. Patton, "Limited-scan arrays," *Proc. 1970 Phased Array Antenna Symp.*, ed. by A. A. Oliner and G. H. Knittel, Dedham: Artech House, pp. 332–343, 1970.

[35] C. Winter, "Phase-scanning experiments with two reflector antenna systems," *Proc. IEEE*, vol. 56, no. 11, pp. 1984–1999, 1968.

[36] R. J. Mailloux and P. Blacksmith, "Array and reflector techniques for precision approach radars," *AGARD Conf. Proc. No. 139 on Antennas for Avionics*, NATO 26–30, November 1973.

[37] W. D. Fitzgerald, "Limited electronic scanning with a near-field Cassegrainian system," *Tech. Rep. 484*, ESD-TR-71-271, Lincoln Lab, 1971.

[38] Hughes Aircraft Company, Ground Systems Group, "Tradex S-band phased array design study," *Interim Rep. FP71-14-3*, Fullerton, California, May 27, 1971.

[39] W. D. Fitzgerald, "Limited electronic scanning with an offset-feed near-field Gregorian system," *Tech. Rep. 486*, ESD-TR-272, Lincoln Lab, MIT, 1971.

[40] Lincoln Lab, "A KREMS phased array radar," report dated April 26, 1971.

[41] C. J. Miller and D. Davis, "LFOV optimization study, final report," prepared by Westinghouse Defense and Electronics Systems Center, Systems Development Division, for MIT Lincoln Lab, Contract No. F19628-70-C-0230, May 1, 1972.

[42] Hughes Aircraft Company Ground Systems Group, "Study program for reflector surface optimization LFOV system (TRADEX/KREMS)," *FP No. 71-14-138*, Fullerton, California, August 19, 1971.

[43] C. J. Sletten, "Caustic matching: a new technique for improving limited-scan antennas," US Air Force Cambridge Research Laboratories, Hanscom Air Force Base, Massachusetts, December 17, 1974.

[44] C. H. Tang and C. F. Winter, final report on Contract No. AF19628-72-C-0213.

[45] M. Born and E. Wolf, *Principles of Optics*, New York: Pergamon Press, 1959.

[46] Hughes Aircraft Company Ground Systems Group, "Limited-scan antenna techniques study," final report on Contract No. F1962B-73-C-0129, Fullerton, California 92634, August 14, 1975.

[47] R. Tang, "Survey of time delay beam steering techniques," *Proc. 1970 Phased Array Antenna Symp.*, ed. by A. A. Oliner and G. H. Knittel, Dedham: Artech House, pp. 254–260, 1972.

[48] N. S. Wong, R. Tang, and E. E. Barber, "A multielement high-power monopulse feed for low side lobes and high aperture efficiency," *IEEE Trans. Antennas Propag.*, vol. AP-22, pp. 402–407, May 1974.

[49] E. C. DuFort, "Optical technique for broadbanding phased arrays," *IEEE Trans. Antennas Propag.*, vol. AP-23, pp. 516–523, July 1975.

[50] J. L. McFarland and J. S. Ajioka, "Multiple beam constrained lens design," *NEREM Rec.*, November 1962.

[51] L. Stark, "High-resolution hemispherical reflector antenna," US Patent No. 3,852,748, assigned to Hughes Aircraft Company, December 3, 1974.

[52] G. V. Borgiotti, "An antenna for limited scan in one plane: design criteria and numerical simulation," *IEEE Trans. Antennas Propag.*, vol. AP-25, no. 2, March 1977.

[53] R. J. Giannini, "An electronically scanned cylindrical array based on a switching and phasing technique," *1969 G-AP Intl. Symp. Program Dig.*, pp. 199–204, 1969.

[54] A. E. Holley, E. C. DuFort, and R. A. Dell-Imagine, "An electronically scanned beacon antenna," *IEEE Trans. Antennas Propag.*, vol. AP-22, no. 1, pp. 3–12, January 1974.

[55] J. E. Boyns, C. W. Gorham, A. D. Munger, J. H. Provencher, J. Reindel, and B. I. Small, "Step-scanned circular array antenna," *IEEE Trans. Antennas Propag.*, vol. AP-18, no. 5, pp. 590–595, September 1970.

[56] P. Sheleg, "A matrix-fed circular array for continuous scanning," *Proc. IEEE*, vol. 56, no. 11, November 1968.

[57] "Proposal for air traffic control radar beacon system (ATCRBS) electronic scan antenna," *RFP No. WA5R-1-0059*, submitted by Hughes Aircraft Company, Ground Systems Group, Fullerton, California, March 19, 1971.